A SEARCH FOR THERMOSPHERIC COMPOSITION PERTURBATIONS DUE TO VERTICAL WINDS

A

THESIS

Presented to the Faculty

of the University of Alaska Fairbanks

in Partial Fulfillment of the Requirements

for the Degree of

DOCTOR OF PHILOSOPHY

By

Matthew P. Krynicki, B.S.

Fairbanks, Alaska

May 2006

A SEARCH FOR THERMOSPHERIC COMPOSITION PERTURBATIONS

DUE TO VERTICAL WINDS

By

Matthew P. Krynicki

RECOMMENDED:

Advisory Committee Chair

Physics Department Head

APPROVED:

Dean, College of Natural Science and Mathematics

Dean of the Graduate School

May 16, 2006

Date

Abstract

The thermosphere is generally in hydrostatic equilibrium, with winds blowing horizontally along stratified constant-pressure surfaces, driven by the dayside-to-nightside pressure gradient. A marked change in this paradigm resulted after *Spencer et al.* [1976] reported vertical wind measurements of 80 $m \cdot s^{-1}$ from analyses of AE-C satellite data. It is now established that the thermosphere routinely supports large-magnitude (~30-150 $m \cdot s^{-1}$) vertical winds at auroral latitudes. These vertical winds represent significant departure from hydrostatic and diffusive equilibrium, altering locally—and potentially globally—the thermosphere's and ionosphere's composition, chemistry, thermodynamics and energy budget. Because of their localized nature, large-magnitude vertical wind effects are not entirely known.

This thesis presents ground-based Fabry-Perot Spectrometer OI(630.0)-nm observations of upper-thermospheric vertical winds obtained at Inuvik, NT, Canada and Poker Flat, AK. The wind measurements are compared with vertical displacement estimates at ~10^4 km^2 horizontal spatial scales determined from a new modification to the electron transport code of *Lummerzheim and Lilensten* [1994] as applied to FUV-wavelength observations by POLAR spacecraft's Ultraviolet Imager [*Torr et al.*, 1995]. The modification, referred to as the column shift, simulates vertical wind effects such as neutral transport and disruption of diffusive equilibrium by vertically displacing the *Hedin* [1991] MSIS-90 $[O_2]/[N_2]$ and $[O]/([N_2]+[O_2])$ mixing ratios and subsequently redistributing the O, O_2, and N_2 densities used in the transport code. Column shift estimates are inferred from comparisons of UVI OI(135.6)-nm auroral observations to their corresponding modeled emission. The modeled OI(135.6)-nm brightness is determined from the modeled thermospheric response to electron precipitation and estimations of the energy flux and characteristic energy of the precipitation, which are inferred from UVI-observed Lyman-Birge-Hopfield N_2 emissions in two wavelength ranges. Two-dimensional column shift maps identify the spatial morphology of thermospheric composition perturbations associated with auroral forms relative to the model thermosphere. Case-study examples and statistical analyses of the column shift

data sets indicate that column shifts can be attributed to vertical winds. Unanticipated limitations associated with modeling of the OI(135.6)-nm auroral emission make absolute column shift estimates indeterminate. Insufficient knowledge of thermospheric air-parcel time histories hinders interpretations of point-to-point time series comparisons between column shifts and vertical winds.

Table of Contents

List of Figures

List of Tables

List of Appendices

Acknowledgements

Thank you to my family, Mom, Dad, Aaron, Janice and Tim, and Uncle Lenny and Aunt Flo for their great support during my years in graduate school. Special thanks to Mom, Dad, Aaron and Uncle Bob for helping me to reach Alaska, twice. Props to my brother Aaron, one who can say he experienced 60 below temperatures, the Midnight Sun and smoke-filled 90° Fairbanks air at least once in his life.

I want to thank my two advisors Mark Conde and Dirk Lummerzheim for their guidance, support and patience as I have completed this work. Special thanks to Dirk for the amazing flights to Inuvik. Thank you to Roger Smith for whispering "vertical winds" in my ear. He knew there was a thesis in there somewhere but expected me to find it myself. Thank you to the rest of my committee, John Craven, John Olson, and Brenton Watkins, for their essential input during the final stages of the thesis. Thank you to Jim and Becky Conner for their friendship and generosity. Thank you to Mamoru Ishii and Gonzalo Hernandez for the use of their wind data. Thank you to Channon Price for working my fingers to the bone in the Mechanics (C, Q and S) courses.

I must gratefully acknowledge the tireless support of the first technician Jeff Allen in Inuvik while he helped first to get the Fabry-Perot spectrometer running up there and then maintaining it through its many idiosyncrasies. Thank you also to Chris Strube, the second technician, who helped resolve numerous equipment failures. Thank you to Debi-Lee Wilkinson, who developed much of the original software used for the analysis of the UVI data in this thesis, and to Ed Hoch, who helps keep the wind data on the Web.

A big thank you to all the former and current graduate students and friends I have known at the GI, on campus and in Fairbanks for their support, companionship, and friendship when I needed it. We had some fun. Last but not least, thanks to my posse from the Detroit area. The music jams and bull sessions are magick.

This work was conducted under grant ATM9720303 from the National Science Foundation, under MOA-01/24/95 from the Japanese Space Agency through Communications Research Laboratory, Japan, and under grants NAG5-10069 and NAG5-13622 from the National Aeronautics and Space Adminstration.

Chapter 1 Introduction to the Thermosphere

1.1 Vertical Winds in the Thermosphere

1.1.1 Horizontal Winds in the Thermosphere due to Solar Radiative Input

Absorption of solar ultraviolet (UV) and X-ray radiation by Earth's thermosphere above ~100 km altitude in the approximate wavelength range of $1 < \lambda < 200$ nm heats and ionizes Earth's dayside upper atmosphere (~100-1000 km) [*e.g. Rishbeth and Garriott*, 1969]. Thermal expansion of the atmosphere associated with the increased dayside temperature generates a global-scale, dayside-to-nightside horizontal pressure gradient that drives a system of nearly-horizontal global-scale thermospheric winds [*e.g. Kohl and King*, 1967]. The neutral winds blow zonally and meridionally across the pressure gradient away from the dayside temperature maximum—referred to as the diurnal bulge—located in the early afternoon sector at ~1400 local time centered near the geographic equator in the summer hemisphere towards the coldest part of the thermosphere, which is located in the early morning sector at ~0300 local time in the winter hemisphere [*e.g. Rishbeth*, 1972]. The wind velocities are controlled by the latitudinally-varying Coriolis force and by the frictional forces of ion drag, which varies with latitude, local time of day and altitude, and viscosity, which is strongest in the upper thermosphere ($\gtrsim$200 km) and begins to smooth out the vertical variation in the horizontal wind velocity at upper-thermospheric altitudes [*Rishbeth*, 1972]. This is in contrast to lower- and middle-atmospheric ($\lesssim$100 km) global-scale horizontal winds, which are controlled primarily by the Coriolis force and generally circulate around pressure highs and lows (clockwise around highs, counter-clockwise around lows in the northern hemisphere, vice versa in the southern hemisphere), the condition referred to as the geostrophic approximation [*Rishbeth*, 1998]. Ions do not flow freely along with the neutrals in the thermosphere because their motion is constrained by Earth's magnetic field, and as a result, ions exert a drag on the neutral air through collisions [*Rishbeth*, 1972]. Above ~150 km, ion drag is the limiting force to the dayside-to-nightside pressure-gradient force [*Rishbeth*, 1998]. Prevailing neutral horizontal wind

speeds due strictly to solar radiative energy input range in magnitude from ~20-50 $m \cdot s^{-1}$ in the lower and middle thermosphere (~100-150 km and ~150-200 km, respectively) to ~50-100 $m \cdot s^{-1}$ in the upper thermosphere [*e.g. Kohl and King*, 1967; *Rishbeth*, 1972; *Dickinson et al.*, 1984], varying in latitude and local time of day and dependent on the intensity of the solar ionizing radiation, which varies daily and from solar minimum to maximum. The Sun's radiative output and variability is outlined in Appendix A. Ion drag is discussed in more detail later and in Appendix B, as is the geostrophic approximation. Collisions and viscosity are discussed in Appendices B and C. The above assertions are incomplete because the thermosphere's global-scale horizontal wind system is also strongly governed by the additional high-latitude magnetospheric-related energy sources of Joule heating and auroral-particle precipitation [*e.g. Roble*, 1977; *Dickinson et al.*, 1984; *Fuller-Rowell et al.*, 1994; *Fujiwara et al.*, 1996], which in general are comparable in magnitude to solar radiative energy input for periods of time in localized regions.

1.1.2 Hydrostatic and Diffusive Equilibrium

The steady-state feature of Earth's atmosphere that characterizes the exponential decrease with altitude and vertical stratification of its pressure and mass density up to the top of the thermosphere (~600-1000 km) is hydrostatic equilibrium. In general, gravity and pressure are the two strongest forces acting vertically in the atmosphere, and any vertical acceleration due to other forces are small compared to these [*e.g. Rishbeth et al.*, 1969]. The atmosphere's upward pressure balances the weight of the atmosphere above it, and this condition is specified by an approximate form of the vertical component of the momentum equation, referred to as the barometric equation,

$$dp = -g\rho dz, \tag{1.1}$$

where g is the gravitational constant, ρ is the mass density, and dp is the differential drop in pressure for a differential upward altitude change of dz. In addition, the ideal gas law,

$$p = \rho RTM^{-1} = nk_BT, \tag{1.2}$$

approximates well the atmosphere's equation of state up to the top of the thermosphere, where p is the pressure, T is the temperature, M is the mean molecular mass, n is the number density, $k_B = 1.38 \times 10^{-23}$ $J \cdot K^{-1}$ is the Boltzmann constant, and $R = 8.314 \times 10^3$

$J \cdot kmol^{-1} \cdot K^{-1}$ is the ideal gas constant. Pressure and mass density decrease exponentially according to Equation 1.1 as a function of altitude z, $\alpha \exp(-z/H)$, where H is referred to as the atmospheric or pressure scale height and is given by $H = RT/Mg = k_B T/mg$ (m is the mass of a given atom or molecule). For typical values of mean molecular mass ($M = 28.9$ amu) and temperature (~150-300 K) that prevail in the lower and middle atmosphere, the scale height ranges from 6-8 km [*e.g. Thomas and Stamnes*, 1999]. The momentum equation is discussed later and described in greater detail in Appendix B.

A property specific to the thermosphere that determines the vertical distribution of its neutral and ionized species, along with hydrostatic balance, is diffusive equilibrium. The lower and middle atmosphere, referred to as the homosphere or turbosphere, is well mixed by turbulence into a composite gas of $M = 28.9$ amu. Because of the thermosphere's positive temperature gradient and its increased temperature relative to the atmosphere below, molecular diffusion, a temperature-dependent process, begins to dominate over turbulent mixing (eddy diffusion) above ~100 km [*e.g. Richmond*, 1983]. This altitude marks the transition region, referred to as the homopause or turbopause, between the lower and middle atmosphere and the upper atmosphere. Above the turbopause, thermospheric species begin to separate under gravity, and any mixing that occurs due to turbulence is strongly inhibited above ~120 km [*Rees*, 1989], resulting in diffusive separation of species. Each species must be considered individually and assumes its own density, partial pressure and scale height distributions, dependent on thermospheric temperature, its own molecular or atomic weight, and the diffusive equilibrium condition [*Rees*, 1989]. For typical values of temperature prevailing in the lower to upper thermosphere, ~200-1500 K, respectively, during most solar and geomagnetic conditions, the thermosphere's three major species of molecular nitrogen (N_2), atomic oxygen (O) and molecular oxygen (O_2; molecular masses of 28, 16, and 32 amu, respectively) have scale heights ranging from ~5-80 km in the lower to upper thermosphere, respectively. The thermosphere's total pressure is the sum of all its major and minor species' partial pressures. Thermospheric composition and diffusive equilibrium are discussed in more detail in Section 1.2. At auroral latitudes, Joule and particle-precipitation heating, sometimes surpassing solar radiative energy input

for periods of time locally, can generate localized vertical motions that disrupt hydrostatic and diffusive equilibrium [*Smith*, 1998], a topic to be discussed in more detail later.

1.1.3 Barometric Motion of the Thermosphere

In general, winds in the thermosphere blow horizontally along isobaric surfaces unless significant departure from hydrostatic balance occurs [*Smith and Hernandez*, 1995]. The constant-pressure surfaces do not remain at fixed altitudes, however, because the pressure of a given layer depends on the atmosphere's temperature and mass density above it. The diurnal cycle of solar radiative heating results in a strong temperature oscillation from day to night in the thermosphere, causing a diurnal oscillation of the isobaric surfaces, a process referred to as breathing [*Smith*, 1998]. The dayside expansion and nightside contraction is slow and smooth, and in general, hydrostatic balance is maintained because the thermosphere has time to adjust to the changing temperature, a topic to be discussed in more detail later. Air parcels flowing horizontally along a given pressure layer will have a small vertical velocity component associated with that pressure layer's changing altitude, which follows the thermosphere's changing scale height. An idealized example described in *Smith* [1998] illustrates the thermosphere's change in scale height from 40 to 50 km at 260 km altitude going from night to day over a 12-hr time period as the temperature increases from 700 K to 1000 K, assuming a mean molecular mass of M = 24 amu. The resulting vertical wind speed is ~1 $m \cdot s^{-1}$, and in general, the thermosphere's upward and downward barometric motion W_B associated with its temperature cycle is $W_B \approx \pm 1\text{-}3\ m \cdot s^{-1}$, peaking in amplitude locally ~2 hr after sunrise and sunset, respectively [*Smith*, 1998]. In general, the mean barometric velocity and displacement of the thermosphere's isobaric surfaces over a 24-hr period due to solar radiative input is zero [*Smith*, 1998], though the altitude of the isobaric surfaces will also vary from day to day, seasonally, and through a solar cycle, dependent on thermospheric temperature, which varies with geomagnetic activity and the Sun's daily, seasonally, and solar-cyclically varying UV and X-ray flux.

1.1.4 Global-scale Divergence in the Thermosphere

As was stated earlier, strict geostrophic flow does not prevail in the thermosphere because ion drag is the primary opposing force to the thermosphere's dayside-to-nightside

pressure-gradient force rather than the Coriolis force, particularly at altitudes ≳150 km [*Rishbeth*, 1998]. Horizontal wind direction of the thermosphere's neutral species is instead governed by the ratio of the Coriolis force to ion drag [*Rishbeth*, 1998], ultimately resulting in some large-scale divergent flow. Conservation of mass requires that vertical motion of air parcels must occur to accommodate horizontal divergence and convergence. *Dickinson and Geisler* [1968] and *Rishbeth et al.* [1969] theorized that at middle latitudes, upper-thermospheric vertical winds due to global-scale divergent and convergent horizontal winds must have a mean amplitude of ~2 $m \cdot s^{-1}$ in order to satisfy the neutral air continuity equation. This vertical motion is in addition to the diurnal rise and fall of the constant-pressure layers. *Burns et al.* [1981] confirmed the *Dickinson and Geisler* [1968] and *Rishbeth et al.* [1969] supposition by inferring the existence of upper-thermospheric, spatially- and temporally-averaged vertical winds resulting from divergent meridional flow at the low-latitude site of Arecibo, Puerto Rico for times around local midnight. The downward wind speeds W_D reached magnitudes of up to 7 $m \cdot s^{-1}$, and the expression

$$W_D = -H\nabla_h \mathbf{U}_h \tag{1.3}$$

was used to estimate the vertical wind speed, where H is the scale height, $\mathbf{U}_h = U_x\mathbf{x} + U_y\mathbf{y}$ is the horizontal wind velocity, and $\nabla_h = (\partial/\partial x)\mathbf{x} + (\partial/\partial y)\mathbf{y}$ is the horizontal derivative. Note that x is eastward and y is northward in this context, and that bold type denotes a vector quantity. Equation 1.3 originates from the three-dimensional continuity equation,

$$\nabla \cdot (\rho\mathbf{U}) = \partial\rho/\partial t, \tag{1.4}$$

the barometric equation, and the ideal gas law, where $\mathbf{U} = U_x\mathbf{x} + U_y\mathbf{y} + W_D\mathbf{z}$ and local mass density changes due to divergent flow are assumed to be small in an incompressible atmosphere; *i.e.*, $\partial\rho/\partial t = 0$ [*e.g. Crickmore*, 1993]. U_x and U_y were determined from Fabry-Perot Spectrometer (FPS) observations of the upper-thermospheric atomic oxygen (OI) λ630.0-nm airglow emission in the four cardinal directions. Chapters 2 and 3 and Appendix D discuss Fabry-Perot spectroscopy in more detail. Estimating vertical wind speeds from Equation 1.3 instead of from zenith-directed FPS observations reduces sensitivity to short-term, small-scale variations in the vertical wind field since the horizontal winds used to estimate the divergence, measured in the spatially-separated four cardinal directions over

a (relatively) long period of time, yield a spatially- and temporally-averaged vertical flow across the FPS field of view [*Smith*, 1998]. However, divergent-flow-inferred vertical wind estimates are more reliable than direct zenith observations [*Burns et al.*, 1981] at middle and low latitudes since, in general, the weak vertical winds prevailing at these latitudes will fall within the range of errors of zenith-looking FPS measurements.

1.1.5 Departure from Equilibrium Conditions

The aforementioned global-scale barometric and divergence-driven vertical winds of ±1-10 $m \cdot s^{-1}$ are indicative of quasi-static thermospheric change that occurs over long time scales (~1-2 hr) and substantial horizontal distances (~10^3 km) [*Rees et al.*, 1984a]. Vertical motion of this sort that is set up by the Sun's continuous radiative energy input into the dayside thermosphere can be crudely regarded as a smoothly-varying, global-scale vertical flow cell [*Smith*, 1998]. Large-scale divergent horizontal flow out of the cell on Earth's dayside in the summer hemisphere and convergent flow on the nightside in the winter hemisphere results in large spatial-scale, long time-scale, quasi-static upward and downward winds of ~5 $m \cdot s^{-1}$, respectively. This motion represents an insignificant perturbation to the state of the thermosphere (*e.g.*, its density and temperature distributions) because hydrostatic balance is preserved while the motion persists, except perhaps locally in the 2-hr time periods around sunrise and sunset when the thermosphere is most disturbed by the Sun's radiative influence or lack there of [*Smith*, 1998].

The validity of this assumption can be tested by evaluating the time scales of these disturbances and the thermosphere's characteristic response time to a perturbation. The thermosphere's time scale for hydrostatic adjustment, τ_{hydr}, due to molecular diffusion during and after a disturbance can be estimated from the expression $\tau_{hydr} \approx H/v_{ther}$ [*Smith*, 1998], where $v_{ther} = (3k_BT/m)^{1/2}$ is the mean molecular thermal speed. For typical values of thermospheric temperature and mean molecular mass at lower- to upper-thermospheric altitudes ($T \sim$ 200-1500 K, $M \sim$ 28-16 amu, respectively), $\tau_{hydr} \approx$ 15-50 s, respectively. Thus, molecular diffusion due to localized pressure and density gradients can be expected to restore hydrostatic stability in ~1-2 min after a disturbance. Molecular diffusion in the thermosphere is described in more detail in Appendix C and Section 1.2.2. In addition,

time scales for changes to the thermosphere's pressure, τ_P, due to these vertical winds can be estimated from the expression $\tau_P \approx H/W_D$ or H/W_B [*e.g. Burnside et al.*, 1981; *Smith*, 1998]. For example, taking W_D or $W_B \approx 5$ m·s^{-1} and $H \approx$ 20-50 km for altitudes $\gtrsim$120 km, $\tau_P \approx$ 1-3 hr. Thus, vertical flow of ~1-10 m·s^{-1} must persist at a specific location (in the reference frame of the horizontal bulk flow) for at least an hour to offset diffusion and appreciably upset hydrostatic balance. Lastly, an estimate of the vertical acceleration of air parcels associated with this vertical motion also illustrates their ineffectiveness in disturbing hydrostatic balance [*Smith*, 1998]. If a +1 m·s^{-1} barometric wind is launched at sunrise, then the acceleration a_B of air parcels due to the onset of radiation deposition is roughly given by $a_B \sim W_B/\tau_{hydr} \approx 1$ m·s^{-1}/50 s = 0.02 m·s^{-2} $\approx g/500$ [*Smith*, 1998]. This is regarded as a negligible departure from hydrostatic stability and confirms the previous assertion that gravity and pressure are the two strongest forces acting vertically in the atmosphere. Thus, depending on altitude, vertical winds of ±1-10 m·s^{-1} lasting for $\lesssim$1 hr at a specific location, given their effects on local equilibrium conditions, are not regarded as significant and are not expected to modify the thermosphere's state locally or globally.

1.1.6 The Thermosphere's Global-scale Horizontal Wind System

The dynamical behavior of the thermosphere is governed primarily by two sources of energy; the dayside absorption of solar X-ray and UV radiation and the ionospheric-magnetospheric-related processes of Joule heating and particle precipitation acting in the auroral zone. Other energy sources do exist, such as the turbulent and viscous dissipation of gravity waves and tidal motions, but these sources are weak when compared to radiation deposition and Joule and particle-precipitation heating, not appreciably affecting the thermosphere's global-scale horizontal wind patterns and depositing only ~0.7 mW·m^{-2} into the thermosphere, mostly at altitudes $\lesssim$100 km where the bulk of the thermosphere's mass is located [*Rishbeth and Garriott*, 1969]. Particle precipitation, Joule heating, and ion drag, in contrast, alter significantly above ~100 km the thermosphere's global-scale horizontal neutral circulation from that of strict geostrophic flow and from the dayside-to-nightside, radiative-driven pattern discussed earlier. The momentum equation does not reduce to the geostrophic approximation horizontally when applied to the thermosphere

because each thermospheric and ionospheric species' compositional, dynamical and energetic behavior must be evaluated individually (particularly at altitudes of ~100-200 km where there are several neutral and ionic species) and because ion drag and viscosity—both of which can exceed the Coriolis force—and electromagnetic forces (which largely govern ionic motion, in turn determining the ion drag force) must all be considered. The application of the momentum equation and other relevant equations to the thermosphere and ionosphere to determine the nature of the upper atmosphere's dynamics is described in more detail in Appendix B, as are thermospheric tidal motions and buoyancy waves.

During solar minimum, photoionization of N_2, O_2, and O by X-ray and UV radiation of wavelengths ~1-100 nm, photodissociation of O_2 by radiation in the Schumann-Runge (SR) continuum, ~130-175 nm, and subsequent chemical reactions deposit ~3 $mW \cdot m^{-2}$ into the thermosphere between the altitudes of ~95-250 km on Earth's dayside [*Hargreaves*, 1992]. Photodissociation of O_2 by SR-UV radiation and subsequent chemical reactions also deposit ~30 $mW \cdot m^{-2}$ at altitudes of ~85-95 km. Energy input is generally 2-3 times this during solar maximum, and total upper-atmospheric radiative energy input generally equals about 10^{11} W globally [*e.g. Hinteregger*, 1979; 1981]. Downward molecular heat conduction, horizontal advection (*i.e.*, winds), and adiabatic expansion redistribute the energy [*e.g. Killeen et al.*, 1997], while thermally-excited infrared (IR) emissions, such as those from the minor thermospheric species of nitric oxide (NO) at 5.3 μm [*e.g. Kockarts*, 1980] and carbon dioxide (CO_2) at 4.3 μm and 15 μm [*e.g. Killeen et al.*, 1997], regulate the thermosphere's global mean ambient temperature. Radiation deposition in the atmosphere (*i.e.*, the optical depth parameter) and the atmosphere's response is described in more detail in Appendix A. The thermosphere's photochemistry is summarized in Section 1.2.1.

In contrast to the Sun's latitudinally- and longitudinally-distributed radiative energy deposition across Earth's dayside (dependent on solar zenith angle, the angle of incidence of the Sun's rays), Joule and particle-precipitation heating processes deposit energy along the latitudinally-narrow region of the auroral oval. Each can deposit energy at rates of ~10-100 $mW \cdot m^{-2}$ [*e.g. Rees et al.*, 1984b] across latitudinally- and longitudinally-extended regions of ~0.1-5° × ~0.1-25° (~10-500 km × ~10-1000 km), respectively, for time periods

of minutes to several hours. Total Joule and particle-precipitation energy input into the thermosphere can be estimated using the solar wind-magnetospheric energy coupling function of *Perreault and Akasofu* [1978] and *Akasofu* [1979; 1980; 1981]. Total energy input values may be as low as ~10^9 W during quiet geomagnetic conditions, but can reach ~10^{12} W during highly-disturbed conditions, exceeding the solar radiative component yet depositing this energy along the latitudinally-narrow region of the auroral oval.

Joule heating and ion drag are due to the differences that exist between the neutral wind velocity and ion drift velocity [*e.g. Rishbeth*, 1972]. Above ~150 km, ion drag affects thermospheric neutral flow at all latitudes [*Rishbeth*, 1998]. Joule heating, however, is only significant at auroral latitudes where the cross-polar cap electric field **E** (mapped down from the magnetosphere to the high-latitude ionosphere) can generate $(\mathbf{E} \times \mathbf{B})/B^2$ ion drifts of up to ~1-2 km·s^{-1} during disturbed geomagnetic conditions [*e.g. Killeen et al.*, 1988]. **B** is Earth's magnetic field strength. Collisional dissipation of the high-latitude ionospheric convection by the thermosphere's neutral species transfers momentum from the ions to the neutrals and converts mechanical energy into thermal energy. The Joule heating rate per unit volume Q_J can be estimated from the expression [*e.g. Richmond*, 1978],

$$Q_J = \mathbf{J} \cdot \mathbf{E} = \ldots = \sigma_P(z) E_\perp^2, \tag{1.5}$$

where **J** is the current density, $\sigma_P(z)$ is the ionospheric Pedersen conductivity, and $E_\perp$ is the local electric field strength normal to Earth's magnetic field. The heating rate per unit volume extends up to ionospheric F1- and F2-region altitudes (~150-200 km, ~200-800 km by day and ~200-500 km at night, respectively) but generally maximizes at the E-region altitudes of ~110-150 km where the Pedersen conductivity is highest [*e.g. Brekke*, 1997].

Like Joule heating, particle-precipitation heating and ionization rates, which depend on the characteristic energy (a quantity indicative of the particles' distribution type and average energy) and flux of the precipitating particles (mostly electrons), generally maximize at altitudes of ~110-150 km [*Rees*, 1989]. The heating and ionization extend to higher altitudes as well as the precipitating electrons collisionally deposit their excess energy while spiraling down Earth's high-latitude magnetic field lines and can also extend downward into the extreme lower thermosphere (~90-100 km) during very high

characteristic energy (>10 keV) precipitation events [*Rees*, 1989]. Enhanced ionization at E-region altitudes due to the collisional excitation further increases the Joule heating rate.

During quiet geomagnetic conditions, the thermosphere's global-scale dynamics is not strongly affected by auroral-zone energy sources [*e.g. Roble*, 1977; see Figure B.2 on page 270 in Appendix B]. During moderate-to-active conditions, however, when the cross-polar cap electric field and ionospheric convection are strongest [*e.g. Heelis et al.*, 1982; *Heppner and Maynard*, 1987], auroral-latitude energy input alters significantly the thermosphere's global-scale wind and temperature patterns. Figure 1.1 below [*Dickinson et al.*, 1984] shows E- and F-region global-scale wind vectors in geographic coordinates at 1200 universal time (UT), computed using the Thermosphere Ionosphere Electrodynamics General Circulation Model (TIEGCM) [*e.g. Dickenson et al.*, 1981, 1984; *Roble et al.*, 1982, 1988; *Richmond et al.*, 1992] at the National Center for Atmospheric Research (NCAR) in Boulder, CO. Temperature deviations from the global mean are also illustrated for each region. The cross-polar cap electric potential used in the calculation was 60 kV, indicative of moderate geomagnetic activity. The largest wind vectors in both the E and F regions (79 $m \cdot s^{-1}$ and 336 $m \cdot s^{-1}$, respectively) are at high latitudes, indicating that during moderate-to-disturbed geomagnetic activity, high-latitude energetic processes are the most significant. In the E region, however, where ion drag is weaker, a strong geostrophic wind component is still apparent, particularly at equatorial and middle latitudes [*Brekke*, 1997].

1.1.7 Vertical Winds in the High-latitude Thermosphere

As was discussed above, ion drag, Joule heating and auroral-particle precipitation largely determine the thermosphere's global-scale horizontal wind patterns during active geomagnetic conditions. During even quiet conditions, the minute energy input ($\sim 10^9$-10^{10} W) due to these processes into the thermosphere is significant in determining along with radiative input the global mean thermospheric and exospheric temperature [*e.g. Roble and Emery*, 1983]. Joule and particle-precipitation heating processes, whether occurring during quiet or active geomagnetic periods, produce nearly-immediate local thermospheric temperature increases at auroral latitudes [*e.g. Smith and Hernandez*, 1995] and generate the mesoscale ($\sim 10^2$-10^5 km) spatial structures (*e.g.*, strong, localized wind shears) that

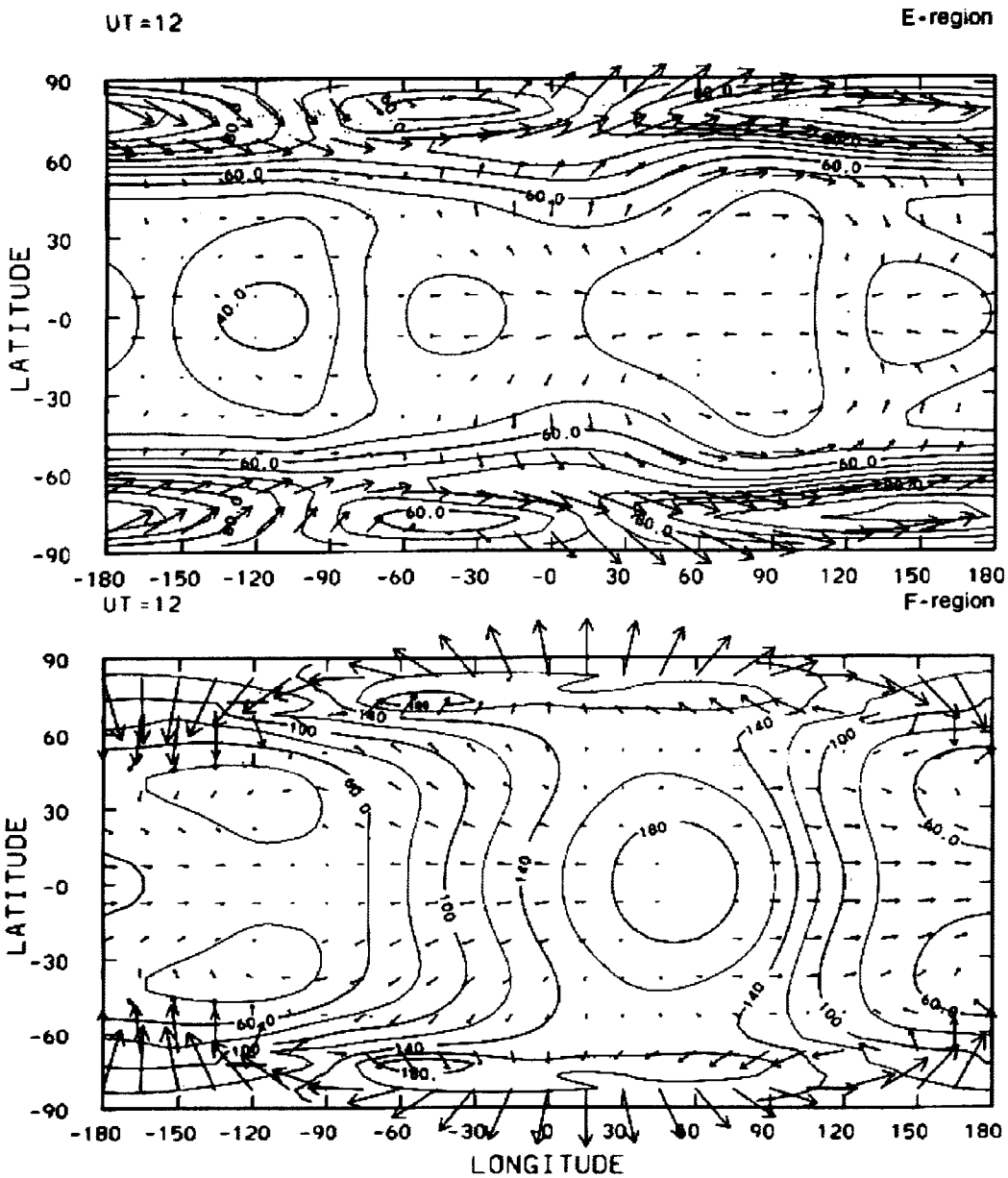

Figure 1.1. E- and F-region temperature structure and horizontal neutral vector winds. Maximum wind vector length in the E region is 79 $m \cdot s^{-1}$, in the F region is 336 $m \cdot s^{-1}$. Temperature contours are deviations from the mean [Figure from *Dickinson et al.*, 1984].

have been predicted to exist [*e.g. Fuller-Rowell*, 1985] and observed [*e.g. Conde and Smith*, 1998; *Conde et al.*, 2001] in the high-latitude neutral horizontal wind field. During active geomagnetic conditions, thermal expansion of the high-latitude thermosphere strongly modifies the thermosphere's global-scale horizontal pressure

gradient. Meridional flow away from the high-latitude thermosphere dominates the global thermospheric circulation [*Roble*, 1977; see Figure B.2 in Appendix B], resulting in delayed thermospheric temperature increases at middle and low latitudes [*e.g. Fuller-Rowell et al.*, 1994; *Fujiwara et al.*, 1996]. The expanded auroral oval is synonymous with an expanded divergent high-latitude horizontal wind field [*Hernandez and Roble*, 1979] that transports regions of heavier (N_2-rich) air across isobaric surfaces from the lower and middle to the upper thermosphere, modifying neutral composition at upper-thermospheric altitudes and pressure levels by decreasing the atomic-oxygen-to-molecular-species mixing ratio, $[O]/([N_2]+[O_2])$ [*e.g. Prölss*, 1980; 1992; *Rishbeth et al.*, 1985; 1987; *Hecht et al.*, 1989; 1999; *Lummerzheim*, 1990; *Fuller-Rowell et al.*, 1996]. The large-scale meridional and zonal flow carries O-depleted (or N_2-rich) air [*e.g. Craven et al.*, 1994] and/or NO-rich air [*e.g. Siskind et al.*, 1989a] from high latitudes to middle and low latitudes and other local time sectors. Convergent thermospheric horizontal winds—often indicative of the mesoscale spatial structures referred to earlier [*e.g. Conde and Smith*, 1998]—produce regions of downwelling that transport O-rich upper-thermospheric air across pressure surfaces, enhancing the $[O]/([N_2]+[O_2])$ at lower altitudes [*e.g. Rishbeth et al.*, 1985; 1987; *Fuller-Rowell et al.*, 1994]. In addition to these and other well-established global-scale thermospheric and ionospheric effects, Joule and particle-precipitation heating also regularly launch and sustain localized vertical winds in the auroral zone of much greater magnitudes than the aforementioned global-scale barometric and divergence-driven vertical winds, no matter the geomagnetic conditions that prevail.

Upward and downward winds, with horizontal spatial scales of $\sim 10^2$-10^5 km^2 and lasting for minutes to an hour, have been observed at high latitudes in the northern and southern hemispheres with both ground- and satellite-based instrumentation, with speeds ranging from 20-50 $m \cdot s^{-1}$ in the lower thermosphere [*e.g. Peterherych et al.*, 1985; *Price et al.*, 1995] to 50-200 $m \cdot s^{-1}$ in the upper thermosphere [*e.g. Spencer et al.*, 1976; 1982; *Smith*, 1980; *Rees et al.*, 1984a; *Conde and Dyson*, 1995; *Price et al.*, 1995; *Smith and Hernandez*, 1995; *Innis et al.*, 1996; 1997; 1999]. The question arises as to whether vertical winds of this sort sufficiently disturb hydrostatic and diffusive equilibrium to appreciably

modify the high-latitude thermosphere's local state, particularly during quiet geomagnetic conditions. Are localized, intermediate- to large-magnitude vertical winds sufficiently energetic and long-lived to transport air parcels from the lower and/or middle to upper thermosphere across isobaric surfaces, and vice versa, and disrupt the diffusive separation of high-latitude thermospheric species? Moreover, what are the necessary conditions to produce and sustain such vertical winds that can alter the local high-latitude thermospheric and ionospheric composition, chemistry and thermodynamics, potentially modifying the thermosphere's global density and temperature distributions via horizontal transport of the modified high-latitude thermospheric composition? Both questions are considered here in detail, and the central goal of this thesis is to examine the validity of the former question.

Localized heating in the high-latitude thermosphere produces localized pressure bulges that deflect the thermosphere's large-scale horizontal bulk flow. The redirected divergent horizontal flow generally will follow the contours of these localized pressure gradients, resulting in vertical winds that at times can be estimated from Equation 1.3. In addition, the onset of sudden intense heating at lower- to middle-thermospheric altitudes may rapidly produce concentrated pressure gradients that can generate strong vertical (upward) flow cells. The pressure change Δp in a vertical flow cell (assuming hydrostatic balance is being disturbed) determines the wind speed W, which can be approximated by the time derivative of the barometric equation [*e.g. Smith*, 1998; *Rishbeth*, 1998],

$$W = \frac{dz}{dt} = -\frac{1}{g\rho}\frac{dp}{dt} \approx -\frac{1}{g\rho}\frac{\Delta p}{\Delta t}, \tag{1.6}$$

where Δt is the duration of the heating and vertical wind event. If significant heat input is maintained into a disturbed region for a sufficient length of time, then a vertical flow cell will persist, with air parcels flowing away from the region's temperature maximum [*Smith*, 1998]. The topic of how much energy input is required and for how long to generate and sustain such a vertical flow cell is discussed below.

Localized divergent flow into a vertical flow cell is required to support upwellings and satisfy conservation of mass, and negative pressure variations at altitudes below a heated region will produce the convergent horizontal winds necessary to sustain a vertical

flow cell from underneath [*Smith*, 1998]. Divergent winds blowing out of a vertical flow cell well above a heated region can deflect and/or merge with large-scale horizontal bulk flow [*Smith*, 1998]. When a heating event is sufficiently intense to generate pressure bulges and locally disrupt hydrostatic equilibrium for a substantial period of time, upward winds that are generated within the vicinity of strong, localized electric fields and ionospheric currents (Joule heating) and/or intense auroral arcs (particle-precipitation heating) may transport lower- and middle-thermospheric air parcels along a column of atmosphere ahead of the thermally-expanding rising constant-pressure surfaces to the hotter, less dense upper thermosphere [*Smith*, 1998]. Air parcels, while retaining their initial temperature and composition, expand adiabatically as they rise due to the atmosphere's exponential decrease in pressure, and increase in speed due to their decreasing mass density since a given air parcel's energy density $\frac{1}{2}\rho W^2$ remains constant. Large-scale upper-thermospheric horizontal winds blowing over such a pressure bulge transport air parcels flowing out of the vertical flow cell away from the heated region. The cooler, slightly-denser air parcels will then either slowly thermalize with the surrounding air (of differing composition) and continue on with the horizontal flow (to other latitudes and local time sectors, modifying composition and chemistry) or, before thermalizing, proceed to sink in the direction of gravity and the negative temperature gradient when sufficiently removed from the heated region, resulting in downward winds. Convergent horizontal winds at upper-thermospheric altitudes can create localized density bulges which also generate strong, localized downward (or upward) winds that transport upper-thermospheric air parcels to lower (or higher) altitudes [*e.g. Smith*, 1998].

Sudden intense heating also launches acoustic and gravity (buoyancy) waves that propagate away from a heated region vertically and horizontally. Large-scale atmospheric gravity waves (AGWs) generated at auroral latitudes within the thermosphere can travel large distances and impart their momentum and energy at middle and low latitudes via turbulent processes [*e.g. Richmond*, 1978, 1979a, b; *Mayr et al.*, 1984a, b; 1987c; *Fuller-Rowell et al.*, 1996]. Thermospheric motion associated with a propagating gravity wave's horizontal component, when observed overhead from the ground with, for example, an

FPS looking in the zenith direction would appear as a vertical wind [*e.g. Hernandez*, 1982]. Buoyancy waves are described in more detail in Appendix B. Gravity waves are effective at perturbing hydrostatic balance and thermospheric composition [*e.g. Hernandez*, 1982], and *Smith* [1998] discusses an idealized example of a vertically-propagating medium-scale gravity wave launched from 125 km altitude and its effect on hydrostatic stability as it travels from the lower to upper thermosphere. Such waves generally have a wavelength comparable to the size of the heated region [*Smith*, 1998] and a period indicative of the thermosphere's buoyancy resonance period at that altitude, referred to as the Brunt-Väisälä period (see Appendix B). For example, a gravity wave of wavelength ~10 km and period ~300 s will propagate at a velocity of 10000 m/300 s $\approx$ 33 m·s^{-1}. The wave will travel from 125 km to 250 km in 125,000 m/33 m·s^{-1} $\approx$ 3800 s, or about one hour. Because vertical wind speed increases with increasing altitude (*i.e.*, with decreasing mass density), a vertical disturbance of this nature may be expected to last $\lesssim$1 hr as the gravity wave propagates upward and increases in speed, even after the heating has subsided. Even less time, ~20-30 min, is required for a +50 m·s^{-1} wind in a vertical flow cell to transport air parcels ~70-80 km through two or three scale heights from the lower to upper thermosphere and modify thermospheric composition along the column of thermosphere at each disturbed pressure level, if the wind persists for long enough and represents a significant-enough perturbation to equilibrium conditions, which is discussed next.

As was described in Section 1.1.5, time scales for changes to the thermosphere's pressure, τ_P, can be estimated from the relation $\tau_P \approx H/W$. For an intermediate-magnitude vertical wind of $W = \pm 30$ m·s^{-1} and for scale heights ranging from H = 10-50 km, $\tau_P \approx$ 10-30 min, which is comparable in duration to auroral-zone heating and vertical wind events. Thus, a 30 min heating event sufficiently energetic (discussed next) to produce and sustain a $\pm$30 m·s^{-1} will significantly upset hydrostatic stability. Vertical acceleration of air parcels associated with gravity wave propagation or in an intense, persistent vertical flow cell can also be estimated, and for a gravity wave traveling at 30 m·s^{-1}, the acceleration of air parcels a_{vert} is roughly $a_{vert} \approx 30$ m·s^{-1}/$\tau_{hydr} = 0.3$ m·s$^{-2} \sim g/30$, which represents a fairly significant departure from hydrostatic balance [*Smith*, 1998]. Even stronger accelerations

of ~$g/10$ are required to produce vertical winds of $\gtrsim$100 m·s^{-1}, though these magnitudes are only observed in the upper thermosphere since the higher mass density of the lower thermosphere requires considerably more energy input to produce and sustain such wind speeds, the topic discussed next. Nonetheless, vertical winds of the kind observed at high latitudes in the lower to upper thermosphere that are associated with ionospheric and auroral phenomena, when attaining speeds of greater than ±30-150 m·s^{-1} and lasting for time intervals of $\gtrsim$15-30 min, may be expected to upset hydrostatic balance such that the local thermosphere significantly departs from equilibrium conditions. Composition at each disturbed thermospheric pressure level may be expected to change in and within the vicinity of a column of heated atmosphere during such wind events [*e.g. Rishbeth et al.*, 1985; 1987], depending on the heating event's intensity, duration and altitudinal extent.

Although vertical winds of ~30-150 m·s^{-1} are regularly observed in the high-latitude thermosphere and indicate significant departure from equilibrium conditions, considerable localized and continuous energy input is required to overcome the stability, maintain the disturbance, and substantially alter the local composition, chemistry and dynamics at each affected pressure level. *Price et al.* [1995], in presenting simultaneous observations of lower- and upper-thermospheric vertical winds, used the approximate expression

$$P/A = \rho H[gW - c_P W(\Gamma - \partial T/\partial z) + c_P(\partial T/\partial t)] \quad (1.7)$$

to estimate the power per unit area P/A necessary to generate a vertical flow cell, where W is the wind speed, ρ is the mass density, H is the scale height, g is the acceleration due to gravity, $\Gamma = -9.8$ K·km^{-1} is the adiabatic lapse rate, and c_P is the specific heat of air at constant pressure. The first term on the right hand side of Equation 1.7 is the mechanical power required to raise a column of air at speed W in the absence of buoyancy. The real atmosphere is of course in hydrostatic equilibrium, so the first term instead needs to be $\rho H[gW + W\rho^{-1}(\partial p/\partial z)]$. The second term is the thermal power required to overcome adiabatic cooling, and the third term accounts for heating. The two thermal power terms are most significant in the lower thermosphere, while the mechanical power is generally the most significant in the upper thermosphere (where $\partial T/\partial z \rightarrow 0$). For example, the thermal power per unit area required to produce a lower-thermospheric, 42 m·s^{-1} vertical

wind (which *Price et al.* [1995] observed) at an altitude of 130 km is 330 $mW \cdot m^{-2}$, while the mechanical power per unit area is only 60 $mW \cdot m^{-2}$, amounting to a total of 390 $mW \cdot m^{-2}$ necessary to produce and sustain a 42 $m \cdot s^{-1}$ vertical wind. At altitudes of $\gtrsim$200 km, the required mechanical power per unit area to produce and sustain a vertical wind of 138 $m \cdot s^{-1}$ is much smaller, only ~10-20 $mW \cdot m^{-2}$, while the required thermal power per unit area is negligible. *Price et al.* [1995] showed that below ~120 km, vertical wind power requirements increase dramatically, reducing the likelihood that vertical flow cells can be generated at these lower altitudes. Above 120 km, however, where Joule and particle-precipitation heating regularly maximize [*e.g. Rees*, 1989], the required power to produce and sustain significant vertical winds that potentially extend from the lower to upper thermosphere does fall within the ranges of Joule heating and particle-precipitation energy input values and their durations. Equation 1.7 will prove to be useful again in Chapter 4.

As has been described, the response of the high-latitude thermosphere to Joule and particle-precipitation heating is nearly immediate in many respects, such as in the formation of pressure bulges due to increases in local temperature. However, collisional coupling between the high-latitude ionospheric circulation and the horizontal neutral flow generally takes much longer. Recall that the high-latitude $(\mathbf{E} \times \mathbf{B})/B^2$ ion drift can reach speeds of 1-2 $km \cdot s^{-1}$ during active geomagnetic conditions. This drift, however, may change direction instantaneously due to the varying cross-polar cap **E** field. Upon a change in direction and the reestablishment of steady ion drift, ~0.5-2 hr may be required for the high-latitude neutral circulation to recouple through collisions to the ionospheric convection [*e.g. Killeen et al.*, 1984; *Conde et al.*, 2001]. In general, at least one hour is required for ion drag to significantly modify the thermosphere's neutral horizontal dynamics [*e.g. Rishbeth and Garriott*, 1969; *Rishbeth*, 1972].

Similarly, when investigating neutral thermospheric vertical motion that may be induced by ion drift's vertical component, collisional coupling between ions and neutrals must persist for ~30-60 min before any substantial neutral vertical motion in the direction of the ions can result. Vertical ion drifts result from a zonally-directed electric field, which produces an upward ion drift for an eastward-directed **E** field and a downward drift

for a westward **E**. This drift is strongest at equatorial latitudes [*Rishbeth*, 1998], and at high latitudes is generally an order of magnitude less than the ions' horizontal drift speed since Earth's magnetic field is very nearly vertical in the high-latitude thermosphere. High-latitude $(\mathbf{E} \times \mathbf{B})/B^2$ vertical ion drifts may impart some frictional heating to neutrals through collisional coupling (increasing the local temperature) and produce some small-scale highly-localized neutral vertical motion (eddy mixing) along a column of atmosphere, but in general, these vertical ion drifts are not sufficiently long-lived to collisionally couple to the neutrals for any considerable length of time and produce strong and persistent neutral vertical winds, particularly of the kind that can significantly perturb hydrostatic balance for long periods of time and potentially modify local composition.

In general, two classes of vertical winds prevail in the thermosphere, those which cause the thermosphere to depart significantly from equilibrium conditions, potentially altering the thermosphere's density, wind, and temperature patterns, and those which do not. Global-scale barometric and divergence-driven thermospheric vertical winds of ±1-10 $m \cdot s^{-1}$ are associated with the thermosphere's radiatively-driven thermal expansion and contraction and dayside-to-nightside horizontal pressure gradient and are indicative of quasi-static atmospheric change that causes the thermosphere to deviate very little from its equilibrium configuration. In contrast, localized Joule and particle-precipitation energy input into the high-latitude thermosphere produces localized vertical winds that regularly attain amplitudes of $\gtrsim$30 $m \cdot s^{-1}$ in the lower thermosphere and $\gtrsim$100 $m \cdot s^{-1}$ in the upper thermosphere, lasting for up to an hour. These intermediate- to large-magnitude winds, produced directly by Joule and particle-precipitation heating and indirectly by localized and/or extended regions of divergent horizontal flow set up from ion drag and the heating (*i.e.*, pressure bulges), significantly disturb hydrostatic stability and may often extend from the lower to upper thermosphere [*e.g. Price et al.*, 1995] in the form of vertical flow cells that can transport air parcels ~70-80 km across isobaric surfaces through two or three scale heights. Gravity waves also will be launched that propagate away from a heated region, perturbing composition and transporting momentum and energy vertically to higher altitudes and horizontally to middle and low latitudes. The local thermospheric and

ionospheric composition, chemistry and thermodynamics at all affected pressure levels in the vicinity of the heating is altered during such heating events, depending on the intensity and duration of the energy input and its altitudinal, latitudinal and longitudinal extent. The thermosphere's global-scale composition, horizontal dynamics, and energy budget are strongly modified during the more highly-disturbed geomagnetic events. Though auroral-related, localized, intermediate- to large-magnitude thermospheric vertical winds are a well-documented phenomenon, as are local [*e.g. Hecht et al.*, 1989; 1999; *Lummerzheim et al.*, 1990; *Germany et al.*, 1990; *Christensen et al.*, 1997] and global [*e.g. Prölss*, 1980; 1992; *Craven et al.*, 1994; *Siskind et al.*, 1989a, b] thermospheric composition variations associated with auroral-zone dynamical and energetic processes, a quantitative link between the two phenomena, the primary focus of this thesis, has yet to be achieved.

1.2 The Thermosphere's Composition

1.2.1 Structure and Composition, Basic Chemistry and Energetics of the Thermosphere and Ionosphere

Like the rest of Earth's atmosphere, the thermosphere's composition has largely been determined by Earth's geologic history. The atmosphere's concentrations of N_2 (~78%), O_2 (~21%) and Argon (Ar, ~1%) are the result of its long-term evolution, and the general outline of Earth's atmosphere and magnetosphere presented in Appendix A describes many more details of the solar-terrestrial environment. Above the mesopause (~90 km) and turbopause (~100 km), however, the nature of the atmosphere changes considerably.

Of the many differences between the thermosphere and the atmosphere's other regions, one is the thermosphere's abundance (relative to its other constituents) of atomic oxygen. Furthermore, the thermosphere is also the region from which most of the visible radiation generated within the atmosphere emanates (*i.e.*, not scattered sunlight); the dayglow, nightglow and aurora. The aurora has amazed and delighted humans for millenia, and spectral emissions of the thermosphere are many and by many sources, including atomic oxygen. It is atomic oxygen's variability and chemistry, however, that influences most of these emissions [*Rees*, 1989], and understanding its daily, seasonal, latitudinal and solar-cyclical variability due to chemical, dynamical and energetic

processes, particularly those associated with the high-latitude thermosphere (*e.g.*, vertical winds), is essential to improving the predictive capabilities of general circulation models such as the TIEGCM at NCAR and the coupled thermosphere ionosphere (plasmasphere) model (CTIM or CTIP) [*Fuller-Rowell and Rees*, 1980,1983; *Fuller-Rowell et al.*, 1987, 1994, 1996b; *Millward et al.*, 1996] of the University College London (UCL), U.K., the University of Sheffield, U.K., and the Space Environment Center, Boulder, CO.

The altitude ranges of the thermosphere's different regions have already been defined and are reiterated here; the extreme lower thermosphere, ~90-100 km, the lower thermosphere, ~100-150 km, the middle thermosphere, ~150-200 km, and the upper thermosphere, ≳200 km. The thermosphere terminates at the thermopause, the nebulous boundary between the thermosphere and exosphere where the thermosphere's temperature maximizes and ceases its exponential increase. The thermopause's altitude (~600-1000 km) and temperature (~700-2000 K) vary with the Sun's daily, seasonally and solar-cyclically varying X-ray and UV radiative flux and with varying geomagnetic conditions. The thermopause resides in an altitude range where the mean free path of the thermosphere's neutral constituents—dependent on their collision cross section [*e.g. Sears and Salinger*, 1975]—becomes comparable to the pressure scale height, quantities which both depend on thermospheric temperature. The thermopause is the atmospheric region where hydrostatic equilibrium begins to break down, collisions become infrequent, and gases are no longer in thermal equilibrium. Fluid mechanics can no longer be used to examine neutral-constituent motion, neutral particles tend to follow ballistic trajectories governed by Earth's gravity, and charged-particle motion is governed by the local configuration of Earth's magnetic field. Collisions, thermal equilibrium, and mean free path in the thermosphere are discussed in more detail in Appendix C.

In general, several criteria are used for defining the altitude ranges of the different thermospheric regions. The extreme lower thermosphere resides between the mesopause and turbopause, the region where the atmosphere's temperature gradient turns positive due to photochemical heating processes (discussed below), but also where eddy diffusion continues to dominate over molecular diffusion, keeping the region well mixed. The

lower thermosphere is the region where the O and O_2 densities become comparable and also where molecular diffusion begins to strengthen sufficiently to offset any turbulent mixing, resulting in diffusive separation of species. The O and N_2 densities become comparable in the middle thermosphere, and the upper thermosphere is where O becomes the dominant species (discussed below). General diffusion principles are outlined in Appendix C. Diffusive equilibrium in the thermosphere is described in detail later.

As was stated earlier, the three major neutral constituents of the thermosphere are N_2, O, and O_2. Because N_2 and O_2 are products of the atmosphere's long-term evolution, their concentrations in the thermosphere are not affected by local sources and sinks, such as chemical reactions [*Rees*, 1989]. Atomic oxygen is produced primarily by the photodissociation of O_2 from radiation in the Schumann-Runge (SR) wavelength range ($\lambda \approx 130$-175 nm), radiation which has enough photonic energy to dissociate O_2 molecules but not to ionize them. The absorption process is described by the reaction equation

$$O_2 + h\nu(\sim 130 \leq \lambda \leq 174.8 \text{ nm}) \rightarrow O_2(B^3\Sigma_u^-) \rightarrow O(^3P) + O(^1D) + \text{K.E.}, \quad (1.8)$$

where $h = 6.63 \times 10^{-34}$ J·s is Planck's constant, ν is the radiation's frequency, K.E. is the residual kinetic energy, and the $O_2(B^3\Sigma_u^-)$ state is one of many excited states of O_2. At auroral latitudes, electron-impact dissociation of O_2 is also a significant contributor to O production. Because O_2 has a large absorption cross section ($\sim 10^{-18}$-10^{-17} cm^2) for radiation at SR-UV wavelengths [*Emery and Roble*, 1983], the bulk of the Sun's SR-UV radiation is absorbed by O_2 at altitudes of ~85-95 km where the O_2 optical depth reaches unity (see Figure A.4 in Appendix A), depositing ~30 $mW \cdot m^{-2}$ during solar minimum. Recall also that some SR-UV radiation is absorbed at higher altitudes, contributing to the thermosphere's heating (~3 $mW \cdot m^{-2}$ during solar minimum) from ~95-250 km along with photoionization processes (discussed below). The $O(^3P)$ state is the ground state of O, and $O(^1D)$ is the weakly excited (1.97 eV), highly metastable (~110 s radiative half-life [*e.g. Rees*, 1989]) state responsible for the λ630.0-nm airglow and auroral "red line" emanating from the upper thermosphere, which takes on a striking blood-red color if seen during proper auroral conditions. Though radiation of wavelengths $\leq$242.2 nm (photons of energy 5.12 eV, the O_2 dissociation threshold) has enough photonic energy to dissociate

O_2, thermospheric O_2 does not absorb radiation of wavelengths $\gtrsim$175 nm strongly because its absorption cross section drops off considerably ($\sim 10^{-21}$ cm^2) for wavelengths $\gtrsim$175 nm [*Roble and Emery*, 1983]. Radiation of wavelengths $\gtrsim$175 nm instead is absorbed by stratospheric O_3 and O_2, where the total atmospheric density is high enough such that it counters the weak O_2 absorption cross section. In general, the O density surpasses the O_2 density in the lower thermosphere at ~125 km [*Rishbeth and Garriott*, 1969] and the N_2 density at ~200 km [*Rees*, 1989]. The altitudes vary with the Sun's variable X-ray and UV radiation input [*e.g. Hedin*, 1991] and the varying high-latitude energy inputs. Hydrogen and Helium are the dominant species at exospheric altitudes, $\gtrsim$600-1000 km.

Atomic oxygen that is produced above the turbopause in the lower through upper thermosphere diffuses slowly downward over many days and ultimately is transported convectively through the turbopause into the extreme lower thermosphere [*Rees*, 1989]. Diffusion time scales, which vary with altitude, are discussed in the next section. Atomic oxygen is destroyed primarily by the exothermic three-body recombination reaction

$$O + O + M \rightarrow O_2 + M + 5.12 \text{ eV}, \qquad (1.9)$$

where M is any third body [*Rees*, 1989]. The reaction occurs below the turbopause at ~90 km and requires the sufficiently high density of the extreme lower thermosphere for three-body collisions to occur at a significant rate. At the base of the thermosphere, the reaction dominates and acts as the main heat source to the upper mesosphere [*Rees*, 1989]. On a global scale, photodissociation of O_2 and the recombination of O act as the primary heat sources to the extreme lower thermosphere (~30 mW·m^{-2}), though, as mentioned, turbulent and viscous dissipation of gravity waves and tidal motions also deposit ~0.7 mW·m^{-2} below ~100 km. Much like N_2 and O_2, local production and loss mechanisms have only a minor effect on O concentrations in general [*Rees*, 1989], but because O is chemically active (discussed below), its concentration is more variable at altitudes of ~80-120 km [*Rishbeth et al.*, 1987]. In general, transport processes are most responsible for the density distributions of the thermosphere's three major constituents [*Rees*, 1989].

Several minor species are present in the thermosphere as well, and in addition to CO_2 and NO, other minor constituents include Ar, He, H and atomic nitrogen (N) [*Rees*, 1989].

Local sources and sinks (discussed more below) strongly govern the concentrations of NO and N [*Rees*, 1989]. Ionized species are also important members of the thermosphere's makeup, and the daytime ionospheric regions have been defined as follows; the D region, ~50-90 km, the E region, ~90-150 km, the F region, comprised of the F1 and F2 layers, ~150-200 km and ~200-800 km, respectively, and the topside ionosphere, ≳800 km (≳500 km at night) [*e.g. Rishbeth and Garriott*, 1969; *Anderson and Fuller-Rowell*, 1999]. Maximum ion number density occurs in the F region at ~300 km during the day and ~400 km at night. The D and F1 regions disappear at night, while the F2 region remains. The E region also remains, but at a very highly reduced density. In general, the ionosphere is characterized by charge neutrality; *i.e.*, the electron density equals the sum of all the ion densities. NO^+ and O_2^+ are the major ions in the E and F1 regions, O^+ is the major ion in the F2 region, and H^+ and He^+ are the major ions at exospheric altitudes, ≳600-1000 km. The D region, which exhibits a very complex chemistry, will not be discussed in any detail here. Figure 1.2 [*Rishbeth and Garriott*, 1969] and Figure 1.3 [*Rees*, 1989] depict a

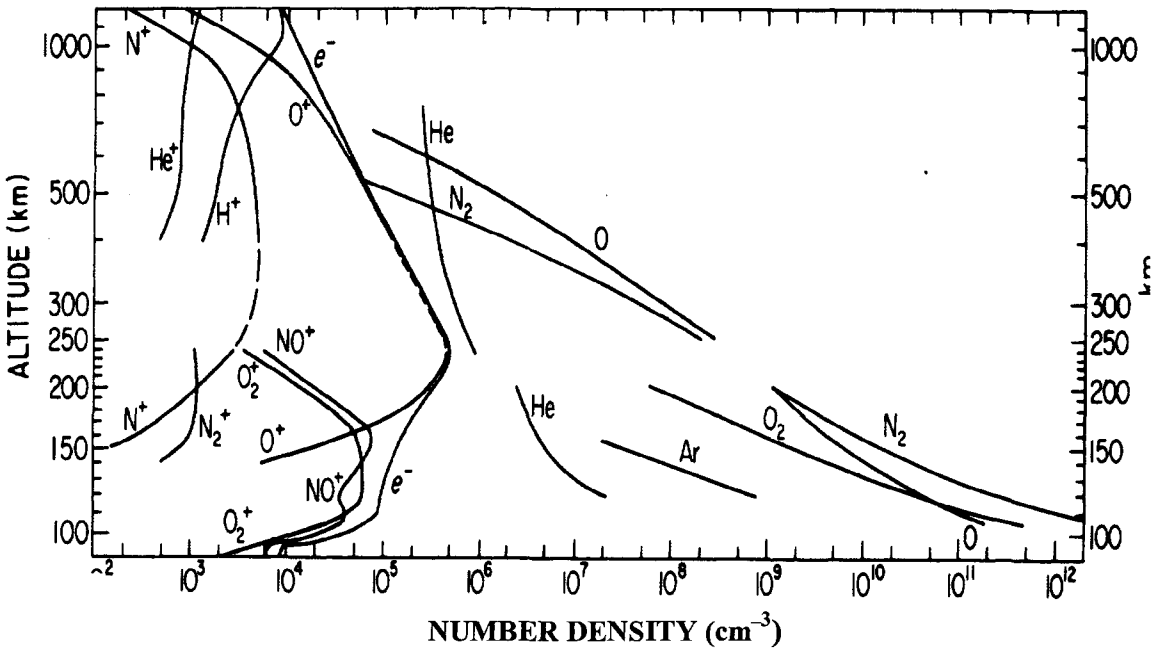

Figure 1.2. Constituents of the thermosphere and ionosphere and their densities. Typical mid-latitude daytime profiles of the neutral and ionized species above 90 km [Figure from *Rishbeth and Garriott*, 1969].

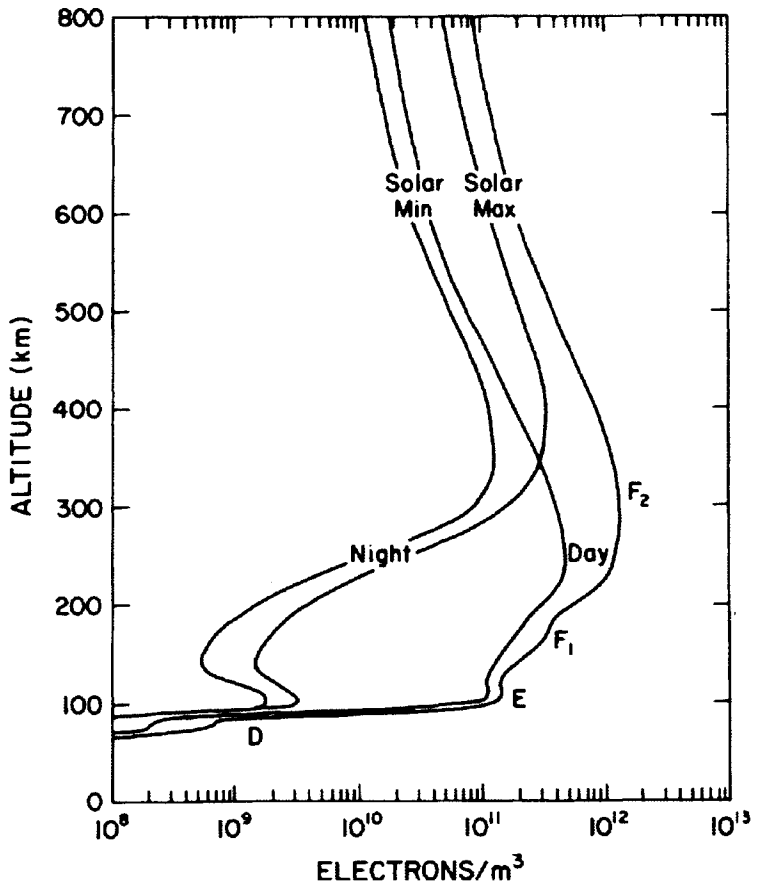

Figure 1.3. Electron density of the ionosphere. Mid-latitude electron density profiles for day and night and for solar minimum and solar maximum conditions are shown. The regions of the ionosphere are identified. The D and F1 regions vanish at night, and the E region nearly vanishes [Figure from *Rees*, 1989].

typical daytime, middle latitude thermosphere and ionosphere and typical middle latitude daytime and nighttime electron densities for solar minimum and solar maximum conditions, respectively.

Many chemical reactions which liberate heat occur in the extreme lower, lower and middle thermosphere; *i.e.*, the upper D, E and F1 regions. Many of these reactions are also responsible for the two dominant ionic species that prevail in the lower and middle thermosphere, NO^+ and O_2^+ [*e.g. Hargreaves*, 1992], where one might expect N_2^+ to be the major ion since N_2 is the dominant neutral species up to ~200 km. Two examples of the nine chemical reactions responsible for the production of NO^+ [*Rees*, 1989] include

$$O^+(^4S) + N_2 \rightarrow NO^+ + N(^4S) + 1.10 \text{ eV} \quad (1.10)$$

and

$$N_2^+ + O \rightarrow NO^+ + N(^4S) + 3.08 \text{ eV}, \quad (1.11)$$

and two examples responsible for the production of O_2^+ include

$$O^+(^4S) + O_2 \rightarrow O_2^+ + O + 1.55 \text{ eV} \quad (1.12)$$

and

$$O^+(^2D) + O_2 \rightarrow O_2^+ + O + 4.87 \text{ eV}. \quad (1.13)$$

Many reactions result in the production and loss of neutral and ionized species (*e.g.*, NO, N, N_2^+), and most of these reactions liberate heat [*Rees*, 1989]. But also obvious from Equations 1.10-13 is the important role O and its ion O^+ play in thermospheric chemistry, demonstrating why a better knowledge of O variability is essential to a better understanding of the thermosphere's and ionosphere's chemical, dynamical and energetic behavior.

Although the photodissociation of O_2 contributes to some of the thermosphere's heating between the altitudes of ~95-250 km, most of the heating at these altitudes (~3 $mW \cdot m^{-2}$ during solar minimum) is due to the photoionization of N_2, O_2, and O. All three major species have fairly large absorption cross sections (~10^{-19}-10^{-17} cm^2) for radiation of wavelengths ~1-100 nm [*Roble and Emery*, 1983] and summarized in Table 1.1 [*Rees*, 1989] are the ionization and dissociation (if applicable) threshold wavelengths and energies of N_2, O_2, and O and several minor species as well. Excess energy leftover from the ionization and dissociation processes imparts kinetic energy to the reaction products and/or leaves the reaction products in excited states. The subsequent exothermic chemical reactions that occur with the other species redistribute the excess energy. The excess energy stored in the daytime chemistry is liberated at night through exothermic recombination reactions and the emission of radiation; *i.e.*, airglow. Thermally-excited IR emissions act as the thermosphere's cooling mechanism. Collisions between species are also an important energy transfer mechanism in the thermosphere, but their contribution is small compared with exothermic chemical reactions [*Rees*, 1989].

Molecular oxygen has a structured and highly variable absorption cross section for radiation between the Far UV (FUV) wavelengths of 102.6 nm (the ionization limit of O_2)

Table 1.1. Ionization and dissociation threshold energies and wavelengths. Major and minor thermospheric species are included [Table from *Rees*, 1989].

Species	Ionization threshold		Dissociation threshold	
	E (eV)	λ (nm)	E (eV)	λ (nm)
N_2	15.58	79.6	9.76	127
O_2	12.08	102.6	5.12	242.2
O	13.61	91.1	–	
N	14.54	85.3	–	
NO	9.25	134.0	6.51	190.5
H	13.59	91.2	–	
He	24.58	50.4	–	

and 130 nm [*Roble and Emery*, 1983], and some of this radiation results in D-region ionization. For example, radiation of wavelengths between 102.7-111.8 nm can reach the mesosphere and ionize O_2 that is already in an excited state. In addition, the H Lyman-α line at λ121.6 nm ionizes mesospheric NO [*Hargreaves*, 1992; see Table 1.1]. However, most radiation in this wavelength range is absorbed in the extreme lower thermosphere and further contributes to the photodissociation of O_2 along with SR-UV radiation. For wavelengths <102.6 nm, the O_2 absorption cross section becomes large again [*Roble and Emery*, 1983], and the absorption of radiation of wavelengths 80-102.6 nm by O_2,

$$O_2 + h\nu(80 \leq \lambda < 102.6 \text{ nm}) \rightarrow O_2^+ + e, \quad (1.14)$$

results in lower-thermospheric (E-region) ionization [*Hargreaves*, 1992]. Equation 1.14 also helps to account for O_2^+ being one of the two major ions of the lower thermosphere, along with such chemical reactions as Equations 1.12-13.

Extreme UV (EUV) radiation of wavelengths ~20-90 nm is absorbed most strongly in the middle thermosphere [*Hargreaves*, 1992], at the altitudes of ~140-170 km where the optical depth reaches unity (see Figure A.4 in Appendix A), accounting for ionization at F1-layer altitudes. N_2, O_2, and O all contribute to this ionization. Radiation of wavelengths $\leq$66.2 nm has enough photonic energy to dissociatively ionize O_2,

$$O_2 + h\nu(\lambda \leq 66.2 \text{ nm}) \rightarrow O^+ + O + e, \quad (1.15)$$

and the little bit of O_2 present above ~150 km that dissociatively ionizes, besides aiding in F1-layer ionization, is responsible for the increasing O density (relatively speaking) of

the middle thermosphere. In addition, dissociatively-ionized O_2, in producing O, indirectly further contributes to F1-layer ionization because O also strongly absorbs EUV radiation of wavelengths ~10-91.1 nm [*Roble and Emery*, 1983],

$$O + h\nu(\lambda \leq 91.1 \text{ nm}) \rightarrow O^+ + e. \quad (1.16)$$

N_2 has a strong and fairly uniform absorption cross section as well for radiation of wavelengths relevant to the F1 layer, ~20-79.6 nm [*Roble and Emery*, 1983],

$$N_2 + h\nu(\lambda \leq 79.6 \text{ nm}) \rightarrow N_2^+ + e. \quad (1.17)$$

Equations 1.14-17 (and Equation 1.19 below) are the main contributors to lower- and middle-thermospheric ionization, and though O_2^+, O^+, and N_2^+ (and some He^+ and N^+) are the primary photoreactive products of these reactions, NO^+ and O_2^+ become the dominant species of both the E and F1 regions through the many chemical reactions that take place, such as Equations 1.10-13 above. Atomic oxygen is the principal absorber of radiation in the upper thermosphere (F2 region)—O^+ by far being the most abundant ion—and He and O dominate any absorption very high up (≳500 km).

Though N_2 is the dominant species up to ~200 km, leading one to think that perhaps N would be in high relative abundance in the thermosphere because of photodissociation processes' similar to O_2, N is only a minor species. This is because the production and loss of N is governed more by chemical reactions than by the photodissociation of N_2. Dissociation of N_2 is complex and involves predissociation states and decay processes, unlike O_2, which dissociates by continuum radiation absorption as well as predissociation and decay [*Rees*, 1989]. Though radiation of wavelengths ≤127 nm has enough photonic energy to dissociate N_2, the N_2 absorption cross section is small for wavelengths of ~100-127 nm. Only radiation of wavelengths ~80-100 nm can result in its dissociation,

$$N_2 + h\nu(\sim 80 \leq \lambda < 100 \text{ nm}) \rightarrow N + N. \quad (1.18)$$

Furthermore, the absorption cross section in this wavelength range, which does reach peaks comparable to values relevant to Equation 1.17 ($\sim 10^{-17}$ cm^2), is highly structured and variable [*Roble and Emery*, 1983], and consequently, direct radiative dissociation of N_2 is not a major source of N [*Rees*, 1989]. In addition, other factors conspire to keep N a minor thermospheric species. Recalling Equations 1.9-10, these are chemical reactions

that lead to the production of N but also of NO^+. Because N is chemically active in general, thermospheric N gets used up quickly by other chemical reactions [*Rees*, 1989], which ultimately results in the further production of NO and NO^+. NO and NO^+ are two particularly important species of the thermosphere because of their IR emission (cooling) properties. One other source of N, and F1-layer ionization, is radiation of wavelengths $\leq$51 nm, which have enough photonic energy to dissociatively ionize N_2,

$$N_2 + h\nu(\lambda \leq 51 \text{ nm}) \rightarrow N^+ + N + e. \quad (1.19)$$

In the high-latitude thermosphere, electron-impact dissociation, ionization and dissociative ionization can all take place similarly to Equations 1.8 and 1.14-19 [*Rees*, 1989]. The subsequent altered composition and enhanced chemistry resulting from these high-latitude processes ultimately results in increased amounts of NO and NO^+ in the high-latitude thermosphere. Thermospheric circulation can carry this excess NO and NO^+—and the increased radiative cooling—to middle and low latitudes [*e.g. Siskind et al.*, 1989a, b].

At night, the D and F1 regions quickly vanish due to dissociative recombination. This process occurs in the E region as well, but because of the thermosphere's absorption of galactic cosmic rays, UV radiation in starlight, and solar UV radiation scattered by Earth's geocorona (the cloud of neutral H atoms surrounding Earth) into the nighttime thermosphere [*Luetzelschwab*, 2004], a perceptible nighttime E region persists, though of highly-reduced density. Chemical reactions applicable to the E and F1 regions include

$$NO^+ + e \rightarrow N + O + 0.38 \text{ eV or } 2.75 \text{ eV} \quad (1.20)$$

and

$$O_2^+ + e \rightarrow O(^1D) + O(^3P) + 5.0 \text{ eV}. \quad (1.21)$$

Although the F1 layer disappears after dark, the F region as a whole endures at a reduced density (see Figure 1.3). This is because O^+ is the dominant ionized constituent of the upper thermosphere, which makes recombination a more complex process. Because O^+ does not easily recombine with electrons [*Rees*, 1989],

$$O^+ + e \rightarrow O^* \rightarrow O^+ + e, \quad (1.22)$$

where O* denotes a highly excited state that quickly autoionizes, recombination in the upper thermosphere requires two steps,

$$O^+ + O_2 \rightarrow O_2^+ + O, \text{ or}$$

$$O^+ + N_2 \rightarrow NO^+ + N, \qquad (1.23a\text{-}b)$$

and then

$$NO^+ + e \rightarrow N + O, \text{ or}$$

$$O_2^+ + e \rightarrow O + O, \qquad (1.24a\text{-}b)$$

respectively. The total rate of reactions 1.23*a* and 1.24*a* together (1.23*b* and 1.24*b* together) is strongly governed by Equation 1.23*a* (*b*) in the upper thermosphere because the rate coefficients of Equations 1.23*a* and *b* are altitude-dependent, decreasing with decreasing density, and thus decreasing with increasing altitude [*Hargreaves*, 1992]. Ultimately, not all of the O^+ ions recombine over the course of the night, which results in the F region enduring through darkness.

An interesting feature of the upper thermosphere is that the ion and electron density maximum of the F2 (nighttime F) region, referred to as N_mF2, and its corresponding altitude, h_mF2 (~300 km during day, ~400 km at night), occur where there is not a strong radiative ionization source, since total optical depth reaches unity lower in the thermosphere for all relevant wavelengths (see Figure A.4 in Appendix A). The reason for this involves three processes. The equilibrium ion and electron density N_P below and up to the F2-layer peak by day is approximately given by the relation [*e.g. Rishbeth and Garriott*, 1969; *Rishbeth*, 1998],

$$N_P \sim q/\beta \sim I_\infty[O]/(k'[O_2]+k''[N_2]). \qquad (1.25)$$

The production rate of electrons q, referred to as the Chapman production function, is dependent on the total ionizing irradiation I_∞ (all relevant wavelengths) and the density of atomic oxygen, [O]. The loss rate of electrons β due to recombination depends on the densities of O_2 and N_2, $[O_2]$ and $[N_2]$, and their rate coefficients, k' and k'', which are indicative of Equations 1.23*a* and *b*, respectively, the governing reactions in the loss of electrons at upper-thermospheric heights. During daytime hours, q and β balance each other up to the F2-layer peak. Above h_mF2, however, Equation 1.25 yields an unrealistic escalating N_P with increasing altitude—though q and β decrease with increasing altitude (decreasing atmospheric density)—because O is the dominating species at upper-

thermospheric altitudes. The upward increase of N_P does cease, however, at the altitude where transport becomes comparable to production and loss. The height at which the upward diffusion of the O^+ ion-electron plasma sufficiently contributes to the loss of electrons along with recombination β loss marks the peak of the F2 layer and occurs where the loss rate $\beta \approx D_P/H_O^2$. D_P is the ion diffusion coefficient (proportional to the inverse of the ion-neutral collision frequency), and H_O is the scale height of atomic oxygen [*Rishbeth*, 1998]. General diffusion principles, ion diffusion, and the derivation of $\beta \approx D_P/H_O^2$ are outlined in Appendix C. Neutral diffusion is discussed in the next section.

Clearly, the N_mF2 and h_mF2 parameters are strongly sensitive to the atomic-oxygen-to-molecular-species mixing ratio, $[O]/([N_2]+[O_2])$, and to processes that modify this ratio (*e.g.*, vertical winds). In addition, there are other numerous ionospheric effects associated with active geomagnetic conditions that have been observed at F-region altitudes [*e.g.* see review, *Field and Rishbeth*, 1997], and some of these effects can be attributed to changes in thermospheric chemistry that are caused by the thermosphere's modified circulation altering the thermosphere's neutral composition. So-called "positive" effects include an initial enhancement of N_mF2 lasting a few hours due to increased particle-precipitation rates as geomagnetic activity intensifies, while enhanced meridional neutral flow away from the auroral zone increases h_mF2 at middle latitudes by pushing ionospheric constituents up the magnetic field lines [*e.g. Prölss*, 1991; *Rishbeth*, 1991]. "Negative" effects lasting for 1-2 days after intense geomagnetic activity include depleted ionospheric densities at F-region altitudes due to increased N_2 concentrations (affecting recombination rates) and decreases in h_mF2 due to poleward neutral flow that has surged across the equator from the opposite hemisphere [*e.g. Fuller-Rowell et al.*, 1994]. The neutral surge across the equator also further decreases ionospheric densities by pushing the ionosphere to lower altitudes where more N_2 (relative to O) resides [*Rishbeth*, 1991].

1.2.2 Diffusion and Diffusive Equilibrium in the Thermosphere

Another feature of the thermosphere that distinguishes it from the atmosphere's other regions, besides its relative abundance of atomic oxygen and its radiative emissions, is diffusive equilibrium. Well above the turbopause, molecular diffusion dominates over

any weak eddy diffusion that occurs (*e.g.*, dissipation of gravity waves and tidal motions) [*Richmond*, 1983], and thermospheric constituents diffusively separate under gravity relative to each other because of their differing molecular masses. Each species must be considered individually, and molecular diffusion introduces a process, not applicable to the atmosphere below, that must be considered when determining each species' partial pressure and number density distributions. As discussed in Section 1.1.7, this scenario is further complicated at auroral latitudes, where Joule heating and particle precipitation produce localized vertical motions that upset hydrostatic and diffusive stability.

The thermosphere, like the rest of the atmosphere, is characterized by large pressure, density and temperature gradients in all three dimensions, making the study of thermospheric diffusive processes and composition response fairly complex. Moreover, the thermosphere's gradients are more variable and extreme relative to the atmosphere's other regions because of the thermosphere's regularly varying energy inputs and its large altitude range (~90 to 600-1000 km). The thermosphere's total mass density decreases by ~7 orders of magnitude from the mesopause to the thermopause while the temperature increases from ~180 to 700-2000 K (dependent on time of day, geomagnetic conditions, and solar cycle). Because the thermosphere's scale size is much smaller in the vertical direction than in the horizontal [*Richmond*, 1983], and because the largest variations in number density and temperature are vertical, diffusive flow is generally vertical. The horizontally-directed large-scale pressure gradients between Earth's dayside and nightside and between auroral and mid-to-low latitudes result in large-scale horizontal bulk flow rather than diffusive flow. In addition, the horizontal flow along the stratified constant-pressure surfaces tends to stay horizontal because hydrostatic balance is reinforced in the thermosphere by the positive temperature gradient in the vertical direction. Lastly, the higher thermospheric temperatures above the turbopause increase the molecular diffusion rate such that it dominates over eddy diffusion above ~120 km [*Richmond*, 1983].

In an isothermal atmosphere that is subject to gravitational, collisional, and pressure-gradient forces, the time-dependent vertical diffusion of a minor gas through the atmospheric background gas is approximately given by the equations [*Hargreaves*, 1992]

$$w = -(D/n)[\partial n/\partial z + n/H] \quad (1.26)$$

and

$$\partial n/\partial t = \partial/\partial z[D(\partial n/\partial z + n/H)], \quad (1.27)$$

where w and n are the diffusion speed and number density of the minor gas, respectively, z is the altitude, H is the scale height, and $D = k_B T/m\upsilon$ is the molecular diffusion coefficient of the minor gas. The diffusion coefficient of the minor gas depends on its collision frequency υ with the background gas, its temperature T, and the mass m of its molecules. However, because the collision frequency also depends on the density of the background gas (see Appendix C), the diffusion coefficient of the minor gas is inversely proportional to the density of the background gas. Therefore, in general, molecular diffusion is stronger high in the thermosphere and becomes weaker as a gas diffuses downward. The derivation of Equations 1.26-27 is described in more detail in Appendix C, and in the upper thermosphere above the F2-layer peak, where the vertical temperature gradient is nearly zero, these equations are suitable for describing the diffusion of plasma (O^+ ions and electrons) through the neutral O atom gas (see Appendix C for more details).

Equations 1.26-27 are derived assuming an isothermal atmosphere, but in examining vertical diffusion of thermospheric neutral species in the lower and middle thermosphere where the vertical temperature gradient is significant, the isothermal condition is no longer valid. Equations 1.26-27 are derived by carrying out a force-balance analysis on the forces due to the vertical pressure gradient, gravitation and collisions (see Appendix C). In this analysis, the derivative of the ideal gas law in the vertical direction, $\partial p/\partial z = k_B T(\partial n/\partial z)$, is employed. When the isothermal condition is relaxed, $\partial p/\partial z = k_B T(\partial n/\partial z)$ is no longer valid, and it is necessary to use $\partial p/\partial z = k_B[T(\partial n/\partial z) + n(\partial T/\partial z)]$. Force balance yields $w = -k_B T(m\upsilon n)^{-1}(\partial n/\partial z) - k_B(m\upsilon)^{-1}(\partial T/\partial z) - g\upsilon^{-1}$, which can be rewritten as

$$w = -(D/n)[\partial n/\partial z + (n/T)(\partial T/\partial z) + n/H]. \quad (1.28)$$

Equation 1.28 is an approximation as well, however, because the diffusion coefficient also depends on temperature, thus varying with altitude. In general, when investigating the non-equilibrium distribution of a lower- to middle-thermospheric neutral gas and the diffusion of that gas through the multi-component background gas, a more exhaustive

treatment of the problem is necessary. A simplified version of the general diffusion equation, which illustrates some key terms, is given by [*e.g. Richmond*, 1983; *Rees*, 1989]

$$v_j(z) - v(z) = \sum_i \frac{n}{n_i} D_{ji} \left[\frac{1}{n_j} \frac{\partial n_j}{\partial z} + \frac{(1+\mu_{ji})}{T} \frac{\partial T}{\partial z} + \frac{m_j g}{k_B T} \right], \tag{1.29}$$

where $v_j(z)$ is the diffusion velocity of the j^{th} species, and is measured with respect to any mass-averaged velocity $v(z)$ of the thermosphere that may be occurring, such as a high-latitude vertical wind. The temperature-gradient term in Equation 1.29 is slightly altered from its corresponding term in Equation 1.28, and μ_{ji} is referred to as the thermal diffusion coefficient between species j and i, analogous to a molecular diffusion coefficient. Generally, $\mu_{ji} \approx 0.35$ for thermospheric species, though it is also temperature dependent [*Rees*, 1989]. D_{ji} is the binary diffusion coefficient between species j and i, n_i is the i^{th} constituent's number density, and n is the mass-averaged total number density. Equation 1.29 does not yield the time-dependence of n_j because an initial steady-state condition is assumed in deriving it, but by utilizing one approximation, Equation 1.29 does yield an analytic equilibrium solution for $n_j(z)$. If there is no net vertical velocity, either diffusive or mass-averaged (*i.e.*, $v_j(z) = v(z) = 0 = \partial n_j/\partial t$), then Equation 1.29 reduces to

$$\frac{\partial n_j}{\partial z} + (1+\mu_j) \frac{n_j}{T} \frac{\partial T}{\partial z} + \frac{n_j m_j g}{k_B T} = 0, \tag{1.30}$$

the differential equation that characterizes diffusive equilibrium. The number density $n_j(z)$ of the j^{th} constituent determined from Equation 1.30 is

$$n_j(z) = n_j(z_0) \left[\frac{T(z_0)}{T(z)} \right]^{(1+\mu_j)} \exp\left[-\int_{z_0}^{z} \frac{m_j(z')g(z')}{k_B T(z')} dz' \right], \text{ or} \tag{1.31}$$

$$n_j(z) \approx n_j(z_0)[T(z_0)/T(z)]^{(1+\mu_j)} \exp[-(z-z_0)/H_j]. \tag{1.32}$$

The distributions of the three major neutral thermospheric species N_2, O, and O_2 generally follow Equations 1.31-32 because time scales for density variations associated with daily and seasonal effects are long [*Rees*, 1989]. As a result, a quasi-equilibrium distribution generally prevails in the thermosphere except around dusk and dawn and during periods of strong geomagnetic activity. Each major species assumes its own number density

distribution, scale height structure and partial pressure dependent on its molecular weight. The thermosphere's total pressure is the sum of all the partial pressures. In addition, density distributions of the major species are dominated by transport processes rather than by local production and loss. As was stated, the presence of N_2 and O_2 in the atmosphere is the result of the atmosphere's long-term evolution, and local sources and sinks do not affect their concentrations. The production and loss of O (photodissociation of O_2 and three-body recombination near the mesopause, respectively) are global-scale processes that affect local O concentrations insignificantly when compared with dynamical processes such as auroral-latitude vertical winds and large-scale horizontal transport [*Rees*, 1989]. When investigating minor thermospheric neutral and ionized species (*e.g.*, NO, NO^+), however, these criteria do not necessarily apply. Local sources and sinks (*e.g.*, chemical reactions, see previous section) play a central role in their concentrations, and production and loss terms must be kept when evaluating the continuity equations of the minor species.

Because of the temperature dependence of Equations 1.31-32, $\alpha\,[T(z_0)/T(z)]^{(1+\mu)}$, the diffusive equilibrium solution differs some from a strictly hydrostatic solution,

$$n_j(z) = n_{j,0}\exp[-(z-z_0)/H_j], \tag{1.33}$$

where $n_{j,0}$ is the density of j^{th} species at altitude z_0. However, in the upper thermosphere, particularly above the F2-layer peak where the temperature becomes nearly constant with altitude, the diffusive equilibrium solution reduces to the hydrostatic solution. This is because $T(z_0)/T(z) \rightarrow 1$ in Equations 1.31-32, and $H_j = k_B T_j/m_j g$ becomes nearly constant. Therefore, the number density of the upper thermosphere's dominant constituent, atomic oxygen, can be written approximately as

$$n_O \approx n_{O,0}\exp[-(z-z_0)/H_O], \tag{1.34}$$

where $n_{O,0}$ is the O density at altitude z_0 (*e.g.*, $z_0 = h_mF2$). This approximation is useful in determining the loss rate γ_P of the O^+ ion-electron plasma, N_P, in the upper thermosphere due to the upward diffusion of the plasma away from the F2-layer peak through the background O gas [*Hargreaves*, 1992]. The diffusion loss rate γ_P of the plasma,

$$\gamma_P \equiv D_P(\delta_P^{-1} - H_P^{-1})(\delta_P^{-1} - H_O^{-1}) \sim D_P/\delta_P^2, \tag{1.35}$$

is derived in Appendix C. D_P is the ion diffusion coefficient, H_P is the plasma scale

height, and $\delta_P = [-N_P^{-1}(\partial N_P/\partial z)]^{-1}$ is the ion's distribution height parameter ($\delta_P \approx H_P$ under equilibrium conditions; *e.g.*, below and up to the F2-layer peak during the day). The determination of δ_P and γ_P which validates the assertion of the previous section that the location of the F2-layer peak occurs at an altitude where upward diffusive loss becomes comparable to recombination loss (*i.e.*, where the recombination loss rate $\beta \approx \gamma_P \approx D_P/H_O^2$) is described in more detail in Appendix C. In general, a distribution height parameter δ_2,

$$\delta_2 = [-n_2^{-1}(\partial n_2/\partial z)]^{-1}, \tag{1.36}$$

and an appropriate diffusion transport rate γ_2,

$$\gamma_2 \equiv D_2(\delta_2^{-1} - H_2^{-1})(\delta_2^{-1} - H_1^{-1}) \sim D_2/\delta_2^2, \tag{1.37}$$

characterizes the diffusion of a species-2 gas through some background species-1 (or multi-component) gas, and in the case of self-diffusion, the rate at which diffusion acts in the thermosphere is roughly given by $\gamma \approx D/\delta^2 \approx D/H^2$ [*Rishbeth and Garriott*, 1969].

Several mechanisms exist that can disturb hydrostatic and diffusive equilibrium in the thermosphere [*Rishbeth et al.*, 1987], and the most effective is high-latitude, auroral-related vertical winds. Once diffusive equilibrium is upset, time is required for molecular diffusion to restore the vertical distribution of species, and the amount of time varies with altitude since the molecular diffusion coefficient varies with altitude. If the rate at which diffusion acts is $\gamma \approx D/H^2$, then the time required to achieve diffusive equilibrium, τ_{eq}, is roughly given by $\tau_{eq} = \gamma^{-1} = H^2/D$ [*Rishbeth and Garriott*, 1969]. *Müller-Wodarg and Aylward* [1998], in investigating the effects of upward propagating tides on diffusive equilibrium in the lower and middle thermosphere, determined that below about 160 km, molecular diffusion is ineffective in reestablishing equilibrium within the time scales of tidal oscillations (tidal motions are summarized in Appendix B). In general, time scales for the establishment of diffusive equilibrium below ~160 km are very long, and Table 1.2 [*Müller-Wodarg and Aylward*, 1998], which gives τ_{eq} at various altitudes for globally averaged conditions, illustrates this fact. At middle and low latitudes, disruptions of diffusive equilibrium are negligible [*Rishbeth et al.*, 1987], but at high latitudes, where the auroral zone resides almost all of the time, energy and momentum are continuously being deposited into the lower and middle thermosphere due to ion drag, Joule heating and

Table 1.2. Time scales for establishing diffusive equilibrium in the thermosphere [Table from *Müller-Wodarg and Aylward*, 1998].

Height	105 km	115 km	125 km	140 km	160 km	180 km	200 km	>200 km
τ_{eq}	410 hr	150 hr	60 hr	24 hr	10 hr	5 hr	2 hr	<1 hr

particle-precipitation processes, whether during quiet or active geomagnetic conditions. Diffusive equilibrium is much less likely to prevail in the lower and middle thermosphere at high latitudes most of the time because Joule and particle-precipitation heating, in perturbing hydrostatic equilibrium, can produce vertical winds that result in large-scale transport of air parcels from the lower and middle thermosphere to upper thermosphere, or vice versa, (intense, persistent heating events) and/or in small-scale eddy mixing along a column of thermosphere (weak, persistent heating). Though the thermosphere responds quickly to perturbations of hydrostatic stability (recalling from Section 1.1.5 that the time scale for hydrostatic adjustment, τ_{hydr}, is given by $\tau_{hydr} \approx H/v_{ther} \approx$ 15-50 s), in a persistent vertical flow cell, disruptions of hydrostatic and diffusive stability are maintained while the heat input and vertical wind persists. Once the heating diminishes, localized horizontal diffusive flow quickly reestablishes hydrostatic balance locally, but depending on the altitude range of the disturbance, the vertical distribution of the thermospheric composition (in the reference frame of the horizontal bulk flow) will remain unsettled for hours to days.

1.3 A Search for Thermospheric Composition Perturbations due to Vertical Winds: Comparing Auroral Observations to Model Predictions

As the previous sections have indicated, ion drag, Joule heating, and auroral-particle precipitation play important roles in the compositional, dynamical and energetic behavior of the thermosphere. One consequence of these thermospheric, ionospheric, and magnetospheric interactions (among many others) in an otherwise hydrostatically-stable, vertically-stratified thermosphere is the regular occurrence of long-lived, intermediate- to large-magnitude vertical winds. The most telling characteristic of these winds, however—their localized nature—is the very thing that makes their compositional, dynamical and thermodynamic effects so difficult to identify and quantify.

In general, auroral-latitude vertical winds are not well represented in global-scale general circulation models because their horizontal spatial scales (~10^2-10^5 km^2) are small compared to model grid sizes [*Smith*, 1998]. Moreover, observing high-latitude vertical winds is problematic since they are restricted in time and space [*Smith*, 1998]. A ground-based, zenith-looking observatory at auroral latitudes must wait for a vertical wind field to move overhead, while an orbiting satellite must travel through a vertical wind field for an onboard instrument to make an *in situ* measurement of the wind. In addition, ground-based observations only record a vertical wind event's time history as it occurs overhead, in general unable to determine the spatial extent of the vertical wind field, where the air parcels were prior to moving overhead, or whether the vertical wind was blowing before or continues to blow after the wind is observed. In contrast, satellite observations of a vertical wind can only ascertain a vertical wind field's spatial extent as the satellite passes through it. Lastly, the causal effect of vertical winds is often not apparent; *i.e.*, whether the wind is associated with adjacent upward- and downward-moving air columns due to direct energetic forcing (a vertical flow cell) [*Smith*, 1998], or is associated with a divergent horizontal wind field or a propagating gravity wave produced by a distant heat source. Depending on the focus of a vertical wind study, other data sets—*e.g.*, horizontal wind measurements (for estimating divergence), magnetometer traces (to infer Joule heating rates), or vertical wind estimates at another nearby location (for resolving a vertical wind field's spatial extent)—may be essential to a detailed investigation of the circumstances accompanying a long-lived, intermediate- to large-magitude vertical wind event.

This thesis presents seven nights of ground-based Fabry-Perot Spectrometer (FPS) zenith observations of the atomic oxygen (OI) λ630.0-nm airglow and auroral emission obtained at Inuvik, NT, Canada (geographic latitude 68.3°N, longitude 226.5°E; L = 9.9), yielding vertical wind estimates in the upper thermosphere. Also presented is an example of one night's upper-thermospheric vertical wind estimates and simultaneous lower-thermospheric vertical winds (determined from observations of the OI(557.7)-nm airglow and auroral emission) obtained at Poker Flat, AK (65.1°N, 212.6°E; L = 5.9) with an FPS owned by the Communications Research Laboratory (CRL) of Japan [*Ishii et al.*, 1997].

The vertical wind measurements presented here exhibit intermediate-to-large amplitude variations (±30-100 $m \cdot s^{-1}$) during a variety of geomagnetic and solar-radiative conditions and are indicative of the geophysically-significant vertical wind events discussed in Section 1.1.7 that disturb hydrostatic and diffusive equilibrium sufficiently to modify the local composition at each affected pressure level. The central goal of this study is to associate these long-lived, intermediate- to large-magnitude vertical wind events identified in the vertical wind time series from Inuvik and Poker Flat with a distinct and quantifiable thermospheric composition response. With this in mind, a second data set was sought that would reveal vertical wind-induced composition perturbations.

Many compelling examples of localized, upper-thermospheric composition perturbations due to vertical winds (which acted as a motivation to this study) exist from the Dynamics Explorer satellite mission. Upper-thermospheric vertical (and zonal) wind observations by the Wind and Temperature Spectrometer (WATS) [*Spencer et al.*, 1981] onboard the Dynamics Explorer 2 (DE2) satellite, which orbited at altitudes of ~300-800 km, were made in conjunction with neutral composition density [*Carignan et al.*, 1981] and ion temperature [*Hanson et al.*, 1981] measurements. Figure 1.4 [*Conde*, 2004, private communication] is one of many examples from the DE2 Unified Abstract data source that definitively illustrates the high correlation between increases in ion temperature (heating), strong (~100 $m \cdot s^{-1}$) upward winds, and perturbations to upper-thermospheric composition (the N_2 density). At ~1520 UT in this example, WATS begins measuring strong upward winds of ~50-100 $m \cdot s^{-1}$, corresponding with increased ion temperatures. The satellite remains within the vertical wind field for about ten minutes, and during this time, the N_2 density is elevated by ~25%, indicating that higher-density air parcels are being transported from lower altitudes to the satellite's altitude. As the satellite emerges from the heated region, the ion temperature decreases, the vertical wind subsides, and the N_2 density returns to characteristic values. Note that the decreasing N_2 density after the heating and vertical wind event follows the increasing altitude of the satellite.

As revealing as Figure 1.4 is in demonstrating the link between heating, vertical winds and composition response, there remains the complication of not being able to track

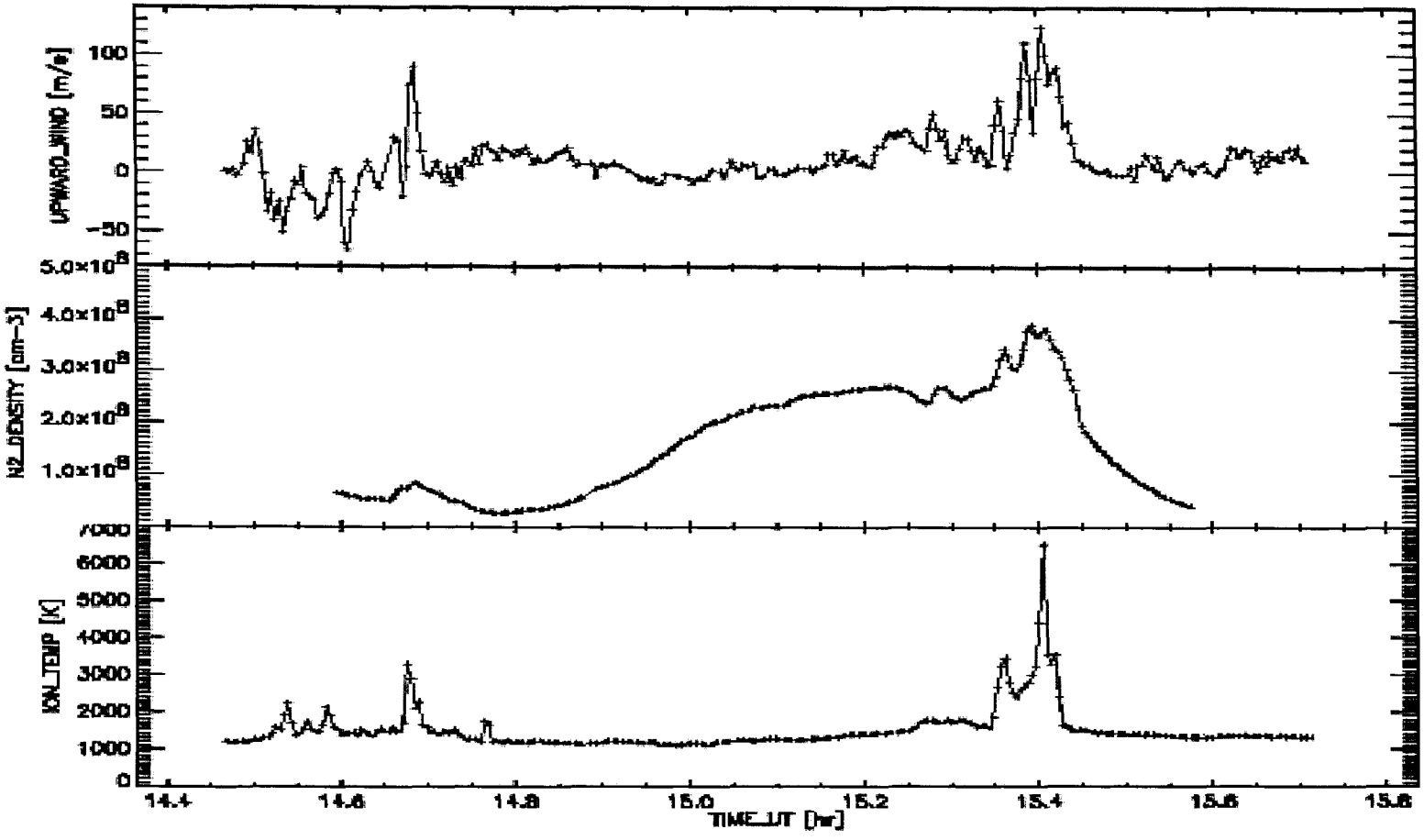

Figure 1.4. Vertical winds, N_2 density, and ion temperature in the upper thermosphere. The data were obtained by instrumentation aboard the Dynamics Explorer 2 satellite during the Dynamics Explorer mission from 1981-1988. This example illustrates a vertical wind-induced composition perturbation. Starting at ~1520 UT, strong upward winds of ~50-100 $m \cdot s^{-1}$ prevail, corresponding with increased ion temperature. The N_2 density is elevated by ~25% while the satellite remains in the vertical wind field [Figure from *Conde*, 2004, private communication].

the time history of the vertical wind or the composition perturbation (in the reference frame of the horizontal bulk flow) because of the *in situ* nature of the measurements. Thus, a possible next step in tracking vertical wind-induced composition perturbations, in conjunction with ground-based vertical wind measurements for example, would be to acquire some sort of two-dimensional (2-D) thermospheric composition map—centered on an observatory's latitude and longitude (local time)—that identifies composition perturbations attributed to significant vertical wind activity and follows the perturbations in subsequent 2-D maps—or, in addition, identifies a vertical-wind induced composition perturbation in previous 2-D maps prior to the observation of a significant vertical wind. One suitable method for investigating the thermosphere's composition is through spectroscopic studies of the aurora. Auroral-imaging techniques utilize spectral intensity measurements of the aurora from the ground or orbit in conjunction with models of the aurora to infer such things as the energy flux and characteristic energy of the precipitating electrons, ionospheric conductances (inferred from the energy flux and characteristic energy), and density perturbations to the model neutral thermospheric composition [*e.g. Lummerzheim et al.*, 1990; *Hecht et al.*, 1989; 1999; *Germany et al.*, 1990; 1994a, b].

The most likely thermospheric bulk property to reveal composition perturbations due to long-lived, intermediate- to large-magnitude vertical winds is the atomic-oxygen-to-molecular-species mixing ratio, $[O]/([N_2]+[O_2])$ [*Rishbeth et al.*, 1985; 1987]. Upward winds adiabatically lift N_2-rich air from the lower and middle thermosphere to the upper thermosphere, while downward winds can transport O-rich, upper-thermospheric air to relevant auroral-emission altitudes (~100-250 km). Auroral emission profiles will change accordingly. Electron transport models [*e.g. Strickland et al.*, 1989; *Lummerzheim and Lilensten*, 1994], which rely on spatially- and temporally-averaged model thermospheric densities such as the Mass Spectrometer and Incoherent Scatter (MSIS) model [*Hedin et al.*, 1977a, b; *Hedin*, 1983; 1987; 1991] and on such quantities as imprecise absorption and emission (cascade plus direct excitation) cross sections to determine volumn emission rates, are not designed to account for mesoscale thermospheric processes that locally perturb equilibrium conditions for unknown periods of time. Discrepancies between a

modeled and observed auroral (or airglow) emission can indicate local (or global) disruptions to the $[O]/([N_2]+[O_2])$ ratio due to, for example, significant vertical wind activity associated with Joule and particle-precipitation heating, or, more generally, to any process associated with geomagnetic activity, such as large-scale horizontal transport or enhanced "photo"chemistry at high latitudes due to electron-impact dissociation and ionization processes (see Section 1.2.1).

In addition to FPS measurements of upper-thermospheric vertical winds, this thesis presents vertical displacement estimates in km at $\sim 10^4$-10^5 km^2 horizontal spatial scales determined from comparisons of POLAR spacecraft Ultraviolet Imager (UVI) [*Torr et al.*, 1995] OI(135.6)-nm auroral observations—obtained on the same nights as the FPS wind measurements—to the modeled OI(135.6)-nm auroral emission. Employing the electron transport code of *Lummerzheim and Lilensten* [1994] in conjunction with UVI observations of the Lyman-Birge-Hopfield (LBH) auroral emissions of molecular nitrogen in two wavelength ranges, energy flux and characteristic energy of the precipitating electrons are determined. The modeled OI(135.6)-nm auroral emission is then determined from the modeled thermospheric response to electron precipitation and the inferred energy flux and characteristic energy. Lastly, discrepancies between the modeled OI(135.6)-nm auroral brightness and its corresponding UVI-observed OI(135.6)-nm brightness identify thermospheric composition perturbations relative to the model thermosphere. The vertical displacement, referred to as the column shift, acts as the composition perturbation to the model thermosphere and is determined by matching the OI(135.6)-nm modeled brightness to the UVI OI(135.6)-nm observations. The column shift is a new modification to the transport code of *Lummerzheim and Lilensten* [1994] that characterizes the time-integrated vertical wind effect of height displacement of air parcels at auroral-emission altitudes in the model neutral thermosphere. The column shift parameterizes such vertical wind effects as bulk neutral transport (due to long-lived, intermediate- to large-magnitude vertical winds), small-scale eddy mixing along a column of thermosphere (due to the random, persistent small- to intermediate-magnitude vertical motion that prevails throughout the thermosphere), and the overall disruption of diffusive

equilibrium by vertically displacing the MSIS-90 neutral model $[O_2]/[N_2]$ and $[O]/([N_2]+[O_2])$ mixing ratios used in the transport code and subsequently redistributing the O, O_2, and N_2 densities at each model thermospheric pressure level to match the new ratios. Modeled auroral emission profiles computed by the transport code depend accordingly on the varying column shift values. Thus, the column shift's interpretation is two-fold; a parameter that reveals the height displacement of air parcels due to vertical winds, and a parameter that also characterizes the discrepancy between the model neutral thermospheric composition and the actual composition in the altitude range of the auroral emissions, which can be the result of vertical wind activity but may also be due to such processes as those mentioned above; *e.g.*, large-scale horizontal transport or enhanced high-latitude "photo"chemistry.

The column shift estimates that are determined from the OI(135.6)-nm observed-to-modeled brightness comparisons are presented here in two formats. The first format is a consequence of the nature of the UVI auroral-brightness observations, which are 2-D images of the aurora collected every 37 s (discussed more in Chapter 2). The UVI auroral-image data are binned according to latitude and magnetic local time at horizontal spatial scales of $\sim 10^4$ km^2 into 2-D maps that are centered about Inuvik (discussed more in Chapter 3). Thus, a time series of 2-D maps of column shift estimates are one by-product of the analysis techniques developed here. Spatial averaging of the column shift values in the vicinity of Inuvik's or Poker Flat's latitude and local time in each 2-D column shift map results in a time series of point-like column shift estimates over the respective site, which is the second data format. The time series of spatially-averaged column shift values can then be compared to the time series of vertical wind measurements.

Although unanticipated limitations associated with modeling of the OI(135.6)-nm auroral emission make the absolute column shift estimates indeterminate, the 2-D column shift maps still characterize the spatial morphology of thermospheric composition variations associated with auroral forms relative to the model neutral thermosphere, similarly to other composition studies that infer thermospheric O density variations from comparisons of auroral-brightness ratios [*e.g. Hecht et al.*, 1989; 1999; *Lummerzheim et*

al., 1990] and even if the variations are not necessarily due to vertical winds (*e.g.*, instead due to horizontal transport). In addition, many of column shift magnitudes do fall within a range that is expected of height displacements of air parcels (~10-80 km at auroral-emission altitudes) due to significant vertical wind activity, and the point-to-point variation in the column shift time series is often reasonable (with some exceptions). Examples of selected 2-D column shift maps from two nights of observations are shown, and some of the difficulties encountered with modeling of the OI(135.6)-nm auroral emission are also illustrated in these examples. These difficulties are discussed later with the presentation of additional analysis of the column shift data sets.

Some correlation is visually apparent between the point-to-point time series comparisons of the spatially-averaged column shift values and the Inuvik and CRL-FPS vertical wind measurements, but in general, cross correlation analysis of the time series proves to be inconclusive except for one night's data. Insufficient knowledge of the time history of the thermospheric air parcels moving through the FPS fields of view during observations significantly hinders the interpretation of these time series comparisons. Initially, it was the goal of this study to definitively correlate thermospheric composition perturbations with vertical wind activity via the comparisons here between the vertical wind and column shift time series, and indeed, several examples are apparent of vertical wind-induced column shifts in the time series comparisons, which are examined in detail. Additionally, one night's column shift and vertical wind data from Inuvik exhibits a high correlation coefficient. Spectral analysis of the vertical wind and column shift time series from this night also identifies matching periodicities in the two data sets, potentially identifying equivalent gravity wave oscillations in the data sets. However, none of the other column shift time series presented here were sufficiently lengthy to warrant a search for periodicities, and it was therefore decided that additional analysis of the column shift and vertical wind data sets be considered in order to establish a more-definitive link between vertical winds and column shifts.

Ultimately, it is an analysis of the distribution of column shift values and vertical wind measurements that convincingly links column shifts to vertical winds. A histogram

analysis of the eight column shift data sets finds that a distinct vertical wind signature is present in the distribution of column shift values. The column shift values from each night's data set are binned in histogram format, including those values inferred from very weak, uncertain auroral data (the criterion is described in Chapters 3 and 4). Seven of the eight histogram distributions are characterized very well by a numerical fit of two distinct Gaussian distributions, one narrow and one broad, prompting further speculation that column shifts, as envisioned, have a physical interpretation. The two-Gaussian distribution of the column shift data sets has a convincing basis for comparison to vertical wind data. Histogram analysis of the Inuvik FPS vertical wind data and of a large data set of upper-thermospheric vertical wind data obtained with an FPS [*Hernandez et al.*, 1990] at the South Pole station during quiet-time geomagnetic conditions at solar minimum and active-time geomagnetic conditions at solar maximum is also presented. The distribution of auroral-latitude vertical wind measurements also exhibits a distinct two-Gaussian distribution of one narrow and one broad Gaussian, indicative of two distinct geophysical phenomena at work in the high-latitude thermosphere. Vertical wind speeds associated with the narrow Gaussian, which has a full-width at half-maximum $\equiv\xi$ of ξ_{nar} = 25-36 m·s^{-1}, are indicative of the random, small- to intermediate-magnitude vertical winds (±1-30 m·s^{-1}) that are due to solar radiative input and weak Joule and particle-precipitation heating which prevails in the auroral-latitude thermosphere almost all of the time. Vertical wind speeds associated with the broad Gaussian, ξ_{brd} = 46-96 m·s^{-1}, are attributed to intermediate- to large-magnitude vertical winds ($\geq$30-50 m·s^{-1}) due to significant Joule and particle-precipitation heating events.

The distribution of column shift values, ideally, should also exhibit the characteristics of a vertical wind distribution, if indeed vertical winds are responsible for the height displacement of air parcels and the UVI-inferred auroral model outputs of energy flux, characteristic energy, modeled OI(135.6)-nm brightness and column shift are valid. In general, the eight column shift histogram distributions are all significantly biased towards the left (the negative end) of the zero column-shift value; *i.e.*, in general, many more negative (downward) column shifts are inferred than positive (upward) shifts,

which is not physically reasonable and speaks to the difficulties encountered here that are associated with the modeling of FUV auroral emissions (discussed more below). The numerically-fitted first Gaussian of each column shift histogram distribution is centrally located around the histogram peak, and is biased towards the negative end of the zero column-shift value. In general, the second Gaussian of each column shift histogram is considerably more biased towards the negative end of the zero column-shift value, is much broader, and is nearly as pronounced as the first Gaussian. A significant number of the column shift values associated with these broad Gaussians are highly negative (less than –100-200 km) and have no physically-realistic interpretation.

Though the column shift distributions are biased towards negative column shift values, the full-width at half-maximum $\equiv \zeta$ of the narrow Gaussian of each column shift data set (ζ_{nar} = 26-37 km for the geomagnetically-quiet Inuvik data) is characteristic of the time-integrated, height-displacement effect of fairly long-lived (*e.g.*, ~15 min), intermediate-magnitude (~30 $m \cdot s^{-1}$) vertical winds; *i.e.*, wind speeds either associated with the narrow Gaussian (ξ_{nar} = 25-36 $m \cdot s^{-1}$) or the broad Gaussian (ξ_{brd} = 46-96 $m \cdot s^{-1}$) in the histogram distributions of the Inuvik FPS and South Pole vertical winds. Depending on the duration and magnitude of a particular intermediate-magnitude vertical wind, the wind would be expected to act in and across 1-2 scale heights in the lower thermosphere and one scale height in the middle-to-upper thermosphere and transport air parcels an amount specified by the range in width of the narrow Gaussians in the column shift distributions, which is comparable to the pressure scale height $H = k_B T/mg \approx$ 10-80 km at the lower- to upper-thermospheric auroral-emission altitudes of ~120-300 km. For example, a 30 $m \cdot s^{-1}$ vertical wind lasting for 15 min will transport air parcels 27 km.

In assessing the significance of the broad Gaussians in the column shift distributions, the full-width at half-maximum of the broad Gaussians is ζ_{brd} = 73-100 km. The low end of this range may be attributed to long-lived (~30 min), large-magnitude ($\gtrsim$50 $m \cdot s^{-1}$) vertical winds of the kind associated with the broad Gaussians of the Inuvik FPS and South Pole vertical wind distributions, transporting air parcels across two or three scale heights ~50-80 km from the lower thermosphere to the upper thermosphere or vice versa.

However, the high end of the ζ_{brd} = 73-100 km range is essentially due to the extent which the highly-negative column shift values of less than –100 km appear in the column shift data sets. These highly-negative column shift values—and the fact that all of the histogram distributions are biased towards negative values—point to the considerable uncertainty associated with modeling of FUV auroral emissions due to such quantities as uncertain emission (cascade plus direct excitation) and absorption cross sections and imprecise model density profiles. The uncertainty in quantities inferred from auroral model outputs such as energy flux, characteristic energy [*e.g. Lummerzheim and Lilensten*, 1994; *Germany et al.*, 2001], and the modeled OI(135.6)-nm emission (discussed in Chapter 3), and experimental uncertainties such as airglow removal from the UVI auroral images may be hindering the interpretation of the column shift data sets (discussed in Chapter 4).

With this in mind, a brighter-aurora criterion was applied to the selection of UVI auroral data to retain. The number of column shift estimates retained with the new criterion is considerably decreased, but the remaining distribution of column shift values from each night is noticeably improved, in that the broad Gaussian is strongly suppressed while the characteristics of the narrow Gaussian are essentially unchanged, $\zeta_{nar,brght}$ = 22-36 km. Furthermore, though the broad Gaussians are strongly suppressed using the brighter-aurora criterion, the brighter-aurora column shift distributions do retain the broad-Gaussian signature. Use of the brighter-aurora criterion gives some credibility to the possibility that the remaining broad-Gaussian column shift values are due to long-lived, large-magnitude vertical wind activity associated with significant auroral-related heating events and are not attributed to experimental or modeling uncertainties. The full-width at half-maximum of the brighter-aurora broad Gaussians is now more closely comparable to two or three thermospheric scale heights, $\zeta_{brd,brght}$ = 51-76 km, and is indicative of an altitude range that a long-lived, large-magnitude vertical wind may be expected to act. Presumably, most of the highly-negative column shift values that are suppressed by the brighter-aurora criterion are associated with such experimental uncertainties as airglow removal from UVI auroral data and skeptically-inferred energy

flux values associated with very weak and suspect auroral data. These topics are discussed in Chapter 4.

Lastly, the dilemma of all of the column shift histogram distributions exhibiting a bias towards negative column shift values is considered. In general, this would indicate that either the auroral model of *Lummerzheim and Lilensten* [1994] is underestimating the OI(135.6)-nm auroral brightness on average when compared to the UVI OI(135.6)-nm observations, or that one or more of the parameters used to infer the modeled OI(135.6)-nm auroral brightness (*i.e.*, energy flux or characteristic energy) is inaccurate. As was stated, possible sources of error in auroral modeling are uncertain cross sections and inaccuracies in the neutral model densities. An assessment of cross-section uncertainties and how these contribute to the discrepancies that exist between auroral models is presented in *Lummerzheim and Lilensten* [1994] and *Germany et al.* [2001] and is discussed further in Chapters 3 and 4. Possible corrections to the MSIS-90 thermospheric O density at auroral-emission altitudes which the column shift inherently introduces into the model density profiles are also considered in Chapter 4. In addition to these sources of error, a statistical analysis of selected 2-D map examples of the observed and modeled OI(135.6)-nm brightnesses reveals an apparent deficiency in the estimation of energy flux at different characteristic energies that affects the estimation of the modeled OI(135.6)-nm auroral brightness. In the examples where the energy flux appears to be underestimated, the determining factor is the range of characteristic energies of the precipitating electrons. Thus, possible avenues of improvement to the MSIS-90 atomic oxygen density profile and to determinations of energy flux from FUV auroral observations are identified that may help with the determination of absolute column shift estimates and ultimately with comparisons between time series of vertical wind measurements and column shift values.

This Chapter 1 has described at length some of the global-scale processes (*e.g.*, solar radiative input, high-latitude Joule and particle-precipitation heating) that are responsible for the composition and density, wind and temperature patterns that are observed in the thermosphere. The review presented in Section 1.1 describes the

thermosphere's horizontal wind system and its quasi-equilibrium configuration associated with the Sun's UV and X-ray radiative input, ending with a discussion of the high-latitude processes that contribute to and modify this wind system and disturb the equilibrium. High-latitude, intermediate-to-large magnitude vertical winds associated with auroral-related processes and their effects on the thermosphere's state are discussed in detail. Section 1.2 presents a general overview of the thermosphere's structure, composition and photochemistry, leading into a discussion of diffusion and diffusion time scales in the thermosphere and diffusive equilibrium. The discussion here in Section 1.3 illustrates the correlation between heating, vertical winds, and composition response and ends with a general overview of the results of this study and what is to be presented in the rest of the thesis.

Chapter 2 describes the instrumentation used for this study. A general overview of Fabry-Perot interferometry is presented in Chapter 2. Appendix D describes some aspects of Fabry-Perot spectrometry in greater detail. The type and overall design of the FPS located at Inuvik, NT, Canada are described in Chapter 2, as are several upgrades to it that make it a workable remote instrument. Relevant spectroscopic quantities of the Inuvik FPS are also presented.

In presenting a review of the Global Geospace mission's POLAR spacecraft Ultraviolet Imager (UVI) [*Torr et al.*, 1995], Chapter 2 discusses in some detail processes relevant to airglow and auroral emissions and how spectroscopic studies of the aurora can be used to infer the characteristic energy and energy flux of precipitating electrons and density perturbations to the neutral model thermosphere. The POLAR spacecraft's orbital trajectory is described, which benefited but also restricted certain aspects of this study, and several spacecraft deficiencies relevant to the analysis of the UVI data are also discussed. The wavelength passbands of the five UVI filters are presented, as is the motivation for the selection of these wavelength ranges.

Chapter 3 discusses the data acquisition and analysis techniques that are employed in this study relevant to the Inuvik FPS and the POLAR spacecraft UVI instrument. In presenting those methods applicable to the Inuvik FPS OI(630.0)-nm observations, two

general prerequisites, scattering and the zero-Doppler shift reference, are considered with regard to thermospheric vertical wind data. The Doppler shift formula and its application to the Inuvik FPS are discussed. The analysis methods of *Conde* [2002] and *Conde* [2001] that were employed in this study to reduce the Inuvik FPS image data first to one-dimensional spectra and then to their respective Doppler shifts, widths, and intensities is described in some detail. The technique that was developed to account for étalon drift in the Inuvik FPS vertical wind measurements (*i.e.*, changes in the étalon's optical path length due to the varying atmospheric pressure and ambient temperature) is described in detail. Lastly, the time series of vertical wind estimates from the seven nights of Inuvik FPS observations are presented with their statistical significance and respective uncertainties in the wind measurements due to these data reduction techniques.

In discussing the techniques in Chapter 3 that were developed to infer the energy flux and characteristic energy, the modeled OI(135.6)-nm auroral emission, and the column shifts from UVI observations of the LBH auroral emissions of molecular nitrogen and the OI(135.6)-nm auroral emission, the method used to remove airglow from the auroral images is first described. The binning process of the UVI auroral image data into horizontal spatial scales comparable to a vertical wind field is also described. Next, a description is presented of how the output from the auroral model of *Lummerzheim and Lilensten* [1994] is merged with the wavelength passband data of the UVI instrument to determine the expected response of the UVI instrument at the prescribed wavelength bandwidths to FUV aurora of 1 $mW \cdot m^{-2}$ of energy flux over a range of characteristic energies. The method of determining the energy flux, characteristic energy, and modeled OI(135.6)-nm emission from the expected UVI instrument response and the UVI observations of the LBH emissions in two wavelength ranges is then described. Finally, the column-shift modification to the MSIS-90 neutral thermospheric density profiles is described. The expected UVI instrument response for a range of column shift values is presented, and selected examples of 2-D column shift maps inferred from the OI(135.6)-nm observed-to-modeled brightness comparisons are discussed, illustrating the technique as to how column shift values are inferred. A discussion is also presented in the midst of

these other discussions of the uncertainties associated with auroral modeling of FUV emissions and how these uncertainties manifest themselves into errors in energy flux, characteristics energy, and column shift values. Time series of column shift values are then presented illustrating these uncertainties. The encouraging results of the modeled-to-observed OI(135.6)-nm brightness comparisons are discussed, as are the unanticipated and perplexing difficulties encountered with the column shift data sets.

Chapter 4 begins with an important distinction between nadir and off-nadir viewing of the aurora, which affected the UVI observations presented here. Because of the unanticipated problems encountered with the column shift data sets, some statistical properties of the column shift data are presented. The brighter-aurora criterion that was employed to try to make the column shift 2-D maps and time series more presentable so as to aid their interpretation is also described. A 2-D map and time series of the relative column shift is presented, and finally, the time series of vertical wind measurements and column shift values are compared. Cross-correlations are computed, and the time series comparisons are discussed. Several examples of vertical wind-induced composition perturbations are identified, and one of the time series comparisons shows a high degree of correlation. In addition, spectral analysis of the time series in the highly-correlated example identifies a significant periodicity of ~3 hr in both time series, which may be attributed to equivalent gravity wave activity identified in these time series.

The second half of Chapter 4 presents the histogram analysis discussed above of the vertical wind measurements and column shift values. A simple interpretation of the nadir- and off-nadir-viewed column shift values with regard to the UVI viewing geometry of the aurora is presented. The column shift histogram distributions and their characteristics are discussed before and after the brighter-aurora criterion is applied to the column shift data sets. The histogram distributions of the Inuvik FPS vertical wind measurements (and South Pole FPS measurements for confirmation) are also presented. The column-shift correction to the MSIS-90 atomic oxygen density profile at auroral-emitting altitudes is discussed based on the histogram analysis of the column shift values. Finally, one-to-one comparisons of the observed and modeled OI(135.6)-nm brightness

are presented which suggest possible areas of improvement in the determination of energy flux from the observed LBH-L brightness measurements.

Chapter 5 reiterates the conclusions of this study and discusses the possible avenues of improvement to auroral modeling and to the column shift technique. Improvements to the Inuvik FPS are discussed, and a possible experiment which would further explore the validity of the column shift technique is explained.

The Appendices present a broad range of material that is relevant to the overall scope of this thesis. Appendix A presents a general overview of Earth's atmosphere and magnetosphere, describes the Sun's radiative output, and describes radiation deposition in the atmosphere; *i.e.*, the Lambert-Beer exponential law and the optical depth parameter are discussed. Appendix A then goes on to describe radiative equilibrium and derives Earth's effective surface temperature. The adiabatic lapse rate is derived, and finally, some significant features of the lower and middle atmosphere are discussed. Appendix B discusses winds, tides and waves in the thermosphere. The application of the momentum equation and other relevant equations to the thermosphere and ionosphere is described, tidal motions of the thermosphere are briefly discussed, and some details of buoyancy wave analysis and gravity wave properties are described. Appendix C discusses particular molecular properties of the thermosphere. Thermal equilibrium, collisions and mean free path in the thermosphere are described, general diffusion principles are discussed, and ion diffusion in the thermosphere is described. Appendix D discusses some general principles of Fabry-Perot spectroscopy. The ideal Fabry-Perot interferometer is described, its relevant spectroscopic quantities are derived, and inevitable deviations from the ideal are discussed. Appendix E discusses two tools used for the analysis of and comparison between unevenly-sampled time series. The cross-correlation calculation between two distinct time series (at different lags) is described, and finally, Lomb-Scargle spectral analysis of unevenly-sampled time series in order to search for periodicities in the time series is described.

Chapter 2 Instrumentation

2.1 Introduction to Fabry-Perot Spectroscopy

The measurement of such upper-atmospheric (≳100 km altitude) quantities as bulk flow speed and temperature is possible through methods devised to take advantage of the thermosphere's airglow and auroral emissions. The Fabry-Perot Spectrometer (FPS) is an instrument that provides this capability. An FPS is a high-resolution spectrometer that can resolve the wavelength spectrum of, for example, a radiative emission emanating from a particular thermospheric (or ionospheric) species, provided the spectrum is sufficiently narrow. In principle, the emission's resolved wavelength spectrum can then be compared to an absolute wavelength reference to yield the emitting species' line-of-sight wind speed through the Doppler formula and its temperature through Maxwell-Boltzmann relations. These quantities, if determined from a neutral emission of sufficient radiative lifetime, are generally characteristic of the bulk flow speed and temperature of all the neutral species prevailing in the altitude range of the emission [*Aruliah and Rees*, 1995].

Fabry-Perot spectroscopy is based upon the optical phenomenon of interference, in which two or more light waves emanating from separate radiative sources, or that have been split from one source, interact by obeying the superposition principle [*e.g. Born and Wolf*, 1999]. The central component of an FPS is the étalon, which utilizes the method of multiple-beam-amplitude splitting interference, also referred to as division-of-amplitude. Essentially, an étalon consists of two semi-transparent mirrors held parallel at a fixed separation. In the étalon cavity, the primary wavefronts of the incident radiation are separated into many components of decreasing electric field scalar amplitudes, which travel different optical path lengths and then are superimposed. An FPS usually only operates at night, though certain FPS arrangements allow for daytime operations, and an étalon can be utilized at a variety of wavelengths. A useful property of the FPS is its large étendue (*i.e.*, its light-gathering capability) when compared with other spectrometers, such as the grating spectrometer and prism [*e.g.*, see *Hernandez*, 1986, and references therein],

making the FPS the spectrometer of choice for high-resolution studies when a source signal is weak. A more detailed introduction of Fabry-Perot spectroscopy and the ideal étalon, such as its reflection and transmission characteristics (the Airy formula) and spectroscopic properties (*e.g.*, finesse, free spectral range), is presented below and in Appendix D. Also in Appendix D are some examples of how a real étalon deviates from the ideal, methods for characterizing these deviations, and methods for determining such quantities as an étalon's reflectance, real finesse and instrument function. The FPS currently located in Inuvik, Northwest Territories, Canada, its hardware and software layout, recent upgrades, and spectroscopic and transmission properties is described next.

2.2. The Inuvik, NT, Canada Fabry-Perot Spectrometer

The Inuvik FPS has been used to measure winds and temperatures in the upper and lower thermosphere through observations of the OI(630.0)-nm and OI(557.7)-nm airglow and auroral emissions, respectively. The Inuvik FPS utilizes a Queensgate Instruments model ET116 fixed-gap, capacitance-stabilized, servo-controlled étalon [*Atherton, et al.*, 1981]. The étalon is open to air and operates at a gap width of 20 mm. The plates were originally polished to $\lambda/100$, where λ is the wavelength of the radiation, and the capaitance-stabilization system generally maintains a gap stability of $\lambda/3000$ [*Hicks, et al.*, 1984].

Several quantities define an étalon's spectroscopic capability, and one is its free spectral range $(\Delta\lambda)_{fsr}$. The wavelength spectrum of a radiation source can be determined from its étalon-induced radial intensity distribution, provided the radiation's bandwidth is small compared with the étalon's free spectral range [*Conde*, 2002]. In general, an étalon's free spectral range [*e.g. Hecht*, 1984; also see Appendix D] is given by

$$(\Delta\lambda)_{fsr} = \lambda^2(2n'h\cos\theta)^{-1}, \tag{2.1}$$

where n' is the index of refraction of the medium between the étalon's mirrored surfaces, h is the gap width, and θ is the incidence angle of the incoming radiation normal to the étalon plates. The index of refraction of air is n'_{air} = 1.000293 at standard temperature and pressure (STP) and is dependent on both these quantities. At STP, the Inuvik FPS has a free spectral range (at near-normal incidence, $\theta \approx 0°$, $\cos\theta \approx 1$) of $(\Delta\lambda)_{fsr,Ivk,557}$ = 0.007773 nm at λ557.7 nm and $(\Delta\lambda)_{fsr,Ivk,630}$ = 0.009920 nm at λ630.0 nm.

Radiation in an étalon cavity is modulated according to the Airy formula (discussed below). An étalon transmits a set of bright circular rings on a dark background and reflects a set of dark rings onto a light background. The rings are referred to as fringes of equal inclination, an example of which is shown below. In the étalon cavity, the phase difference δ between the interfering wavefronts [*e.g. Hecht*, 1984; also see Appendix D] is given by

$$\delta = kP \pm \phi \approx 4\pi n' h \lambda^{-1} \cos\theta = 2\pi m, \qquad (2.2)$$

where $k = 2\pi\lambda^{-1}$ is the vacuum wave number, $P = (2n'h)\cos\theta$ is the optical path length between interfering wavefronts, ϕ is the phase shift due to the étalon's mirrored surfaces (generally negligible if h is sufficiently large), and m is the orders of interference of the fringes, $m = 0, 1, 2, 3,\ldots$ The order of interference of the Inuvik étalon's central fringe at STP is $m_{cent,557.7} = 71744$ at λ557.7 nm and $m_{cent,630.0} = 63510$ at λ630.0 nm. The orders of interference will drift, however, with the changing optical path length, which varies with the varying index of refraction of air due to ambient pressure and temperature changes.

The Inuvik FPS is referred to as an imaging spectrometer. The term "imaging" has different meanings for different applications, but here, an imaging FPS is one that images the étalon's fringes onto a 2-D detector, such as a TV camera [*e.g. Sivjee et al.*, 1980] or a charged-coupled device (CCD), as opposed to an FPS that employs a one-dimensional (1-D) detector such as a photomultiplier tube (PMT), only utilizing the étalon's central order of interference [*e.g. Hernandez and Mills*, 1973]. A simple representation of an imaging FPS is shown in Figure 2.1 [*Conde*, 2002]. The spectroscopic variable relevant to this arrangement is the incident angle θ of the radiation, and because of this design, a focusing lens behind the étalon can provide a 1:1 mapping of the étalon's viewing direction onto position coordinates x and y of a 2-D image [*Conde*, 2002]. The technique as it applies to the Inuvik FPS is described in more detail later and in Chapter 3. Of particular advantage to this design is its utilization of several orders of interference of the étalon—increasing the amount of usable signal collected by the FPS—rather than merely the central order like such 1-D arrangements as the one described in *Hernandez and Mills* [1973].

The Inuvik FPS has several features that make it particularly useful for observing thermospheric winds at auroral latitudes and foremost is its portability. A general lack of

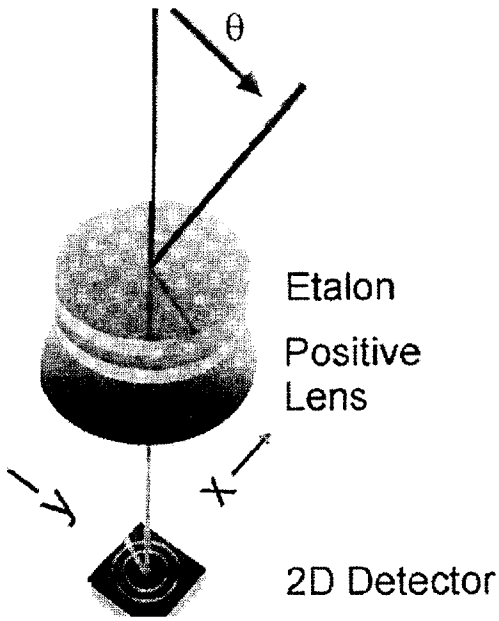

Figure 2.1. Schematic representation of the major components of an imaging FPS. Radiation of incident θ is mapped onto a two-dimensional detector of coordinates x and y. Thus, the orders of interference m, which are a function θ, can be written in terms of x and y [Figure from *Conde*, 2002].

data coverage on such upper-atmospheric quantities as densities, winds, temperatures, and electric field strengths (particularly at auroral latitudes where it is often difficult to deploy ground-based instrumentation because of harsh winters and sometimes-lacking social and technological infrastructure) is always a problem for modelers in the upper-atmospheric research community who require real-time or near real-time input parameters from around the globe to make upper-atmospheric wind and temperature predictions based on existing geomagnetic conditions. The Inuvik FPS was designed with this very issue in mind and was assembled within a deployable trailer that can travel anywhere there are roads, electricity, and, preferably, little extraneous light. A simple block diagram of the current configuration of the Inuvik FPS is shown in Figure 2.2.

As a deployable spectrometer, the Inuvik FPS has evolved considerably from its original design because of several upgrades during its seven years in Inuvik. The FPS was deployed in December, 1998, and initially was configured to measure upper-thermospheric horizontal and vertical winds through observations of the OI(630.0)-nm emission in the

four horizontal directions of magnetic north, south, east and west and the zenith direction, respectively. The FPS was reconfigured for strictly zenith observations (as indicated in Figure 2.2) in February, 2000, and all but two of the vertical wind data sets presented in this thesis are of upper-thermospheric vertical winds acquired with the FPS from February, 2000 to January, 2001. Two other vertical wind data sets presented here were acquired at Poker Flat, AK in March, 2001 with an FPS owned and operated by the Communications

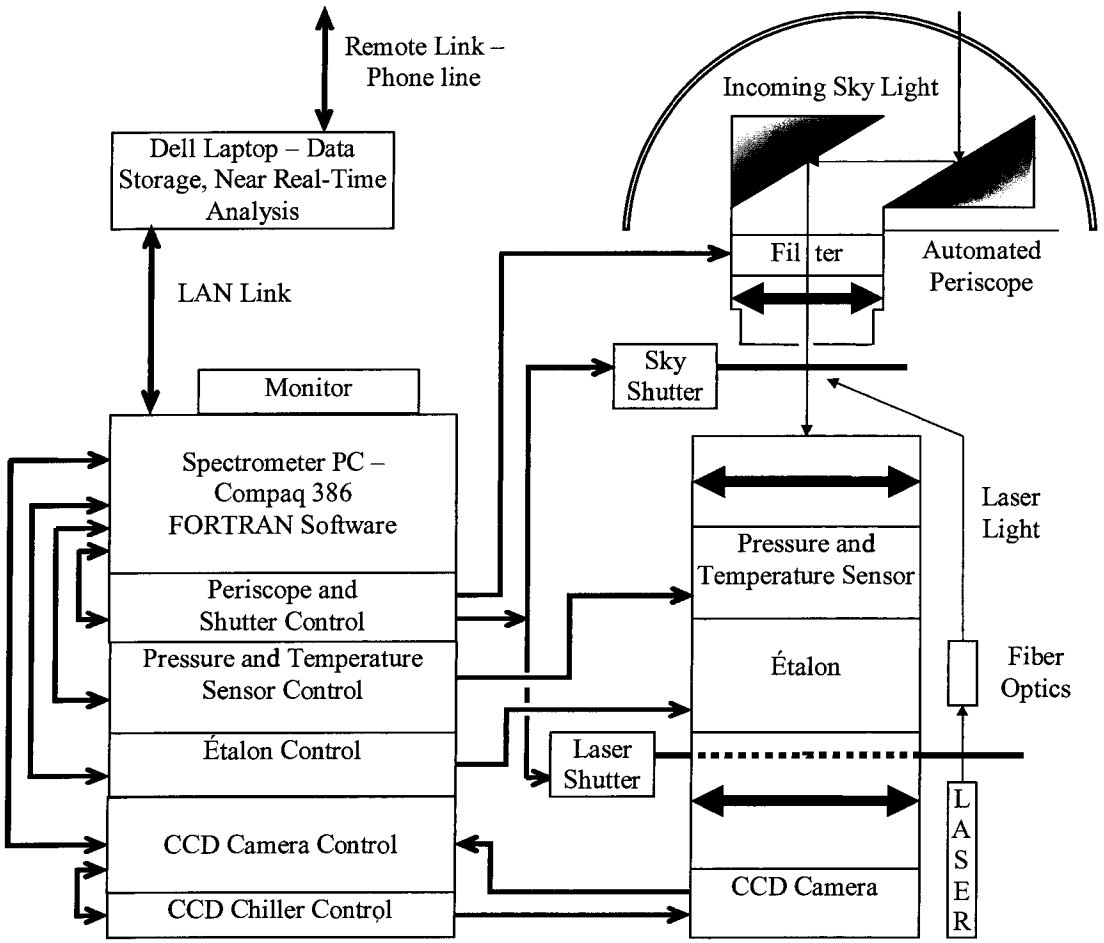

Figure 2.2. Block diagram indicating the major components of the Inuvik FPS. The bold, straight black lines with arrows on each end, ↔, on the diagram's right-hand side represent lenses. The bold black line coming from the right-hand side of the sky shutter box represents the actual sky shutter, and the bold straight-dashed-straight black line is the actual laser shutter. The two shaded triangles represent the mirrors that reflect skylight into the FPS assembly. The curved shape on the top, right-hand side represents the dome on the trailer roof. See the text for a discussion of the various components.

Research Laboratory (CRL) of Japan [*Ishii et al.*, 1997]. Currently, the Inuvik FPS mode of operation is to observe of the OI(557.7)-nm airglow and auroral emission emanating from altitudes of ~100-140 km strictly in the zenith, measuring vertical winds and temperatures in the lower thermosphere in support of the NASA TIMED satellite mission.

The Inuvik FPS begins and ends operations when the solar depression angle reaches 8°, and can acquire data from mid-August to late April, though data coverage is minimal at the ends of this range. Pre-selected FPS exposure times that provide enough signal-to-noise during even the weakest airglow are 200 s at λ630.0 nm and 140 s at λ557.7 nm. Data processing between observations, however, sets the temporal resolution of the wind measurements at ~4 and ~3 min, respectively. The FPS has a narrow field of view of ~1.5°, allowing it to observe with only minor concerns of contamination from moonlight, and can measure vertical winds in the zenith and horizontal winds in eight azimuthal directions (at angle of 30° off the horizon) because of its automated periscope system. The FPS 2-D detector is a Photometrics PM512 CCD with a pixal array of 512 × 512, operating at an optimum temperature of –45 °C maintained by a chiller unit.

The current location of the Inuvik FPS (geographic latitude 68.3°N, longitude 226.5°E; L = 9.9) is unique in that it is located where the quiet-time auroral oval resides. Time series of thermospheric vertical wind measurements display a variety of characteristics at high latitudes, such as large-magnitude wind events, diurnal variation, and periodicities due to gravity waves [*e.g. Rees et al.*, 1984; *Smith and Hernandez*, 1995; *Innis et al.*, 1996; 1997], and the ability of an FPS to estimate wind speed is limited only by its ability to resolve the wavelength spectrum of a radiation source. Though wind speed estimates of <1 $m \cdot s^{-1}$ are possible with the existing stability of Queensgate étalons [*Hicks et al.*, 1984], wind speeds that fall within the range of typical FPS wind-measurement errors, ±5-30 $m \cdot s^{-1}$, due to other sources of error are in general considered unreliable. This topic is discussed in much greater detail in Chapter 3. These concerns are not a significant issue to scope of this study since the study focuses on the long-lived, intermediate- to large-magnitude vertical winds of the kind described in Chapter 1. During even quiet geomagnetic conditions, the Inuvik FPS often still observes these

geophysically-significant vertical wind events that are associated with the small oval's narrowly-confined energy inputs.

The Inuvik FPS has seen past service in Fort Nelson, British Columbia, Canada and Eagle, AK and was originally designed and built by current UAF Geophysical Institute Director Roger W. Smith in the early 1990s. The instrument has been altered some from its initial configuration, although the major components (*e.g.*, the étalon, CCD camera, periscope) have not changed, and the layout shown in Figure 2.2 is not much different from the original design. However, the software and hardware modifications that I have made to the FPS during its time in Inuvik as part of this thesis work have allowed it to run much more reliably than before, with better day-to-day characterization of instrument parameters, and without the necessity of near-constant attention from technical personnel.

Simply put, the Inuvik FPS operates as follows: at night, thermospheric airglow and auroral light, depicted in the upper right-hand corner of Figure 2.2, enters the FPS via a zenith-looking mirror (depicted in Figure 2.2 as a shaded triangle), which reflects the light towards a second mirror attached to a periscope. The periscope mirror redirects the light downward along the optical axis of the FPS assembly, with a filter blocking out any extraneous light. The airglow and auroral radiation passes through the filter, a pinhole aperture and then through the étalon, which modulates the radiation according to the Airy formula (described below and in Appendix D). A lens focuses the sky-light fringe image onto the CCD detector. Lenses are indicated in Figure 2.2 by the bold black lines with arrows on each end, ↔. The CCD detector has a small door that is opened and closed by commands issuing from the CCD Camera Control—which is controlled by FORTRAN code running on a Compaq 386 Spectrometer PC (indicated in Figure 2.2 on the left-hand side)—exposing the detector to the modulated radiation for a specified amount of time. Fringe images are transferred from the CCD camera to the Spectrometer PC and stored on the PC hard disk. The process continues throughout the course of a data-acquistion period, with regular laser exposures taken in between sky exposures to characterize étalon performance. Raw image data is periodically dumped from the Spectrometer PC to a LAN-linked Dell laptop that performs data storage, executes the raw image data's

high-end analysis (wind and temperature determination), and sends the analysis files back to the Geophysical Institute in Fairbanks. FPS hardware and functionality, in general, is controlled by the FORTRAN code running on the Spectrometer PC, which communicates with and controls the different peripheral components of the FPS, such as opening and closing the sky shutter when night or day arrives, respectively, opening and closing the CCD shutter during exposure times, turning the periscope, and updating the Spectrometer PC screen with the parameters relevant to the data analysis and FPS operations. The Spectrometer PC's operating system is DOS 6.22, and the laptop runs Windows 2000.

An important first modification to the FPS after its deployment was to repair the FORTRAN code running on the Spectrometer PC. Data acquisition would often cease during operation at any moment without warning, and dependable operation of the FPS did not occur until the software bugs were traced and corrected. One other vital software modification initially implemented by Roger Smith and updated several times by me was to include actual data storage of the raw Fabry-Perot fringe patterns that are imaged onto the CCD camera. The new data item was an addition to a reduction-to-radius-squared procedure (described briefly in Chapter 3) that was used previously for determination of the wavelength spectrum. The significance of raw FPS image data is discussed later.

Two hardware modifications I implemented to the instrument's overall design have contributed significantly to its remote-site reliability. First, a second shutter assembly over the laser (see Figure 2.2) was installed in November, 2001, permitting laser exposures to be acquired during nighttime operations. Prior to this, a technician would enter the trailer once or twice a week and execute laser exposures separate from normal night-to-night operations, providing étalon characterization only then. During data compaigns, I would execute laser exposures more often, generally several times a day. The étalon's instrument function (*i.e.*, the mathematical function describing its working passband) is determined from the laser exposures (described more below and in Chapter 3).

With the new configuration, nighttime operations begin with a laser exposure while the sky shutter is closed. The laser shutter then closes as five sky exposures are acquired. The sky shutter closes as the laser shutter reopens and another laser exposure is obtained.

This procedure continues through the night and allows for the étalon's characterization during operation instead of on only a weekly basis. This procedure also, ideally, allows for étalon drift correction in the estimated fringe peak positions of the 1-D sky spectra, which have been inferred from the 2-D sky fringe images (described in detail in Chapter 3). Because the étalon's optical path length changes during operation due to changes in the ambient pressure and temperature, the location of the orders of interference of a frequency-stabilized laser will drift with the varying optical path length. This information can be used to correct for the drift in the sky-spectra peak position information.

The last major hardware upgrade to the Inuvik FPS involved the installation of the Dell laptop computer identified in Figure 2.2. The laptop acts as the storage device for raw FPS image data and also executes the analysis of the fringe images; *i.e.*, conversion of FPS raw image data into wind, temperature, and relative airglow- and auroral-intensity estimations. Installation of a network card into the Spectrometer PC and its configuration was required to facilitate LAN communications between the laptop and PC. Significant modifications to the DOS batch files running the PC were also required to implement communication procedures, in general and particularly during FPS operation times.

The laptop's large hard disk permits image data to be stored using 16 bits rather than 8 bits, which was the case originally when the FPS used ZIP disks to store the raw images. The laptop also provides remote access by phone, and data or software files can be downloaded from or uploaded to it. Software upgrades can also be uploaded to the Spectrometer PC if necessary via a PC batch file command that has the PC search for software updates on the laptop once per day. Lastly, the laptop provides near real-time analysis of the previous night's data by executing each day a software package described in *Conde* [2002] and *Conde* [2001]. Currently, the laptop's analysis computes estimates of lower-thermospheric vertical winds and temperature and the relative OI(557.7)-nm airglow and auroral intensity. These data are uploaded once per day to the Geospace Environment Data Display System (GEDDS) server at the Geophysical Institute.

The analysis software of *Conde* [2002] and *Conde* [2001] is described in detail in Chapter 3, and one of its major benefits is its determination of the étalon's real finesse N

and instrument function directly from modulated laser light without *a priori* knowledge of the reflectance R of the étalon plates' mirrored surfaces or any existing plate defects (see Appendix D for a discussion of étalon reflectance and defects). The sharpness of an étalon's fringes is defined by several quantities, and one of these quantities is an étalon's ideal reflectivity finesse N_R, which is given by [*e.g. Hecht*, 1984; also see Appendix D]

$$N_R = \pi R^{1/2}/(1-R). \tag{2.3}$$

For typical values of reflectance, $R \sim 0.9$, $N_R \approx 30$, and an increasing R and N_R implies tighter fringes. In general, the real finesse N of an étalon is less than its ideal reflectivity finesse because of real-world effects, which is discussed more below and in Appendix D.

As stated earlier, the transmitted flux density I_T of an ideal étalon is described by the Airy formula $\tilde{A}(\delta)$ [*e.g. Hecht*, 1984; also see Appendix D], which is given by

$$\tilde{A}(\delta) \equiv \frac{I_T}{I_0} = \left[\frac{1}{1+F\sin^2(\delta/2)}\right], \tag{2.4}$$

where I_0 is the incident radiation's flux density, δ is the phase difference between fringes defined in Equation 2.2, and $F = 4R/(1-R)^2$ is the coefficient of finesse. The Airy formula is periodic in δ, and when $\delta = 2\pi m$ for the transmitted beams, constructive interference is said to occur. The beams are in phase, and $\tilde{A}(\delta) = 1$. Destructive interference occurs when $\delta = 2\pi(m + 1/2)$. The beams are out of phase, and $\tilde{A}(\delta) = (1 + F)^{-1}$.

An étalon's transmission properties are modified from the ideal by real-world effects, such as plate-coating defects, deviations from parallelism, and the plates' finite size. The real transmission passband will be broadened relative to the Airy profile that is characteristic of that étalon's measured reflectance R [*e.g. Wilksch*, 1985] and determined from Equation 2.4. A typical fringe image from a He-Ne λ632.8-nm laser exposure acquired with the Inuvik FPS is shown in Figure 2.3a, illustrating an étalon's transmission properties. The retrieved 1-D laser spectrum inferred from this image, shown in Figure 2.3b, represents this étalon's working passband; *i.e.*, its instrument function. Also shown in Figure 2.3b is an Airy formula fit to the 1-D spectrum. Reducing the reflectance R of the fitted function has the effect of broadening it, and represents the same effect that a plate defect or a lack of parallelism would have on the étalon's instrument function. The fit

shown in Figure 2.3b uses a reduced reflectance $R_{Rd} = 0.61$, and the étalon's performance capability can now be determined by calculating its real finesse N_{Ivk} using Equation 2.3 and replacing R with R_{Rd}. Thus, $N_{Ivk} \approx \pi R_{Rd}^{1/2}/(1 - R_{Rd}) = 6.29$, which seems low when

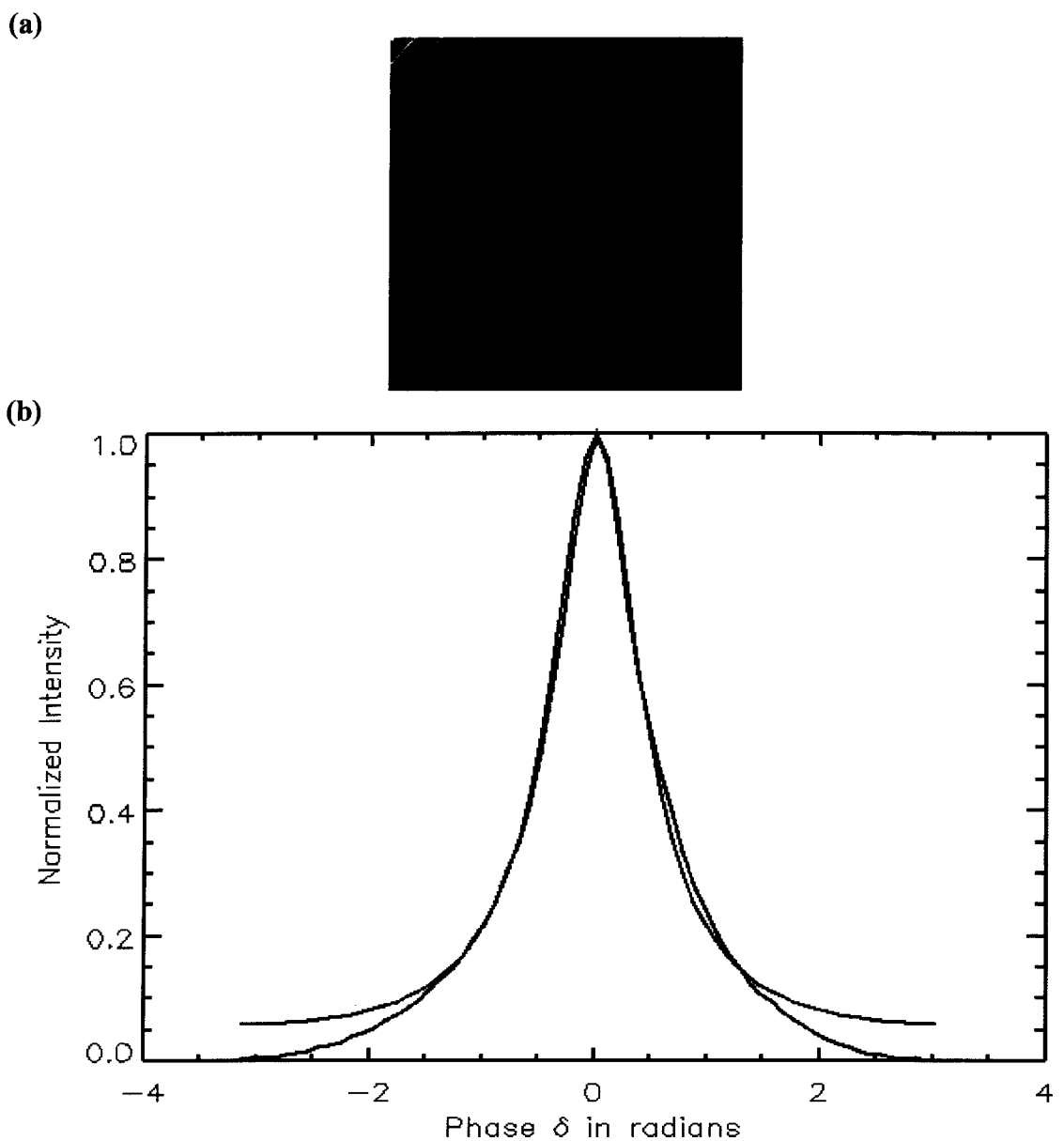

Figure 2.3. Modulated laser light from the Fabry-Perot étalon at Inuvik, the retrieved instrument function, and the Airy formula fit. **(a)** Modulated laser (λ632.8 nm) light. **(b)** The retrieved instrument function and Airy formula fit. The instrument function is in black, and the fitted function is in red. The fitted function used a reduced reflectance $R_{Rd} = 0.61$, which gives a real finesse $N_{Ivk} = 6.29$ for the Inuvik étalon.

compared with the ideal value of $N_R = 30$ for $R = 0.9$. However, N_{Ivk} is comparable to the real finesses of other recent Fabry-Perot spectrometers [*e.g. Biondi et al.*, 1985].

Using N_{Ivk}, it is now possible to determine other spectroscopic characteristics of the Inuvik FPS. For example, the resolving power **R** of a spectrometer expresses its ability to discriminate between the wavelengths in a spectrum when more than one wavelength is present in that spectrum [*e.g. Hecht*, 1984; see Appendix D for more details]. The Inuvik FPS resolving power $\mathbf{R}_{Ivk}$ is given by

$$\mathbf{R}_{Ivk} \approx 2n'h\lambda^{-1}N_{Ivk} = 0.97mN_{Ivk}, \tag{2.5}$$

and the resolving limit $(\Delta\kappa)_{min,Ivk}$ is given by

$$(\Delta\kappa)_{min,Ivk} \approx (2n'hN_{Ivk})^{-1}. \tag{2.6}$$

At λ557.7 nm, the étalon's resolving power is $\mathbf{R}_{Ivk,557.7} \approx 4.5 \times 10^5$ at STP, and at λ630.0 nm is $\mathbf{R}_{Ivk,630.0} \approx 4 \times 10^5$. These values are comparable to a diffraction grating's resolving power, and in general an order of magnitude greater than that of a prism's. An ideal étalon with a reflectance of ~0.9 and $n'h$ ~ 10-20 mm (n of air is ~1) observing visible wavelengths will have a resolving power of $\mathbf{R}_{FPS} \approx 10^6$. Thus, for all the minor problems the Inuvik étalon may have (*e.g.*, reduced true reflectance R due to age and heat; parallelism issues) as illustrated by its low reduced reflectance R_{Rd}, it's resolving power is not reduced much relative to the ideal case and is still fully capable of resolving the wavelengths of interest here. The resolving limit is $(\Delta\kappa)_{min,Ivk} \approx 0.04$ cm^{-1}, and presented in Table 2.1 are the étalon's relevant spectroscopic characteristics. There is one final item to mention concerning the resolving power and limit of the Inuvik FPS. The FPS images the fringe patterns onto a 2-D detector, and in general, the resolving power and limit are functions of θ, $\mathbf{R}_{Ivk} = 2hn'\lambda^{-1}N_{Ivk}\cos\theta$, $(\Delta\kappa)_{min,Ivk} \approx (2n'hN_{Ivk}\cos\theta)^{-1}$ (see Appendix D for their derivations). However, because the field of view of the FPS is small, ~1.5°, the resolving power and limit change very little across the extent of the 2-D fringe images.

One final parameter of the Inuvik FPS to discuss is its étendue U_{Ivk}. The OI(557.7)-nm and OI(630.0)-nm airglow emissions can be very weak ($\leq 10^3$ Rayleighs), and in the absence of aurora, a spectrometer with a large étendue can compensate for weak signal. The étendue U of a Fabry-Perot spectrometer in general is given by the expression

Table 2.1. Spectroscopic properties of the Inuvik FPS.

Spectroscopic variable	λ = 630.0 nm,	λ =557.7 nm
Free spectral range $(\Delta\lambda)_{fsr,Ivk}$ (at STP)	0.009920 nm	0.007773 nm
Central Order of Interference "	63510	71744
Resolving power $\mathbf{R}_{Ivk}$ "	4.0×10^5	4.5×10^5
Real finesse N_{Ivk}	6.29	–
Resolving limit $(\Delta\kappa)_{min,Ivk}$	0.04 cm^{-1}	–
Étendue U_{Ivk}	172 $cm^2 \cdot sr$	–

$$U = A_{plate}\Omega, \tag{2.7}$$

where A_{plate} is the usable (coated) étalon plate area, and Ω is the collection solid angle at the étalon plates. The Inuvik FPS étendue U_{Ivk} is relatively high because it utilizes several orders of interference of the étalon and also because the Queensgate ET116 model's plate area is fairly large. It has a usable plate diameter of 116 mm, and thus, a plate area of $A_{plate} \approx 106$ cm^2. The collection solid angle Ω at the plates is determined from the θ_{max}, the radiation's maximum angle of incidence at the étalon relative to the plate normal. The maximum angle of incidence is determined by examining the laser fringe pattern in Figure 2.3a, which shows that there are approximately five orders of interference being detected at the CCD. The maximum angle of incidence is determined from the condition

$$m_\perp - m_\theta = j, \tag{2.8}$$

where $m_\perp$ is the order of interference at the fringe pattern's center, m_θ is the order of interference at incident angle θ, and j is the fringe number at θ. Recalling that the Airy formula $\tilde{A}(\delta) = [1 + F\sin^2(\delta/2)]^{-1}$ is dependent on the phase difference $\delta = (4\pi n'h\lambda^{-1})\cos\theta = 2\pi m$, a fringe pattern's orders of interference can be written in general as

$$m = 2n'h\lambda^{-1}\cos\theta. \tag{2.9}$$

In Equation 2.8, $m_\perp = 2n'h\lambda^{-1}$ since $\theta = 0°$ at the center of the fringe pattern, and $m_\theta = 2n'h\lambda^{-1}\cos\theta$. Thus, j is given by

$$j = 2n'h\lambda^{-1} - 2n'h\lambda^{-1}\cos\theta = 2n'h\lambda^{-1}(1 - \cos\theta). \tag{2.10}$$

For small incident angles θ, $\cos\theta \approx 1 - \theta^2/2$, and therefore,

$$j \approx 2n'h\lambda^{-1}[1-(1-\theta^2/2)] = n'h\theta^2\lambda^{-1}. \quad (2.11)$$

From this, $\theta = (j\lambda/n'h)^{-1/2}$, and when $j = 5$, $\theta = \theta_{max}$. Therefore, $\theta_{max} \approx 0.013$ radians = 0.72° relative to the étalon normal. The solid angle Ω subtended by θ_{max} in steradians (sr) is approximately given by $\Omega = \pi\theta^2_{max} = 1.63$ sr. With these values, the Inuvik FPS étendue is $U_{Ivk} \approx 172$ cm^2·sr, which is comparable to other FPS étendues [*e.g. Biondi et al.*, 1985; *Rees and Greenaway*, 1983].

The combination of the Inuvik FPS's portability, high étendue, equitable finesse, and recently-increased reliablity and functionality makes it a suitable spectrometer for use at auroral latitudes. How vertical wind measurements are determined from Inuvik FPS raw sky fringe images by the data analysis software of *Conde* [2002] and *Conde* [2001] is described in more detail in Chapter 3. The techniques that were developed to account for the étalon's drift, that is, the changing optical path length of the étalon cavity due to the varying ambient pressure and temperature, are also outlined in Chapter 3.

2.3 Inferring Thermospheric Composition Perturbations from Observations of the Airglow and Aurora

The thermosphere's airglow and auroral emissions are the result of energy deposition and redistribution processes associated with the Sun's UV and X-ray radiative input into the thermosphere and the solar wind's influence on the magnetosphere and ionosphere, and many details of this broad subject are discussed in Appendices A and B and Chapter 1. The neutral and ionized thermosphere's UV dayglow emissions outside of the auroral zone are the result of excitation by photoelectrons and resonance and fluorescent scattering of the solar radiation [*Rees*, 1989]. Because few chemical reactions are energetic enough to excite these UV energy states [*Lummerzheim et al.*, 1990], dayglow chemistry is fairly simple, and dayglow emissions are fairly well understood [*Gladstone*, 1994]. As Earth's rotation takes thermospheric constituents out of the sunlight or as large-scale bulk flow transports material away from the dayside, chemistry takes over as the dominant excitation mechanism. During quiet geomagnetic conditions, the nighttime ionosphere rapidly decays energetically as chemical and recombination reactions liberate heat (except the F region which decays over timescales of many hours;

see Chapter 1 and Appendix C), leaving some species in excited states which lead to UV and visible emissions. IR airglow that regulates the thermosphere's ambient temperature is the result of chemistry and thermally-excited collisional reactions. Apart from auroral-related energy input, solar radiative energy input is the driver to these processes, and modeling of the airglow in general requires knowledge of FUV, EUV and X-ray energy deposition rates into the upper atmosphere and of the daytime and nighttime thermospheric and ionospheric composition and chemistry [*e.g. Roble and Emery*, 1983].

Auroral emissions are a consequence of energy deposition as well, but the energy deposition is due to highly-energized electrons (and some protons) spiraling down Earth's high-latitude magnetic field lines and colliding with the polar thermosphere's species. Collisional heating, excitation, and ionization of neutrals occurs, and ionospheric density and conductances are enhanced due to the production of secondary electrons. High current densities and conductances in the vicinity of and within the auroral oval significantly increase the Joule heating rate. Collisional deactivation of constituents' excited energy states may occur, but so will radiative deactivation; *i.e.*, the aurora. Elevated thermospheric temperatures ultimately result in increased thermally-excited IR emission rates from such species as NO, NO^+, O and CO_2 [*e.g. Killeen et al.*, 1997].

Within the dayside auroral oval, UV emissions associated with auroral processes occur in addition to dayglow UV emissions, and the two radiative components must be separated from one another if the processes responsible for each are to be investigated. UV nightglow emissions that occur at auroral latitudes are generally weak ($\trianglelefteq$ kR) [*Rees*, 1989], but must also be accounted for if processes that produce UV aurora are to be properly investigated separate from processes that produce UV nightglow. Though quantum mechanics explains how auroral and airglow emissions originate at the atomic level, it is energy deposition into the thermosphere associated with solar radiative and magnetospheric processes which ultimately supplies the energy that results in the excitation of these radiative states in the thermosphere's species. The manner in which this energy input occurs can be investigated, for example, through a sequence of point-like or spatially-extended airglow- and/or auroral-intensity measurements, which can

yield an evolving map of the energetic solar radiative, magnetospheric and thermospheric processes that produce these airglow and auroral emissions.

As was discussed at the end of Chapter 1, auroral-brightness measurements, in conjunction with an auroral model, can yield such quantities as the energy flux and characteristic energy of auroral-particle precipitation, high-latitude ionospheric conductances, and thermospheric composition changes relative to the model thermosphere. Differences between modeled and observed airglow or auroral emissions are characteristic of real thermospheric composition changes that are not well described in temporally- and spatially-averaged model thermospheres such as MSIS-90 [*Hedin*, 1991]. *Craven et al.* [1994], for example, identified a 25-55% decrease in the OI(130.4)-nm dayglow intensity across a spatially-extended region of ~10^7 km^2 in the morning sector after a period of strong geomagnetic activity by comparing Dynamics Explorer 1 photometer [*Frank et al.*, 1981] observations of the OI(130.4)-nm emission to a quiet-time modeled emission. The decrease was attributed to Joule and particle-precipitation heating that thermally expands the thermosphere and reduces the O column density relative to the molecular nitrogen column density across large areas. The same phenomenon is also perceptible at smaller spatial scales within the auroral-oval region, and *Lummerzheim et al.* [1990] used ground-based photometer measurements from Poker Flat, AK of the visible auroral wavelengths of λ427.8 nm from N_2^+, λ630.0 and λ844.6 nm from O, and λ732.0 nm from O^+ to infer the characteristic energy and energy flux of the precipitating electrons, and an atomic oxygen density scaling factor. Data from the night of September 25, 1987 revealed a depletion of the O column density over Poker Flat of 50% relative to the model. Quantities such as energy flux and characteristic energy can be inferred from both ground-based brightness measurements of the visible aurora [*e.g. Hecht*, 1989; *Lummerzheim*, 1990] and from satellite observations of UV aurora [*e.g. Germany et al.*, 1990; 1994a], the latter of which is described below and in Chapter 3. Modeling of the aurora, however, requires an exposition of the Boltzmann transport equation, which is beyond the scope of this thesis. Nonetheless, the electron transport code of *Lummerzheim and Lilensten* [1994] has provided the necessary tool to utilize

global-scale UV auroral images acquired by the Global Geospace (GGS) POLAR spacecraft Ultraviolet Imager (UVI) [*Torr et al.*, 1995] and search for thermospheric composition perturbations associated with auroral activity that may be attributed to the geophysically-significant vertical wind events observed with the Inuvik FPS.

2.4 A Brief History of Satellite Imaging

In general, photometry is the comparison of the luminous intensities of two radiant sources; *e.g.*, a background or calibration source and a source of particular or unknown properties. A photometric sensor has the property of converting radiant energy that is incident upon it into some other form, and the first photometers where chemical in nature; *i.e.*, photographic film. Imaging of the aurora from satellite was first achieved with film, but since then, the development of such electronic sensors as PMTs and CCDs has improved considerably some aspects of the process of photometric observations from satellite; *e.g.*, increased temporal resolution.

The first two-dimensional observations of the aurora from satellite were obtained by the Canadian satellite ISIS-II in 1973 [*Anger et al.*, 1973; *Shepherd et al.*, 1973]. The satellite imaged the N_2^+ first negative emission at λ391.4 nm and the OI(557.7)-nm and OI(630.0)-nm emissions using three scanning photometers. Only partial coverage of the auroral oval was possible because of the satellite's relatively low altitude (~10^3 km), and only one image per orbit could be obtained because the photometers on board used the satellite's orbital trajectory to provide one of the dimensions in the images' pixel array.

The United States Air Force's first Defense Meterorological Satellite Program (DMSP) spacecraft soon followed the ISIS-II satellite in 1974 [*Rogers et al.*, 1974], and orbited at about 850 km, obtaining broad band images of the partial oval in the visible and IR wavelength range of 400-1130 nm. Both DMSP and ISIS-II were limited to the nightside because they imaged at visible wavelengths. The first dayside pictures in the far-ultraviolet wavelength range of 120-140 nm were obtained by the Japanese satellite Kyokko [*Kaneda et al.*, 1977], which had a remarkably good temporal resolution of two minutes per image compared to DMSP and ISIS-II.

A number of satellites launched in the 1980s advanced the field of auroral imaging considerably. The first, Dynamics Explorer 1 (and 2), was launched in 1981, and is discussed below. HILAT in 1984 [*Meng and Huffman*, 1984] and Polar BEAR in 1987 [*Meng et al.*, 1987] both orbited at low altitudes and had spectrometers of high enough resolution to distinguish between the OI(130.4)-nm and OI(135.6)-nm emissions. Viking in 1987 [*Anger et al.*, 1987] orbited at an altitude of 13,500 km, allowing it to take images of the entire auroral oval. The OI(130.4)-nm and OI(135.6)-nm emissions and the various molecular nitrogen vibrational and rotational transitions of the Lyman-Birge-Hopfield (LBH) bands between 120 and 200 nm were imaged using CCD technology, giving Viking images a temporal resolution of twenty seconds. The most productive of the 80s imagers, however, were the three photometers aboard the Dynamics Explorer 1 (DE1) satellite [*Frank et al.*, 1981], launched in 1981 and orbiting from altitudes of ~600 to 23,000 km. DE1 provided hundreds of thousands of images over its nine-year life-span. Images at wavelengths of λ391.4 nm, λ557.7 nm and λ630.0 nm and within a broad band FUV range of 120-170 nm had a temporal resolution of twelve minutes. DE1 was also launched in conjunction with Dynamics Explorer 2 (DE2), which had a low orbiting altitude of ~300-800 km. Instruments aboard DE2 made *in situ* measurements of such quantities as neutral winds and temperature [*Hays et al.*, 1981; *Spencer et al.*, 1981] and composition [*Carignan et al.*, 1981], among many others. The Freja mission [*Murphree et al.*, 1992], launched in 1992, was a continuation of the Viking program, and imaged at the same wavelengths as Viking but with a faster temporal resolution of six seconds. However, Freja orbited at a much lower altitude of ~600-1750 km, providing much better spatial resolution at the expense of global coverage.

In February of 1996, the POLAR spacecraft was launched as part of the Global Geospace mission, joining its partner satellite WIND (launched in 1995) in orbit. The International Solar Terrestrial Program (ISTP), which is responsible for the SOHO and GEOTAIL satellites, is also part of the GGS mission. Along with the Ultraviolet Imager (the topic of the next section), POLAR has a variety of instruments for making various *in situ* measurements, and in addition, images the λ394.1-nm emission of N_2^+, the O

emissions at λ557.7 nm and λ630.0 nm, the O^+ emission at λ732.0 nm, and the hydrogen λ656.3-nm emission using the two cameras of the Visible Imaging System (VIS) [*Frank et al.*, 1995]. A third camera of VIS images the FUV wavelength range of 124-149 nm, separate from the UVI system. Since POLAR, there have been several satellites launched into orbit with imaging capabilities, none of which will be mentioned here.

2.5. The Global Geospace POLAR Spacecraft Ultraviolet Imager (UVI)

A comprehensive review of the Ultraviolet Imager's characteristics and the POLAR spacecraft it resides upon is presented in *Torr et al.* [1995], and some of the material discussed here is a survey of the forementioned paper. However, much of the calibration information presented in *Torr et al.* [1995] is preliminary because it is based only on engineering data. It was George Parks of the University of Washington who completed the final stages of the imager's development, including the laboratory and orbital calibration [*Lummerzheim*, 2004, private communication]. A considerable amount of the most recent calibration information on the UVI instrument remains unpublished, and is included here or in Chapter 3 where appropriate.

The POLAR spacecraft has a highly-elliptical polar orbit ranging between the altitudes of approximately 1.8 R_E and 9 R_E, with an orbital period of approximately 18 hr. The data sets presented in this thesis extend from February, 2000 to March, 2001, and POLAR's coverage of the northern hemispheric high-latitude region from the more advantangeous altitudes of 4-9 R_E was extensive during this time period, though POLAR's orbit had already apsidally precessed towards the equator to some extent by this time (discussed more below). POLAR's apsidal precession rate is 15° per yr, and as of January, 2006, POLAR views the southern hemisphere when at apogee.

The UVI is mounted upon a despun platform that permits the imager to remain nadir viewing or to be stepped through increments of 0.02° to any offset angle that is desired (in the plane normal to the spacecraft's spin axis). The imager's circular field of view is 8°, giving it the capability of imaging the entire high-latitude region at magnetic latitudes of ~60° and higher when the spacecraft is located at ~6 R_E and outward. This spatial coverage spans a total of ~9 hr of the 18-hr orbital period during the trip from

~6 R_E to ~6 R_E through apogee, though UVI's orientation relative to the auroral oval (discussed more below) hinders this coverage somewhat during the February, 2000-March, 2001 time period when data was being collected for this thesis. The temporal coverage of ~9 hr is advantageous, however, in that it permits uninterrupted viewing of the auroral oval during a time frame when several auroral substorms may occur or when a magnetic storm is taking place. Measurement of the appropriate emission brightnesses provides the information needed to infer, for example, the auroral-related energy deposition rate over the entire extent of the oval at each imaging step, and—because of UVI's image repetition rate of 37 seconds (though integration times of 9, 18, and 36 can be selected)—to infer a reliable time-integrated total energy input into the thermosphere during an entire magnetic storm or substorm [*e.g. Germany et al.*, 1997; *Lummerzheim et al.*, 1997].

When the spacecraft is at altitudes of $\lesssim$6 R_E, the imager can no longer view the entire oval, and at ~4 R_E, it can observe only about one quarter of the auroral region [*Torr et al.*, 1995], depending on the despun platform's pointing direction. Below this altitude, global coverage quickly diminishes, though spatial resolution is now considerable, which allows for the possibility of imaging smaller-scale features of the aurora. At 8 R_E, the imager's 8° field of view (FOV) translates to a latitudinal spatial coverage of 66° and a CCD spatial resolution of ~40 km·pixel^{-1} × 35 km·pixel^{-1}. At 2 R_E, the decreased latitudinal spatial coverage is 16°, and the increased spatial resolution is ~10 km·pixel^{-1} × 9 km·pixel^{-1} [*Torr et al.*, 1995]. Figure 2.4 [*Torr et al.*, 1995] illustrates the imager's 8° FOV projected onto a typical auroral oval when the spacecraft is at 9 R_E and at 4 R_E. Figure 2.4 is representative of very early in POLAR's lifetime, when at apogee it viewed the northern-hemispheric region essentially from over the magnetic pole. When at 9 R_E, POLAR's location relative to Earth was ~80-90° geomagnetic latitude, and at 4 R_E, POLAR was at a latitude of ~45°. Because of its ~18-hr orbital period, POLAR generally reached apogee at times of ~0000, ~1800, ~1200, ~0600, ~0000 UT,... It is also important to note that the "jitter" of the despun platform and the "wobble" of the spacecraft (discussed more below) reduce the spatial resolution relative to the values quoted above. The POLAR

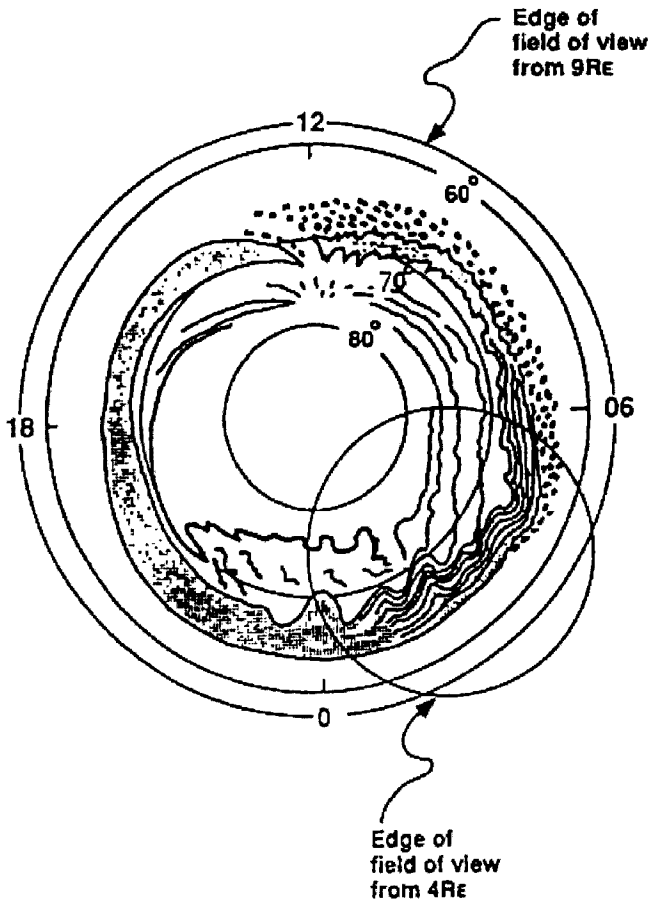

Figure 2.4. Schematic representation of the 8° FOV of the UVI. The projected FOV at 9 R_E and at 4 R_E onto a typical auroral oval are shown [Figure from *Torr et al.*, 1995].

spacecraft's current and past orbital information can be checked on NASA's website at the URL http://www-spof.gsfc.nasa.gov/orbits/menu_orbits.html.

Overall, the imager's extensive temporal coverage of the high-latitude northern hemisphere over ~10-11-hr periods, occurring every two-thirds of a day due to POLAR's 18-hr orbital period, was highly advantageous to the scope of this thesis. The Fabry-Perot spectrometer at Inuvik generates time series of thermospheric vertical wind estimates for time spans of up to nearly 18 hr per day during the winter solstice months of December and January. Vertical wind estimates from Inuvik from the data seasons of 1999-2000 and 2000-2001 were acquired in conjunction with the POLAR UVI observations of February, 2000 to March, 2001. POLAR's favorable orbital trajectory provided lengthy coverage

of UVI auroral brightnesses over the entire polar region, including Inuvik, during several nights when lengthy vertical wind observations at Inuvik were also collected, allowing for the time history of potential vertical wind composition effects to be investigated.

The enthusiasm created by the coverage UVI provides was tempered some by a variety of data acquisition and analysis concerns. One simple reason was Inuvik's weather. There were many occasions when good UVI coverage during active aurora was available, but cloudy conditions prevailed at Inuvik, or there were clear nights at Inuvik but no UVI coverage, or clear nights at Inuvik and good UVI coverage but no aurora. Care must taken when determining vertical winds from the Doppler shifts of thermospheric emissions because the scattering of airglow and auroral signal from non-zenith sources into the FPS field of view by molecules, aerosols and clouds in the lower atmosphere renders vertical wind measurements uninterpretable. This is because the FPS is no longer viewing airglow and aurora from strictly overhead but also from other parts of the sky or the entire sky if overcast conditions prevail; *i.e.*, the FPS is measuring some unquantifiable combination of horizontal and vertical winds from different parts of the thermosphere. The data sets that are presented here were the few available when all three criteria were met. Scattering is discussed in more detail as it applies to thermospheric wind measurements in Chapter 3.

As was stated earlier, another principal data acquisition issue was the orientation of UVI relative to the auroral oval. During the years of 1999 to 2001, POLAR's ~9 R_E-apogee location relative to Earth was ~30-45° geomagnetic latitude. This is illustrated in Figure 2.5, which shows the POLAR orbit on February 28, 2000 from ~0000-1800 UT. Depicted in Figure 2.5 are projections of the polar orbit in the *x*-*z* and *y*-*z* planes in Solar Magnetic (SM) coordinates. The SM coordinate system has its *z*-axis along Earth's magnetic dipole, while the *x*-*z* plane contains the solar direction, with *x* roughly towards the Sun. The labels next to the asterisks along the orbital trajectory indicate the UT time.

During POLAR's initial journey towards apogee, the imager's view of the northern hemispheric polar-latitude region was essentially from the side; *i.e.*, Earth's limb was the imager's FOV, and thus, the imager would be viewing the auroral oval from the side. Not until ~0600 UT did POLAR begin to view the oval from a ~45° angle and not until its

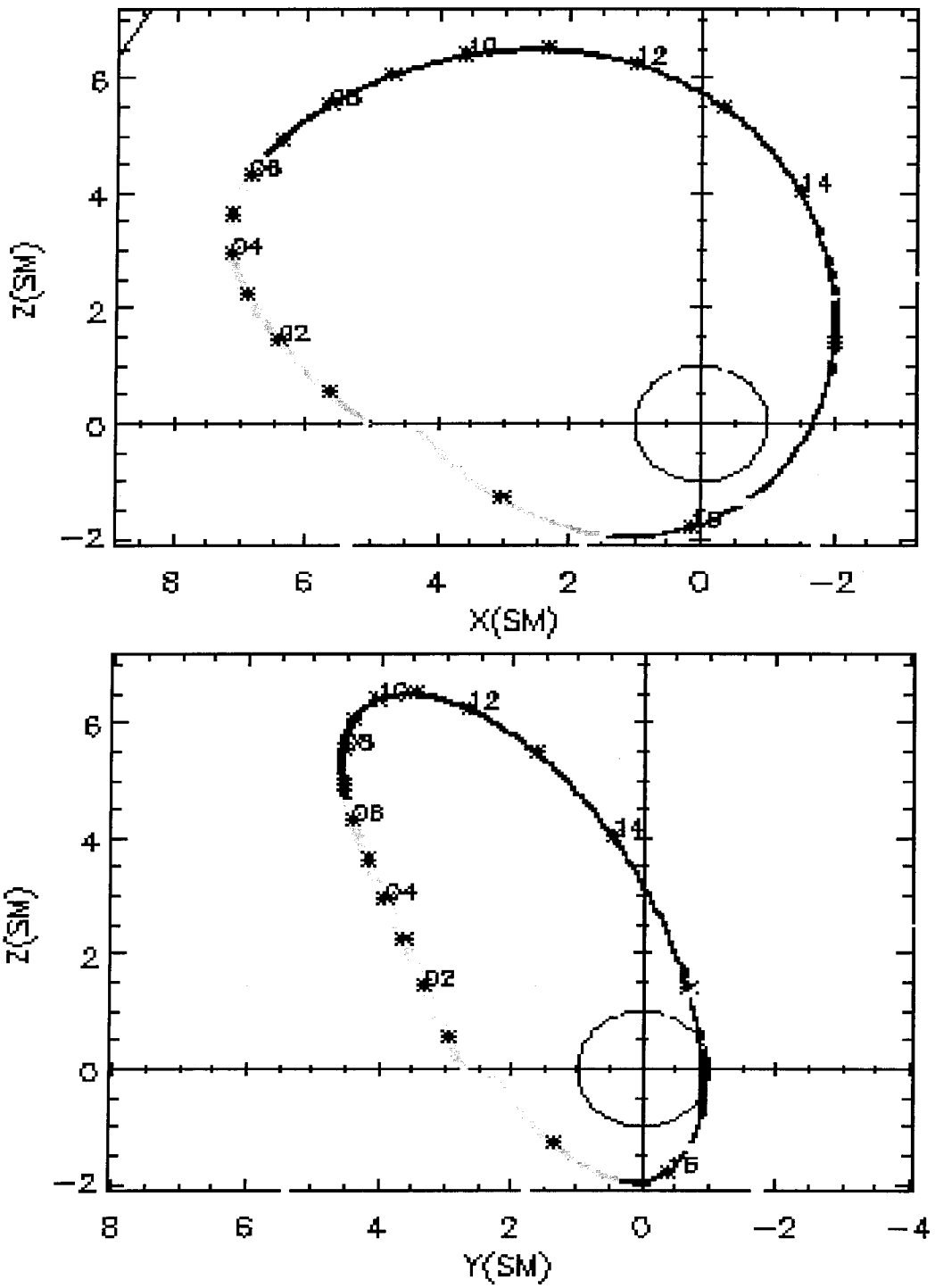

Figure 2.5. The POLAR spacecraft orbital trajectory on February 28, 2000 from 0000-1800 UT. Projections of the polar orbit are in the *x-z* and *y-z* planes in Solar Magnetic (SM) coordinates. The numbers next to the asterisks along the orbital trajectory indicate the UT time [Figure obtained on March 18, 2005 from the internet at the NASA website, http://www-spof.gsfc.nasa.gov/orbits/menu_orbits.html].

journey towards perigee did the imager's view of the northern hemispheric high-latitude region become advantageous. Only when POLAR reached altitudes of ~7-3 R_E during its descent was the imager looking nearly vertically down on the high-latitude region. These orientation concerns are important because an auroral model's interpretation of column-integrated auroral brightness measurements assumes that the brightness measurements are being made while an imager is nadir viewing; *i.e.*, auroral models are one-dimensional. In general, auroral models compute altitude profiles of ionization, energy deposition, and volume emission rates along only one column of thermosphere, and assume that the precipitating electrons stream into the thermosphere parallel to the column. When an imager views the aurora from off-nadir angles, it may be observing two or more columns of thermospheric air parcels, some which may be radiatively excited, others which are not. Thus, such scenarios as resonance scattering of radiation into the imager's FOV can result in overestimations of measured auroral brightnesses, as may be the case for the OI(135.6)-nm emission, or extinction of radiation emanating from a radiatively-excited column of thermosphere by an unexcited column, leading to, for example, underestimations of energy flux inferred from emission brightnesses. This issue is a concern in some of the UVI analysis presented here, but rather than exclude the suspect data, the suspect data's interpretation requires more caution and skepticism. The UVI data that are presented here which have this concern are marked and discussed accordingly in Chapter 4.

Another issue relevant to UVI data analysis is airglow contamination in the auroral data. As was already stated, thermospheric airglow is always present, whether on the nightside or dayside, though nightglow is generally weak ($\leq$1 kR). However, when inferring energy flux from measured UVI auroral brightnesses, even weak nightglow contamination in the auroral data will yield, for example, overestimations of energy flux. This issue has been addressed by the use of an airglow-removal algorithm, which will be discussed further in Chapter 3. Background subtraction (*i.e.*, dark count subtraction) from the UVI images is also required, and a simple procedure in the UVI analysis software identifies an averaged-background value and removes it from the UVI data accordingly.

One final issue relevant to the analysis of the UVI data concerns the stability of the despun platform, referred to as the jitter, and of the spacecraft, referred to as the wobble. The jitter is on the order of 1-2 pixels of the detector and is due to a slight shuddering of the despun platform when the platform's motor engages or disengages. The wobble is more invasive, on the order of 10 pixels, and is due to a misalignment of the spin axis of the despun platform and the spin axis of the satellite. Both have the effect of "smearing" the aurora as imaged by the 2-D detector, thus reducing spatial resolution, and if wobble occurs normal to an auroral curtain during an image exposure, the smearing can have the effect of making the auroral curtain appear much broader than it is. If the wobble is along the track of an auroral curtain during an exposure, then the smearing effect of the aurora is negligible. This is an ongoing issue for UVI analysts, and new techniques that account for the wobble and jitter are developed as new information becomes available. The spatial averaging that is performed to the UVI data presented here (and on UVI data in general) is intended to minimize these effects and is described in Chapter 3.

The UVI instrument measures column-integrated auroral brightnesses in five wavelengths ranges with the use of five filters. Two of the wavelengths are the λ130.4-nm and λ135.6-nm emissions of atomic oxygen. Two other filters select out the Lyman-Birge-Hopfield-Short (LBH-S) band of molecular nitrogen, centered at λ150.0 nm, and the LBH-Long (LBH-L) band centered at λ170.0 nm. A fifth filter centered at λ190.0 nm measures the scattered sunlight continuum. Figure 2.6 [*Torr et al.*, 1995] shows the passbands of each filter superimposed on an FUV spectrum.

The reasons for measuring the OI(135.6)-nm, LBH-S and LBH-L auroral emissions are explained in great detail in *Germany et al.* [1990; 1994], and as has been stated, these wavelengths in conjunction with an auroral model can be used to infer the properties of the precipitating electrons and thermospheric composition variations relative to model densities. Simply put, an auroral model is an electron transport model [*e.g. Lummerzheim and Lilensten*, 1994; *Strickland et al.*, 1989]. The model assumes an incident flux of energetic electrons that are precipitating into a model high-latitude thermosphere and ionosphere from the magnetosphere, and numerically solves the Boltzmann transport

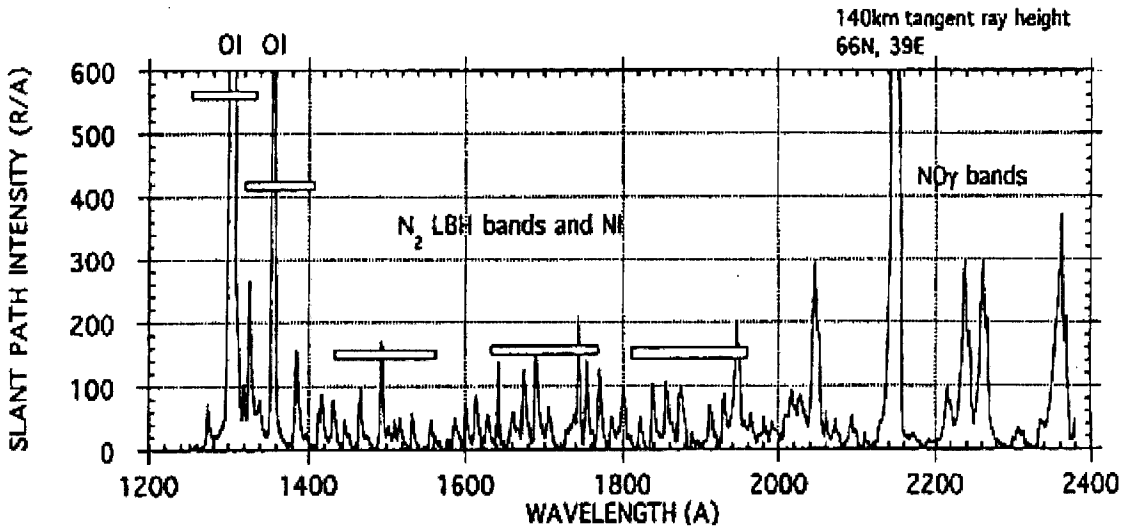

Figure 2.6. FUV spectrum and the five filter passbands of the UVI instrument [Figure from *Torr et al.*, 1995].

equation that describes the electrons' transport into the model thermosphere from above. The transport model goes on to determine the total collisional energy input due to the precipitating electrons into the model thermosphere, and predicts the ionization rates and the numerous volume emission rates of the model thermosphere's constituents being energized. In addition, the emission rates of certain species that are predicted by the auroral model for the specified precipitating-electron properties can be integrated along a line of sight while taking into account absorption and scattering by other thermospheric species, yielding emission brightnesses. These brightnesses can then be convolved with a particular instrument's passband function, yielding height-integrated nadir-viewing total column emission rates emanating from that model thermosphere that the instrument will measure. Comparision of these predicted brightnesses to actual measured brightnesses can then determine the precipitating electrons' properties (flux and characteristic energy) during a particular auroral event, and composition discrepancies between the real and model thermosphere, such as in the form of an atomic oxygen scaling factor [*e.g. Hecht et al.*, 1989; *Lummerzheim et al.*, 1990], or, as is the case here, in the form of the column shift parameter that vertically displaces the neutral model $[O_2]/[N_2]$ and $[O]/([N_2]+[O_2])$

ratios and redistributes the O, N_2, and O_2 densities at each model thermospheric pressure level.

For the purposes of this thesis, the electron transport code of *Lummerzheim and Lilensten* [1994] was used to precipitate an isotropic Maxwellian distribution of electrons at nine different characteristic energies and thirty-one column shift values at 1 $mW \cdot m^2$ of energy flux into the MSIS-90 model thermosphere and compute the volume emission rates of the FUV emissions relevant to the UVI instrument (as well as ionization rates and a variety of other emission rates). For the case of UVI-observed FUV emissions, the energy flux of the precipitating electrons in $mW \cdot m^{-2}$ is inferred directly from the LBH-L brightness, and the characteristic energy of the electrons in keV is inferred from the ratio of the LBH-S to LBH-L brightnesses. The ratio of the OI(135.6)-nm to LBH-L brightnesses can also be used to infer characteristic energy [*Germany et al.*, 1990].

Recall from Chapter 1 that the Schumann-Runge (SR) continuum of molecular oxygen lies in the wavelength range of ~130-175 nm, where the absorption cross section of O_2 becomes very large, as Figure 2.7 shows [data provided by *Lummerzheim*]. Because the UVI LBH-L filter passband lies at the far edge of the SR continuum (as indicated in Figure 2.7), the molecular nitrogen auroral emissions that the LBH-L filter monitors are only weakly reabsorbed by any molecular oxygen that lies above the peak auroral-emission altitude. The LBH-L height-integrated column emission brightness that the UVI instrument measures can then be compared to the auroral model's prediction of the total emission brightness at, for example, an energy flux of 1 $mW \cdot m^{-2}$, regardless of an aurora's peak emission altitude. The relative difference between the measured LBH-L brightness and its predicted brightness at 1 $mW \cdot m^{-2}$ of energy flux determines the total energy flux associated with that particular auroral event.

Conversely, the OI(135.6)-nm emission and the emissions which the LBH-S filter monitors (see the LBH-S passband in Figure 2.7) are strongly absorbed by molecular oxygen. Because the peak auroral-emission altitude is dependent on the precipitating electrons' characteristic energy [*Rees*, 1989] (*i.e.*, the more energetic the precipitation, the deeper the precipitation penetrates into the thermosphere), LBH-S and OI(135.6)-nm

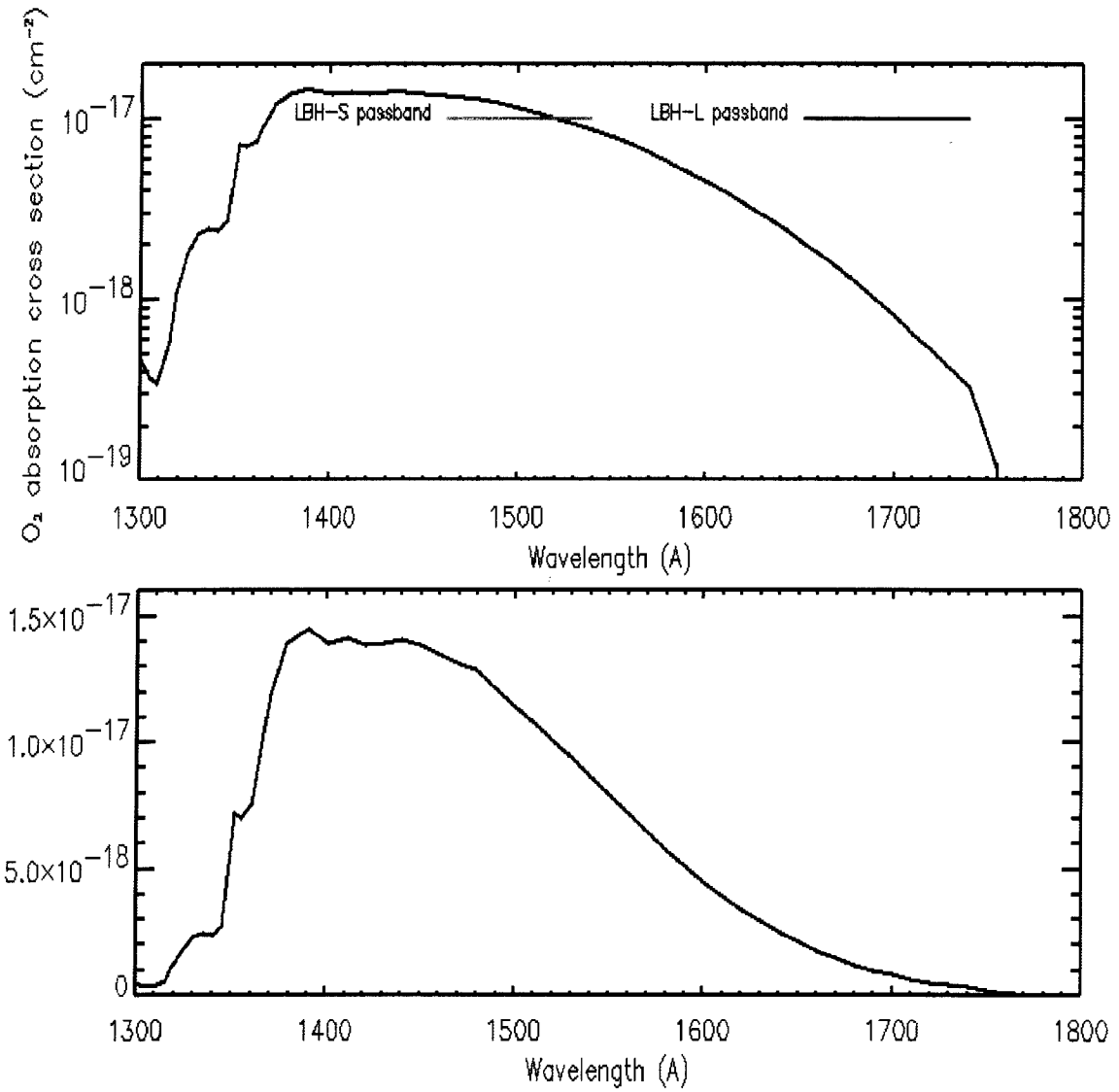

Figure 2.7. Absorption cross section for molecular oxygen. The top plot shows the cross section on a logarithmic scale. The bottom plot shows the cross section on a linear scale. The wavelength passbands of the LBH-S and LBH-L filters are also indicated [data provided by *Lummerzheim*].

emissions that originate lower in the thermosphere will be more strongly attenuated by the SR continuum of O_2. Therefore, the LBH-S and OI(135.6)-nm volume emission rates are dependent on both the energy flux and the characteristic energy of the electrons, while the LBH-L emission rate is dependent mostly on the flux. Thus, if the auroral model computes particular LBH-L and LBH-S emission rates for an energy flux of 1

$mW \cdot m^{-2}$ and a range of characteristic energies, then the ratio of the LBH-S to LBH-L brightnesses is representative of that range of characteristic energies. Comparison of the measured LBH-S/LBH-L ratio to the predicted ratio range determines the characteristic energy of the precipitating electrons associated with a given aurora.

Once the energy flux and characteristic energy are determined from the measured LBH brightnesses, the technique can be pushed further by inferring a modeled OI(135.6)-nm brightness. The electron transport model computes OI(135.6)-nm emission rates at an energy flux of 1 $mW \cdot m^{-2}$ and a range of characteristic energies, and once the measured characteristic energy and flux are known, the modeled OI(135.6)-nm brightness can be inferred. Going even one more step, the modeled OI(135.6)-nm brightness can then be compared with the measured OI(135.6)-nm brightness. Discrepancies between the two can be attributed either to uncertainties in the model, such as inaccurate neutral densities (which are temporally- and spatially-averaged quantities) or absorption and emission (cascade plus direct excitation) cross sections, or to geophysical phenomena, such as chemistry and transport. The purpose of this thesis is to ascertain the likelihood of the latter variety; *i.e.*, the geophysical phenomenon of high-latitude thermospheric vertical winds. With this in mind, the new column shift parameter was introduced into the electron transport code of *Lummerzheim and Lilensten* [1994]. As was already stated, the column shift simulates the potential effects of long-lived, intermediate- to large-magnitude thermospheric vertical winds such as the disruption of diffusive equilibrium and vertical transport of thermospheric species by vertically displacing the neutral model $[O_2]/[N_2]$ and $[O]/([N_2]+[O_2])$ ratios and redistributing the O, N_2, and O_2 densities at each model thermospheric pressure level. The effect of the column shift parameter on the MSIS-90 model thermosphere is described in more detail in Chapter 3, as is the column shift's effect on the modeled LBH and OI(135.6)-nm brightnesses computed by the auroral model of *Lummerzheim and Lilensten* [1994].

Chapter 3 Data Acquisition, Analysis and Observations

3.1 Fabry-Perot Observations of Upper-Thermospheric Vertical Winds at Inuvik

3.1.1 Vertical Winds: General Considerations

Measurement of thermospheric winds using Fabry-Perot interferometry is a time-honored technique dating back to the 1960s [*e.g. Armstrong*, 1969]. Many practical data reduction requirements must be considered, however, before it is feasible to make sensible determinations of upper-atmospheric wind measurements from a given night's accumulated unprocessed Fabry-Perot interferometric observations. Two of these general prerequisites, scattering and the zero-velocity reference, as they apply to zenith-looking image data of the Inuvik FPS are described here.

3.1.1.1 The Zero Doppler-shift Reference

As was discussed in Chapter 1, the thermosphere's diurnally-varying global-scale barometric and divergence-driven vertical winds of ±1-10 $m \cdot s^{-1}$ associated with its radiatively-driven thermal expansion and contraction and dayside-to-nightside horizontal pressure gradient are indicative of quasi-static thermospheric change that does not significantly perturb hydrostatic balance, occurring over long time scales (~1-2 hr) and substantial horizontal distances (~10^3 km). Over the course of a 24-hr period, a given air parcel's vertical displacement associated with this motion is generally assumed to average out to zero (unless there is significant change in the solar UV and X-ray radiative flux into the thermosphere from one day to the next), and air parcel vertical motion relative to its own pressure level is also zero [*Smith*, 1998]. Furthermore, thermospheric vertical motion associated with geomagnetic activity (*i.e.*, due to Joule and particle-precipitation heating and divergent horizontal winds set up by ion drag and pressure bulges at auroral latitudes) is also generally assumed to vary diurnally and average out to zero, if not on a day-to-day basis then when averaged over days or weeks. The assumption is essentially based on the law of conservation of mass, which basically requires that what goes up must eventually come down (see the discussion in Chapter 1, Section 1.1.4). *Smith and Hernandez* [1995]

confirmed this supposition through simultaneous observations using a 2-Channel FPS [*Hernandez et al.*, 1990] of lower- and upper-thermospheric vertical winds over the South Pole station (90°S, 75°INV) from June 1-15, 1991 during a period of geomagnetic activity when K_P ranged from 1 to 9. The FPS ran continuously during the 15-day period (the South Pole was in total darkness), and the lower- and upper-thermospheric vertical winds, when averaged over thirteen of the fifteen days (two days were cloudy), exhibited a diurnal variation with average amplitudes of 10 $m \cdot s^{-1}$ and 40 $m \cdot s^{-1}$, respectively.

In general, this reasoning applies to 24-hr-averaged thermospheric vertical motion relative to any observatory's location, and consequently, it has become common practice in the field of FPS upper-atmospheric studies to use the vertical wind component as measured at a ground-based site over the course of an observation period to determine the zero-velocity reference for thermospheric wind measurements, and, in addition, to monitor changes in the optical path length of an FPS étalon cavity; *i.e.*, monitor an étalon's drift [*Aruliah and Rees*, 1995]. This method of establishing the zero Doppler-shift reference of a particular thermospheric emission line is useful when one is determining Doppler shifts of emission lines for which there is not a convenient laboratory source that provides a stable, long-term absolute wavelength reference at an automated, remote observatory, which is the case for the OI(630.0)-nm airglow and auroral emission [*Aruliah and Rees*, 1995]. Furthermore, because vertical wind speeds are generally small, ±1-10 $m \cdot s^{-1}$ [*Aruliah and Rees*, 1995], and an order of magnitude less than horizontal wind speeds (except at auroral latitudes), and because time series of vertical wind measurements are often stochastic in appearance (indicative of the random fluctuations of the many small and large wave fields that prevail in the thermosphere, essentially averaging to no vertical motion), experience has revealed that slow and smooth variations in an étalon's optical path length (~1-10% of the étalon's free spectral range per hour) due to slow changes in ambient temperature (~1-3°C·hr^{-1}) and characterisitic changes in atmospheric pressure (~1-2 mmHg·hr^{-1})—if, for example, the étalon is not temperature-controlled or pressure-sealed like the Inuvik FPS—are readily identified in the time series of sky spectra peak positions inferred from a given night's FPS zenith-looking fringe images. Fluctuations in the time series of sky

spectra peak positions that are due to actual thermospheric vertical wind activity are generally on the order of ~0.1-1% of one free spectral range and are superimposed onto the more smoothly-varying oscillations in the sky-spectra peak position time series that are due to changes in the optical path length. This topic is discussed in more detail later.

Determining the zero Doppler-shift reference for a given night's thermospheric wind measurements by assuming that the average vertical wind speed is zero over the course of the observation period does have its limitations. Most FPSs only run at night, and zenith observations over only part of a 24-hr period will not likely produce a mean vertical wind of zero, particularly at high-latitude sites where long-lived, intermediate- to large-magnitude vertical winds will result in a net upward or downward thermospheric motion as measured over the site, biasing the zero-velocity reference [*Aruliah and Rees*, 1995]. In addition, vertical wind activity as measured at a high-latitude site depends on geomagnetic conditions since the site may be equatorward, within or poleward of the auroral oval, depending on the time of day and the level of geomagnetic activity. Studies have suggested that downwelling occurs more regularly at the equatorward edge of the auroral oval [*e.g. Crickmore et al.*, 1991], while upwelling occurs more regularly at the poleward edge [*e.g. Innis et al.*, 1996; 1997]. Within the oval, both will generally occur with equal frequency [*e.g. Price et al.*, 1995] (described in greater detail in Chapter 1, Section 1.1.7). Lastly, the length of the data-acquistion period for nighttime observations at high-latitude sites has a large seasonal dependence, and thus, also determines how many nighttime hours (along with geomagnetic activity) a site spends within the auroral oval.

Aruliah and Rees [1995], in examining 1242 nights of OI(630.0)-nm upper-thermospheric vertical wind observations obtained at the high-latitude site of Kiruna, Sweden (68°N, 20°E) from November, 1981 to April, 1990, determined that the mean vertical wind at Kiruna exhibited systematic variations dependent on geomagnetic activity, season and solar cycle. For example, in averaging the wind data according to season, *Aruliah and Rees* [1995] found that the mean vertical wind speed for dates around the equinoxes, for which there were wind measurements from 1700-0500 UT, was of much larger amplitude (±10-30 $m \cdot s^{-1}$) than the mean vertical wind for dates around winter

solstice (±10 $m \cdot s^{-1}$), for which the wind measurements spanned times of 1500-0700 UT. The equinox winds were also statistically more significant and exhibited considerable systematic variation (*i.e.*, lengthy periods of downward winds, then upward winds, *etc.*) when compared with the winter-solstice winds, which in general varied randomly about zero. In averaging the wind data according to geomagnetic activity (using K_P), *Aruliah and Rees* [1995] found that the mean vertical winds were comparable (±10 $m \cdot s^{-1}$) for both quiet geomagnetic conditions ($K_P < 2$) and moderate conditions ($2 < K_P < 5$) but that the moderate-condition winds were statisically more significant (like the equinox winds) and showed greater systematic variation when compared with the quiet-condition winds, which in general varied randomly about zero. Ultimately, *Aruliah and Rees* [1995] concluded that the assumption that the thermosphere's vertical wind speed over the course of an observation period averages out to zero is generally not valid, and only under conditions of low geomagnetic activity when the observation period is long (~17 hr) did the vertical wind data support this assumption. *Aruliah and Rees* [1995] determined that if the vertical wind component over the course of one night's observations was to be used in isolation to determine the zero-velocity reference for that night's wind measurements, then in general, one could expect an error of about ±5 $m \cdot s^{-1}$ or less in the zero-velocity baseline during periods of quiet geomagnetic activity near winter solstice, but a systematic error of ±5-20 $m \cdot s^{-1}$ in the zero-velocity baseline during periods of elevated geomagnetic activity and during other seasons when the observation period is reduced to 12 hr or less.

The method of averaging all zenith observations to zero to establish a zero Doppler-shift reference is used in this study, and in general, most standard analysis techniques that yield wind estimates from Fabry-Perot observations apply here; *e.g.*, fitting a Gaussian function convolved with an étalon's instrument function to sky spectra [*Conde*, 2001] to determine their spectral peak positions and widths. An incorrect zero-velocity level can adversely affect horizontal wind estimates, causing apparent convergences or divergences to appear in the horizontal wind field that do not exist [*Aruliah and Rees*, 1995]. However, studies that focus only on the relative vertical wind speed, such as those that search for periodicities in vertical wind time series due to gravity waves [*e.g. Innis et al.*,

1996; 97], are not affected by the zero-velocity baseline since the systematic variations in the vertical wind time series are still valid. This study, which emphasizes the long-lived, intermediate- to large-magnitude vertical winds discussed in Chapter 1 that occur in the auroral zone, also is not concerned with the zero-velocity baseline since the vertical wind data sets presented here exhibit obvious intermediate- to large-magnitude vertical wind events (*i.e.*, significant variation in Doppler shifts over an observation period), regardless of any error in the zero-velocity baseline. Furthermore, of the seven Inuvik FPS vertical wind time series presented here, six are from around winter solstice, spanning ~15-17 hr of observations, and five of the six data sets were collected during geomagnetically-quiet conditions ($A_P \sim 10$). The error in the zero-velocity reference is negligible on these nights.

One analysis technique employed here that is new to the methods of Fabry-Perot interferometric analysis is the procedures described in *Conde* [2002]. Because the Inuvik FPS images the observed fringe patterns onto a CCD detector, some method must be used to reduce the 2-D fringe images to 1-D spectra. One method for reducing an FPS fringe image to a 1-D spectrum is referred to as the reduction-to-radius-squared procedure, which was briefly mentioned in Chapter 2. The method involves dividing an FPS image into sets of concentric annuli of equal area and summing the pixel brightness in each successive ring, yielding a 1-D spectrum. The subsequent fitting of a Gaussian function convolved with the étalon's instrument function, for example, will yield the spectral peak location. However, FPS fringes are rarely perfectly circular due to étalon defects (such as those described in Chapter 2 and Appendix D) and optical aberrations (discussed more below), and precise determination of a fringe image's center location is also problematic. Thus, the reduction-to-radius-squared procedure was replaced in favor of the novel analysis method of *Conde* [2002], which is discussed in more detail below. Errors introduced into the wind measurements by the analysis procedures of *Conde* [2001] are also discussed, as are errors associated with the procedures designed to account for the étalon's drift.

3.1.1.2 Scattering

Ground-based FPS observations of Doppler-shifted thermospheric emissions are inherently assumed to be emanating from the source region being viewed by the FPS line

of sight [*Abreu et al.*, 1983]. As was stated earlier, thermospheric vertical winds are generally of much smaller magnitudes than horizontal winds, and thus, when making FPS zenith observations, it is necessary to ensure that the vertical wind measurements are not contaminated by the horizontal wind component. Ground-based FPS airglow and auroral observations of regions of weak emission which are near large intensity gradients may be contaminated by light that is being Rayleigh scattered by air molecules or Mie scattered by aerosols and clouds in the lower atmosphere from the regions of strong emission into the FPS field of view [*Abreu et al.*, 1983]. In the case of horizontal winds, apparent divergences or convergences may appear in the thermosphere's horizontal wind field relative to the observatory's location [*Abreu et al.*, 1983]. In the case of vertical winds, contamination of vertical wind measurements with the horizontal wind component may result in apparent upwellings or downwellings as measured over the observatory [*Price et al.*, 1995], or may conceal an actual vertical wind if the scattered signal has an oppositely-directed Doppler shift to the vertical wind Doppler-shifted zenith signal.

The possibility that scattering can influence the measurement of a vertical wind is investigated more closely in *Price et al.* [1995], which presents three nights of lower- and upper-thermospheric vertical wind and temperature estimates obtained at Poker Flat, AK during Spring, 1991 from simultaneous observations of the OI(557.7)-nm and OI(630.0)-nm airglow and auroral emissions, respectively, with a 2-Channel FPS [*Hernandez and Mills*, 1973]. Vertical wind data from two nights exhibited simultaneous long-lived, large-magnitude upwellings in the lower and upper thermosphere. Lower-thermospheric vertical wind data from the third night showed an apparent downwelling coinciding with a sharp increase in the OI(557.7)-nm brightness but no corresponding downwelling in the upper-thermospheric vertical winds. *Price et al.* [1995], which had the benefit of horizontal wind observations to complement the vertical wind data, considered three questions [see *Price et al.*, 1995 and references therein] in exploring the possibility that the measured vertical winds were caused by horizontal wind contamination; was the direction of the potentially-biased, large-magnitude vertical wind consistent with the direction of the horizontal wind as measured from the region of enhanced auroral intensity, and, did the

potential bias show up in both the lower-thermospheric OI(557.7)-nm and upper-thermospheric OI(630.0)-nm vertical wind data, since scattering is less likely to occur at λ630.0 nm because of the longer wavelength [*Price et al.*, 1995]? The third question focused on whether the lower-thermospheric OI(557.7)-nm zenith temperatures were influenced by scattering from the brighter non-zenith source region, since temperature as inferred from the Doppler width of thermospheric emissions is not particularly sensitive to scattering; *i.e.*, scattering of signal is not a concern when the measured temperature difference between different regions of the thermosphere is $\gtrsim$100 K [*Abreu et al.*, 1983].

On the night of March 21, 1991, *Price et al.* [1995] observed a long-lived (~30 min), large-magnitude vertical wind simultaneously in both the lower and upper thermosphere, with upward wind speeds reaching magnitudes of 42 $m \cdot s^{-1}$ and 138 $m \cdot s^{-1}$, respectively. An intense auroral arc was located south of Poker Flat at the time of the upwelling, and the lower-thermospheric meridional wind as measured north of the site was 150 $m \cdot s^{-1}$ in the equatorward direction. *Price et al.* [1995] inferred from this information that if auroral signal was scattered from the southern arc into the FPS zenith field of view, then a red shift (*i.e.*, upward wind) would be measured by the FPS, assuming a uniform horizontal wind field over the site. Thus, the possibility that scattering produced the observed upward wind could not be eliminated based on the direction of the horizontal wind. However, the upward wind was also observed in the OI(630.0)-nm wind data, which is not as readily scattered as the OI(557.7)-nm emission. Furthermore, a temperature increase of 210 K had been observed in the lower thermosphere coinciding with the upward wind, but as the southern arc moved overhead, the lower-thermospheric temperature decreased. Thus, if scattering of the OI(557.7)-nm signal emanating from the auroral arc had occurred during the measurement of the upwelling, then the lower-thermospheric temperature associated with the arc would have been measured by the FPS, which was not the case. Thus, scattering was determined to not have an influence on the measurement of this upwelling.

An example of when scattering was determined to be responsible for an apparent vertical wind occurred on March 10, 1991. On this night, *Price et al.* [1995] observed a large (55 $m \cdot s^{-1}$), fairly long-lived (~20 min) downwelling in the lower thermosphere, just

prior to a sharp increase in the OI(557.7)-nm zenith brightness. Auroral arcs prevailed both south and east of the site, and the lower-thermospheric zonal wind was 150 $m \cdot s^{-1}$ and westward as measured east of the site. Scattered signal emanating from the eastern arc would appear as a downward wind in the zenith. Furthermore, there was no significant vertical motion observed in the OI(630.0)-nm wind data, and finally, the lower-thermospheric temperature measured in the east was within 60 K of the zenith-measured temperature, in addition to the measured relative OI(557.7)-nm brightness being about the same amount in the east and the zenith. Some thin clouds were also observed as the aurora brightened in the zenith. Thus, the measured lower-thermospheric downward wind was concluded to be the result of scattering of auroral light from the arc located east of the site into the zenith-looking FPS field of view.

The time series of upper-thermospheric vertical wind measurements over Inuvik presented in this thesis have been determined from FPS zenith observations of the OI(630.0)-nm emission. These vertical wind data sets, first and foremost, were selected based on the generally clear weather prevailing at Inuvik. As was stated earlier, scattering by molecules and aerosols in the lower atmosphere of the OI(630.0)-nm emission is not as much of a concern as it is with shorter-wavelength emissions, and furthermore, intensity gradients in the OI(630.0)-nm auroral emission are much less significant than in, for example, OI(557.7)-nm aurora [*e.g. Rees*, 1989]. As a result, the vertical wind observations of the Inuvik FPS presented here are considered reliable and in general representative of the upper thermosphere's vertical wind activity on those nights.

3.1.2 The Doppler-shifted Atomic Oxygen (OI) λ630.0-nm Emission

The OI(630.0)-nm airglow and auroral emission emanates from the upper thermosphere in the altitude range of ~200-400 km, with a peak emission altitude of ~240 km, though the altitude can vary, as is the case for mid-latitude stable auroral red arcs which emanate from a height of ~400 km [*Rees*, 1989]. The OI(630.0)-nm night airglow emission rate is $\lesssim$1 kR, and during auroral events, the total emission rate can reach ~5 kR [*Rees*, 1989]. The long radiative lifetime of the $O(^1D)$ atomic state that is responsible for the λ630.0-nm emission, which has a half-life of ~110 s [*e.g. Rees*, 1989], prevents the

emission from originating lower in the thermosphere (≲200 km) due to collisional deactivation of the elevated energy state since collision frequency increases with increasing density, and therefore decreasing altitude. However, the long lifetime of the $O(^1D)$ state ensures that the Doppler shift of the OI(630.0)-nm emission due to the velocity of the emitting species is representative of the neutral thermosphere's bulk flow speed at upper-thermospheric altitudes [*Aruliah and Rees*, 1995] since the neutral upper thermosphere is composed primarily of atomic oxygen. The mathematical expression that determines the line-of-sight wind speed of a radiation-emitting source when the FPS-determined peak wavelength of the source is compared to an absolute wavelength reference is the Doppler shift equation, which is given by

$$\Delta\lambda = \lambda - \lambda_0 = \lambda_0(v/c). \tag{3.1}$$

Here, λ_0 is the rest wavelength, λ is the measured peak wavelength, v is the line-of-sight bulk flow speed of the emitting particles, and c is the speed of light. Thus, the line-of-sight wind speed is given by $v = c[(\lambda - \lambda_0)/\lambda_0] = c(\Delta\lambda/\lambda_0)$. In general, the precision required for measuring thermospheric winds is a few meters per second, which corresponds to wavelength Doppler shifts $\Delta\lambda$ of 1 part in 10^8 [*Conde*, 2002], emphasizing the extreme accuracy needed in the determination of the 1-D sky spectra peak locations.

Because the Inuvik FPS is configured for high-resolution studies, its free spectral range $(\Delta\lambda)_{fsr,Ivk}$ is necessarily very small, and a wavelength spectrum whose bandwidth is greater than the étalon's free spectral range will result in the overlapping of orders, impairing the resolving capability of the FPS (see Appendix D for more discussion). Thus, the bandwidth of the observed emission line necessarily must be smaller than the étalon's free spectral range. Recall that the free spectral range of the Inuvik FPS is

$$(\Delta\lambda)_{fsr,Ivk} = \lambda_0^2(2n'_{air}h\cos\theta)^{-1} = 0.009920 \text{ nm} \tag{3.2}$$

when observing the OI(630.0)-nm emission and operating at a gap width of h = 20 mm under STP conditions, with n'_{air} = 1.000293. As is generally required of FPS studies, the Inuvik FPS free spectral range is known to a very high precision, recalling from Chapter 2 that the capaitance-stabilization system of Queensgate étalons generally maintains a gap stability of $\lambda/3000$ [*Hicks, et al.*, 1984].

As was discussed earlier, in general, an étalon's orders of interference will drift due to changes in its optical path length $P = (2n'h)\cos\theta$ (see Appendix D for more details on optical path length). Because the Inuvik FPS étalon is not pressure-sealed or temperature-controlled, its optical path length changes with the varying ambient temperature and atmospheric pressure (both of which alter air's index of refraction). As was stated earlier, experience has revealed that slow changes (~1-3°C·hr^{-1}) in the ambient temperature and characteristic changes in the atmospheric pressure (~1-2 mmHg·hr^{-1}) result in drifts of ~1-10% of the étalon's free spectral range per hour, which are readily identified in a given night's time series of zenith-looking sky spectra peak determinations. Fluctuations in sky spectra peak positions due to thermospheric vertical wind activity are generally on the order of 0.1-1% of the orders of interference and are superimposed onto the more smoothly-varying oscillations in the sky-spectra peak position curve that are due to changes in the optical path length, noting that vertical winds generally range from ±1-100 m·s^{-1}. The free spectral range at λ630.0 nm, when expressed in velocity dimensions, $v_{fsr,Ivk}$, reveals this information and further emphasizes the extreme precision required of FPS data analysis procedures to determine the peak positions of 1-D sky spectra inferred from FPS fringe images in order to determine thermospheric wind speeds. The Doppler relation, $\Delta\lambda/\lambda_0 = v/c$, can be used to determine $v_{fsr,Ivk}$ by substituting $\Delta\lambda$ with $(\Delta\lambda)_{fsr,Ivk}$,

$$v_{fsr,Ivk} = c[(\Delta\lambda)_{fsr,Ivk}/\lambda_0] = c\lambda_0(2n'h)^{-1} = 4720.3482 \text{ m·s}^{-1}. \quad (3.3)$$

Thus, one order of interference of the Inuvik étalon, operating at a gap width of 20 mm (stability of $\lambda/3000$) and observing the OI(630.0)-nm emission at STP, corresponds to 4720.35 m·s^{-1} of wind velocity. The required precision of a few meters per second for measuring thermospheric winds corresponds to ~1/1500 of $v_{fsr,Ivk}$. This also represents the relative change in the radii r_m of the orders of interference (assuming the fringes are fairly circular) if there is a change of ~3 m·s^{-1} in a line-of-sight wind measurement [*Conde*, 2002]. The radius r_m of each fringe is given by

$$r_m = f[2 - m\lambda_0/n'_{air}h(1 - v/c)]^{1/2}. \quad (3.4)$$

where m is the order of interference, and (referring to Figure 2.1 in Chapter 2) f is the focal length of the lens sitting below the étalon that focuses the transmitted fringe pattern

onto a 2-D detector. Equation 3.4 originates from Equation 2.2, $\delta = 4\pi n'_{air} h\lambda^{-1}\cos\theta = 2\pi m$, which describes the phase difference δ between the interfering wavefronts, and the trigonometric relation $\tan\theta = r_m/f$ describing the radiation incident-angle dependence of the fringe radii at the detector. For small incident angles θ, $\cos\theta \approx 1 - \theta^2/2$ and $\tan\theta \approx \theta$. Thus, $m\lambda \approx 2n'h(1 - \theta^2/2)$ and $\theta \approx r_m/f$. These two relations yield an expression for r_m, $r_m = f(2 - m\lambda/n'_{air}h)^{1/2}$, and substitution of the Doppler shift relation into this expression yields Equation 3.4. For an FPS operating at a gap width of $h = 20$ mm and observing the OI(630.0)-nm emission at STP, Equation 3.4 yields $r_m = 0.0045819f$ when the line-of-sight wind speed is zero and $r_m = 0.0045841f$ when the line-of-sight wind speed is 3 $m \cdot s^{-1}$, resulting in a relative change in the fringe radii of ~1/1500. It is clear from this discussion that great care must be taken during the acquisition of the FPS fringe data to ensure that circularity of the fringes is maintained as much as is instrumentally possible, and in addition, to identify the precise center of the fringes during the analysis and also account for potential fringe non-circularities, if possible, in the software-reduction of the fringe patterns to 1-D spectra and their peak and width determinations. The necessary precision in locating accurately the orders of interference and their center position is obtained by the FPS image analysis techniques of *Conde* [2002], which are described next.

3.1.3 Generating One-Dimensional Spectra from Inuvik FPS Fringe Images

Actual Fabry-Perot interference fringe images are rarely circular and the difficulties faced in characterizing a fringe pattern's distortions, magnification, and center position all potentially contribute to the error in the measurement of thermospheric winds. Optical aberrations consist of two main types; chromatic aberrations, which arise from the fact that the index of refraction is a function of wavelength, and monochromatic aberrations [*e.g. Hecht*, 1984]. Chromatic aberrations are not a concern here since air's index of refraction does not change appreciably in the range of wavelength Doppler shifts (1 part in 10^7-10^8) that the Inuvik FPS measures. However, monochromatic aberrations, which fall into two subcategories, can result in both image deterioration and deformation. Such monochromatic aberrations as coma and astigmatism will deteriorate the image, making it unclear, while others, such as Petzval field curvature and distortion, will deform the

image [*Hecht*, 1984]. Some of these aberrations are discussed in more detail below, and it is the FPS fringe image analysis procedures described in *Conde* [2002] that are able to produce 1-D spectra from the Inuvik FPS 2-D fringe patterns while carefully minimizing the flaws in the inferred 1-D spectra due to these potential aberrations. The analysis procedures of *Conde* [2002] accomplish this by modeling the orders of interference of an étalon's calibration image (generally a laser image) with the 2-D Airy formula. The model fit is evaluated at each detector pixel locaton while including adjustable parameters that can account for image distortions and magnification, and an unknown center location.

Initially, it is helpful to examine how the orders of interference m of an étalon's transmitted fringe image without distortions are modeled, and more details on the material discussed in this section are presented in *Conde* [2002]. Recalling from Chapter 2 that the Airy formula $\tilde{A}(\delta) = [1 + F\sin^2(\delta/2)]^{-1}$ is a function of the phase difference $\delta = 4\pi n' h\lambda^{-1}\cos\theta = 2\pi m$ between interfering wavefronts, then the orders of interference m of an image are given by $m = 2n'h\lambda^{-1}\cos\theta$, where n' is the index of refraction, h is the gap width, λ is the wavelength, and θ is the angle of incidence of the radiation relative to the étalon normal. For small incident angles θ, $\cos\theta \approx 1 - \theta^2/2$, and thus,

$$m(\theta) \approx 2n'h\lambda^{-1} - n'h\theta^2\lambda^{-1} = m_0 - n'h\theta^2\lambda^{-1}, \tag{3.5}$$

where $m_0 = 2n'h\lambda^{-1}$ is the nominal central order of interference. As is shown in Figure 2.1 in Chapter 2, a lens behind the étalon uniquely maps the incidence angle θ of the radiation to the x and y coordinates of the detector. For circular fringes, $\theta = L_\theta(x, y)$ is given by

$$\theta = L_\theta(x, y) = \alpha[(x - x_0)^2 + (y - y_0)^2]^{1/2}, \tag{3.6}$$

where α is the magnification, and (x_0, y_0) is the fringe's center location. Inserting this into Equation 3.5 yields an expression for $m(x, y)$,

$$m(x, y) = m_0 - \beta[(x - x_0)^2 + (y - y_0)^2], \tag{3.7}$$

where β is also a magnification term, given by $\beta = \alpha^2 n'h\lambda_0^{-1}$. In this basic model, it is necessary to fit four parameters, m_0, β, x_0, and y_0, which physically represent a fringe pattern's phase, magnification, and x and y center positions, respectively.

Equation 3.7 represents the orders of interference m as perfect circles, and in order to account for potential distortion effects in the mapping of both the radiation's axial and

azimuthal incidence angles, θ and ϕ, respectively, to x and y coordinates, a more elaborate set of expressions describing the orders of interference is necessary. Thus, several types of aberration terms are introduced into the model for m, which are chosen to represent an instrument's typical first-order departures from Equation 3.7 [*Conde*, 2002]. In general, several types of image aberrations are possible. For example, warping of the circular fringes corresponds to variations in a fringe's radius as a function of azimuthal angle ϕ around the fringe [*Conde*, 2002]. To account for warping in the model, the x and y distances from the fringe center are replaced by the new quantities u and v, which are given by [*Conde*, 2002]

$$u = (x - x_0) + \gamma_x |x - x_0|, \; v = (y - y_0) + \gamma_y |y - y_0|, \tag{3.8a-b}$$

respectively, where γ_x and γ_y account for the variation of a fringe's radius at each x and y.

Another image aberration is the elliptical distortion, which is due to magnifications in x, y, or xy. It is included in the model by replacing u and v with another function $\psi(x, y)$, which is given by

$$\psi(x, y) = \beta_x u^2 + \beta_y v^2 + \beta_{xy} uv, \tag{3.9}$$

where β_x, β_y, and β_{xy} are the magnification terms. Finally, the last aberration accounted for in the model, which depends on $\varepsilon\psi^2(x, y)$, where ϵ is another coefficient, is due to radially-varying magnification, which is more familiar as the barrel (when $\epsilon < 0$) and pincushion (when $\epsilon > 0$) aberrations [*Hecht*, 1984]. This aberration arises because the focal length and magnification of a focusing lens may vary across the lens [*Hecht*, 1984].

Consequently, there are nine free parameters, m_0, x_0, y_0, γ_x, γ_y, β_x, β_y, β_{xy}, and ϵ, in the analysis procedures of *Conde* [2002] that characterize the mapping of θ and ϕ to the detector's x and y coordinates. The orders of interference $m(x, y)$ are then written as

$$m(x, y) = m_0 - \psi(x, y) + \varepsilon\psi^2(x, y). \tag{3.10}$$

Figures 3.1a-d below [presented by *Conde* at the CEDAR conference, June, 2003, Longmont, CO] illustrate the effect of these aberrations on the transmission properties of an étalon by incorrectly representing modeled virtual étalon transmitted fringes (in blue) using inaccurate model parameters. The virtual étalon fringes are superimposed on an observed laser calibration image (in orange) obtained from the Inuvik FPS.

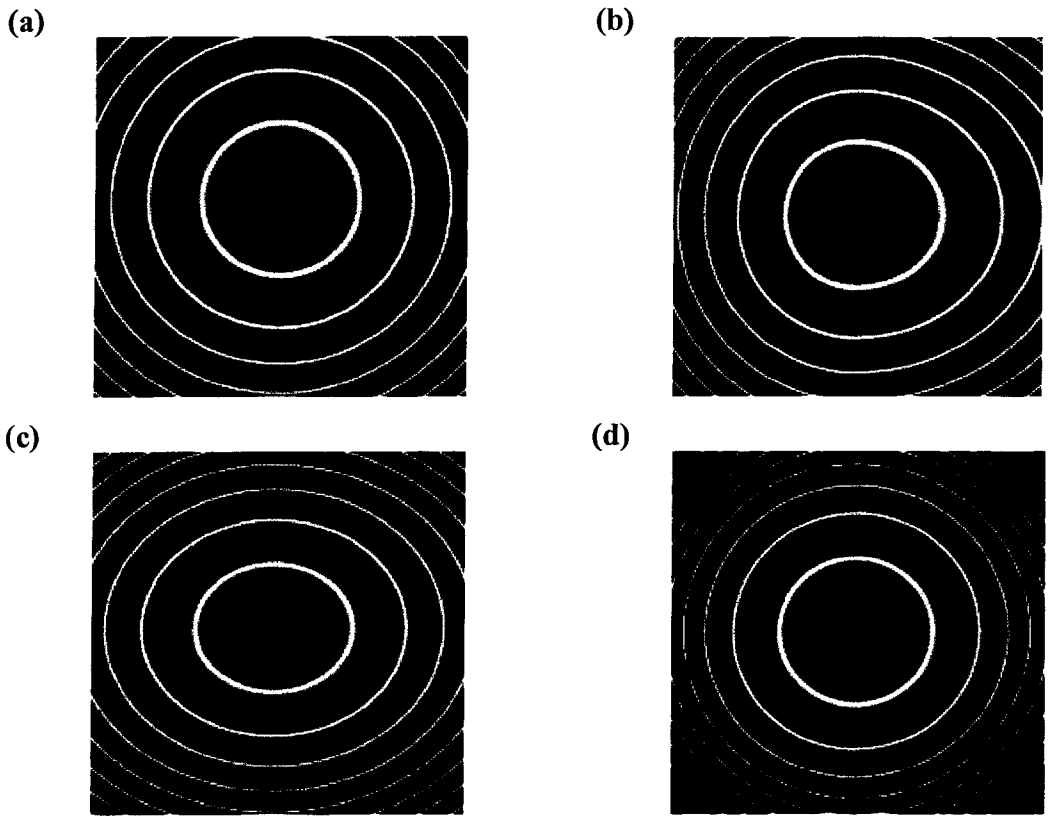

Figure 3.1. Visualizing étalon transmission distortions. The virtual étalon's fringes are in blue, and the laser image is in orange, which was obtained with the Inuvik FPS. **(a)** An inaccurate y center position, y_0. **(b)** Incorrect warping in the x direction, γ_x. **(c)** Incorrect magnification in the x direction, β_x. **(d)** The barrel aberration, incorrect ϵ [Figures presented by *Conde* at the CEDAR conference, June, 2003, Longmont, CO].

The best choice for the nine model parameters determined by the fitting routines are quantified by calculating the discrete 2-D cross-correlation value, κ, between the observed and modeled fringes. These nine best parameters are assumed to maximize the value of κ, which is given by the expression

$$\kappa = \sum_{x=1}^{N_x} \sum_{y=1}^{N_y} \{\bar{A}_M[m(x,y)] \times \bar{B}_C(x,y)\}, \tag{3.11}$$

where N_x and N_y are the number of pixels in the x and y dimensions, respectively. The observed laser calibration fringes are represented by $B_C(x, y)$, and $\bar{B}_C(x, y)$ in Equation 3.11 is given by $\bar{B}_C(x, y) = B_C(x, y) - \min[B_C(x, y)]$. The model fringe pattern is represented by

$A_M[m(x, y)]$, and $\bar{A}_M[m(x, y)]$ is given by $\bar{A}_M[m(x, y)] = A_M[m(x, y)] - \min\{A_M[m(x, y)]$. Each parameter is varied using a grid search until the highest cross correlation is obtained, yielding a set of virtual étalon fitted fringes that accurately overlay the laser calibration fringes, as Figure 3.2 shows [presented by *Conde* at the CEDAR conference, June, 2003, Longmont, CO]. A test that determines whether or not the iteration process converges on some local maxima of κ rather than its global maximum is described below.

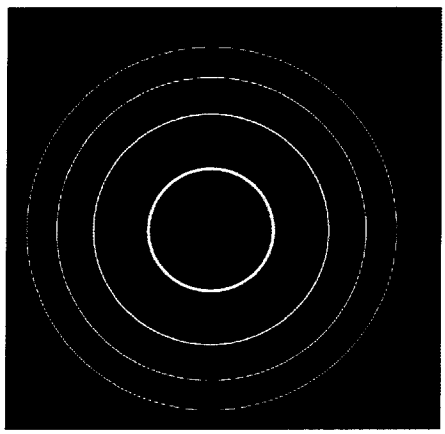

Figure 3.2. Fitted virtual étalon fringes overlayed on a real laser fringe pattern. The fitted fringes are in blue, and the laser image is in orange. The laser image was obtained with the FPS owned and operated by the Communications Research Laboratory (CRL) of Japan. This FPS currently resides at Poker Flat, AK [Figure presented by *Conde* at the CEDAR conference, June, 2003, Longmont, CO].

In the analysis of a given night's Inuvik FPS observations, the laser images are first sorted from the sky images. Recall the discussion from Chapter 2 concerning the Inuvik FPS upgrades that prior to November, 2001, laser exposures were performed only once or twice per week by the on-site technician (or several times per day if I was at the site) separate from nighttime observations. Since the November, 2001 upgrade, laser exposures are performed during nighttime observations approximately every twenty minutes, and the next step in the analysis of a night's data set is to determine the nine parameters m_0, x_0, y_0, γ_x, γ_y, β_x, β_y, β_{xy} for each laser image. This information is saved, and once the virtual étalon's parameterization is complete for each image, a 1-D laser

spectrum is obtained from each laser image by varying m_0 in the model (in Equation 3.10) over one free spectral range. This is equivalent to scanning the virtual étalon by varying its virtual gap width, so that the model fringes expand in radius as m_0 increases. The laser fringes are sampled for each m_0 (*i.e.*, at a slightly different order of interference) by performing a cross correlation between the model fringes and the laser fringes at each step. Each sampling generates a scalar value of the irradiance at that step number, referred to as the channel number, ultimately yielding the wavelength spectrum as a function of channel number. Currently, the virtual étalon is configured to step scan through 64 channels. Recall from Chapter 2 (see Figure 2.3b) that each 1-D laser spectrum (if that laser image contains no defects, discussed more below) represents the étalon's instrument function at the time of the exposure. Experience has revealed that on rare occasions, the iteration process that searches for the nine best parameters will sometimes converge to some local maxima of κ rather than the global maximum, usually because of some minor flaw in a particular laser image but sometimes because of no obvious reason. This generally results in elongated virtual étalon fitted fringes (as in Figure 3.1c) that clearly do not overlay the laser calibration fringes, ultimately resulting in a flawed inferred instrument function. An analysis procedure described in *Conde* [2001] calculates the width of each laser spectrum, referred to as the laser temperature, by fitting an Airy formula function to the inferred laser spectra. In general, the widths of the flawed laser spectra are significantly different from the widths of the acceptable laser spectra, and experience has identified a criterion for disregarding the flawed laser spectra.

The next step in the analysis of a night's observations is to generate 1-D sky spectra from the sky fringe images. A sky spectrum is obtained from each sky image similarly to how the laser spectra are obtained, by varying m_0 in the model over one free spectral range. The sky fringes are sampled for each m_0, generating a wavelength spectrum for each image as a function of channel number. Below in Figure 3.3 is an example of a sky observation obtained with the Inuvik FPS at λ630.0 nm on the night of January 3, 2001. The étalon's instrument function that was used to analyze that night's data set is shown in Figure 3.4. The sky spectrum inferred from the sky image in Figure 3.3 by the analysis

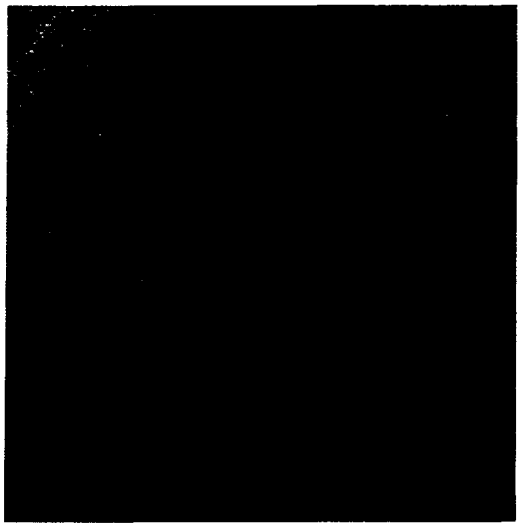

Figure 3.3. FPS observation of the OI(630.0)-nm airglow and auroral emission obtained at Inuvik. This image was obtained on the night of Jan 3, 2001 at 0352 UT.

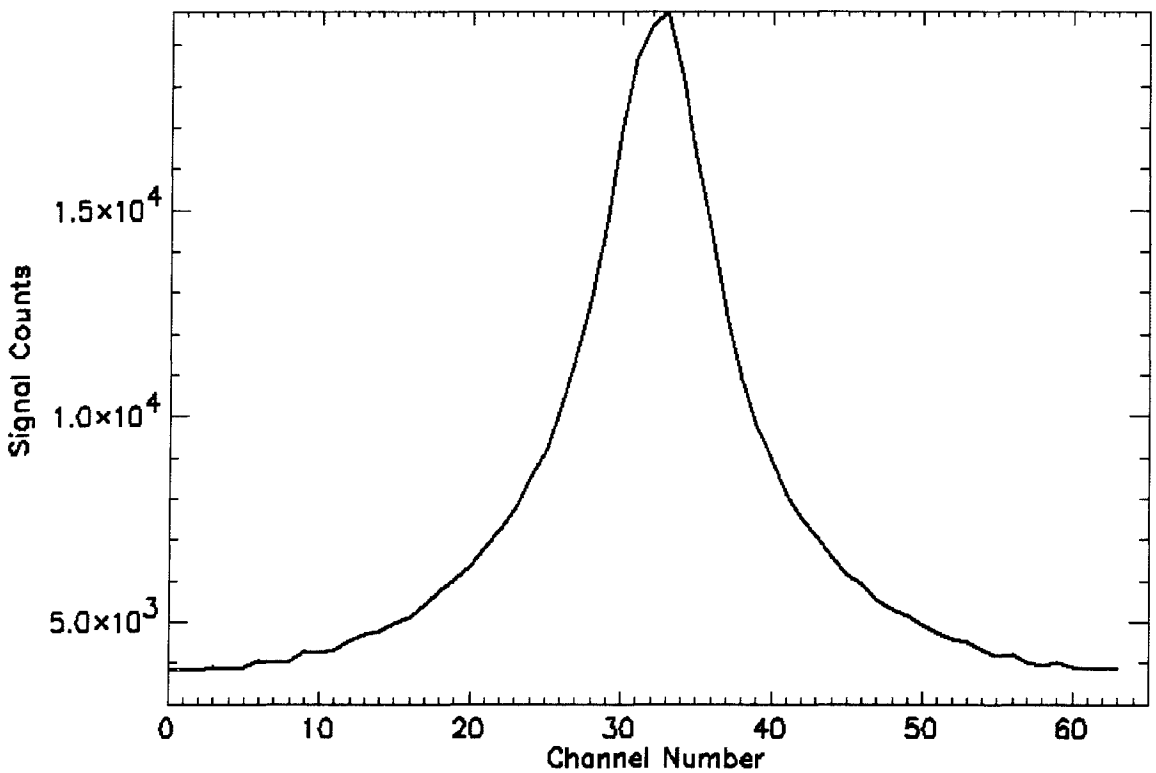

Figure 3.4. The étalon's instrument function on Jan 3, 2001. The instrument function is determined from He-Ne (λ632.8 nm) laser observations and the virtual étalon procedures of *Conde* [2002]. The instrument function is plotted as a function of channel number. This instrument function was used to analyze the sky images obtained on Jan 3, 2001.

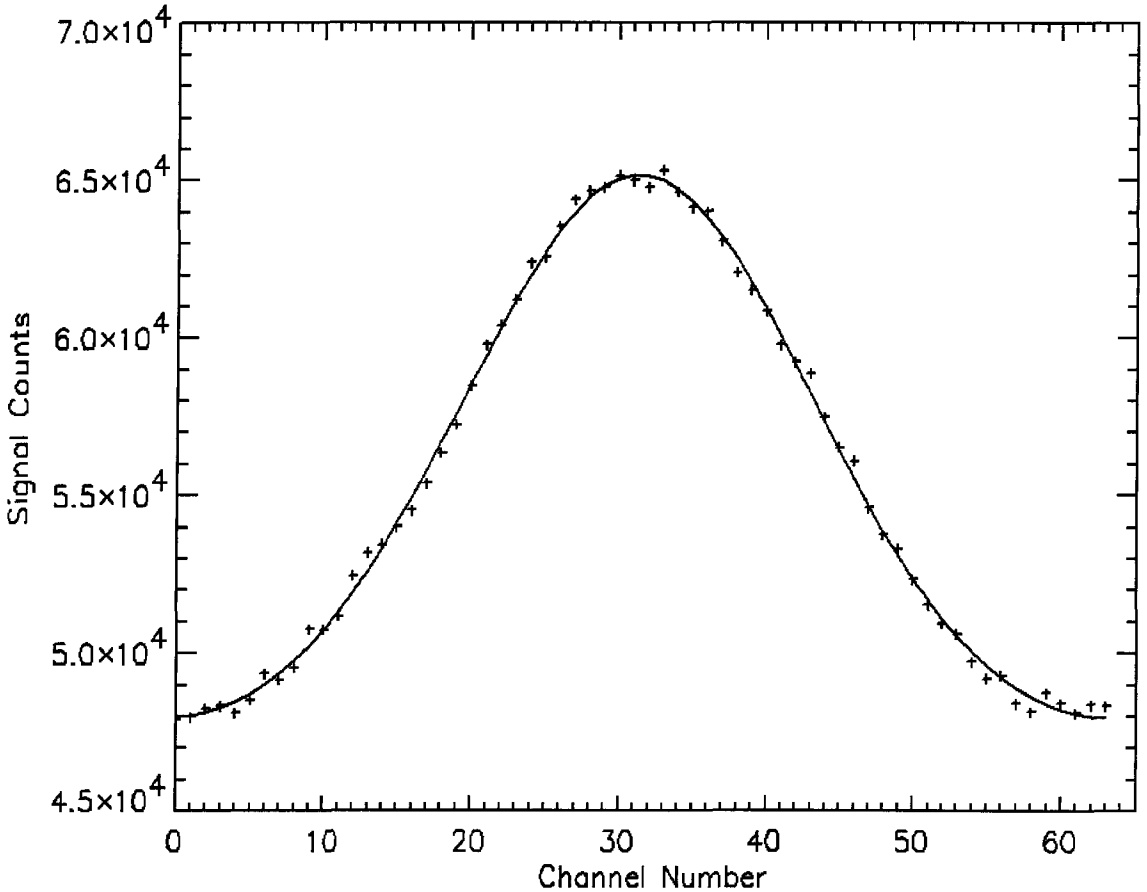

Figure 3.5. Sampled 1-D spectrum inferred from the OI(630.0)-nm sky image in Figure 3.3. The sky spectrum is obtained by the virtual étalon procedures of *Conde* [2002]. The spectrum is indicated by the cross marks. The numerical fit is in black, and is the convolution of a Gaussian function with the instrument function in Figure 3.4.

procedures of *Conde* [2002] is shown in Figure 3.5, along with a numerical fit to the sky spectrum. The numerical fit is performed by the analysis procedures described in *Conde* [2001], and is the best least-squares fit to the data. The analysis procedures are capable of fitting to FPS or LIDAR wavelength spectra, and if required, can account for emission backscatter due to atmospheric molecules or aerosols that are often present in LIDAR spectra. For the sake of Inuvik FPS fitting procedures, the numerical fit is the convolution of a Gaussian function and the instrument function with three adjustable model parameters $\{p_j\}$. The numerical fit yields an estimated value of the sky spectra peak location in channel number units (CNU), the spectral width (used to determine the emitting atom's

temperature), and brightness. The uncertainty in the three parameters is also provided (discussed more below). A chi-squared χ^2 goodness-of-fit indicator [*Conde*, 2001],

$$\chi^2 = \sum_{n=0}^{N-1} \frac{(y_n - s_n)^2}{\sigma_n^2}, \tag{3.12}$$

is performed between the observed sky spectrum and its fitted spectrum at each iteration of the fitting process to identify the best set of model parameters $\{p_j\}$, where N is the number of samples (*i.e.*, channels) in the observed sky spectrum, $\{y_n\}$ is the set of measured values of the observed spectrum, $\{s_n\}$ is the set of modeled values of the fitted spectrum, and σ_n^2 is the variance of the n^{th} element of the observed spectrum y_n. The best possible choice of $\{p_j\}$ will yield the minimum χ^2 when

$$\frac{\partial \chi^2}{\partial p_j} = 0 \tag{3.13}$$

for all j [*Press et al.*, 1992]. It is generally not possible to solve for the peak position and width parameters analytically [*Conde*, 2001], so a grid search is utilized by the analysis procedures of *Conde* [2001] to numerically evaluate χ^2, where χ^2 is minimized with respect to each model parameter while the other parameters are held fixed. Optimization of $\{p_j\}$ is repeated cyclically until a fit is found that meets the criterion for adequate convergence described by Equation 3.13. Linear least-squares fitting methods are discussed again in a little more detail in the next section. The analysis procedures of *Conde* [2001] also calculate the variance in the estimated spectral peak position, width, and brightness simultaneously using a generalized method that standard non-linear, least-squares fitting techniques provide, such as those outlined in *Bevington* [1969] (see *Conde* [2001] for more details), ultimately yielding the uncertainty in the wind, temperature and relative brightness estimates (discussed more below) associated with the numerical fit.

In the analysis of Inuvik FPS observations, the virtual étalon, which is configured with the same parameters as the Inuvik étalon (*e.g.*, same gap width, wavelength of observation), step scans through one free spectral range, $v_{fsr,Ivk}$ = 4720.3482 m·s^{-1}, by stepping through 64 channels. Thus, one channel corresponds to 73.7554 m·s^{-1} in velocity units. To convert the raw FPS OI(630.0)-nm spectral peak position information from a

given night's observations to actual thermospheric wind speeds, the peak positions are first collected together and averaged to zero, as was discussed in Section 3.1.1.1 in which a given night's FPS zenith-looking component is used to estimate the zero Doppler-shift reference for that night's wind measurements. Multiplying the shifted-to-zero-level peak positions by 73.7554 $m \cdot s^{-1}$ converts the spectral peak positions from CNU to velocity units. These are not the final wind speed estimates, however, since the étalon's drift must also be removed from the spectral peak position information. As was also discussed in Section 3.1.1.1, the error in the Inuvik FPS vertical wind measurements associated with the zero-velocity baseline is generally ± 5 $m \cdot s^{-1}$ or less for most of the data sets presented in this thesis since geomagnetic activity was quiet on these nights and FPS observations spanned ~17 hr during the winter solstice period of late November, December and early January. The vertical wind data sets presented in this thesis that do not meet these criteria are discussed accordingly. The error in the Inuvik vertical wind measurements associated with the zero-velocity baseline is implied and is not included in the final presented form of the Inuvik vertical wind measurements; *i.e.*, this error is not included in the wind-measurement error bars. In addition, this implied error does not change the interpretation of the vertical wind measurements presented here since this thesis is concerned with the long-lived, intermediate- to large-magnitude vertical wind events discussed in Chapter 1.

As was stated above, the uncertainty in the OI(630.0)-nm spectral peak positions, widths and intensities associated with the numerical fitting procedures is determined by computing the variances in these model parameters. In addition to calculating these variances, the analysis procedures of *Conde* [2001] also compute the signal-to-noise ratio (SNR) of the observed sky spectra. The SNR of a given sky spectrum is calculated from its power spectrum, and is defined as the power spectrum's fundamental component divided by its averaged high-frequency, noise-dominated components [*Conde*, 2001]. For the data sets presented in this thesis, the estimated uncertainty in each peak position value, σ_{pk}, is generally $\sigma_{pk} \approx \pm 0.010$-$0.200$ CNU, corresponding to an error in each vertical wind measurement of approximately ± 0.75-15.00 $m \cdot s^{-1}$. For example, the uncertainty in the peak position of the sky spectrum shown in Figure 3.5 determined from its numerical

fit is σ_{pk} = ±0.054 CNU, corresponding to an error of ±3.99 m·s^{-1} in the vertical wind measurement inferred from that spectrum. The observed sky spectrum shown in Figure 3.5 is an example of a sky spectrum with a high (≳2000) SNR. In general, sky spectra with a low SNR (~100-500) yield wind measurements with much larger errors than the example shown in Figure 3.5. This is illustrated in Figure 3.6, which is an example of a sky spectrum from the night of December 22, 2000 with the overlayed numerical fit. The

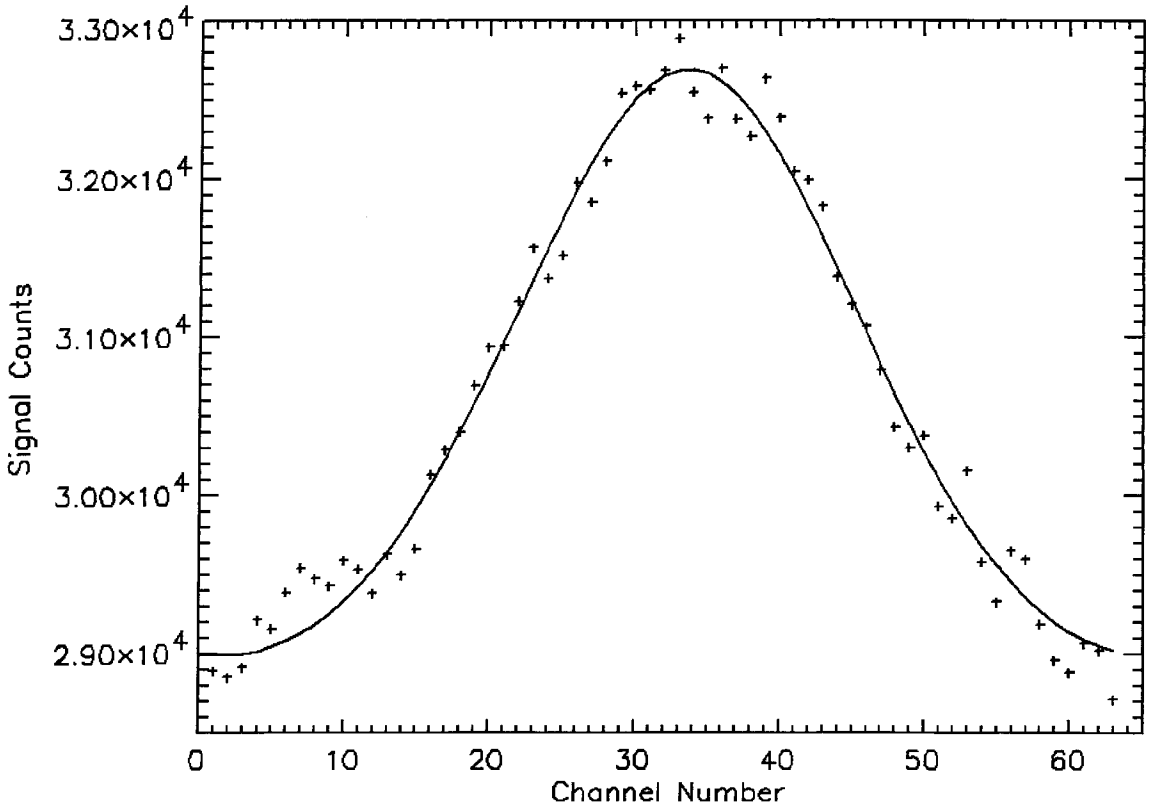

Figure 3.6. Sampled 1-D spectrum inferred from a OI(630.0)-nm sky image obtained on the night of December 22, 2000. The cross marks designate the observed spectrum, which is an example of a spectrum with a low SNR (~100-500). The numerical fit is in black. The peak position determined from the fit had an uncertainty of σ_{peak} = ±0.145 CNU.

uncertainty in the peak position determined from the fit is much larger for this spectrum, σ_{pk} = ±0.145 CNU, than for the example shown in Figure 3.5, and corresponds to a wind-measurement uncertainty of ±10.70 m·s^{-1}. Finally, as has been mentioned, there is also

one other source of error to the Inuvik FPS vertical wind estimates that is associated with the correction for the étalon's drift in the OI(630.0)-nm sky-spectra peak position data. This topic is discussed in the next section along with the final presentation of the Inuvik FPS vertical wind data.

The analysis procedures of *Conde* [2002] and *Conde* [2001] also have been applied to Fabry-Perot image data obtained by the FPS operating at Poker Flat, AK owned by the Communications Research Laboratory (CRL) of Japan [*Ishii et al.*, 1997]. The CRL-FPS is a narrow field-of-view (1.4° full angle), zenith-looking, imaging spectrometer employing a Queensgate étalon that observes the OI(630.0)-nm and OI(557.7)-nm emissions simultaneously with a temporal resolution of 2 min, producing vertical wind estimates in the lower and upper thermosphere, respectively. Comparisons between CRL-FPS OI(630.0)-nm upper-thermospheric vertical wind estimates and OI(630.0)-nm vertical wind measurements obtained with the Scanning Doppler Imager FPS (SDI-FPS) of *Conde and Smith* [1995; 1997; 1998] at Poker Flat were presented by *Conde* at the CEDAR conference, June 2003, Longmont, CO. The comparisons turn out to be an excellent exercise in discussing Fabry-Perot instrumentation and data in general and the significant differences between the CRL-FPS and SDI-FPS instruments in particular.

The SDI-FPS is an all-sky imaging spectrometer that scans over ~1.5 orders of interference of the étalon at λ630.0 nm by piezo-electrically varying the étalon's spacing about a nominal gap width of 20 mm. The reasons for scanning the étalon are described in more detail in *Conde and Smith* [1998]. An all-sky lens and optical relay system maps an approximately 65° half-angle field of view of the sky onto 5 orders of interference at the étalon [*Conde and Smith*, 1997], which are then imaged onto a 2-D detector with a focusing lens. The SDI-FPS uses analysis procedures different from those described in *Conde* [2002] and *Conde* [2001] to compute its thermospheric wind estimates [see *Conde and Smith*, 1998 for more details], and during the time period that the CRL-FPS and SDI-FPS were making these observations (November, 1998 through February, 1999), the SDI-FPS was configured to simultaneously measure the line-of-sight wind speed from 25 independent regions of the thermosphere that map from the sky onto the instrument's 2-D

detector as sectors of four concentric, annular rings centered about the zenith [*Conde and Smith*, 1998]. The rings are spaced uniformly in relation to the zenith angle, with the outermost ring edge at 65°. The inner zone maps to ~35° of the all-sky lens viewing angle centered about the zenith, and the three rings centered about the central sector contain 4, 8 and 12 sectors, respectively. The division of the SDI-FPS field of view into 25 sectors is performed entirely by the analysis software of *Conde and Smith* [1995; 1997; 1998]. A spectrum is acquired from each sector, and the spectra are analyzed for their Doppler shifts and widths. The instrument's ~130° field of view translates to a circular area of $\sim 8 \times 10^5$ km^2 (~1000 km diameter) at an altitude of ~240 km (the λ630.0-nm peak emission altitude). Because the SDI-FPS separates the observed auroral (and airglow) signal into 25 detector sectors, longer integration times are generally necessary to provide enough signal-to-noise per sector for meaningful wind measurements. Consequently, the SDI-FPS temporal resolution during the winter data season of 1998-99 was generally about 8 min. The SDI-FPS is primarily intended for measuring thermospheric horizontal winds in the auroral zone, and thus, the analysis procedures described in *Conde and Smith* [1998] are designed to transform the line-of-sight wind speeds of the 25 viewing sectors into a thermospheric horizontal vector wind field across the instrument's ~130° field of view. Vertical wind estimates from the central sector are also a product of these analysis procedures.

The comparisons between the CRL-FPS and SDI-FPS OI(630.0)-nm vertical wind data, of which an example will be discussed accordingly, give confidence that in general, the analysis procedures of *Conde* [2002] and *Conde* [2001], when applied to Fabry-Perot observations of Doppler-shifted thermospheric emissions, produce wind results that are reliable. However, because of the significant differences between the two instruments, the general criterion that is used to compare the two time series is that the Doppler shifts of the OI(630.0)-nm emission as measured by each instrument only display similar behavior [*Ishii et al.*, 2001]. Because the SDI-FPS is primarily intended for measuring horizontal winds, its configuration and some of the analysis procedures that are used to transform the raw Doppler shifts into wind measurements will influence the magnitudes

of the vertical wind estimates, as opposed to the narrow field-of-view, zenith-looking CRL-FPS, which is configured strictly for the measurement of vertical winds. Therefore, comparisons of the absolute wind speeds as measured by each instrument are not emphasized, but general trends in the vertical wind variations as measured by each instrument, when similar, are regarded as reliable [*Ishii et al.*, 2001]. Furthermore, when the vertical wind variations of each instrument are dissimilar, the discrepancies can generally be attributed to the significant differences between the two instruments.

For example, because the SDI-FPS has a large zenith field of view of ~35°, which is the equivalent of $\sim 2 \times 10^4$ km^2 in circular area (~150 km diameter) at ~240 km altitude, any localized upward or downward motion that occurs in one part of the instrument's zenith field of view may be averaged by oppositely-directed vertical motion in some other part of that field of view if the vertical wind field is not uniform across the SDI-FPS zenith field of view. Recall from Chapter 1 that vertical wind fields in the auroral zone in general have horizontal spatial scales of $\sim 10^2$-10^5 km^2 [*Smith*, 1998]. Putting this another way, what in actuality may be adjacent upward- and downward-moving thermospheric air columns across the SDI-FPS zenith field of view (each of areas, say $\sim 5 \times 10^3$ km^2, and perhaps reaching vertical wind speeds of ± 100 m·s^{-1} at upper-thermospheric altitudes, respectively) may appear as an ~0 m·s^{-1} vertical wind to the SDI-FPS when spatially averaged over that field of view.

Another contributing factor to the averaging effect of the SDI-FPS vertical wind estimates is the instrument's ~8 min time resolution. For example, any significant vertical wind that occurs during an exposure will be temporally averaged by smaller amplitude or oppositely-directed winds that also occur during that exposure. Put another way, the CRL-FPS, with its 2 min time resolution, may have the opportunity, for example, to observe a significant vertical wind event from its beginning to its end, measuring a 10 m·s^{-1} upward wind speed with one exposure, then 25 m·s^{-1} with the next exposure, then 45 m·s^{-1} with the third exposure, 60 m·s^{-1} with the fourth exposure, 60 m·s^{-1} with the fifth exposure, 45 m·s^{-1} with the sixth exposure, 20 m·s^{-1} with the seventh exposure, and 10 m·s^{-1} with the eighth exposure. Conversely, the SDI-FPS during this sixteen minute

time span will make only two temporally-averaged wind measurements, each of ~35 $m \cdot s^{-1}$, assuming the vertical wind field that the CRL-FPS samples is uniform across the larger SDI-FPS field of view. These 35 $m \cdot s^{-1}$ wind measurements, when isolated from other wind measurements, give the impression that the vertical wind event being observed by both instruments is not as energetic as the CRL-FPS wind measurements in fact reveal.

Another condition of the SDI-FPS that will in general influence its vertical wind estimates is the fairly simple method used for correcting for the étalon drift during the 1998-99 winter data season. Because the SDI-FPS étalon is temperature-controlled and pressure-sealed and consequently is very stable, its drift over the course of a night's observations is generally small, only ~0.1% of one free spectral range, which is the equivalent of ~10-20 $m \cdot s^{-1}$ [*Ishii et al.*, 2001]. The method used to remove this drift from the wind data is to high-pass filter the zenith-looking spectral peak positions, based on the assumption that the spatial and temporal average of the vertical wind is small over sufficiently long time periods [*Ishii et al.*, 2001]. The width of the high-pass filter window is generally large, up to 1/3 of the vertical wind data set, and the high-pass filter's effect is to crudely zero the vertical wind data [*Ishii et al.*, 2001], similarly to what was discussed above in Section 3.1.1.1. While removing the étalon's drift from the wind estimates, the technique also introduces an uncertainty in the wind speeds similar in magnitude to the drift, ±5-20 $m \cdot s^{-1}$ [*Conde and Smith*, 1998]. The technique is generally adequate when applied to the SDI-FPS horizontal wind measurements, and does not affect their interpretation since horizontal winds are usually an order of magnitude larger than vertical winds. However, the interpretation of the vertical winds, particularly their magnitudes, may be significantly affected by this uncertainty.

Also affecting the reported SDI-FPS vertical wind magnitudes is the λ630.0-nm rest wavelength reference; *i.e.*, the zero Doppler-shift reference. The method used by the analysis procedures of *Conde and Smith* [1998] is different from the one described in Section 3.1.1.1 in which all the zenith-looking FPS observations from a night's observations are averaged to zero. Instead, the analysis procedures of *Conde and Smith* [1998] identify a rest wavelength for a night's observations by first sorting each sky

exposure's 25 spectra according to their peak determinations. The two highest and lowest values from each set of 25 spectra are rejected, and a mean wavelength peak for each sky exposure is then determined from the remaining spectra. Using each sky exposure's mean value, a time series of mean wavelengths is obtained from over the night's observation period, which is then smoothed. The smoothed result acts as the time-varying estimate of the zero-Doppler shift. The uncertainty in the SDI-FPS wind measurements associated with this inferred zero-velocity reference is comparable to the uncertainty in zero-velocity baseline that was discussed in Section 3.1.1.1, ±5-20 $m \cdot s^{-1}$ [*Conde and Smith*, 1998], and total uncertainty in SDI-FPS wind measurements (whether vertical or horizontal) due to all sources of error rarely exceed ±20-25 $m \cdot s^{-1}$ [*Conde and Smith*, 1998].

The typical uncertainty in CRL-FPS vertical wind estimates is generally much less than the uncertainty in the SDI-FPS vertical wind estimates. As was stated, the analysis of the CRL-FPS image data here involves the usage of the procedures of *Conde* [2002] and *Conde* [2001] to generate the 1-D sky spectra and determine their peak position, width and intensity. Uncertainty in the CRL-FPS wind velocities due to these procedures are comparable to what was described above concerning the Inuvik FPS image data in Figures 3.3-6. In addition to this error, the CRL-FPS analysis procedures also utilize the technique described in Section 3.1.1.1 to determine the zero Doppler-shift reference, in which a night's raw Doppler shifts are averaged to zero, potentially resulting in a constant offset in the vertical wind variation [*Ishii et al.*, 2001]. Lastly, the CRL-FPS analysis procedures account for étalon drift by making observations of a frequency-stabilized laser every 20 min during a night's data-acquistion period [*Ishii et al.*, 2001]. The peak positions of the inferred 1-D laser spectra act as a time-varying estimate to the étalon drift, which is subtracted from the sky-spectra peak position curve. Subsequent errors in the fit to the laser peak positions are included in the error to the vertical wind estimates. Total uncertainty in the CRL-FPS vertical wind measurements is generally ±5-15 $m \cdot s^{-1}$. Ultimately, it is important to realize that only comparisons of the general trends in the vertical wind variations of the two instruments are valid, implying that both instruments

identify similar Doppler shifts at λ630.0 nm, albeit with different uncertainties and spatial and temporal scales, while comparisons of the absolute wind speeds should be avoided.

Figure 3.7 [presented by *Conde* at the CEDAR conference, June 2003, Longmont, CO] shows vertical wind measurements obtained at λ630.0 nm from both instruments on the night of December 25, 1998. Discrepancies between the two time series do exist, but through much of the night, the variation in the vertical wind measurements are similar. For example, during the time period of ~1200-1630 UT, the general trends of the two time series are highly similar. In addition, both instruments identify a significant upward wind at ~0945 UT, then a dropoff to near-zero wind speeds until ~1015 UT. Before ~0945 UT, however, the CRL-FPS wind measurements exhibit significant variation between ± 30 $m \cdot s^{-1}$, while the SDI-FPS vertical winds show very little variation. This, however, is attributed to the large SDI-FPS ~35° zenith field of view. Examination of the SDI-FPS horizontal vector wind measurements between 0800 UT and 0945 UT from this night reveals that significant structure was present in the horizontal wind field over Poker Flat during this time period, particularly in the horizontal winds just outside the SDI-FPS zenith field of view. These localized horizontal wind fields of varying wind speeds in and around the SDI-FPS zenith field of view would produce highly-localized upward and downward winds that, when averaged over the zenith field of view, would result in SDI-FPS vertical wind estimates of ~0 $m \cdot s^{-1}$, which is what is seen in Figure 3.7 from 0800-0945 UT. The narrow field of view of the CRL-FPS (1.4° full angle, ~30 km^2 circular area) reveals the significant structure in the vertical wind field over Poker Flat during the 0800-0945 UT time period that is associated with these variable and structured horizontal winds identified by the SDI-FPS, while the SDI-FPS vertical wind measurements, with their spatial- and temporal-averaging, are unable to identify the vertical wind variation.

Comparisons of this sort between two distinct vertical wind data sets obtained at the same location gives confidence that the analysis procedures of *Conde* [2002] and *Conde* [2001] are indeed performing to satisfaction. In addition, these analysis procedures have been applied to a large body of Fabry-Perot interferometric OI(630.0)-nm and OI(557.7)-nm image data from Inuvik spanning several years of observations. The upper- and lower-

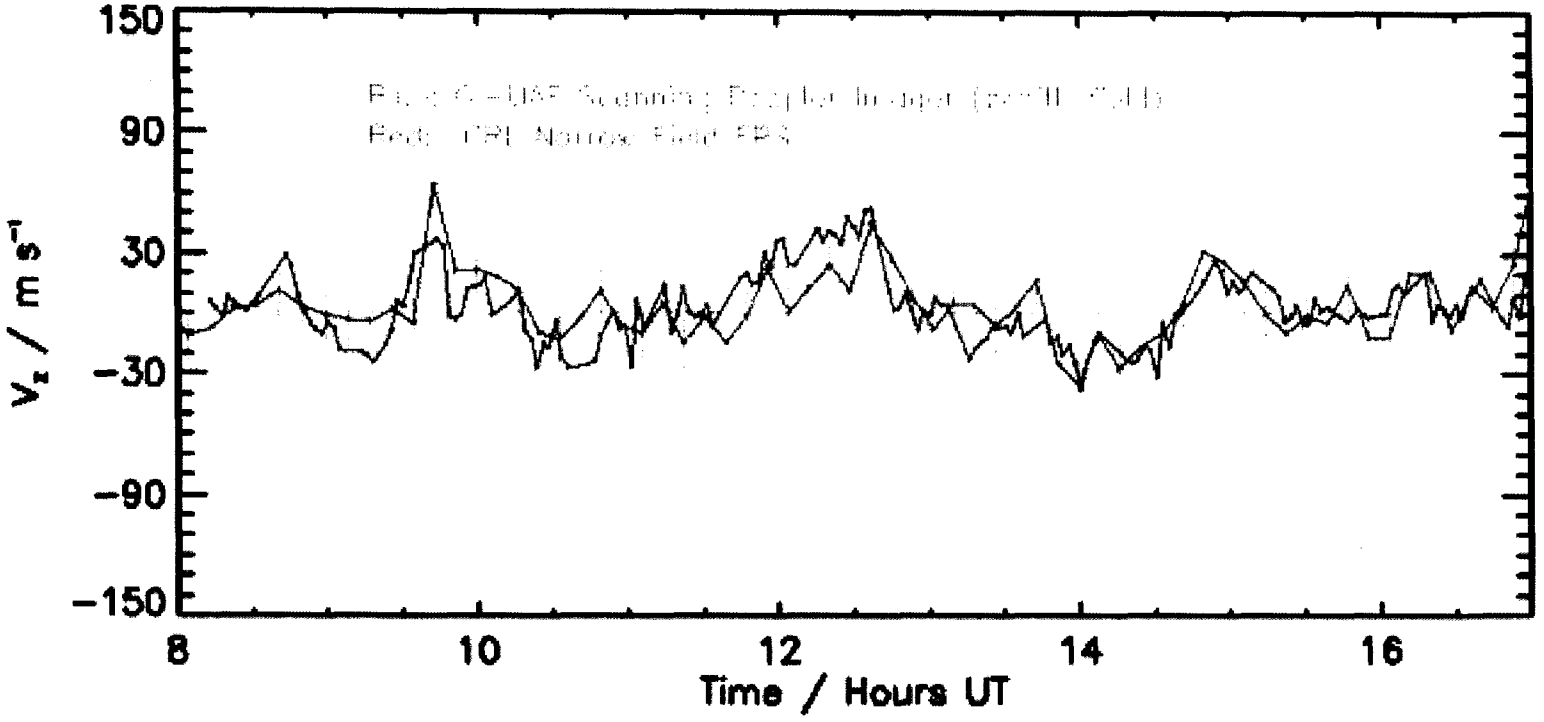

Figure 3.7. Upper-thermospheric vertical wind measurements from the night of December 25, 1998 obtained with the CRL-FPS and the SDI-FPS at Poker Flat, AK. The red line indicates the vertical winds measured with the CRL-FPS,, which were computed using the analysis procedures of *Conde* [2002] and *Conde* [2001] as described in the text. The blue line indicates the vertical winds measurements obtained with the SDI-FPS, which were computed using the analysis procedures of *Conde and Smith* [1995; 1997; 1998]. The general trends in the variations of the vertical wind time series are similar through most of the night, giving confidence that the analysis procedures of *Conde* [2002] and *Conde* [2001] are performing adequately. Discrepancies between the two time series can be attributed to the significant differences between the two instruments, which is discussed in the text. [Figure presented by *Conde* at the CEDAR conference, June, 2003, Longmont, CO].

thermospheric vertical wind data sets from Inuvik that have been computed using these analysis procedures in general have similar characteristics (*e.g.*, typical wind speeds, wave structure, large-magnitude wind events) to vertical wind data obtained at other high latitude sites [*e.g. Rees et al.*, 1984; *Price et al.*, 1995; *Innis et al.*, 1996; 1997], providing further confidence that the analysis procedures of *Conde* [2002] and *Conde* [2001] are accurately reducing the Inuvik FPS raw image data to 1-D sky and laser spectra and their respective spectral widths, Doppler shifts and intensities. After these analysis procedures are executed on a given data set of Inuvik FPS fringe images and the raw spectral peak positions are averaged to zero to determine the zero Doppler-shift reference (recall from Section 3.1.1.1), the last step in the reduction of the image data to actual wind measurements is to correct for the étalon's drift in the spectral peak position information.

3.1.4 Correcting for Étalon Drift and the Inuvik Vertical Wind Time Series

In the previous section, two techniques were outlined in the context of the CRL-FPS and SDI-FPS wind observations that attempt to correct for an étalon's drift which occurs over the course of an observation period. For the case of the SDI-FPS, the étalon's drift is generally negligible since the étalon is temperature-controlled and pressure-sealed, and consequently, the analysis procedures of *Conde and Smith* [1998] use the fairly simple method of high-pass filtering the zenith peak position data to determine the time-varying estimate of the étalon drift. The CRL-FPS, conversely, employs a Queensgate étalon that is open to air, and therefore, its optical path length changes with the varying ambient pressure and temperature like the Inuvik étalon. These changes in the étalon's optical path length are monitored by imaging the fringes of radiation from a frequency-stabilized laser at regular intervals during a given observation period. The laser fringes are reduced to their 1-D spectra and spectral peak positions, and the laser peak position values determine a time-varying estimate to the drift that is subtracted from the sky-spectra peak position information. This method was also attempted at Inuvik. Regrettably, the He-Ne λ632.8-nm laser utilized at Inuvik that was intended for this drift-correction technique (in addition to determination of the étalon's instrument function) is not stable in frequency as the manufacturers guaranteed, making drift correction by this method impossible. Thus,

alternative means were developed to account for the étalon drift in the Inuvik vertical wind measurements presented here. The laser is still capable of providing a reliable étalon instrument function, except when the laser "mode-hops" during an exposure.

For the case of a fixed-gap étalon that is open to air, the optical path length $P = (2n'h)\cos\theta$ will vary with air's varying index of refraction n', which changes with the changing pressure and temperature. The drift-correction technique devised for the Inuvik FPS data involves regular monitoring of the pressure and temperature in the FPS housing (the trailer) with a pressure and temperature sensor that is located near the étalon (see the block diagram Figure 2.2 in Chapter 2). A pressure and temperature measurement is made at the end of each laser or sky exposure, and the data are collected in an ASCII file at the end of the night. The pressure and temperature data act as basis functions (discussed below) for the OI(630.0)-nm sky spectra peak positions from which a linear least-squares fit to the peak position data is computed, with error estimates of the fit also provided. Linear-least square fitting methods were presented in the previous section [*e.g. Bevington*, 1969; *Jenkins and Watts*, 1968], and are described in a bit more detail here.

Suppose the output $\{x_j, q_j\}$ of a system (*e.g.*, q_j is the raw spectral peak positions, x_j is time) has been measured at time steps $j = 1,\ldots, J$, and is known to vary with K external sources $\{x_j, b_k(x_j)\}$, $k = 1,\ldots, K$ (*e.g.*, pressure and temperature), which also have been measured at time steps $j = 1,\ldots, J$. In addition, the system output may have some, as yet, unknown functional form that follows the variation in x_j of the external sources. In general, the functional form of $q(x)$ that attempts to predict the relationship between q_j and x_j may be expressed in model form by a linear combination of any G specified functions (*e.g.*, polynomials, Fourier series, Gaussian) of x [*Press et al.*, 1992],

$$q(x) = a_0 + \sum_{g=1}^{G} a_g X_g(x), \tag{3.14}$$

where $X_g(x)$ are the arbitrary fixed functions of x, referred to as the basis functions, and the term "linear" refers strictly to the model's dependence on the adjustable parameters $\{a_g\}_{g = 1,\ldots, G}$ [*Press et al.*, 1992], which are determined from the numerical fitting procedures (discussed below). When attempting to determine the functional form of $q(x)$

that follows the variation in x of the external sources $b_k(x)$, the data sets of $b_k(x_j)$ can serve as the basis functions for the linear model. The functional form of $q(x)$ is then given by

$$q(x) = a_0 + \sum_{k=1}^{K} a_k b_k(x). \tag{3.15}$$

The numerical fitting procedures determine the relative strength of each external source by determining the values of the coefficients $\{a_k\}_{k=1,\ldots,K}$.

For the case of the Inuvik FPS drift correction, the basis functions are the pressure-variation data set $b_1(x_j)$ and what is referred to as the temperature-variation-response data set $b_2(x_j)$. The reason for using a temperature-variation-response data set as a basis function rather than the actual temperature-variation values is discussed more below. The functional form $q(x)$ of the drift correction is then given by

$$q(x) = a_0 + a_1 b_1(x) + a_2 b_2(x), \tag{3.16}$$

a_0, a_1, and a_2 are determined from the numerical fitting procedures, and $q(x_j)$, the value of $q(x)$ at $j = 1,\ldots, J$, is the drift of the étalon (in CNU) at x_j due to the varying pressure and temperature. The new, drift-corrected spectral peak positions $\{p_j(x_j)\}_{j=1,\ldots,J}$ are given by

$$p_j(x_j) = q_j(x_j) - q(x_j), \tag{3.17}$$

where the deviations in the OI(630.0)-nm spectral peak positions about the function $q(x)$ are now geophysically significant in that they represent Doppler shifts (about the zero Doppler-shift reference) due to vertical wind activity.

The numerical fitting procedures estimate the values of the coefficients a_0, a_1, and a_2 and test for the validity of the fit $q(x)$ by performing a χ^2 check at each time step j. Mathematically, the χ^2 test for this example is given by [*Press et al.*, 1992]

$$\chi^2 = \sum_{j=1}^{J} \left[\frac{q_j(x_j) - q(x_j)}{\sigma_j} \right]^2, \tag{3.18}$$

where σ_j is the standard deviation of the j^{th} peak position value $q_j(x_j)$. As was stated in the previous section, the best possible choice of $\{a_k\}$ will yield the minimum χ^2 when

$$\frac{\partial \chi^2}{\partial a_k} = 0 \tag{3.19}$$

for all k. Rather than numerically evaluate χ^2 using a grid search like the analysis methods

of *Conde* [2001] (see the previous section), where χ^2 is minimized with respect to each model parameter while the other parameters are held fixed, here, the model parameters $\{a_k\}$ which minimize χ^2 are evaluated using the method of singular value decomposition outlined in [*Press et al.*, 1992]. The material presented in [*Press et al.*, 1992] on singular value decomposition is beyond the scope of this discussion, but the numerical procedures, in determining the fit coefficients a_0, a_1, and a_2, also compute their uncertainties through a calculation of their respective variances [*Press et al.*, 1992]. The subsequent uncertainty σ_{pt} (in CNU) associated with the pressure-temperature drift-correction fit $q(x_j)$ in the spectral peak position values $p_j(x_j)$ at each x_j is combined with the uncertainty σ_{pk} in each individual peak position that was determined from the numerical fitting procedures of *Conde* [2001] (recall from the previous section), resulting in an uncertainty $\sigma_{pk,pt}$ in the spectral peak positions (relative to the zero Doppler-shift reference) that is given by

$$\sigma_{pk,pt} = [\sigma_{pk}^2 + \sigma_{pt}^2]^{1/2} \text{ (CNU)}. \tag{3.20}$$

In general, the uncertainty σ_{pt} in the individual peak position values due to the pressure-temperature drift correction is $\sigma_{pt} \approx \pm 0.010$-$0.200$ CNU, corresponding to an error in the vertical wind measurements of ± 0.75-15.00 m·s^{-1} (recall from the previous section that 1 CNU = 73.7554 m·s^{-1}). The previous section observed that the error in the wind speeds associated with the uncertainty σ_{pk} is also generally ± 0.75-15.00 m·s^{-1}. However, there are no instances in the Inuvik FPS vertical wind data sets presented here of a large uncertainty σ_{pk} combining with a large uncertainty σ_{pt}, and in general, the combined error $\sigma_{wnd,pk,pt}$ in the wind measurements associated with both sources of uncertainty is $\sigma_{wnd,pk,pt}$ = ± 2.00-15.00 m·s^{-1}. The pressure-temperature drift-correction numerical fits to each night's data set are discussed in more detail below with the presentation of the seven time series of Inuvik FPS OI(630.0)-nm peak position values. In addition, one other source of error in the wind measurements due to a last-resort drift correction is also discussed.

In general, changes in the étalon's optical path length due to pressure and/or temperature variations are easily recognized in the spectral peak position information, as the examples presented here will illustrate. On the nights where there was considerable variation in the trailer's temperature but little variation in the pressure, the effect of the

varying temperature on the peak position values is clearly identified. Similarly, on the nights where there was significant pressure variation but little temperature variation, the variation in the peak position values due to the changing pressure is easily recognized. As several of the spectral peak position examples will show (each of which will be discussed accordingly), increases in the trailer temperature (in °C) increase the value of the peak positions (in CNU) and vice versa, and decreases in the pressure (in mmHg) increase the peak position values and vice versa. Under these circumstances, the pressure-temperature drift-correction fits generally follow the slow and smooth variations in the étalon's optical path length (~1-5 CNU·hr^{-1}) that are attributed to either the varying trailer temperature (~1-3°C·hr^{-1}) or varying pressure (~1-2 mmHg·hr^{-1}). Furthermore, on nights where there was variation in both pressure and temperature, their competing effects on the étalon's drift (*i.e.*, on the spectral peak position values) can be discussed appropriately. It is also noted that with the way the analysis methods are implemented here, positive excursions in the peak position values about the zero Doppler-shift reference, when attributed to thermospheric wind activity, are representative of blue Doppler shifts (*i.e.*, towards the observer), and negative excursions represent red Doppler shifts (away from the observer). Therefore, positive excursions in the peak position values about the zero-velocity reference represent downward winds, and negative excursions indicate upward winds.

Returning to the discussion of the basis functions, the reason for using a temperature-variation-response data set $b_2(x_j)$ as a basis function rather than the actual temperature-variation values is because the FPS is not expected to respond immediately to temperature changes in the trailer. The heaters are located in different parts of the trailer relative to the temperature-pressure sensor and étalon. Furthermore, though the étalon is open to air and is also fairly close and thermally-coupled to the temperature-pressure sensor (through their respective mountings to the FPS optical-axis assembly), the étalon plates are surrounded by a robust metal jacket that houses the plates and capacitance-stabilization system, thermally distancing the étalon cavity from the temperature-pressure sensor more than the étalon's exterior. Consequently, variations in the trailer temperature due to the cycling of the heaters alter the sensor's reading before influencing, first, the exterior of

the étalon, and second, the étalon's plates, capacitance-stabilization components, and cavity; *i.e.*, increasing or decreasing the temperature of the air between the plates, thus changing the index of refraction in the étalon cavity. Therefore, a temperature-variation-response data set $b_2(x_j)$ that is derived from the temperature-variation data set is instead employed in an attempt to simulate the overall response of the étalon's optical path length to temperature variations in the trailer.

In essence, the temperature-variation-response data set $b_2(x_j)$ is a numerically-differentiated, shifted, and smoothed version of the trailer's temperature variation. Experience with hundreds of nights of Inuvik FPS OI(630.0)-nm and OI(557.7)-nm observations and subsequent attempts to account for the étalon drift in these data sets using this technique has revealed that shifting forward the original temperature variation values by the equivalent of ten minutes (*i.e.*, the sensor's measured temperature changes, the optical path length responds ~10 min later) yields a temperature-variation-response data set that, in most instances, functions as a basis function from which a reasonable drift-correction fit to the raw OI(630.0)-nm or OI(557.7)-nm spectral peak position data is computed. In general, these drift-correction fits remove the slow and smooth variations in the étalon's optical path length that are easily identified in the time series of peak positions and that can be attributed specifically to the smooth variations in temperature, providing confidence that the temperature-variation-response data set does in actuality simulate to a large extent the étalon's overall response to temperature variations in the trailer. Two examples presented here in particular illustrate this assertion.

However, the various linear and/or non-linear responses of the étalon's metal exterior, glass plates, and capacitance-stabilization components (which have different thermal properties), and of the étalon cavity's index of refraction, to temperature variations are not known and/or calibrated. In addition, difficulities with heating the trailer interior on some of the colder night's (*e.g.*, when the outside temperature was very cold, –40°C) resulted in a lower average trailer temperature during observations. For example, the mean trailer temperature during the December 22, 2000 FPS observations was ~23.5°C, but was ~20.5°C during the January 4, 2001 observations. These varying

temperature ranges from night to night may result in different linear and/or non-linear responses of the étalon components, though this statement cannot be confirmed. Ultimately, the sum total of the étalon's drift associated with these varying temperature responses of the étalon's components, and also due to changes in the relative humidity (which is not measured in the trailer but is temperature dependent and also contributes to étalon drift), is likely combined into the value of the a_2 coefficient, though this statement also cannot be confirmed. Nonetheless, it is the a_2 coefficient that exhibits the most variability from peak position data set to data set (whereas the a_1 pressure coefficient is much less variable) and which would most isolate the various responses of the étalon's components to temperature and humidity variations during observations and to the mean temperature and humidity from night to night, since it is this coefficient in the linear least-squares fit that is meant to account the étalon's response to temperature changes. Table 3.1 below shows the a_0, a_1, and a_2 drift coefficients for the seven nights of Inuvik FPS observations, along with their corresponding uncertainties, σ_{a_0}, σ_{a_1}, and σ_{a_2}. The

Table 3.1. Inuvik FPS pressure and temperature drift-correction coefficients. Their corresponding uncertainties are also shown. The drift correction $q(x_j)$ at each x_j is given by $q(x_j) = a_0 + a_1 b_1(x_j) + a_2 b_2(x_j)$, where $b_1(x_j)$ is the pressure-variation data set and $b_2(x_j)$ is the temperature-variation-response data set. The coefficients and uncertainties are in channel number units (CNU).

Date	a_0	$\pm$ σ_{a_0}	a_1	$\pm$ σ_{a_1}	a_2	$\pm$ σ_{a_2}
Jan 03, 2001	–0.20	0.07	–0.54	0.02	0.69	0.16
Dec 09, 2000	0.50	0.04	–0.64	0.22	3.24	0.13
Dec 22, 2000	0.02	0.03	–0.13	0.03	–0.25	0.12
Feb 28, 2000	0.24	0.06	–0.33	0.09	1.61	0.29
Jan 04, 2001	0.94	0.04	–0.43	0.03	1.99	0.05
Jan 26, 2001	–0.02	0.03	–0.57	0.08	1.49	0.12
Nov 28, 2000	0.43	0.06	–0.21	0.05	2.41	0.27

drift coefficients from each night's pressure-temperature drift correction are discussed more below along with the presentation of each night's time series of peak position values and the corresponding pressure-temperature drift-correction fits.

In general, étalon drift due to pressure, temperature, and humidity variations should be quantifiable in terms of well-defined coefficients that describe an étalon's average response in terms of physical laws, yielding the index of refraction of air in the étalon cavity as a function of these three factors. Experience has shown, however, that this is not always the case, and drift correction by any method is often an imperfect tool. Thus, a weighted 3rd- and 5th-degree polynomial fit is also applied to the peak position curves after the pressure-temperature drift correction. Before the pressure-temperature drift-correction method was developed, a polynomial fit was the only method applied to the time series of peak positions to account for étalon drift. Generally, a 7th- or 9th-degree polynomial was used, which usually succeeded in removing clearly-recognized étalon drift but also had the potential to remove geophysically-significant wave structure from the time series. The 3rd- and 5th-degree polynomial fit is a last resort to remove any variation in the peak positions that may be due to factors besides pressure and temperature; *e.g.*, those associated with the étalon's non-linear temperature response or with variations in the relative humidity, or due to potential artifacts introduced into the time series caused by inaccurate pressure-temperature drift correction. Error estimates are returned from the fit, and in general, the uncertainty σ_{py} in the peak position values due to the polynomial fit is $\sigma_{py} \approx \pm 0.020\text{-}0.250$ CNU, corresponding to wind measurement errors of $\pm 1.50\text{-}18.50$ $m \cdot s^{-1}$. The exception is the November 28, 2000 data set, which exhibited uncertainties of $\sigma_{py} \approx \pm 0.090\text{-}0.490$ CNU; *i.e.*, wind measurement errors of $\pm 7.00\text{-}36.00$ $m \cdot s^{-1}$. Total error in the peak position values σ_{tot} associated with the peak determinations of *Conde* [2001], the pressure-temperature drift correction, and the polynomial fit are given by

$$\sigma_{tot} = [\sigma_{pk,pt}^2 + \sigma_{py}^2]^{1/2} \text{ (CNU)}. \tag{3.21}$$

Any variation about the zero Doppler-shift reference remaining in the time series of peak position values after these drift-correction procedures are applied is presumed to be geophysical in nature, as discussed in Chapter 1; *i.e.*, vertical winds. In general, the total error $\sigma_{tot,wnd}$ in the Inuvik FPS vertical wind measurements presented here is $\sigma_{tot,wnd} = \pm 3.00\text{-}19.00$ $m \cdot s^{-1}$, except for the November 28, 2000 vertical winds, which have total wind measurement errors of $\sigma_{tot,wnd} = \pm 7.50\text{-}38.00$ $m \cdot s^{-1}$.

Figures 3.8a-b below show the pressure-temperature and polynomial drift-correction analysis for the night of January 3, 2001. Recalling from the previous section, the virtual étalon of the *Conde* [2002] analysis procedures is configured to scan through one free spectral range by stepping through 64 channels when sampling the FPS images. Thus, the 1-D sky spectra are returned as a function of channel number (see Figures 3.5 and 3.6), and their peak position estimates are in CNU. Figure 3.8a presents the time series of raw

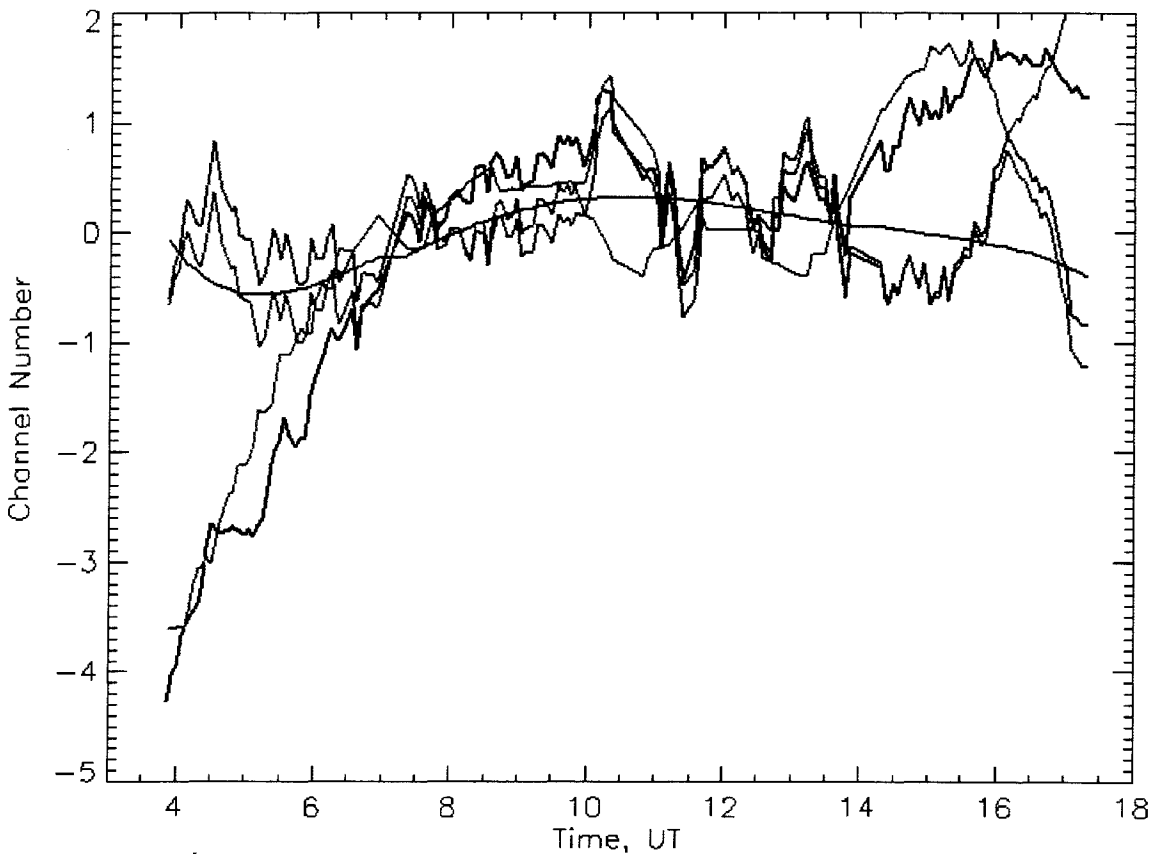

Figure 3.8. Étalon drift-correction analysis on the night of Jan 3, 2001. **(a)** The OI(630.0)-nm raw peak positions determined from the analysis procedures of *Conde* [2002] and *Conde* [2001] are in black. The raw peak position values shown here and in subsequent plots have been averaged to zero to determine the zero Doppler-shift reference. The pressure-temperature drift-correction fit to the peak position curve is in green. The orange curve represents the peak position values after the pressure-temperature drift-correction fit (green curve) has been subtracted from the raw peak positions (black curve). The blue curve is the polynomial fit to the orange curve, and the red curve is the orange curve minus the blue curve; *i.e.*, the final peak position values. See the text for a discussion of the material shown here.

OI(630.0)-nm peak position values in black. The values have already been averaged to zero, determining the zero Doppler-shift reference (recall from Section 3.1.1.1). The pressure-temperature drift-correction fit to the black peak position curve is shown in green. The orange curve represents the peak position values after the green curve has been subtracted from the black peak position curve. The blue curve is the polynomial fit to the orange curve, and the red curve is the orange curve minus the blue curve; *i.e.*, the red curve represents the final peak position values.

The peak position data set from the night of January 3, 2001 is an example of FPS observations that occurred during significant pressure variation but little temperature variation over the course of the night, and consequently, the slow and smooth drift of the étalon associated with the pressure variation is easily recognized in the peak position time series. Figure 3.8b below shows the raw peak positions in black and the pressure-temperature drift-correction fit in green. The absolute pressure is averaged to a zero-reference level similarly to the peak positions, and the relative pressure variation in mmHg is shown in blue. The trailer's relative temperature variation in °C is shown in orange, and the red curve represents the étalon's temperature-variation response. The "arbitrary units" designation to the *y*-axis refers to the peak positions, temperature, pressure and temperature-response.

At first glance, the pressure-temperature drift-correction numerical fit (green curve) may not look like a good representation of the black peak position curve. For example, from ~1000-1100 UT, the variation in the green curve certainly does not follow the variation in the black curve. However, it is important to remember that the pressure-temperature fit is not a best least-squares fit of, for example, some polynomial series but is the best least-squares fit using the given basis functions. Consequently, though the green curve may appear as a poor fit to the black curve during some time periods, the green curve in actuality does represent the drift of the étalon—within the determined uncertainties—due to pressure and temperature variations.

This example illustrates the general effect that pressure variations have on the étalon's optical path length. As the orange curve indicates in Figure 3.8b, the trailer's

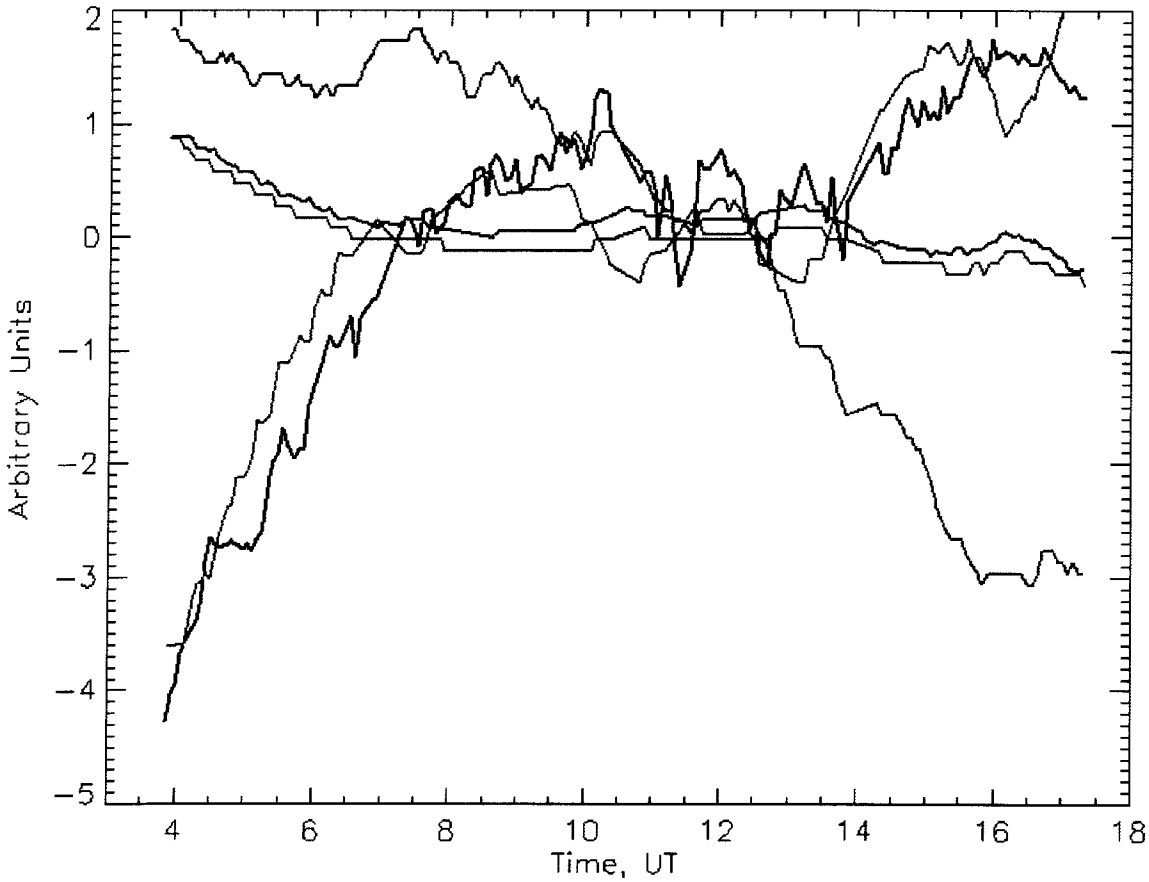

Figure 3.8 cont. Étalon drift-correction analysis on the night of Jan 3, 2001. **(b)** The raw peak positions (in CNU) are in black. The absolute pressure variation is averaged to a zero-reference level similarly to the peak position values, and the relative pressure variation (in mmHg) is shown in blue. The relative temperature variation (in °C) is shown in orange. The étalon's temperature-variation response is in red. The linear least-squares fit in green utilizes the pressure-variation $b_1(x_j)$ and temperature-variation-response $b_2(x_j)$ data sets as basis functions. See the text for a discussion of the material shown here.

temperature exhibited little variation during the night, and the substantial amount of slow, positive drift observed in the time series of peak position values that occurred during observations, approximately –4.5 to +2 CNU, is unquestionably due to the significant decrease in overall pressure, 5 mmHg, from the beginning of the night to the end. This assertion is also validated by the negligible error in the a_1 coefficient, $a_1 = -0.54 \pm 0.02$ CNU. Thus, some simple insight is acquired from this example; pressure decreases increase the optical path length of the étalon and vice versa. This insight benefits the

overall interpretation of the pressure-temperature numerical fits to the raw peak position curves from all the data sets. Here, the pressure-temperature drift-correction fit in general agrees well with the black peak position curve, although some clear discrepencies remain, which are presumed to be either geophysical in nature or are due to uncertainties in the fit. For example, the relatively large error in the a_2 coefficient, $a_2 = 0.69 \pm 0.16$ CNU, indicates that though there is some negligible étalon drift due to the weakly-varying temperature, the fitting procedures are not able to quantify it with certainty, and in general, the most significant error in the January 3, 2001 vertical wind measurements associated with the pressure-temperature drift correction are due to the uncertainty in quantifying the temperature-related drift. This is apparent during the ~1000-1100 UT time period, for example. The errors in the wind measurements increase from ~6 $m \cdot s^{-1}$ to ~8-10 $m \cdot s^{-1}$ over this time span, and illustrate the relative poorness of the fit associated with the slight temperature and pressure increases that occur concurrently. The presentation of the December 9, 2000 peak position data set next will clearly illustrate temperature-induced étalon drift, and the January 3, 2001 pressure-temperature fit in Figure 3.8b during the ~1000-1100 UT time period instead appears to follow the slight increase in pressure that occurred. This same scenario is obvious later on in the observations as well, from ~1545-1700 UT, where there is a leveling-off then slight increase in the pressure and another slight increase in the temperature. The pressure-temperature fit appears to follow the leveling-off and increase in the pressure instead of the slight temperature increase. Nonetheless, the pressure-temperature fit does indicate that some étalon drift occurred in these time spans, even if the fit is less reliable, and the drift is apparently associated with the pressure variation. Still, it is these examples illustrating where the pressure-temperature fit does not account for the étalon drift with certainty that led to the idea of using a last-resort polynomial fit to remove any remaining drift that may be present in the peak position time series. The polynomial fit (the blue curve in Figure 3.8a) has some weak variation to it about the zero-reference level and removes some long time scale undulation in the time series. The red curve in Figure 3.8a represents the final peak positions after the drift-correction procedures are complete.

When converted into velocity units, the red curve in Figure 3.8a yields the time series of vertical wind estimates from January 3, 2001 shown in Figure 3.9. Total error in the wind estimates are ~6-18 $m \cdot s^{-1}$. This time series exhibits several vertical wind events of fairly large magnitudes for extended periods of time; *e.g.*, one downward wind event beginning at ~1000 UT and lasting ~30 min, reaching magnitudes of –60 $m \cdot s^{-1}$, another upward event at ~1130 UT lasting for ~15 min, reaching magnitudes of up to ~60 $m \cdot s^{-1}$, and one at ~1300 UT, reaching magnitudes of –50 $m \cdot s^{-1}$. The question of whether these large wind speeds are statistically significant or not is answered by computing the standard deviation SD_{wnd} of the time series, which is given by [*e.g. Press et al.*, 1992]

$$SD_{wnd} = \left[\frac{1}{N-1} \sum_{j=0}^{N-1} (W_j - \overline{W})^2 \right]^{1/2}, \tag{3.22}$$

where N is the total number of wind measurements, W_j is the j^{th} wind measurement, and $\overline{W}$ is the mean wind speed, which is given by

$$\overline{W} = \frac{1}{N} \sum_{j=0}^{N-1} W_j . \tag{3.23}$$

The mean and standard deviation of the January 3, 2001 vertical wind time series are $\overline{W}$ = –0.92 $m \cdot s^{-1}$ and SD_{wnd} = 22.98 $m \cdot s^{-1}$, respectively. Because the magnitudes of these winds during the respective events reach values of ~2-3 times the standard deviation of the time series, these magnitudes represent significant wind activity relative to the typical wind activity that was occurring this night. Furthermore, because the standard deviation of the time series is greater than the typical error in the wind estimates, the measured wind speeds are truly representative of the vertical wind activity in the thermosphere this night. Lastly, the mean wind being close to zero implies that the drift-correction procedures performed adequately by not biasing the wind measurements positively or negatively. The other Inuvik FPS vertical wind measurements are discussed in more detail here after the completion of the drift-correction discussion and in Chapter 4 with the concurrent presentation of the column shift estimates. Table 3.2 presented at the end of this section lists the mean wind, standard deviation and typical error in the wind measurements for each Inuvik FPS data set presented here.

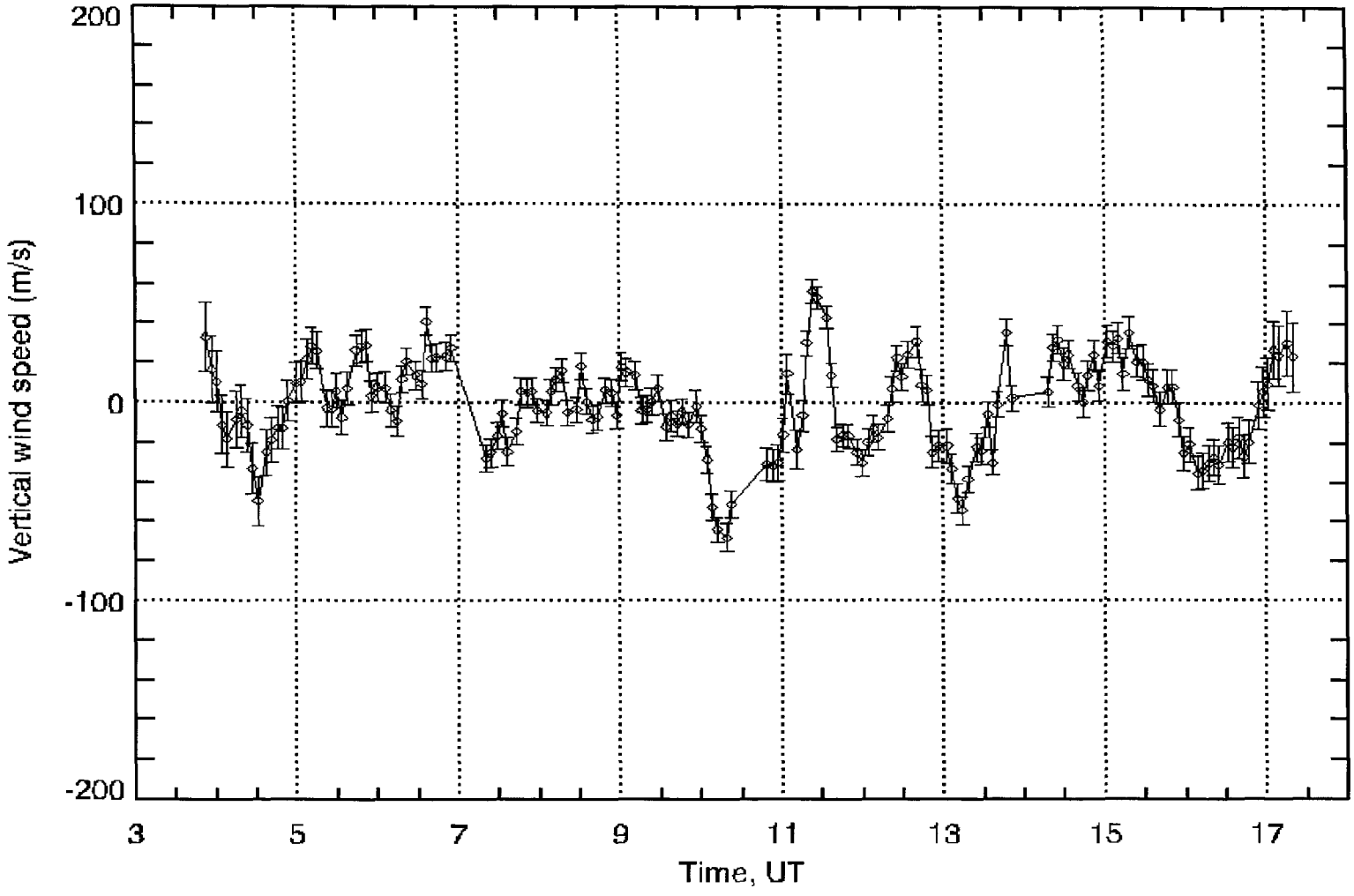

Figure 3.9 Upper-thermospheric vertical wind speeds on the night of Jan 3, 2001. Wind speeds are determined from the red curve in Figure 3.8a above. The error bars shown here include errors associated with the analysis procedures of *Conde* [2001], the pressure-temperature drift-correction, and polynomial drift-correction procedures.

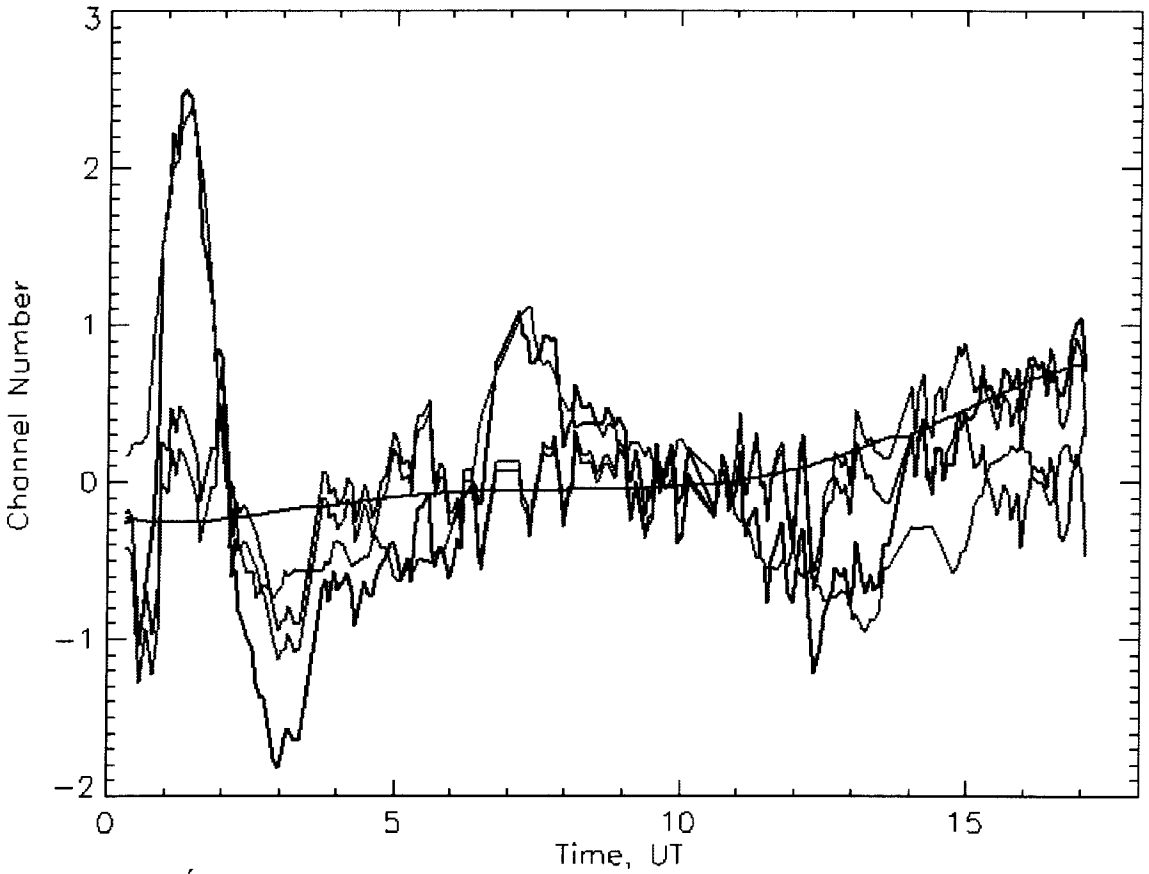

Figure 3.10. Étalon drift-correction analysis on the night of Dec 9, 2000. **(a)** The color scheme used in the previous (a) figure applies. The raw OI(630.0)-nm peak positions in CNU are shown in black, the green curve is the pressure-temperature drift-correction fit to the black curve, the orange curve is the black curve minus the green curve, and the blue curve is the polynomial fit to the orange curve. The red curve is the orange curve minus the blue curve, and represents the final peak positions. See the text for discussion.

Figures 3.10a-b show the pressure-temperature and polynomial drift correction for the night of December 9, 2000. This is an example where the pressure variation was negligible throughout the night, but the temperature variation was significant. There was considerable difficulty maintaining a steady temperature in the trailer on this night, and the étalon drifted accordingly. Using the same color scheme as in Figures 3.8a-b, Figure 3.10a shows the raw OI(630.0)-nm peak position values in black. The values have been averaged to zero, determining the zero Doppler-shift reference. The pressure-temperature drift correction fit to the black curve is shown in green. The orange curve is the peak

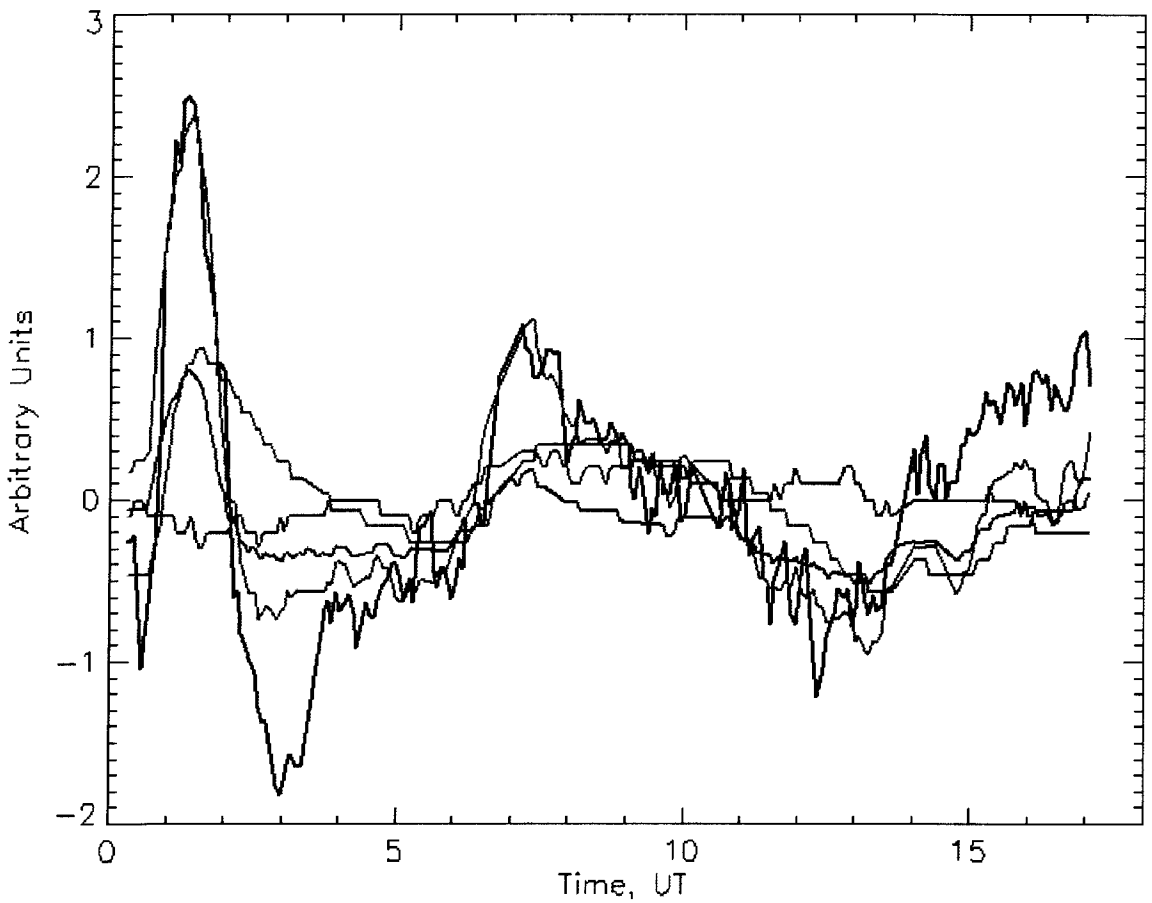

Figure 3.10 cont. Étalon drift-correction analysis on the night of Dec 9, 2000. **(b)** The color scheme used in the previous (b) figure applies. The raw peak positions are in black, the green curve is the pressure-temperature fit to the black curve, the blue curve is the relative pressure variation, the red curve is the relative temperature variation, and the orange curve is the étalon's temperature-variation response. See the text for discussion.

position values after the green curve has been subtracted from the black curve. The blue curve is the polynomial fit to the orange curve, and the red curve, which represents the final peak position values, is the orange curve minus the blue curve. In Figure 3.10b, the peak positions are again shown in black, and the pressure-temperature drift-correction fit is in green. The absolute pressure is averaged to a zero-reference level similarly to the peak positions, and the relative pressure variation is shown in blue. The trailer's relative temperature variation is shown in orange, and the red curve represents the étalon's temperature-variation response.

As the blue curve indicates in Figure 3.10b, the atmospheric pressure exhibited very little variation during observations, but the temperature, indicated by the orange curve, was highly variable. The varying temperature over the course of the night resulted in significant étalon drift that is easily recognizable in the time series of peak position values. For example, a temperature increase of 1.5°C from ~0030-0145 UT resulted in an increase in the optical path length of approximately +0.2 to +2.3 CNU based on the pressure-temperature fit's computation. In addition, the fitting procedures identified the decrease in the optical path length as the temperature slowly decreased from ~0130-0600 UT, the increase in optical path length as the temperature again increased from ~0600-0700 UT, and the decrease in optical path length as the temperature leveled off then slowly decreased from ~0700-1330 UT. The assertion that the pressure-temperature fit accurately removes the étalon's drift associated with the varying temperature is further validated by the relatively (*e.g.*, compared to the January 3, 2001 data set) negligible error in the a_2 coefficient, $a_2 = -3.24 \pm 0.13$ CNU.

Using this example, it is observed that increases in the temperature increase the optical path length of the étalon and vice versa. As with the pressure variation in the January 3, 2001 example, the information acquired from this example contributes to a better understanding of étalon drift in general. This understanding in particular will benefit the discussion concerning the Inuvik FPS peak position data set presented next. Here, the pressure-temperature drift-correction fit in general agrees with the black peak position curve very well, except after ~1400 UT, where the pressure-temperature fit does follow the upward trend of the slowly-increasing temperature but is not centered on the peak positions. This may be attributed to uncertainty in the fit since the pressure coefficient was considerably more uncertain in this example than in the January 3, 2001 data set, $a_1 = -0.64 \pm 0.22$ CNU, or it may have geophysical significance. Nonetheless, the polynomial fit removes this potential artifact of the pressure-temperature drift subtraction, as is illustrated by the blue curve's variation after ~1300 UT in Figure 3.10a, which is the fit to the orange curve. The vertical wind estimates from this night, determined from the red curve in Figure 3.10a, are shown in Figure 3.11.

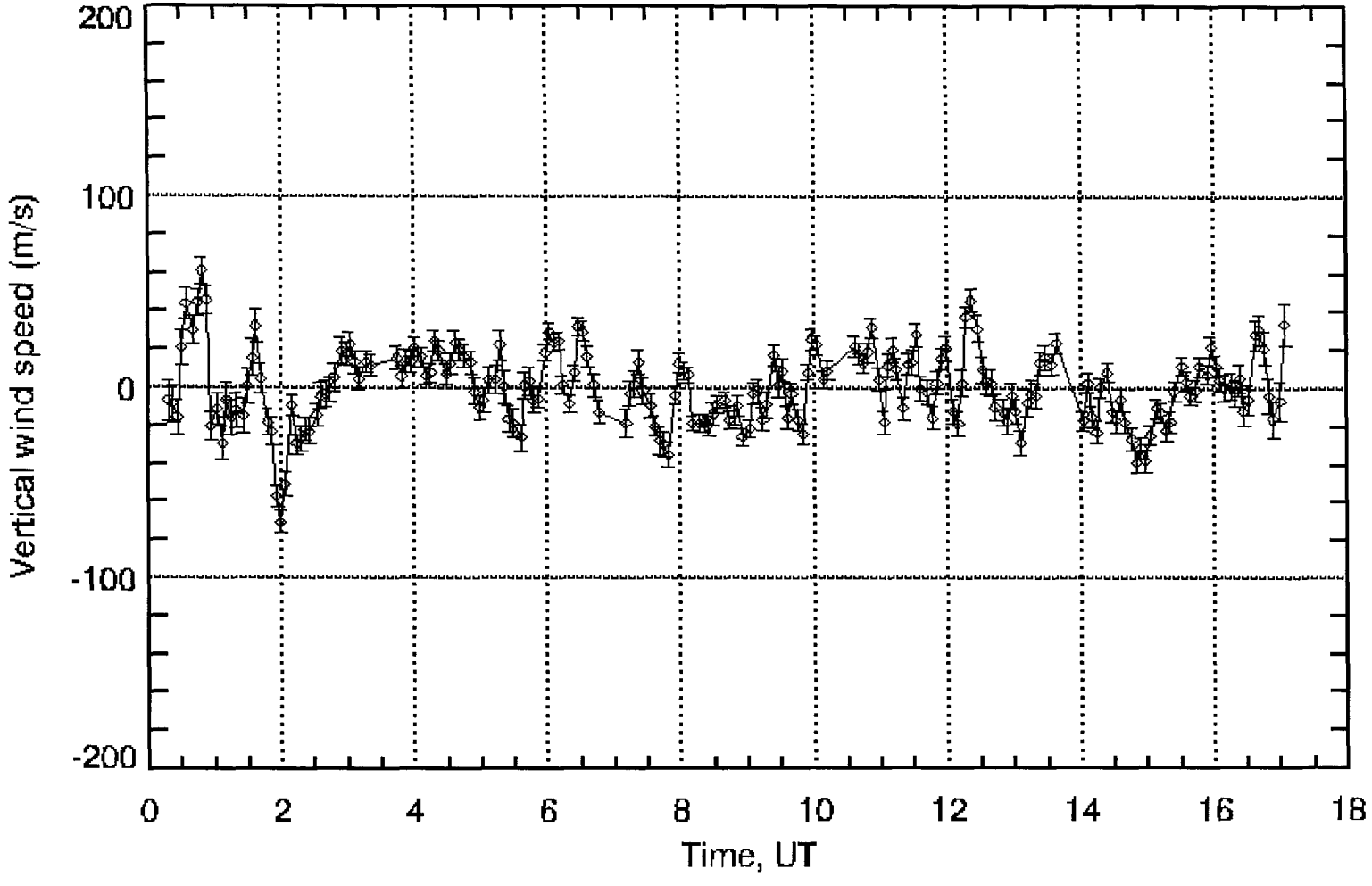

Figure 3.11 Upper-thermospheric vertical wind speeds on the night of Dec 9, 2000. Wind speeds are determined from the red curve in Figure 3.10a above. The error bars shown here include errors associated with the analysis procedures of *Conde* [2001], the pressure-temperature drift-correction, and polynomial drift-correction procedures.

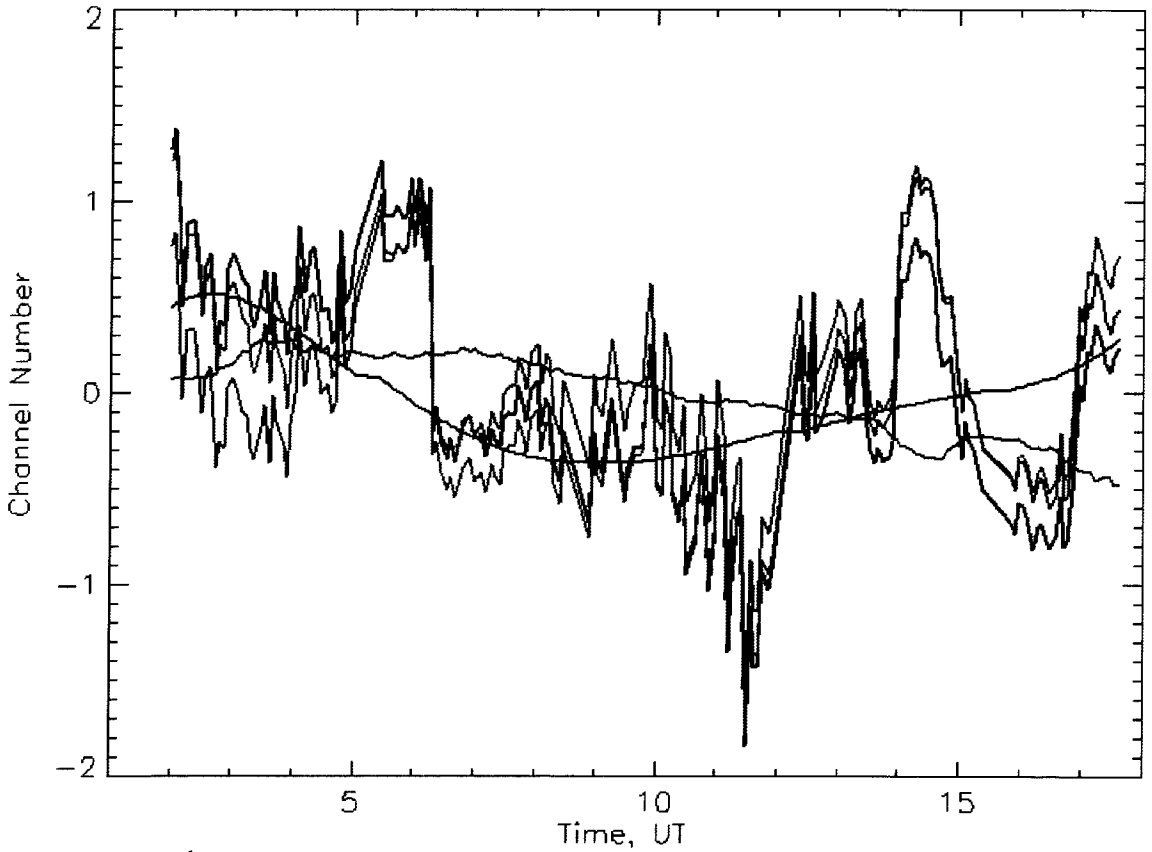

Figure 3.12. Étalon drift-correction analysis on the night of Dec 22, 2000. **(a)** The color scheme used in previous (a) figures applies. The black curve indicates the raw OI(630.0)-nm peak position values, the green curve is the pressure-temperature fit to the black curve, the orange curve = black – green, the blue curve is the polynomial fit to the orange curve, red = orange – blue is the final peak position values. See the text for discussion.

An example of what initially appears to be poor pressure-temperature drift correction is shown in Figures 3.12a-b. This data set was obtained on December 22, 2000, a night that exhibited significant positive and negative variation in both the pressure and temperature. A preliminary inspection of the pressure-temperature drift-correction fit (green curve) in Figure 3.12a seems to reveal that the fit does not follow very well at all the significant variation in the peak position values (black curve). In addition, the a_0, a_1, and a_2 coefficients are all close to zero, and this is also the only peak position data set in which the a_2 coefficient was determined to be negative (though considerably uncertain), $a_2 = -0.25 \pm 0.12$ CNU. However, upon closer examination, much of the variation in the

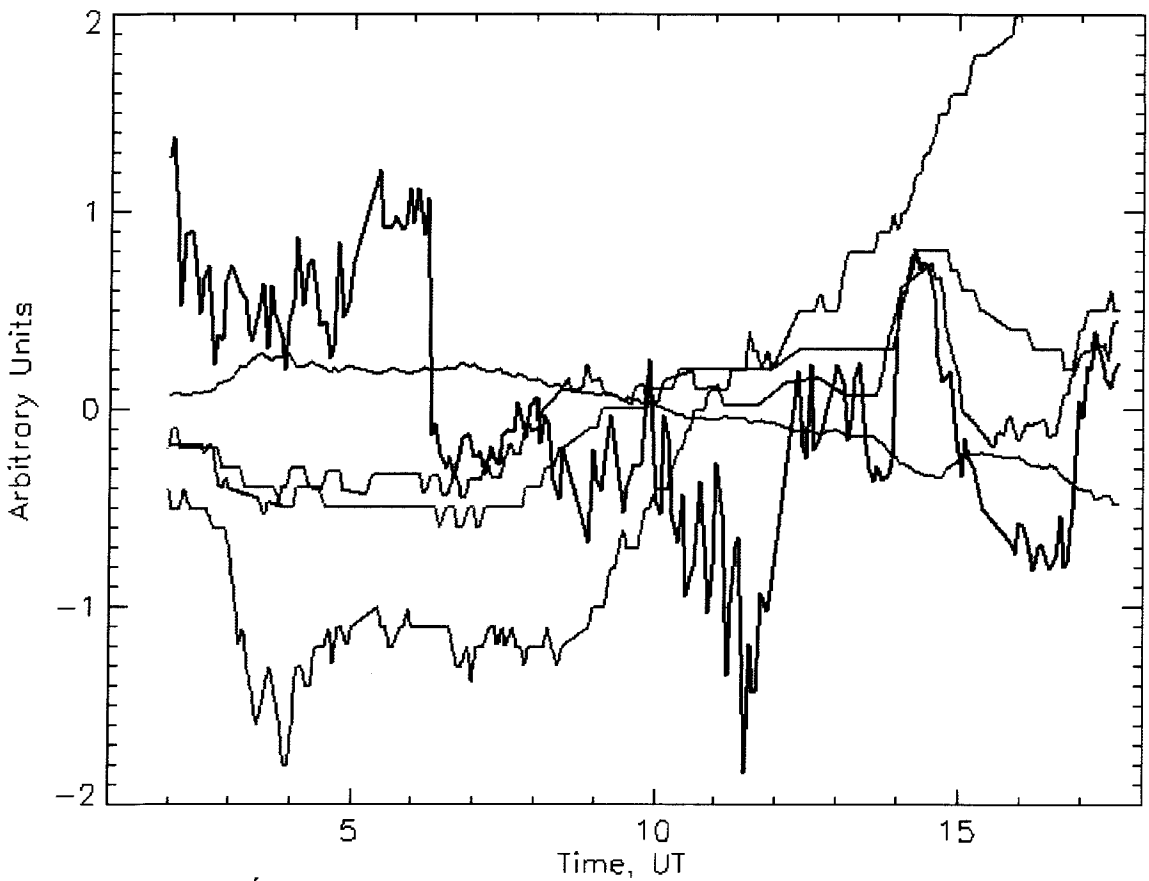

Figure 3.12 cont. Étalon drift-correction analysis on the night of Dec 22, 2000. **(b)** The color scheme used in previous (b) figures applies. The black curve represents the raw peak position values, the green curve is the pressure-temperature fit to the black curve, the blue curve indicates the relative pressure variation, the orange curve is the relative temperature variation, and the red curve is the étalon's temperature-variation response. See the text for discussion.

peak position values can be attributed specifically to vertical wind activity, ~0.1-1 CNU·min^{-1}, and not to étalon drift of ~1-5 CNU·hr^{-1}. This is because throughout much of the night, the competing influences of either positive pressure variation (resulting in negative drift) and positive temperature variation (resulting in positive drift) occur concurrently or negative pressure variation (*i.e.*, positive drift) and negative temperature variation (*i.e.*, negative drift) occur concurrently, as Figure 3.12b illustrates. Thus, the overall effect of these competing influences would be little or no étalon drift, which the pressure-temperature fit seems to indicate. For example, from ~0800 UT to the end of

observations, the pressure increased considerably, >3 mmHg. Significant negative étalon drift of ~5 CNU would normally accompany this pressure change based on the January 3, 2001 example, but also occurring during this time period are several temperature increases (orange curve), which would typically result in positive étalon drift based on the December 9, 2000 example. According to the pressure-temperature fit, the subsequent weak étalon drift (+0.2 to –0.5 CNU) that occurs over this 10-hr time period due to these competing influences follows the positive pressure change while being moderated by the positive temperature change. Furthermore, in the midst of this broad pressure and temperature increase is an interesting smaller feature. From ~1400-1430 UT, there is a temperature increase of 0.5 °C, which normally would cause a positive étalon drift ~0.7 CNU based on the December 9, 2000 example. However, the pressure also increases considerably during this time period, 0.5 mmHg, which would normally result in a drift of ~0.7 CNU based on the January 3, 2001 example. The pressure-temperature fitting procedures actually determine that negative étalon drift of ~0.2 CNU occurs from ~1400-1430 UT, confirming the results of the previous two examples within the range of uncertainties, while the peak position values appear to follow the temperature increase during this ~1400-1430 UT time period. Overall, the errors in the wind measurements associated with the pressure-temperature drift correction are larger here than for the two data sets already presented, and this error is clearly due to the difficulty in quantifying the drift due to temperature variations, as illustrated by the significant uncertainty in the a_2 coefficient. The a_1 coefficient here was computed with greater certainty, $a_1 = -0.13 \pm 0.03$ CNU. The vertical wind estimates from this night are shown in Figure 3.13.

The February 28, 2000 drift-correction procedures are shown in Figures 3.14a-b. This is an example where the variations in pressure and temperature were minimal, but the changes in pressure and temperature that do occur through much of the night act to compete against each other in terms of the étalon drift. There is also an interval when a fairly significant increase in the trailer temperature occurred (orange curve in Figure 3.14b). Nonetheless, the pressure-temperature numerical fit (green curve in Figures 3.14a-b) overall performs well here within the ranges of uncertainty. For example, from

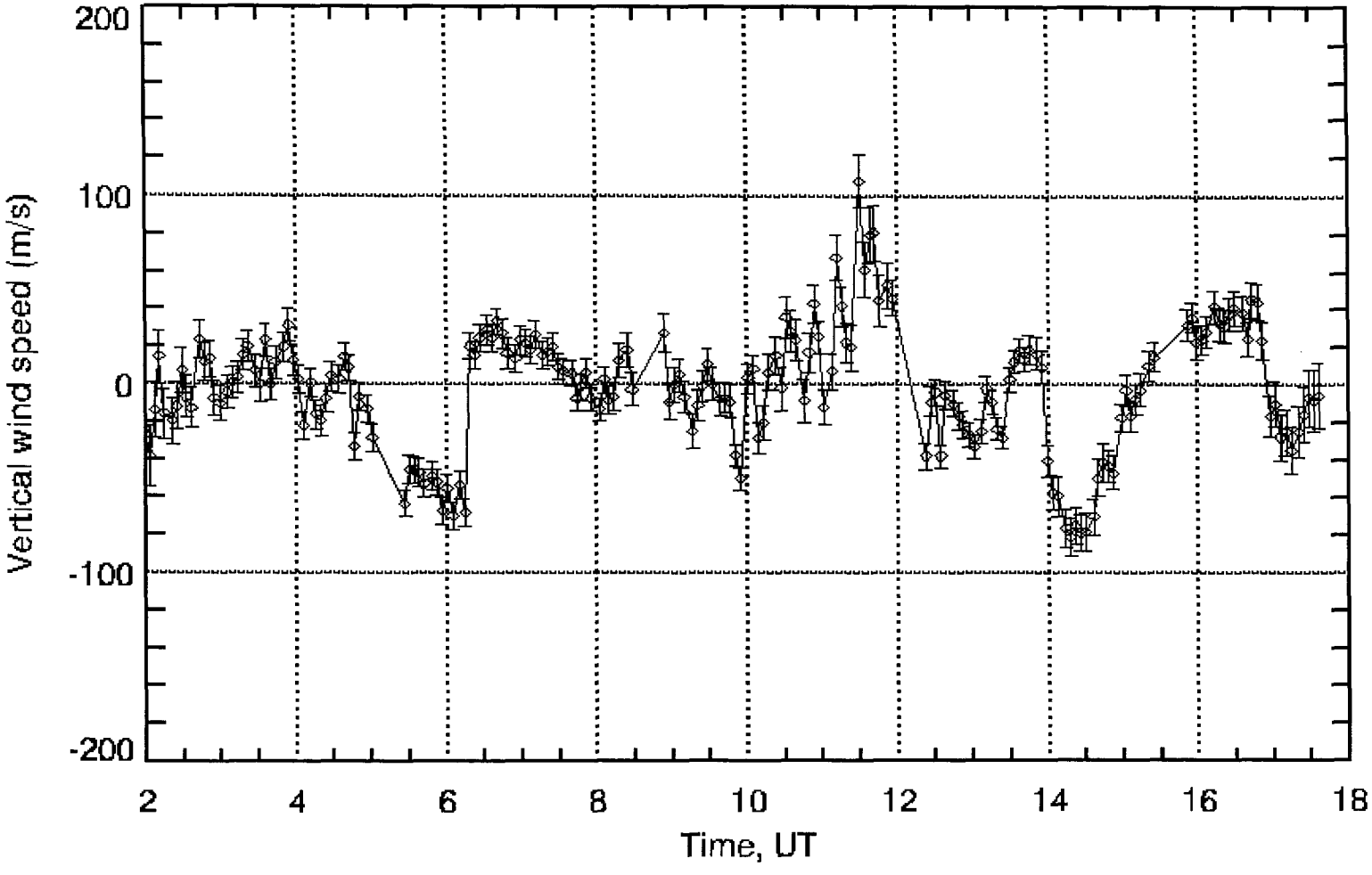

Figure 3.13 Upper-thermospheric vertical wind speeds on the night of Dec 22, 2000. Wind speeds are determined from the red curve in Figure 3.12a above. The error bars shown here include errors associated with the analysis procedures of *Conde* [2001], the pressure-temperature drift-correction, and polynomial drift-correction procedures.

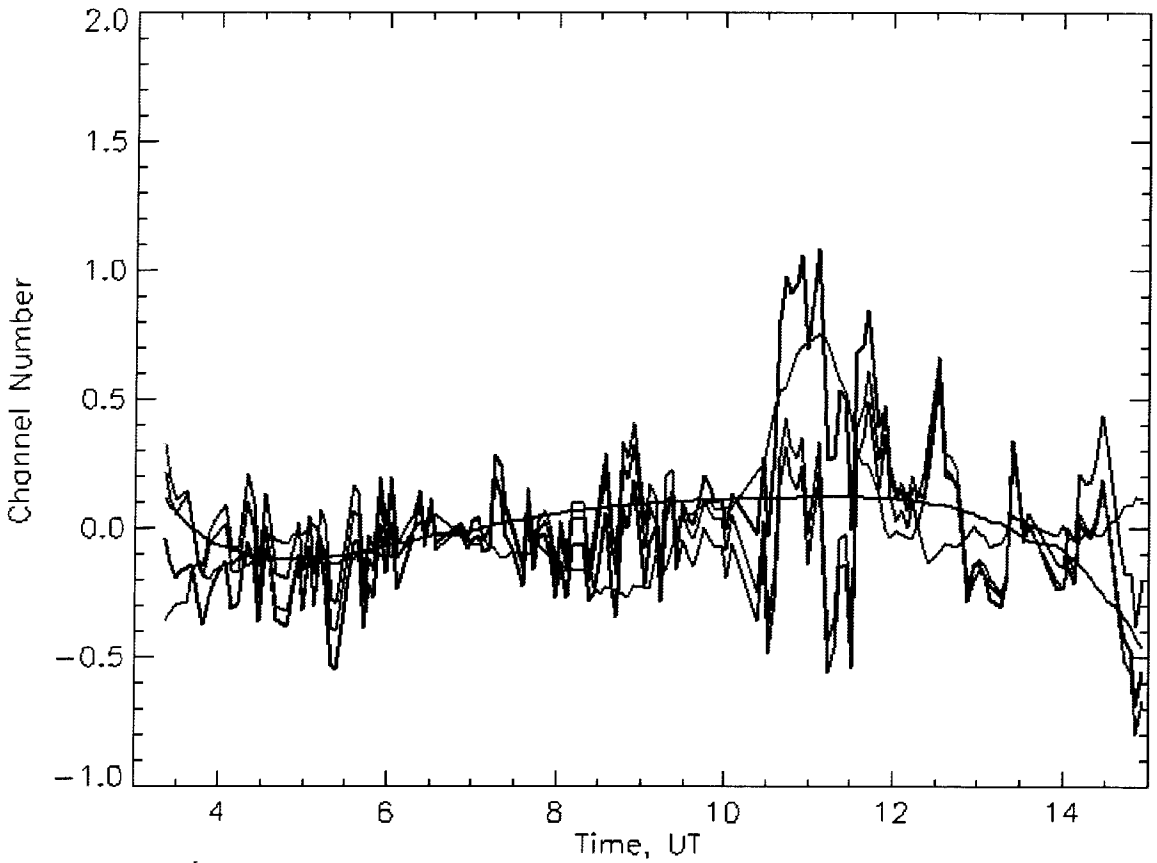

Figure 3.14. Étalon drift-correction analysis on the night of Feb 28, 2000. **(a)** The color scheme used in the previous (a) figures applies. Black is the raw OI(630.0)-nm peak position values, green is the pressure-temperature fit to black, orange = black – green, blue is the polynomial fit to orange, red = orange – blue is the final peak position. See the text for discussion.

~0315-0645 UT, the pressure decreases by 1 mmHg, which would result in a positive drift of ~1.3 CNU based on the above discussions, while the temperature slowly decreases by 0.2 °C, which would result in a negative drift of ~0.3 CNU based on the above discussions. During this ~0315-0645 UT time span, the fit identifies a drift of approximately –0.4 to +0.1 CNU, which does not quite match the total drift of 1.3 – 0.3 = 1.0 CNU that would occur based on the above discussions, but does follow the overall positive trend. Furthermore, from ~0645-0900 UT, during which time the pressure levels off, the pressure-temperature fit generally follows the continuing decrease in temperature. And from ~0900-1200 UT, the pressure-temperature fit follows the increase in peak

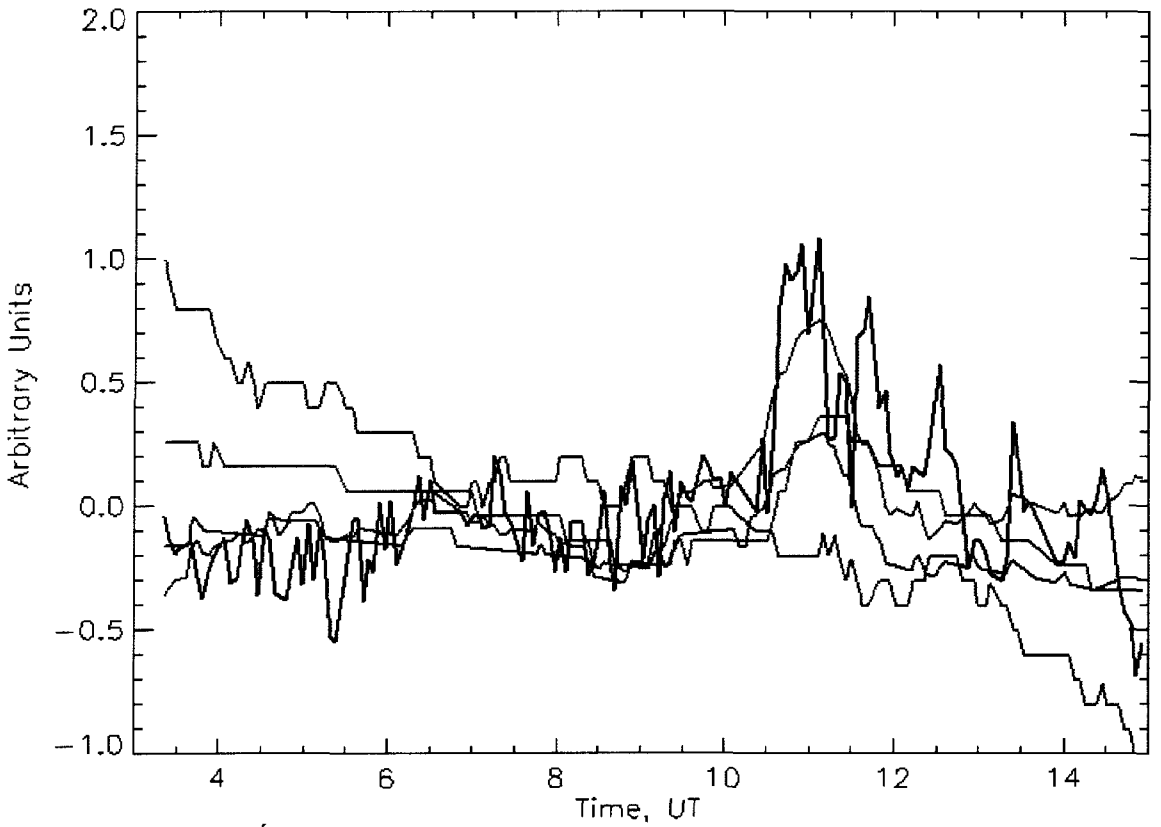

Figure 3.14 cont. Étalon drift-correction analysis on the night of Feb 28, 2000. **(b)** The color scheme used in previous (b) figures applies. The black curve represents the raw peak position values, the green curve is the pressure-temperature fit to the black curve, the blue curve indicates the relative pressure variation, the orange curve is the relative temperature variation, and the red curve is the étalon's temperature-variation response. See the text for discussion.

position values attributed to the increasing temperature. After ~1200 UT, the pressure-temperature fit appears to have more difficulty removing the étalon drift, which is now attributed to the decreasing temperature competing with the decreasing pressure. The greater uncertainty in the pressure-temperature fit is illustrated by the wind measurement errors after ~1200 UT, which increase from ~4 $m \cdot s^{-1}$ to ~5-10 $m \cdot s^{-1}$, and the polynomial fit, which takes on significantly more variation after ~1300 UT. The total uncertainty in the pressure-temperature fit can be attributed to the fit's uncertainty in quantifying both the pressure and temperature drifts, based on similar relative errors in the fit coefficients, $a_1 = -0.33 \pm 0.09$ CNU and $a_2 = 1.61 \pm 0.29$ CNU. The estimated vertical winds from this

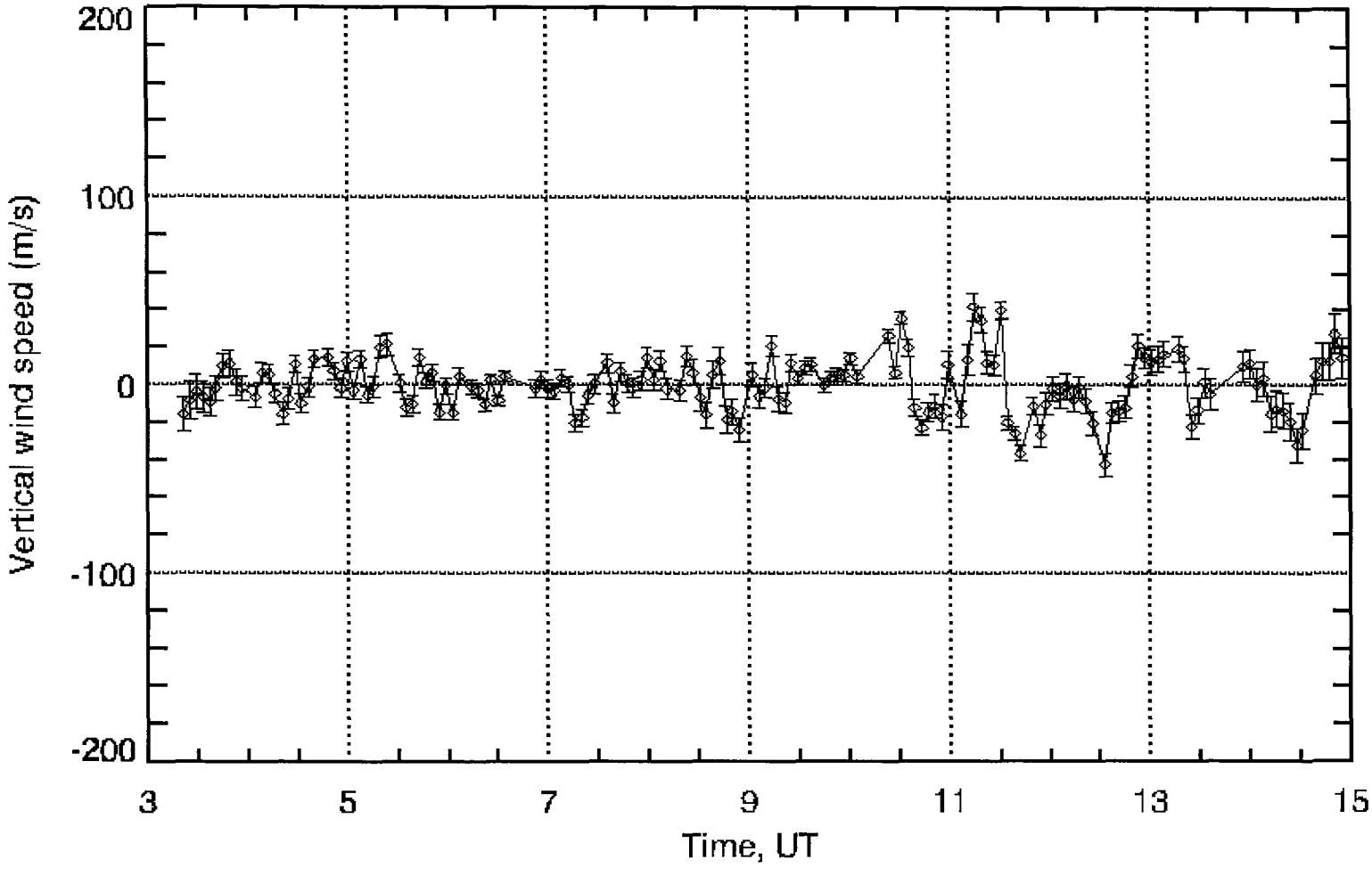

Figure 3.15 Upper-thermospheric vertical wind speeds on the night of Feb 28, 2000. Wind speeds are determined from the red curve in Figure 3.14a above. The error bars shown here include errors associated with the analysis procedures of *Conde* [2001], the pressure-temperature drift-correction, and polynomial drift-correction procedures.

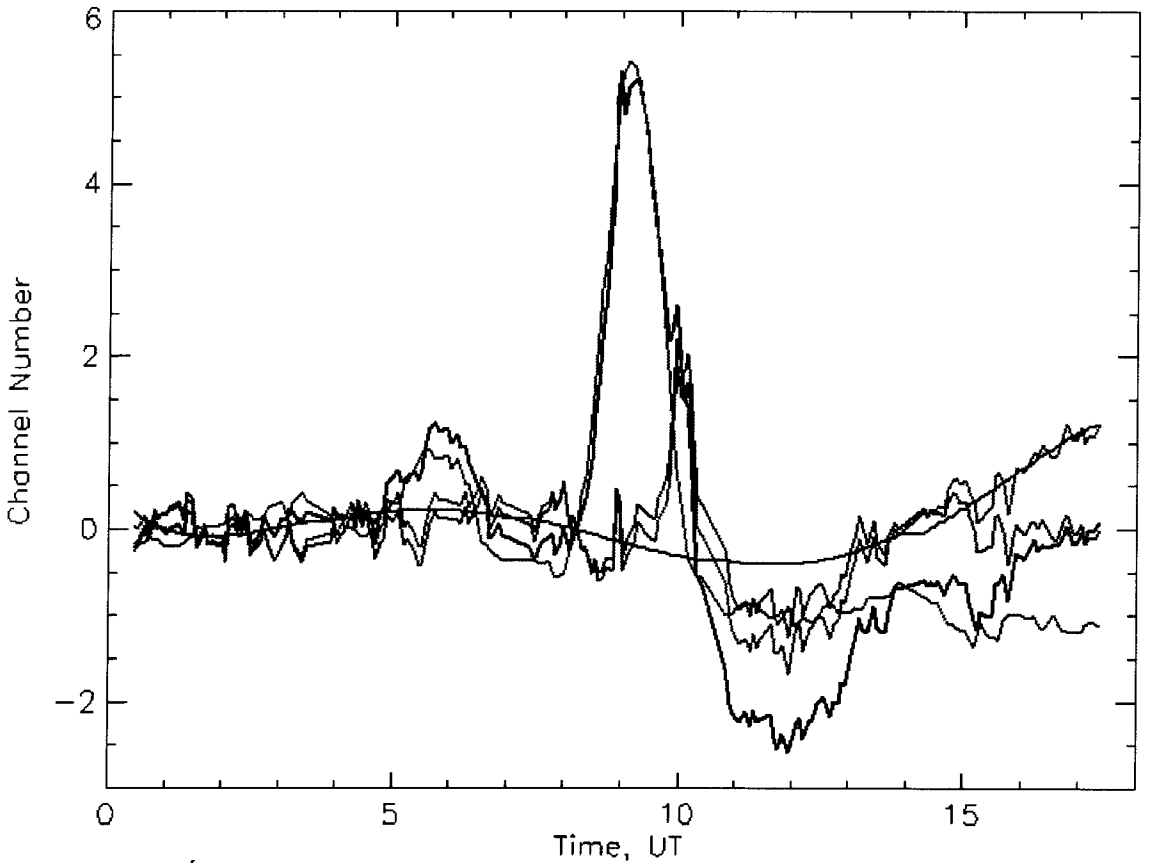

Figure 3.16. Étalon drift-correction analysis on the night of Jan 4, 2001. **(a)** The color scheme used in the previous (a) figures applies. Black is the raw OI(630.0)-nm peak position values, green is the pressure-temperature fit to black, orange = black – green, blue is the polynomial fit to orange, red = orange – blue is the final peak position. See the text for discussion.

night are shown in Figure 3.15 above. As was stated earlier, time series of vertical winds are often stochastic in appearance, and this is apparent in the February 28, 2000 vertical winds early in the night. Two fairly significant vertical wind events do occur later.

The January 4, 2001 drift-correction procedures are shown in Figures 3.16a-b. This is an example where the variations in both the pressure and temperature were negligible early in the night but significant later on, and the changes in pressure and temperature that occurred later the night acted to compete against each other in terms of étalon drift. Between ~0000-0500 UT, the pressure (blue curve in Figure 3.16b) remained fairly steady, but after that, the pressure increased steadily by 3 mmHg, which would result in a drift of

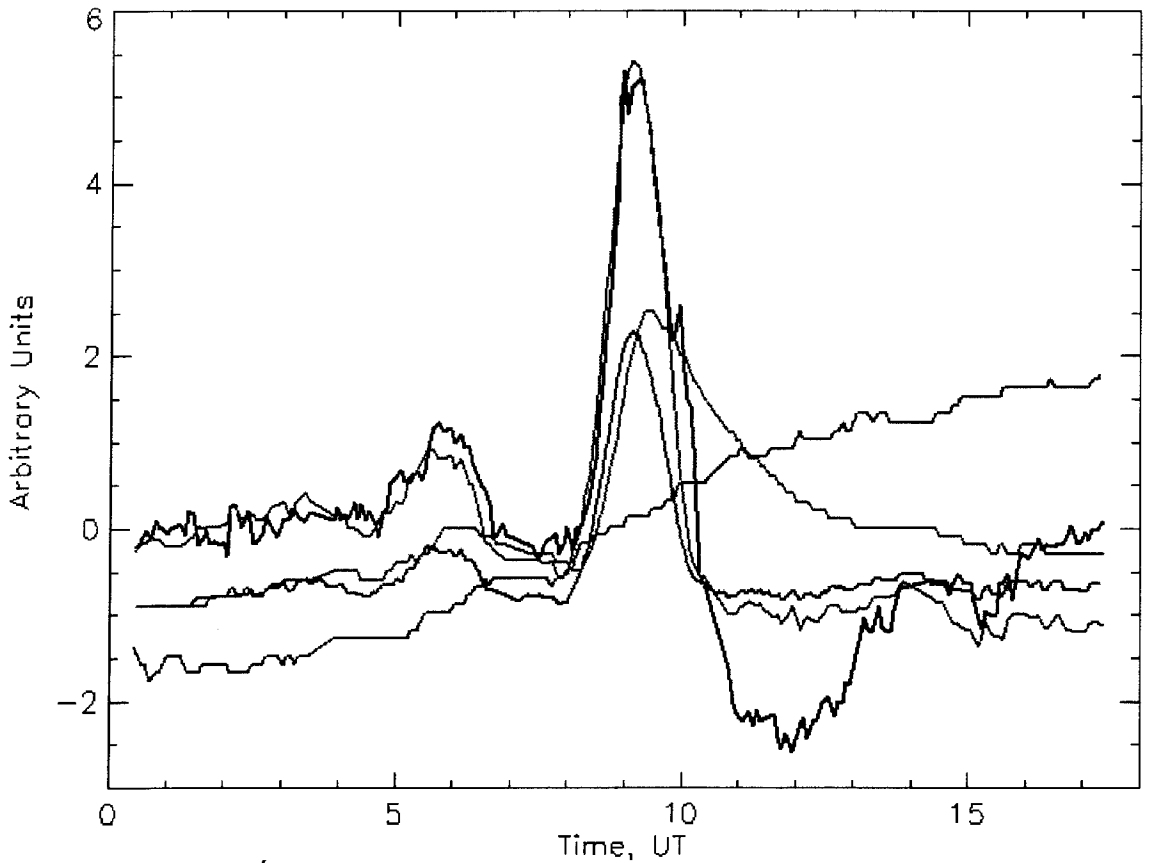

Figure 3.16 cont. Étalon drift-correction analysis on the night of Jan 4, 2001. **(b)** The color scheme used in the previous (b) figures applies. Black is the raw peak position, green is the pressure-temperature fit to black, blue is the pressure variation, red is the temperature variation, and orange is the étalon temperature-variation response. See the text for discussion.

of 4 CNU based on the previous discussions. Between ~0000-0445 UT, the temperature (orange curve in Figure 3.16b) also remained fairly steady, and accordingly, the variation in the peak position values (black curve in Figures 3.16a-b) is essentially about the zero Doppler-shift reference, as is the pressure-temperature fit, indicating that little or no étalon drift was occurring during this time span. After ~0445 UT, however, the temperature became highly variable, and after ~0500 UT, the pressure began its steady increase. The étalon drifted accordingly.

In general, the pressure-temperature fit (green curve) succeeds here in removing the étalon drift from the raw peak position data set. This assertion is validated by the

negligible uncertainty in both the a_1 and a_2 coefficients, $a_1 = -0.43 \pm 0.03$ CNU and $a_2 = 1.99 \pm 0.05$ CNU, and is also readily identified in the pressure-temperature fit. For example, from ~0445-0600 UT, there is a moderate increase in the pressure of 0.4 mmHg accompanied by a moderate increase in the temperature of 0.6 °C. The total resulting positive drift due to both sources would be (according to the previous discussions) ~0.3 CNU, which the peak positions and numerical fit exhibit during this time span within the ranges of uncertainty. From ~0600-0800 UT, the pressure becomes steady while the temperature slowly decreases, and the negative drift identified in the peak position values associated with the slow temperature decrease is suitably removed by the pressure-temperature fit. From ~0800-0915 UT, there is a large increase in the temperature of 3 °C, accompanied by a large increase in peak position values of 5 CNU. After 0915 UT, the temperature begins to decrease, and the étalon's optical path length begins to recover, slowly returning to pre-temperature-increase values between 0915 UT and 1015 UT. The pressure-temperature fit, which clearly follows the smooth variation in the peak position values due to the increasing-then-decreasing temperature, visibly removes the étalon drift during this ~0800-1015 UT time period.

Examination of the orange curve (the black curve minus the green curve) and red curve (the orange curve minus the blue polynomial fit) in Figure 3.16a shows that there is significant variation remaining in the peak position values around 1000 UT after the drift-correction procedures. The time series of vertical wind measurements from this night is shown in Figure 3.17, which exhibits a significant downward wind event at ~1000 UT. One may question the validity of these wind measurements as not being attributable to Doppler shifts due to vertical wind activity, but instead due to uncertainty in the pressure-temperature drift correction. However, upon closer inspection of the original black curve, a deviation in the peak position values of ~0.4 CNU at 1000 UT is superimposed on the smoother downward trend in the peak positions associated with the slowly-decreasing temperature. This small deviation in the black curve around 1000 UT is not the sort of peak position perturbation that can be attributed to smooth drift over long time scales, ~1-5 CNU·hr^{-1}, but instead is the kind of fluctuation that would be attributed to the

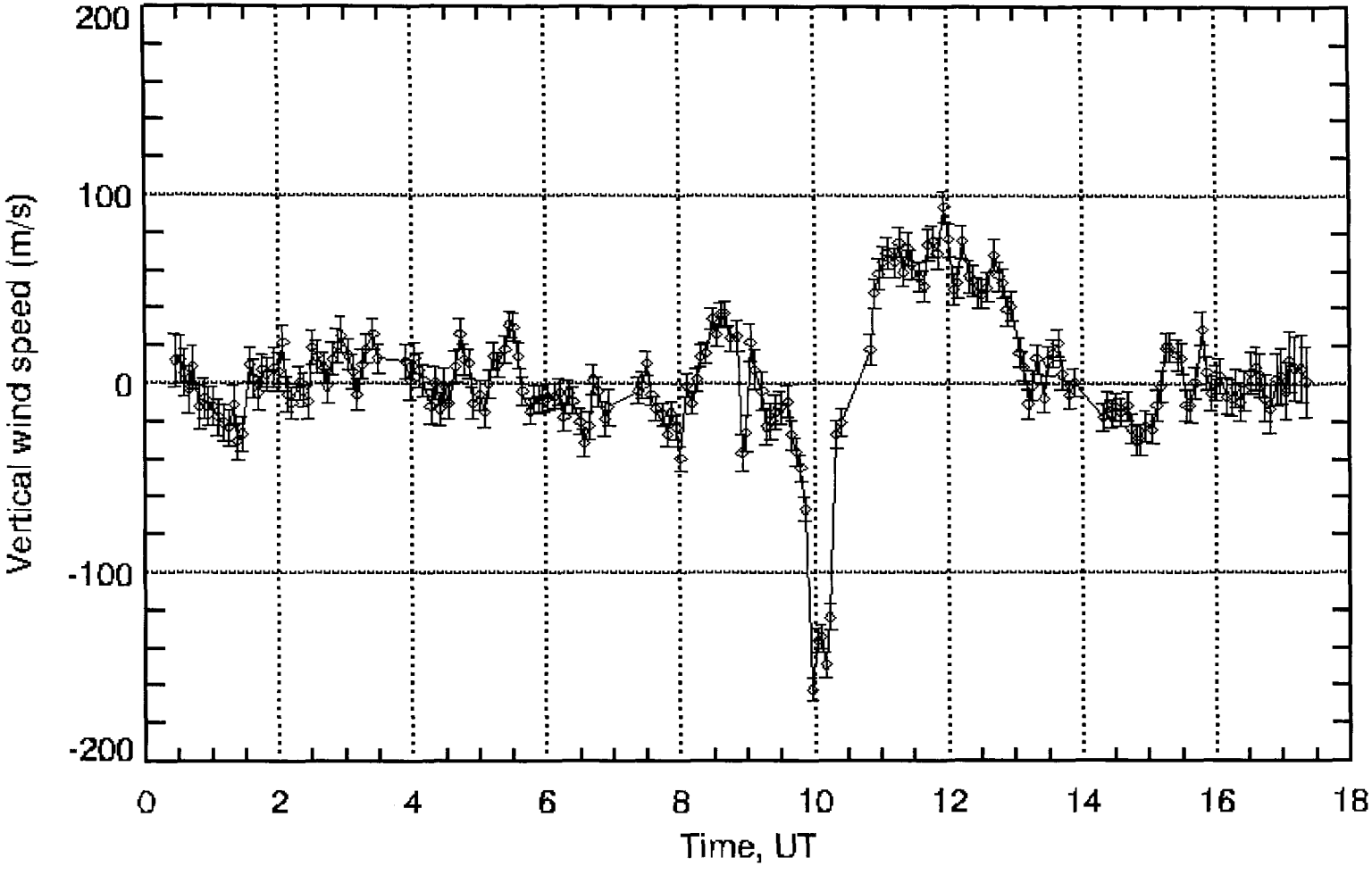

Figure 3.17 Upper-thermospheric vertical wind speeds on the night of Jan 4, 2001. Wind speeds are determined from the red curve in Figure 3.16a above. The error bars shown here include errors associated with the analysis procedures of *Conde* [2001], the pressure-temperature drift correction, and polynomial drift correction procedures.

Doppler shift of the λ630.0-nm emission over short time scales, ~0.1-1 CNU·min^{-1}, due to a vertical wind activity. Thus, this small deviation is attributed to vertical wind activity. Furthermore, an examination of the Inuvik FPS relative OI(630.0)-nm airglow and auroral intensity, shown in Figure 3.18, indicates a significant increase in the OI(630.0)-nm emission intensity at ~1000 UT concurrent with the downward winds. Experience with many nights of Inuvik FPS observations has revealed that relative intensity estimates of ~1-5 by the Inuvik FPS generally indicate that only OI(630.0)-nm airglow emissions are prevalent, while anything >5 indicates that aurora is present. The brightest OI(630.0)-nm auroras reach ~30-40 on the Inuvik FPS intensity scale. On January 4, 2001 at ~1000 UT, the Inuvik FPS measured in conjunction with the downward winds of ~150 m·s^{-1} a 200% increase in the OI(630.0)-nm emission intensity. This intensity increase is indicative of a

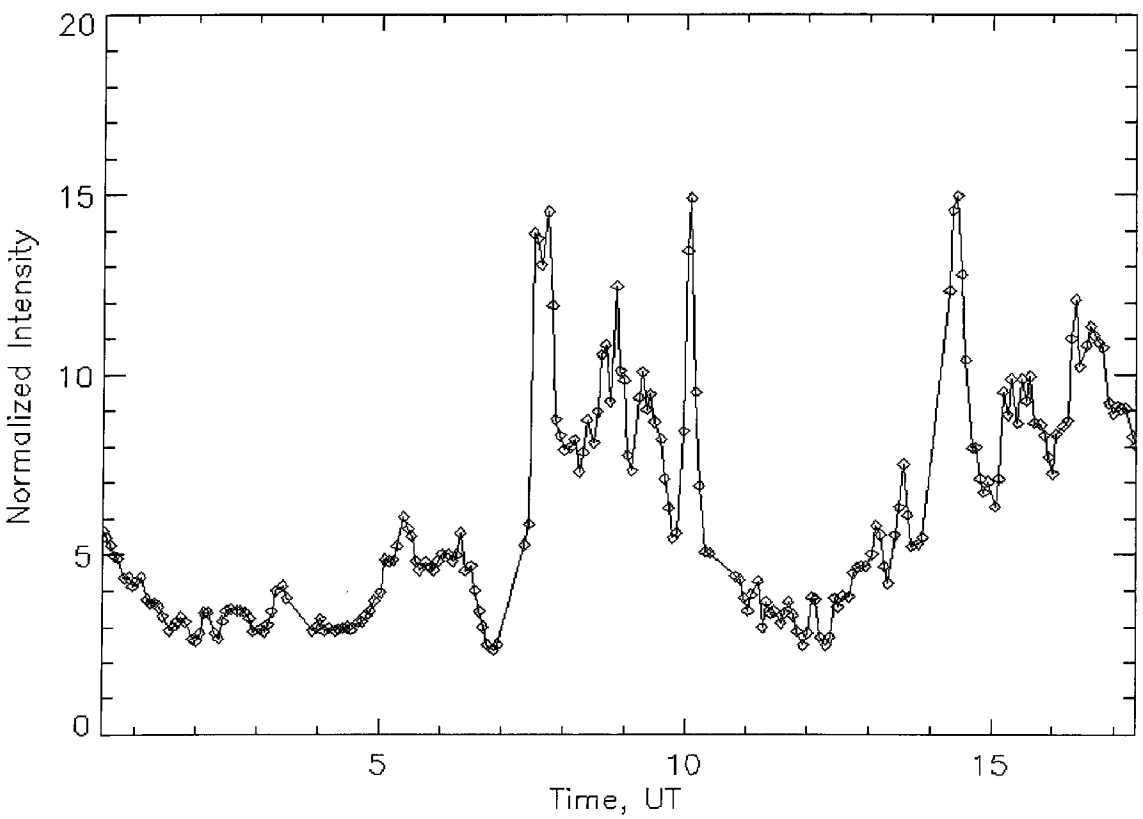

Figure 3.18. Inuvik FPS OI(630.0)-nm relative intensity on the night of Jan 4, 2001. The significant increase in the OI(630.0)-nm auroral emission that occurs at ~1000 UT is concurrent with a significant downward wind event.

downward wind bringing O-rich air from high thermospheric altitudes (≳250 km) to relevant OI(630.0)-nm auroral emission heights (~200-240 km), and gives further evidence that indeed, the significant downward winds measured at ~1000 UT are valid.

Inspection of the raw peak positions (black curve in Figure 3.16b) and the pressure-temperature fit (green curve in Figure 3.16b) in the January 4, 2001 data set from ~1100-1300 UT reveals the one occasion where the pressure-temperature drift correction appears to perform inadequately. However, this deficiency is attributed to the étalon's behavior and not to the pressure-temperature fit. After ~0915 UT, the trailer temperature begins to slowly decrease. As the temperature decreases, the temperature-variation-response curve (red curve in Figure 3.16b) and pressure-temperature fit follow the slow recovery of the étalon's optical path length until ~1030 UT as the peak position values smoothly decrease from +5 CNU to –0.5 CNU. Beginning at ~1100 UT after a 25 min break in observations, however, the peak position values lie in a range around –2 CNU, whereas the pressure-temperature fit remains around –1 CNU. Because the pressure-temperature fit estimates that the peak position values should be around –1 CNU (based on the existing pressure and temperature data) and the peak position values actually lie in the range around –2 CNU, it is presumed here that as the optical path length recovers from the temperature spike, the optical path length overshoots its pre-temperature increase-then-decrease amount. Of course, this statement cannot be easily confirmed, and it is not clear what may be the cause, though perhaps it is related to the capacitance-stabilization system's recovery from the temperature spike. However, from ~1200-1300 UT, it is evident that the peak positions trend towards the presumed pressure-temperature fit values of about –1 CNU. Furthermore, this overshoot effect is also evident in the December 9, 2000 data at ~0300 UT, although the effect is not nearly so pronounced as in the January 4, 2001 data, and the étalon appears to recover more quickly. Ultimately, the conclusion concerning this étalon trait is that the large-magnitude vertical wind estimates of ~50-100 $m \cdot s^{-1}$ from ~1100-1300 UT are not realistic in the January 4, 2001 data. If the pressure-temperature fit estimation of –1 CNU is believed to represent realistic peak position values from ~1100-1300 UT, then the resulting vertical wind speeds are likely ~0 $m \cdot s^{-1}$ during this time.

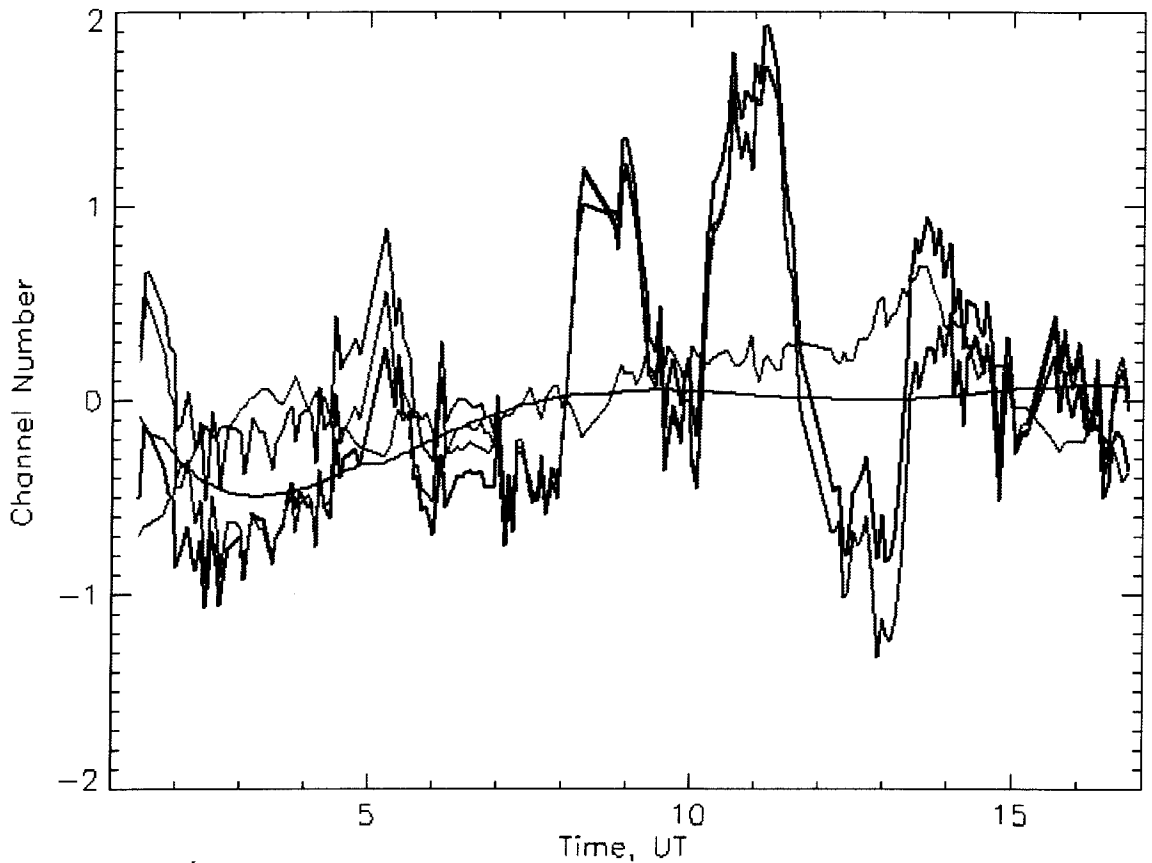

Figure 3.19. Étalon drift-correction analysis on the night of Jan 26, 2001. **(a)** The color scheme used in the previous (a) figures applies. Black is the raw OI(630.0)-nm peak position values, green is the pressure-temperature fit to black, orange = black – green, blue is the polynomial fit to orange, red = orange – blue is the final peak position. See the text for discussion.

The drift-correction procedures for the January 26, 2001 data set are shown in Figures 3.19a-b. The data set is similar to the December 22, 2000 data set, in that a preliminary inspection of the pressure-temperature drift-correction fit (green curve in Figures 3.19a-b) seems to reveal that it does not follow the variations in the raw peak positions (black curve) very well. However, upon closer examination, it is observed that the significant pressure and temperature variations which occurred during observations in general competed against each other in terms of étalon drift, similarly to the December 22, 2000 data set. A more detailed inspection of the pressure-temperature fit reveals that the étalon's drift followed the variations in pressure and temperature accordingly.

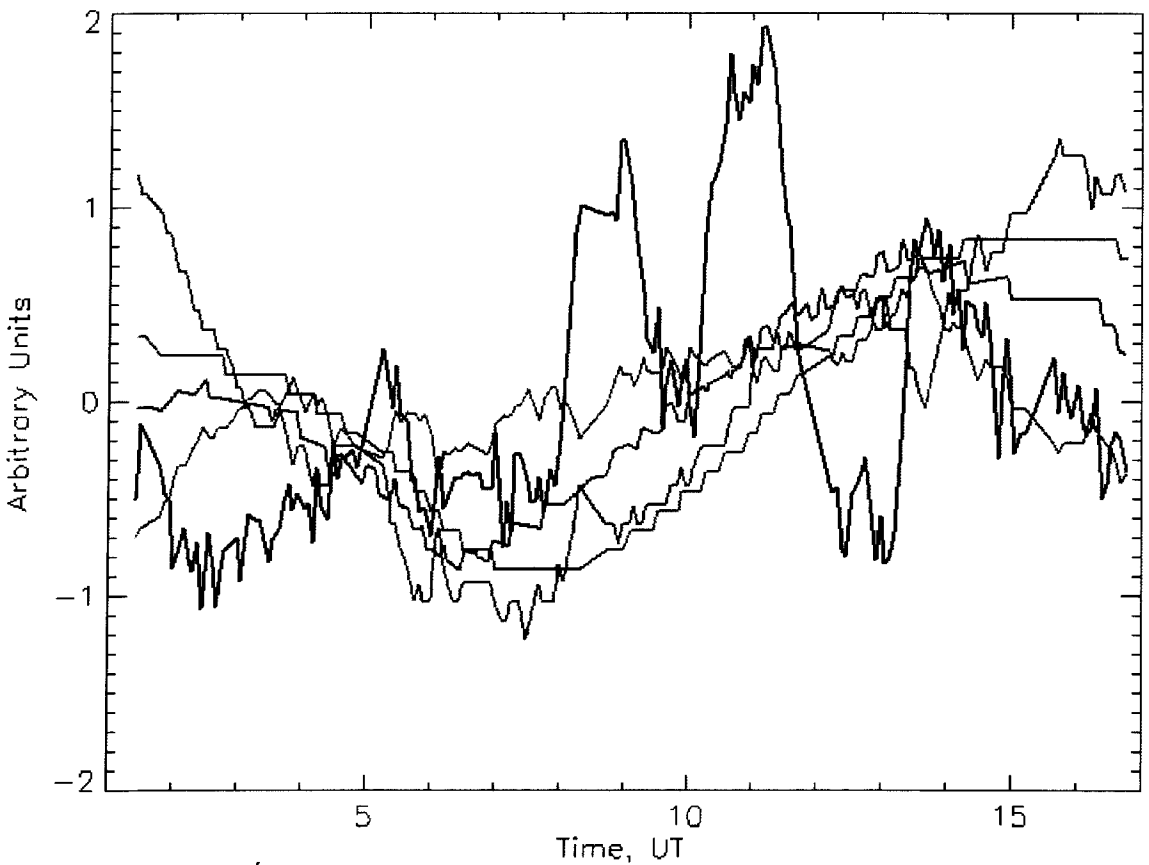

Figure 3.19 cont. Étalon drift-correction analysis on the night of Jan 26, 2001. **(b)** The color scheme used in the previous (b) figures applies. Black is the raw peak position, green is the pressure-temperature fit to black, blue is the pressure variation, red is the temperature variation, and orange is the étalon temperature-variation response. See the text for discussion.

For example, from ~0100-0300 UT, there was a significant decrease in pressure of 1.2 mmHg, which would result in a positive drift of 1.6 CNU based on previous discussions. The temperature dropped by 0.2 °C during this time, which would result in a negative drift ~0.3 CNU based on previous discussions. According to the pressure-temperature fit, the total positive drift that did occur was 0.7 CNU, which does not match the drift estimate based on the previous discussions but does conform with the general trends that have been determined from these data sets associated with pressure- and temperature-induced drift. From ~0300-0700 UT, the pressure slowly decreased by 1 mmHg while the temperature decreased by 1 °C. The competing effects resulted in little

drift, which the pressure-temperature fit reveals. From ~0700-1300 UT, both the pressure and temperature increase considerably. The pressure-temperature fit indicates a slow and small positive drift associated with the increasing temperature being moderated by the increasing pressure. As the temperature levels off after ~1300 UT, the drift follows the variable pressure, which the pressure-temperature fit identifies. Overall, the pressure-temperature fit is successful in identifying the drift of the étalon in this data set, an assertion which is further validated by the relatively small uncertainty in both the a_1 and a_2 coefficients, $a_1 = -0.57 \pm 0.08$ and $a_2 = 1.49 \pm 0.12$. The vertical wind estimates from this night, which exhibit a great deal of wave structure, are shown in Figure 3.20 below.

The drift-correction procedures for the November 28, 2000 data set are shown in Figures 3.21a-b. Much of the slow, negative étalon drift that occurred in the first half of the night is attributed to the large change in pressure of 3 mmHg that occurred from ~0100-1100 UT. The temperature varied little during this time period, and only began to slowly decrease after ~0900 UT. Overall, the pressure-temperature fit here removed the slow drift due to the large change in pressure, similarly to the January 3, 2001 example. After ~1100 UT, the pressure leveled off and the slow, negative drift is now attributed to the slow temperature decrease that occurred until ~1600 UT. In general, the pressure-temperature fit works reasonably well here in removing the étalon's drift derived from the varying pressure and temperature basis functions, based on what was presented earlier concerning the general trends observed in peak position values due to varying pressure and temperature (*e.g.*, increasing pressure → negative drift; increasing temperature → positive drift). However, the relative uncertainty in the drift coefficients is larger here than for some of the other data sets ($a_1 = -0.21 \pm 0.05$, $a_2 = 2.41 \pm 0.27$), and this can be attributed to the model attempting to fit a function based on pressure and temperature data to a time series of highly-variable peak position values. Nonetheless, this data set was acquired during a period of several days of intense geomagnetic activity, when the 3-hr magnetic index A_P ranged from 67 late November 26 to 94 early on the 27th to 48 on the 28th to 111 early on the 29th. The upper-thermospheric vertical wind speeds measured at Inuvik on this night, shown in Figure 3.22, are not surprising given these conditions.

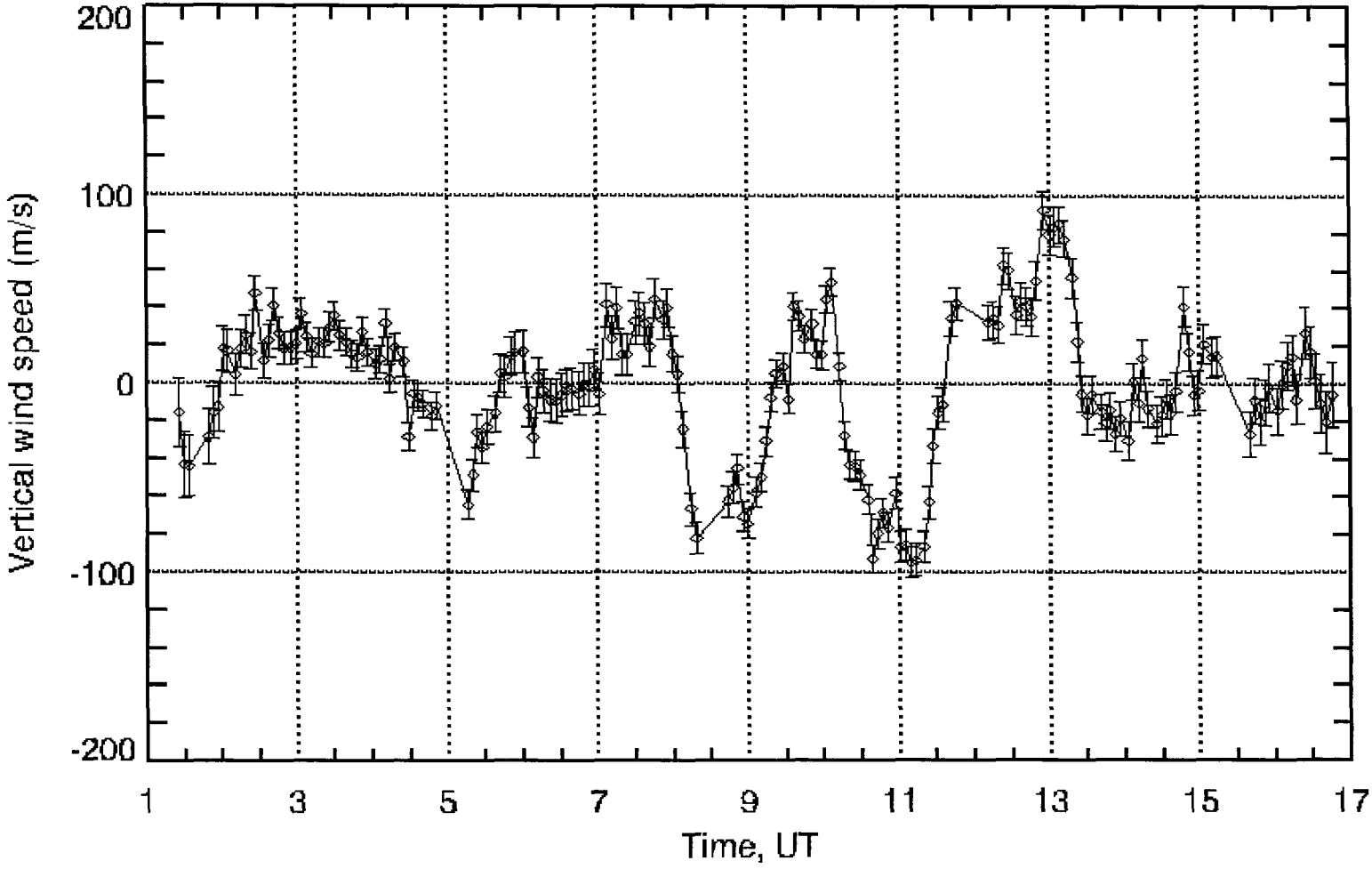

Figure 3.20 Upper-thermospheric vertical wind speeds on the night of Jan 26, 2001. Wind speeds are determined from the red curve in Figure 3.19a above. The error bars shown here include errors associated with the analysis procedures of *Conde* [2001], the pressure-temperature drift-correction, and polynomial drift-correction procedures.

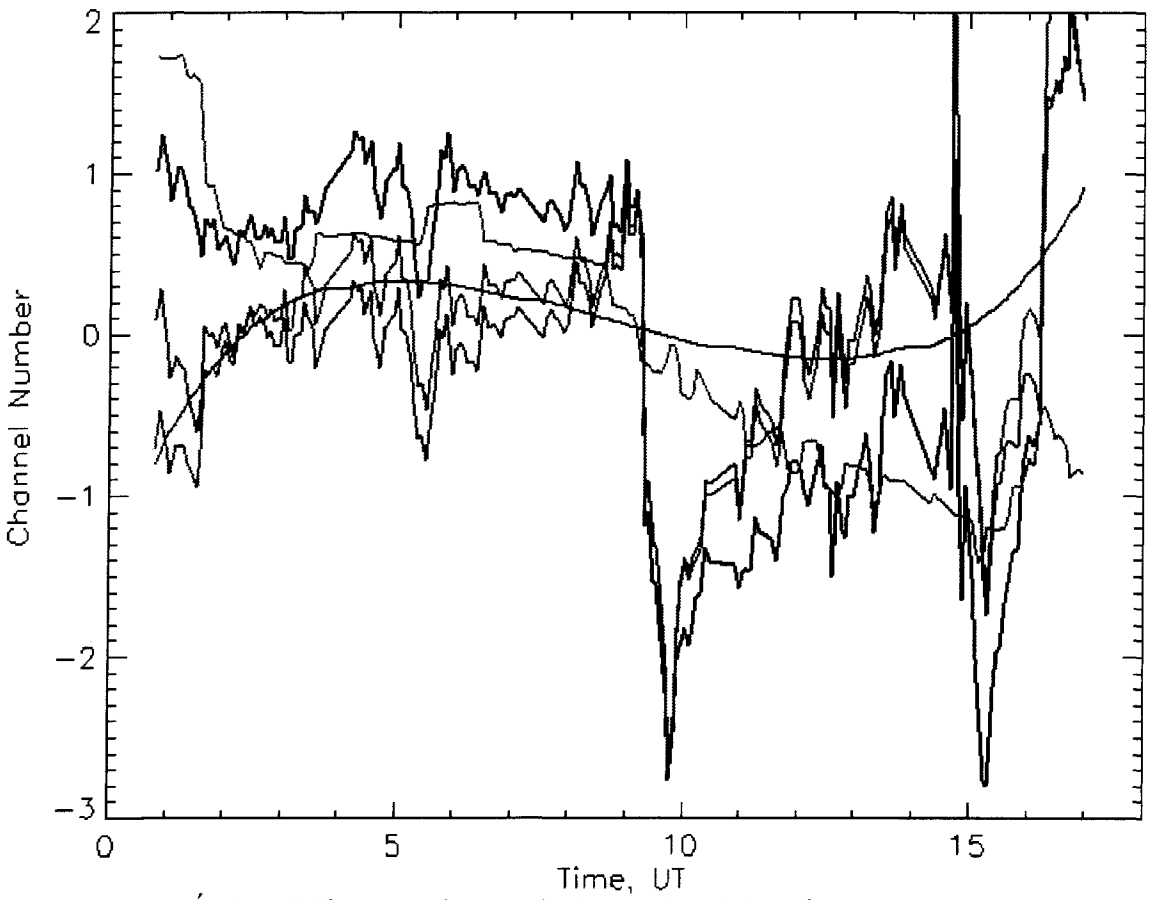

Figure 3.21. Étalon drift-correction analysis on the night of Nov 28, 2000. **(a)** The color scheme used in the previous (a) figures applies. Black is the raw OI(630.0)-nm peak position values, green is the pressure-temperature fit to black, orange = black – green, blue is the polynomial fit to orange, red = orange – blue is the final peak position.

Though minor flaws in the Inuvik FPS drift-correction procedures are evident from the discussions concerning these seven upper-thermospheric vertical wind data sets, the overall success of the drift-correction analysis and the analysis procedures of *Conde* [2002] and *Conde* [2001] justify the belief that these vertical wind time series exhibit the sort of long-lived, intermediate- to large-magnitude, geophysically-significant vertical winds that were discussed in Chapter 1. The question as to whether these wind events are also statistically-significant was addressed with regards to the January 3, 2001 data set. Table 3.2 below presents the mean wind $\overline{W}$, the standard deviation SD_{wnd}, the typical wind measurement error $\sigma_{tot,wnd}$, and the magnitudes and durations of the significant wind

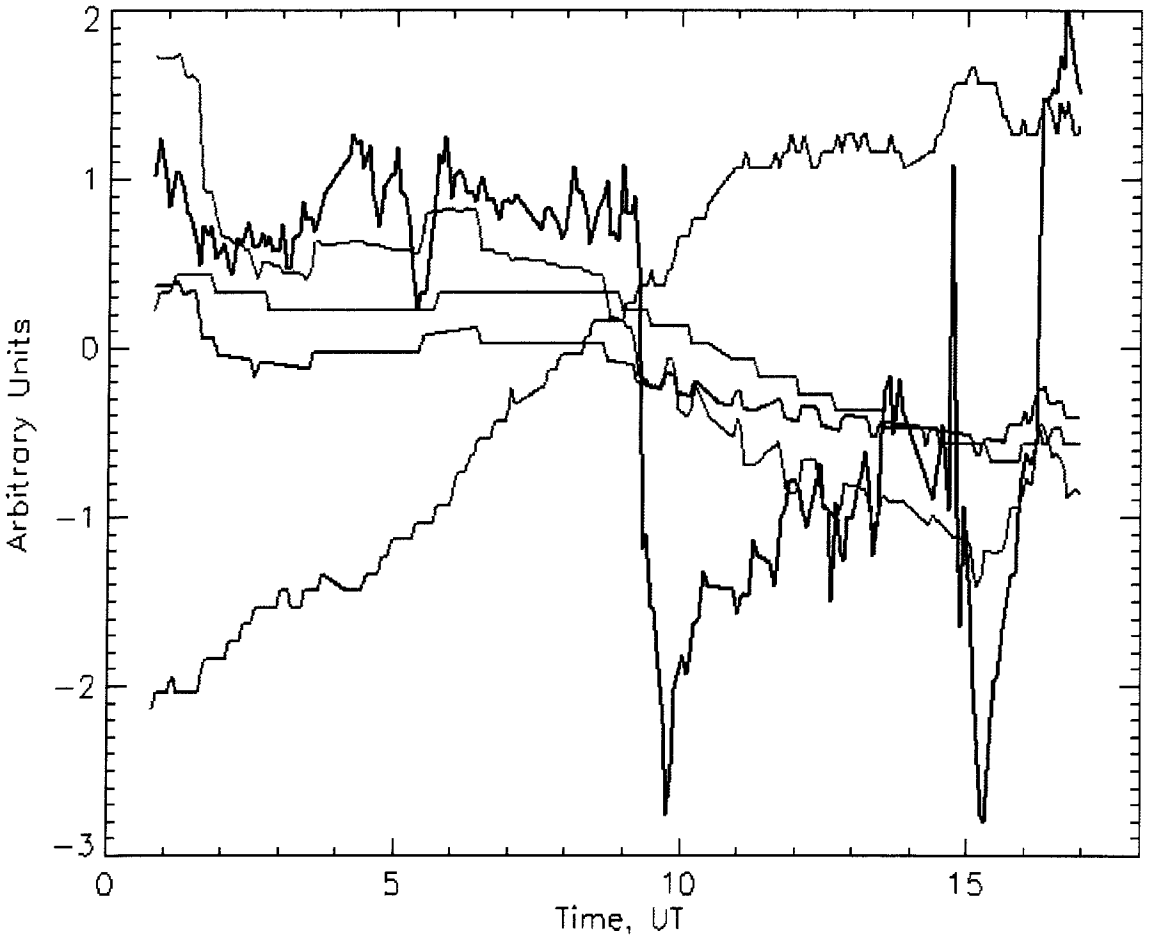

Figure 3.21 cont. Étalon drift-correction analysis on the night of Nov 28, 2000. **(b)** The color scheme used in the previous (b) figures applies. Black is the raw peak position, green is the pressure-temperature fit to black, blue is the pressure variation, red is the temperature variation, and orange is the étalon temperature-variation response.

events, W_{max} and τ_{wnd}, respectively, for each of the seven Inuvik FPS vertical wind data sets. The geophysical significance of the wind events is discussed in specific detail in Chapter 4 with the concurrent presentation of the column shift data. As the information in Table 3.2 illustrates, the large-magnitude vertical wind events from each night are statistically-significant as well as geophysically-significant. For example, on February 28, 2000, the largest upward wind speeds observed only reached magnitudes of ~40 $m \cdot s^{-1}$. However, the standard deviation of the night's data set was $SD_{\text{Feb 28, 2000}} = 14.27\ m \cdot s^{-1}$, making the ~40 $m \cdot s^{-1}$ wind speed a statistically-significant measurement. Furthermore,

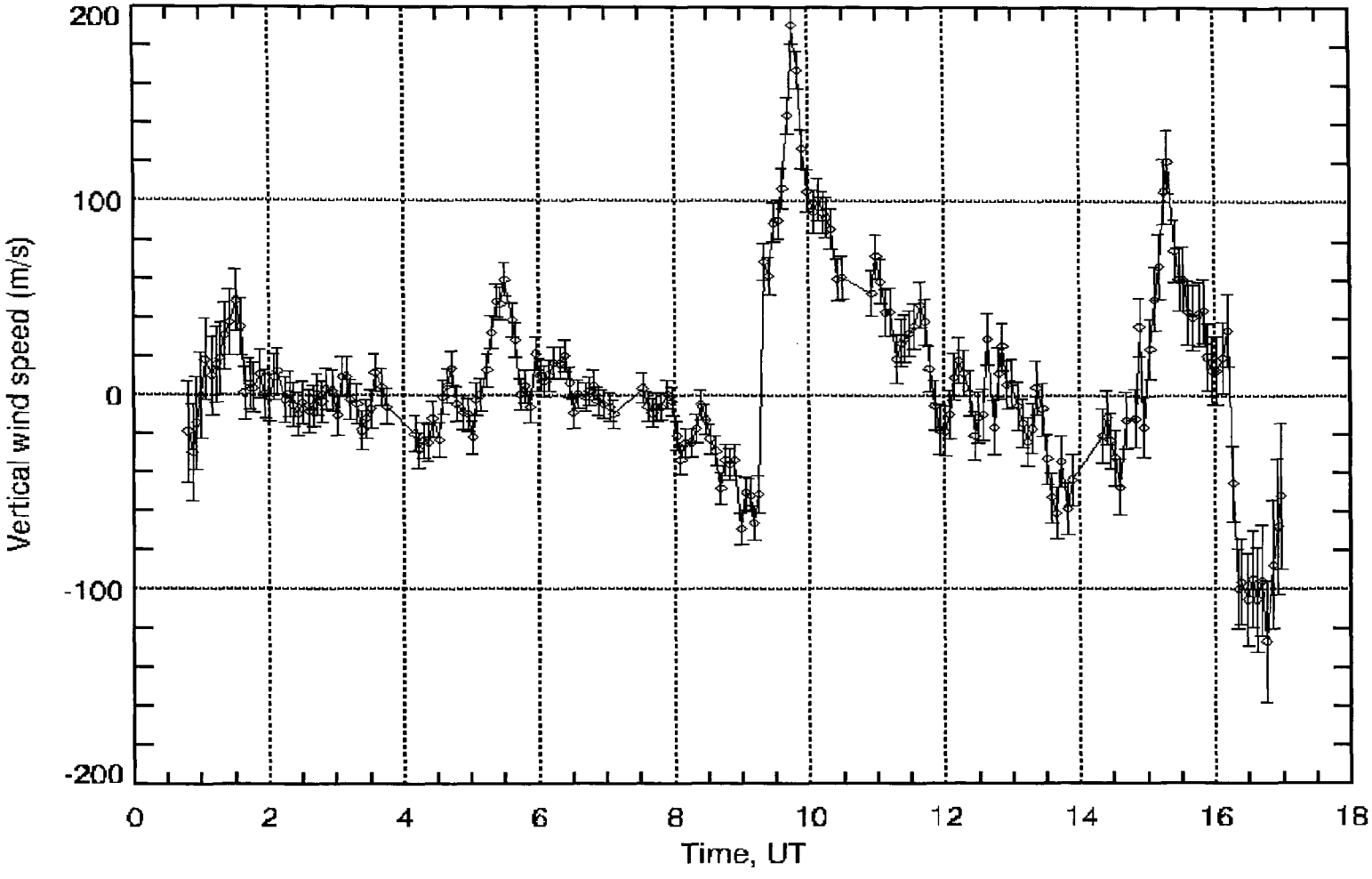

Figure 3.22 Upper-thermospheric vertical wind speeds on the night of Nov 28, 2000. Wind speeds are determined from the red curve in Figure 3.21a above. The error bars shown here include errors associated with the analysis procedures of *Conde* [2001], the pressure-temperature drift-correction, and polynomial drift-correction procedures.

Table 3.2. Statistical quantities of the Inuvik FPS vertical wind data sets.

Date	$\overline{W}$ ($m \cdot s^{-1}$)	SD_{wnd} ($m \cdot s^{-1}$)	$\sigma_{tot,wnd}$ ($m \cdot s^{-1}$)	W_{max} ($m \cdot s^{-1}$)	τ_{wnd} (min)
Jan 03, 2001	–0.92	22.98	6-18	–60; +60; –50	30; 15; 20
Dec 09, 2000	0.49	19.49	4-11	+60; –70	20; 10
Dec 22, 2000	–2.01	32.02	6-18	+100; –80	10; 40
Feb 28, 2000	0.03	14.27	3-11	+40	15
Jan 04, 2001	3.89	35.33	7-19	–160	20
Jan 26, 2001	–0.21	37.02	7-19	–80; –100; +90	40; 50; 30
Nov 28, 2000	6.60	46.67	7-38	+60; +200	30; 40

the standard deviation exceeds the total wind measurement error for each night's data set, indicating that the winds are a real thermospheric phenomenon. Lastly, some general insight into the drift-correction procedures is revealed from the mean wind calculation. On nights where the mean wind was significantly different than 0 $m \cdot s^{-1}$ (*e.g.*, December 22, 2000; January 04, 2001; November 28, 2000), indicating that the drift correction biased the wind measurements relative to the zero Doppler-shift reference, the error estimates were generally larger and the drift correction was relatively inferior (compared to the other data sets). This deficiency was attributed to the pressure-temperature fit's failure to precisely remove the étalon drift due to the competing processes of pressure-induced negative drift and temperature-induced positive drift or vice versa. The exception is the November 28, 2000 data set, whose large wind measurement errors near the beginning and end of observations are due to the significant uncertainty in the polynomial fit.

3.2 Characterization of Precipitating Electrons

The spectacular auroral displays that can be seen at high latitudes are the result of plasma sheet electrons which have been expelled towards Earth by (presumed) magnetic reconnection processes and further energized near the topside ionosphere. The energized electrons spiral down Earth's magnetic field lines into the high-latitude thermosphere and deposit their kinetic energy through the many collisions they make with the thermosphere's constituents. Some of the collisionally-excited thermospheric species release their excess energy through radiative processes, producing the wondrous visual

display known as the aurora. As was discussed in Chapter 1, thermospheric energy deposition associated with electron precipitation and Joule heating processes can modify the thermosphere's global composition, circulation and temperature relative to solar-radiative-driven patterns, and knowledge of the precipitating electrons' characteristic energy and energy flux provides the information required to predict, for example, the ionization rate or total energy input due to the precipitation. As was discussed in Chapter 2, auroral intensity measurements can be used to infer characteristic energy and energy flux of precipitating electrons and composition changes relative to model estimates, thus providing the information required to model the thermosphere's response to geomagnetic activity. How the characteristic energy and energy flux are determined from the UVI observations as it applies to the needs of this thesis is explained here.

3.2.1 Airglow Removal from the UVI LBH-S, LBH-L and OI(135.6)-nm Auroral Observations

Chapter 2 provided some detail on how the characteristic energy and energy flux of precipitating electrons can be determined from UVI auroral brightness measurements. Before this can be achieved, the airglow signature that is present in the auroral images must be removed. Otherwise, the energy flux inferred from the LBH-L brightness will be overestimated, and the inferred characteristic energy will be incorrect, since the airglow signatures in the LBH-S and LBH-L images are not necessarily the same and do not divide out when their ratio is taken. Furthermore, incorrect energy flux and characteristic energy estimates will result in an incorrectly modeled OI(135.6)-nm emission. Lastly, the airglow signature must be removed from the OI(135.6)-nm auroral images if the composition effects associated with auroral processes are to be properly inferred.

Techniques for removing airglow from POLAR UVI auroral images were originally developed in the 1980s and 1990s for airglow removal from DE-1 auroral images [*e.g.*, *Lummerzheim*, 2004, private communication; *Craven*, 2004, private communication; *Immel et al.*, 1997], and subsequently modified to fit the needs of the UVI data. Airglow signatures in the auroral images can be modeled as a function of solar zenith angle, and the method developed for modeling the airglow proceeds in two steps. First, the auroral

oval is identified in any particular auroral image, preferably one showing a well defined oval. An exclusion zone in magnetic latitude coordinates is specified by the individual by approximating the location of the auroral oval, indicating to the software to avoid the pixels in this region when modeling the airglow signature in the image. The remaining pixels are binned by their solar zenith angle, and an averaged counts·pixel^{-1} as a function of solar zenith angle is determined. It is noted here that UVI investigators often quote auroral brightnesses in counts·pixel^{-1} rather than Rayleighs·pixel^{-1}.

The next step is to numerically fit a 4th-degree polynomial to the averaged airglow signature as a function of solar zenith angle, generating four coefficients. Normally, a 4th-degree polynomial has five coefficients, but this particular function, which has the form

$$B_{Arglw}(x) = a(x - x_0)^4 + b(x - x_0)^2 + c, \tag{3.24}$$

where a, b, c, and x_0 are the coefficients, takes advantage of the assumption that x_0 is the terminator location; *i.e.*, the shadow height, the point in space where the atmosphere is no longer illuminated by direct or scattered sunlight. Generally, this location, which is estimated by the x_0 coefficient, resides at solar zenith angles of ~100°-110° on Earth's nightside at thermospheric altitudes. The function $B_{Arglw}(x)$ yields a good approximation to the airglow signature if the aurora is in the vicinity of the terminator, which of course is the region of interest in the image if there is aurora located there. The fit is cutoff at the terminator, and extended into the nightside by assuming a constant nightglow. This is an approximation to night airglow values based on other studies [*e.g. Immel*, 1998], but is generally considered sufficient for estimating nightglow when its signature is being removed from nightside auroral data [*Lummerzheim*, 2004, private communication]. A given pixel sitting at a certain solar zenith angle will have an airglow value associated with that angle as defined by $B_{Arglw}(x)$. The airglow values at each pixel are then subtracted away from the entire auroral image, including the auroral-region exculsion-zone pixels.

Seven of the eight UVI data sets used in this thesis were collected during the deep winter months of late November, December and January, when the polar cap is in darkness, so dayglow is not a concern. The weak nightglow present in the auroral images from these months must still be accounted for, and generally, an averaged constant

nightglow of 3-4 counts·pixel^{-1} is removed from them. This amount corresponds to ~5-30% of the OI(135.6)-nm total image brightness, and ~1-30% of the LBH-L and LBH-S total image brightness. One example illustrating the dayglow procedures is shown below.

Figures 3.23a-g are an example of auroral images that contain some amount of dayglow. The images were acquired on March 20, 2001 at ~0635 UT, with the polar cap illuminated on the dayside. Figure 3.23a shows the results of the polynomial fit procedures, giving the airglow corrections for the LBH-S, LBH-L, and OI(135.6)-nm images in counts·pixel^{-1} as a function of solar zenith angle near the terminator. The curves indicate that near the terminator, there is dayglow that must be accounted for in the

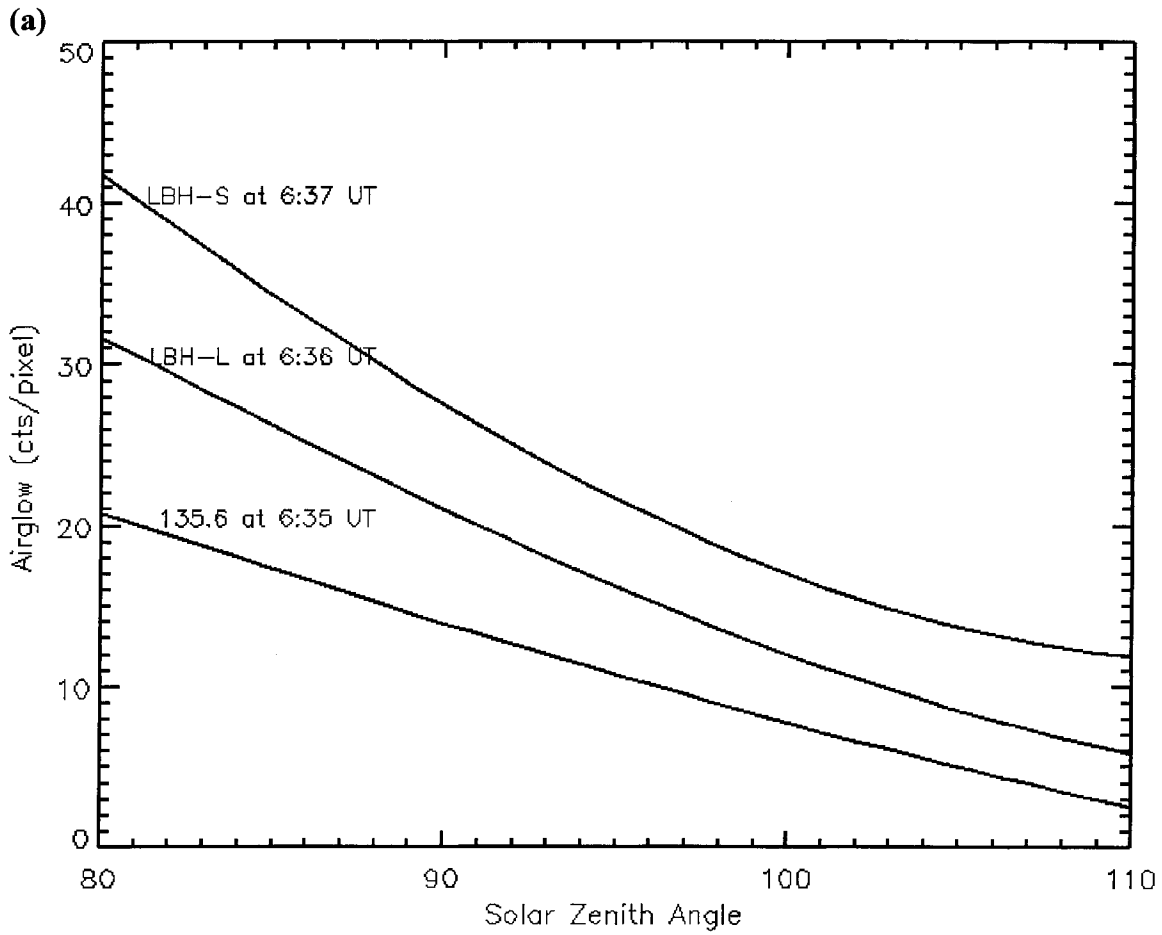

Figure 3.23. Airglow-removal procedures for UVI observations of LBH-S, LBH-L, and OI(135.6)-nm auroral images. **(a)** Airglow correction polynomial fits for the UVI LBH-S, LBH-L and OI(135.6)-nm auroral images obtained at 0635 UT on Mar 20, 2001.

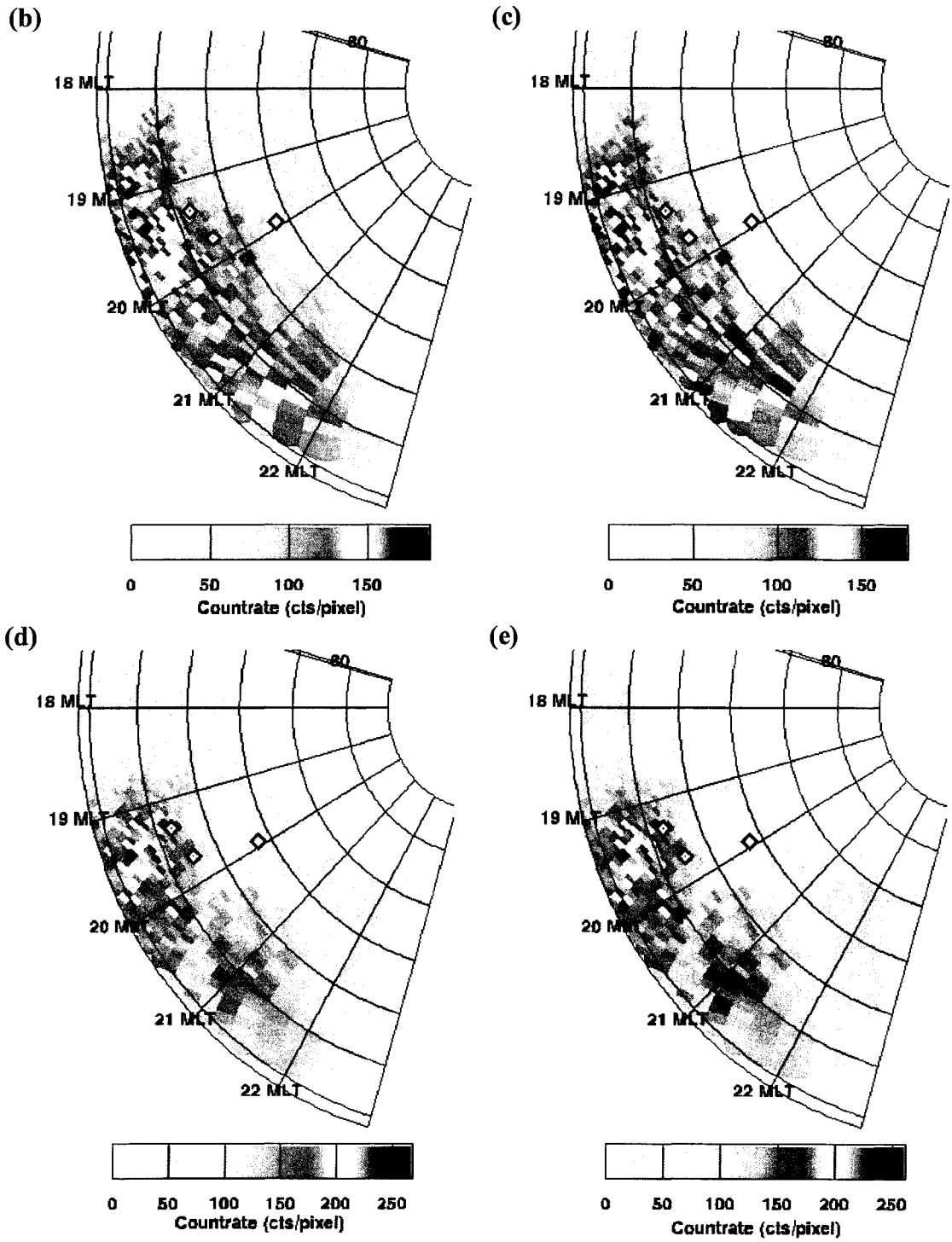

Figures 3.23 cont. Airglow-removal procedures for UVI observations of LBH-S, LBH-L, and OI(135.6)-nm auroral images. **(b), (c)** UVI LBH-S auroral images at 0637 UT and **(d), (e)** LBH-L auroral images at 0636 UT before and after airglow removal, respectively. The marked points on the plots are Inuvik, NT at 71° magnetic latitude, and Eagle and Poker Flat, AK, at 66.1° and 65.2°, respectively.

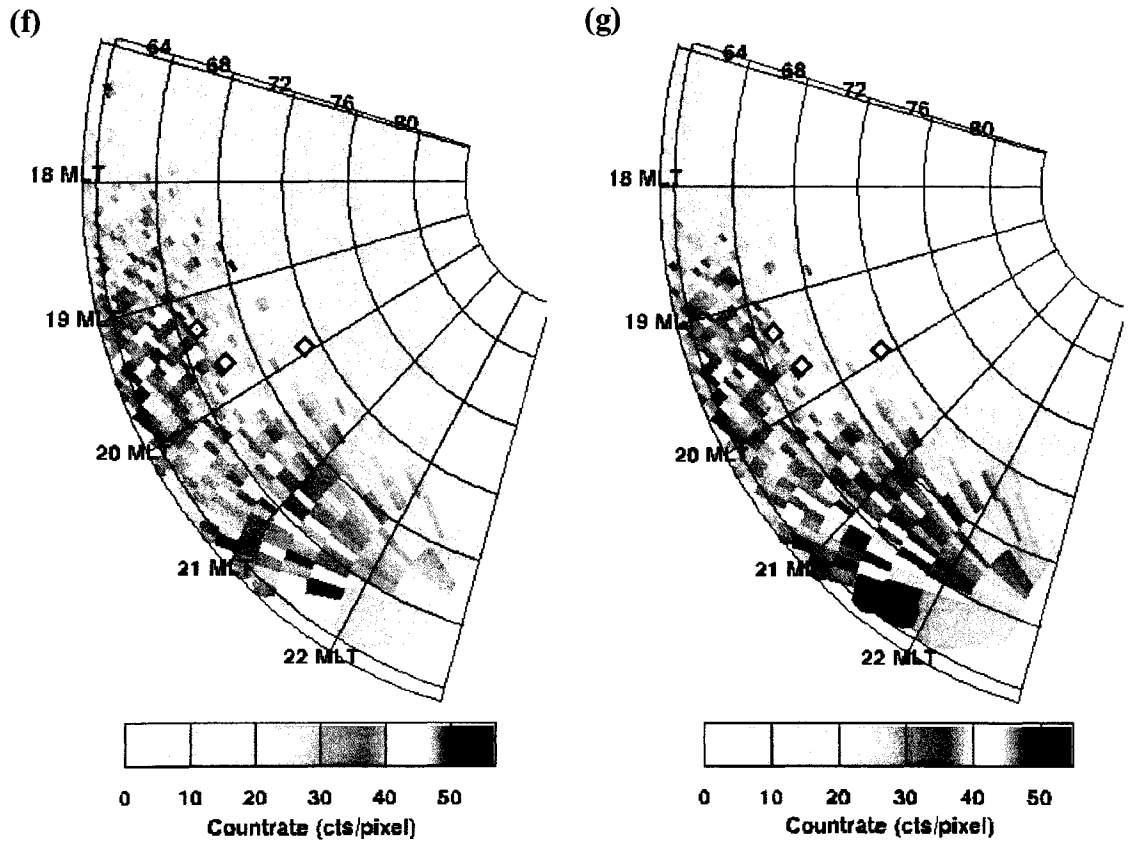

Figures 3.23 cont. Airglow-removal procedures for UVI observations of LBH-S, LBH-L, and OI(135.6)-nm auroral images. **(f)** and **(g)** UVI OI(135.6)-nm auroral images at 0635 UT before and after airglow removal, respectively.

the auroral images if dayside auroral processes are to be investigated. As the solar zenith angle increases, the airglow signature across the image becomes weak, until on Earth's nightside, the airglow reduces to nightglow values of 3-4 counts·pixel^{-1}. The curves shown in Figure 3.23a are applied to the UVI data on a pixel-by-pixel basis, with Figures 3.23b-g illustrating the effect of the airglow removal on the LBH-S, LBH-L, and OI(135.6)- nm images, respectively, by showing a sector of the image before and after airglow removal. Though the effect of the airglow removal is not visually dramatic, examination of the late-afternoon sector at ~1800 magnetic local time (MLT) and of the polar cap region of the images reveals that there is a noticable difference between the before-and-after-airglow images that the eye can distinguish.

3.2.2 Inferring Energy Flux and Characteristic Energy from UVI LBH-L and LBH-S Auroral Observations

In general, a great deal of preliminary analysis was performed on the UVI auroral data before energy flux and characteristic energy could be inferred from the LBH-L and LBH-S images, and before composition perturbations could be inferred from comparisons between the observed and modeled OI(135.6)-nm images. Removal of airglow from the LBH-L, LBH-S, and OI(135.6)-nm images was only the first step. Spatial averaging of the raw images was of primary concern in order to minimize (*i.e.*, smear out) the effects of the jitter in the despun platform and the wobble in the spacecraft (discussed in Chapter 2), and also to address the need of having statistically-significant, reasonably-averaged quantities. The auroral images shown in the previous section in Figures 3.23b-g illustrate the UVI data in their least-averaged form, which were plotted on a pixel-by-pixel basis using a polygon-filling software routine to color in the spaces between the pixels. In addition, the spatial averaging of the auroral data was done so as to organize the data in such a manner as to support the investigation of mesoscale thermospheric processes; *i.e.*, spatially-extended processes such as vertical winds which potentially occur over areas of $\sim 10^4$-10^5 km^2. A good representation of this notion is shown in Figure 3.24 [*Price et al.*, 1995], which illustrates a large-magnitude, mesoscale vertical wind field blowing from the lower thermosphere into the upper thermosphere. Energy deposition due to Joule heating and electron precipitation in the lower thermosphere can drive spatially-extended regions ($\sim 10^4$ km^2) of lower-thermospheric air parcels upward, which travel into the upper thermosphere and subsequently expand adiabatically. *Price et al.* [1995], in presenting simultaneous lower- and upper-thermospheric vertical wind measurements, determined that lower-thermospheric vertical wind fields may expand outward horizontally at upper-thermospheric altitudes to areas of up to 6 times that of the wind's spatial extent in the lower thermosphere. This is illustrated in Figure 3.24, which shows a lower-thermospheric vertical wind field of radius 160 km (area $\approx 8 \times 10^4$ km^2) expanding outward to a radius of 400 km (area $\approx 5 \times 10^5$ km^2) as the air parcels are transported to upper-thermospheric pressure levels. The spatial averaging of the UVI auroral images that are presented here yields resolutions on the order of the area scales discussed in *Price et al.* [1995].

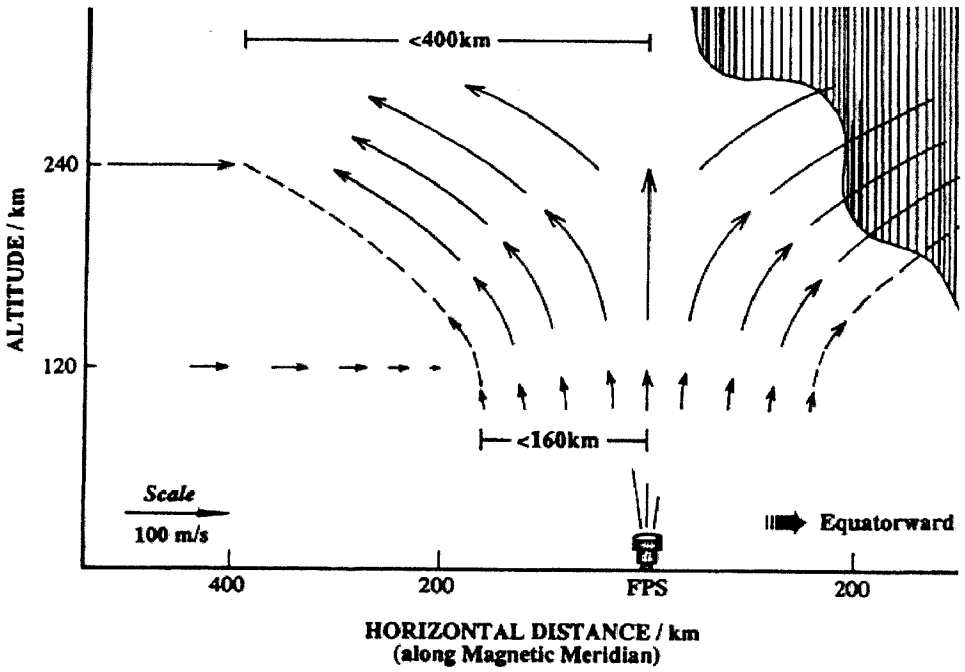

Figure 3.24. Schematic representation of a large-magnitude, spatially-extended thermospheric vertical wind field. The upward wind illustrated here occurs poleward of an auroral arc, and its spatial scales in the lower and upper thermosphere are shown [Figure from *Price et al.*, 1995].

Chapter 2 presented the basic methodology as to how the UVI LBH-L and LBH-S auroral-brightness observations can be used to infer the energy flux and characteristic energy of precipitating electrons. Except for the H Lyman-α line at λ121.6 nm, the most prominent UV auroral emissions are the OI(130.4)-nm and OI(135.6)-nm lines and the N_2 LBH bands [*Germany et al.*, 1990]. The OI(130.4)-nm emission undergoes multiple scattering at a high efficiency, and thus, is limited in its use for auroral imaging, though it has potential as an indicator of O concentrations [*Germany et al.*, 1990]. The OI(135.6)-nm and N_2 LBH band emissions also experience multiple scattering, but at significantly smaller efficiencies [see *Germany et al.*, 1990 and references therein]. Thus, muliple scattering is generally ignored in the sort of UV auroral-emission studies done here and in such works as *Germany et al.* [1990] and *Germany et al.* [1994].

Recalling from Chapter 2, molecular oxygen's absorption of radiation of wavelengths in the Schumann-Runge (SR) continuum, $\lambda \approx$130-175 nm, strongly attenuates

the OI(135.6)-nm emission and the N_2 auroral emissions in the wavelength range of the UVI LBH-S filter (centered at 150 nm), while auroral emissions monitored via the UVI LBH-L filter (centered at 170 nm) remain mostly unattenuated. The only significant excitation mechanism of the N_2 LBH states is electron impact since the LBH transitions are electric dipole forbidden [*Germany et al.*, 1990]. Thus, LBH airglow signatures are very weak, and the emission may function as a direct measure of the total energy flux of precipitation into the thermosphere [*Germany et al.*, 1990]. The longer wavelength LBH bands can be used as an indicator of total energy flux since these wavelengths mostly lie outside the range of the SR continuum [*Germany et al.*, 1990]. The O_2 column abundance above the aurora's local production region determines how much of the OI(135.6)-nm and LBH-S band emissions are attenuated, while the altitude of maximum auroral emission depends on the characteristic energy of the precipitating electrons. Thus, the deeper the peneration of the precipitating electrons into the thermosphere, the lower is the peak emission altitude, and thus, the more O_2 that is available above the peak emission altitude to absorb the OI(135.6)-nm and LBH-S band emissions. The ratio of either the OI(135.6)-nm emission or the LBH-S band emissions to the LBH-L band emissions can be used to infer the mean energy of the precipitating electrons [*Germany et al.*, 1990].

Figures 3.25a-b emphasize the significant differences that can exist between auroral events due to precipitating electrons of different characteristic energies. Figure 3.25a illustrates the modeled brightnesses of FUV wavelengths between 130 nm and 190 nm due to an energy flux of 1 $mW \cdot m^{-2}$ of precipitating electrons with a characteristic energy of 1 keV. Figure 3.25b illustrates the same quantities for a characteristic energy of 7 keV. The figures also illustrate the effect of O_2 absorption on UVI-observed auroral emissions. The LBH-L, LBH-S, and OI(135.6)-nm filter bandwidths and sensitivities are represented by the black curves using the sensitivity scale at the right-hand ordinate. Using the brightness scale at the left-hand ordinate, the black columns represent the model calculation of the unattenuated column-integrated brightness at each particular wavelength, which is determined from the respective volumn emission rates computed by the transport code of *Lummerzheim and Lilensten* [1994]. This model computation does not

take into account the reabsorption of the radiation by O_2 in the vicinity of the emissions. The red columns represent the model calculation of the column-integrated brightnesses

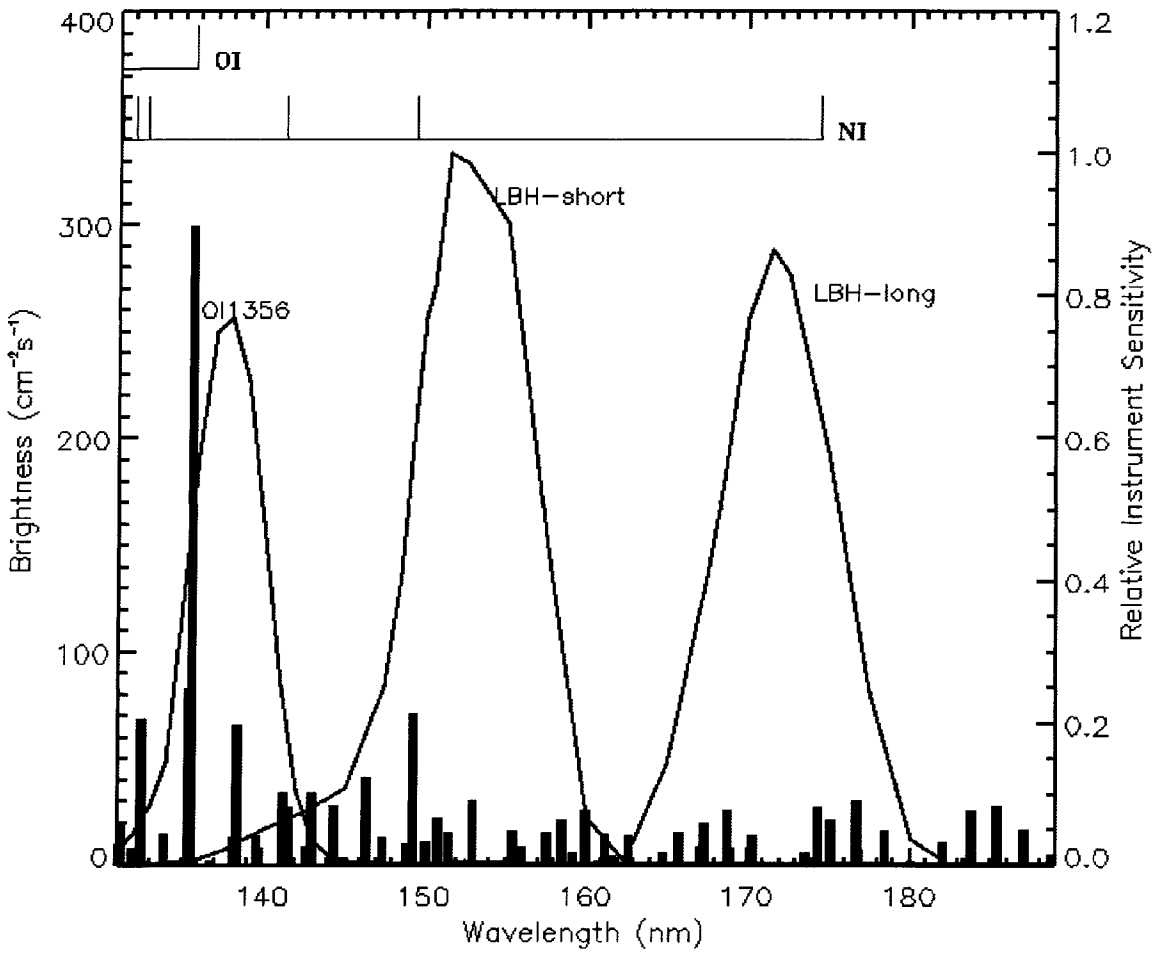

Figure 3.25. UVI instrument response to FUV aurora produced by 1-keV and 7-keV electron precipitation at 1 $mW \cdot m^{-2}$ of energy flux. **(a)** 1-keV electron precipitation. The UVI LBH-L, LBH-S, and OI(135.6)-nm filter bandwidths and sensitivities are represented by the black curves using the sensitivity scale at the right-hand ordinate. Using the brightness scale at the left-hand ordinate, the black columns represent the model calculation of the unattenuated column-integrated brightness at each particular wavelength, which is determined from the respective volumn emission rates computed by the transport code of *Lummerzheim and Lilensten* [1994]. This computation does not take into account the reabsorption of the radiation by O_2. The red columns represent the model calculation of the column-integrated brightnesses taking into account absorption by O_2, which is the brightness measurement that the UVI instrument would make of this modeled aurora. The absolute difference between the black and red columns represents the amount that the emission brightness is reduced by O_2 attenuation.

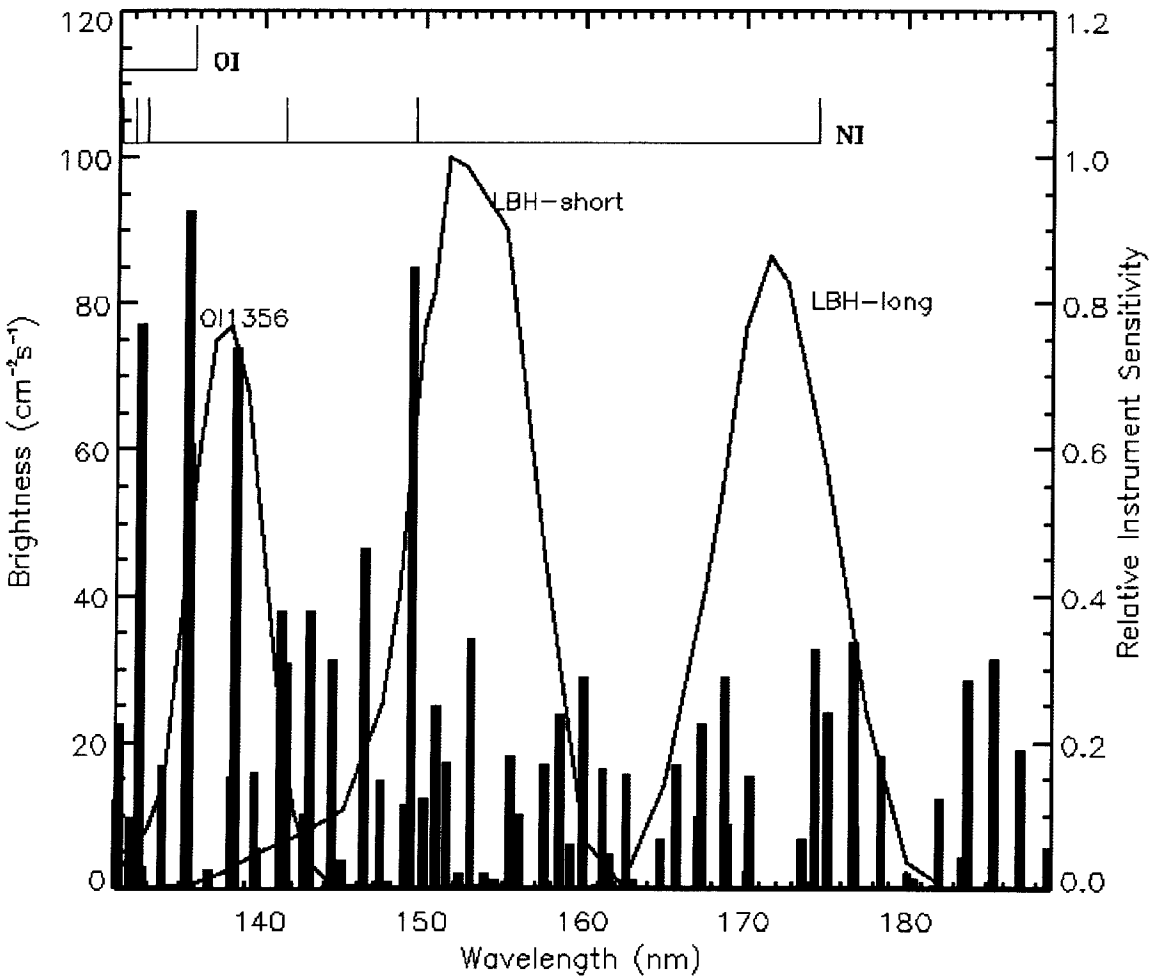

Figure 3.25 cont. UVI instrument response to FUV aurora produced by 1-keV and 7-keV electron precipitation. **(b)** 7-keV electron precipitation. Same format as for **(a)**. The penetration of the 7-keV electrons deeper into the thermosphere results in a lower peak emission altitude. Thus, more of the OI(135.6)-nm emission and the N_2 band emissions monitored via the UVI LBH-S filter are absorped by O_2.

taking into account absorption by O_2, which is the brightness measurement that the UVI instrument would make of this modeled aurora. Because the instrument resides at an altitude well above the aurora's peak emission altitude, O_2 above the aurora's local production region reabsorbs some of the radiation as the radiation propagates upward toward the instrument. The absolute difference between the black and red columns represents the amount that the emission brightness is reduced by O_2 attenuation. As the red columns indicate, N_2 band emissions that are monitored via the UVI LBH-L filter are

mostly unattenuated by O_2, though attenuation does increase with decreasing peak emission altitude; *i.e.*, with increasing characteristic energy of the precipitating electrons. In addition, because the O_2 column abundance above the peak emission altitude for the 7-keV aurora is much greater than for the 1-keV case (on the order of a scale height more of O_2), the 7-keV auroral emissions within the SR wavelength range are much more strongly attenuated by O_2 than for the 1-keV aurora; *i.e.*, in the wavelength range monitored via the UVI LBH-S and OI(135.6)-nm filters. Thus, the measured relative brightnesses of the LBH-L and LBH-S bands relative to each other during auroral events of differing characteristic energies should be indicative of those differing characteristic energies.

The FUV brightness calculations of the kind shown in Figures 3.25a-b predicted by the transport code of *Lummerzheim and Lilensten* [1994] are used to produce reference curves that estimate the response of the UVI instrument at the prescribed filter wavelength bandwidths on a pixel-by-pixel basis, in Rayleighs·pixel^{-1} or counts·pixel^{-1}, to electron precipitation at 1 mW·m^{-2} of energy flux as a function of characteristic energy. Recall from Chapter 2 that the transport code of *Lummerzheim and Lilensten* [1994] was used to precipitate a Maxwellian distribution of eight streams of electrons at nine characteristic energies and thirty-one column shift values at 1 mW·m^2 of energy flux into the MSIS-90 model thermosphere, predicting the volume emission rates of the FUV emissions relevant to the UVI instrument. This was executed using two different sets of MSIS-90 model parameters. The two model runs used MSIS-90 thermospheric densities representative of low-to-moderate geomagnetic and solar minimum conditions and moderate-to-high geomagnetic and solar maximum conditions, respectively, at Inuvik's geographic latitude and longitude (68.3°N, 226.5°E) and magnetic-midnight local time of 0200 AM (1000 UT) for nights in early January. The MSIS-90 solar and geomagnetic parameters are outlined in Table 3.3. The reference data describing the modeled UVI-measured brightnesses of the OI(135.6)-nm and LBH-L and LBH-S band emissions due to electron precipitation at 1 mW·m^{-2} of energy flux as a function of characteristic energy is shown below in Figures 3.26a-b for the two different model runs. The reference data describing the modeled UVI-measured brightnesses as a function of column shift is discussed later.

Table 3.3. MSIS-90 model parameters. Geographic latitude, 68.3°N; longitude, 226.5°E. Magnetic local time of 0200 AM (1000 UT).

	Solar and Geomagnetic activity	
	Low-to-moderate	Moderate-to-high
$F_{10.7}$ cm Flux	164	160
Averaged $F_{10.7}$ cm Flux	168	188
A_P Magnetic Activity Index	9	126
Day of Year	3	26

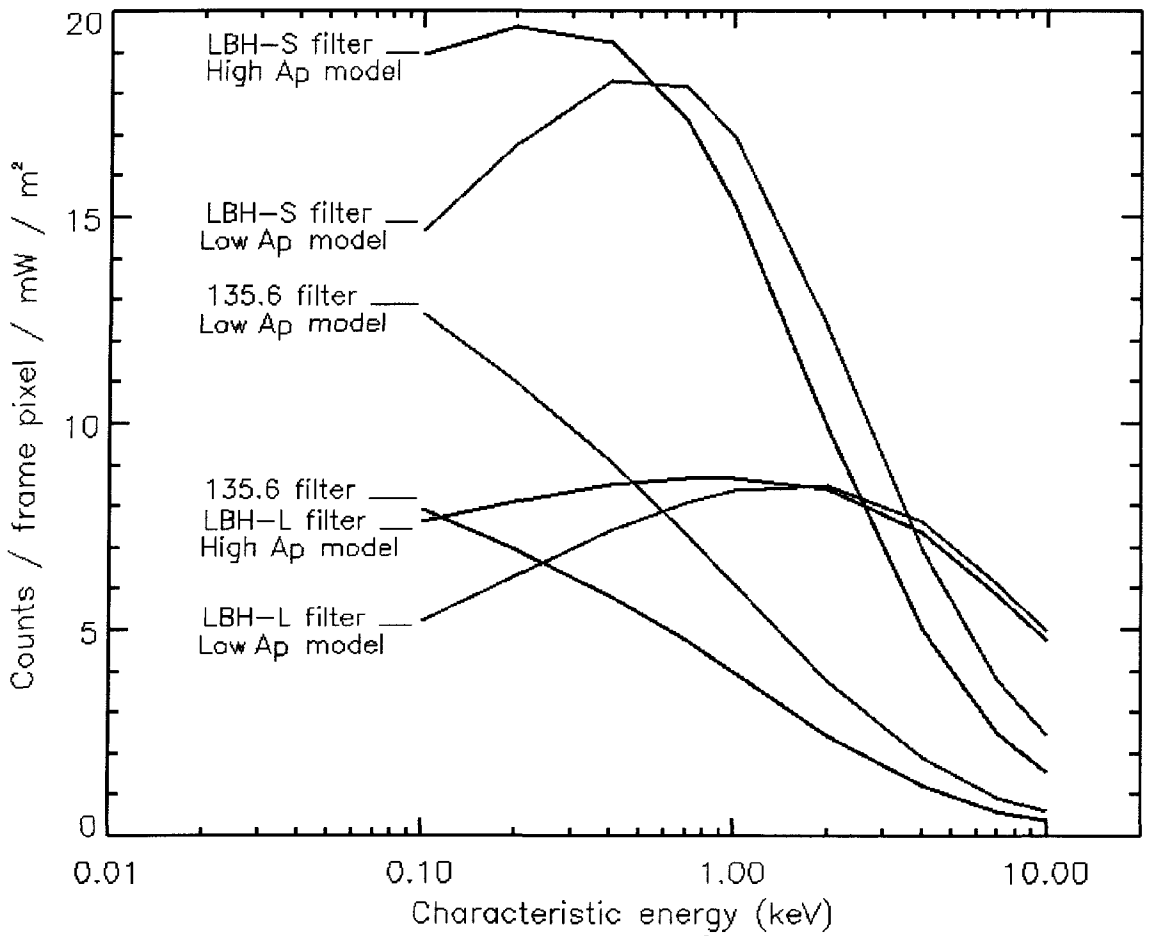

Figure 3.26. UVI instrument response to 1 $mW \cdot m^{-2}$ of energy flux as a function of characteristic energy for two levels of geomagnetic and solar activity. **(a)** The low-A_P model run is shown in red. The energy flux associtated with a given aurora is estimated from the observed LBH-L brightness using the LBH-L reference curves shown here. See the text for discussion. The characteristic energy of the precipitating electrons is estimated from the modeled ratio of LBH-S/LBH-L, shown in **(b)**.

Inspection of the LBH-L reference curves in Figure 3.26a from both model runs helps illustrate how energy flux of the precipitating electrons is inferred directly from the UVI-measured LBH-L emission brightness. For example, if the modeled UVI-measured brightness of the LBH-L band emission is 8.5 counts·pixel^{-1} at 1 mW·m^{-2} of energy flux and the UVI instrument measures a 180 count·pixel^{-1} LBH-L brightness, then the energy flux associated with that aurora is (180/8.5) = 21.2 mW·m^{-2}. However, this example relies on the assumption that the LBH-L reference curves in Figure 3.26a are straight lines of zero slope; *i.e.*, the modeled UVI-measured brightness of the LBH-L band emission at 1 mW·m^{-2} of energy flux is 8.5 counts·pixel^{-1} for all characteristic energies. This implies that there is no absorption of the LBH-L band emissions by O_2 for all characteristic energies, which is obviously not correct based on the significant differences that are seen between the 1-keV and 7-keV auroras illustrated in Figures 3.25a-b. During higher characteristic energy ($\gtrsim$1 keV) auroras, there is considerably more absorption of the LBH-L band emissions (particularly between 160-170 nm) by O_2 compared to low characteristic energy auroras. This is because the aurora's peak emission altitude of $\lesssim$130 km [*e.g.*, see *Lummerzheim and Lilensten*, 1994 and references therein] is sufficiently low such that the total column abundance of O_2 above the local production region is greater by an order of magnitude or more compared to the higher peak emission altitudes (~140-200 km) of low characteristic energy (~0.2-0.9 keV, respectively) auroras, where the N_2 density is diminished relative to the O density but so is the O_2 density. For very low characteristic energy ($\lesssim$0.2 keV) auroras, electron precipitation does not penetrate much below ~200 km, and consequently, O emissions dominate, such as the λ630.0-nm red line.

For the sake of inferring energy flux here from UVI-measured LBH-L brightnesses, a straight line of zero slope is assumed, and for UVI workers in general, energy flux is estimated by using a constant factor of 9.3 counts·pixel^{-1} per 1 mW·m^{-2} of energy flux [*Lummerzheim*, 2001, private communication]. The essential reason for this involves the large amount of uncertainty between electron transport models that accompanies model brightness estimates of FUV auroral emissions. For example, neither of the LBH-L reference curves produced by the transport code of *Lummerzheim and Lilensten* [1994]

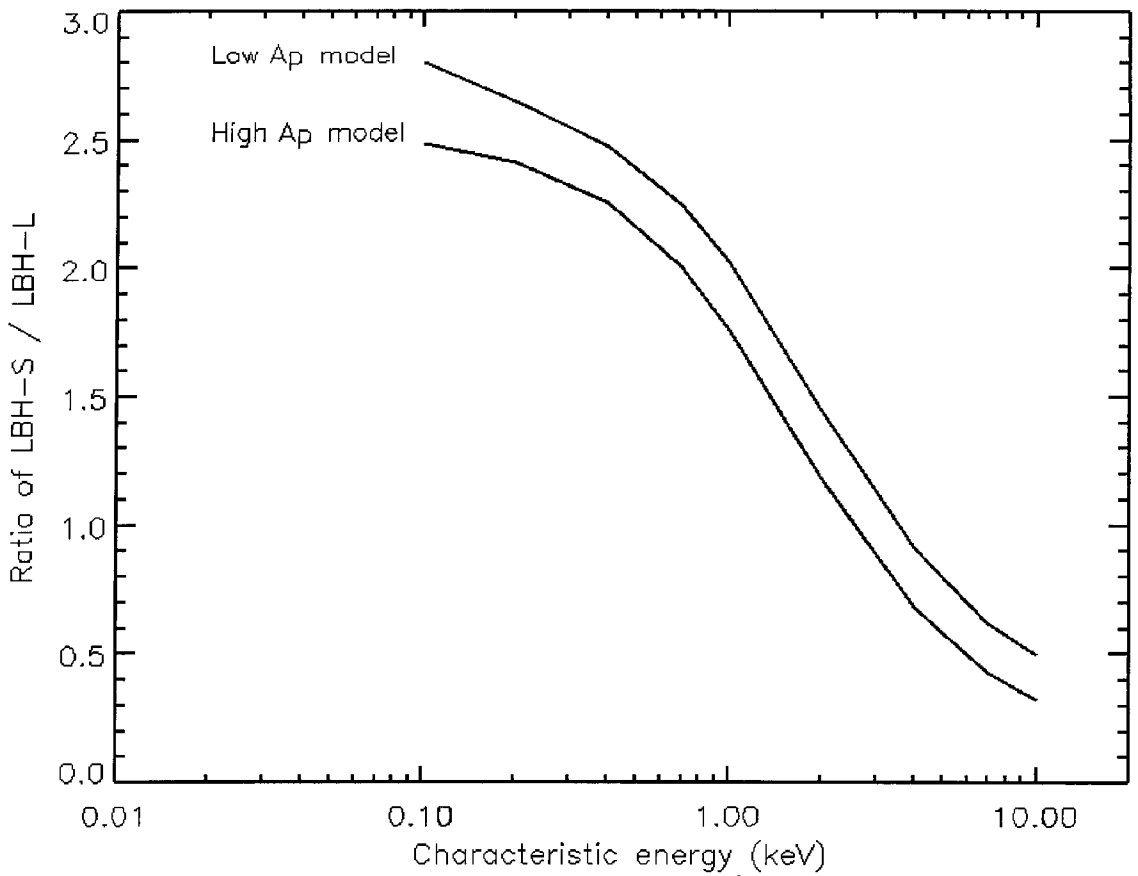

Figure 3.26 cont. UVI instrument response to 1 $mW \cdot m^{-2}$ of energy flux as a function of characteristic energy for two levels of geomagnetic and solar activity. **(b)** The ratio of the LBH-S/LBH-L modeled brightnesses as a function of characteristic energy for 1 $mW \cdot m^{-2}$ of electron precipitation. The LBH-S and LBH-L curves in **(a)** give the curves here. An observed LBH-S to LBH-L brightness ratio is compared to these curves to estimate characteristic energy. See the text for discussion.

that are presented in Figure 3.26a is a horizontal line, and furthermore, neither of the LBH-L reference curves attains 9.3 $counts \cdot pixel^{-1}$ at any characteristic energy, though the high-A_P reference curve does come close in the 0.7-0.9 keV mean energy range. However, LBH-L reference curves produced by other UVI workers using other electron transport models [*e.g. Richards and Torr*, 1990], while exhibiting similar trends compared to the output of the *Lummerzheim and Lilensten* [1994] model, also display dissimilar features. For example, the modeled LBH-L emission brightness computed as a function of characteristic energy by the transport model of *Richards and Torr* [1990] has been shown

to have a slope much closer to zero than the reference curves shown in Figure 3.26a [*e.g. Germany et al.*, 1990]. Similarly, the UVI LBH-L reference curve computed by the *Richards and Torr* [1990] model has a slope close to zero, and in addition, a value of ~10 counts·pixel^{-1} [*Lummerzheim*, 2004, private communication]. Many UVI studies have been concerned with estimating total energy flux into the thermosphere during auroral substorms and magnetic storms [*e.g. Germany et al.*, 1997; *Lummerzheim et al.*, 1997], and it was generally agreed upon by UVI workers that a standard value of 9.3 counts·pixel^{-1} of LBH-L emission brightness equating to 1 mW·m^{-2} of energy flux must be used so that comparisons between UVI studies could be properly conducted without concerns that the differences between the auroral models were influencing the comparisons. The LBH-L emission brightness of 9.3 counts equating to 1 mW·m^{-2} of energy flux is used here as well. Uncertainties associated with auroral modeling of FUV emissions (*e.g.*, uncertain emission and absorption cross sections) and their effects on energy flux and characteristic energy determinations are discussed more below. In order to determine the characteristic energy of precipitating electrons from the UVI observations, the ratio of the measured LBH-S to LBH-L auroral brightness is determined and then interpolated to a characteristic energy value that lies along the reference curves shown in Figure 3.26b.

The MSIS-90 thermospheric models used with two different levels of geomagnetic and solar activity to create these UVI reference curves at first glance appear to result in large differences between the two model cases. However, the effect on the reference curves is easily understood. The LBH-L and LBH-S reference curves have basically the same slope at high characteristic energies for both the low- and high-A_P model runs, and only begin to diverge at the lowest characteristic energies ($\lesssim$0.8 keV). For the case of the high-A_P reference curves, higher brightnesses are predicted for the LBH-L and LBH-S band emissions at lower characteristic energies (relative to the low-A_P model) because the thermally-expanded hotter thermosphere in the high-A_P model lifts N_2 to higher altitudes, altering the $[O]/([N_2]+[O_2])$ mixing ratio at each altitude and repartitioning the collisional energy and excitation between the different thermospheric species. Thus, more N_2 is available at higher altitudes in the high-A_P model for excitation during low characteristic

energy precipitation events. Comparison of the low- and high-A_P reference curves at high characteristic energies reveals that LBH-L brightnesses are essentially unaffected by changing geomagnetic conditions since LBH-L band emissions are mostly unattenuated by O_2, whether the O_2 resides at lower altitudes in a low-A_P cool thermosphere or resides at higher altitudes in a high-A_P hot thermosphere. However, because LBH-S band emissions are attenuated by O_2, it is relevant how much O_2 resides in the column above the auroral emission. Determination of energy flux is insensitive to the A_P effect at high characteristic energies, while careful examination of the ratio curves in Figure 3.26b shows that if the high-A_P model was used to estimate characteristic energies determined from auroral brightnesses measured during a low-A_P time period, the inferred characteristic energies would be reduced by about a factor of two relative to the low-A_P model estimates. The OI(135.6)-nm reference curves shown in Figure 3.26a, which clearly show the most variability between the low- and high-A_P cases, are discussed in the next section.

As was stated earlier, spatial averaging of the auroral images was necessary in order to address the platform jitter and spacecraft wobble problems (discussed in Chapter 2), the statistical significance of the measurements, and the potential for examining mesoscale thermospheric processes. The raw LBH-L, LBH-S and OI(135.6)-nm auroral images were binned latitudinally and longitudinally into square regions (*i.e.*, boxes) of 1° latitude × 3° longitude, resulting in areas of ~110 km × ~120 km = 1.3×10^4 km^2, respectively. The auroral images were acquired by the spacecraft in a sequence shown in Table 3.4. The filter sequence allowed the required data to be acquired in an order that allowed determination of the necessary parameters, since comparisons between the observed and modeled OI(135.6)-nm emission are of interest here; *i.e.*, the precipitation's energy flux and characteristic energy that prevailed at the acquisition time of the OI(135.6)-nm auroral image is desired. How this was addressed is explained more below. The binning process averaged the 18 and 36 second exposures together, resulting in pixel totals of 10-40 pixels per region; *i.e.*, box. The term "box" is used hereafter to describe each binned region. Examples of the UVI LBH-L and LBH-S auroral images and the inferred energy flux and characteristic energy as determined by the above procedures are presented in

Table 3.4. UVI-filter sequence. Integration times shown and the order of auroral-image acquisition.

UVI Filter	Integration time
Home (Dark frame)	18 seconds
Home	36 s
OI(130.4) nm	18 s
OI(130.4) nm	36 s
OI(135.6) nm	18 s
OI(135.6) nm	36 s
LHB-L	18 s
LBH-L	36 s
LHB-S	18 s
LBH-S	36 s

Figures 3.27a-d and 3.28a-d from the nights of January 3, 2001 and February 28, 2000, respectively. The figures below are presented in the described format, where each box of an image is 1° latitude × 3° longitude.

After spatial binning was completed, further averaging involved linear interpolation in time. If a modeled OI(135.6)-nm auroral brightness was to be compared to an observed OI(135.6)-nm brightness acquired at a particular time, then the energy flux and characteristic energy at that time would be desired, ideally. The method for achieving this task was to take the LBH-L and LBH-S binned brightnesses measured before and after each OI(135.6)-nm image, and interpolate those brightnesses to the time of the OI(135.6)-nm image. For example, if an LBH-L brightness in a given box is 80 counts at 1005 UT and 160 counts at 1011 UT, then the box's brightness is 120 counts at the 1008 UT time of the OI(135.6)-nm brightness measurement. This linear interpolation of the LBH-S and LBH-L brightnesses to the time of the OI(135.6)-nm measurements was deemed better than simply averaging the before-and-after LBH-S and LBH-L brightnesses together in order to provide a better estimation of the energy flux and characteristic energy flux at the times of the OI(135.6)-nm images. The time between successive OI(135.6)-nm images was approximately six minutes, and large-scale auroral forms can change dramatically on time scales much shorter than this, potentially adding artifacts to estimates

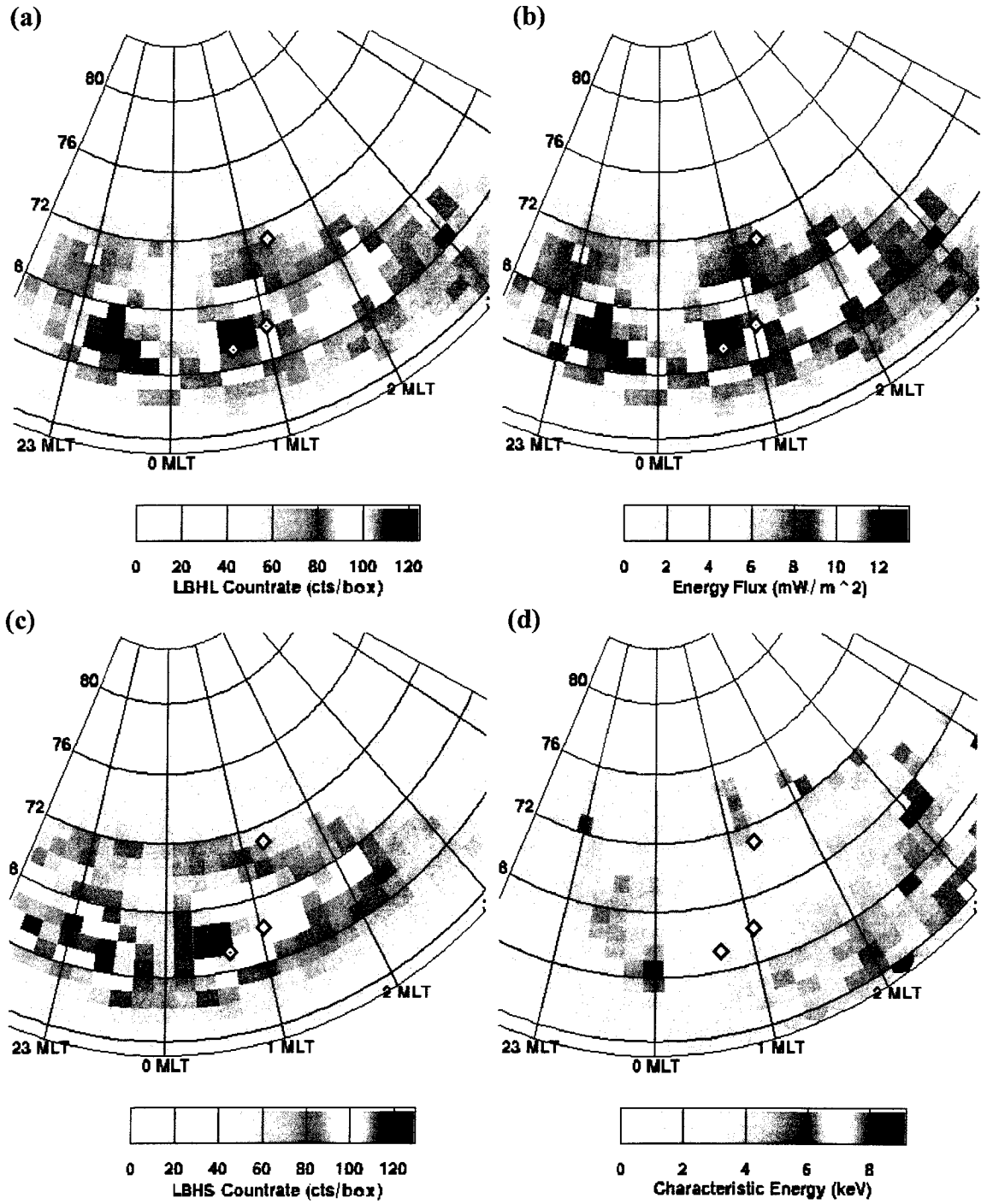

Figures 3.27. UVI-observed LBH-L and LBH-S auroral images, inferred energy flux and characteristic energy at 1139 UT on Jan 3, 2001. **(a)** The LBH-L brightness, binned according to the discussion in the text. **(b)** Inferred energy flux from the LBH-L brightness. **(c)** The LBH-S brightness. **(d)** The LBH-S/LBH-L inferred characteristic energy. Each box represents a region of ~110 km × ~120 km, the potential size of a spatially-extended vertical wind field.

of interpolated LBH-L and LBH-S brightnesses. More averaging, however, was deemed excessive, given the issues of platform jitter and spacecraft wobble.

In general, auroral-model outputs are regarded as reliable by the aeronomy community because auroral parameters derived from model-to-observation brightness comparisons generally fall within the ranges that are expected for aurora, of which the energy flux and characteristic energy estimates presented in Figures 3.27a-d and 3.28a-d are typical examples. Nonetheless, significant uncertainty exists in these inferred auroral parameters due to the respective uncertainty in the absorption and emission (cascade plus direct excitation) cross sections of N_2, O_2, and O, all of which contribute to the uncertainty in model estimates of auroral FUV emissions and inferred energy fluxes and characteristic energies. For example, the total uncertainty in the emission cross section for the LBH band emissions is ~20% [*Ajello and Shemansky*, 1985], and is ~25% for the OI(135.6)-nm emission [see *Doering and Gulcicek*, 1989 and references therein]. An internal check of energy conservation by *Lummerzheim and Lilensten* [1994] in their model found that numerical procedures also introduce an error of $\lesssim$5% in the results. In general, propagation of errors through an auroral model tends to lead to unrealistically-high errors in model estimates of the FUV emission brightnesses and inferred auroral parameters [*Germany et al.*, 2001], and a study performed by *Germany et al.* [2001] on cross section limits examined this issue. In one model run, a set of cross section values was used, and in another run, cross section values at the other end of their respective uncertainty ranges was used. The study found that energy flux and characteristic energy values derived from UVI observations and the two model runs differed by 16% and 23%, respectively.

Error estimates of the energy flux and characteristic energy in this study are comparable to the values quoted above. Rather than propagate uncertainties through the auroral model of *Lummerzheim and Lilensten* [1994], a difficult and unrealistic venture [*Lummerzheim*, private communication], the uncertainty in energy flux and characteristic energy can be easily estimated from simple expressions. If the energy flux F_e is given by

$$F_e = k(L) = c_1 \cdot L, \tag{3.25}$$

where L is the mean LBH-L brightness in counts·box^{-1}, k is some function of L, and c_1 is

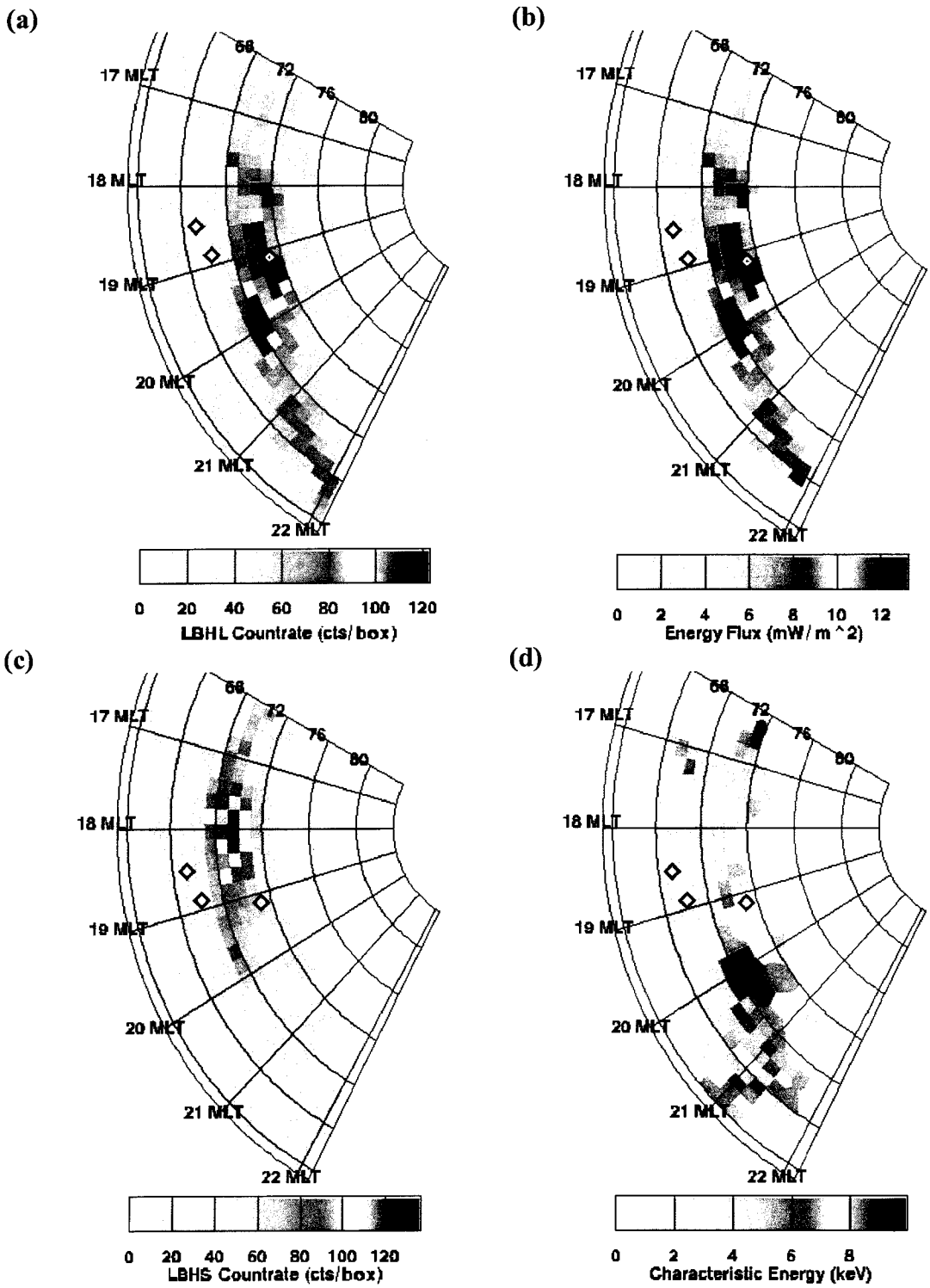

Figures 3.28. UVI-observed LBH-L and LBH-S auroral images, inferred energy flux and characteristic energy at 0552 UT on Feb 28, 2000. Same layout as Figure 3.27. **(a)** The LBH-L brightness. **(b)** Inferred energy flux. **(c)** The LBH-S brightness. **(d)** The LBH-S/LBH-L inferred characteristic energy.

the constant that converts LBH-L brightness measurements into energy flux values, c_1 = 9.3 counts/1 mW·m^{-2}, then the percentage error $\delta F_e/F_e$ in the energy flux F_e is given by,

$$\delta F_e/F_e = [(\delta c_1/c_1)^2 + (\delta L/L)^2]^{1/2}, \quad (3.26)$$

where the uncertainty in the constant c_1 is analogous to the uncertainty in the emission cross section; *i.e.*, $\delta c_1/c_1 = 0.2$ [*Ajello and Shemansky*, 1985]. The statistical uncertainty δL in an LBH-L brightness measurement L of a particular box is given by

$$\delta L = \left[\frac{1}{N}\sum_{i=1}^{N}\frac{(x_i - L)^2}{N-1}\right]^{1/2}, \quad (3.27)$$

where N is the total number of pixels per box, and x_i is the LBH-L brightness value of each pixel. In general, the statistical uncertainty percentage $\delta L/L$ is $0.05 \lesssim \delta L/L \lesssim 0.25$ for the total number of pixels per box of 10-40. For the values of $\delta L/L$ quoted here, the total percentage error in the inferred energy fluxes is ~20-35%. Similarly, if the characteristic energy E_c is given by

$$E_c = j(S, L) = c_2 \cdot (S/L), \quad (3.28)$$

where S is the mean LBH-S brightness in counts·box^{-1}, j is some function of S and L, and c_2 is the constant that converts LBH-S/LBH-L brightness ratios into characteristic energies, then the percentage error $\delta E_c/E_c$ in the characteristic energy is given by,

$$\delta E_c/E_c = [(\delta c_2/c_2)^2 + (\delta L/L)^2 + (\delta S/S)^2]^{1/2}, \quad (3.29)$$

where $\delta c_2/c_2 = \delta c_1/c_1 = 0.2$, and $\delta S/S = \delta L/L \approx 0.5$-$0.25$. In general, the percentage error in the derived characteristic energies is ~20-40%. These expressions are used later in the error estimations of the modeled OI(135.6)-nm brightness and column shift.

During the preliminary stages of these studies (*i.e.*, in the initial derivations of energy flux and characteristic energy from the LBH-L and LBH-S auroral images), only boxes exhibiting energy flux values of 1 mW·m^{-2} (*i.e.*, 9.3 counts·box^{-1}) or greater were retained. Any boxes exhibiting LBH-L brightnesses below this threshold were discarded. The selection of the 9.3 counts·box^{-1} brightness threshold was arbitrary, but some method was necessary to select data which would provide statistically-meaningful estimates of energy flux and characteristic energy. The 9.3 counts·box^{-1} LBH-L brightness threshold was considered a reasonable estimate that significant aurora prevailed in a particular

region. In addition, boxes that contained characteristic energy values extending outside the range of the model runs (*i.e.*, boxes with characteristic energies <0.1 keV or >10 keV) were also discarded, the reason being that these characteristic energy estimates were not interpolated quantities but instead were extrapolated. As can be seen in Figures 3.27 and 3.28, the LBH-L and LBH-S images contain a great deal of very low signal count outside of the auroral regions that remains even after background subtraction and airglow removal from the raw images. It is this low signal data that was generally disregarded by the above criteria when inferring the energy flux and characteristic energy. However, it was determined later that 9.3 counts·box^{-1} was too low a threshold for selection of auroral data to retain for the purposes of this study, and subsequently, the threshold was increased to 15 counts·box^{-1}. The energy flux and characteristic energy maps in Figures 3.27 and 3.28 were produced using the 15 counts·box^{-1} threshold, and the reasons for this higher threshold are discussed more below and in detail in Chapter 4.

3.2.3 Modeling the OI(135.6)-nm Auroral Emission

Once the energy flux and characteristic energy were determined, the next step in the search for vertical wind-induced thermospheric composition perturbations was to compute the model OI(135.6)-nm auroral brightness and compare it to UVI OI(135.6)-nm brightness observations. The modeled OI(135.6)-nm brightness is determined from the response of the model thermosphere's OI density profile to the estimated energy flux and characteristic energy of the precipitating electrons; *i.e.*, from the expected brightness of the resulting auroral emissions, and the expected UVI observation of those emissions using the OI(135.6)-nm reference curve of Figure 3.26a. Discrepancies between the two potentially indicate mesoscale-size regions of vertical uplifting or downwelling. A region where the observed OI(135.6)-nm brightness was greater than the modeled brightness would indicate O-rich air in the region, due perhaps to a downward vertical wind transporting air parcels from high in the upper thermosphere to auroral-emission altitudes. Upward winds which adiabatically lift N_2-rich air from the lower thermosphere into the middle and upper thermosphere would potentially result in the observed OI(135.6)-nm brightness being less than the expected OI(135.6)-nm brightness.

Furthermore, the electron transport code does not necessarily model accurately the OI(135.6)-nm emission at mesoscale sizes of ~10^4 km^2 because the MSIS-90 atmosphere used in the transport code to describe the thermosphere's neutral densities is an averaged atmosphere, both spatially and temporally, which smooths out composition variations that would exist at mesoscale sizes in the real thermosphere. Therefore, the discrepancies between the observed and modeled OI(135.6)-nm emissions have the potential to describe mesoscale-sized perturbations that occur in the real thermosphere relative to a model thermosphere. Recall also from Chapter 1 that atomic oxygen's daily, seasonal, latitudinal, and solar-cyclical variability, and its variability associated with high-latitude thermospheric processes, remains an outstanding question of thermospheric studies.

The technique for modeling the OI(135.6)-nm auroral emission was simple, once the energy flux and characteristic energy were predicted from the LBH-L and LBH-S brightnesses. For an estimated characteristic energy associated with a particular box, the UVI instrument response curve at λ135.6 nm—either of the two OI(135.6)-nm reference curves shown in Figure 3.26a, depending on geomagnetic conditions—was used to infer the modeled OI(135.6)-nm brightness as measured by the UVI instrument for 1 mW·m^2 of flux in that box. The inferred energy flux associated with that box was then multiplied by the modeled OI(135.6)-nm brightness of the box at 1 mW·m^2 to compute the modeled OI(135.6)-nm brightness particular to that box's energy flux. Mathematically, the modeled OI(135.6)-nm auroral brightness M can be written as

$$M = g(c_3, F_e, E_c) = c_3 \cdot F_e \cdot [c_4 \cdot \log(E_c)], \tag{3.30}$$

where g is some function of energy flux F_e and characteristic energy E_c, c_3 is analogous to the OI emission cross section at λ135.6 nm, and c_4 is the value of the OI(135.6)-nm reference curve at the inferred characteristic energy in Figure 3.26a which estimates the modeled OI(135.6)-nm brightness at 1 mW·m^2 of energy flux at that characteristic energy. Equation 3.30 will prove to be useful later in the estimation of the uncertainty in the modeled OI(135.6)-nm brightness. Because the integro-differential equation that describes electron transport into the atmosphere is linear in electron intensity, the solution for electron intensity is linearly dependent on energy flux F_e [*Lummerzheim et al.*, 1990].

Thus, simple linear scaling by F_e of the modeled OI(135.6)-nm emission M at 1 $mW \cdot m^{-2}$ is justified. Figures 3.29a-b and 3.30a-b show the observed and modeled OI(135.6)-nm brightnesses from the data sets of January 3, 2001, 1139 UT and February 28, 2000, 0552 UT, respectively. Figures 3.29b and 3.30b are determined from Equation 3.30, using the energy flux and characteristic energy data of Figures 3.27 and 3.28, respectively, and the low-A_P OI(135.6)-nm reference curve of Figure 3.26a. LBH-L and LBH-S brightnesses were also modeled using this same method to check for consistency, and in general, the modeled LBH-L and LBH-S brightnesses were consistent with their respective UVI-observed brightnesses, with one caveat. When the standard LBH-L reference curve of 9.3 counts·pixel^{-1} and zero slope was used, the results were consistent; when the low-A_P or high-A_P LBH-L reference curves of Figure 3.26a were used (depending on the data set being analyzed), the model underestimated the LBH-L and LBH-S brightnesses compared to the observed brightnesses. This would be expected since the energy flux was originally inferred from the LBH-L reference curve of 9.3 counts·pixel^{-1} and zero slope.

As the figures here indicate, the broad-scale features of the modeled OI(135.6)-nm brightness appear to match the observed brightness. This is encouraging. Inspection of Figures 3.29a-b reveals similar bright auroral structures around 2300 MLT and 0100 MLT, with a weaker region of brightness at 0000 MLT between the sectors of greater brightness. Similarly, Figures 3.30a-b reveal comparable auroral structures and brightnesses from ~1700-2100 MLT and ~64°-72°, with some discrepancies from box to box. However, the one thing that is clearly evident from both examples, and particularly the January 3, 2001 data, is that on average, the modeled OI(135.6)-nm auroral brightness is weaker than the observed brightness. As was discussed at the end of Chapter 1, this was the case through all the data sets presented in this thesis. The topic is examined later and in Chapter 4.

The uncertainty in the modeled OI(135.6)-nm brightness is estimated similarly to how error estimates were determined for the energy flux and characteristic energy. Using Equation 3.30, the uncertainty δM in the modeled OI(135.6)-nm brightness M is given by

$$\delta M = \{[(\partial g/\partial c_3)\cdot\delta c_3]^2 + [(\partial g/\partial F_e)\cdot\delta F_e]^2 + [(\partial g/\partial E_c)\cdot\delta E_c]^2\}^{1/2}. \quad (3.31)$$

From this expression and Equations 3.26 and 3.29, the percentage error $\delta M/M$ in the

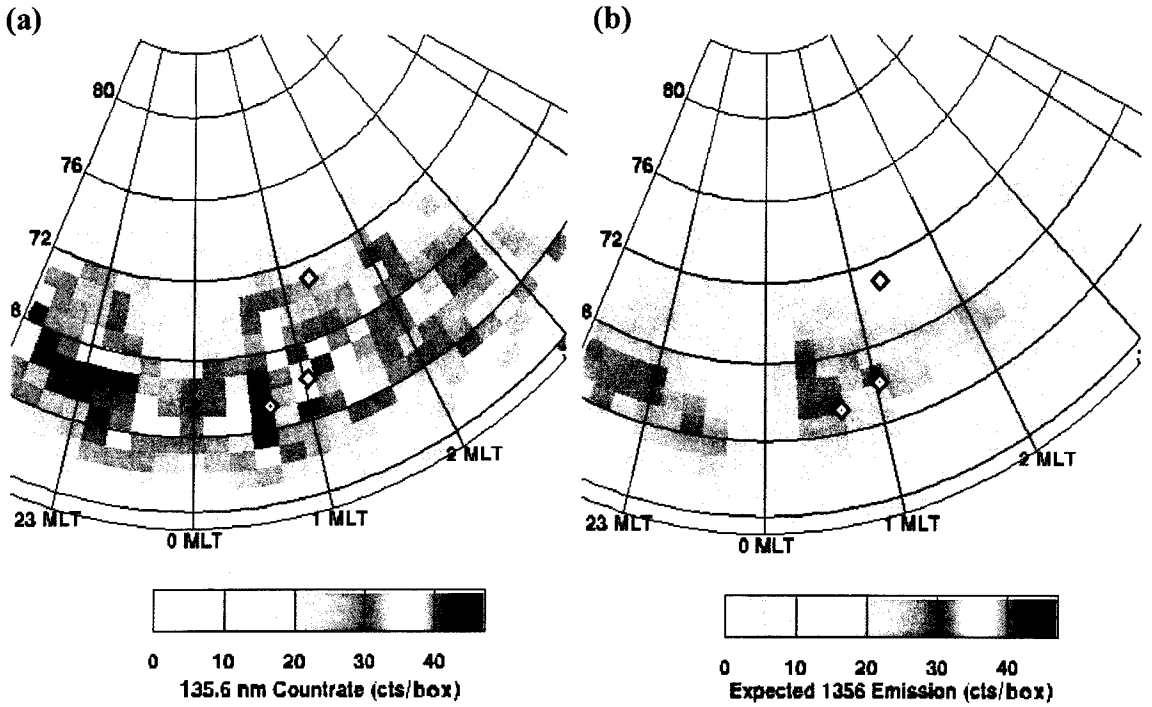

Figure 3.29. UVI-observed and modeled OI(135.6)-nm auroral brightnesses at 1139 UT on Jan 3, 2001. **(a)** UVI-observed OI(135.6)-nm brightness. **(b)** Modeled OI(135.6)-nm brightness. In general, discrepancies between the brightnesses on a box-by-box basis may indicate vertical wind composition effects. However, the large amount of difference between the two brightnesses here, on average, is attributed to problems with the modeling process. See the text here and in Chapter 4 for discussion.

modeled OI(135.6)-nm brightness is found to be

$$\delta M/M = [(\delta c_1/c_1)^2 + (\delta c_2/c_2)^2 + (\delta c_3/c_3)^2 + 2\cdot(\delta L/L)^2 + (\delta S/S)^2]^{1/2}, \quad (3.32)$$

where $\delta c_3/c_3 = 0.25$ [*e.g.*, see *Doering and Gulcicek*, 1989 and references therein] is the uncertainty in the OI emission cross section at λ135.6 nm, and $\delta c_1/c_1 = \delta c_2/c_2 = 0.2$ [*Ajello and Shemansky*, 1985]. Equation 3.32 is used in the next section in the estimation of the error in the column shift values. In general, the total percentage error in modeled OI(135.6)-nm brightness values based on Equation 3.32 is 38-58%. Clearly, this error is considerable, and initially, it was not certain if the significant on-average systematic difference between the modeled and observed OI(135.6)-nm brightnesses through all the data sets was attributed to this uncertainty in the model estimates. However, because the modeling process systematically underestimated the OI(135.6)-nm brightness compared

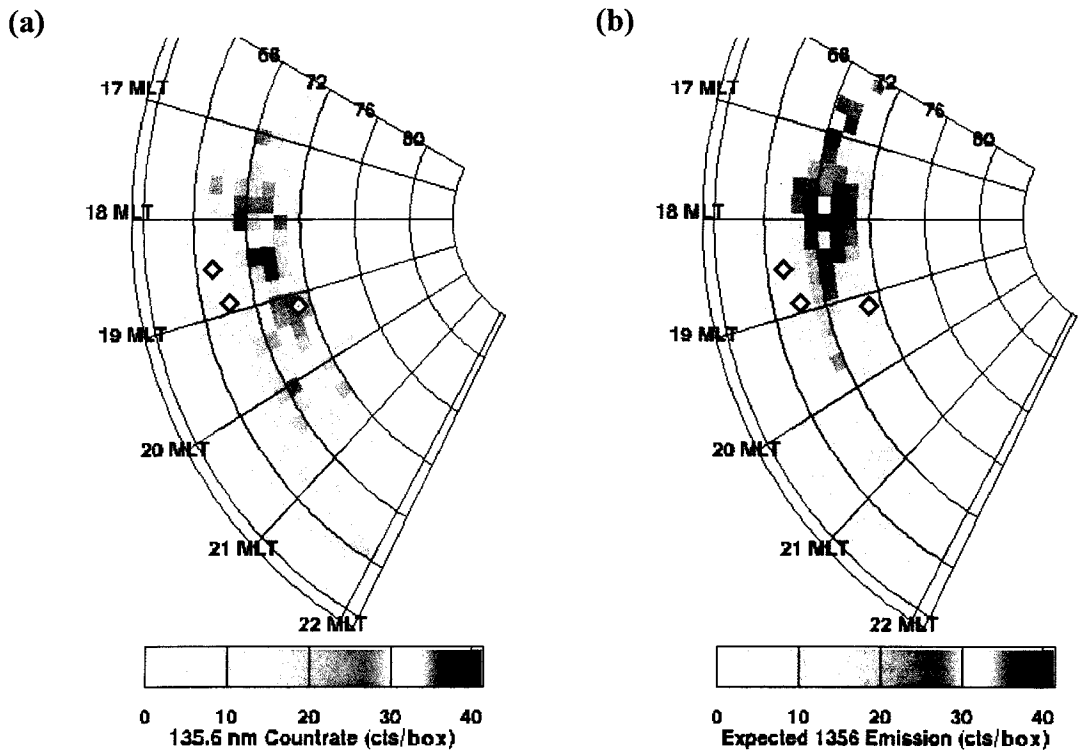

Figure 3.30. UVI-observed and modeled OI(135.6)-nm auroral brightnesses at 0552 UT on Feb 28, 2000. **(a)** UVI-observed OI(135.6)-nm brightness. **(b)** Modeled OI(135.6)-nm brightness. Same layout as Figure 3.29a-b.

to the observed brightness through all the data sets, it was decided that some other, as yet unknown, deficiency in the modeling process was likely responsible.

Initially, the observed-to-modeled OI(135.6)-nm brightness comparisons were presented as percent and standard-deviation differences [*Krynicki et al.*, 2000 CEDAR conference, June, 2000, Boulder, CO]. This was useful for identifying the statisically-significant composition variations in the observed-to-modeled OI(135.6)-nm brightness comparisons so that these variations potentially could be correlated with vertical wind activity. However, this method of presentation provided no further insight into a significant vertical wind's effect on thermospheric structure, such as height displacement of air parcels or mixing. It was also decided that presenting the OI(135.6)-nm brightness comparisons in terms of an atomic oxygen scaling factor like *Hecht et al.* [1989] or *Lummerzheim et al.* [1990] would yield no more insight than the percent and standard-

deviation difference presentations, since the scaling factor has no physical interpretation beyond indicating that some mechanism depleted or enhanced the O density within a column of thermosphere, which in essence the percent and standard-deviation difference presentations also stated. Thus, a model parameter which could be subject to a physical interpretation—height displacement—and which simulated and parameterized vertical wind composition effects such as transport, mixing and disruption of diffusive equilibrium was envisioned. This turned out to be the column shift, the subject of the next section.

3.2.4 Vertical Displacement and Disruption of Diffusive Equilibrium: The Column Shift Parameter Modification to the MSIS-90 Model Thermosphere Density Structure

As was discussed at the end of Chapter 1, the most likely thermospheric bulk property to reveal auroral-related vertical wind composition effects is the atomic-oxygen-to-molecular-species mixing ratio, $[O]/([N_2]+[O_2])$. For example, *Rishbeth et al.* [1987] modeled high-latitude vertical wind effects by defining a diffusive equilibrium parameter P in terms of the O and N_2 partial pressures. In general, regions of enhanced P were found where heating and strong upwelling prevailed, while regions of reduced P were produced by downwelling. Long-lived, intermediate- to large-magnitude upward winds due to large pressure or density gradients that are set up by Joule and particle-precipitation heating may transport air parcels of a given $[O]/([N_2]+[O_2])$ from the lower and middle thermosphere to the upper thermosphere. Air parcels expand adiabatically due to the one-to-two order of magnitude pressure change between the lower and upper thermosphere, but their low $[O]/([N_2]+[O_2])$ will remain intact relative to the surrounding air's higher $[O]/([N_2]+[O_2])$ (though continuing to blow along with the large-scale horizontal flow) since, recalling from Chapter 1, times scales for diffusive processes to reestablish diffusive equilibrium, given by $\tau_{eq} = H^2/D$, where H is the scale height and D is the molecular diffusion coefficient, are ~2 hours at ~200 km. Remembering also that such a region of uplifted air, though mesoscale in size, is still rather large ($\sim 10^2$-10^5 km^2), the region will not immediately respond to the surrounding air's different mixing ratio relative to its own. Since a mesoscale-sized region of a given $[O]/([N_2]+[O_2])$ is fairly long-lived, its auroral-emission output, presumably, would reflect that density distribution.

Large-magnitude downward winds of the kind observed in the high-latitude upper thermosphere are not as easily understood, compared to what drives an upward wind. However, these winds are presumably due to either the adiabatic compression of upper-thermospheric air parcels that happen to be much cooler and denser than the surrounding air, causing the cooler, denser air parcels to sink in the direction of gravity and negative temperature gradient, or are due to convergent upper-thermospheric horizontal winds which can produce localized density bulges that generate strong, localized downward or upward winds, transporting upper-thermospheric air parcels to lower or higher altitudes, respectively [*e.g. Smith*, 1998]. Large magnitude, upper-thermospheric downward winds may transport air parcels of a high $[O]/([N_2]+[O_2])$ down to altitudes of a lower $[O]/([N_2]+[O_2])$, and the auroral emission output of that particular thermospheric column will change accordingly. With these issues in mind, a parameter referred to as the column shift was introduced into the MSIS-90 model thermosphere [*Hedin*, 1991] used by the electron transport code of *Lummerzheim and Lilensten* [1994]. The purpose of this modification was to simulate these potential mesoscale vertical wind composition effects that the MSIS-90 model cannot replicate because of its inherently averaged nature.

The column shift's implementation proceeded first by utilizing the notion that the $[O_2]/[N_2]$ and $[O]/([N_2]+[O_2])$ mixing ratio of a given pressure level (altitude) in the MSIS-90 model could be imposed at another pressure level, but that total mass density must be maintained at each pressure level in order to maintain the pressure in that level; *i.e.*, hydrostatic equilibrium is maintained. In reality, a mixing ratio change at a given altitude will result in a minimal pressure change based on the ideal gas law $p = nk_BT$, but hydrostatic equilibrium will be quickly restored, since, recalling from Chapter 1, the altitude-dependent time constant is $\tau_{hydr} \approx$ 15-50 s. The column shift parameter would not be a meaningful quantity unless hydrostatic equilibrium was maintained in the model, and in general, pressure is maintained to 1 part in 10^3-10^4 at each pressure level. Furthermore, the largest differences in the pressure are at very high altitudes in the model thermosphere, $\gtrsim$300 km. The column shift's overall effect was to redistribute the [O], $[O_2]$, and $[N_2]$ at each pressure level while maintaining the total mass density (and pressure) at

each level. This effect represents a disruption of diffusive equilibrium that is physically reasonable since recovery from diffusive equilibrium disturbances takes much longer in the real thermosphere than from hydrostatic balance disturbances. Mathematically, the modification was implemented in the MSIS-90 model by using two criteria. First, total mass density is the same for the two different sets of mixing ratios at each altitude z,

$$\rho_{tot}(z) = \rho'_{tot}(z), \tag{3.33}$$

where $\rho_{tot}(z)$, in units of amu per unit volume, is the total mass density with the original mixing ratio at each altitude z, given by

$$\rho_{tot}(z) = 16 \cdot n_O(z) + 28 \cdot n_{N_2}(z) + 32 \cdot n_{O_2}(z), \tag{3.34}$$

and $\rho'_{tot}(z)$ is the total mass density with the new mixing ratio at each altitude z, given by

$$\rho'_{tot}(z) = 16 \cdot n'_O(z) + 28 \cdot n'_{N_2}(z) + 32 \cdot n'_{O_2}(z). \tag{3.35}$$

Here, $n_O(z)$, $n_{N_2}(z)$, $n_{O_2}(z)$, $n'_O(z)$, $n'_{N_2}(z)$, and $n'_{O_2}(z)$ are the number densities of atomic oxygen, molecular nitrogen, and molecular oxygen for the original mixing ratio and new mixing ratio, respectively, and 16, 28, and 32 are the molecular weight of O, N_2, and O_2 in amu, respectively. The second criterion assumes that the mixing ratio of the primed densities is the ratio of the unprimed densities at some displaced altitude ΔZ,

$$\frac{n'_{O_2}(z)}{n'_{N_2}(z)} = \frac{n_{O_2}(z+\Delta Z)}{n_{N_2}(z+\Delta Z)} \equiv \sigma(z+\Delta Z), \tag{3.36}$$

and

$$\frac{n'_O(z)}{n'_{N_2}(z) + n'_{O_2}(z)} = \frac{n_O(z+\Delta Z)}{n_{N_2}(z+\Delta h) + n_{O_2}(z+\Delta Z)} \equiv \xi(z+\Delta Z). \tag{3.37}$$

Thus, there are three Equations, 3.33, 3.36, and 3.37 and three unknowns, $n'_O(z)$, $n'_{N_2}(z)$, and $n'_{O_2}(z)$. The expressions for the primed densities are then given by

$$\begin{aligned}
n'_{N_2}(z) &= \frac{1}{[28+32\sigma+16\xi(\sigma+1)]} \cdot [28 n_{N_2}(z) + 32 n_{O_2}(z) + 16 n_O(z)] \\
n'_{O_2}(z) &= \frac{\sigma}{[28+32\sigma+16\xi(\sigma+1)]} \cdot [28 n_{N_2}(z) + 32 n_{O_2}(z) + 16 n_O(z)], \\
n'_O(z) &= \frac{\xi(\sigma+1)}{[28+32\sigma+16\xi(\sigma+1)]} \cdot [28 n_{N_2}(z) + 32 n_{O_2}(z) + 16 n_O(z)]
\end{aligned} \tag{3.38a-c}$$

and though these expressions may appear complicated, the method used to implement the modification in the code was simple. If the transport code was to be run for a given characteristic energy and a given column shift, the new neutral densities as defined by Equations 3.38a-c were determined by first making a call to the MSIS-90 subroutine, yielding the model thermospheric neutral densities at the altitude $z+\Delta Z$. This information determines $n_{N_2}(z+\Delta Z)$, $n_{O_2}(z+\Delta Z)$, and $n_O(z+\Delta Z)$, and thus, $\xi(z+\Delta Z)$ and $\sigma(z+\Delta Z)$. Another call is then made to the subroutine, this time at altitude z, giving $n_{N_2}(z)$, $n_{O_2}(z)$, and $n_O(z)$. Thus, $n'_{N_2}(z)$, $n'_{O_2}(z)$, and $n'_O(z)$ are determined from $n_{N_2}(z), n_{O_2}(z)$, $n_O(z)$, $\xi(z+\Delta Z)$ and $\sigma(z+\Delta Z)$. These new densities at altitude z are employed in the transport code in place of the MSIS-90 neutral densities that would normally prevail at altitude z.

The electron transport model of *Lummerzheim and Lilensten* [1994] generally utilizes an MSIS-90 atmosphere of 200 layers extending from 80 km to 500 km, and what is performed in the code by the column shift parameter is better explained by a simple example. If a column shift of $\Delta Z = -50$ km was used to redistribute the neutral densities, then what is done by the code is to take the $[O_2]/[N_2]$ and $[O]/([N_2]+[O_2])$ ratios from 130 km to 550 km, impose these ratios at 80 km to 500 km, and then redistribute the densities according to Equations 3.38a-c. The column shift's overall modification to the MSIS-90 model's [O], $[O_2]$, and $[N_2]$ profiles as a function of altitude are illustrated below in Figures 3.31a-c. Figure 3.31a is a standard output from the MSIS-90 model for a set of input parameters, such as latitude, longitude, time, $F_{10.7}$ cm flux and magnetic index A_P. The O, O_2, and N_2 denstities are shown from an altitude of 80 km to 300 km, as is the atomic-oxygen-to-molecular-species mixing ratio. The MSIS-90 model output can be verified at the National Space Science Data Center's space physics model website, at the URL http://nssdc.gsfc.nasa.gov/space/model/models/msis.html.

The effect of an upward column shift of 50 km is illustrated in Figure 3.31b. The $[O_2]/[N_2]$ and $[O]/([N_2]+[O_2])$ ratios from 30-450 km altitude are imposed at altitudes of 80 km to 500 km, and the densities are redistributed accordingly, conforming to Equations 3.38a-c. Examination of Figure 3.31b reveals an unavoidable feature of the column shift modification that is physically unreasonable but fortunately not too important. Because

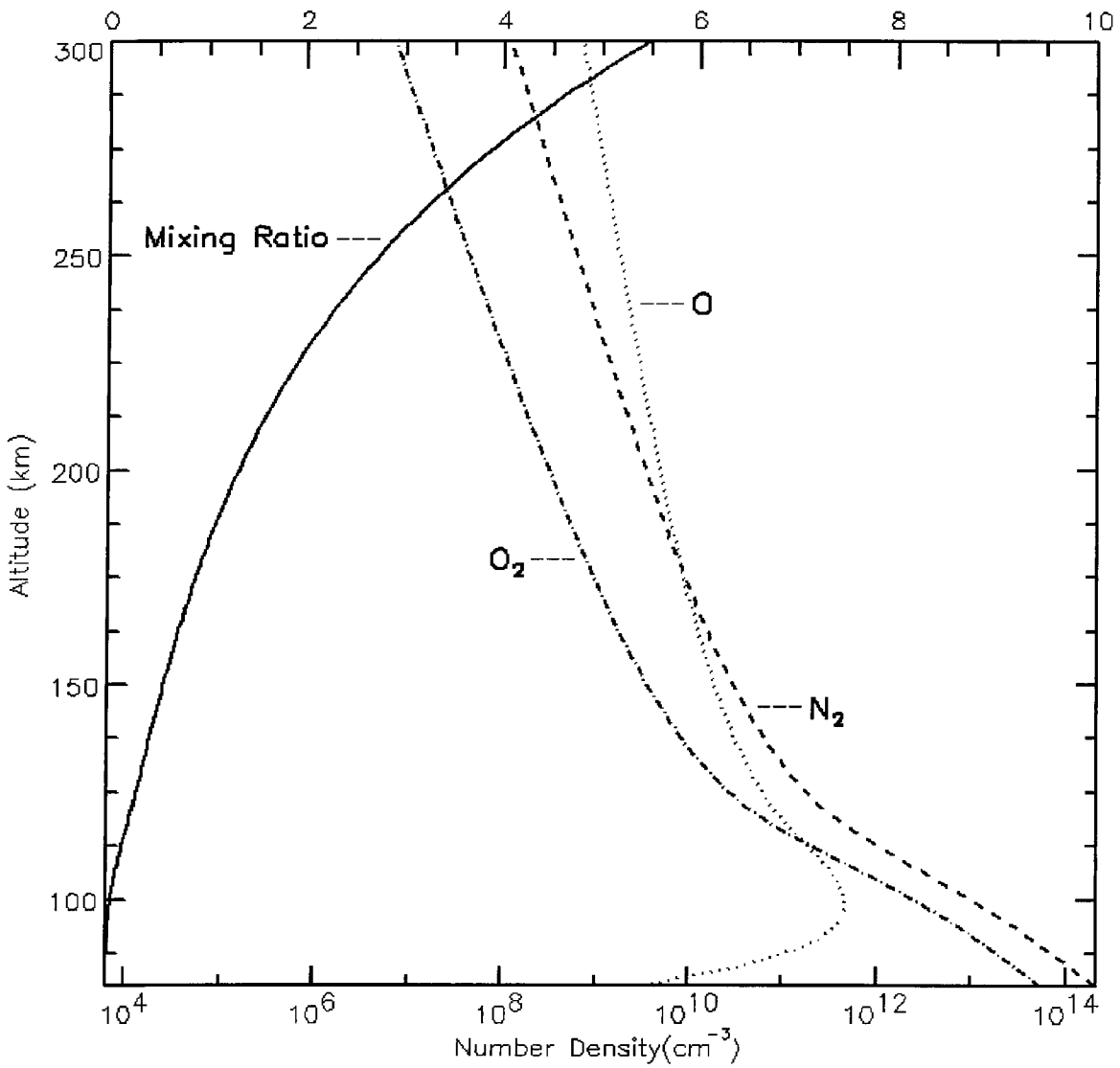

Figure 3.31. MSIS-90 model output of neutral density profiles for O, N_2, and O_2 at three column shifts. **(a)** Standard MSIS-90 model output of the neutral density profiles of O, N_2, and O_2 for zero column shift. The dashed line is the N_2 profile, the dash-dotted line is the O_2 profile, and the dotted line is the O profile. Also shown is the mixing ratio ξ = [O]/([N_2]+[O_2]) by the solid line. Conditions for the MSIS-90 model were A_P = 9 and $F_{10.7}$ cm flux = 164. The location is Inuvik, NT (68.3° N, 226.5° E), and the time is 1000 UT (0200 AM local time), which is magnetic midnight at Inuvik. The abscissa on the top of the graph gives the mixing ratio as a function of altitude. The MSIS-90 model output can be verified at the URL http://nssdc.gsfc.nasa.gov/space/model/models/msis.html.

the MSIS-90 model does not extend O density profiles below an altitude of 72.5 km, an upward shift of 50 km has the effect on the MSIS-90 model output of removing essentially

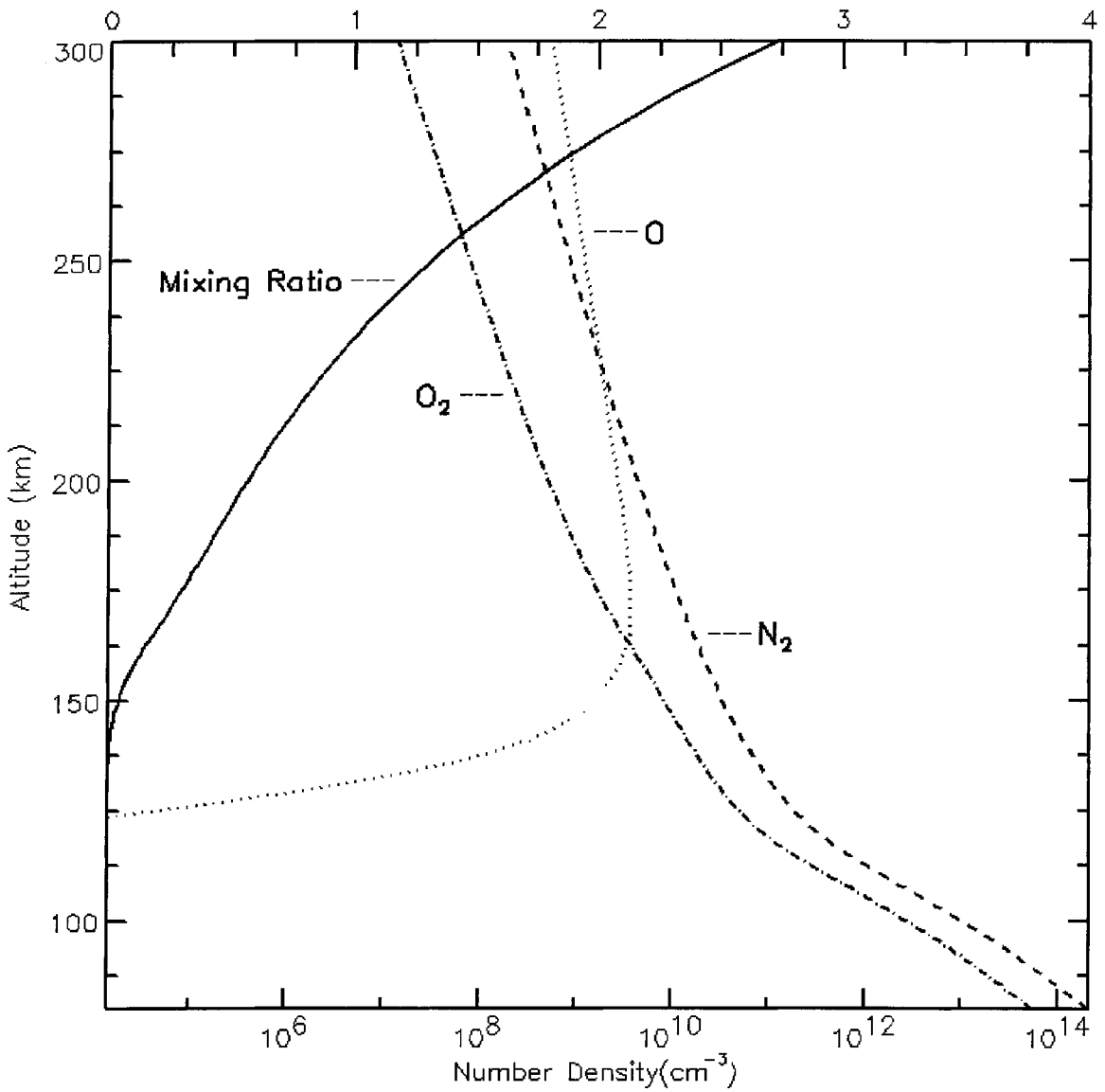

Figure 3.31 cont. MSIS-90 model output of neutral density profiles for O, N_2, and O_2 at three column shifts. **(b)** MSIS-90 model output with an upward column shift of 50 km. Same layout as (a). The upward shift has the overall effect of redistributing the neutral densities of O, N_2, and O_2. The effect is most pronounced in the O density profile. The O density below ~125 km is unphysical. See the text for discussion.

all of the atomic oxygen in the thermosphere below ~125 km, which is, of course, physically unrealistic. In reality, lower-thermospheric convergent horizontal winds will supply air with a mixing ratio indicative of that altitude into a given thermospheric column and maintain some level of atomic oxygen in the vicinity of the vertical wind field.

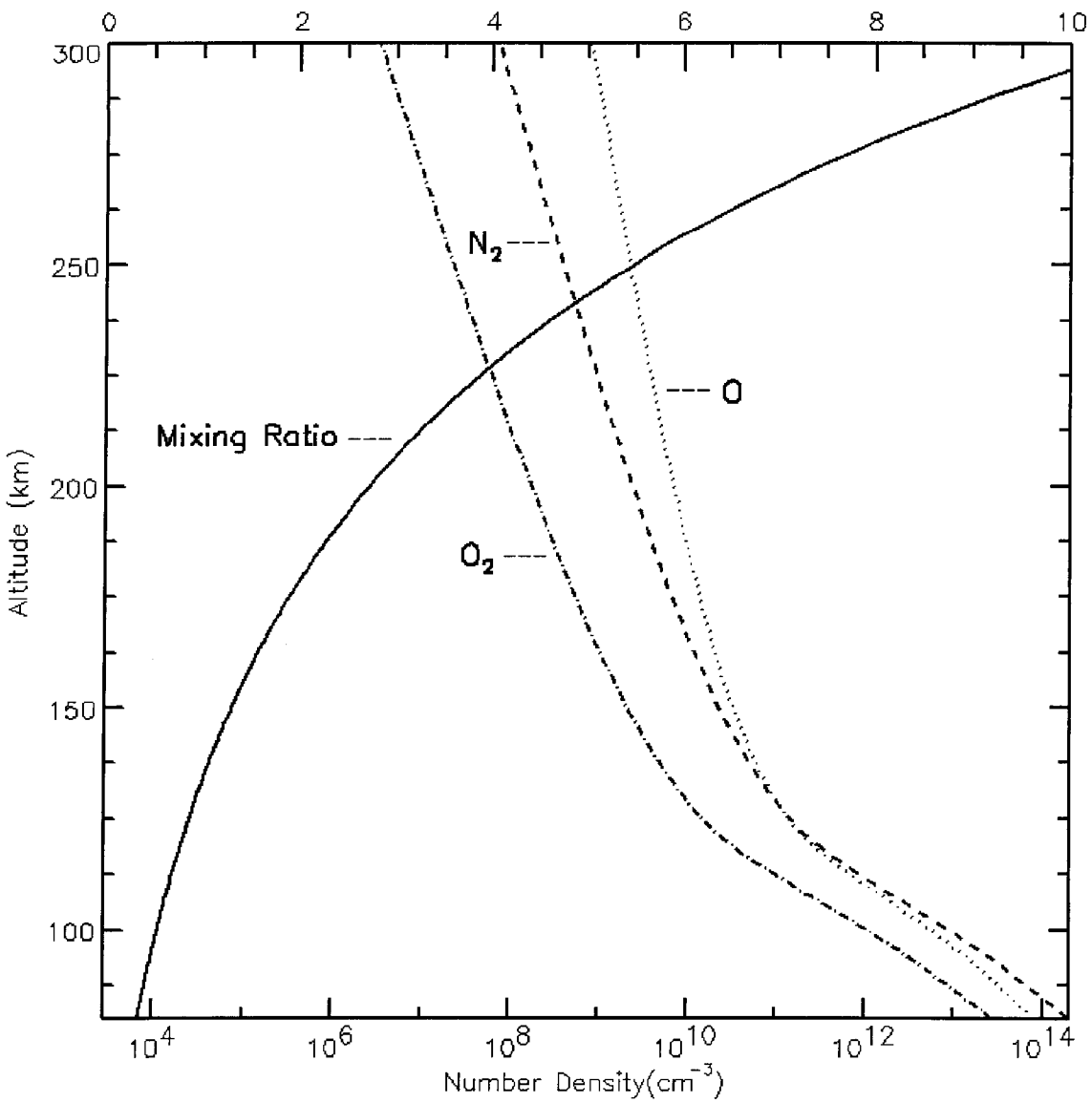

Figure 3.31 cont. MSIS-90 model output of neutral density profiles for O, N_2, and O_2 at three column shifts. **(c)** MSIS-90 model output with a downward column shift of 50 km. Same layout as **(a)** and **(b)**. The downward shift has the overall effect of redistributing the neutral densities of O, N_2, and O_2. The effect is most pronounced in the O density profile. The O density below ~100 km is unphysical. See the text for discussion.

However, as a model parameter, the upward shift still represents a disruption of diffusive equilibrium, and does encapsulate the overall effect of a long-lived, intermediate- to large-magnitude vertical wind. Atomic oxygen is depleted in a given thermospheric column at the auroral-emitting altitudes of ~125-300 km, and is replaced with N_2 and O_2 from lower

in the thermosphere. Certainly, auroral emissions from altitudes $\lesssim$125 km are relevant, particularly during moderate-to-high characteristic energy precipitation events ($\gtrsim$1-2 keV) [*e.g. Lummerzheim and Lilensten*, 1994], but what is more relevant to this study is that significantly less OI(135.6)-nm radiation will be observed by an instrument in orbit during these scenarios due to attenuation by O_2 above the peak emission altitude. As can be seen from Figures 3.31a-b, the O_2 number density at 125 km altitude is nearly twice as much for the ΔZ = 50 km case, $n_{O_2} = 4.5 \times 10^{10}$ cm^{-3}, as it is for the ΔZ = 0 km case, $n_{O_2} = 2.3 \times 10^{10}$ cm^{-3}, so OI(135.6)-nm aurora due to higher characteristic energy precipitation will be absorbed by O_2 that has been transported to higher altitudes by a vertical wind. For example, a particular model run of the *Lummerzheim and Lilensten* [1994] transport code predicts that for 4 keV precipitation, the OI(135.6)-nm column-integrated brightness is 0.1050 kR for the ΔZ = 0 km case (0.0678 kR at the spacecraft) and 0.0113 kR for the ΔZ = 50 km case (0.0111 kR at the spacecraft). For 0.2 keV precipitation, the transport code predicts that the OI(135.6)-nm column-integrated brightness is 0.6304 kR for the ΔZ = 0 km case (0.6271 kR at the spacecraft) and 0.3689 kR for the ΔZ = 50 km case (0.3669 kR at the spacecraft). Thus, an upward column shift reduces the column-integrated amount of O, replaces it with N_2 and O_2, and reduces the total column-integrated brightness of the OI(135.6)-nm emission, no matter the characteristic energy of the precipitation.

Figure 3.31c shows the effect of a downward column shift of 50 km, which also results in unrealistic values of O densities below about 100 km. However, the column shift analysis is not concerned with altitudes below ~100 km because the OI(135.6)-nm emission generally originates at altitudes above 100 km [*Lummerzheim and Lilensten*, 1994]. As was just discussed, high characteristic energy OI(135.6)-nm aurora emitted below 100 km will be absorbed by O_2. The redistribution of the O density at and above ~100 km due to the downward column shift of 50 km is likely realistic, in the sense that a large-magnitude downward wind will bring O from higher in the thermosphere down to auroral-emitting altitudes. Lastly, the overall effect of the column shifts on the N_2 density profile is negligible compared to the column shift effect on the O density profile, though it is the ratio of these two that is most important. The density of O relative to N_2

is what is meaningful, since these are the two most abundant thermospheric constituents between ~125 km and ~300 km competing for collisions with the precipitating electrons.

In order to infer column shift estimates from observed-to-modeled OI(135.6)-nm brightness comparisons, the transport code must provide auroral-brightness estimates for a number of column shifts, similarly to what was done in Figures 3.26a-b where the UVI-measured auroral brightness is determined as a function of characteristic energy at 1 $mW \cdot m^{-2}$ of energy flux. Generally, the transport code is run for nine characteristic energies in order to get the reference curves of Figures 3.26a-b. For the case of the column shifts, the transport code was run for nine different characteristic energies and for thirty-one different column shift cases. This produced a family of reference curves which was used to infer the column shift value for a given characteristic energy (determined from the LBH-S/LBH-L ratio) and a modeled OI(135.6)-nm emission brightness (dependent on the energy flux). Figure 3.32 shows this family of reference curves that determines the UVI instrument response at λ135.6 nm for nine different characteristic energies and thirty-one column shift values at 1 $mW \cdot m^{-2}$ of energy flux using the low-A_P model.

Two examples of 2-D maps of column shifts inferred from the observed-to-modeled OI(135.6)-nm brightness comparisons centered on Inuvik's location (the marked point on the plots at 71° magnetic latitude) are shown in Figures 3.33a-b. Figure 3.33a shows the inferred column shifts on January 3, 2001 at 1139 UT, derived from the comparison of the observed OI(135.6)-nm brightness shown in Figure 3.29a and its modeled counterpart in Figure 3.29b. Figure 3.33b shows the inferred column shifts on February 28, 2000 at 0552 UT from the comparison of the observed OI(135.6)-nm brightness in Figure 3.30a and its modeled brightness in Figure 3.30b.

Examination of Figures 3.33a-b reveals that structures are present in both of the examples, prompting speculation that the column shift maps are distinguishing the spatial morphology of thermospheric composition variations associated with auroral forms. The color scheme used here is synonymous with the Doppler shifting of an emission's wavelength which is due to motion of the emitting species; *i.e.*, for a red shift, the emitting species is moving away from a potential observer on the ground and for a blue shift, the

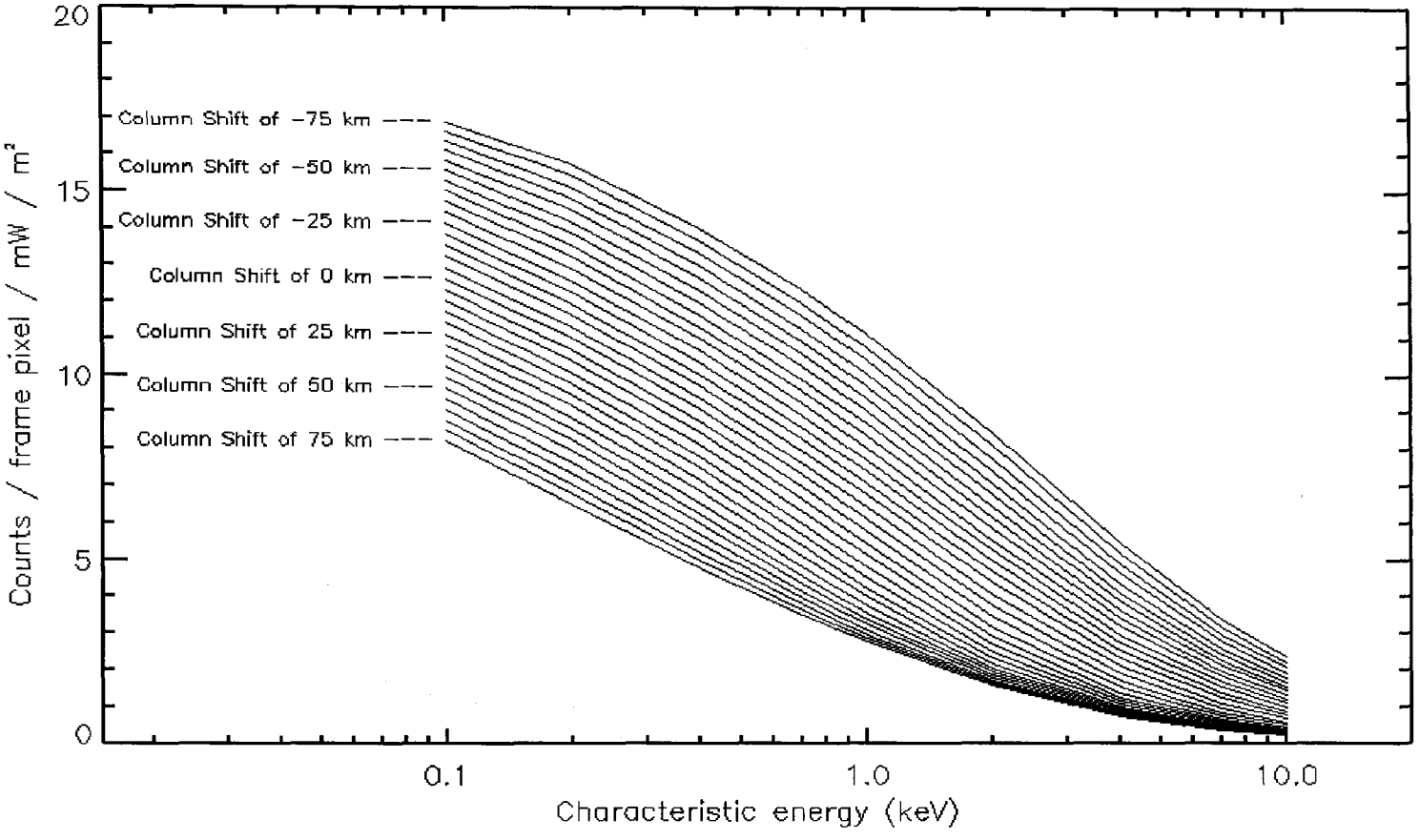

Figure 3.32 UVI instrument response at λ135.6 nm to 1 mW·m^{-2} of energy flux for nine different characteristic energies and thirty-one column shift values for the low-A_P model. The conditions, location, and time which produced the MSIS-90 model neutral thermosphere are the same as in Figure 3.31a-c. The curve for zero column shift here is the same curve as shown in Figure 3.26a describing the UVI instrument response at λ135.6 nm for the low-A_P model. The high-A_P model UVI reference curves exhibit similar behavior as a function of characteristic energy compared with the low-A_P reference curves here, but the range of the instrument response at 0.1 keV for the high-A_P is 6-11 counts·frame pixel for column shifts of +75 km to −75 km, respectively.

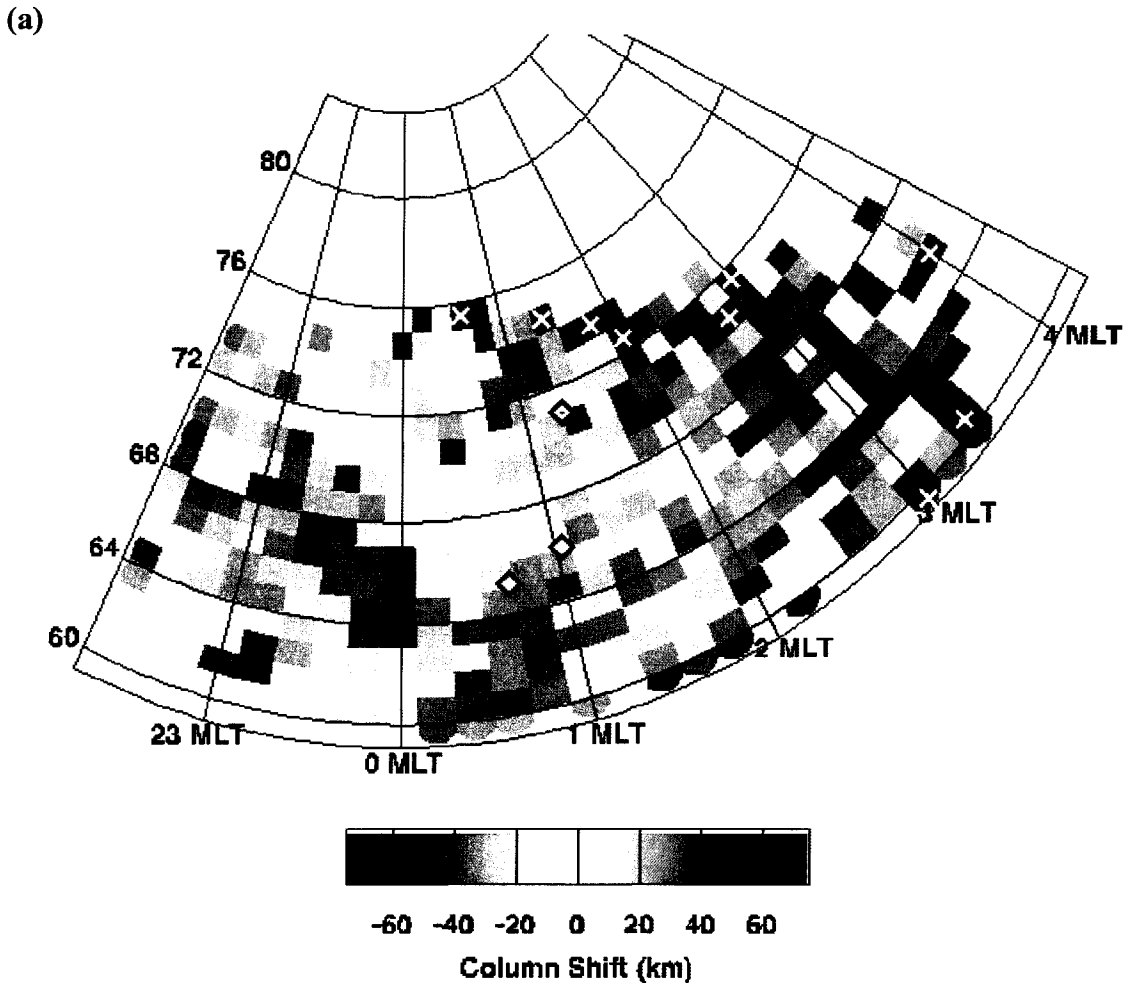

Figure 3.33. 2-D map of column shifts inferred from comparisons of the observed to the modeled OI(135.6)-nm auroral brightness. **(a)** UVI-inferred column shifts at 1139 UT on Jan 3, 2001. The color scheme used here is synonymous with the Doppler shifting of an emission's wavelength which is due to motion of the emitting species; *i.e.*, for a red shift, the emitting species is moving away from the observer, for a blue shift, the emitting species is moving toward the observer. The red color here represents upward column shifts, which would be indicative of upward winds, and the blue color represents downward column shifts. The red boxes with "*X*"s in them indicate upward column shifts which exceeded 75 km, and the blue boxes with *X*s indicate downward column shifts which are less than –75 km. See the text for discussion. As was stated earlier, the marked points on the plots are Inuvik, NT at 71° magnetic latitude, and Eagle and Poker Flat, AK, at 66.1° and 65.2°, respectively.

emitting species is moving toward the observer. The red color here represents upward column shifts, which would be indicative of upward winds, and the blue color represents

(b)

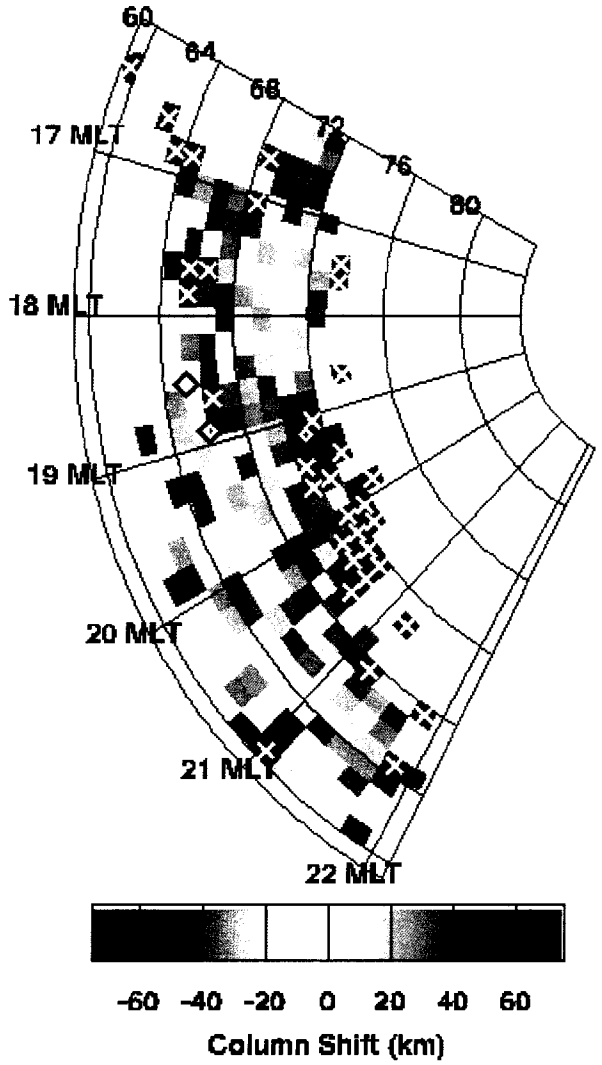

Figure 3.33 cont. 2-D map of column shifts inferred from comparisons of the observed to the modeled OI(135.6)-nm auroral brightness. **(b)** UVI-inferred column shifts at 0552 UT on Feb 28, 2000.

downward column shifts. The deeper the shade of red or blue, the larger the magnitude of the column shift. The "*X*"s located in some of the boxes represent values of the column shift which either exceed 75 km or are less then –75 km, representing invalid column shift estimates. While the height displacement of air parcels of ±75 km across two or three scale heights in an energetic vertical wind field extending from the lower to upper thermosphere is entirely plausible (based on previous studies [*e.g. Price et al.*, 1995] and

the discussions in Chapter 1), column shift estimates of greater than 75 km and less than –75 km are not valid here because they represent values that fall outside the range of the transport model runs; *i.e.*, these values were extrapolated and not interpolated. Nonetheless, column shift values that attain magnitudes of ~80 km are within reason.

As was stated earlier, auroral-model outputs are generally regarded as reliable by the aeronomy community since such auroral parameters as energy flux and characteristic energy derived from model-to-observation brightness comparisons fall within the ranges that are expected for aurora, even though their respective uncertainties are generally very large. Similarly, the absolute magnitude of the UVI-inferred column shifts under many circumstances falls within the range that would be expected of height displacements of air parcels due to vertical winds, of which Figure 3.33b is a good example. However, there also appears to be a constant negative offset to the column shift magnitudes in each data set, of which Figure 3.33a is an example, and in addition, many column shift values fall well outside of the expected range. As was discussed in Chapter 1, the column shift parameter, if representative of persistent intermediate- to large-magnitude vertical winds, can be expected to have a range of one to three scale heights in the lower through upper thermosphere, which is ~10-80 km at auroral-emission altitudes of ~120-300 km. When column shift variations are considered relative to some mean value in each data set, the majority of the column shift values for the data sets presented here do fall within the ±10-80 km range. The uncertainty in column shift magnitudes due to the auroral-model output uncertainties is described more below. The prevalence of the unreasonable column shifts in the data sets, the significance of the constant negative offset, and the determination of a sensible mean column shift value is discussed more below and in Chapter 4.

In many instances, the column shift maps function well as an indicator of composition variations associated with auroral forms, of which Figure 3.33b is a good example. For example, a band of red boxes extending from ~1700-2100 MLT and ~64°-72°, presumably due to a period of Joule and particle-precipitation heating and sustained upward winds, is clearly identified in the figure. Scattered among this swathe of red boxes are blue boxes, possibly associated with adjacent upward- and downward-moving air columns due to the

energetic forcing. The band of red boxes also agrees with previous studies that infer O density variations from comparisons of auroral-brightness ratios [*Hecht et al.*, 1989; 1999; 2000; *Lummerzheim et al.*, 1990], which in general have found that O is depleted in the vicinity of aurora. The blue boxes clustered together on the map edges may be attributed to downward flow that occurs far away from the heated region. Some of these blue boxes are *X*-ed out, however, indicating that the values may have been inferred in error.

The column shift parameter, apart from its interpretation as a height-displacement parameter due to vertical wind activity, can be regarded more generally as a parameter that, in matching the modeled OI(135.6)-nm brightness to the observed brightness, simply indicates the real thermosphere's composition relative to the model composition; *i.e.*, the column shift potentially represents how far off the MSIS-90 model is in its prediction of thermospheric O densities (if all other aspects of the model are assumed correct), whether the differences are due to vertical winds or to some other phenomenon. For example, if the modeled OI(135.6)-nm brightness is less than the observed brightness in a given box, one could infer that more O was present in that region of the real thermosphere compared to the model thermosphere. A downward column shift can account for a lack of O in the model theremosphere, which the column shift maps would then identify. This is clearly apparent in Figure 3.33a, the January 3, 2001 example, which exhibits some upward column shifts around ~0000 MLT from 68°-72°, but on average is blue column-shifted throughout the map. This tendency is indicative of the trend already discussed at the end of Chapter 1 observed in all the column shift data sets; that the modeled OI(135.6)-nm brightness on average is less than the observed OI(135.6)-nm brightness. The column shift maps identify this trend by showing more blue column shifts on average, which has the effect of bringing more atomic oxygen down to auroral-emission altitudes.

The tendency for this trend to show up in all of the column shift data sets is addressed more fully in the next chapter and initially hindered the interpretation of the column shift parameter. It was not until a statistical study was performed on the column shift data sets and vertical wind measurements (presented in Chapter 4) that some insight was acquired into the modeling difficulties encountered here, and a definitive link was

established between vertical winds and column shifts. Nonetheless, the preliminary results discussed here—that auroral structures prevailing in the UVI OI(135.6)-nm observations can be properly modeled on average, that a parameter which simulates vertical wind effects and corrects the model thermospheric O density by a physically-realistic mechanism can be used to perturb the model to match the modeled OI(135.6)-nm brightness to the observed brightness, that such 2-D column shift maps as Figure 3.33b function well as an indicator of composition perturbations associated with the aurora, and finally, that the majority of the column shift values fall within the ranges that would be expected of height displacements due to significant vertical wind activity—gives some confidence that this column shift technique offers genuine geophysical insight.

In order to definitively establish that column shifts prevailing in and around the sites of Inuvik, NT and Poker Flat, AK were due to significant vertical wind activity, the column shift values of the boxes around the sites were spatially averaged. Thus, a time series of column shift estimates over each site, averaged over a region comparable in size to a vertical wind field, was produced from successive column shift maps, which could then be compared to the vertical wind measurements of the Inuvik FPS and the narrow field-of-view CRL-FPS [*Ishii et al.*, 1997] at Poker Flat described earlier. In addition to the presentation of the column shift data in this time series format, the uncertainty in each box's column shift value was also estimated. If the column shift Z is given by

$$Z = f(O, M), \tag{3.33}$$

where O is the UVI-observed OI(135.6)-nm auroral brightness, M is the modeled brightness given by Equation 3.30, and f is some function of O and M, then the uncertainty δZ in the column shift estimate is given by

$$\delta Z = \left[\left(\frac{\partial f}{\partial O} \delta O \right)^2 + \left(\frac{\partial f}{\partial M} \delta M \right)^2 \right]^{1/2}, \tag{3.34}$$

where δO is the statisical uncertainty in the observed OI(135.6)-nm brightness, and δM is given by Equation 3.31. As was stated earlier, the statistical uncertainty percentage $\delta O/O$ in the UVI brightness estimates is $\delta O/O = \delta L/L = \delta S/S \approx 0.05\text{-}0.25$. The derivative of f with respect to O and with respect to M is approximately given by

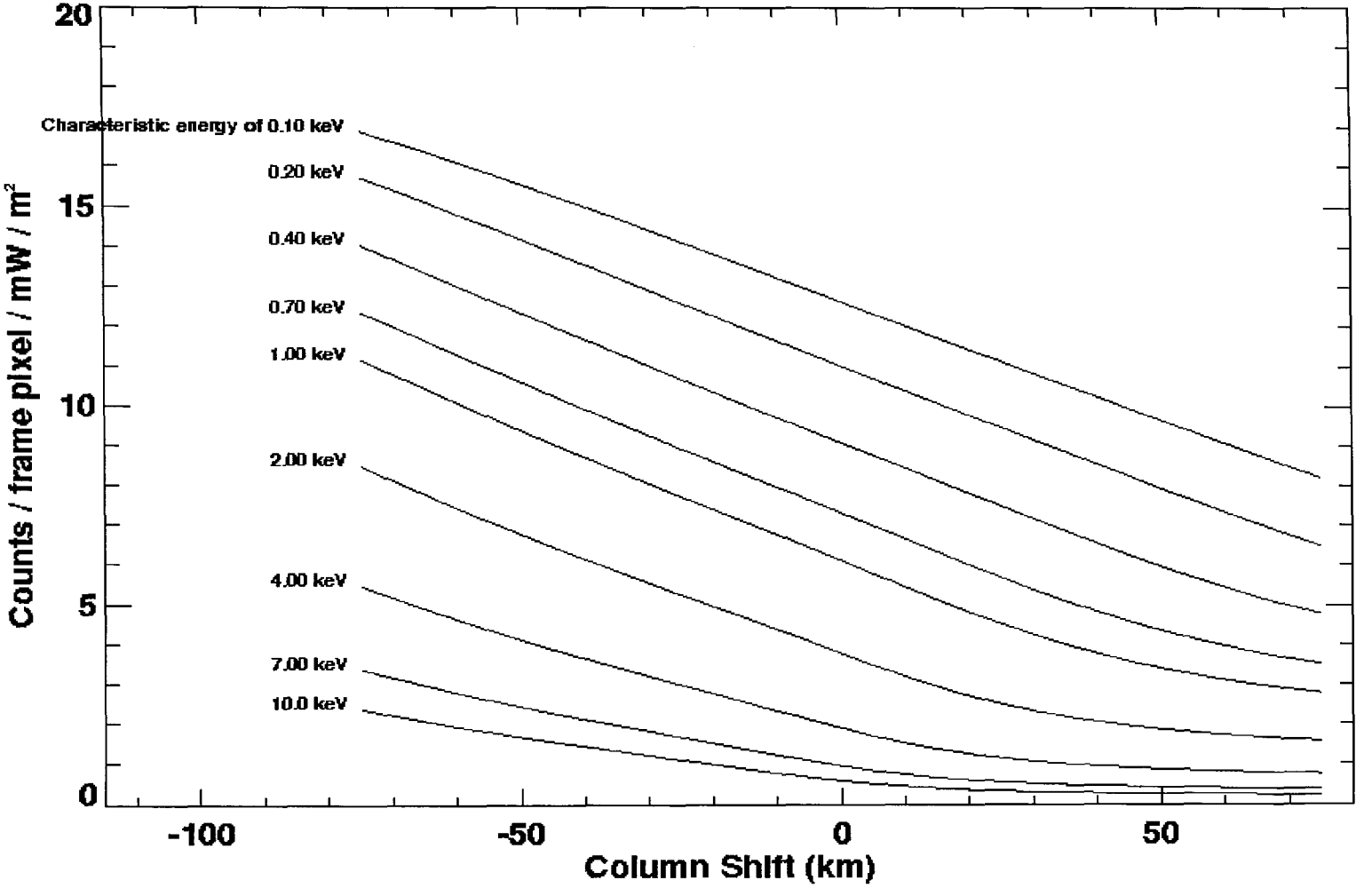

Figure 3.34 UVI instrument response at λ135.6 nm to 1 $mW \cdot m^{-2}$ of energy flux as a function of column shift for nine characteristics energies. The transport model run used the low-A_P MSIS-90 model thermosphere to produce these reference curves. The information presented here is essentially the same information in Figure 3.32.

$$\frac{\partial f}{\partial O} = \frac{f(O,M) - f(O+\Delta O,M)}{\Delta O}, \frac{\partial f}{\partial M} = \frac{f(O,M) - f(O,M+\Delta M)}{\Delta M}, \quad (3.35a\text{-}b)$$

respectively, and is estimated from the references curves that describe the UVI instrument response at λ135.6 nm for 1 mW·m^{-2} of energy flux as a function of column shift. The reference curves for the low-A_P model run are shown in Figure 3.34, and basically present the same information as Figure 3.32. Furthermore, because column shifts are inferred from comparisons of UVI OI(135.6)-nm brightness observations to model predictions of those UVI observations, essentially $\partial f/\partial O = \partial f/\partial M$, which is measured in km·counts^{-1}.

In order to determine the uncertainty in the column shift value of each box on the 2-D maps, it is necessary to determine $\partial f/\partial M$ for that box. First, an OI(135.6)-nm reference curve corresponding to the prevailing characteristic energy of each box is inferred from the modeled reference curves of Figure 3.34 by interpolation. This new reference curve is then scaled by the energy flux prevailing in that box. Finally, $\partial f/\partial M$ is estimated by computing an average slope of this inferred reference curve. As can be seen from Figure 3.34, this average slope is close to the actual value of the reference curve's $\partial f/\partial M$ for characteristic energies of $\lesssim$1 keV. For characteristic energies $\gtrsim$1 keV, the approximation of $\partial f/\partial M$ by this average slope is more uncertain. However, given the large error in the modeled OI(135.6)-nm brightness ($\delta M/M$ = 38-58%) determined from Equation 3.32, $\partial f/\partial M$ is less of a concern. Finally, using Equation 3.32, the uncertainty δZ in the column shift estimates is

$$\delta Z = \left(\frac{\partial f}{\partial M}\right)\left\{\delta O^2 + M^2\left[\left(\frac{\delta c_1}{c_1}\right)^2 + \left(\frac{\delta c_2}{c_2}\right)^2 + \left(\frac{\delta c_3}{c_3}\right)^2 + 2\left(\frac{\delta L}{L}\right)^2 + \left(\frac{\delta S}{S}\right)^2\right]\right\}^{1/2}, \quad (3.36)$$

recalling that $\delta c_2/c_2 = \delta c_1/c_1 = 0.2$, $\delta c_3/c_3 = 0.25$, $\delta S/S = \delta L/L \approx 0.5\text{-}0.25$, M is the modeled OI(135.6)-nm brightness, and δO is the statistical uncertainty in the UVI-observed OI(135.6)-nm brightness. In general, the uncertainty in column shift values determined from Equation 3.36 is $\delta Z = \pm$20-90 km, with a few outlying column shifts that have errors reaching ±130 km. This range is obviously very large, but is not unexpected based on the previous discussions of the uncertainty in other auroral-model outputs. The error in each respective column shift value is in general reduced compared to the $\delta Z = \pm$20-90 km range

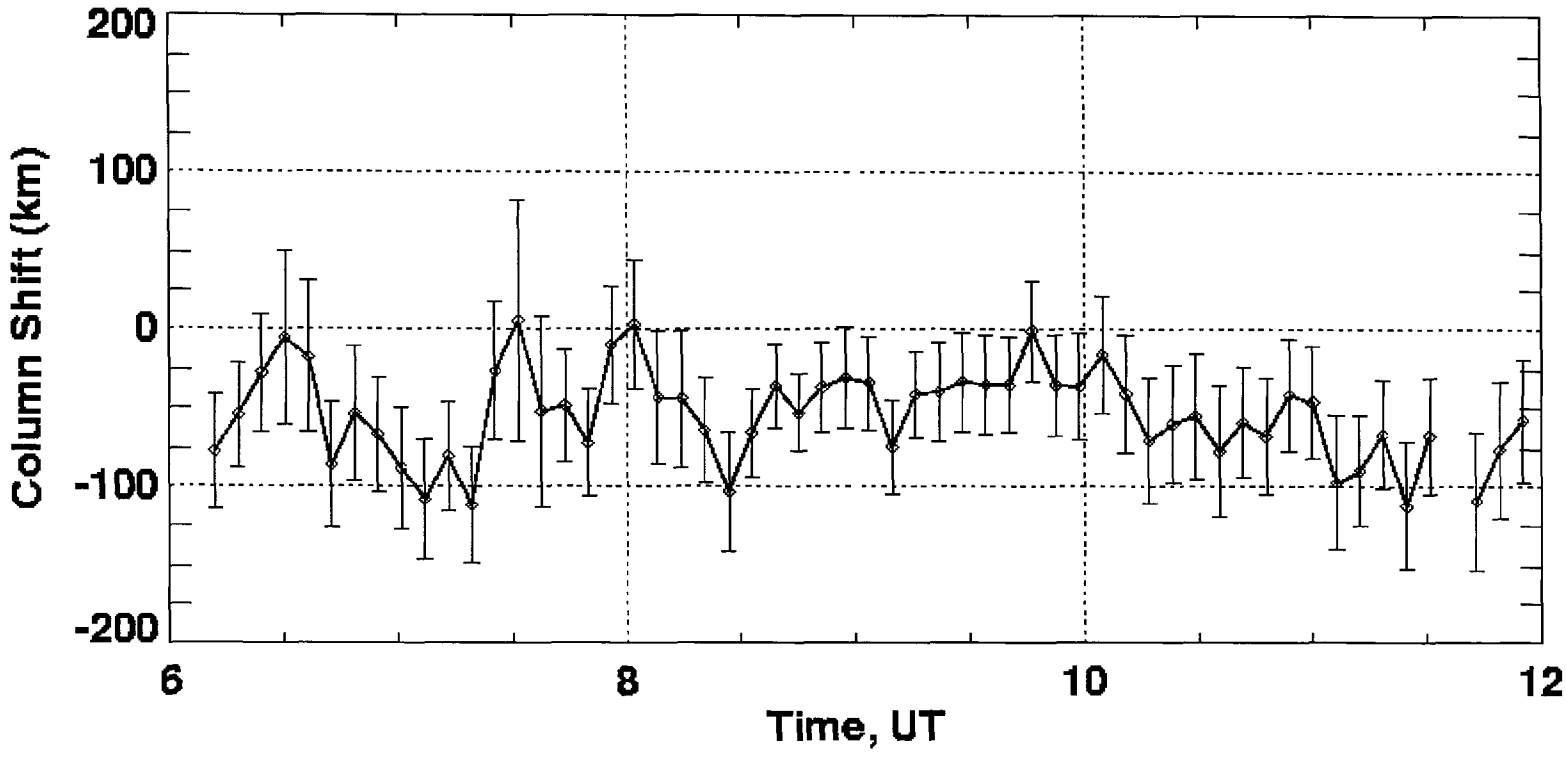

Figure 3.35 UVI-inferred column shift estimates over Inuvik, NT on Dec 22, 2000. The column shift values measured over Inuvik are averaged over an area centered on Inuvik of 3° latitude × 9° longitude, which is ~340 km × ~370 km = 1.26×10^5 km^2, the equivalent of nine boxes. This is generally considered the largest extent that a vertical wind field will have. The criterion used here to retain column shift data was the LBH-L brightness threshold of 9.3 counts·box^{-1}. The uncertainty in the column shift estimates is ±27-77 km. See the text for more discussion. The geophysical significance of these column shift estimates is discussed more fully in Chapter 4 with the concurrent presentation of the vertical wind measurements.

when a more stringent criterion is applied to the UVI auroral data to retain. This criterion is discussed more later and in Chapter 4.

Three examples of time series of column shift estimates over Inuvik with their respective uncertainties are shown here. These examples were chosen for presentation here because of the robust quality of the column shift data set, illustrating what was initially believed to be "good" data; *i.e.*, data sets which would hopefully yield insightful interpretations of the column shift parameter. Figure 3.35 above shows the time series of column shift values from December 22, 2000, Figure 3.36 shows the December 9, 2000 data set, and Figure 3.37 shows the January 3, 2001 data set. The column shift values shown here are averaged over an area centered on Inuvik's location of 3° latitude × 9° longitude, which is ~340 km × ~370 km = 1.26×10^5 km^2, the equivalent of nine boxes from the 2-D maps. This is generally considered the largest extent that a vertical wind field will have [*Smith*, 1998]. Rather than use the LBH-L brightness threshold of 15 counts·box^{-1} which was used in the presentation of Figures 3.27-3.30 and Figure 3.33, the criterion used here to retain column shift data was the LBH-L brightness threshold of 9.3 counts·box^{-1} discussed in Section 3.2.2. The reason for this was to illustrate the more significant problems with the column shift data sets, which the 15 counts·box^{-1} criterion would exclude. The presentation here leads into the Chapter 4 presentations.

In general, these column shift time series illustrate the unanticipated and perplexing difficulties that were initially encountered in the process of accumulating these data sets, such as the January 3, 2001 column shift values of –100-200 km from ~0900-1100 UT. These highly-negative column shift values were inferred during periods of what is considered weak and uncertain aurora (based on analysis presented in Chapter 4) when the LBH-L brightness was close to 9.3 counts·box^{-1}. As was stated earlier, these column shift values fall well out of the range of the *Lummerzheim and Lilensten* [1994] transport model outputs that run from –75 km to 75 km. No rational explanation was forthcoming of these highly-negative column shift values, and no physical mechanism exists in the thermosphere that could readily explain their appearance in the data sets. Furthermore, the one thing that is clearly evident from these time series is the systematic trend for each

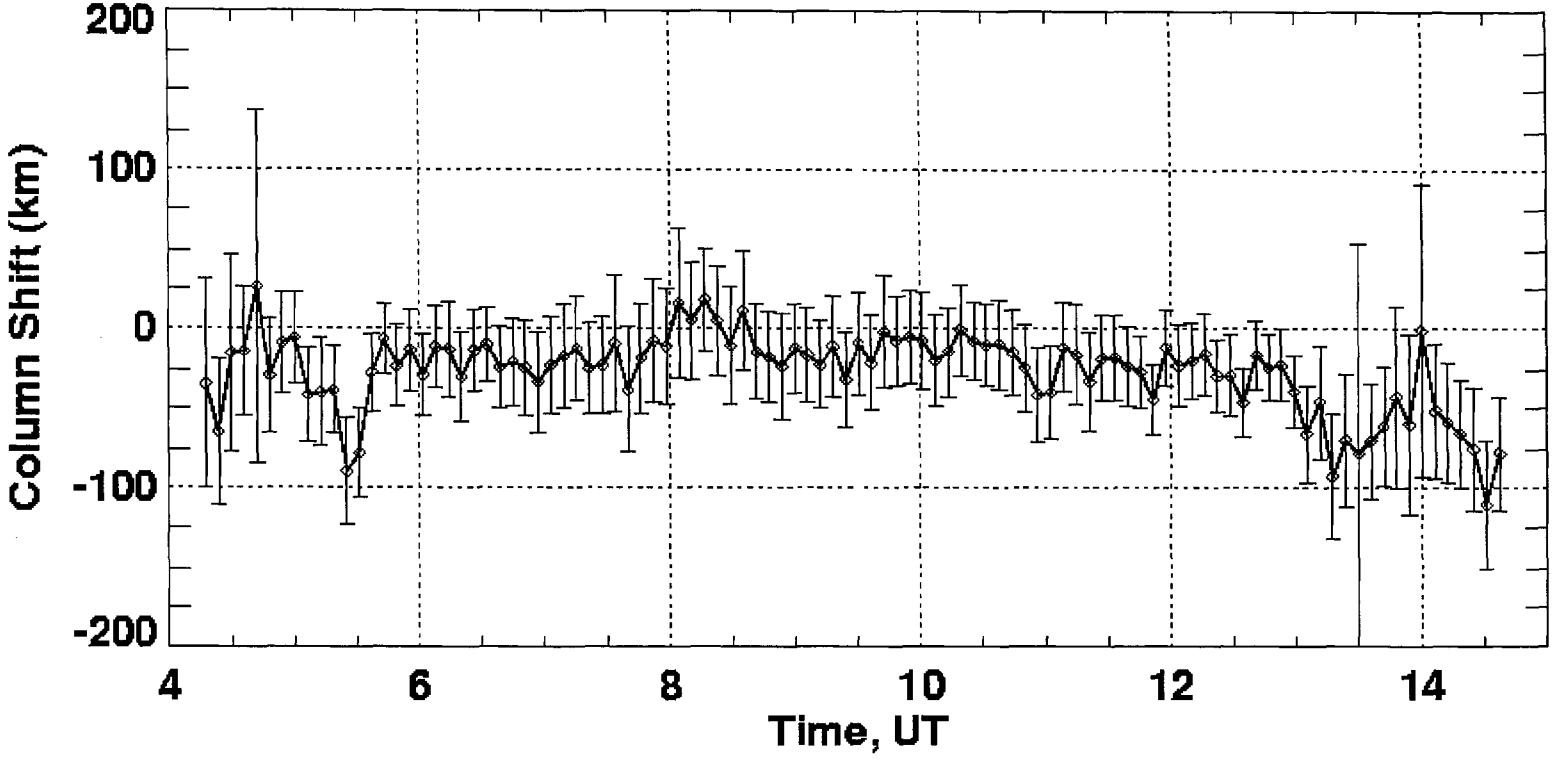

Figure 3.36 UVI-inferred column shift estimates over Inuvik on Dec 09, 2000. The relative variation in the column shifts from one measurement to the next was fairly small for much of this night. See the text for more discussion of this topic. The uncertainty in the column shift estimates is ±21-132 km. See the text for more discussion. The geophysical significance of these column shift estimates is discussed more fully in Chapter 4 with the concurrent presentation of the vertical wind measurements.

column shift time series to exhibit, on average, a negative value, indicating as previously discussed that the modeled OI(135.6)-nm auroral brightness is less than, on average, the UVI-observed OI(135.6)-nm brightness. The relative variation of the column shift values for each data set generally appears to be about some mean value that is less than zero.

This systematic trend towards downward column shifts runs contrary to the previous studies of *Hecht et al.* [1989; 1999; 2000] and *Lummerzheim et al.* [1990] which found that O is depleted in the vicinity of aurora, not enhanced as the data sets here would require if MSIS-90 thermospheric O densities are inaccurate. Nonetheless, the systematic underestimation of the modeled OI(135.6)-nm brightness that is seen here has been independently confirmed using the transport code of *Lummerzheim and Lilensten* [1994; *Lummerzheim*, 2004, private communication]. Initially, it was presumed that this average negative value of each column shift data set was in some way characterizing the deficiency in the modeling process of the OI(135.6)-nm auroral brightness; that, for example, the MSIS-90 model grossly underestimates the O density—which seems unlikely if the previous studies of *Hecht et al.* [1989; 1999; 2000] and *Lummerzheim et al.* [1990] are correct—or that energy flux or characteristic energy estimates inferred from FUV auroral emissions in conjunction with transport model outputs are inaccurate.

These other serious concerns aside, the relative variation in the time series from one measurement to the next about some mean column shift value is entirely plausible, and the variations often fall within the range that would be expected of air parcel height displacements due to intermediate- to large-magnitude vertical wind events. For example, the relative variation in the December 9 and 22, 2000 column shifts is generally in the ~10-50 km range (with some notable exceptions) and is also very often ~0 km, which would be expected under many circumstances. If there is little significant vertical wind activity for extended periods of time in a particular region, then one may expect that air parcel height displacements will be ~0 km and that thermospheric composition would remain fairly uniform in the region during that period. Thus, a composition-perturbation sampling of this region like the column shift parameter would exhibit little relative variation. This is evident for example in the December 22, 2000 column shift data in the

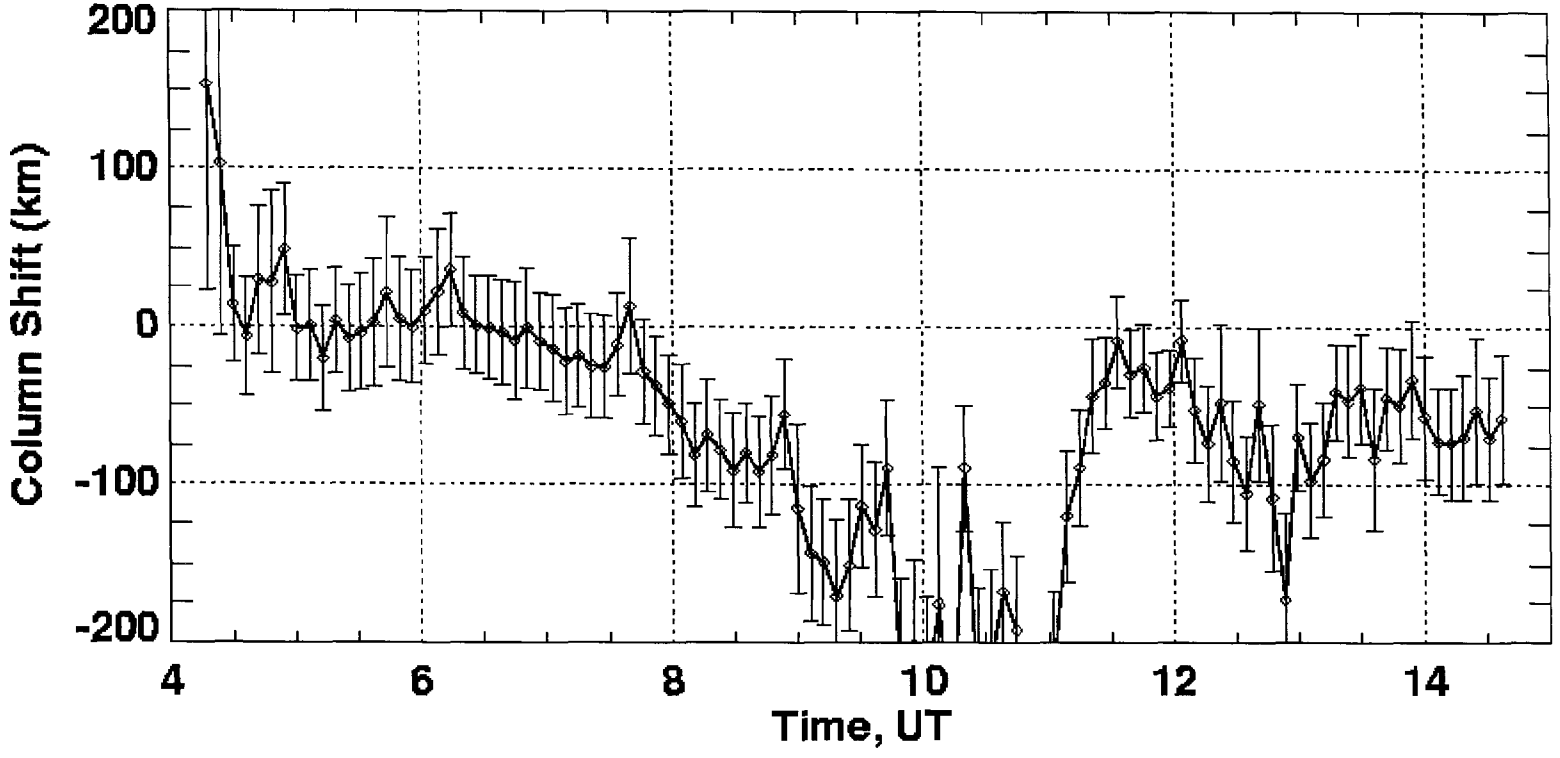

Figure 3.37 UVI-inferred column shift estimates over Inuvik on Jan 03, 2001. The relative variation in the column shift values from one measurement to the next is more significant during several time periods on this night than in the previous examples from Dec 09 and 22, 2000. See the text for more discussion of this topic. The uncertainty in the column shift estimates is ±24-87 km, except for the first two column shifts where the error was ±131 km and ±109 km, respectively. See the text for more discussion. The very large magnitude negative column shifts measured between 0900 and 1100 UT were inferred during periods of weak aurora when the LBH-L brightness was close to 9.3 counts·box^{-1}. The geophysical significance of these column shift estimates is discussed more fully in Chapter 4 with the concurrent presentation of the vertical wind measurements.

time period around 0930 UT. The relative variation in column shifts on this night appears to be about a mean value of about –40-50 km. Examination of the vertical wind data from Inuvik on this night in Figure 3.13 on page 130 shows that there was negligible vertical wind activity during the 0915-0945 UT time period. Wind speeds varied randomly between –20 and +10 $m \cdot s^{-1}$. If the relative state of the thermosphere's composition at auroral-emitting altitudes at ~0930 UT is characterized by the effect that a –40 km column shift has on thermospheric composition (*e.g.*, see Figure 3.31c), then the state of the thermosphere's composition would be expected to remain approximately the same if there is no significant vertical wind activity prevailing around these times.

An example of an intermediate-magnitude vertical wind effect is also evident in the January 3, 2001 column shift time series. From 0555-0615 UT, there is a relative increase in the column shift values of 0 km to +36 km. Examination of the vertical wind data from Inuvik on this night (Figure 3.9 on page 122) shows that an intermediate-magnitude vertical wind event lasting from 0540-0555 UT reaching wind speeds of ~30 $m \cdot s^{-1}$ precedes the increase in the column shifts. A 15 min, 30 $m \cdot s^{-1}$ vertical wind will result in an air parcel height displacement of 27 km, which is confirmed by the column shift values within the range of the wind and column shift uncertainties. This example is investigated in greater detail in Chapter 4, along with other similar examples.

Admittedly, there are many periods in these column shift time series where the variation cannot be attributed to vertical winds, and there are periods in the vertical wind wind time series where a significant wind event occurs but no corresponding height displacement is identified in the column shift data. This would be expected when comparing data from two semi-random phenomena. There will be random periods of correlation, anti-correlation, and no correlation. Furthermore, other thermospheric processes can produce variations in the column shift data similarly to vertical winds or mask vertical wind-induced effects so that the height displacement effect is not identified in the column shift data. However, when correlations do occur like here in the January 3, 2001 example and the vertical wind-computed height displacement matches the relative

variation in the column shift data within the range of uncertainties, some degree of credibility seems warranted.

The overall geophysical significance of these column shift estimates is explored further in Chapter 4 with the concurrent presentation of the vertical wind measurements from Inuvik and Poker Flat and the statistical analysis of the column shift and vertical wind data sets. The Chapter 4 presentation of these time series does not include the error bars of the respective vertical wind measurements or column shift values as it would further clutter an already elaborate display of data, though the uncertainties are quoted in the text. This is why some examples of the time series of column shift values are shown here, and the seven examples of the Inuvik vertical wind data were shown in Section 3.1.4, so as to illustrate the respective uncertainties in the vertical wind and column shift estimates. The Chapter 4 presentations do however further address the difficulties that were encountered in the interpretation of the column shift data sets, and the methods that were used to attempt to understand the column shift parameter and present the column shift data sets in a suitable format. Several examples similar to the January 3, 2001 example discussed above are presented in Chapter 4, and cross correlation analysis of is performed. Except for one time series comparison which exhibits a high correlation, the cross correlation analysis prove to be a mostly unsuccessful endeavor. Therefore, statistical analysis of the column shift data sets and the vertical wind measurements is also explored, which ultimately provides the most insight into the column shift parameter.

Chapter 4 Analysis and Discussion of Observations and Results

4.1 Comparison of the Time Series of Vertical Wind Measurements to Column Shift Estimates

At the end of Chapter 3, two-dimensional maps of UVI-inferred column shifts were presented at specific times from the January 3, 2001 and February 28, 2000 data sets. In addition, three time series of spatially-averaged column shift values over Inuvik from the nights of December 22, 2000, December 9, 2000 and January 3, 2001 were also presented with their respective uncertainties. The difficulties encountered with the column shift data sets as discussed at the end of Chapter 3 initially hindered the column shift parameter's interpretation, and some criterion was sought that would establish whether or not a given column shift was in fact representative of a vertical wind's effects and facilitate the comparison of the time series of column shift values to the vertical wind measurements from Inuvik and Poker Flat. Initial comparisons such as the example presented at the end of Chapter 3 of the January 3, 2001, 0540-0615 UT vertical winds and column shifts give confidence that column shift variations can at times be attributed to vertical wind activity.

The presentation of seven nights of column shift time series over Inuvik is extended here with the concurrent presentation of the Inuvik FPS upper-thermospheric vertical winds measurements. The technique employed to further facilitate these comparisons is described and discussed. One night of vertical wind data obtained at Poker Flat with the CRL-FPS (discussed in Chapter 3) provided the opportunity to compare a time series of column shift estimates with vertical wind measurements at a different auroral-zone latitude and in addition, in two different altitude ranges. General correlations between the vertical wind and column shift time series are also discussed, and cross correlation coefficients are computed at different time lags. Several case study examples of intermediate-magnitude vertical wind-induced composition perturbations similar to the January 3, 2001 example are discussed. In addition, the one time series comparison which exhibits a high correlation coefficient is further examined. Both time series exhibit

significant wavelike structure, and spectral analysis using the Lomb-Scargle normalized periodogram method identifies a strong periodicity at $\tau \approx 3$ hr in both time series.

Before the presentation of the aforementioned data sets, an important caveat concerning column shift estimates and the UVI viewing geometry must be addressed. As was already discussed in Chapter 2, an auroral model's interpretation of column-integrated auroral brightness measurements and estimations of energy flux and characteristic energy assumes that the brightness measurements are being made while an imager is nadir viewing; *i.e.*, the electron transport code is one-dimensional. Auroral models in general compute altitude profiles of ionization, energy deposition, and volume emission rates along only one column of thermosphere and assume that the precipitating electrons stream into the thermosphere parallel to the column. When an imager views the aurora from off-nadir angles, it may be observing two or more columns of thermospheric air parcels, some which may be radiatively excited, others which are not. Thus, such scenarios as resonance scattering of radiation into the imager's field of view can result in overestimations of measured auroral brightnesses, as may be the case for the OI(135.6)-nm emission, or extinction of radiation emanating from a radiatively-excited column of thermosphere by an unexcited column, leading to, for example, underestimations of energy flux inferred from LBH-L emission brightnesses.

Referring again to Figure 2.5 on page 74, the POLAR spacecraft's ~9 R_E apogee location relative to Earth was ~30-45° geomagnetic latitude during the years of 1999 to 2001. The UVI view of the northern-hemispheric polar-latitude region was from the side during POLAR's initial journey towards apogee, and thus, the imager would be viewing the auroral oval from the side. Not until POLAR's journey towards perigee did the imager's view of the northern hemispheric high-latitude region become nearly nadir-viewing. For the sake of the results and discussion presented here, reasonably "good" UVI-viewing of the aurora is considered to be from ~45° to nadir, and greater than 45° is "bad." Admittedly, this is a very generous definition of what should be considered good viewing geometry, but as will shown here later, column shifts estimates from bad viewing angles in general have the same characteristics as column shifts from good

viewing angles. Table 4.1 shows the time periods covered by the data sets presented here and whether the UVI was viewing from good or bad look-angles during these times. The UVI-inferred column shifts that were measured at the bad look-angles may be regarded with skepticism because of an auroral model's dependence on an imager's viewing geometry. Nonetheless, a simple interpretation of these off-zenith column shift values is presented in Section 4.2 based on analysis presented there.

Table 4.1. UVI-viewing geometry. Dates of the data sets are given, and the times when "bad" viewing, 90°-45°, and good viewing, 45°- nadir, are given. See the text for more discussion.

Date	Bad viewing times (UT)	Good viewing times (UT)
Jan 3, 2001	0400 – 0915	0915 – 1445
Dec 9, 2000	0400 – 0915	0915 – 1430
Feb 28, 2000	0200 – 0900	0900 – 1300
Dec 22, 2000	0600 – 0915	0915 – 1200
Jan 4, 2001	N/A	0500 – 0900
Jan 26, 2001	N/A	0500 – 0915
Nov 28, 2000	N/A	0330 – 0630
Mar 20, 2001	0430 – 0830	N/A

As was discussed at the end of Chapter 3, there was no explanation as to why each column shift data set exhibited a mean value of <0 km, or why many column shifts were unrealistically negative like the –100-200 km values from 0900-1100 UT in the January 3, 2001 time series shown in Figure 3.37. As was also discussed, however, many of the column shifts did fall within a range that was expected of air parcel height displacements due to vertical wind activity, and in addition, the relative variation in the point-to-point column shift values was often plausible. In addition, broad-scale auroral structures in the modeled OI(135.6)-nm brightness appeared to match (with anticipated discrepancies) the same auroral structures in the observed LBH-L, LBH-S, and OI(135.6)-nm maps, even though the modeled OI(135.6)-nm brightness on average was less than the UVI-observed OI(135.6)-nm brightness. Thus, it was presumed that the OI(135.6)-nm modeling process

was working to some degree and that the column shift parameter may still prove to be a useful tool for investigating vertical wind effects if criteria could be found that excluded suspect column shift estimates and/or explained the modeling deficiencies.

Initially, in comparing the time series of column shifts and vertical winds, it was determined that even though absolute column shift values could not be established, the variation in the column shifts relative to some mean value of the entire data set or relative to the column shift values prior to a vertical wind event's onset may still reveal vertical wind effects, such as in the January 3, 2001, 0540-0615 UT example discussed in Chapter 3. Thus, it was decided that averaging the column shift values to a zero-reference level—similarly to how Doppler shifts of OI(630.0)-nm zenith observations are averaged to zero to determine a zero-velocity reference—may distinguish the relative variation in the column shifts more clearly, particularly in such 2-D maps as the January 3, 2001, 1139 UT example in Figure 3.33a where the relative variation in the column shifts would now be centered about ~0 km (white color) on the blue-to-red color scale. The 2-D column shift map in Figure 3.33b from the February 28, 2000 data set at 0552 UT is an example where averaging of the map was deemed to not be necessary since the spatial morphology of the thermospheric composition perturbations associated with the aurora was already apparent in the map, with most of the column shift values falling into the expected range of ±10-80 km. Obviously, it was not yet clear why some column shift maps were like the February 28, 2000, 0552 UT example and some like the January 3, 2001, 1139 UT example.

Table 4.2 shows the mean and median values, $\bar{Z}$ and Z_{med}, respectively, and the standard deviation SD_{clm} of each night's column shift data set. All the column shift values from each 2-D map over each night's set of observations were compiled into one array of values, and the median and mean values and standard deviation of this array were computed. Table 4.2 also shows the total number of column shift estimates compiled from each night of observations. As was the case at the end of Chapter 3 in the presentation of the column shift time series, the criterion here to retain UVI auroral data was to use the 9.3 counts·box^{-1} LBH-L brightness threshold. It was also decided that averaging the column shift values to a zero-reference level using the median value of each

Table 4.2. Mean and median values and standard deviation of each column shift data set. The criterion used here to retain UVI auroral data and column shift values is the 9.3 counts·box^{-1} LBH-L brightness threshold. The large difference between the mean value $\overline{Z}$ and the median value Z_{med} is due to the significant number of unrealistically-negative column shift values that are part of each data set, which bias the mean value. The standard deviation SD_{clm} is also unrealistically large. See the text for more discussion.

Date	Total # of column shifts	$\overline{Z}$ (km)	Z_{med} (km)	SD_{clm} (km)
Jan 3, 2001	37468	–68.7	–32.7	185.9
Dec 9, 2000	42540	–50.2	–27.4	105.7
Feb 28, 2000	34005	–153.5	–79.5	283.0
Dec 22, 2000	14000	–80.9	–38.7	172.2
Jan 4, 2001	10954	–63.2	–23.2	190.9
Jan 26, 2001	13224	–49.5	–15.3	131.8
Nov 28, 2000	4969	–123.2	–69.8	234.2
Mar 20, 2001	11249	–204.6	–68.8	828.4

night's column shift data set was the appropriate method to apply. Because many of the column shifts of each data set were unrealistically negative (much less than –100 km), particularly in the March 20, 2001, February 28, 2000, and November 28, 2000 data sets, the mean and standard deviation of each data set was biased by these values, as Table 4.2 indicates. Thus, the median correction method was used. The January 3 and 4, 2001 and December 22, 2000 data sets also exhibited many unrealistically-negative column shifts, and the March 20, 2001 data set, based on its statistics, appeared severely flawed.

Figures 4.1a-b illustrate the effect of the median correction on a column shift map. The example shown here is from the January 3, 2001 column shift data set at 1139 UT. This example is also shown in Figure 3.33a on page 184, but Figures 4.1a-b use the 9.3 counts·box^{-1} LBH-L brightness threshold as the criterion to retain column shift data rather than the 15 counts·box^{-1} LBH-L brightness threshold used in the Chapter 3 examples. As is seen in Figures 4.1a-b, the range of the color bar is –100 km to +100 km, rather than the –75 km to +75 km range used in the Chapter 3 examples. The reason for this was because when the column shift data sets were first being produced, many of the unrealistically-negative column shifts of less than –100 km were present in the data sets. Since it was not clear why column shift values were falling into this range, it was decided that a larger range

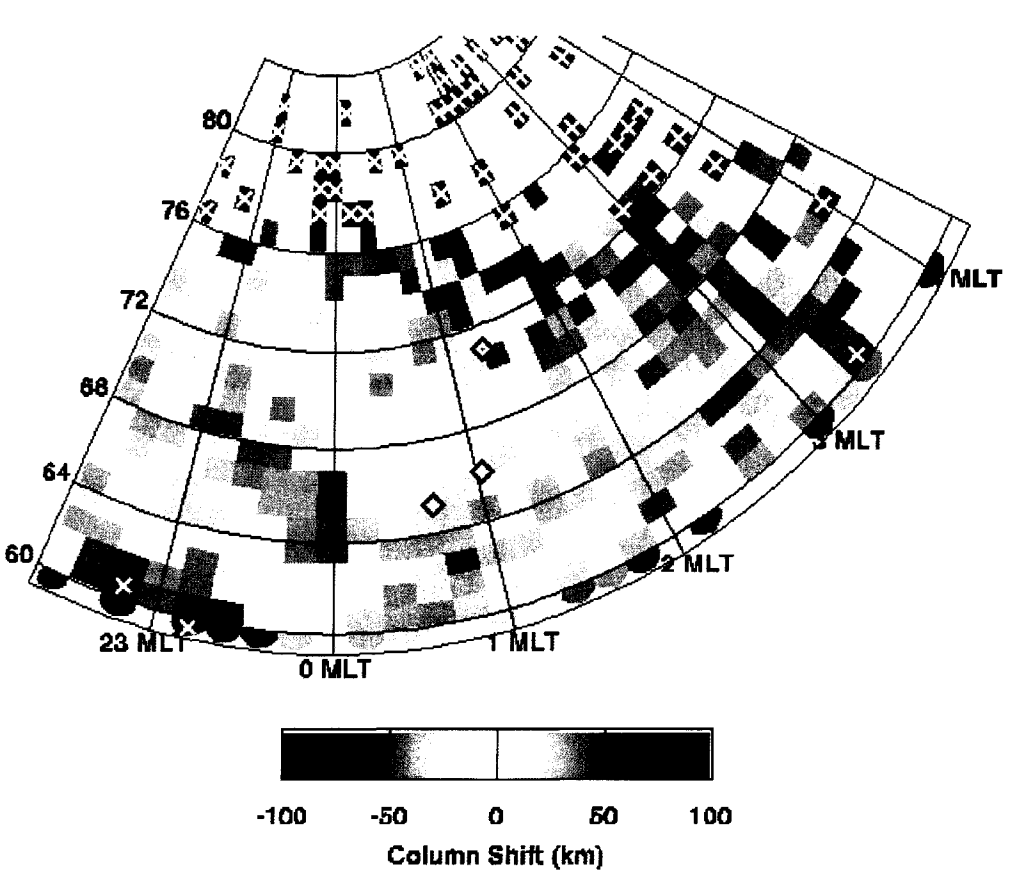

Figure 4.1. Column shift maps before and after median correction from the Jan 3, 2001 data set. **(a)** UVI-inferred column shifts at 1139 UT before median correction. This example uses the 9.3 counts·box^{-1} LBH-L brightness threshold as the criterion to retain column shift values, in contrast to the 15 counts·box^{-1} brightness threshold used in the column shift maps shown in Chapter 3. See the text for more discussion. The "*X*"s in the boxes here represent values that either exceed 100 km or are less than –100 km, rather than the 75 km to –75 km range of the examples shown in Chapter 3. See the text for more discussion. As was stated in Chapter 3, the marked points located around 0100 MLT indicate Inuvik, NT (71° magnetic latitude) and Poker Flat (65.2°) and Eagle (66.1°), AK.

of values should be retained in terms of the color bar's presentation until an explanation of their presence was forthcoming. The "*X*"s here represent values that either exceed 100 km or are less than –100 km, rather than the 75 km to –75 km range used in Figure 3.33a.

Figure 4.1b is produced by subtracting the median value of –32.7 km of the entire January 3, 2001 column shift data set from Figure 4.1a. The relative variation of the column shift values is now centered about a ~0 km value according to the color bar. Recall from

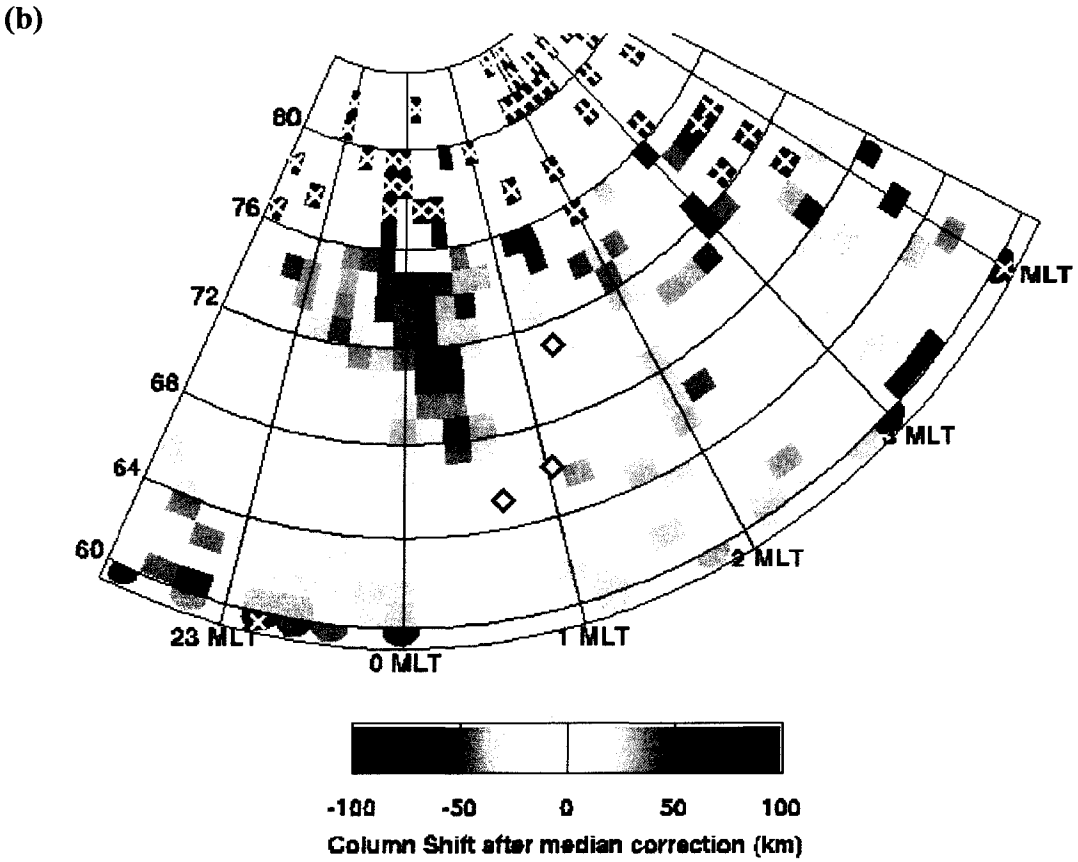

Figure 4.1 cont. Column shift maps before and after median correction from the Jan 3, 2001 data set. **(b)** UVI-inferred column shifts at 1139 UT after median correction. A median value of the entire Jan 3, 2001 column shift data set of –32.7 km (see Table 4.2) is subtracted from the **(a)** map to produce this map. The relative variation of the column shift values is now centered about a ~0 km value. See the text for more discussion.

Chapter 3 that Figure 4.1a is an example of a column shift map which illustrates that the modeled OI(135.6)-nm auroral brightness is underestimated on average relative to the observed OI(135.6)-nm brightness. The January 3, 2001, 1139 UT, observed-to-modeled OI(135.6)-nm brightness comparison on page 172 is shown again here as Figure 4.2.

Inspection of Figures 4.2a-b and Figure 4.1a identifies a band of weak-to-moderate OI(135.6)-nm aurora (~10-20 counts·box^{-1}) and subsequent band of upward column shifts between ~2345-0030 MLT and ~76°-68°. The band of upward column shifts runs contrary to the overall trend of this column shift map to indicate that the modeled OI(135.6)-nm brightness is weaker on average than the observed brightness; *i.e.*, in this region, the model

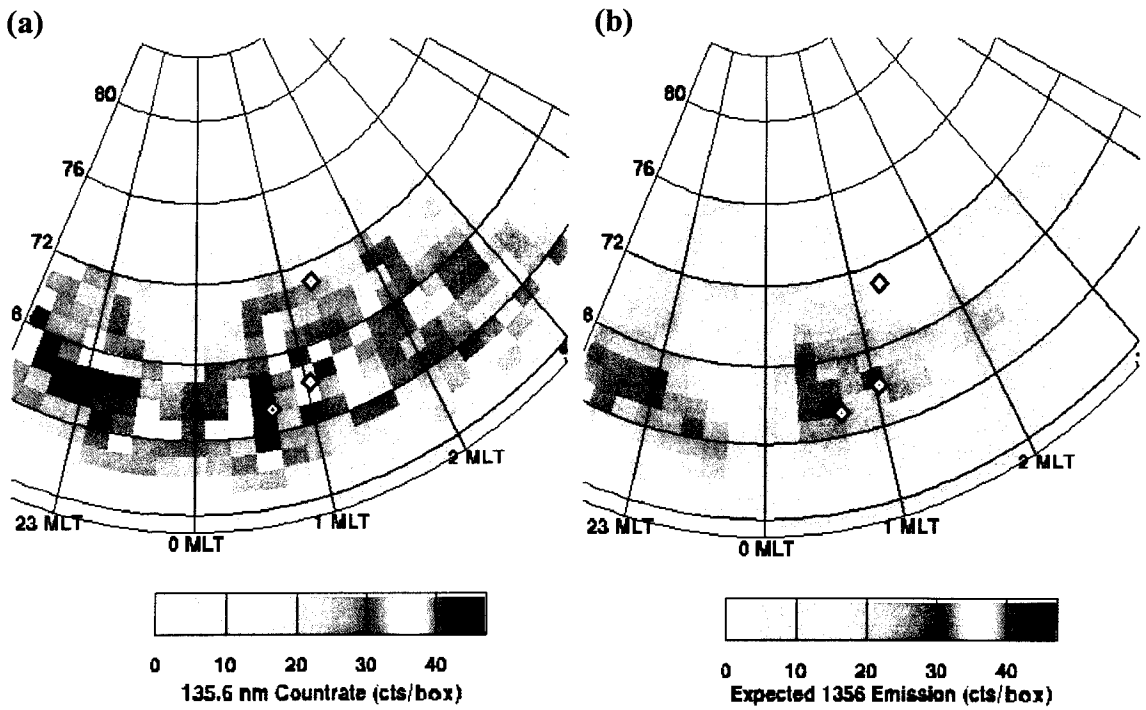

Figure 4.2. UVI-observed and modeled OI(135.6)-nm auroral brightnesses at 1139 UT on Jan 3, 2001. **(a)** UVI-observed OI(135.6)-nm brightness. **(b)** Modeled OI(135.6)-nm brightness. Previously shown as Figure 3.29 on page 172.

computes, based on energy flux and characteristic energy values prevailing in these boxes (see Figures 3.27b and 3.27d), that the OI(135.6)-nm emission should be brighter than what is actually being observed. This fact on its own is intriguing because it may indicate why the model works in some instances and not in others in predicting the OI(135.6)-nm auroral brightness. In addition, when the –32.7 km column shift median value is subtracted from Figure 4.1a, the upward column shift structure prevailing at ~2345-0030 MLT and ~76°-68° becomes more pronounced, as is seen in Figure 4.1b. The question becomes whether it is valid or not to infer that the upward column shifts in this region are larger based on Figure 4.1b. However, if the modeled OI(135.6)-nm brightness on average is underestimated by an amount that the –32.7 km column shift would correct—*i.e.*, by increasing the O density at auroral-emission altitudes an amount specified by a –32.7 km column shift—then a density correction to the MSIS-90 O density profile would increase the modeled OI(135.6)-nm brightness in the 2345-0030 MLT, 68°-76° region relative to

the brightness values of the region in Figure 4.2b. Hence, much larger upward column shifts would prevail in this region. Of course, the only way to confirm whether or not the relative column shift (to the median correction) is valid and attributable to vertical winds is to compare the time series of column shift values to vertical wind measurements.

Before discussing the time series comparisons, a comparison of Figures 4.1a-b to the column shift map of Figure 3.33a on page 184 and Figures 4.2a-b above (which use the 15 counts·box^{-1} LBH-L brightness threshold) reveals that many of the highly-negative column shift values are inferred at latitudes which sit outside of the auroral-oval region. While these boxes may have an LBH-L auroral signature of ≥9.3 counts, it is more likely these boxes have a count total of ≥9.3 because the background and/or airglow-removal procedures did not perform adequately. For example, excess airglow signal of 1-2 counts remaining from the procedures adds to a weak auroral signature in these boxes and causes the total signal to exceed 9.3 counts, preventing the boxes from being excluded from their respective data set. There are many values like this in the February 28, 2000, 0552 UT example shown in Figure 4.3, which uses the 9.3 counts·box^{-1} LBH-L brightness threshold rather than the 15 counts·box^{-1} criterion in Figure 3.33b on page 185. Boxes residing at magnetic latitudes of ≳72° and ≲64° for times of ~1600-2000 MLT exhibit column shift values which are very likely the result of poor dayglow removal. This topic is discussed more below, and led to the first inclinations to increase the LBH-L brightness threshold.

Initially, the median correction to the column shift values using the 9.3 counts·box^{-1} LBH-L brightness threshold was applied to the column shift time series before it was decided to increase the LBH-L brightness threshold. Figures 4.4a-b show the time series of column shifts over Inuvik from December 22, 2000 without the median correction (Figure 3.35) and with the median correction of –38.7 km. The column shifts measured over Inuvik are averaged over an area centered on Inuvik of 3° latitude × 9° longitude, which is ~340 km × ~370 km = 1.26×10^5 km^2, the equivalent of nine boxes. As is evident from Figures 4.4a-b, the median correction to the column shift time series does little in terms of helping visualize the relative variation of the column shifts over a site as it does with the 2-D maps across an area. Nonetheless, the median correction does bring the column shift

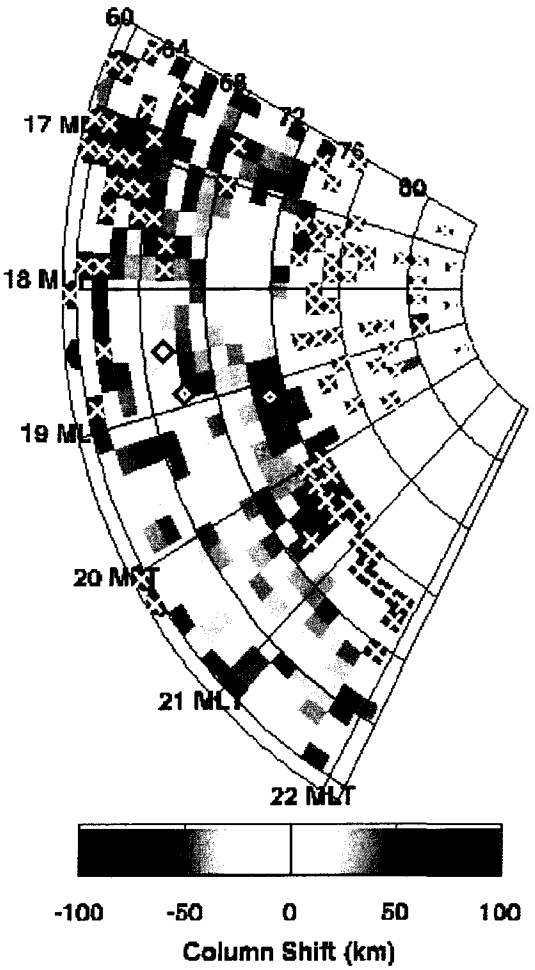

Figure 4.3. 2-D map of the UVI-inferred column shifts at 0552 UT on Feb 28, 2000. The example here uses the 9.3 counts·box^{-1} LBH-L brightness threshold to retain column shift values rather than the 15 counts·box^{-1} LBH-L brightness threshold. The lower threshold retains many boxes that fall outside of the auroral-oval latitude region and that exhibit column shift values of much less than –100 km. See the text for discussion.

values to an approximate zero-reference level, potentially for better visual comparison to vertical wind estimates.

As was just stated, the 9.3 counts·box^{-1} LBH-L brightness threshold retained UVI image data that often was located outside of auroral-oval latitudes. In addition, the column shifts associated with these boxes outside of the auroral oval were almost exclusively of unrealistically-large and negative values, suggesting that what was originally considered a reasonable estimate for what represented significant aurora prevailing in a region, ≥9.3

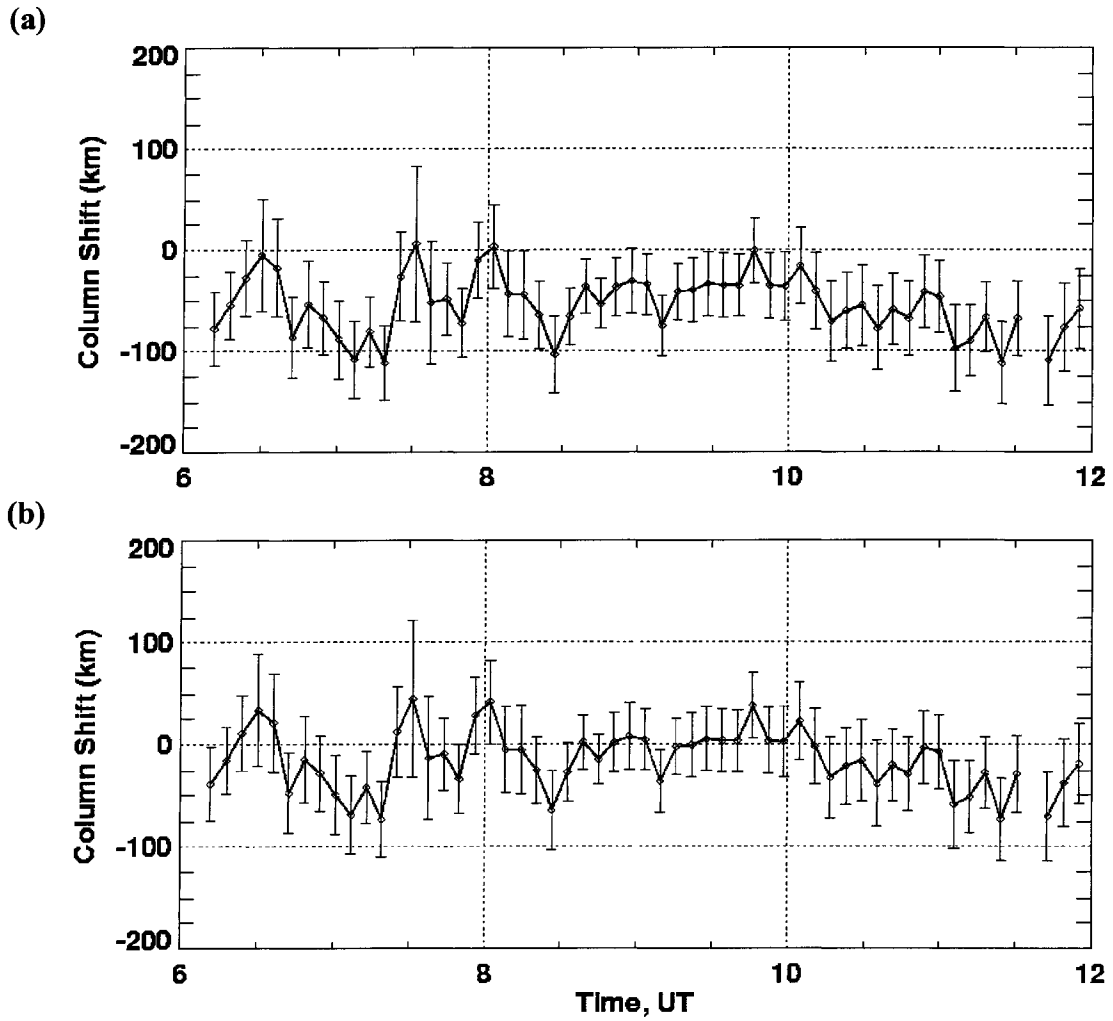

Figure 4.4. UVI-inferred column shift estimates over Inuvik, NT on Dec 22, 2000 without and with median correction. **(a)** Column shift values before median correction. **(b)** Column shift values after the median correction of –38.7 km; *i.e.*, –38.7 km is subtracted from the absolute column shift value of each box determined from the observed-to-modeled OI(135.6)-nm brightness comparisons. The criterion used here to retain column shift data was the LBH-L brightness threshold of 9.3 counts·box^{-1}. The uncertainty in the column shift estimates for this night are generally ±27-77 km. See the text for more discussion.

LBH-L counts·box^{-1} (1 mW·m^{-2} of energy flux), was a poor choice. The reasons for this could be many. For example, a given box may have an excess of LBH and OI(135.6)-nm airglow signal that the airglow-removal procedures do not eliminate accurately. If this excess airglow signal is significant (*e.g.*, 2-5 counts), particularly in boxes affected by

dayglow (which is much more variable than nightglow [*e.g., Rees*, 1989]), and the auroral signal is weak (*e.g.*, 10 counts), then the inferred energy flux and modeled OI(135.6)-nm brightness estimates will be significantly overestimated, and the effect on the inferred characteristic energy will be unclear. In contrast, excess airglow signal in the original UVI OI(135.6)-nm images will increase the observed OI(135.6)-nm brightness relative to what the model indicates the OI(135.6)-nm brightness would be based on the prevailing energy flux and characteristic energy of a given box. This leads to the unrealistically-negative column shift values that these data sets exhibit using the 9.3 LBH-L counts·box^{-1} criterion, as Figures 4.1a-b and 4.3 and Table 4.2 indicate. In addition to these scenarios, energy flux values inferred from very weak LBH-L observations (9.3-15 counts) may not indicate that significant aurora prevailed in a given box compared to energy flux values inferred from bright LBH-L observations (*e.g.*, 150 counts). If the uncertainty in a 1 mW·m^{-2} energy flux value is 35%, then the low end of the energy flux range from this LBH-L observation is 0.65 mW·m^{-2}, which is even lower if airglow-removal procedures leave an excess of LBH-L signal in the original UVI image. Does this weak energy flux indicate significant aurora, enough to indicate possible vertical winds and column shifts?

From these deliberations, it was ultimately determined that the LBH-L brightness threshold to retain UVI auroral data should be increased. The last deliberations on this issue involved an analysis of the distribution of column shift values, which is presented and discussed in Section 4.2 and resulted in meaningful conclusions on the column shift parameter. From the results of the distribution analysis, a reasonable LBH-L brightness threshold was determined to be 15 counts·box^{-1}. This value is a better indicator that 1 mW·m^{-2} of energy flux prevails in a given box when considering the discussion of the previous paragraph and the range of uncertainty of 20-35% in energy flux estimates (see Chapter 3). Furthermore, it was also determined from the column shift distribution analysis that increasing the LBH-L brightness threshold beyond 15 counts·box^{-1} did not significantly modify the results of the distribution analysis or in any way alter their conclusions. Thus, 15 counts·box^{-1} was the decided LBH-L threshold value to indicate significant aurora and proceed further with interpretations of the column shift parameter.

With the application of the new LBH-L brightness criterion to the column shift data sets, the column shift results improved markedly in that virtually all the boxes on the 2-D maps retaining weak auroral signal outside of the auroral-oval region were discarded, (see Figures 4.1a and 4.3 compared to Figures 3.33a-b on pages 184-185), that many of the unrealistically-negative column shifts also were discarded, and that the uncertainty in the spatially-averaged column shift values over each site was generally reduced. The mean and median values of the column shift data sets also became comparable and were reduced considerably, as was the standard deviation. This is seen in Table 4.3, which reiterates the information in Table 4.2 for comparison and shows the total number of column shift values remaining in each data set after the 15 counts·box^{-1} LBH-L criterion was applied.

For example, the February 28, 2000 column shift data set was reduced by more than half, the mean and median values were reduced by a factor of ~3 and the standard deviation by ~4. It was concluded for this particular data set that, presumably, UVI auroral data was retained inappropriately using the old LBH-L brightness criterion because residual dayglow signal likely remained in the auroral images after the removal procedures, potentially adding to weak auroral signal in the boxes of each 2-D map. The February 28, 2000 UVI data set is long, with observations beginning at 0200 UT, and significant portions of the 2-D maps observed early in the data set extend well into the dayside (0000-0600 UT; see Figure 4.3) where the thermosphere is sunlit. The dayglow signature of a given box deviating from the average dayglow signal determined from the numerical fit $B_{Arglw}(x)$ of Equation 3.24 would likely cause the total LBH-L signal per box to increase above the 9.3 counts·box^{-1} threshold. This is the case for the March 20, 2001 data set as well, which was also sunlit. With the application of the new LBH-L brightness threshold, the standard deviation of the March 20, 2001 data set was reduced by a factor of 8.

However, the application of the new LBH-L brightness threshold did not elevate the mean value of the new column shift data sets to ~0 km, demonstrating that the modeling process continued to underestimate the OI(135.6)-nm auroral brightness on average relative to the observed OI(135.6)-nm brightness. This was discouraging at first. However, because the column shift maps were improved so markedly (*i.e.*, cleaned up,

Table 4.3. Mean and median values and standard deviation of each column shift data set using the old and new LBH-L auroral brightness thresholds. The information in Table 4.2 is reiterated here for comparison. The new LBH-L brightness threshold used to retain UVI auroral data and column shifts is 15 counts·box^{-1}. The mean and median values and standard deviations are reduced considerably using the new brightness criterion. Also, the large difference between the mean and median values that exists using the old brightness criterion is not nearly as apparent. See the text for more discussion.

LBH-L criterion	New	Old	New	Old	New	Old	New	Old
Date	Total # of column shifts		$\bar{Z}$ (km)		Z_{med} (km)		SD_{clm} (km)	
Jan 3, 2001	22234	37468	–20.5	–68.7	–17.8	–32.7	42.3	185.9
Dec 9, 2000	28574	42540	–22.8	–50.2	–18.6	–27.4	31.2	105.7
Feb 28, 2000	15456	34005	–40.7	–153.5	–29.6	–79.5	67.0	283.0
Dec 22, 2000	5170	14000	–13.2	–80.9	–10.8	–38.7	33.7	172.2
Jan 4, 2001	6936	10954	–16.4	–63.2	–12.4	–23.2	28.1	190.9
Jan 26, 2001	8406	13224	–6.8	–49.5	–6.3	–15.3	31.6	131.8
Nov 28, 2000	3462	4969	–50.1	–123.2	–48.1	–69.8	91.6	234.2
Mar 20, 2001	8245	11249	–64.7	–204.6	–46.0	–68.8	104.2	828.4

removal of many *X*ed-out boxes) and because the mean and median values and standard deviation of each column shift data set were reduced so markedly, it was believed that the remaining column shifts associated with the brighter-aurora criterion may represent actual composition perturbations associated with the aurora relative to the model thermosphere, and furthermore, that the relative variation in the column shift time series may be truly representative of vertical wind activity. In addition, the new mean and/or median values of the column shift data sets may be a better indicator of what was actually ailing the OI(135.6)-nm auroral-modeling process. Thus, the column shift maps were revisited (as the Chapter 3 examples on pages 184-185 show), and the time series of column shifts over Inuvik and Poker Flat were reproduced using the new LBH-L brightness criterion.

Figure 4.5 shows the Inuvik FPS upper-thermospheric vertical winds compared to the UVI-inferred spatially-averaged column shift values over Inuvik on January 3, 2001 using the 15 counts·box^{-1} LBH-L brightness threshold. The median value of –17.8 km of of the entire January 3, 2001 column shift data set has been subtracted from the column shift time series (see Table 4.3). The error bars of the wind measurements and column shift estimates are not included in Figure 4.5 and in the other comparisons of vertical wind

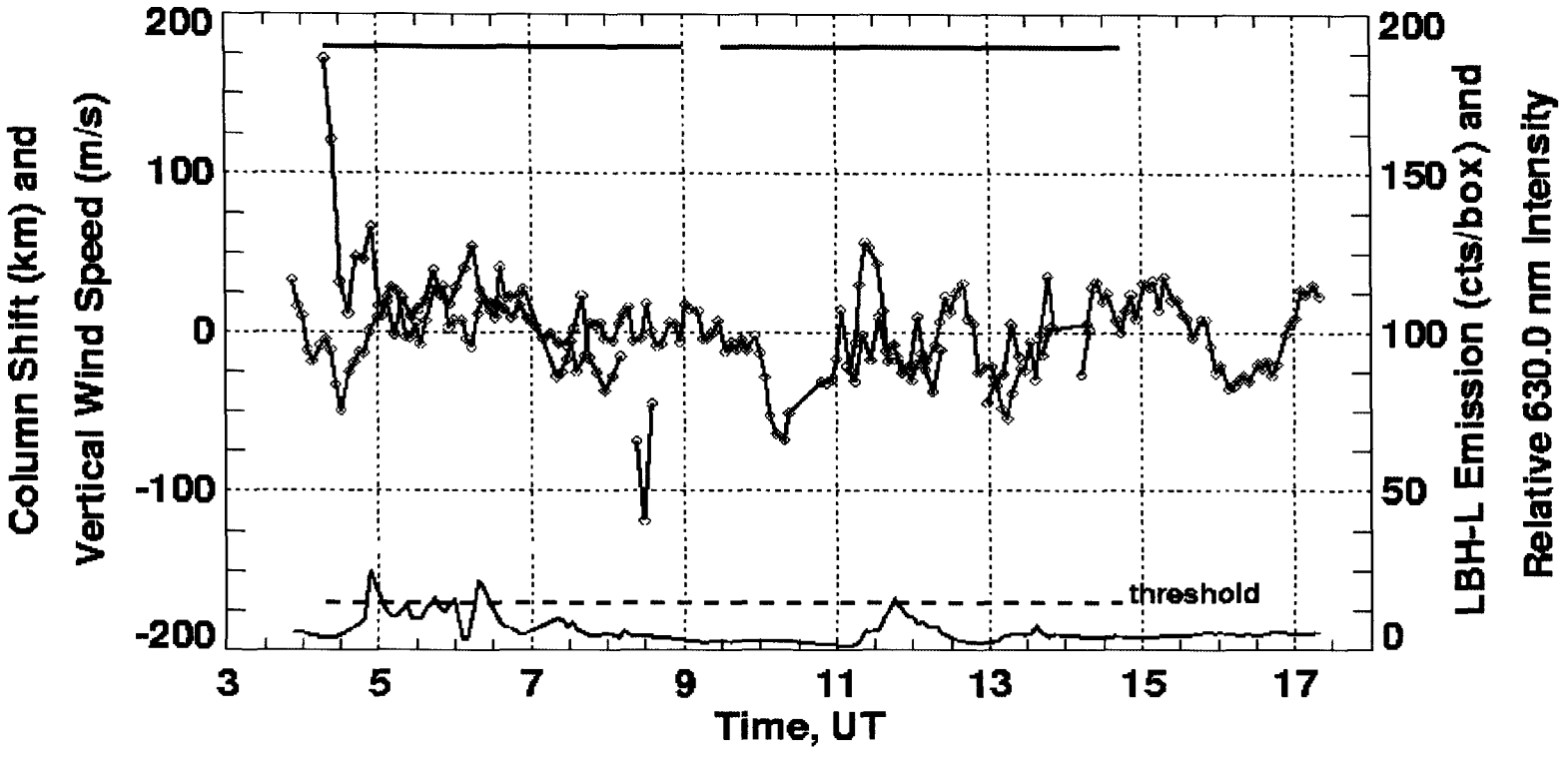

Figure 4.5. Upper-thermospheric vertical wind estimates and the UVI-inferred column shift measured over Inuvik, NT on Jan 3, 2001. The column shift values are in black, and the vertical winds are in red. Also shown is the UVI-measured LBH-L brightness over Inuvik in purple, and the FPS-measured relative OI(630.0)-nm brightness (also in red) using the brightness scale at the right-hand ordinate. As was stated earlier, the column shift values are averaged over an area centered on Inuvik of 3° latitude × 9° longitude (~340 km × ~370 km), the equivalent of nine boxes from the 2-D maps. The dashed line indicates the 15 counts·box^{-1} LBH-L brightness threshold. Geomagnetic and solar conditions for this night are in Table 4.4. The median value of –17.8 km was subtracted from the column shift time series. In general, the error in the wind measurements and column shift values is ±6-18 m·s^{-1} and ±24-58 km, respectively. See the text for discussion. The blue line at the top of the plot indicates when the UVI had poor viewing geometry, as discussed in Table 4.1. The red line indicates good viewing geometry.

and column shift time series presented here. Recall that Chapter 3 presents the seven Inuvik FPS vertical wind time series with their respective uncertainties separately from the column shift data, and the error in the January 3, 2001 wind measurements is $\sigma_{tot,wnd}$ = ±6-18 m·s^{-1} (see Figure 3.9 on page 122). In general, the error in the January 3, 2001 column shift values over Inuvik is δZ = ±24-58 km, except for the first two column shifts in the time series where the error was ±131 km and ±109 km, respectively. The general uncertainty range of the column shifts here is reduced compared to the uncertainty range of δZ = ±24-87 km when using the 9.3 LBH-L counts·box^{-1} criterion, as seen in Figure 3.37 on page 195. Comparison of Figure 3.37 to Figure 4.5 also reveals that many of the column shifts over Inuvik retained with the 9.3 LBH-L counts·box^{-1} criterion are no longer present in the new column shift time series using the 15 LBH-L counts·box^{-1} criterion, particularly those column shift values from ~0900-1100 UT.

The night of January 3, 2001 was fairly active aurorally at Inuvik for periods of time, as the UVI LBH-L brightness (in purple) and FPS OI(630.0)-nm relative intensity (in red) in Figure 4.5 indicate. Recall from Chapter 3 that in general the FPS OI(630.0)-nm relative intensity is ~1-5 units when strictly airglow prevails, and reaches ~30-40 units during the brightest auroras. The OI(630.0)-nm relative intensity is shown simply to indicate whether the FPS was observing OI(630.0)-nm aurora or airglow. In general, the OI(630.0)-nm relative intensity and LBH-L brightness show similar brightness variations (with some exceptions), indicating whether the aurora was weak or strong and providing more confidence in the column shift estimates; *i.e.*, brighter aurora → more particle-precipitation heating and ionization → higher conductivities → more Joule heating → vertical winds → column shifts. The brightest LBH-L auroras generally reach 150-200 counts·pixel^{-1}, and on very rare occasions, 300 counts·pixel^{-1}. The OI(135.6)-nm auroral brightness generally ranges from 15-45 counts·pixel^{-1}, and on rare occasions reaches 60-70 counts·pixel^{-1}.

Geomagnetically, it was quiet on January 3, 2001 as the A_P magnetic index indicates, A_P = 9, but weak to moderate aurora persisted over Inuvik for much of the night. This was the case over Inuvik for all the geomagnetically-quiet data sets presented

here, indicative of a quiet-time contracted auroral oval. The geomagnetic and solar conditions for the eight data sets are outlined in Table 4.4. The vertical winds in Figure 4.5 are depicted in red and the column shifts in black, using the scale at the left-hand ordinate. The straight blue and red lines at the top of the figure indicate when the UVI was viewing from good look angles (red, <45° to nadir) or bad look angles (blue, >45°). The dashed line indicates the 15 counts·box^{-1} LBH-L brightness threshold.

Table 4.4. Geomagnetic and solar conditions for the dates of observations. Magnetic midnight at Inuvik, NT is approximately 1000 UT.

Date	A_P magnetic index	$F_{10.7}$ cm flux	90-day mean $F_{10.7}$ cm flux
Jan 3, 2001	8	164	169
Dec 9, 2000	18	131	173
Feb 28, 2000	16	215	162
Dec 22, 2000	6	184	172
Jan 4, 2001	11	169	169
Jan 26, 2001	11	161	169
Nov 28, 2000	31	190	175
Mar 20, 2001	74	152	155

There are complexities here that hinder these time series comparisons. For example, the column shift is a time-integrated quantity, and an air parcel's time history is unknown to the FPS viewing it. The wind measured by the FPS at a given time is not necessarily the wind that was acting on that air parcel 10 or 20 min earlier, and horizontal transport can bring air parcels into the FPS field of view which may not represent the thermospheric composition that the FPS was viewing only a few minutes earlier. Another obstacle is that the OI(630.0)-nm emission emanates from the upper thermosphere, while the peak emission altitude of OI(135.6)-nm aurora depends on the characteristic energy of the precipitation. At times when a significant vertical wind event is observed in the upper thermosphere, the column shift variation may indicate a lower-thermospheric effect that does not correlate with the wind event because the bulk of the OI(135.6)-nm emission is emanating from lower altitudes. In addition, column shift variations may identify a

significant lower- or middle-thermospheric vertical wind that has not yet reached the upper thermosphere. Upper-thermospheric vertical wind observations are useful, however, because they may indicate when a lower- or middle- to upper-thermospheric vertical flow cell prevails, set up by a sufficiently long-lived and energetic heating event. If significant column shift variation correlates with significant upper-thermospheric wind observations, this may indicate either that composition is being modified throughout the thermospheric column or locally at upper-thermospheric altitudes (see the next paragraph).

Generally, what was looked for in these comparisons of vertical wind and column shift time series was three types of impulsive vertical wind-induced column shifts. It was expected that the column shift (relative to either some zero column-shift reference or the column shift values prior to the onset of a vertical wind event) would demonstrate either a delayed or an immediate vertical wind effect, or, in contrast, would indicate an upcoming vertical wind event. For example, if a significant vertical wind extending from the lower or middle to upper thermosphere set up by particle-precipitation and Joule heating has only recently begun to blow, composition will not yet have been significantly modified along the thermospheric column, the observed OI(135.6)-nm auroral emission profile will not yet have been altered relative to the model prediction, and the column shift variation due to the vertical wind will be delayed relative to the vertical wind's onset. In contrast, if a significant vertical wind field moved into the FPS field of view that had already prevailed for some time, the column shifts will be expected to show an immediate change associated with the observed vertical wind; *i.e.*, the vertical wind has already modified composition along the thermospheric column, the observed OI(135.6)-nm emission profile has changed relative to the model prediction, and the wind and column shift variations are simultaneous. In addition, an immediate or nearly-immediate vertical wind effect may be evident at upper-thermospheric altitudes if the electron precipitation is soft to moderate (<1-2 keV). Inspection of the *Lummerzheim and Lilensten* [1994] 8-stream model output reveals that energy deposition due to moderate precipitation (~10^9-10^{10} eV·cm^{-2}·s^{-1}) is nearly as significant at middle- to upper-thermospheric altitudes (~180-250 km) as at lower- to middle-thermospheric altitudes (~100-180 km). Column shift variations during

such events may indicate a middle- to upper-thermospheric composition perturbation that coincides simultaneously or nearly-simultaneously with significant upper-thermospheric vertical wind observations. Lastly, if significant column shift variation occurs during a period of weak upper-thermospheric vertical winds, the column shifts may indicate a significant lower-thermospheric vertical wind event that has not yet extended into the upper thermosphere. Thus, an FPS observation of the upper-thermospheric vertical wind associated with this wind event will be delayed relative to the onset of the column shift variation, if the wind event is sufficiently long-lived and energetic to reach upper-thermospheric altitudes and spatially-extended to remain in the FPS field of view.

In general, the vertical wind activity over Inuvik on January 3, 2001 is indicative of the sort of wind activity that was desired for this study. There are several upward and downward intermediate- to large-magnitude wind events that occur over Inuvik on this night. For example, there is a significant downward wind event from 1000-1100 UT in which the winds reach speeds of ~65-70 $m \cdot s^{-1}$. Aurora did not prevail over Inuvik during this time, however, so column shift data could not be examined, and the downward wind observations are likely associated with a large-scale horizontally-propagating gravity wave passing over Inuvik. Other studies have identified gravity wave perturbations in vertical wind time series [*e.g. Hernandez*, 1982; *Johnson et al.*, 1995; *Innis et al.*, 1996; 1997; *Innis and Conde*, 2001], and the January 3, 2001 vertical wind time series exhibits significant wavelike features. Spectral analysis of the wind data using the Lomb-Scargle normalized periodogram method for unevenly-sampled time series [*e.g. Press et al.*, 1992] confirms this, identifying a strong periodicity at $\tau \approx 1.5$ hr. Lomb-Scargle analysis is described in more detail in Appendix E. Atmospheric gravity waves (AGWs) in the thermosphere have been categorized into two classes; large-scale and medium-scale perturbations [*e.g. Mayr et al.*, 1984; see references therein]. In general, gravity waves have a period greater than or equal to the buoyancy resonance period τ_B of the thermosphere, referred to as Brunt-Väisälä period [*e.g. Brekke*, 1997], and at upper-thermospheric altitudes, $\tau_B \approx$ 10-15 min. Large-scale AGWs generated by auroral-related processes have wavelengths of ~1000-4000 km and periods of ~1-3 hr [*Mayr et al.*, 1984] and can potentially travel

large distances, depositing their energy at middle and low latitudes. Gravity wave analysis methods and gravity wave properties are described in more detail in Appendix B. Lomb-Scargle spectral analysis of the column shift time series did not confirm the 1.5 hr periodicity, but this is attributed to the significant lack of column shift data coverage after the 15 counts·box^{-1} LBH-L brightness threshold was applied to the column shift data set.

What is still apparent in Figure 4.5—even after the 15 counts·box^{-1} LBH-L criterion is applied—is the vertical wind-induced composition perturbation example discussed in Chapter 3. This is an example of a delayed composition effect that occurs in the middle-to-upper thermosphere. From 0540-0555 UT, an intermediate-magnitude upward wind prevailed over Inuvik, reaching speeds of ~30 m·s^{-1}. A 36 km increase in the column shift relative to the column shift values that prevailed prior to the onset of the vertical wind is evident in the column shift time series, occurring from 0555-0615 UT. The height displacement of air parcels of 27 km that a 15 min, +30 m·s^{-1} vertical wind would produce is confirmed by this relative increase of 36 km in the column shift values (within the uncertainty range of the winds and shifts). Furthermore, the delay between the onset of the vertical wind and the initial increase in the column shift is 15 min, indicating that the vertical wind, which lasted for 15 min as measured over Inuvik, apparently had only just begun to blow as it was being observed by the Inuvik FPS. It took 15 min for the column shift variation over Inuvik to reveal the vertical wind-induced composition effect. In addition, the precipitation's characteristic energy over Inuvik during this time was 1.3-1.9 keV, indicating that the precipitation was depositing a significant portion of its energy and producing aurora at middle- to upper-thermospheric altitudes. Lastly, the energy flux prevailing over Inuvik during this time frame was 2.8-4.1 mW·m^{-2}. An estimate of the mechanical power per unit area P/A required to generate upward speeds of 30 m·s^{-1} at 200 km altitude can be determined using the first term from Equation 1.7 [*Price et al.*, 1995], $P/A = \rho HgW = \rho k_B TWm^{-1}$, where W is the vertical wind speed, k_B is Boltzmann's constant, m is the mass of the atoms and/or molecules (assume an average of 24 amu), and ρ and T are the total mass density and temperature at 200 km, $\rho = 3.049 \times 10^{-10}$ kg·m^{-3} and T = 1089 K, respectively, in the low-A_P MSIS-90 model thermosphere. The mechanical

power per unit area is found to be P/A = 3.4 mW·m^{-2}, recalling that the thermal energy terms in Equation 1.7 are negligible at upper-thermospheric altitudes. Thus, the energy flux prevailing over Inuvik during this time frame is high enough to generate the upward wind speeds observed by the Inuvik FPS at the OI(630.0)-nm emission altitude range of ~200-240 km. The column shift variation here is therefore indicative of a composition perturbation that occurs at middle- to upper-thermospheric altitudes since the vertical wind's duration is not long enough nor its magnitude large enough to indicate a lower- to upper-thermospheric composition disturbance.

Besides the above example, there is little correlation between the other significant vertical wind events that occurred over Inuvik on this night and the column shifts. For instance, another upward wind event occurred from 1120-1140 UT, reaching a magnitude of ~55 m·s^{-1}. The column shifts showed only a slight upward trend and in general hovered around ~0 km. There are times, however, where the gradual trend of the column shifts does appear to follow the gradual trend of the vertical winds. For example, there is a slow downward trend in the winds and column shifts, with random fluctuations about this trend, from 0615 UT to 0730 UT. Admittedly, this random, small-magnitude vertical motion is not significant in terms of the discussions of Chapter 1, but these wind measurements can be attributed to the random vertical motion of the thermospheric air parcels [*e.g. Conde and Dyson*, 1995] and/or their respective pressure layers emitting airglow and aurora. At times, this weak, random motion is also revealed in the relative column shift variation.

There are more times, however, where the trends do not match, and there is no basis to state with any degree of reliability whether or not the trends that do match are correlated. Cross correlation analysis of the time series proves to be inconclusive. Figure 4.6a shows the cross correlation calculation of the vertical winds and column shifts from ~0400-0845 UT. Because there is a long break in column shift data coverage from ~0845-1100 UT, a cross correlation coefficient (at different time lags) is computed between the winds and each portion of column shift data. Figure 4.6b shows the cross correlation calculation of the vertical winds and column shifts from 1100-1430 UT. Because the vertical winds and column shifts were sampled with different temporal

resolutions (~4 and ~6 min, respectively), wind values were interpolated to the times of the column shifts before the cross correlation coefficient was calculated. Cross correlation

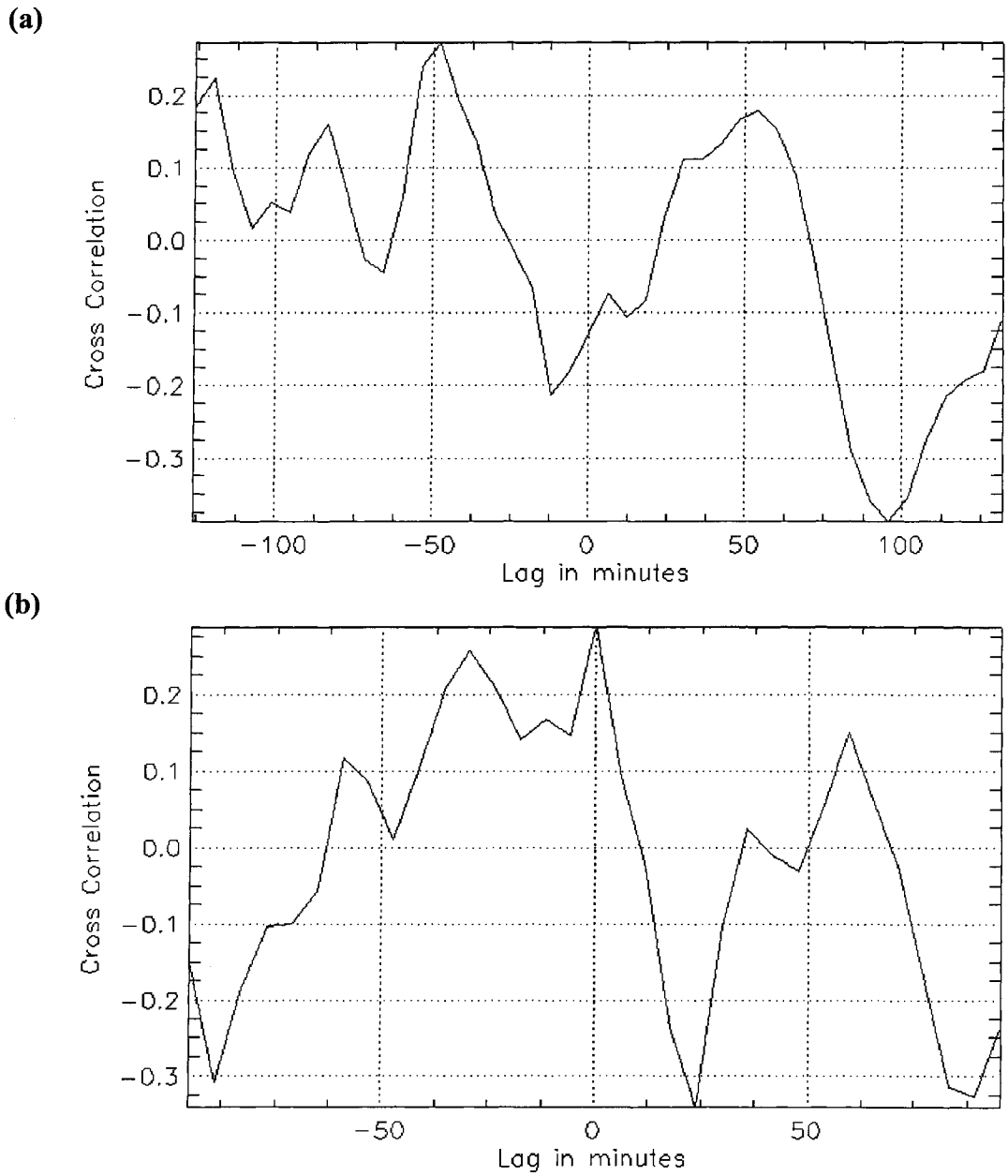

Figure 4.6. Cross correlation calculation between the time series of vertical wind measurements and column shift values on Jan 3, 2001. **(a)** For times between 0400 and 0830 UT. The maximum correlation coefficient of –0.38 occurs at a time lag of 95.8 min. **(b)** For times between 1100 and 1330 UT. The maximum correlation coefficient of –0.34 occurs at a time lag of 23.7 min. See the text for more discussion.

analysis is described in more detail in Appendix E. The maximum correlation coefficient in Figure 4.6a of –0.38 occurs at a time lag of 95.8 min, and the maximum correlation coefficient of –0.34 in Figure 4.6b occurs at a lag of 23.7 min. Table 4.5 shows the maximum correlation coefficient between the time series of vertical winds and column shifts for all the data sets presented here. Neither correlation coefficient in Figures 4.6a-b is large enough to indicate any definitive correlation between the two time series, but as was stated in Chapter 3, this is generally expected when comparing data from two semi-random phenomena. There will be random periods of correlation, anti-correlation, and no correlation. And as was also stated, other phenomena can produce variations in the relative column shift data similarly to vertical winds and/or mask a vertical wind-induced effect so that the height displacement effect is not identified in the column shift data. However, when definitive examples such as the 0540-0615 UT vertical winds and column shifts do occur, mere coincidence does not always explain these correlations.

Table 4.5. Cross correlation calculation between the time series of vertical winds and column shifts. Maximum correlation coefficients are shown at their respective time lags. See the text for more discussion.

Date	Max. correlation coeff.	Time lag (min)
Jan 3, 2001 -- 0400-0830 UT	–0.38	95.8
-- 1100-1330 UT	–0.34	23.7
Dec 9, 2000	–0.25	184
Feb 28, 2000 -- 0500-0715 UT	–0.50	23.1
-- 0845-1245 UT	–0.51	–23.8
Dec 22, 2000	–0.49	24.5
Jan 4, 2001	0.33	–83.0
Jan 26, 2001	0.73	–77.9
Mar 20, 2001 -- OI(630.0)-nm winds	0.48	18.4
-- OI(557.7)-nm winds	0.54	18.4
Nov 28, 2000	0.41	10.4

Figure 4.7 shows the Inuvik FPS upper-thermospheric vertical winds compared to the UVI-inferred column shift estimates over Inuvik (using the 15 counts·box^{-1} LBH-L brightness criterion) on December 9, 2000. The median value of –18.6 km of the entire

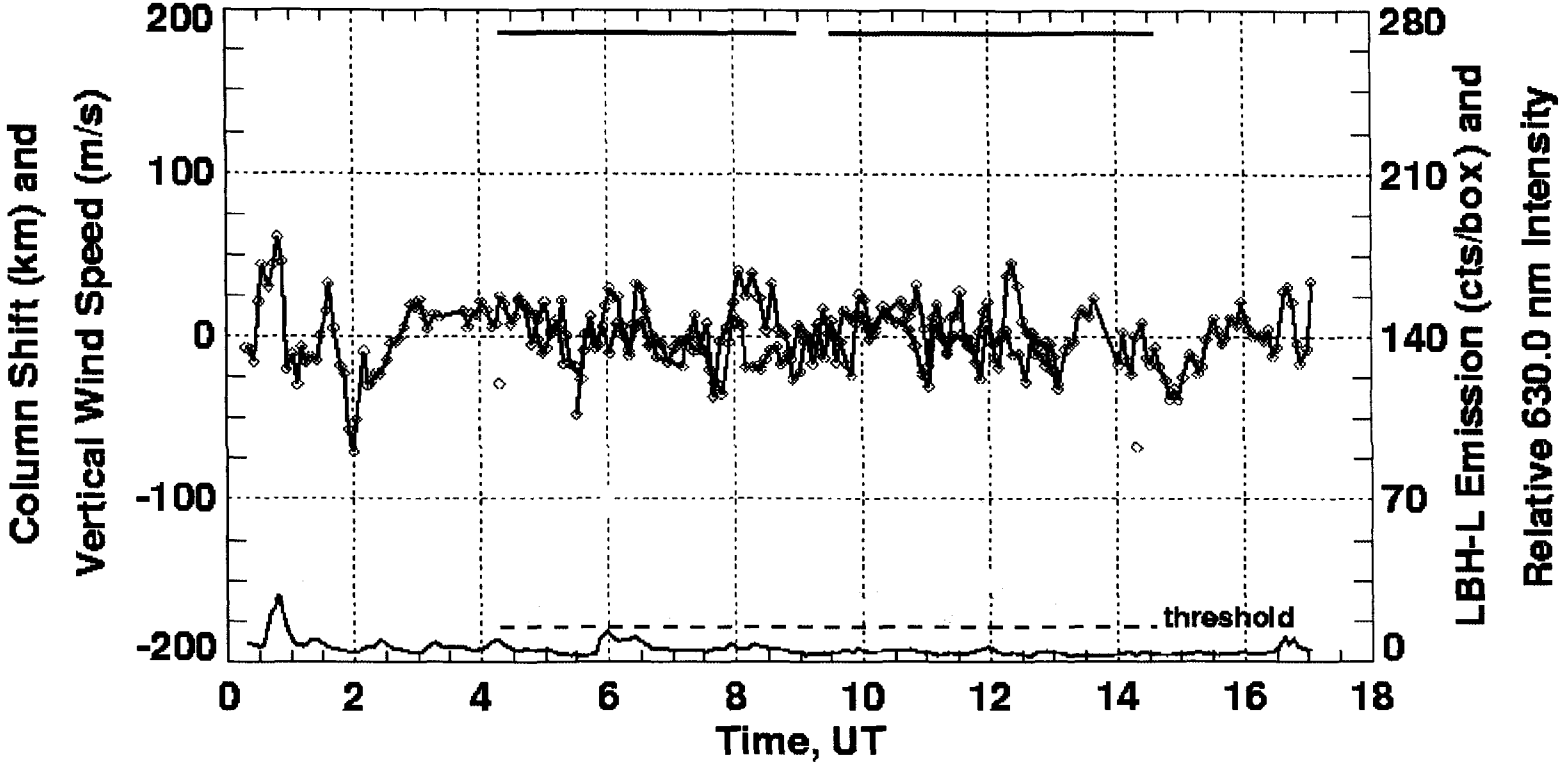

Figure 4.7. Upper-thermospheric vertical wind estimates and the UVI-inferred column shift measured over Inuvik, NT on Dec 9, 2000. Same layout as Figure 4.5. Solar and geomagnetic conditions for this night are outlined in Table 4.4. A median shift of –18.6 km was subtracted from the column shift time series. The error in the wind measurements and column shift values is ±4-11 $m \cdot s^{-1}$ and ±20-43 km, respectively. See the text for discussion.

December 9, 2000 column shift data set has been subtracted from the column shift time series (see Table 4.3). The uncertainty in the vertical wind measurements for this night are ±4-11 $m \cdot s^{-1}$ (see Figure 3.11 on page 126), and the errors in the column shift values are ±20-43 km, compared to the ±21-132 km range of uncertainty seen in Figure 3.36 on page 193 for the column shift data using the 9.3 $counts \cdot box^{-1}$ LBH-L criterion.

Though there are periods apparent in Figure 4.7 where the column shifts and vertical winds appear to coincide, such as the time intervals of 0400-0800 UT and 1000-1200 UT when the up and down trends in the column shifts and vertical winds follow each other (potentially indicative of the random motion of the thermospheric air parcels and/or pressure layers as discussed above), there are other intervals where the column shift does not indicate of a vertical wind-induced effect. For example, fairly insignificant downward winds (0 to –20 $m \cdot s^{-1}$) prevailed during the ~0800-0845 UT time period when sustained upward column shifts of ~40 km occurred (relative to the zero-reference level). Another example is apparent just after 1200 UT when a sustained upward wind, peaking at +50 $m \cdot s^{-1}$

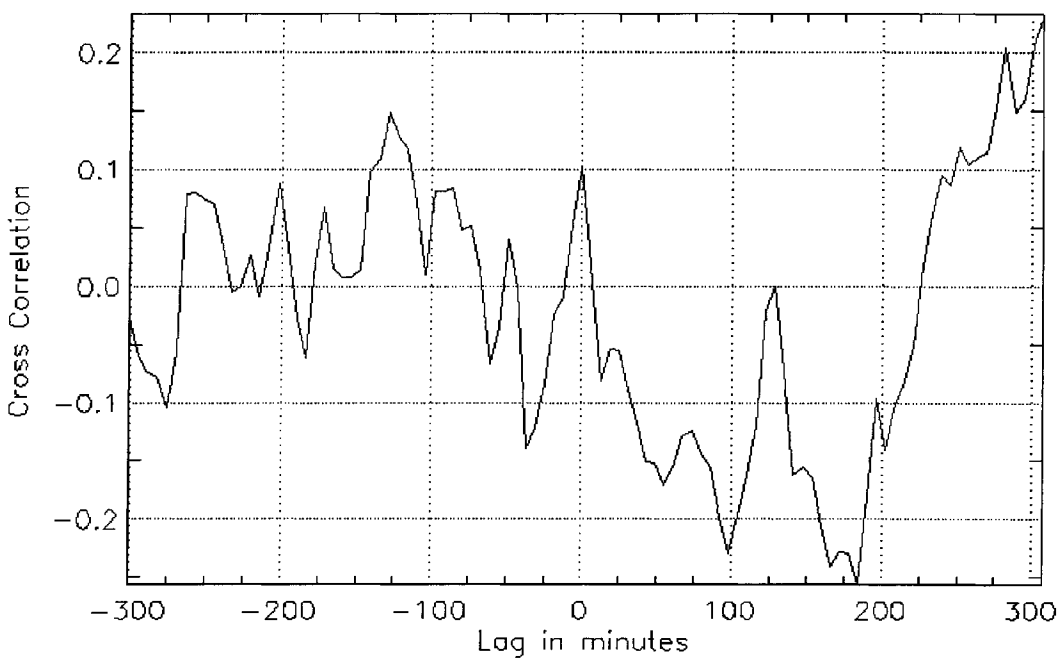

Figure 4.8. Cross correlation calculation between the Dec 9, 2000 vertical wind and column shift time series. The maximum correlation coefficient of –0.25 occurs at a time lag of 184 min. See the text for more discussion.

and lasting for 20 min, occurred. The column shift variation does not reveal an immediate or delayed effect due to the upward wind, and instead indicates a shift of –40 km. The column shift does return to a ~0 km level, and from 1245-1315 UT follows the downward trend in the vertical winds, which reach a magnitude of –30 $m \cdot s^{-1}$. Nonetheless, the cross correlation calculation between the time series, shown above in Figure 4.8, proves to be inconclusive. The maximum correlation coefficient of –0.25 occurs at a time lag of 184 min. There is one time series comparison that will be discussed accordingly which shows much better correlation than the January 3, 2001 and December 9, 2000 data sets.

Figure 4.9 shows the Inuvik FPS upper-thermospheric vertical winds compared to the UVI-inferred column shift estimates over Inuvik (using the 15 $counts \cdot box^{-1}$ LBH-L brightness threshold) on February 28, 2000. The median value of –29.6 km of the entire February 28, 2000 column shift data set has been subtracted from the column shift time series (see Table 4.3). The uncertainty in the vertical wind measurements for this night is ±3-11 $m \cdot s^{-1}$ (see Figure 3.15 on page 133), and the error in the column shift values is ±19-118 km, compared to a ±19-151 km uncertainty range for the column shift data using the 9.3 $counts \cdot box^{-1}$ LBH-L criterion. As can be seen in Figure 4.9, the column shifts up until 0500 UT are highly variable and mostly unrealistic in magnitude, and the largest error in the ±19-118 km uncertainty range is associated with these column shifts. In addition, these column shifts were inferred during periods of generally weak aurora when the LBH-L brightness was 15-35 $counts \cdot box^{-1}$ and the thermosphere over Inuvik was sunlit, as was discussed above and at the end of Chapter 3. Potentially inadequate estimations of the dayglow count per box likely resulted in the LBH-L, LBH-S and OI(135.6)-nm brightness being either over- or underestimated, adversely affecting the inferred energy flux, characteristic energy, modeled OI(135.6)-nm auroral brightness, and column shifts. Only when the LBH-L brightness increased considerably after 0500 UT did the inferred column shifts assume more reasonable values and relative variation in those values.

There is one example in the February 28, 2000 data set where the vertical winds and column shifts coincide. From 1110-1130 UT, there is a period of sustained upward winds, reaching a magnitude of +40 $m \cdot s^{-1}$ on two occasions. During this time frame, the column

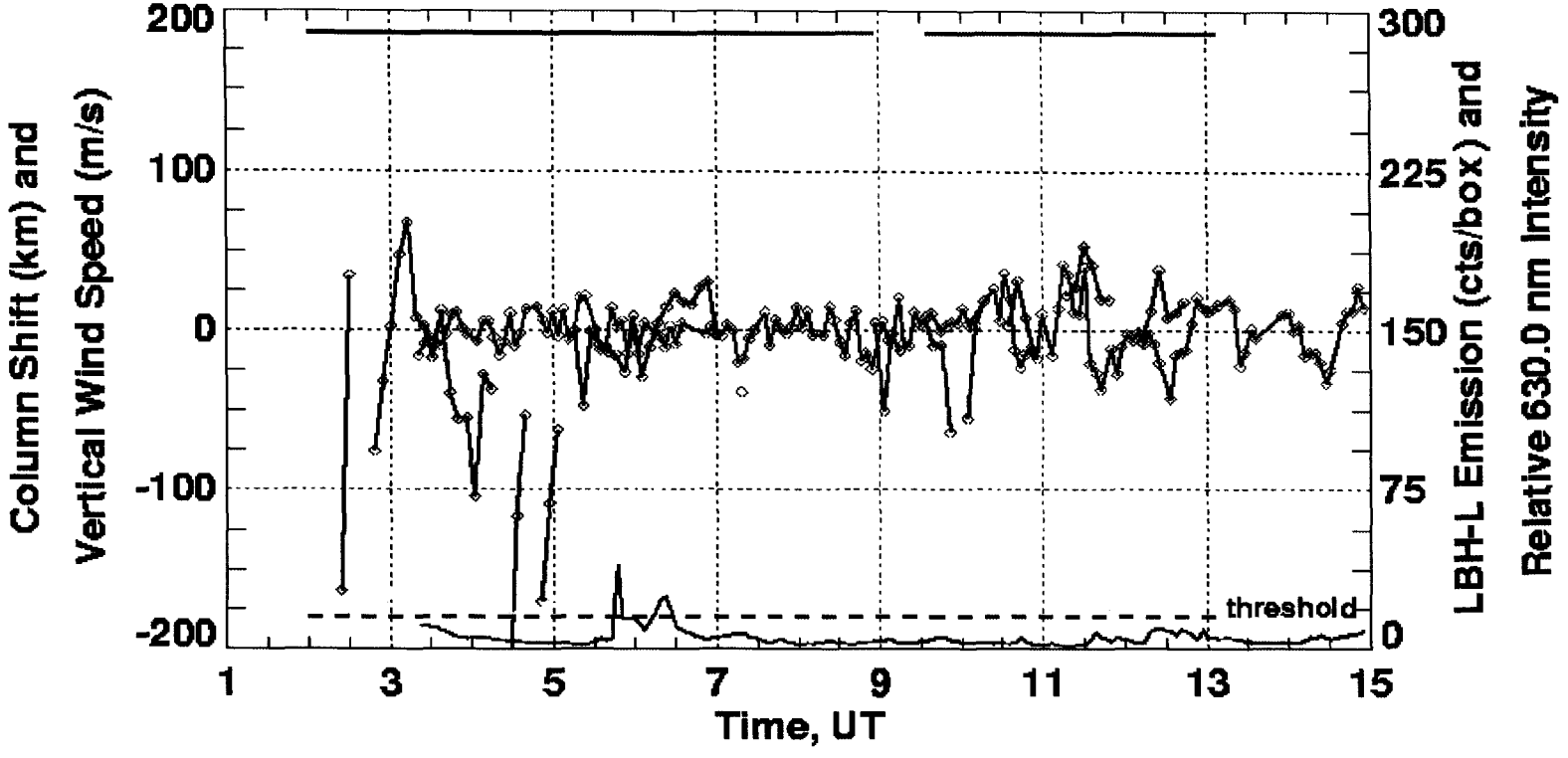

Figure 4.9. Upper-thermospheric vertical wind estimates and the UVI-inferred column shift measured over Inuvik, NT on Feb 28, 2000. Same layout as previous figures. See Table 4.4 for the solar and geomagnetic conditions on this night. A median column shift of –29.6 km was subtracted from the column shift time series. The error in the wind measurements and column shift values is ±3-11 $m \cdot s^{-1}$ and ±19-118 km, respectively. The largest column shift errors are associated with the column shifts inferred before ~0500 UT. See the text for discussion.

shift increased by 40 km relative to its value prior to the onset of the upward wind. A +40 $m \cdot s^{-1}$, 20 min upward wind will transport air parcels an altitude of 48 km, which the relative column shift of 40 km confirms. In addition, the delayed column shift variation here is again indicative of a middle- to upper-thermospheric composition perturbation, similarly to the January 3, 2001 example discussed above. The chararacteristic energy of the electron precipitation ranges from 1.2-2.1 keV during this time frame, the energy flux ranges from 2.0-3.1 $mW \cdot m^{-2}$, and the duration of the vertical wind event is not sufficiently long or its magnitude sufficiently large to produce a lower- to upper-thermospheric composition disturbance.

Other than this example, however, the February 28, 2000 vertical wind and column shift time series comparison is also one that does not yield much insight because of the overall lack of data coverage after the application of the 15 counts·box^{-1} LBH-L brightness threshold to the column shift data set. Ignoring the column shift data prior to 0500 UT, the cross correlation calculation between the time series for the two time periods of 0500-0715 UT and 0845-1245 UT yields maximum correlation coefficients of –0.50 at a lag of 23.1 min and –0.51 at a lag of –23.8 min, respectively. These correlation coefficients, while large compared to the January 3, 2001 and December 9, 2000 examples, are not large enough to warrant serious consideration.

Figure 4.10 shows the Inuvik FPS upper-thermospheric vertical winds compared to the UVI-inferred column shift estimates over Inuvik (using the 15 counts·box^{-1} LBH-L brightness threshold) on December 22, 2000. The median value of –10.8 km of the entire December 22, 2000 column shift data set has been subtracted from the column shift time series. The uncertainty in the vertical wind measurements for this night is ±6-18 $m \cdot s^{-1}$ (see Figure 3.13 on page 130), and the error in the column shift values is ±21-50 km, compared to the ±27-77 km range of uncertainty seen in Figures 4.4a-b on page 208 for the column shift data using the 9.3 counts·box^{-1} LBH-L criterion. However, comparison of Figures 4.4a-b to Figure 4.10 also reveals that many of the column shifts over Inuvik retained with the 9.3 LBH-L counts·box^{-1} criterion are no longer present in the new time series using the 15 LBH-L counts·box^{-1} criterion, similarly to the January 3, 2001 data set.

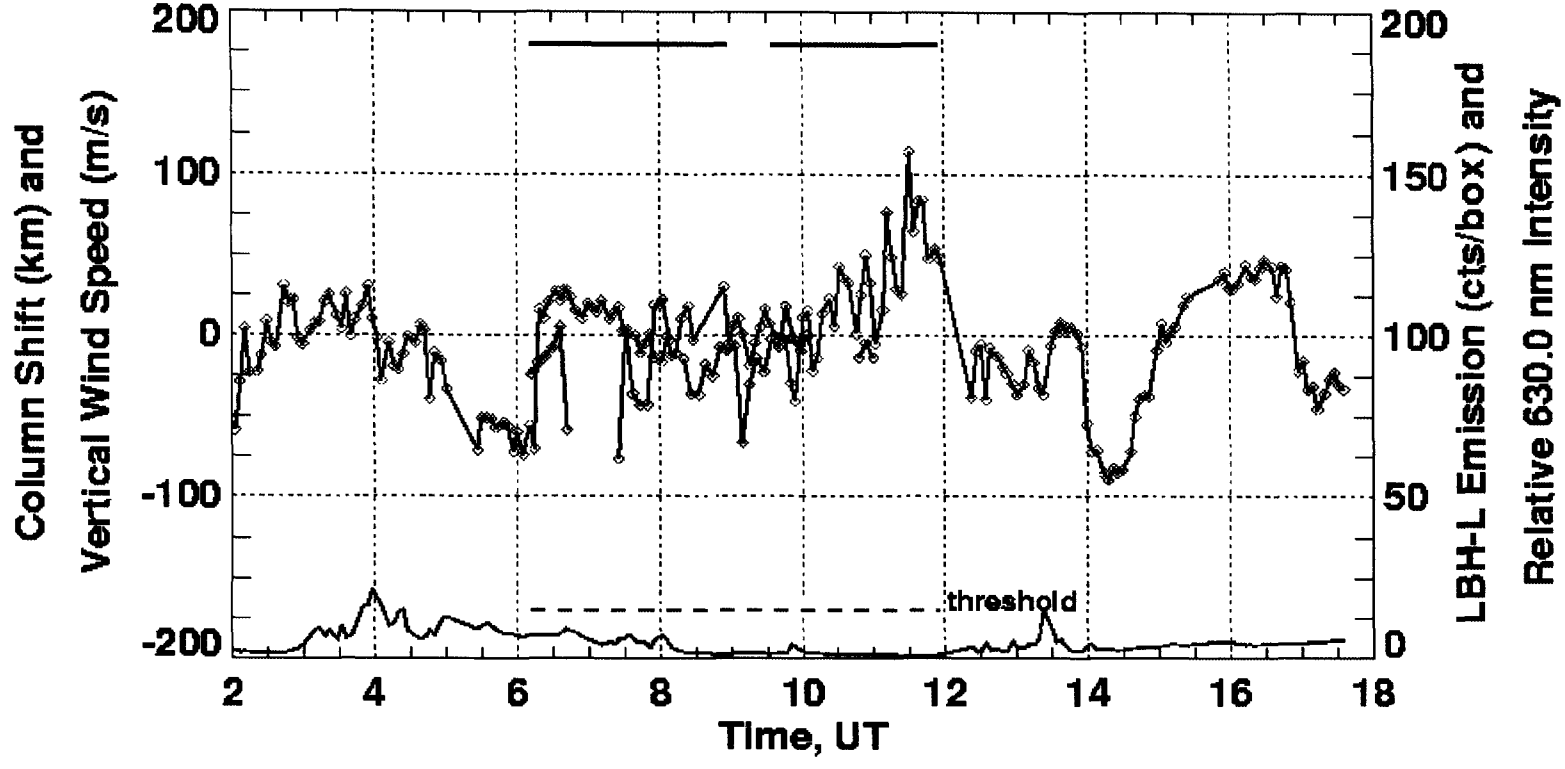

Figure 4.10. Upper-thermospheric vertical wind estimates and the UVI-inferred column shift measured over Inuvik, NT on Dec 22, 2000. Same layout as previous figures. See Table 4.4 for the solar and geomagnetic conditions on this night. A median column shift of –10.8 km was subtracted from the column shift time series. The error in the wind measurements and column shift values is ±6-18 $m \cdot s^{-1}$ and ±21-50 km, respectively. See the text for discussion.

The vertical winds over Inuvik on this night exhibit a variety of interesting characteristics. The time series exhibits several long-lived, large-magnitude vertical wind events, such as the downward wind events from ~0530-0600 UT and ~1400-1500 UT. In addition, the vertical wind time series also exhibits considerable wavelike structure, and Lomb-Scargle spectral analysis of the vertical wind measurements identifies a significant periodicity at τ = 1.7 hr in the time series of vertical winds (see Appendix E). Lomb-Scargle analysis of the column shift time series, however, does not identify the 1.7 hr periodicity, and this is again attributed to the lack of column shift data coverage after the 15 LBH-L counts·box^{-1} criterion is applied, similarly to the January 3, 2001 data set. Though the column shift data coverage does not coincide with the significant vertical wind events, the gradual trend of the column shifts (with random fluctuations about this trend) does follow the gradual trend of the vertical winds from ~0815-0930 UT, similarly to the examples discussed in the January 3, 2001 and December 9, 2000 data sets. However, because of the overall lack of column shift data coverage, this time series comparison does not yield any insight into vertical wind-induced composition variations. The cross correlation calculation finds a maximum correlation coefficient of –0.49 at a time lag of 24.5 min (see Table 4.5). As with the other examples, the correlation coefficient is not sufficiently high nor is the column shift data coverage sufficiently robust to warrant serious consideration.

Figure 4.11 shows the Inuvik FPS upper-thermospheric vertical winds compared to the UVI-inferred column shift estimates over Inuvik (using the 15 counts·box^{-1} LBH-L brightness threshold) for the night of January 4, 2001. The median value of –12.4 km of the entire January 4, 2001 column shift data set has been subtracted from the column shift time series (see Table 4.3). The uncertainty in the vertical wind measurements for this night is ±7-19 m·s^{-1} (see Figure 3.17 on page 137), and the error in the column shift values is ±25-34 km, compared to an uncertainty range of ±26-66 km for the column shift estimates using the 9.3 counts·box^{-1} LBH-L criterion.

The vertical wind activity over Inuvik on this night is significant. The large-magnitude downward wind event that occurs at ~1000 UT was already discussed at length

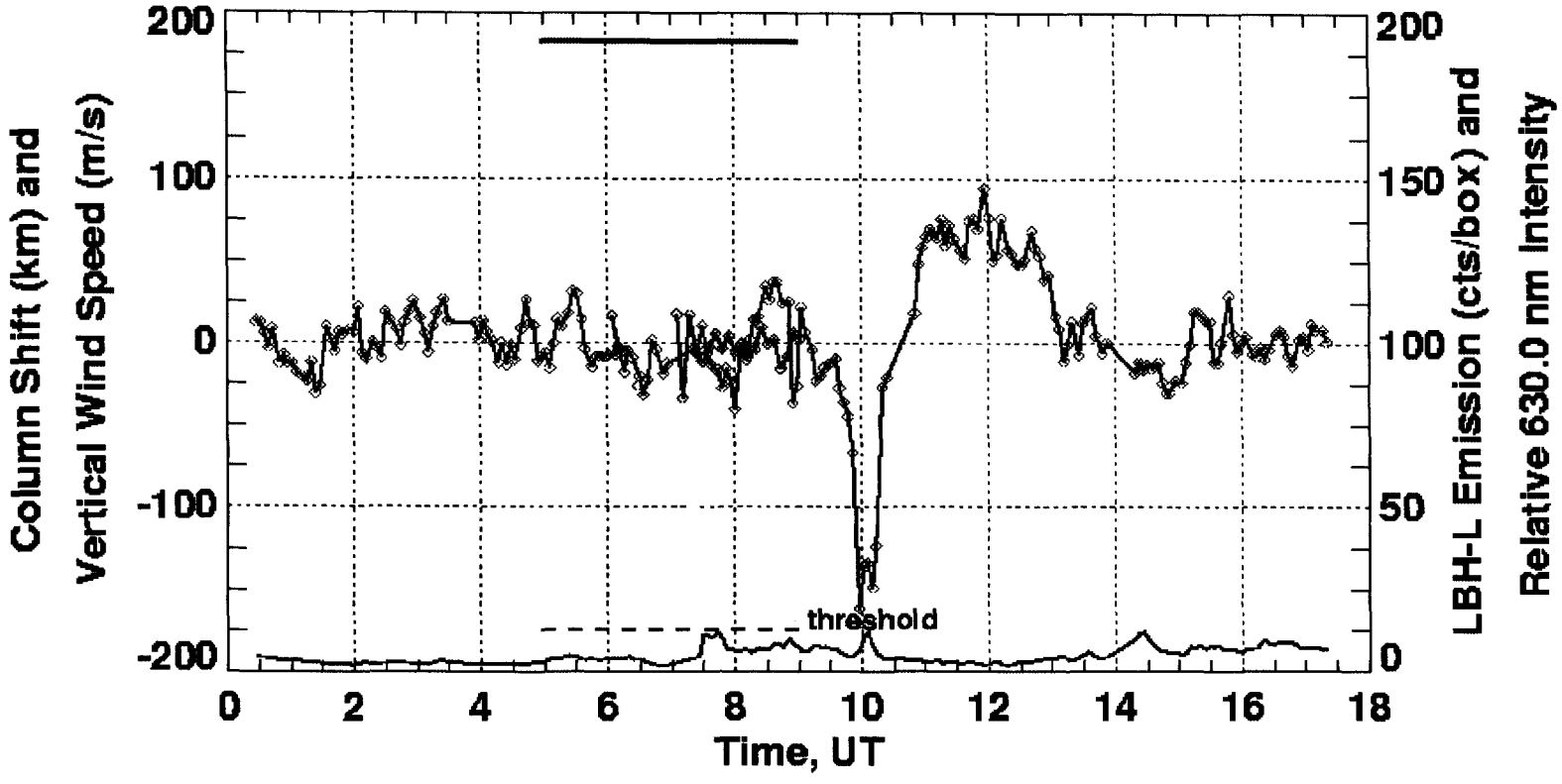

Figure 4.11. Upper-thermospheric vertical wind estimates and the UVI-inferred column shift measured over Inuvik, NT on Jan 4, 2001. Same layout as previous figures. See Table 4.4 for the geomagnetic and solar conditions for this night. A median shift of –12.4 km was subtracted from the column shift time series. The error in the wind measurements and column shift values is ±7-19 $m \cdot s^{-1}$ and ±25-34 km, respectively. See the text for discussion.

in Chapter 3, recalling that there was some question as to how well the drift-correction procedures eliminated the étalon's drift from the Doppler-shifted OI(630.0)-nm spectral information. The ~100 $m \cdot s^{-1}$ upward winds from 1100-1300 UT are questionable based on the drift-correction discussion in Chapter 3, but the concurrent 200% increase in the FPS OI(630.0)-nm relative intensity at the time of the 150 $m \cdot s^{-1}$ downward wind—which would bring O-rich air from high in the thermosphere to the OI(630.0)-nm emission altitudes of ~200-240 km—strongly supports the validity of the wind measurement. There is no UVI coverage at ~1000 UT, however, and the time series comparison of vertical winds and column shifts from this night yields no further insight into vertical wind-induced composition effects. The column shift data coverage is sparse, and in general, the relative variation in the column shifts do not follow the vertical wind variations. The maximum correlation coefficient of 0.33 occurs at a time lag of –83.0 min.

Figure 4.12 shows the Inuvik FPS upper-thermospheric vertical winds compared to the UVI-inferred column shift estimates over Inuvik (using the 15 counts·box^{-1} LBH-L brightness threshold) on January 26, 2001. The median value of –6.3 km of the entire January 26, 2001 column shift data set has been subtracted from the column shift time series. The uncertainty in the vertical wind measurements for this night is ±7-19 $m \cdot s^{-1}$ (see Figure 3.20 on page 143), and the error in the column shift values is ±21-38 km, compared to ±21-57 km for the column shift estimates using the 9.3 counts·box^{-1} LBH-L criterion.

The vertical winds over Inuvik on January 26, 2001 exhibit a number of features similar to the December 22, 2000 vertical winds. Several long-lived, significant vertical wind events occur, and in addition, the vertical wind time series exhibits considerable wavelike structure. At first glance, however, an obvious connection between the vertical winds and column shifts is not apparent. For example, there are no immediate or delayed impulsive column shifts associated with the significant vertical wind activity, like the intermediate-magnitude wind event examples identified previously in the January 3, 2001 and February 28, 2000 vertical wind and column shift data sets. However, as the cross correlation calculation for the January 26, 2001 data set indicates (see Table 4.5), the two time series are highly correlated. The maximum correlation coefficient of 0.73 occurs

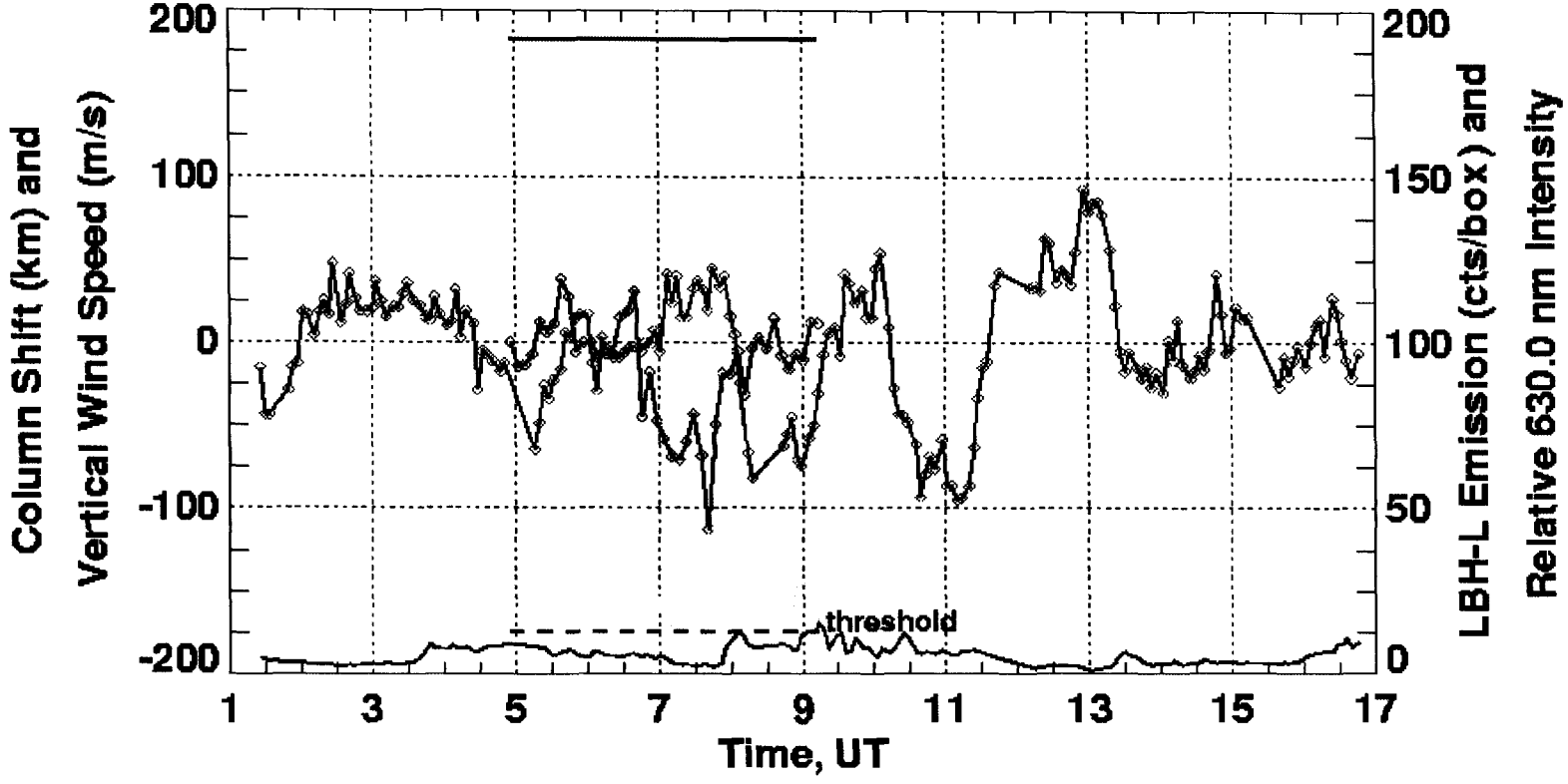

Figure 4.12. Upper-thermospheric vertical wind estimates and the UVI-inferred column shift measured over Inuvik, NT on Jan 26, 2001. Same layout as previous figures. See Table 4.4 for the geomagnetic and solar conditions for this night. A median shift of –6.3 km was subtracted from the column shift time series. The error in the wind measurements and column shift values is ±7-19 $m \cdot s^{-1}$ and ±21-38 km, respectively. See the text for discussion.

at a time lag of –77.9 min. Furthermore, Lomb-Scargle spectral analysis of the vertical wind time series identifies a significant 3.2 hr periodicity (see Appendix E) and a 3.4 hr periodicity in the column shift time series.

This analysis of the January 26, 2001 vertical wind and column shift time series appears to establish a definitive link between them, and a plausible explanation for high correlation between these two time series at the determined time lag is that a large-scale AGW of period ~3 hr propagating over Inuvik and launched by some distant source is inducing vertical wind and displacement perturbations at lower- and upper-thermospheric altitudes. Gravity wave sources (see Appendix B) generally have an altitude range of two to four scales heights [*Richmond*, 1978], and a sudden intense heating event at lower-thermospheric altitudes will perturb the scale height layer H via a temperature increase and subsequent pressure bulge [*Richmond*, 1978], launching a large-scale gravity wave. The lower-thermospheric perturbation will require considerable time to reach upper-thermospheric altitudes, recalling the example described in *Smith* [1998] and outlined in Section 1.1.7. The 78 min lag computed by the cross correlation calculation between the column shift and vertical wind time series (*i.e.*, the lower-thermospheric perturbation leads the upper-thermospheric perturbation by ~78 min) is not unreasonable. Based on the Lomb-Scargle spectral analysis of the OI(630.0)-nm vertical wind time series, an estimation of the gravity wave's amplitude (see Appendix E) is ~30 $m \cdot s^{-1}$ at the OI(630.0)-nm emission altitudes of ~200-240 km. This wave would have a smaller amplitude at lower altitudes, and a ~30 $m \cdot s^{-1}$ disturbance will require ~70 min to propagate from, for example, the lower thermosphere at 125 km (where the heating maximized) to the upper thermosphere at 250 km. Based on this speculation, the column shifts and vertical winds from January 26, 2001 offer a different perspective on the potential link between vertical wind activity, composition perturbations and gravity wave oscillations. This example is also consistent with a recent study by *Innis and Conde* [2002] using AGW theory which examined several large-scale wavelike events identified in vertical and horizontal wind, temperature and composition measurements obtained with the DE2 Wind and Temperature Spectrometer (WATS) and Neutral Atmosphere Composition Spectrometer

(NACS) instruments. The study found that the wavelike perturbations identified in the different data sets were consistent with acoustic-gravity wave oscillations.

The last two column shift data sets to be discussed here were acquired during nights of high geomagnetic activity, March 20, 2001 and November 28, 2000. The energy flux, characteristic energy, modeled OI(135.6)-nm auroral emission, and column shifts were inferred from UVI observations using the high-A_P model reference curves (see Figures 3.26a-b on pages 159-161), and as was discussed earlier, the column shift data from these nights were more perplexing based on their respective mean and median values and standard deviations (see Table 4.3) compared to the low-A_P data sets. Nonetheless, the variation in the column shift values relative to some zero-reference level or to column shift values prior to a significant vertical wind event may still be valid.

Figures 4.13 and 4.14 show the CRL-FPS OI(630.0)-nm upper- and OI(557.7)-nm lower-thermospheric vertical winds, respectively, compared to the UVI-inferred column shift estimates over Poker Flat (using the 15 counts·box^{-1} LBH-L brightness threshold) for the night of March 20, 2001. The CRL-FPS observations provided the opportunity to compare column shift data to vertical winds at a different auroral-zone latitude and from two altitude ranges, recalling that the OI(557.7)-nm auroral emission emanates from ~100-140 km. The median value of –46.0 km of the entire March 20, 2001 column shift data set has been subtracted from the column shift time series (see Table 4.3). The uncertainty in the vertical wind measurements for this night is ±2-3 m·s^{-1} for the upper-thermospheric data and ±2-10 m·s^{-1} for the lower-thermospheric data [*Ishii et al.*, 2001]. The application of the 15 counts·box^{-1} LBH-L brightness threshold to the March 20, 2001 column shift data did not significantly reduce the uncertainty in the column shift values over Poker Flat (±45-98 km) compared to the 9.3 counts·box^{-1} LBH-L criterion, but, as was noted earlier in Table 4.3, did significantly reduce the data set's standard deviation from the highly-unreasonable value of SD_{clm} = 828 km to a more realistic value of SD_{clm} = 104 km.

Geomagnetic activity on March 20, 2001 was very active, as the A_P index of 74 indicates, and the CRL-FPS upper- and lower-thermospheric observations both exhibit significant vertical wind activity. Examining first the upper-thermospheric wind data in

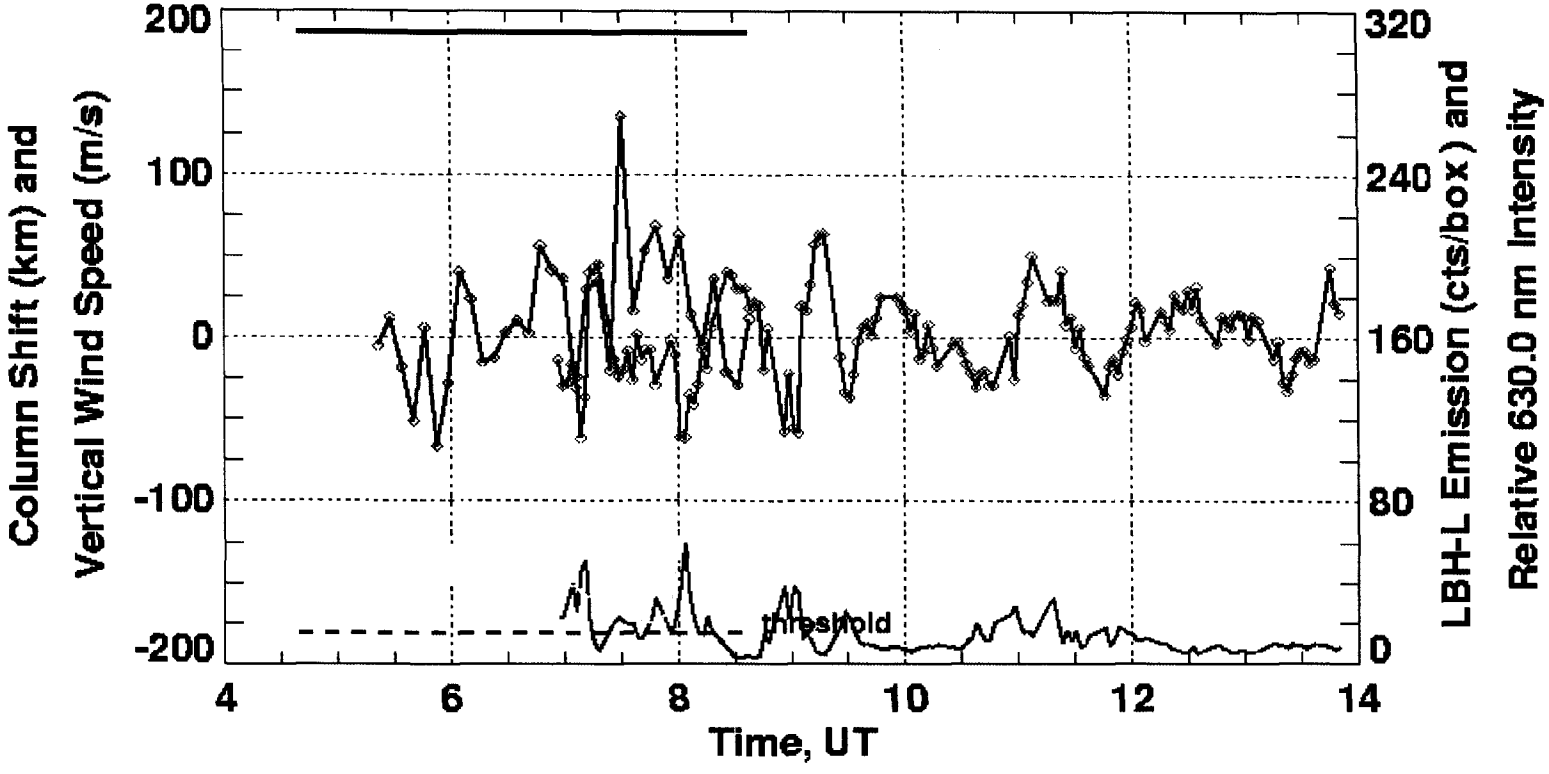

Figure 4.13. Upper-thermospheric vertical wind estimates and the UVI-inferred column shift measured over Poker Flat, AK on Mar 20, 2001. The wind data were obtained with the CRL-FPS [*Ishii et al.*, 1997]. See Table 4.4 for the geomagnetic and solar conditions for this night. A median shift of –46.0 km was subtracted from the column shift time series. The UVI data collected on this night was analyzed using the high-A_P model. The error in the wind measurements and column shift values is (2-3 $m \cdot s^{-1}$ and ±45-98 km, respectively. See the text for discussion.

Figure 4.13, one wind event in particular stands out, from ~0700-0730 UT. This is an example of an immediate composition effect at middle- to upper-thermospheric altitudes associated with the observed vertical winds, implying that the winds had prevailed for some time as they moved into the CRL-FPS field of view and had already modified composition along the thermospheric column. The CRL-FPS had just begun observations at ~0700 UT and was measuring downward wind speeds of –15-30 $m \cdot s^{-1}$ before measuring a large-magnitude downward wind of –60 $m \cdot s^{-1}$. Concurrently, the CRL-FPS measured a ~100% increase in the OI(630.0)-nm relative intensity compared with the previous value, confirming that the thermospheric column which the CRL-FPS was observing was already rich in O due to a prevailing –30-60 $m \cdot s^{-1}$ wind that had transported O-rich air from high in the thermosphere to relevant OI(630.0)-nm emission altitudes. Immediately following the downward wind was a short period of upward winds reaching speeds of +45 $m \cdot s^{-1}$. A concurrent 300% decrease in the OI(630.0)-nm relative intensity compared with the previous value confirmed that the thermospheric column the CRL-FPS was now observing was O-depleted due to a prevailing +45 $m \cdot s^{-1}$ upward wind that had transported N_2 from below to relevant OI(630.0)-nm emission altitudes. This example is likely illustrative of adjacent, highly-localized upward- and downward-moving air columns due to direct energetic forcing at middle- to upper-thermospheric altitudes moving through the FPS field of view. The precipitation's characteristic energy during this time frame was 0.5-2.2 keV, indicating that significant energy was being deposited at middle- to upper-thermospheric altitudes, and the energy flux was 2.7-4.2 $mW \cdot m^{-2}$, perhaps high enough to induce upward wind speeds of ~45 $m \cdot s^{-1}$ at upper-thermospheric altitudes but not lower.

The relative variation in the column shift data from the ~0630-0730 UT time period confirms these conclusions. From ~0630-0700 UT, the column shifts hovered around +40 km (relative to the zero-reference level). With the onset of the –60 $m \cdot s^{-1}$ downward wind, the column shift immediately decreased to a value of –30 km. After this, when the ~45 $m \cdot s^{-1}$ upward winds prevailed, the column shift value returned to a pre-downward wind value of about +30 km. This column shift behavior indicates that the vertical wind had prevailed for some time and had already modified composition in the thermospheric

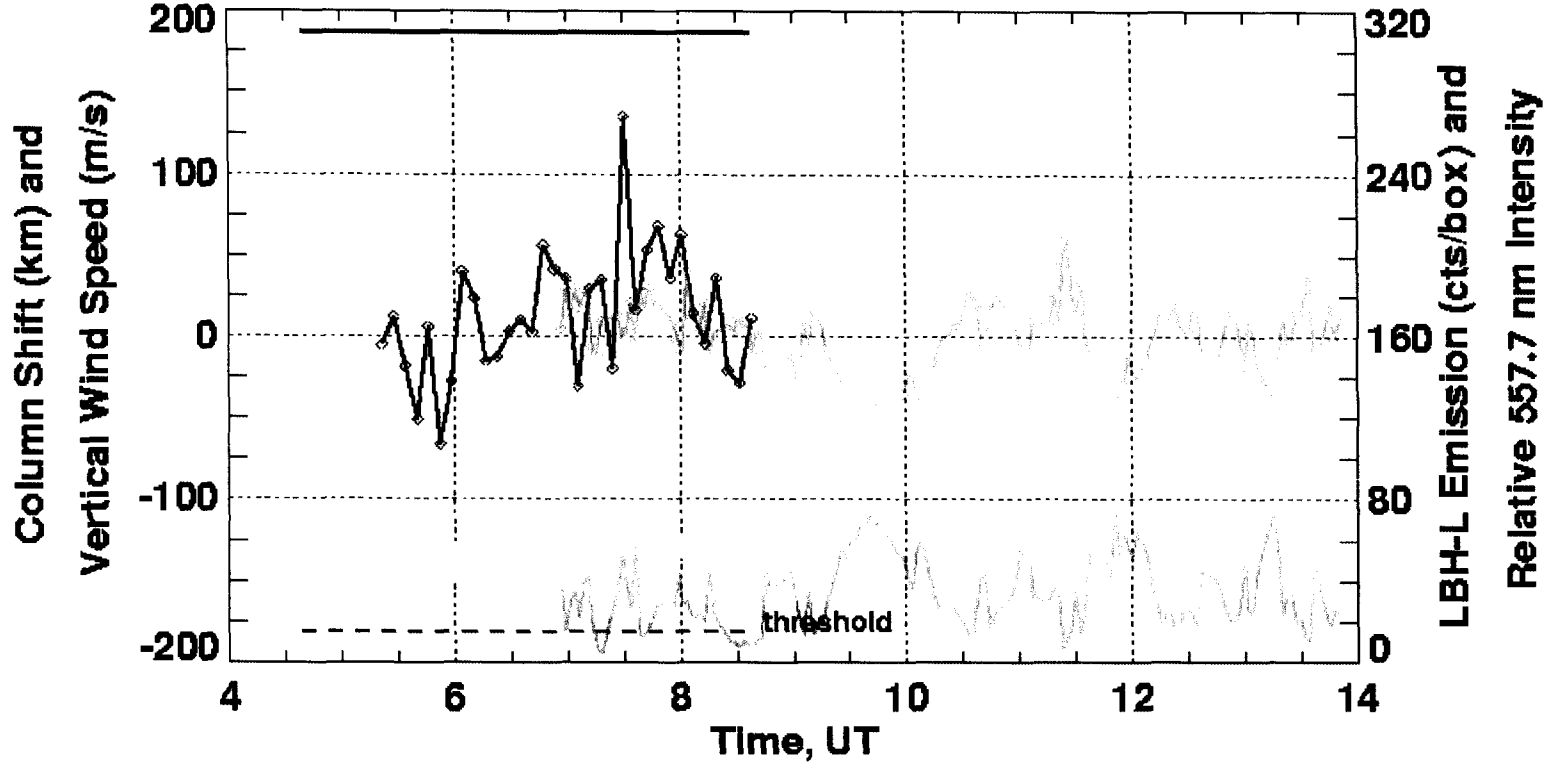

Figure 4.14. Lower-thermospheric vertical wind estimates and the UVI-inferred column shift measured over Poker Flat, AK on Mar 20, 2001. The wind data were obtained with the CRL-FPS [*Ishii et al.*, 1997]. The OI(557.7)-nm relative intensity is shown in green at the bottom of the graph. See Table 4.4 for the geomagnetic and solar conditions for this night. A median shift of –46.0 km was subtracted from the column shift time series. The UVI data collected on this night was analyzed using the high-A_P model. The error in the wind measurements and column shift values is (2-10 $m \cdot s^{-1}$ and ±45-98 km, respectively. See the text for discussion.

column. For example, the short life of the –60 $m \cdot s^{-1}$ wind as measured over Poker Flat is clearly not long enough to induce a relative downward shift of +40 km to –30 km = –70 km. However, the +40 km column shift values (relative to the zero-reference level) can be considered indicative of the thermosphere's state prevailing over Poker Flat before the adjacent downward- and upward-moving air columns move overhead. When the downward wind field (which had prevailed for some time) moves into the FPS field of view, the composition in this thermospheric column has already been modified by the downward wind, which the relative column shift of –70 km and ~100% increase in the OI(630.0)-nm relative intensity confirm. When the upward wind field moves overhead, the column shifts return to the pre-downward wind values of +30 km. The lifetime of the downward and upward wind fields can also be estimated using this information. If a –60 $m \cdot s^{-1}$ wind has produced a relative column shift of –70 km, then the downward wind field had prevailed for t = (70,000 m)/(60 $m \cdot s^{-1}$) $\approx$ 20 min. Likewise, the +45 $m \cdot s^{-1}$ wind produced a relative column shift of +60 km, and thus the upward wind field had prevailed for $t \approx$ 22 min. Another example of a short-lived –60 $m \cdot s^{-1}$ wind event occurs at ~0800 UT, and this also appears to be a composition-variation example similar to the previous one. The concurrent ~150% increase in the OI(630.0)-nm relative intensity and relative decrease in the column shift from +68 km to –4 km confirms this. The OI(630.0)-nm relative intensity decreases again after the downward wind field moves out of the FPS field of view, and the column shift also recovers to a pre-downward wind value.

Admittedly, there are examples where the column shift variations do not match the wind activity. For example, after 0730 UT, the wind speeds decrease from +40 $m \cdot s^{-1}$ to ~0 $m \cdot s^{-1}$. The column shift decreases to ~0 km concurrently, but from ~0730-0800 UT, while the winds continue to hover at ~0 $m \cdot s^{-1}$, the column shifts increase again. On a geomagnetically-active day like March 20, 2001, however, other thermospheric processes will certainly account for some column shift variation. The cross correlation calculation between the upper-thermospheric vertical wind time series and the column shift time series is inconclusive, and the maximum correlation coefficient of 0.48 occurs at a time lag of 18.4 min. In addition, the cross correlation calculation between the lower-

thermospheric vertical wind time series and column shift time series is also inconclusive, with a maximum correlation coefficient of 0.54 occurring at a time lag of 18.4 min. There also do not appear to be any definitive lower-thermospheric, vertical wind-induced composition perturbations in the column shift data. However, this may be expected, since a lower- to upper-thermospheric vertical wind-induced composition perturbation requires considerably more energy input than that which occurs during the OI(630.0)-nm vertical wind-induced composition perturbation examples discussed above. The time frame when one could perhaps investigate lower-thermospheric composition perturbations due to heating and vertical winds is 0600-0700 UT. During this time frame, the characteristic energy of the precipitation over Poker Flat was 2.7-4.4 keV, indicating that most of the auroral-related energy deposition and ionization was at lower- to middle-thermospheric altitudes, which would enhance E-region ionospheric conductances and thus increase the Joule heating rate. In addition, the LBH-L brightness reached fairly high values of ~150 counts·box^{-1} (energy flux values of ~15 mW·m^{-2}) during this time frame. Although this energy input is not enough on its own to generate intermediate- to large-magnitude vertical winds at lower-to middle-thermospheric altitudes based on the calculations of Equation 1.7, the enhanced Joule heating rate combined with the increased energy flux values may have resulted in significant lower-thermospheric vertical wind activity. This cannot be confirmed, however, since the CRL-FPS had not yet begun observations.

Figure 4.15 shows the Inuvik FPS upper-thermospheric vertical winds compared to the UVI-inferred column shifts over Inuvik (using the 15 counts·box^{-1} LBH-L brightness threshold) on November 28, 2000. The median value of –48.1 km of the November 28, 2000 column shift data set has been subtracted from the column shift time series (see Table 4.3). The uncertainty in the vertical wind measurements is generally ±7-20 m·s^{-1}, except for early and late in the night when the errors reached ±25-38 m·s^{-1} (see Figure 3.22 on page 146). Similarly to the March 20, 2001 column shift data set, the application of the 15 counts·box^{-1} LBH-L brightness threshold to the November 28, 2000 column shift data did not significantly reduce the error in the column shift values over Poker Flat (±58-80 km) compared to the 9.3 counts·box^{-1} LBH-L criterion (±58-88 km), but, as noted

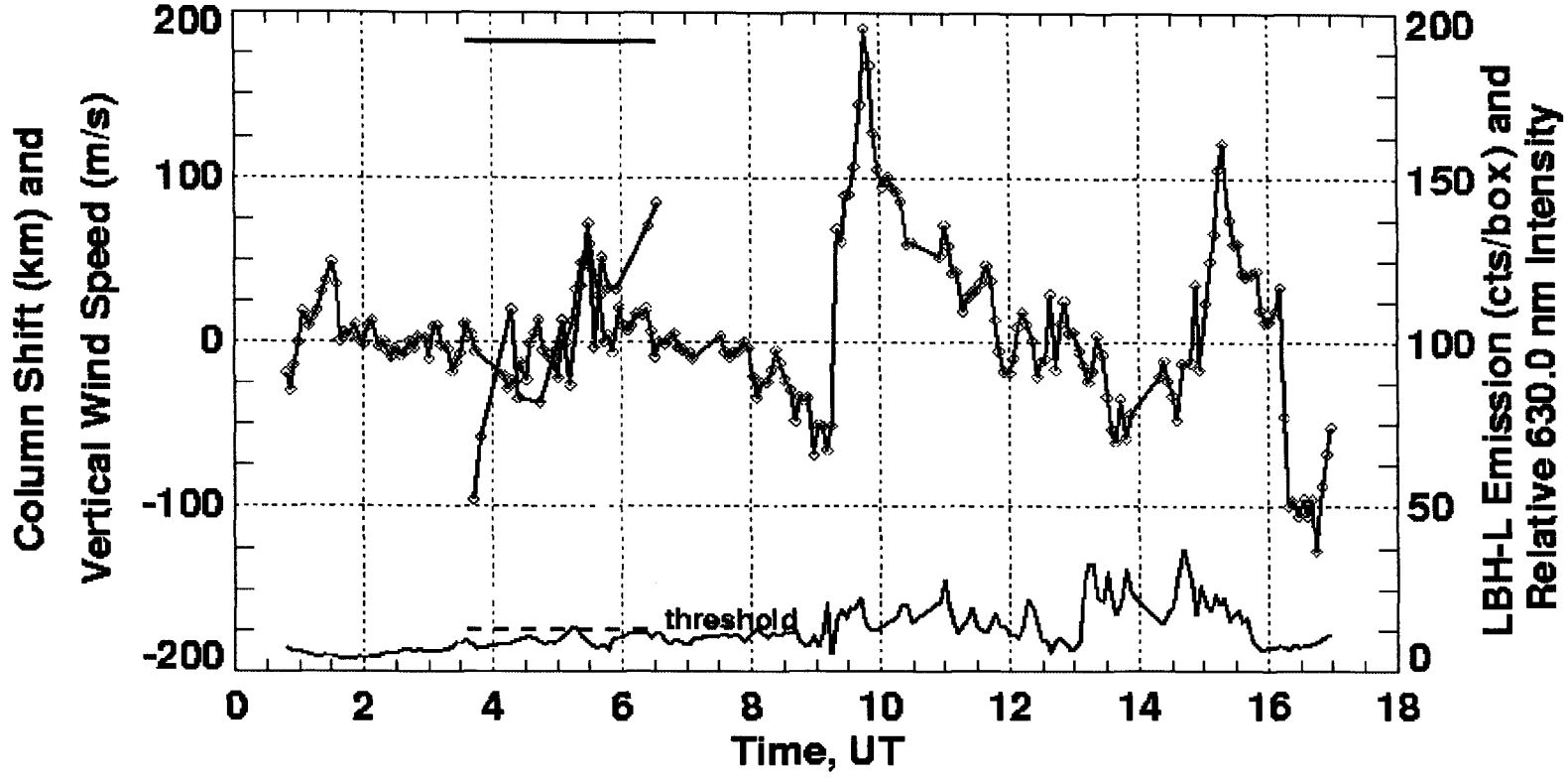

Figure 4.15. Upper-thermospheric vertical wind estimates and the UVI-inferred column shift measured over Inuvik, NT on Nov 28, 2000. See Table 4.4 for the geomagnetic and solar conditions for this night. A median shift of –48.1 km was subtracted from the column shift time series. The UVI data collected on this night was analyzed using the high A_P model. The error in the wind measurements and column shift values is ±7-38 $m \cdot s^{-1}$ and (58-80 km, respectively. See the text for discussion.

earlier in Table 4.3, did significantly reduce the data set's standard deviation from a value of SD_{clm} = 234.2 km to a more realistic value of SD_{clm} = 91.6 km.

The November 28, 2000 vertical winds were obtained during a 4-day period when geomagnetic activity was very intense. The A_P index ranged from 67 late November 26 to 94 early on the 27th to 48 on the 28th to 111 early on the 29th, and consequently, the highly-variable and significant vertical wind events that occur on the 28th over Inuvik are not surprising. The very large-magnitude upward wind of ~200 m·s^{-1} that occurs at ~1000 UT is unusual but not unprecedented [*Innis et al.*, 1999], and although there is no UVI coverage during this particular vertical wind event, there is UVI coverage during a large-magnitude upward wind event that occurs from 0515-0545 UT. Otherwise, UVI coverage was minimal this night, and the column shift variations that occur separately from the 0515-0545 UT time frame do not correlate with the vertical wind observations. The maximum correlation coefficient of 0.41 occurs at a time lag of 10.4 min.

However, the 0515-0545 UT upward wind event is another example of an immediate or nearly-immediate, middle- to upper-thermospheric composition effect associated with the observed vertical winds, similarly to the March 20, 2001 examples discussed above. Here, the upward wind field had likely prevailed for some time before moving into the Inuvik FPS field of view, and had already modified composition to some extent in the thermospheric columns prevailing over Inuvik during the wind event. This conclusion is supported by the characteristic energy and energy flux values prevailing over Inuvik during the time interval, the relative decrease in the Inuvik FPS OI(630.0)-nm intensity, and the concurrent variations in the column shift data.

From 0515-0530 UT, the Inuvik FPS measured ~30-50 m·s^{-1} upward winds, and at 0530 UT, the wind peaked at +60 m·s^{-1}. The winds persisted until 0545 UT, with speeds of +30-40 m·s^{-1}, and finally decreased to ~5 m·s^{-1} after 0545 UT, presumably due to the wind field moving out of the FPS field of view. The characteristic energy of the precipitation prevailing over Inuvik during this time period was generally 0.7-2.1 keV, with some of the boxes in the vicinity of Inuvik—recall, the 1° latitude × 3° longitude regions on the 2-D maps—exhibiting values of <<0.7 keV. This indicates that a

significant portion of the energy deposition was occurring at middle- to upper-thermospheric altitudes. Furthermore, the energy flux values of 2.3-3.9 $mW \cdot m^{-2}$ were high enough to perhaps induce intermediate- to large-magnitude vertical winds at middle- to upper-thermospheric altitudes but not lower.

With the initial onset of the upward wind, the Inuvik FPS OI(630.0)-nm relative intensity decreased by 50% and further decreased by 100% by 0530 UT relative to pre-wind-event values. The OI(630.0)-nm relative intensity remained at this reduced level until the upward wind subsided, and nearly recovered to pre-wind-event values after the wind field moved out of the FPS field of view. The variations in the OI(630.0)-nm relative intensity during the upward wind event support the wind measurements; *i.e.*, an upward wind produced at middle- to upper-thermospheric altitudes was transporting O-depleted (N_2-rich) air along the thermospheric column from lower in the thermosphere to relevant OI(630.0)-nm emission altitudes.

The variations in the column shifts over Inuvik further support this conclusion. The column shift value prevailing over Inuvik at 0511 UT (before the upward wind event began) was approximately –25 km (relative to the zero-reference level). By 0523 UT, the column shift had increased dramatically to +35 km, and by 0529 UT, the column shift had increased to +72 km. There was a large reduction in the column shift to –3 km at 0535 UT, but the column shift again increased to +50 km by 0541 UT, remaining at about +30 km for another 10 min. Clearly, the upward wind had not prevailed long enough over Inuvik for it to induce a –25 km to +35 km = +60 km column shift increase over Inuvik from 0511 UT to 0523 UT. Thus, the upward wind field must have persisted for some time before moving into the Inuvik FPS field of view and had already modified thermospheric composition to some extent. The –25 km column shift prevailing over Inuvik (relative to the zero column-shift reference) prior to the onset of the upward wind event was likely indicative of the thermosphere's state, and as the wind field moved into the FPS field of view, the new column shift value of +35 km was indicative of the thermosphere's state in that particular thermospheric column; *i.e.*, the +35 km column shift is indicative of the upward wind's time-integrated effect on the thermospheric

column, implying that the upward wind had prevailed for some time and had already modified the column's composition. Assuming that the average wind speed from 0511-0523 UT was +40 $m \cdot s^{-1}$, the initial +60 km relative column shift would require that the upward wind field had already prevailed for t = (60,000 m)/(40 $m \cdot s^{-1}$) = 25 min. The initial decrease in the FPS OI(630.0)-nm relative intensity of 50% at the onset of the upward wind event also confirms that the vertical wind field had prevailed for some time and had already modified composition along the thermospheric column. The continued decrease in the OI(630.0)-nm relative intensity and further increase in the column shift values until the vertical wind's peak magnitude was reached supports the supposition that indeed, composition along the thermospheric column had been and was being modified by the vertical wind.

There is one column shift value over Inuvik during the upward wind event that does not support the above conclusions. However, the –3 km column shift measurement at 0535 UT can be explained through a closer examination of the 2-D column shift maps from this time. Figures 4.16a-b show the column shift maps at the times of 0529 UT and 0535 UT, respectively, when the column shift over Inuvik was estimated to be +72 km and –3 km, respectively. Before examining the –3 km column shift measurement in more detail, however, a discussion of these column shift maps is essential. These column shift maps were produced using the 15 counts·box^{-1} LBH-L brightness threshold. In addition, these maps present the absolute column shift values; *i.e.*, the raw values which were inferred directly from the observed-to-modeled OI(135.6)-nm brightness comparisons. Figures 4.16a-b have not been median-corrected like the January 3, 2001, 1139 UT example in Figure 4.1b above or the column shift time series. Recall that the median value of the entire November 28, 2000 column shift data set is –48.1 km, which was subtracted from the 3° latitude × 9° longitude, 9-box, spatially-averaged column shift values over Inuvik in the Novemeber 28, 2000 time series. The column shift values at 0529 UT and 0535 UT over Inuvik after the median correction are +72 km and –3 km, respectively, and thus, the raw column shift values determined from the initial 9-box spatial averaging, before the median correction, are +24 km and –51 km, respectively.

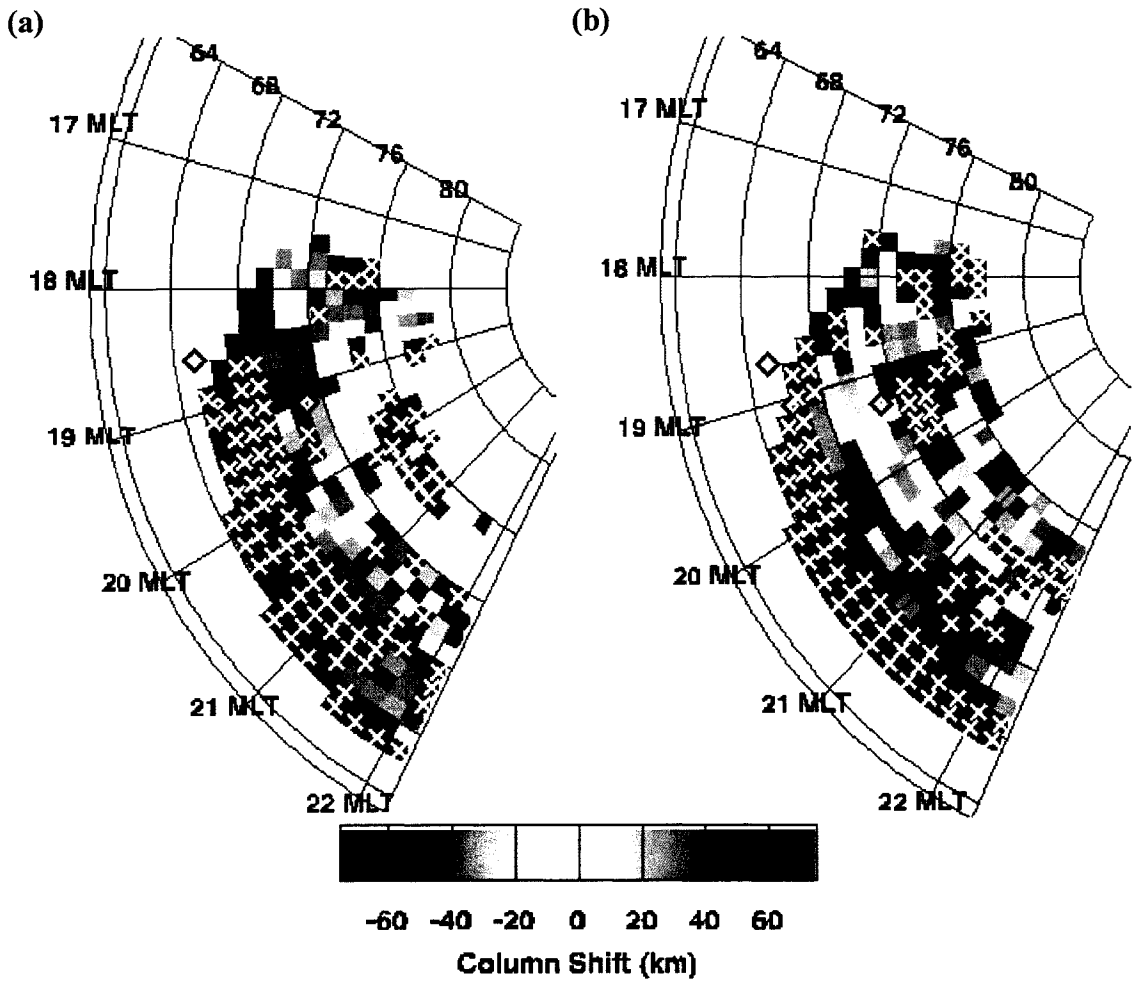

Figure 4.16. 2-D maps of the column shift at 0529 UT and 0535 UT on Nov 28, 2000. **(a)** The column shifts at 0529 UT. **(b)** The column shifts at 0535 UT. These column shift maps were produced using the 15 counts·box^{-1} LBH-L brightness threshold, like the Jan 3, 2001 and Feb 28, 2000 examples shown in Figures 3.33a-b. Thus, the *X*ed-out red boxes indicate upward column shifts which exceed 75 km, and the *X*ed-out blue boxes indicate downward column shifts which are less than –75 km. Also note that these maps have not been median-corrected. See the text for discussion. The large number of *X*ed-out blue boxes are a further indication of the problems that were encountered with the modeling of the OI(135.6)-nm auroral emission.

The large number of *X*ed-out blue boxes that are apparent here in Figures 4.16a-b along the equatorward and poleward edges of the column shift maps are pervasive throughout the November 28, 2000 and March 20, 2001 column shift data sets. These generally-unrealistic column shift values remained in the data sets even with the

application of the 15 counts·box^{-1} LBH-L brightness threshold to the data sets, and are responsible for the highly-biased negative mean and median values and the larger standard deviation of the two data sets compared with the low-A_P model data sets (see Table 4.3). The two high-A_P data sets certainly were more perplexing in their evaluation than the low-A_P data sets because of their statistical characteristics and the continued pervasiveness of *X*ed-out blue boxes, but what is apparent from Figures 4.16a-b and the mean and median values of the high-A_P data sets is that under some circumstances, the modeled OI(135.6)-nm auroral emission is grossly underestimated.

There is a plausible explanation as to why the high-A_P auroral model sometimes grossly underestimates the OI(135.6)-nm auroral brightness, like the column shifts along the equatorward and poleward edges of Figures 4.16a-b indicate, and under other circumstances, will still correctly estimate the brightness, like the swathe of column shifts between ~68-72° and ~1800-2100 MLT apparently indicate. The column shift values in the ~68-72°, ~1800-2100 MLT region exhibit similar characteristics as the column shifts in the February 28, 2000 0552 UT example in Figure 3.33b on page 185. The column shifts here generally fall into the range expected for height displacements due to vertical wind activity, as the 0515-0545 UT example discussed above validates. Furthermore, the general pattern of column shifts from box to box through this ~68-72°, ~1800-2100 MLT region is indicative of adjacent upward- and downward-moving air columns due to the energetic forcing, as was discussed concerning Figure 3.33b, with pockets of red and blue boxes adjacent to one another. Thus, throughout this region, the column shift map apparently functions well as an indicator of composition variations associated with the aurora, indicating that the high-A_P model does indeed work under certain circumstances. However, the column shifts on the edges of the maps are clearly not valid.

The most reasonable explanation for these highly-negative column shifts pervading the November 28, 2000 and March 20, 2001 data sets is that these column shifts are associated with boxes which exhibit high characteristic energies ($\gtrsim$4 keV). For example, Figures 4.17a-d show the energy flux, characteristic energy, and observed and modeled OI(135.6)-nm auroral brightnesses at 0535 UT, respectively. Examination of Figure 4.17a

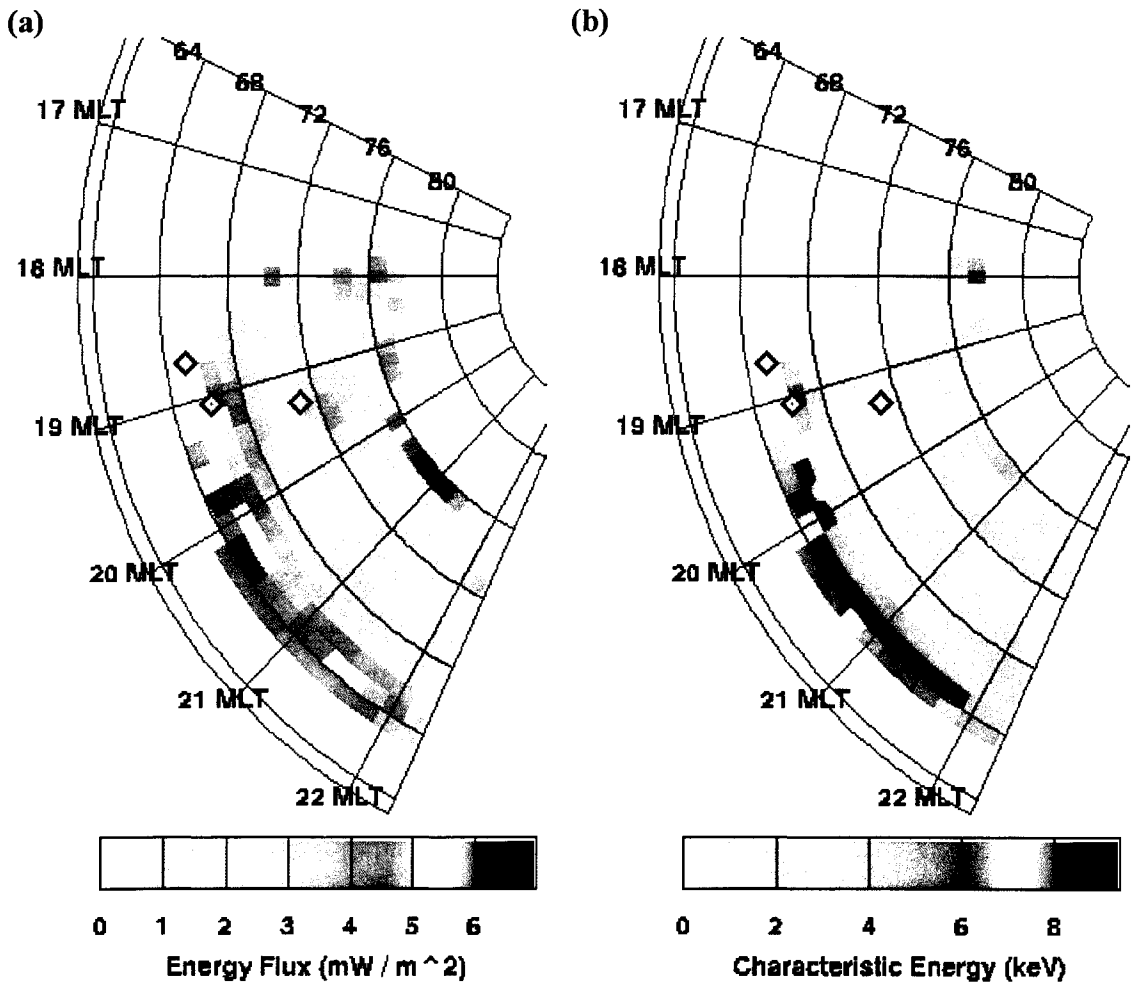

Figure 4.17. 2-D maps of energy flux, characteristic energy, observed and modeled OI(135.6)-nm auroral brightnesses at 0535 UT on Nov 28, 2000. **(a)** The energy flux at 0535 UT. **(b)** The characteristic energy at 0535 UT. See the text for discussion.

reveals that fairly significant energy flux of ~4-7 $mW \cdot m^{-2}$ prevailed along the equatorward edge of the map from ~1900-2200 MLT and ~64-68°. However, this energy flux was associated with precipitation of high characteristic energy, $\gtrsim$4 keV, which is revealed in Figure 4.17b and indicates that the most significant energy deposition and auroral excitation occurred at lower- to middle-thermospheric altitudes (~100-180 km) in the ~64-68°, ~1900-2200 MLT region. The UVI-observed OI(135.6)-nm auroral brightness in this region is fairly signficant, reaching values of ~15-25 $counts \cdot box^{-1}$, as Figure 4.17c indicates, but the high-A_P model predicts that the OI(135.6)-nm auroral brightness should

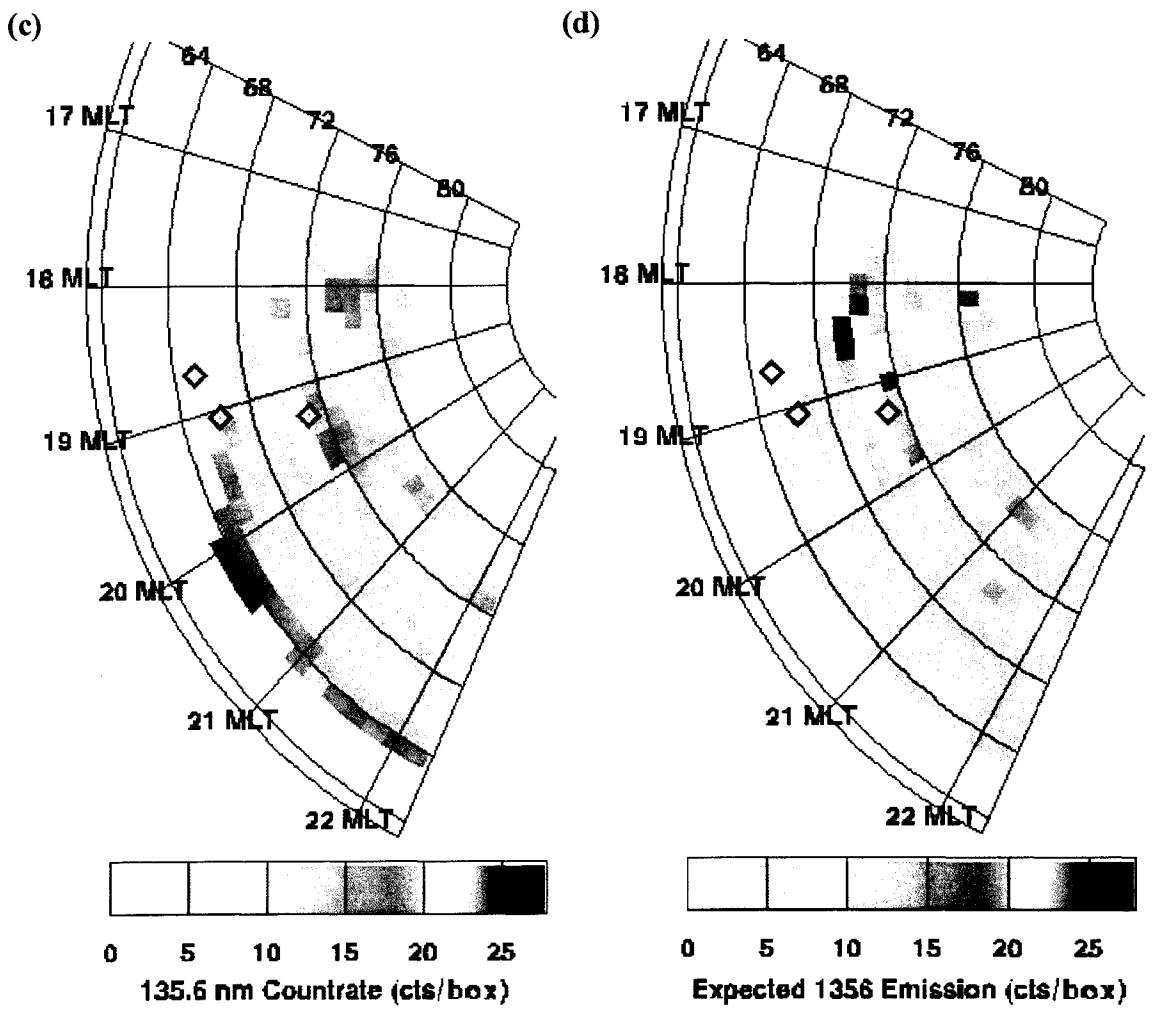

Figure 4.17 cont. 2-D maps of energy flux, characteristic energy, observed and modeled OI(135.6)-nm auroral brightnesses at 0535 UT on Nov 28, 2000. **(c)** The observed OI(135.6)-nm brightness at 0535 UT. **(d)** The modeled OI(135.6)-nm brightness at 0535 UT. See the text for discussion.

be very low, ~5 counts·box^{-1}, based on the energy flux and characteristic energy values prevailing in this region, a percent difference of 65-80%. One may expect that absorption of the OI(135.6)-nm emission by O_2 above the ~100-120 km peak emission altitude will occur in the real thermosphere during high characteristic energy precipitation events, which would explain the reduced OI(135.6)-nm auroral brightness that is predicted by the model. Nonetheless, the observed OI(135.6)-nm brightness is much larger than the model prediction, and consequently, the highly-negative downward column shifts in this region

are a direct consequence of the high-A_P model's poor estimation of the OI(135.6)-nm auroral brightness relative to the observed OI(135.6)-nm brightness, which was the case throughout both high-A_P column shift data sets. The only plausible explanation for this poor estimation of the OI(135.6)-nm auroral brightness at high characteristic energies is that the MSIS-90 neutral model significantly underestimates the O density at low altitudes for high geomagnetic model parameters, and furthermore, that absorption of the OI(135.6)-nm auroral emission by O_2 residing above the peak emission altitude during high characteristic energy events is significantly overestimated.

Recall from Table 3.3 on page 159 that the high-A_P model used an A_P magnetic index of 126. This value is indicative of highly-disturbed geomagnetic activity, and consequently, thermospheric dynamics and energetics will be strongly affected by high-latitude processes. A high-A_P, hot thermosphere will be significantly expanded, and pressure levels will reside at higher altitudes (relative to a low-A_P, cooler thermosphere). Consequently, the presumption is that in general less atomic oxygen will reside at low altitudes and more molecular oxygen at high altitudes in a high-A_P thermosphere. For example, MSIS-90 predicts that at 115 km altitude, the atomic oxygen number density in the low-A_P model is 1.399×10^{11} cm^{-3} and 7.460×10^{10} cm^{-3} in the high-A_P model. This is a difference of 47%, and clearly, the high-A_P model would predict a lower OI(135.6)-nm auroral brightness than the low-A_P model at high characteristic energies. Futhermore, MSIS-90 predicts that at 150 km altitude, the O_2 number density is 3.180×10^9 cm^{-3} in the low-A_P model and 6.948×10^9 cm^{-3} in the high-A_P model, a difference of 54%. Clearly, high-A_P model predictions of auroral emissions that reside in Schumann-Runge (SR) continuum, ~130-175 nm, will be significantly affected by O_2 number density estimations in MSIS-90. This is certainly the case here in the November 28, 2000 and March 20, 2001 data sets, and it is likely that MSIS-90 does not estimate the O number density well at low thermospheric altitudes and the O_2 number density well at middle-to-upper thermospheric altitudes for disturbed geomagnetic conditions, which resulted in the large number of highly-negative column shifts associated with high characteristic energy precipitation that pervade the November 28, 2000 and March 20, 2001 data sets.

These modeling issues aside, the high-A_P model does perform adequately under certain circumstances in inferring column shifts, of which the swathe of intermixed red and blue column shifts from ~68-72° and ~1800-2100 MLT in Figures 4.16a-b and the 0515-0545 UT vertical wind-induced column shifts are an example. The precipitation's characteristic energy is soft to moderate (<1-2 keV) under these circumstances, and the column shifts are thus representative of a middle- to upper-thermospheric composition perturbation. In fact, the soft precipitation that prevails in the ~68-72°, ~1800-2100 MLT region explains why a –3 km column shift was estimated over Inuvik at 0535 UT.

The –3 km column shift measured at 0535 UT, when the vertical wind had reached its peak value of +60 $m \cdot s^{-1}$, does not corroborate the other column shift values that prevailed over Inuvik during the 0515-0545 UT upward wind event. However, examination of Figure 4.16b reveals that the column shifts just south of Inuvik along a longitudinally-extended region from ~1830-2000 MLT had not been estimated in the 0535 UT map. This is because the characteristic energies determined by the auroral model output along this longitudinally-extended region were <0.1 keV. Recall from Chapter 3 that the electron transport model was run at nine characteristic energies, with a range of 0.1-10 keV. Inferred characteristic energies extending outside of this range are discarded throughout the rest of the analysis because the values have been extrapolated rather than interpolated. Nonetheless, UVI observations indicated that aurora prevailed along this longitudinally-extended region. The LBH-L brightness in this region was ~20-40 $counts \cdot box^{-1}$, while the LBH-S brightness was ~60-120 $counts \cdot box^{-1}$. Thus, the ratio of LBH-S to LBH-L was ~3, which does not fall within the range of calculated ratios as a function of characteristic energy for the high-A_P model, as seen on page 161 in Figure 3.26b and shown again below as Figure 4.18. The characteristic energies that would be inferred from these ratios fall below 0.1 keV using the high-A_P model reference curves (in fact, also using the low-A_P model reference curves), and consequently would be discarded. Thus, it is reasonable to assume that very soft precipitation, <0.1 keV, prevailed along this longitudinally-extended region just south of Inuvik. In addition, examination of Figure 4.17c reveals that soft precipitation of <<1 keV prevailed

throughout the ~68-72°, ~1800-2100 MLT region, which would result in significant energy deposition at upper-thermospheric altitudes, and in all likelihood, upward winds and upward column shifts. The Inuvik FPS vertical wind measurements confirm this, and furthermore, the 0529 UT column shift map in Figure 4.16b reveals that significant upward column shifts did prevail six minutes earlier along this longitudinally-extended region just south of Inuvik. Thus, it is reasonable to assume that the –3 km spatially-averaged column shift value over Inuvik at 0535 UT is in error and is likely closer to the value of +50 km at 0541 UT or +72 km at 0529 UT.

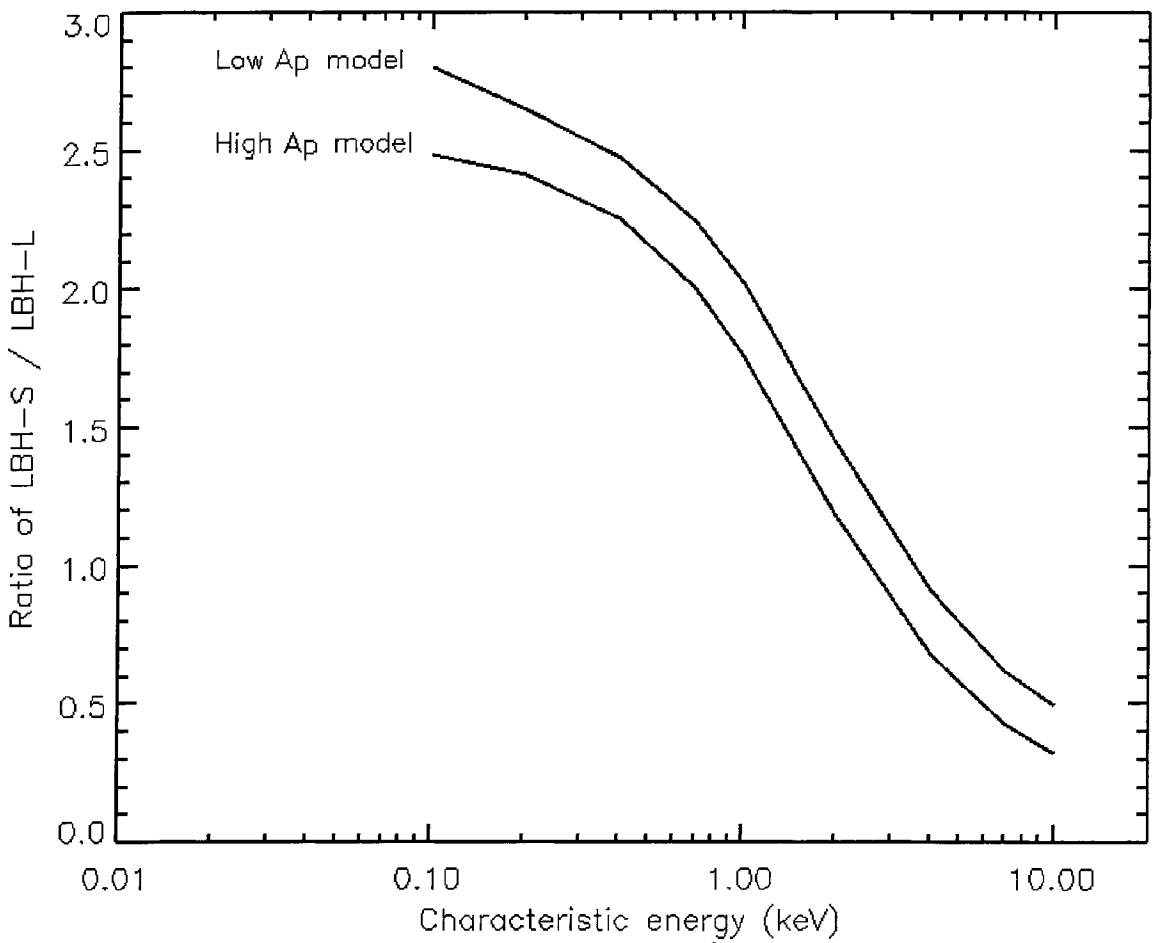

Figure 4.18. UVI instrument response to 1 $mW \cdot m^{-2}$ of energy flux as a function of characteristic energy for two levels of geomagnetic and solar activity. The ratio of the LBH-S/LBH-L modeled brightnesses as a function of characteristic energy for 1 $mW \cdot m^{-2}$ of electron precipitation. Shown originally on page 161 as Figure 3.26b.

This section has presented seven time series comparisons of FPS OI(630.0)-nm upper-thermospheric vertical wind measurements and column shift estimates over Inuvik, NT, Canada and one time series comparison of column shifts to the CRL-FPS OI(630.0)-nm upper-thermospheric and OI(557.7)-nm lower-thermospheric vertical winds over Poker Flat, AK. Statistical characteristics of the column shift data sets were presented using both a weaker- and brighter-aurora criterion, which both illustrated the inherent difficulties that accompanied modeling of the OI(135.6)-nm auroral emission, but also suggested, aside from the modeling concerns, possible avenues of understanding of the column shift parameter and a helpful method in its presentation. This insight is further explored in the next section with the presentation of an analysis of the distribution of column shift values. Cross correlation analysis of the vertical wind and column shift time series comparisons did not establish a definitive link between the time series except in the January 26, 2001 data set, but there are certainly several examples in the vertical wind and column shift time series comparisons, which, when examined in detail, reveal intermediate- to large-magnitude vertical wind-induced composition perturbations. Furthermore, the variations in the Inuvik FPS and CRL-FPS OI(630.0)-nm relative intensity generally support this conclusion. None of the vertical wind-induced column shift variations (relative to the zero column-shift reference) presented here were indicative of a lower- to upper-thermospheric vertical flow cell, like the kind that *Price et al.* [1995] identified in lower- and upper-thermospheric vertical wind data. Instead, the column shift variations here represent middle- to upper-thermospheric composition perturbations based on the low energy flux values (2-4 $mW \cdot m^{-2}$) and soft-to-moderate precipitation ($\lesssim$1-2 keV) that prevailed over Inuvik and Poker Flat at the times of the significant vertical winds. Soft-to-moderate precipitation deposits a significant percentage of its energy at middle- to upper-thermospheric altitudes (180-250 km), and energy flux values of ~4 $mW \cdot m^{-2}$ are only high enough to induce significant vertical wind speeds at middle- to upper-thermospheric altitudes, based on the simple calculation that estimates the mechanical power per unit area, $P/A = \rho HgW$, required to generate and sustain a vertical wind of speed W in a scale height layer H at a mass density ρ.

The several examples presented in Section 4.1 of vertical wind-induced composition perturbations give confidence that the column shift parameter is capable of identifying composition variations relative to the model thermosphere that are attributed to significant vertical wind activity, even under the difficult circumstances of comparing data from two semi-random phenomena. The 2-D column shift maps presented above and in Chapter 3 also perform adequately under certain circumstances in identifying the spatial morphology of composition variations associated with auroral forms relative to the model thermosphere. Nonetheless, these particular examples are buried in the larger problems of understanding why the eight column shift data sets presented here are biased towards negative column shift values; *i.e.*, why the auroral model, on average, underestimates the OI(135.6)-nm auroral brightness relative to the UVI-observed OI(135.6)-nm brightness. The next section presents an analysis of the column shift distributions and case-by-case comparisons of the observed-to-modeled OI(135.6)-nm auroral brightness. The column shift distribution analysis, in identifying a possible improvement to the MSIS-90 atomic oxygen density profile, also establishes a definitive link between vertical wind speeds and column shift values. The observed-to-modeled OI(135.6)-nm brightness comparisons, in revealing a possible improvement to determinations of energy flux from FUV auroral observations, identify an apparent deficiency in the estimation of energy flux at different characteristic energies that affects the estimation of the modeled OI(135.6)-nm auroral brightness. Both improvements can aid with the determination of absolute column shift estimates and ultimately with comparisons between time series of vertical wind measurements and column shift values.

4.2 Column Shift and Vertical Wind Distributions and Discrepencies between the Observed and Modeled OI(135.6)-nm Auroral Emission

The statistical characteristics of the eight column shift data sets displayed in Table 4.3 indicate that the auroral model on average underestimates OI(135.6)-nm brightnesses relative to UVI observations. As was discussed at the end of Chapter 3 and the beginning of Section 4.1, this auroral model deficiency significantly hindered initial interpretations of the column shift parameter, and some criterion was sought that would establish

whether or not a given column shift was representative of a vertical wind's effects and help facilitate the time series comparisons of column shift values to vertical wind measurements. However, it also was presumed that the OI(135.6)-nm modeling process did work under certain circumstances, based on such examples as Figure 3.33b on page 185 showing the February, 28, 2000 0552 UT column shift map, recalling that this map distinguishes the spatial morphology of thermospheric composition variations associated with the aurora and exhibits column shift values which fall within the range expected of height displacements due to intermediate- to large-magnitude vertical winds. In addition, the relative variation in the time series of point-to-point column shift values was often plausible. Thus, it was believed that column shift variations may be attributable to significant vertical wind activity if criteria could be found that excluded suspect column shift estimates and/or explained the modeling deficiencies.

The statistical properties of the column shift data sets suggested that subtraction of each column shift data set's median value (and not the mean value) from the 2-D column shift maps may help to distinguish the spatial morphology of thermospheric composition variations by raising each map's column shift values to a ~0 km column-shift reference level. The same median correction to the time series of spatially-averaged column shift values did not modify the point-to-point relative variation in the column shifts, but did elevate the time series to a ~0 km column-shift reference for easier comparison to the vertical wind time series. Furthermore, the application of the LBH-L 15 counts·box^{-1} brighter-aurora criterion to the UVI auroral data to retain significantly reduced the mean and median values and standard deviation of each column shift data set compared to the original data sets—which used the LBH-L 9.3 counts·box^{-1} brightness threshold—by excluding almost all of the unrealistically-negative column shifts of less than –100 km (except in the high-A_P data sets).

Use of the LBH-L 9.3 counts·box^{-1} brightness criterion (the equivalent of 1 mW·m^{-2} of energy flux) frequently retained UVI auroral data that fell outside of the auroral zone. The column shifts that prevailed in the boxes at these non-auroral-oval latitudes were almost exclusively of values less than –100 km, as the column shift maps in Figures 4.1

and 4.3 indicate. It was speculated that imprecise airglow removal from the raw UVI images in combination with very weak auroral signal (<9.3 LBH-L counts) elevated the total LBH-L signal above 9.3 counts in the non-auroral-oval boxes. Generally, the model predicted very low OI(135.6)-nm brightnesses (~1 count) for these boxes, and if the boxes contained excess OI(135.6)-nm airglow signal along with very weak auroral signal, then the total OI(135.6)-nm signal would be well above the predicted brightness, resulting in unrealistically-negative column shifts. In addition to this concern, energy flux values inferred from very weak LBH-L observations (9.3-15 counts) may not have indicated that significant aurora prevailed in a given box compared to energy flux values inferred from bright LBH-L observations (*e.g.*, 150 counts). Recall from Chapter 3 that the uncertainty range in energy flux values is 20-35%. If the uncertainty in a 1 $mW \cdot m^{-2}$ energy flux value is 35%, then the low end of the energy flux range from this LBH-L observation is 0.65 $mW \cdot m^{-2}$, which is even lower if airglow-removal procedures leave an excess of LBH-L signal in the original UVI image. This weak energy flux is almost certainly not enough to indicate significant aurora, vertical winds or column shifts.

With the application of the new LBH-L brightness threshold, the total number of column shifts remaining in each data set was reduced considerably (see Table 4.3). The application of the new LBH-L brightness threshold did not elevate the mean value of the new column shift data sets to ~0 km—demonstrating that the modeling process continued to underestimate the OI(135.6)-nm auroral brightness on average relative to the observed OI(135.6)-nm brightness—but because the statistical properties of each data set were reduced so markedly and virtually all the boxes on the 2-D maps retaining weak signal outside of the auroral-oval region were discarded, the belief was that the remaining column shifts were more credible and more likely to be attributed to significant vertical wind activity. In addition, the new mean and/or median values of the column shift data sets may be a better indicator of what was actually ailing the OI(135.6)-nm auroral-modeling process. The final deliberations on why the LBH-L brightness threshold was increased and what may be ailing the OI(135.6)-nm auroral-modeling process involved an investigation of the distribution of column shift values from each night's data set.

The initial motivation to investigate the distribution of column shift values of the eight data sets arose from prior analyses of distributions of vertical wind data sets. Random, small- to intermediate-magnitude vertical winds (±1-30 $m \cdot s^{-1}$) in the thermosphere generally assume a Gaussian distribution centered about a peak of ~0 $m \cdot s^{-1}$ if the assumption that the average vertical wind speed over the course of a 24-hr period is zero [*e.g. Conde and Dyson*, 1995]. These winds are attributed to solar radiative input and the weak Joule and particle-precipitation heating that prevails in the auroral-latitude thermosphere almost all of the time. Deviations from this weak-and-random-wind Gaussian distribution are generally representative of the intermediate- to large-magnitude vertical winds ($\geq$30-50 $m \cdot s^{-1}$) observed at auroral latitudes due to significant heating events, which are characterized by a separate Gaussian distribution.

For example, a preliminary investigation of upper-thermospheric vertical wind data [*Krynicki et al.*, CEDAR conference, June, 1998, Boulder, CO] obtained with an FPS [*Hernandez et al.*, 1990] at the South Pole station (90°S, 75°INV) and collected during both quiet geomagnetic conditions at solar minimum and active geomagnetic conditions at solar maximum binned the vertical wind data in histogram format and numerically fitted one Gaussian function to the histogram distribution of geomagnetically-quiet and -active vertical wind measurements, respectively. The Gaussian fit characterized fairly well each histogram distribution around the peak. The Gaussian fit's full-width at half-maximum $\equiv$ ξ for the quiet-time vertical wind data was $\xi = +34.0$ $m \cdot s^{-1}$, with the peak at $\chi = +0.3$ $m \cdot s^{-1}$. The width and peak of the active-time data was $\xi = +46.0$ $m \cdot s^{-1}$ and $\chi = -0.2$ $m \cdot s^{-1}$, respectively. The wings of the histograms, however, were not well characterized by the Gaussian fit, particularly in the active-time data set. A simple conclusion of the study was that vertical winds are a real thermospheric phenomenon since the width of the Gaussian fits are greater than the typical error in the wind measurements (±5-15 $m \cdot s^{-1}$).

Subsequent analysis of the South Pole vertical wind data sets, presented in Figures 4.19a-b, found that a numerical fit of two distinct Gaussian functions, one narrow and one broad, characterized the vertical wind histogram distributions much better than a single Gaussian. In general, both the narrow and broad Gaussians are centrally located

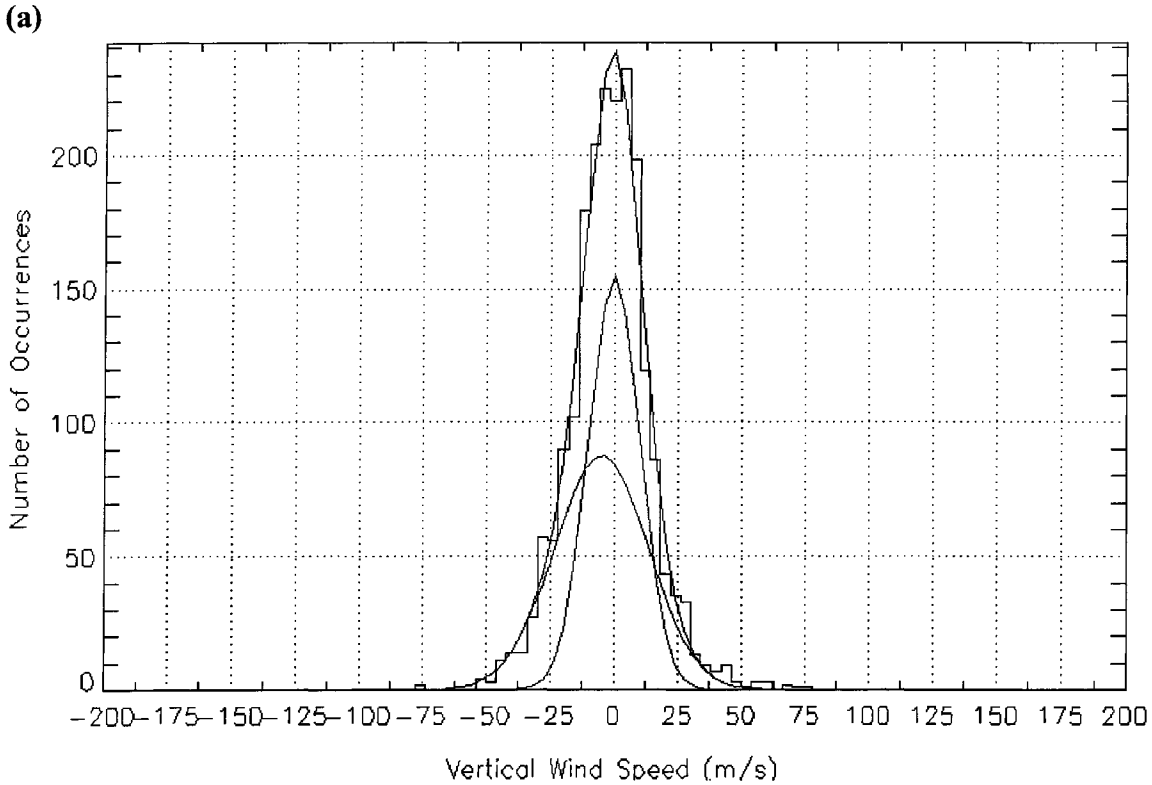

Figure 4.19. Distribution of upper-thermospheric vertical wind measurements at South Pole during quiet and active geomagnetic conditions. **(a)** The quiet-time vertical wind distribution. The quiet-time wind data was obtained during Apr and May in the solar minumum years of 1996 and 1997. The peak and width of the quiet-time narrow and broad Gaussians is –0.2 $m \cdot s^{-1}$ and 25.3 $m \cdot s^{-1}$, and –6.3 $m \cdot s^{-1}$ and 45.7 $m \cdot s^{-1}$, respectively. This data set is comprised of 2006 wind measurements. Typical uncertainty in the wind measurements is 5-15 $m \cdot s^{-1}$. The histogram bin size is 5 $m \cdot s^{-1}$.

about the ~0 $m \cdot s^{-1}$ peak. The width ξ of the narrow and broad Gaussians in the quiet-time data is $\xi_{nar,qt}$ = +25.3 $m \cdot s^{-1}$ and $\xi_{brd,qt}$ = +45.7 $m \cdot s^{-1}$, respectively, and is $\xi_{nar,ac}$ = +26.9 $m \cdot s^{-1}$ and $\xi_{brd,ac}$ = +83.3 $m \cdot s^{-1}$ in the active-time data, respectively. Vertical wind speeds associated with the broad Gaussian are attributed to intermediate- to large-magnitude vertical wind activity due to significant Joule and particle-precipitation heating events, while vertical wind speeds associated with the narrow Gaussian are indicative of the random, small- to intermediate-magnitude vertical winds mentioned above. The greater width of the active-time vertical-wind distribution compared to the quiet-time distribution is attributed to more active solar and geomagnetic conditions causing larger-magnitude

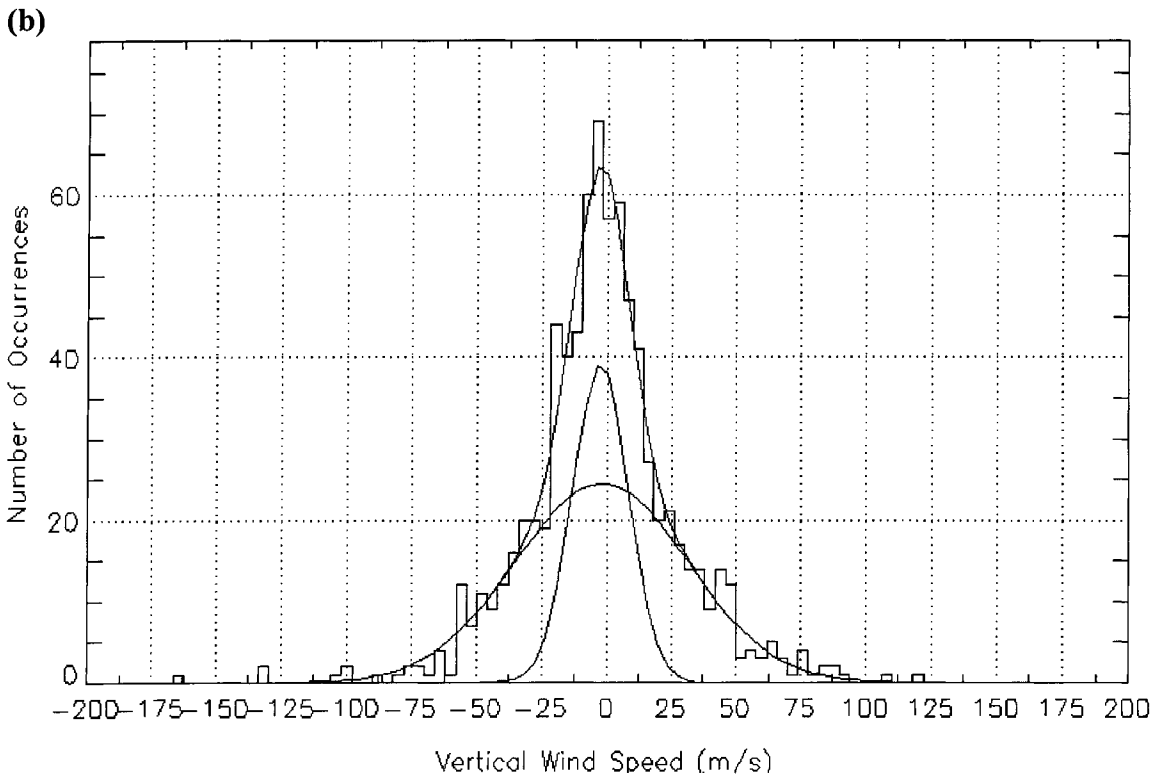

Figure 4.19 cont. Distribution of upper-thermospheric vertical wind measurements at South Pole during quiet and active geomagnetic conditions. **(b)** The active-time vertical wind distribution. The active-time data was obtained during the geomagnetically-active, solar maximum period of Jun 1-15, 1991. The peak and width of the active-time narrow and broad Gaussians is –3.4 $m \cdot s^{-1}$ and 26.9 $m \cdot s^{-1}$ and –2.5 $m \cdot s^{-1}$ and 83.3 $m \cdot s^{-1}$, respectively. This data set is comprised of 783 wind measurements.

random vertical motion in the auroral-latitude thermosphere and a greater number of large-magnitude vertical wind events.

Similarly to the South Pole vertical wind data, the distribution of Inuvik FPS vertical wind measurements from the seven nights of observations, shown in Figure 4.20, is also characterized quite well by a numerical fit of two Gaussian functions. The peaks χ_{Ivk} and widths ξ_{Ivk} of the narrow and broad Gaussians are $\chi_{Ivk,nar} = -2.6$ $m \cdot s^{-1}$ and $\xi_{Ivk,nar} = +35.9$ $m \cdot s^{-1}$, and $\chi_{Ivk,brd} = +6.2$ $m \cdot s^{-1}$ and $\xi_{Ivk,brd} = +95.7$ $m \cdot s^{-1}$, respectively. Table 4.6 lists the peaks and widths of the South Pole and Inuvik FPS vertical wind distributions for comparison. The greater widths of both the narrow and broad Gaussians of the Inuvik FPS data set compared to the South Pole data sets is attributed to the particular selection of

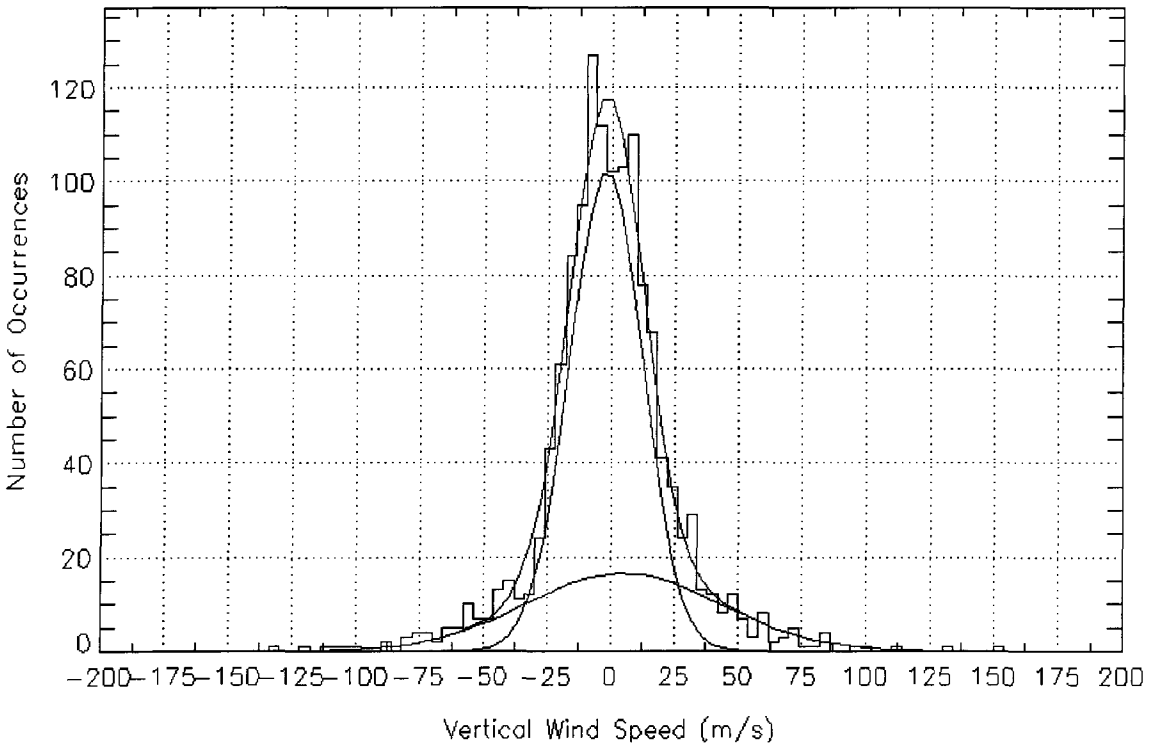

Figure 4.20. Distribution of the upper-thermospheric vertical wind measurements obtained at Inuvik, NT, Canada from Feb, 2000 to Jan, 2001. The peak and width of the narrow and broad Gaussians is –2.6 $m \cdot s^{-1}$ and 35.9 $m \cdot s^{-1}$ and 6.2 $m \cdot s^{-1}$ and 95.7 $m \cdot s^{-1}$, respectively. This data set is comprised of 1326 wind measurements.

Table 4.6. Peaks and widths of the distributions of South Pole and Inuvik FPS vertical wind measurements. The narrow and broad Gaussian distribution properties are shown.

Vertical wind	Narrow Gaussian		Broad Gaussian	
data set	χ_{nar} ($m \cdot s^{-1}$)	ξ_{nar} ($m \cdot s^{-1}$)	χ_{brd} ($m \cdot s^{-1}$)	ξ_{brd} ($m \cdot s^{-1}$)
South Pole				
-- Quiet time	–0.2	+25.3	–6.3	+45.7
-- Active time	–3.4	+26.9	–2.5	+83.3
Inuvik, NT	–2.6	+35.9	+6.2	+95.7

of Inuvik FPS vertical wind data that exhibit significant, large-magnitude wind events, thus biasing the Gaussian distributions towards larger widths.

Because distributions of auroral-latitude vertical winds in general exhibit a distinct two-Gaussian signature, indicative of two distinct geophysical phenomena at work in the

high-latitude thermosphere, it was speculated that the distribution of column shift values, ideally, should exhibit similar characteristics as an auroral-latitude vertical wind distribution, if indeed vertical winds are responsible for the height displacement of air parcels and the UVI-inferred auroral model outputs of energy flux, characteristic energy, modeled OI(135.6)-nm brightness and column shift are valid. Initially, histograms representing the distributions of the absolute column shift values of each data set were constructed and examined using the LBH-L 9.3 counts·box^{-1} brightness threshold. Based on the <0 km mean value of each column shift data set presented in Table 4.3, the column shift distributions were obviously not expected to be centered about ~0 km. Nonetheless, the column shift distributions proved to be valuable in the interpretation of the column shift parameter by establishing a link between vertical wind speeds and column shift values and identifying a criterion for disregarding suspect column shift estimates (by discarding very weak and suspect energy flux values).

As the presentations at the beginning of Section 4.1 revealed, application of the LBH-L 15 counts·box^{-1} brightness threshold to the column shift data sets significantly reduced the statistical characteristics of the data sets. The most convincing insight into this LBH-L brightness increase involved an examination of the column shift distributions using the LHB-L 9.3 counts·box^{-1} brightness threshold compared to the distributions using the LHB-L 15 counts·box^{-1} criterion. As was stated earlier, the column shift data sets using the original LBH-L brightness threshold included an excessive amount of highly-negative column values of less than –100 km. Three histogram distribution examples which illustrate this from December 22, 2000, February 28, 2000, and January 3, 2001 using the LBH-L 9.3 counts·box^{-1} brightness criterion are shown in Figures 4.21a-c. The February 28, 2000 and December 22, 2000 data sets both exhibited considerable aurora, but the auroral brightness was generally low (<50 LBH-L counts·box^{-1}) on these nights. Also, as was discussed at the beginning of Section 4.1, the February 28, 2000 data set included a large number of column shift estimates from very early in the day, ~0200-0600 UT, during which the thermosphere was sunlit. Although the airglow-removal routine was applied to this data set, it likely did not remove the total dayglow

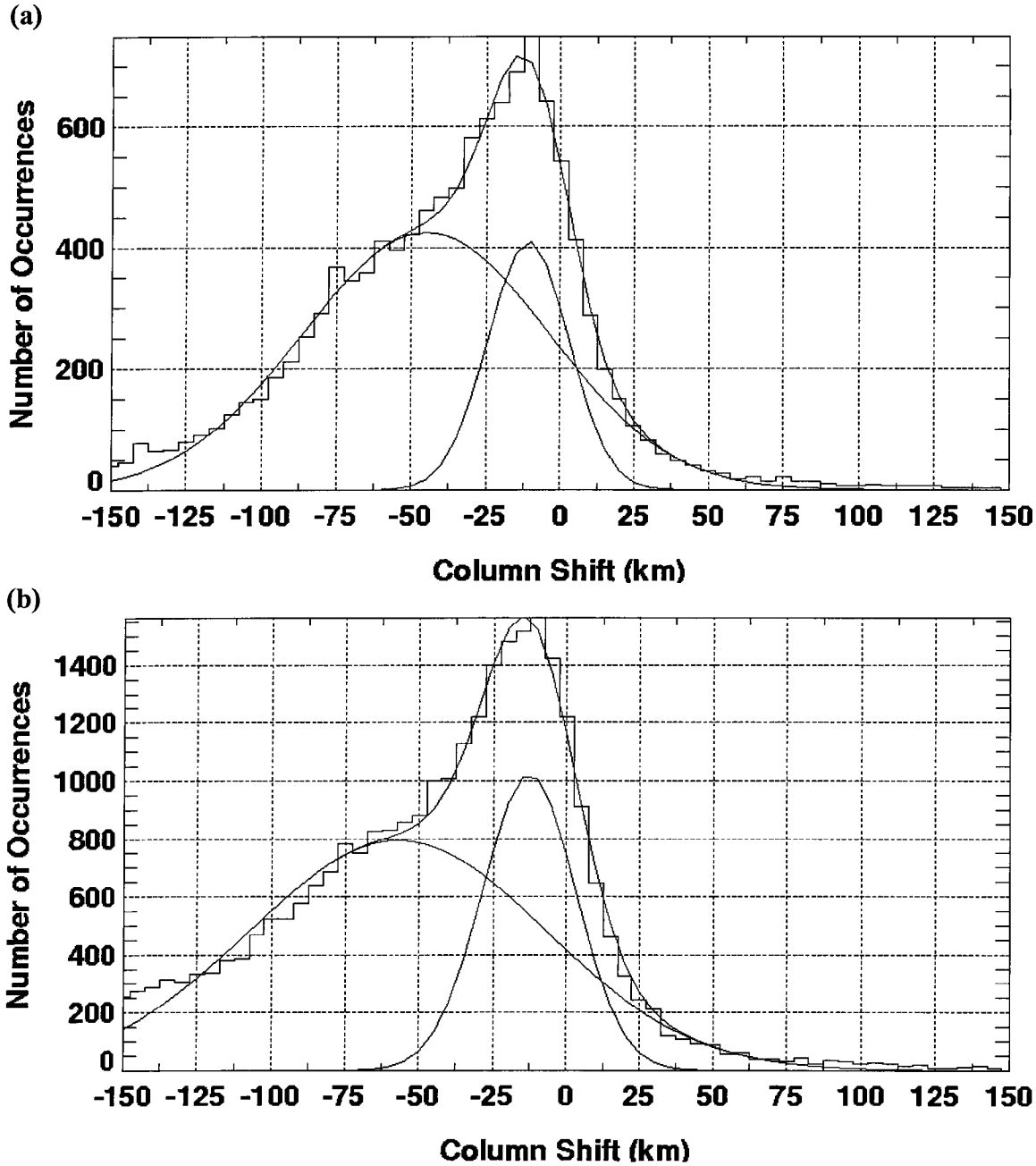

Figure 4.21. Column shift distributions using the LBH-L 9.3 counts·box^{-1} brightness threshold with a two-Gaussian numerical fit applied. The histogram bin size is 5 km. **(a)** Distribution of the Dec 22, 2000 column shift estimates. This data set is comprised of 14,000 column shift estimates. The peak and width of the narrow Gaussian is –10.7 km and 27.1 km, respectively, and the peak and width of the broad Gaussian is –45 km and 82.4 km, respectively. **(b)** Distribution of the Feb 28, 2000 column shift estimates. This data set is comprised of 34,481 column shift estimates. The peak and width of the narrow Gaussian is –12.7 km and 31.8 km, respectively, and the peak and width of the broad Gaussian is –57.1 km and 100 km, respectively.

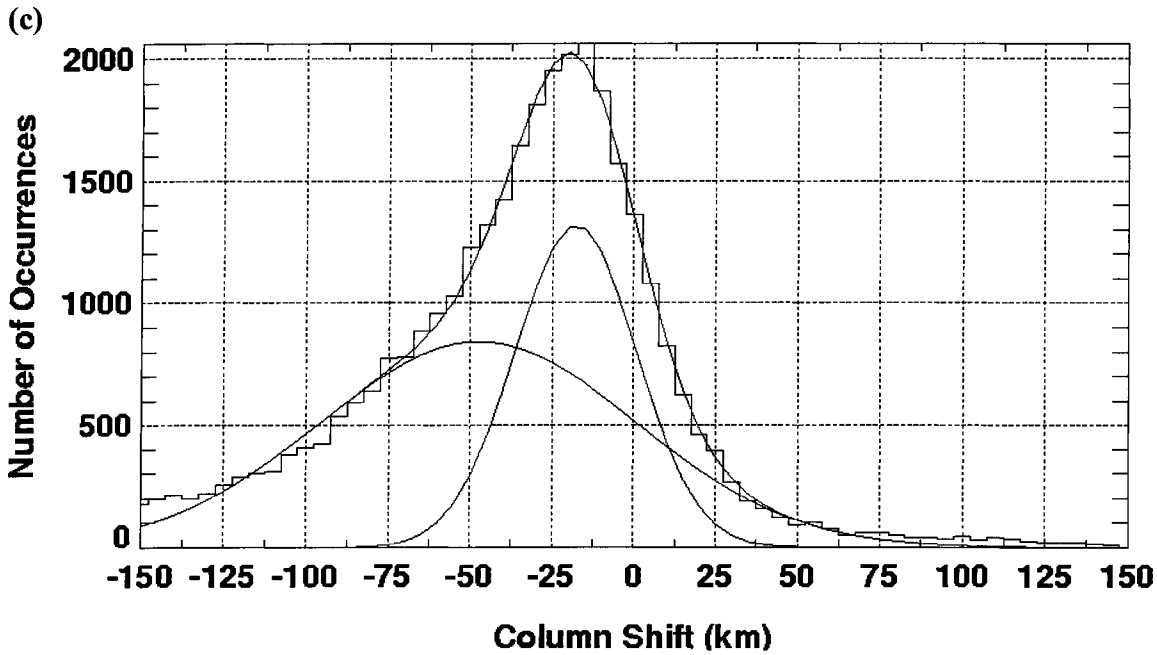

Figure 4.21 cont. Column shift distributions using the LBH-L 9.3 counts·box^{-1} brightness threshold with a two-Gaussian numerical fit applied. **(c)** Distribution of the Jan 3, 2001 column shift estimates. This data set is comprised of 37,468 column shift estimates. The peak and width of the narrow Gaussian is –17.7 km and 37.1 km, respectively, and the peak and width of the broad Gaussian is –47.4 km and 96.3 km, respectively.

signature from each respective box on the 2-D maps. Excess dayglow signal (*e.g.*, 2-5 counts) adding to very weak auroral signal (<9.3 counts) caused many boxes at non-auroral-oval latitudes to be retained in the data set. This was also the case for the March 20, 2001 data set.

A two-Gaussian numerical fit was applied to the distributions, and invariably, a two-hump distribution was identified, which was the case for all the column shift data sets presented in this thesis except for the November 28, 2000 data set. In each of the examples shown in Figures 4.21a-c, the narrow Gaussian displays the characteristics of a distribution of vertical displacements due to small- to intermediate-magnitude vertical winds. If indeed vertical winds are responsible for the height displacement of air parcels, then the full-width at half-maximum of the narrow Gaussian $\equiv \zeta_{nar}$ of each column shift data set, ζ_{nar} = 26-37 km for the six geomagnetically-quiet Inuvik data sets, is indicative

of the time-integrated, height-displacement effect of fairly long-lived (~15 min), intermediate-magnitude vertical winds (~30 $m \cdot s^{-1}$) acting over perhaps one scale height in the middle-to-upper thermosphere or 1-2 scale heights in the lower thermosphere. Table 4.7 lists the peaks, η_{nar} and η_{brd}, respectively, and widths, ζ_{nar} and ζ_{brd}, respectively, of the narrow and broad Gaussians for each column shift data set using the LBH-L 9.3 counts·box^{-1} brightness threshold. The total number of column shift estimates in each data set is also included. The November 28, 2000 column shift data set did not exhibit a two-Gaussian distribution, but numerical-fitting procedures were able to fit a single Gaussian function to the column shift histogram.

Table 4.7. Column shift distribution peaks and widths using the LBH-L 9.3 counts·box^{-1} brightness threshold. Note that March 20, 2001 and November 28, 2000 data sets were analyzed using the high-A_P model. See the text for more discussion.

Date	Total # of column shifts	η_{nar} (km)	ζ_{nar} (km)	η_{brd} (km)	ζ_{brd} (km)
Jan 3, 2001	37468	–17.7	37.1	–47.4	96.3
Dec 9, 2000	42540	–15.7	31.8	–45.1	73.2
Feb 28, 2000	34005	–12.7	31.8	–57.1	100
Dec 22, 2000	14000	–10.7	27.1	–45.0	82.4
Jan 4, 2001	10954	–11.2	26.1	–44.3	74.5
Jan 26, 2001	13224	–8.7	28.9	–33.0	84.4
Nov 28, 2000	4969	–56.6	110	N/A	N/A
Mar 20, 2001	11249	–32.7	76.5	–112	168

In evaluating the meaning of the broad Gaussians in the column shift distributions, the full-width at half-maximum ζ_{brd} of the broad Gaussians for the six geomagnetically-quiet Inuvik data sets is ζ_{brd} = 73-100 km. The low end of this range may be attributed to long-lived (~30 min), large-magnitude ($\gtrsim$50 $m \cdot s^{-1}$) vertical winds of the kind associated with the broad Gaussians of the Inuvik FPS and South Pole vertical wind distributions, transporting air parcels across two or three scale heights ~50-80 km from the lower or middle to upper thermosphere or vice versa. However, the high end of the ζ_{brd} = 73-100 km range is essentially due to the extent which the highly-negative column shift values of

less than –100 km appear in the column shift data sets. The appearance of these highly-negative column shift values and the significant number of them in the data sets (illustrated by the prominence of the broad Gaussians in the distributions), and the fact that the distributions were biased towards negative values, significantly hindered a constructive interpretation of the absolute column shift estimates. These concerns led to different methods that were developed to better evaluate the 2-D column shift maps and column shift time series, some of which were discussed in the previous section. Nonetheless, the two-Gaussian signature of the column shift distributions yielded an explicit link to the distribution of auroral-latitude vertical wind measurements; *i.e.*, if two distinct types of vertical winds are responsible for air-parcel height displacements in the auroral-latitude thermosphere, then the UVI- and auroral model output-inferred column shift parameter under certain circumstances was identifying this effect. The distinct two-Gaussian signature of vertical wind and column shift distributions was too pronounced to ignore and if some criterion could be established that disregarded suspect column shifts, then a valid relationship between vertical winds and column shifts may be found.

After much speculation and trial-and-error, a suitable criterion was identified for discarding certain column shift estimates, which was to increase the LBH-L brightness threshold. Based on the previous discussions concerning the possible contamination of UVI auroral data with unaccounted-for airglow signal and the considerable uncertainty (20-35%) in the UVI- and auroral model output-inferred energy flux values, a brighter-aurora criterion was applied to the column shift data sets. The LBH-L brighter-aurora threshold of 15 counts·box^{-1} was a better indicator that 1 mW·m^{-2} of energy flux prevailed in a given box, considering the uncertainty range. Also recall from the previous section that even weak energy flux values (2-4 mW·m^{-2}) can induce intermediate-magnitude vertical winds at upper-thermospheric altitudes. In addition, the brighter-aurora threshold significantly reduced the size of the column shift data sets and discarded essentially all the boxes residing at latitudes outside of the auroral-oval region, boxes which generally exhibited column shift values less than –100 km. Ultimately, the LBH-L 15 counts·box^{-1}

brightness threshold was definitively established through an examination of the column shift distributions after the brighter-aurora criterion was applied.

When the threshold on the LBH-L brightness was increased, the broad Gaussians in each of the column shift distributions was strongly suppressed without disappearing, while the information associated with the narrow Gaussians was essentially left intact. Figures 4.22a-c show the histogram distributions from the same three nights of December 22, 2000, February 28, 2000, and January 3, 2001 using the LBH-L brightness threshold of 15 counts·box^{-1}. Comparison of Figures 4.21a-b to Figures 4.22a-b, respectively, reveals how significantly the broad Gaussian was suppressed in some of the data sets. The December 22, 2000 data set was reduced by a factor of almost 3 with the application of the new LBH-L criterion, yet the peak, height and width of the narrow Gaussian essentially remained unchanged, while all three characteristics of the broad Gaussian

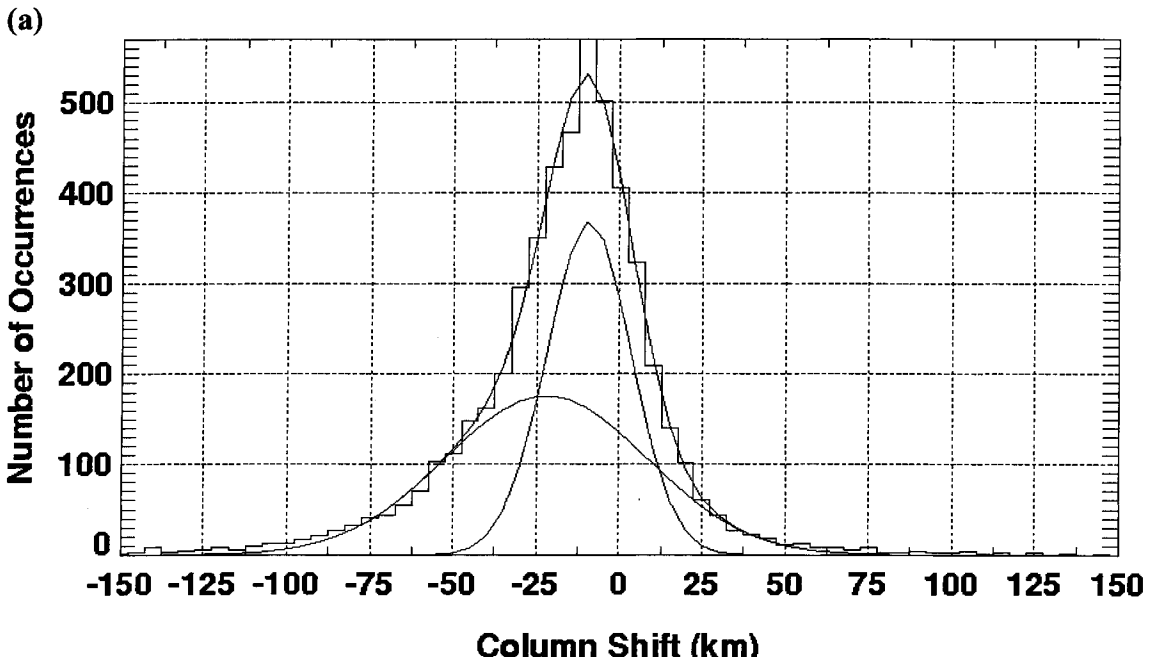

Figure 4.22. Column shift distributions using the LBH-L 15 counts·box^{-1} brightness threshold with a two-Gaussian numerical fit applied. The histogram bin size is 5 km. **(a)** Distribution of the Dec 22, 2000 column shift estimates. This data set is comprised of 5170 column shift estimates. The peak and width of the narrow Gaussian is –9.3 km and 25.4 km, respectively, and the peak and width of the broad Gaussian is –22.0 km and 60.6 km, respectively.

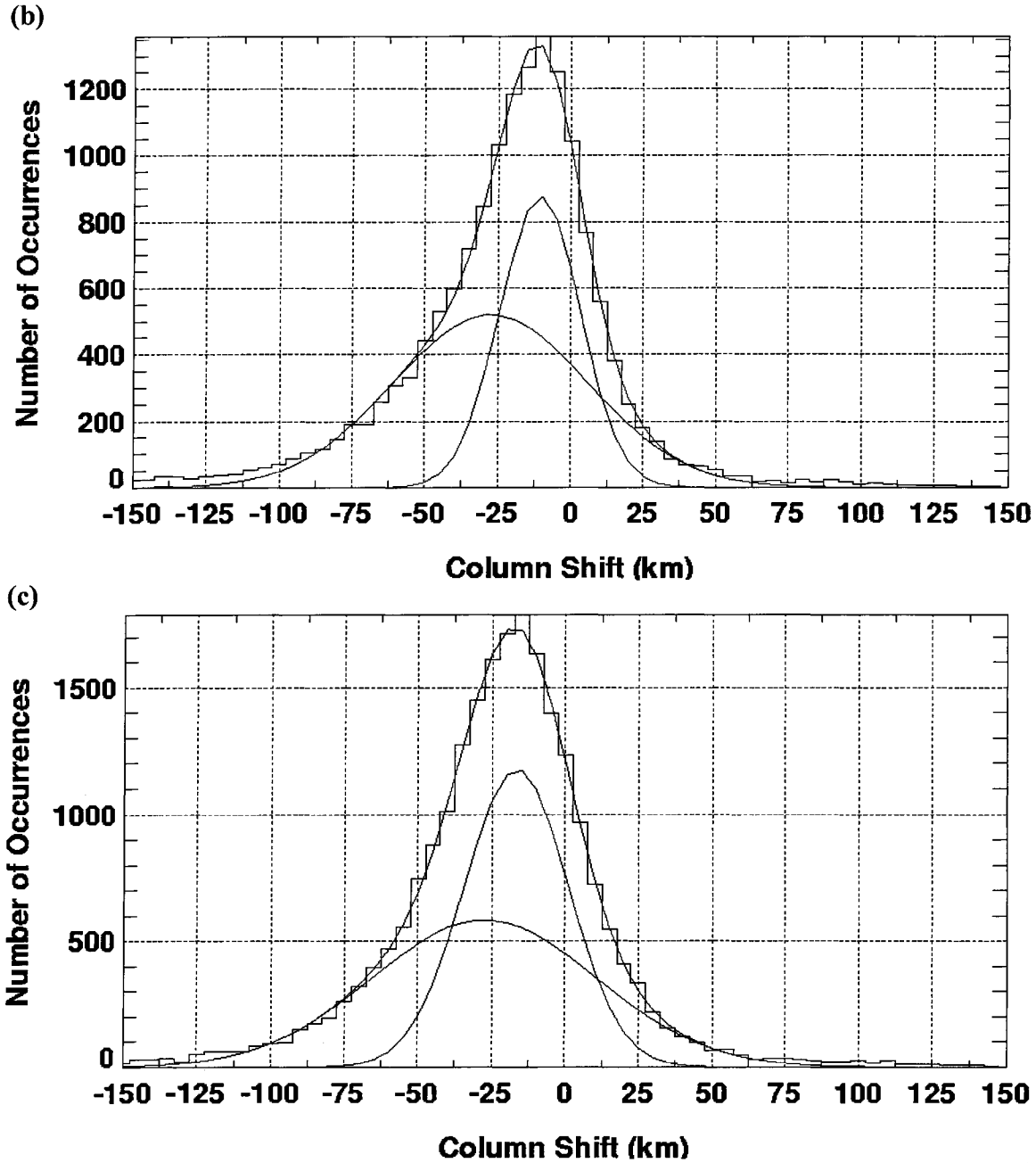

Figure 4.22 cont. Column shift distributions using the LBH-L 15 counts·box^{-1} brightness threshold with a two-Gaussian numerical fit applied. **(b)** Distribution of the Feb 28, 2000 column shift estimates. This data set is comprised of 15,475 column shift estimates. The peak and width of the narrow Gaussian is –10.5 km and 27.7 km, respectively, and the peak and width of the broad Gaussian is –27.1 km and 66.7 km, respectively. **(c)** Distribution of the Jan 3, 2001 column shift estimates. This data set is comprised of 22,234 column shift estimates. The peak and width of the narrow Gaussian is –16.6 km and 35.5 km, respectively, and the peak and width of the broad Gaussian is –27.4 km and 76.1 km, respectively.

dramatically changed. This was also the case for the February 28, 2000 data set, which was reduced by a factor of 3. With the application of the new LBH-L brightness threshold, the widths $\zeta_{nar,brght}$ of the narrow Gaussians for the six geomagnetically-quiet Inuvik column shift distributions, $\zeta_{nar,brght}$ = 22-36 km, did not significantly change compared to ζ_{nar} = 26-37 km for the LBH-L 9.3 counts·box^{-1} criterion. Thus, the interpretation of the column shift values associated with the narrow Gaussians remained unchanged; *i.e.*, random, small- to intermediate-magnitude vertical winds due to solar radiative input and the weak Joule and particle-precipitation heating that prevails at auroral latitudes almost all of the time are responsible for the small- to intermediate-magnitude (±1-30 km) column shifts that occur at lower- to upper-thermospheric altitudes. Table 4.8 lists the peaks and widths of the narrow and broad Gaussians using the LBH-L 15 counts·box^{-1} brightness threshold.

Table 4.8. Column shift distribution peaks and widths using the LBH-L 15 counts·box^{-1} brightness threshold. See the text for more discussion.

Date	Total # of column shifts	$\eta_{nar,brght}$ (km)	$\zeta_{nar,brght}$ (km)	$\eta_{brd,brght}$ (km)	$\zeta_{brd,brght}$ (km)
Jan 3, 2001	22234	–16.6	35.5	–27.4	76.1
Dec 9, 2000	28574	–13.6	28.3	–31.1	55.1
Feb 28, 2000	15475	–10.5	27.7	–27.1	66.7
Dec 22, 2000	5170	–9.3	25.4	–22.0	60.6
Jan 4, 2001	6936	–9.6	22.2	–24.6	51.3
Jan 26, 2001	8406	–7.8	27.4	–15.2	68.4
Nov 28, 2000	3462	N/A	N/A	N/A	N/A
Mar 20, 2001	8245	–29.8	72.3	–77.8	131

While the peaks, widths and heights of the narrow Gaussians did not change considerably after the application of the LBH-L brighter-aurora criterion, the characteristics of the generally less-pronounced broad Gaussians did. The range of widths $\zeta_{brd,brght}$ of the brighter-aurora broad Gaussians shown in Table 4.8 for the six geomagnetically-quiet Inuvik data sets is now more closely comparable to two or three

thermospheric scale heights, $\zeta_{brd,brght}$ = 51-76 km, and is indicative of the altitude range that a long-lived, large-magnitude vertical wind due to significant heating may be expected to act, the sort of large-magnitude vertical wind speeds associated with the broad Gaussians of the vertical wind distributions. Thus, the distributions of column shifts now closely resemble the distributions of vertical winds, albeit in a vertical-displacement sense; *i.e.*, the two distinct classes of vertical winds that prevail in the auroral-latitude thermosphere which are identified in the distributions of vertical wind measurements—random, small- to intermediate-magnitude vertical winds (~1-30 $m \cdot s^{-1}$) due to solar radiative input and weak, persistent heating and intermediate- to large-magnitude vertical winds (>30 $m \cdot s^{-1}$) due to significant heating events—are responsible for two distinct types of composition perturbations identified in the distributions of column shifts—small- to intermediate-magnitude (±1-30 km) column shifts that occur in or across 1-2 scale heights at lower- to upper-thermospheric altitudes and intermediate- to large-magnitude column shifts (>30 km) that occur across 1-3 scale heights.

Presumably, most of the highly-negative column shift values which were discarded by the brighter-aurora criterion are associated with the aforementioned issues of airglow removal from the original UVI auroral images and skeptically-inferred energy flux values associated with very weak and suspect auroral data. In support of this supposition, the distribution of column shifts for LHB-L brightnesses of <15 $counts \cdot box^{-1}$ for the January 3, 2001 data set is shown in Figure 4.23. Almost all the column shift estimates using this criterion are highly-negative and unrealistic in value. The distributions from all of the column shift data sets using this criterion display the same characteristics.

Up to this point, only the widths of the narrow and broad Gaussians in the column shift distributions have been discussed in any detail. As indicated in Table 4.8, the peaks of the narrow and broad Gaussians remained <0 km even with the application of the new LBH-L brightness threshold, illustrating that the auroral model continued to underestimate the OI(135.6)-nm auroral brightness relative to UVI observations under certain circumstances. One concern which was potentially causing this underestimation of the OI(135.6)-nm brightness under some circumstances was the use of off-nadir looking

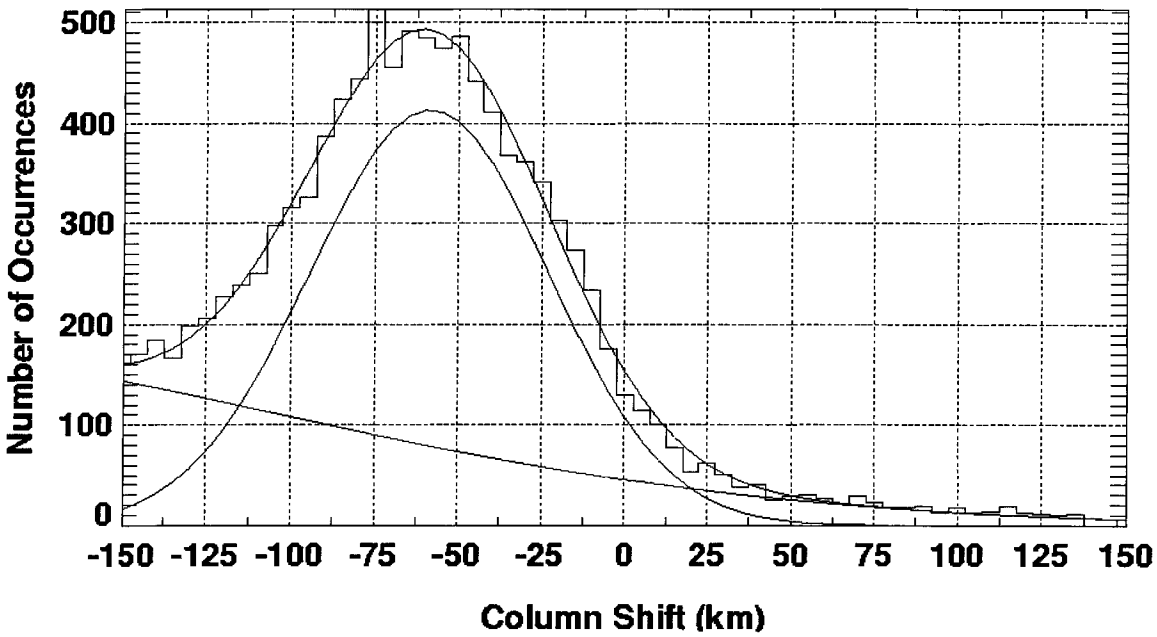

Figure 4.23. Distribution of Jan 3, 2001 column shifts for LBH-L brightnesses of less than 15 counts·box^{-1}. This data set is comprised of 15,234 column shift estimates. In general, these column shift estimates are associated with boxes from the 2-D maps that resided at non-auroral-oval latitudes and which exhibited very weak, suspect energy flux values.

UVI data; *i.e.*, was the OI(135.6)-nm auroral brightness being underestimated only for off-nadir looking angles, thus negatively biasing the distributions of column shifts. Recall from the previous section that reasonably "good" UVI-viewing of the aurora is considered to be from ~45° to nadir, and greater than 45° is considered "bad." Table 4.1 on page 200 lists the times when UVI viewed the aurora from each geometry. Generally, bad viewing geometry occurred early in each of the data sets, before ~0900 UT.

An investigation of the column shift distributions from February 28, 2000, December 9 and 22, 2000 and January 3, 2001 for good and bad looking angles revealed that column shifts inferred from the bad off-nadir angles early in the data sets have the same characteristics as column shifts inferred from the nearly-nadir viewing angles from later in those nights. Figures 4.24a-b from December 22, 2000 show the column shift distribution for times early in the data set and for times later in the data set. The peak, height and width of the narrow Gaussians from early in the data set and later are essentially

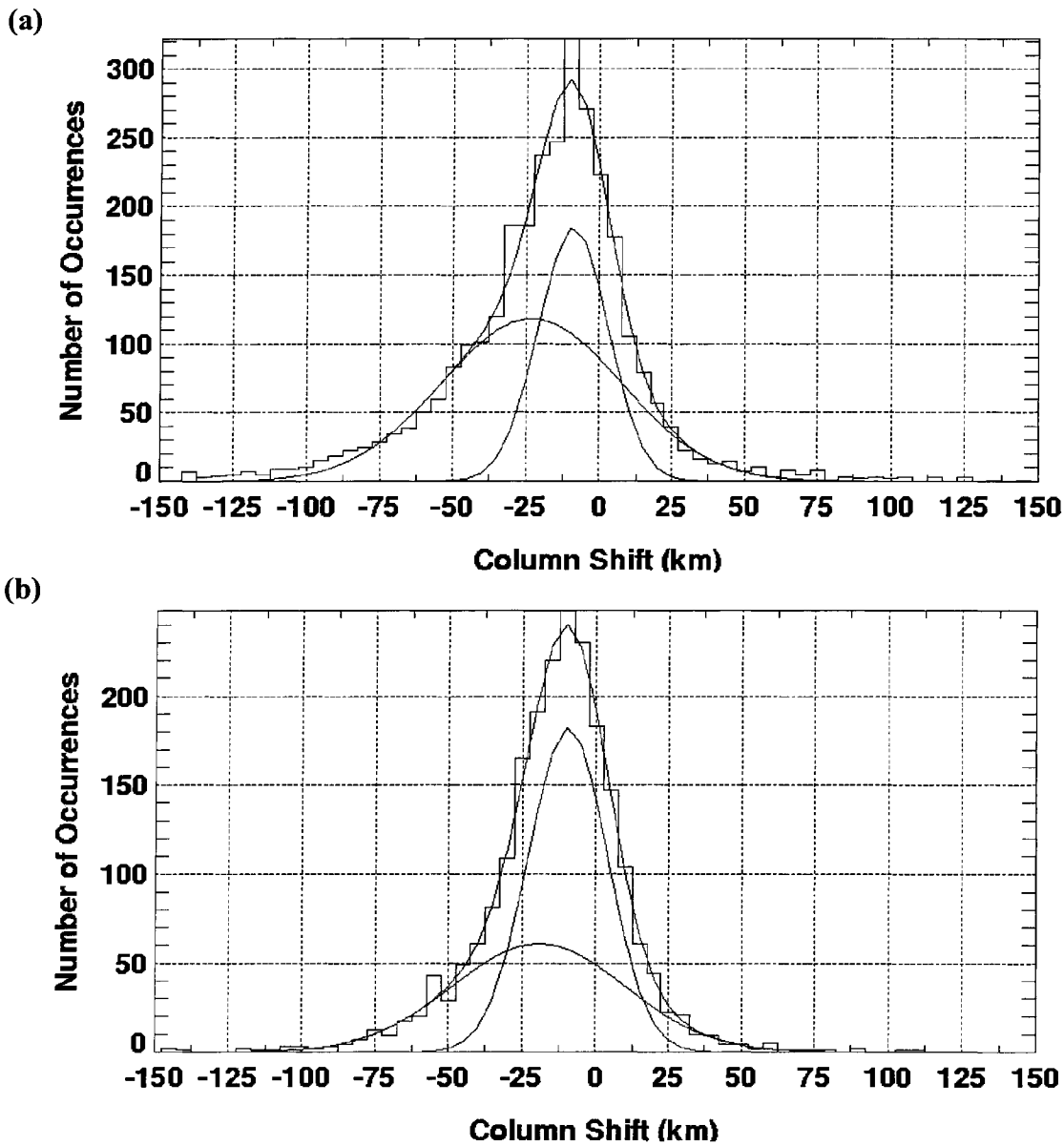

Figures 4.24. Column shift distributions on Dec 22, 2000 for UVI off-nadir bad look angles and near-nadir good look angles with a two-Gaussian fit applied using the LBH-L brightness threshold of 15 counts·box^{-1}. **(a)** Distribution of the column shifts for times 0600-0915 UT when the UVI was viewing the aurora from bad look angles. The peak and width of the narrow Gaussian is –9.0 km and 23.7 km, respectively, and the peak and width of the broad Gaussian is –23.1 km and 61.0 km, respectively. **(b)** Distribution of the column shifts for times 0915-1200 UT when the UVI was viewing the aurora from good look angles. The peak and width of the narrow Gaussian is –9.5 km and 26.7 km, respectively, and the peak and width of the broad Gaussian is –19.2 km and 58.6 km, respectively. The peak, height and width of the narrow Gaussians from the non-nadir viewed and nearly-nadir viewed look angles are essentially the same. The broad Gaussian is noticably more pronounced in the off-nadir estimates.

the same. The peak and width of the broad Gaussians are also similar, though the height of the broad Gaussian in the off-nadir column shift distribution is considerably larger. However, because the narrow and broad Gaussians for the different viewing geometries in general exhibit similar characteristics, and because column shifts represent composition perturbations due to two distinct classes of auroral-latitude vertical winds relative to the model thermosphere, it appears that non-nadir inferred column shifts also identify real composition perturbations in the thermosphere due to heating and vertical winds, even though the knowledge was inferred with auroral observations from a poor viewing geometry. The fact that non-nadir inferred column shifts can still identify real thermospheric composition perturbations is not unexpected and is discussed more below. Furthermore, it was clear that the viewing geometry concerns were not responsible for the negative biasing of the column shift distributions; *i.e.*, there was another reason why the modeled OI(135.6)-nm auroral brightness on average was less than UVI OI(135.6)-nm observations.

Poor viewing geometry makes auroral parameters such as energy flux and characteristic energy indeterminate because the UV imager may be observing aurora from two distinct auroral sources. For example, if the imager views along a slant path 30° from nadir, it may be observing aurora from two separate auroral curtains, one behind the other, and possibly due to precipitation of different energy flux and characteristic energy. The inferred energy flux value determined from LBH-L observations will likely end up being overestimated (assuming the imager had been viewing from nadir and observing only one curtain), but could be some weighted amount associated with both curtains if the LBH-L emission from one curtain was, for example, being attenuated. In addition, the inferred characteristic energy determined from LBH-L and LBH-S observations will end up being some sort of weighted value associated with both auroral arcs, depending on attenuation, and consequently, the modeled OI(135.6)-nm brightness will either be overestimated because of the overestimated energy flux or some sort of weighted amount associated with both curtains. However, this modeled brightness is then compared to some sort of weighted or overestimated observed OI(135.6)-nm

brightness (depending on attenuation) to determine some sort of weighted column shift estimate. Putting this another way, if heating along two auroral arcs results in vertical winds, then a column shift parameter sampling of this region using off-nadir looking UVI data will identify some sort of weighted composition perturbation associated with both arcs. Thus, off-nadir column shift estimates do represent a real thermospheric composition perturbation that may still be attributed to vertical winds, even when the column shift is being inferred from separate auroral sources, as long as the vertical wind field producing the column shift is spatially extended between the auroral sources. The more-pronounced broad Gaussian in the off-nadir column shift distribution may indicate that at times, the off-nadir column shift estimates are inaccurate, but under these circumstances, it may become important to compare the spatially-averaged point-to-point off-nadir column shift values to vertical wind measurements in order to confirm whether the off-nadir column shift estimates are valid or not.

The LBH-L 15 counts·box^{-1} brightness threshold provided a means of filtering out unrealistically-negative column shift estimates associated with non-auroral-oval boxes on the 2-D maps and UVI auroral data which represented very weak, uncertain energy flux values. Several examples presented in the previous section of intermediate-magnitude vertical wind-induced column shifts at middle- to upper-thermospheric altitudes due to soft-to-moderate precipitation of 2-4 mW·m^{-2} energy flux were identified in the time series comparisons, giving confidence that at times, the two semi-random phenomena of vertical winds and column shifts can be correlated. In addition, one of the time series comparisons showed a high degree of correlation at a realistic time lag, with both time series exhibiting the same periodicity, indicative of equivalent gravity wave oscillations present in both data sets. Furthermore, the distributions of auroral-latitude Inuvik (and South Pole) vertical wind measurements and UVI- and auroral model output-inferred column shift estimates both exhibit the distinct character of two Gaussians, one narrow and one broad, indicative of the two classes of vertical winds that prevail at auroral latitudes. After the application of the LBH-L 15 counts·box^{-1} brightness threshold to the column shift data sets, the range of widths of the narrow and broad Gaussians, $\zeta_{nar,brght}$ =

22-36 km and $\zeta_{brd,brght}$ = 51-76 km, respectively, identified in each column shift distribution are characteristic of the expected vertical wind-induced height displacement of air parcels over 1-2 scales heights due to small- to intermediate-magnitude vertical winds for the case of the narrow Gaussians and 1-3 scale heights due to long-lived, intermediate- to large-magnitude vertical winds for the case of the broad Gaussians. All the OI(135.6)-nm auroral modeling concerns aside, variations in the column shifts relative to the model thermosphere can at times be attributed to vertical wind activity. An explanation as to why the auroral model underestimated the OI(135.6)-nm auroral brightness compared to UVI observations, however, was not forthcoming.

Although not shown here, a similar column shift histogram analysis was performed using LBH-L, LBH-S, and OI(135.6)-nm auroral data observed with the GUVI instrument [*Paxton et al.*, 1999] aboard the TIMED satellite. The behavior of the GUVI column shift histograms in all respects was identical to those from UVI, despite the fact that the two instruments are fundamentally different; *i.e.*, a distinct two-Gaussian signature was identified in the GUVI-inferred column shift histograms. The width of the GUVI-inferred narrow and broad column shift Gaussians was comparable to the width of the UVI-inferred narrow and broad column shift Gaussians. In addition, the peak of the GUVI-inferred narrow and broad Gaussians was significantly <0 km, indicating that, like UVI, the GUVI- and auroral model output-inferred OI(135.6)-nm brightness was on average underestimated compared to GUVI OI(135.6)-nm observations. Clearly, the identical characterisics found in the UVI-inferred and GUVI-inferred column shift histograms do not have their origins in UV imaging techniques or in the instruments themselves and must be a consequence of auroral-modeling techniques.

At the end of the previous section, one possible flaw in the auroral model was identified that could contribute to underestimations of the OI(135.6)-nm brightness. In the evaluation of the column shift data sets from November 28, 2000 and March 20, 2001, which were analyzed using the high-A_P model, it was determined that column shifts of less than –100 km were prevalent in the data sets even after the LBH-L 15 counts·box^{-1} brightness threshold was applied. These highly-negative column shifts are

responsible for the highly-biased negative mean and median values and the larger standard deviation of the two data sets compared with the low-A_P model data sets (see Table 4.3). The peaks and widths of the narrow and broad Gaussians from the March 20, 2001 column shift distribution, –29.8 km and 72.3 km, and –77.8 km and 131 km, respectively, and the fact that the fit routines did not even converge in the case of the November 28, 2000 column shift distribution, were further indication of the perplexing difficulties that accompanied the evaluation of these high-A_P data sets. The modeled OI(135.6)-nm auroral emission was grossly underestimated at times in these two data sets.

A specific feature that was identified concerning these data sets was that when the characteristic energy prevailing in a given box was high ($\gtrsim$4 keV), the column shift estimated for that particular box was in general much less than –100 km. A plausible explanation for this was that absorption of the OI(135.6)-nm emission by O_2 above the ~100-120 km peak emission altitude may occur in the real thermosphere during high characteristic energy precipitation events, which would explain the reduced OI(135.6)-nm auroral brightness that was predicted by the model. Nonetheless, the observed OI(135.6)-nm brightness was much larger than the model prediction in these data sets, and consequently, the highly-negative downward column shifts are a direct consequence of the high-A_P model's poor estimation of the OI(135.6)-nm auroral brightness relative to the observed OI(135.6)-nm brightness. One possible explanation for this poor estimation of the OI(135.6)-nm auroral brightness at high characteristic energies is that the MSIS-90 neutral model significantly underestimates the O density at low altitudes for high geomagnetic model parameters, and furthermore, that absorption of the OI(135.6)-nm auroral emission by O_2 residing above the peak emission altitude during high characteristic energy events is significantly overestimated. The model thermosphere in high-A_P auroral model would be highly agitated due to intense geomagnetic activity, and consequently, a high-A_P, hot thermosphere will be significantly expanded, with pressure levels residing at higher altitudes relative to a low-A_P, cooler thermosphere. The presumption is that less atomic oxygen resides at low altitudes and more molecular oxygen at high altitudes in a high-A_P thermosphere, which is what MSIS-90 predicts.

High-A_P model predictions of auroral emissions that reside in SR continuum will be significantly affected by O_2 number density estimations in MSIS-90. This is certainly the case here in the November 28, 2000 and March 20, 2001 data sets, and it is likely that MSIS-90 does not estimate the O number density well at low thermospheric altitudes and the O_2 number density well at middle-to-upper thermospheric altitudes for disturbed geomagnetic conditions, which resulted in the large number of highly-negative column shifts associated with high characteristic energy precipitation that pervade the November 28, 2000 and March 20, 2001 data sets.

If indeed the atomic oxygen number density profile is underestimated by MSIS-90, even in the low-A_P model thermosphere (an ongoing topic of thermospheric research), then this fact would explain, at least partially, why the OI(135.6)-nm auroral brightness is underestimated. For example, the observed-to-modeled OI(135.6)-nm brightness comparison from January 3, 2001 at 1139 UT is shown again below in Figure 4.25. The mean value of the modeled OI(135.6)-nm auroral brightness across the entire 2-D map is 14.3 counts, and the mean value of the observed OI(135.6)-nm brightness is 21.9 counts, a percent difference of 34%. Other observed-to-modeled OI(135.6)-nm brightness comparisons exhibited differences of up to 50%, while others, on average, showed almost no difference. This topic is examined in more detail below.

One way to increase the atomic oxygen number density in MSIS-90 at the auroral-emission altitudes of ~100-300 km is to apply a downward column shift to the MSIS-90 $[O]/([N_2]+[O_2])$ mixing ratio and redistribute the O, N_2 and O_2 number densities accordingly before implementing the electron transport code. Furthermore, the mean value of the column shift data sets or the peak location of the narrow Gaussian in the column shift distributions would be indicative of the downward column shift to apply. For example, if a downward column shift of –10 km were applied to the MSIS-90 number densities, then the atomic oxygen number density would be increased by a factor of 2-3 at auroral-emission altitudes relative to the original MSIS-90 estimate of the O number density. Figure 4.26 illustrates this effect, showing the original MSIS-90 O density profile and $[O]/([N_2]+[O_2])$ mixing ratio, and the new MSIS-90 O density profile

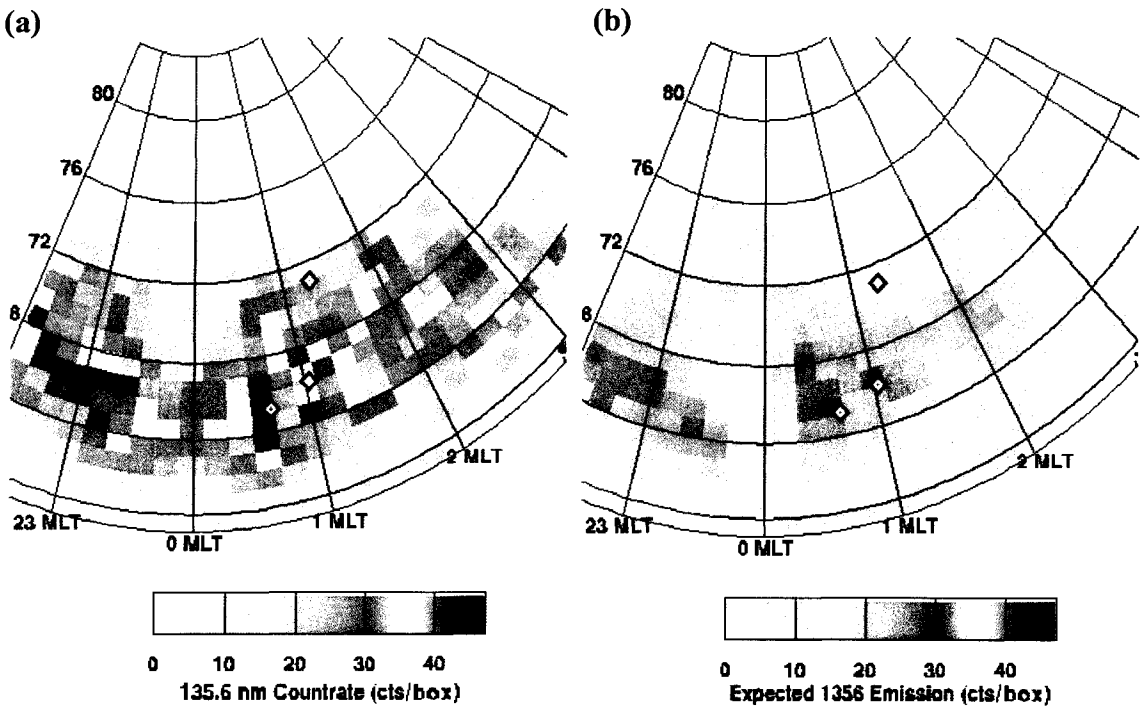

Figure 4.25. UVI-observed and modeled OI(135.6)-nm auroral brightnesses at 1139 UT on Jan 3, 2001. **(a)** UVI-observed OI(135.6)-nm brightness. **(b)** Modeled OI(135.6)-nm brightness. Previously shown as Figure 3.29 on page 172.

and $[O]/([N_2]+[O_2])$ mixing ratio after a downward column shift of –10 km is applied. This is not to say that the entire thermosphere is shifted downward by 10 km, but merely to show that if MSIS-90 is underestimating the O number density for a particular night, the implementation of a downward column shift to the $[O]/([N_2]+[O_2])$ mixing ratio and subsequent redistribution of the number densities before the electron transport code is executed can account for the initial discrepancy between the observed and modeled OI(135.6)-nm auroral brightness. The downward column shift of –10 km is representative of the fact that the unperturbed MSIS-90 prediction of atomic number densities at auroral-emission altitudes on a particular night was 2-3 times less than what the real thermosphere actually exhibited.

Another factor which may result in the underestimation of the modeled OI(135.6)-nm brightness is the inferred energy flux. Figure 3.26a from Chapter 3, shown again here

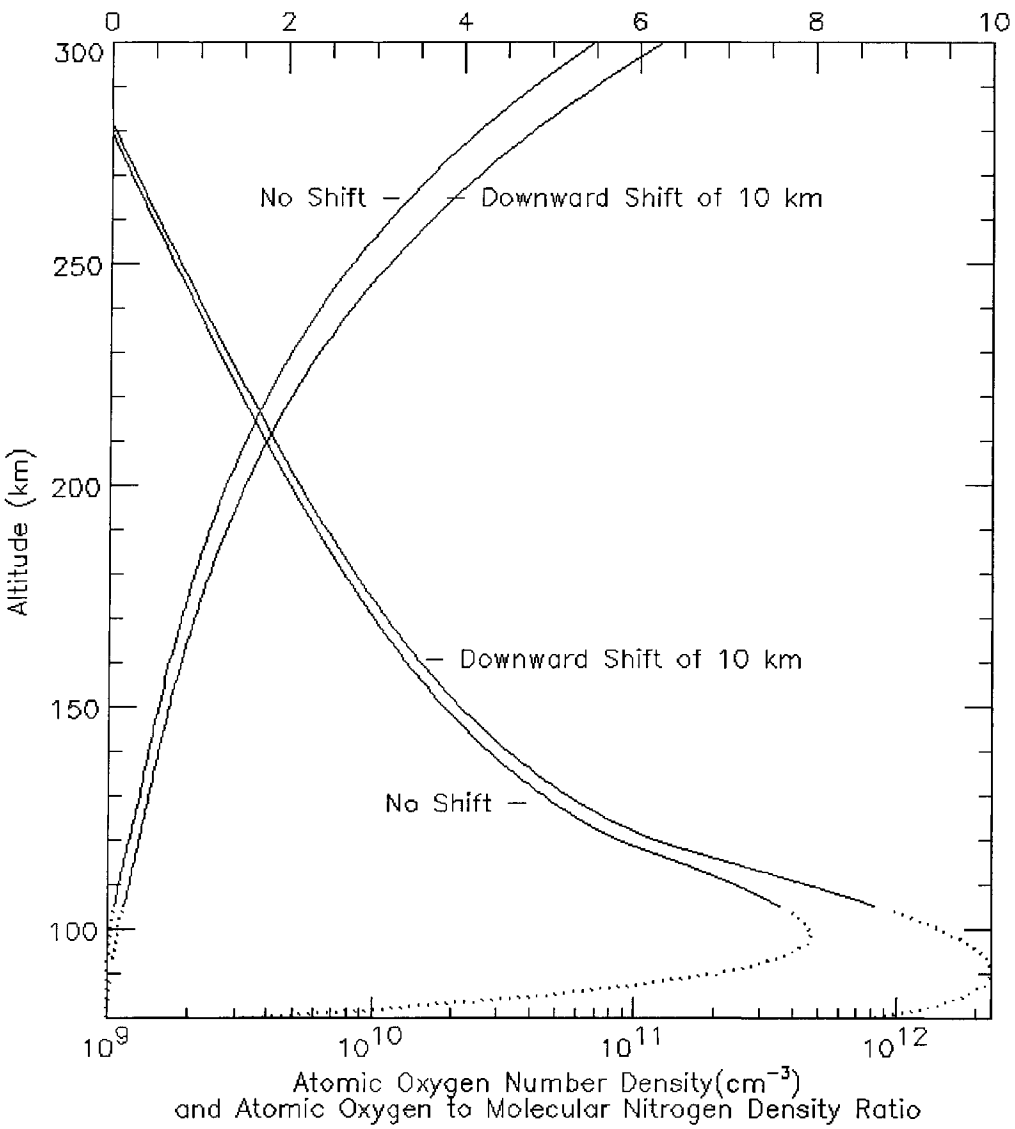

Figure 4.26. Columm shift correction to the MSIS-90 atomic oxygen number density. A column shift of –10 km is applied to the $[O]/([N_2]+[O_2])$ mixing ratio and densities are subsequently redistributed. An MSIS-90 thermosphere represented by the new mixing ratio has 2-3 times more atomic oxygen at the auroral-emission altitudes of ~100-300 km.

in Figure 4.27 to aid the discussion, describes the UVI instrument response to 1 $mW \cdot m^{-2}$ of energy flux. Upon determination of characteristic energy (from the LBH-S and LBH-L brightnesses), the modeled OI(135.6)-nm brightness due to 1 $mW \cdot m^{-2}$ of flux is inferred as a function of characteristic energy for the OI(135.6)-nm instrument response. Recall from Chapter 3 that because the integro-differential equation describing electron

transport into the atmosphere is linear in electron intensity, the solution for electron intensity is linearly dependent on energy flux F_e [*Lummerzheim et al.*, 1990]. Thus, simple linear scaling by the energy flux of the modeled OI(135.6)-nm brightness at 1 $mW \cdot m^{-2}$ is justified. The energy flux as determined from the LBH-L brightness in essence acts as a scaling factor to the OI(135.6)-nm instrument response curve, and therefore is multiplied by the modeled OI(135.6)-nm brightness for 1 $mW \cdot m^{-2}$ in order to infer the modeled OI(135.6)-nm brightness due to a given energy flux. However, if the inferred energy fluxes are underestimated because, for example, a particular electron

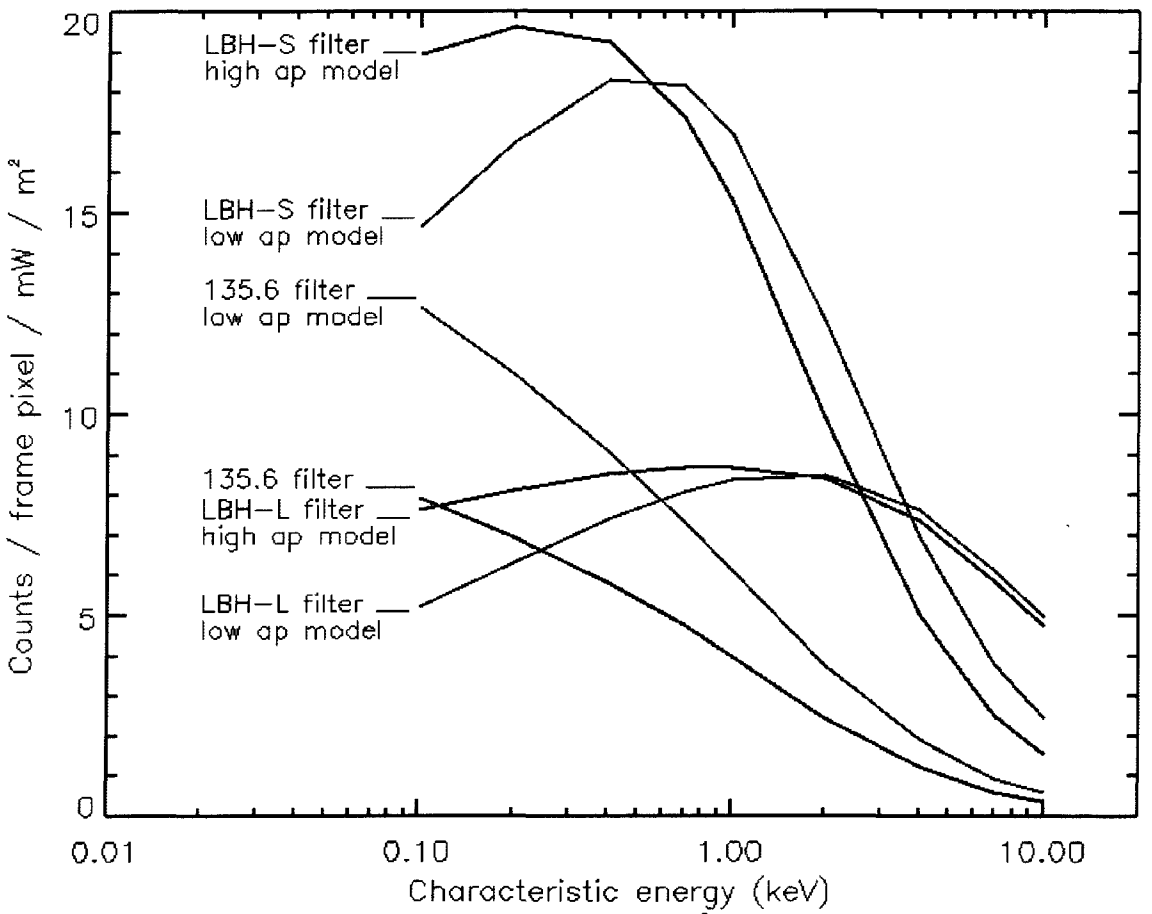

Figure 4.27. UVI instrument response to 1 $mW \cdot m^{-2}$ of energy flux as a function of characteristic energy for two levels of geomagnetic and solar activity. The low-A_P model run is shown in red. The energy flux associtated with a given aurora is estimated from the observed LBH-L brightness using the LBH-L reference curves shown here. See the text for discussion.

transport code predicts a higher LBH-L brightness for 1 $mW \cdot m^{-2}$ of energy flux at a particular characteristic energy than another electron transport model, then the inferred energy flux depends on the output of that particular auroral model. Recall from Chapter 3 that the consensus agreement among UVI auroral modelers is to use 9.3 $counts \cdot pixel^{-1}$ to indicate 1 $mW \cdot m^{-2}$ of energy flux, which is greater than any point on the LBH-L instrument response curve produced by the transport code of *Lummerzheim and Lilensten* [1994] shown in Figure 4.27. However, as was discussed in Chapter 3, other transport codes have predicted an LBH-L instrument response curve of 10 $counts \cdot pixel^{-1}$ with a slope much closer to zero [*Lummerzheim*, 2004, private communication]. Thus, the consensus agreement was to use 9.3 $counts \cdot pixel^{-1}$ to indicate 1 $mW \cdot m^{-2}$ of energy flux as a compromise between the different auroral model predictions. Reducing this factor increases energy flux estimates from UVI LBH-L observations.

An example which illustrates this is shown Figures 4.28a-c. Figure 4.28a shows a scatter plot of the modeled OI(135.6)-nm auroral brightness versus the observed OI(135.6)-nm brightness at the time of 1133 UT on the night of January 3, 2001. The mean value of the observed OI(135.6)-nm brightness across the entire 1133 UT 2-D map is 22.6 counts. The mean value of the modeled OI(135.6)-nm brightness is 14.5 counts, a percent difference of 36% which indicates that the modeled brightness was underestimated in this example. The column shift map inferred from the comparison of the observed OI(135.6)-nm brightness is shown in Figure 4.28b, and is, on average, strongly downward column shifted, which would be expected based on the scatter plot. The slope of the linear regression line to the scatter plot is not equal to one, which indicates that as auroral brightness increases, the modeled OI(135.6)-nm brightness is systematically lower. If the energy flux is being increasingly underestimated as characteristic energy increases, then the modeled OI(135.6)-nm brightness will be attenuated. The characteristic energy map shown in Figure 4.28c indicates that mostly hard (~4-6 keV) electrons were precipitating across the region at this time, and recall that this is similar to the example discussed in Figures 4.17 for the night of November 28, 2000, where the high characteristic energies observed at 0535 UT at ~66° from 1900-2200

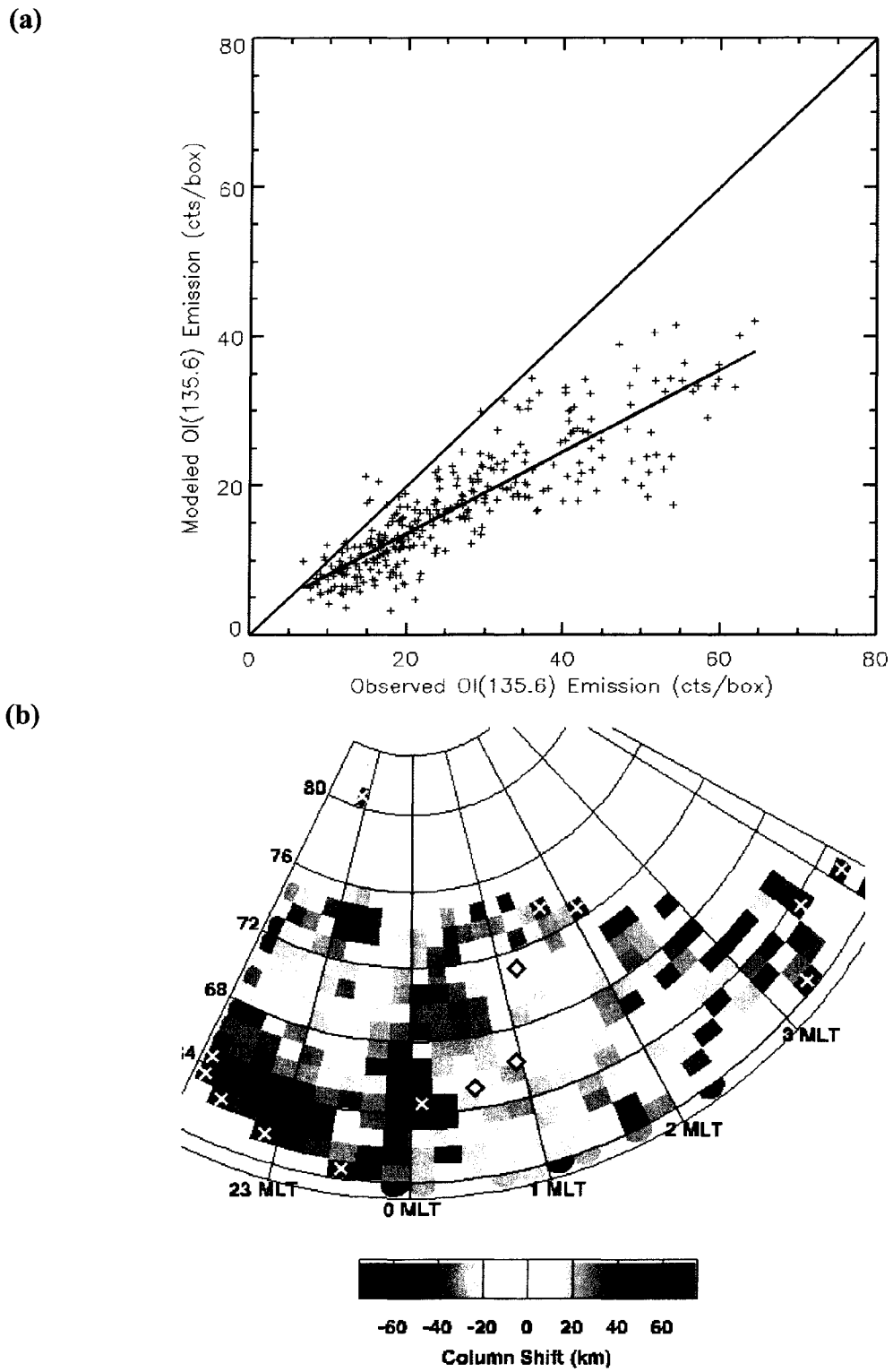

Figure 4.28. Observed versus modeled OI(135.6)-nm brightness, column shift, and characteristic energy at 1133 UT on Jan 3, 2001. **(a)** The scatter plot is indicative an underestimated modeled OI(135.6)-nm brightness. **(b)** The inferred column shifts.

(c)

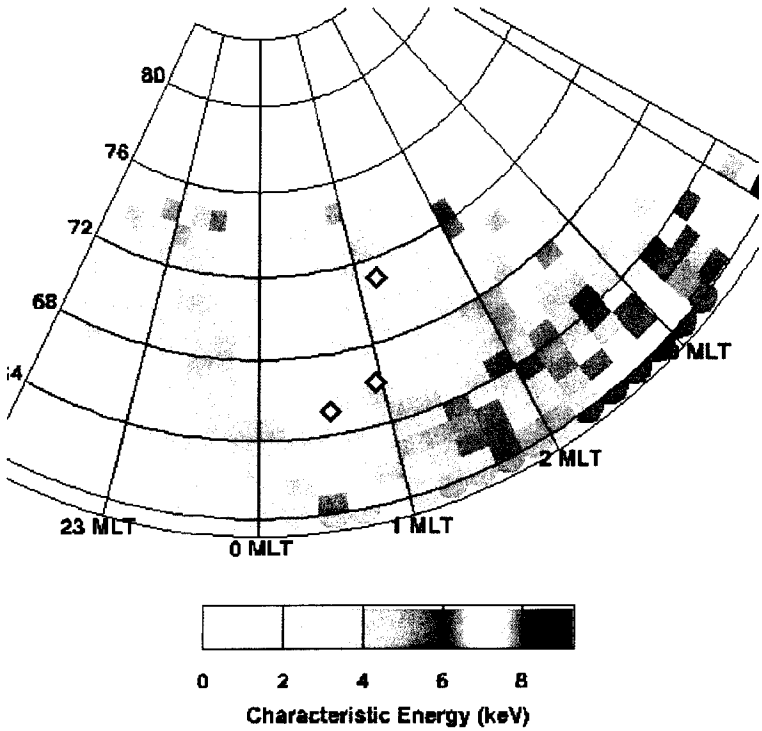

Figure 4.28 cont. Observed versus modeled OI(135.6)-nm brightness, column shift, and characteristic energy at 1133 UT on Jan 3, 2001. **(c)** The inferred characteristic energies.

MLT resulted in a very weak modeled OI(135.6)-nm brightness (~1 count·box^{-1}), whereas the observed OI(135.6)-nm brightness was much brighter. During these high characteristic energy auroras, the modeled OI(135.6)-nm auroral brightness was clearly underestimated compared to the observed OI(135.6)-nm auroral brightness.

An example of softer electron precipitation producing a modeled OI(135.6)-nm auroral brightness that more closely matches the observed brightness is seen in Figures 4.29a-c from the January 3, 2001 data set at 0632 UT. The mean value of the observed OI(135.6)-nm brightness across the entire 2-D map is 14.0 counts, and the mean value of the modeled OI(135.6)-nm brightness is 12.6 counts, a percent difference of 10%. The scatter plot indicates that the observed and modeled OI(135.6)-nm brightness values fall on average about a line of slope equal to one, and the correlation coefficient between the vector of observed OI(135.6)-nm brightness values and vector of modeled OI(135.6)-nm

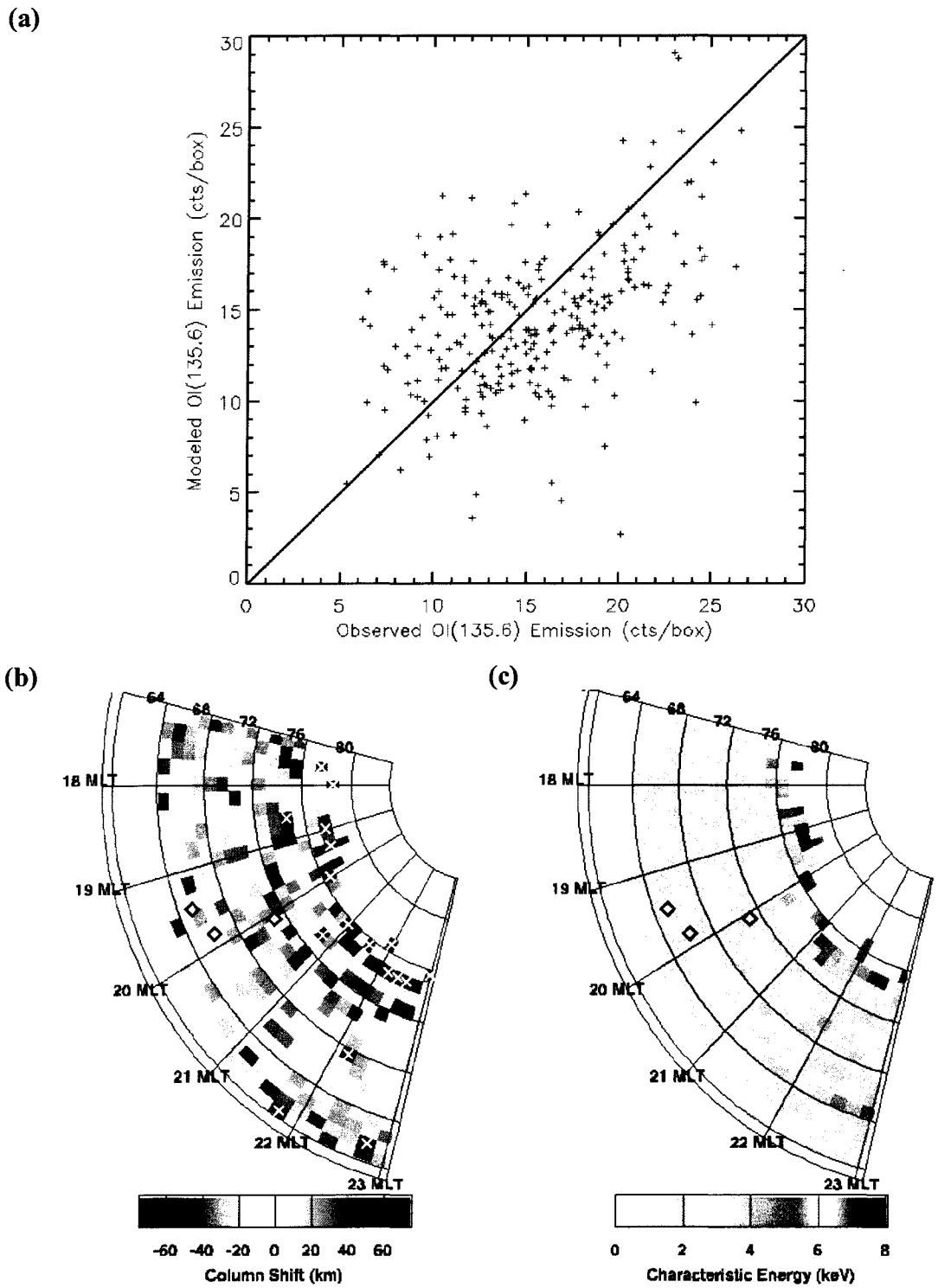

Figure 4.29. Observed versus modeled OI(135.6)-nm brightness, column shift, and characteristic energy at 0632 UT on Jan 3, 2001. **(a)** The scatter plot is indicative of a modeled OI(135.6)-nm brightness that on average matches the observed OI(135.6)-nm brightness. **(b)** The inferred column shifts. **(c)** The inferred characteristic energies.

brightness values is 0.63, which indicates a high degree of correlation and a fit to a linear model. Furthermore, the column shift map of Figure 4.29b has the character of a map similar to the February 28, 2000 0552 UT example shown in Figure 3.33b. The column shift values generally fall within the range of ±10-80 km expected for the height displacement of air parcels due to intermediate- to large-magnitude vertical winds, and the column shift map appears to function well as an indicator of composition variations associated with the aurora. Bands of red boxes, presumably due to periods of Joule and particle-precipitation heating and sustained upward winds, are clearly identified in Figure 4.29b, and scattered among the red boxes are regions of blue boxes, likely associated with adjacent upward- and downward-moving air columns due to the energetic forcing.

The characteristic energy map shown in Figure 4.29c indicates that there was much softer precipitation, ~1-4 keV, occurring across the region during this aurora, and as the LBH-L instrument response curve in Figure 4.27 reveals, an LBH-L brightness closer to 9.3 counts·box^{-1} equates to 1 mW·m^{-1} at these characteristic energies. Thus, the standard of 9.3 counts·box^{-1} used for UVI analysis may only be realistic for 1 keV aurora, and for higher characteristic energies, the conversion factor between LBH-L brightness and energy flux should be reduced. Examination of the LBH-L instrument response curve indicates that a conversion factor of 7 counts·box^{-1} = 1 mW·m^{-2} might be appropriate for higher characteristic energies, but this would only improve the modeled OI(135.6)-nm brightness by ~10-20%, generally not enough, on average, to match the modeled OI(135.6)-nm brightness to the observed brightness. Furthermore, the character of the LBH-L response curve deviates considerably from auroral model to auroral model, as discussed in Chapter 3, and estimation of the mean of the curve is also uncertain from model to model [*Germany et al.*, 2001]. It was determined by the UVI team that 9.3 counts·pixel^{-1} of LBH-L brightness = 1 mW·m^{-1} be the standard conversion factor for inferring energy flux from LBH-L measurements based on the many uncertainties associated with the different auroral models being applied to UVI analysis.

The several examples presented in Section 4.1 of intermediate-magnitude vertical wind-induced column shifts at middle- to upper-thermospheric altitudes indicate that the

column shift parameter at times can be used for comparison to single point-to-point measurements of vertical winds from the ground. The Inuvik FPS vertical wind measurements were shown to have geophysical and statistical significance based on the presentations of the vertical wind time series in Chapter 3. Furthermore, an analysis of the distributions of vertical winds and column shifts presented here identifies a distinct two-Gaussian signature in both data sets, indicative of two distinct classes of vertical winds that prevail in the auroral-latitude thermosphere. In general, column shift values fall within the range of ±10-80 km that is expected for the height displacement of air parcels due to vertical winds, particularly when a bright-aurora criterion is used to distinguish reliable column shifts. The 2-D column shift maps characterize the spatial morphology of thermospheric composition variations associated with the aurora over spatial scales of ~100-1000 km, even when the column shift variation is relative to a mean (or median) column shift value. Subject to the improvements suggested here, absolute column shift estimates may also be possible, yielding a more reliable parameter for comparison to vertical wind measurements.

Chapter 5 Discussion, Conclusions and Future Work

5.1 Discussion and General Conclusions

This thesis has presented seven time series of OI(630.0)-nm upper-thermospheric vertical wind measurements obtained with a Fabry-Perot spectrometer at the auroral-latitude location of Inuvik, NT, Canada. One time series of upper- and OI(557.7)-nm lower-thermospheric vertical wind measurements obtained at Poker Flat, AK with the CRL-FPS [*Ishii et al.*, 1997] were also presented. The goal was to identify thermospheric composition perturbations which could be attributed to the significant vertical wind events associated with auroral-heating processes that were evident in these vertical wind time series. Consequently, a second data set was utilized to explore this possibility. POLAR spacecraft UVI auroral observations of the LBH emissions of molecular nitrogen and the OI(135.6)-nm emission in conjunction with the outputs of the *Lummerzheim and Lilensten* [1994] auroral model provided the means to infer a vertical displacement parameter referred to as the column shift. The column shift approximates such vertical wind effects as transport, mixing and disruption of diffusive equilibrium in the auroral model by vertically displacing the MSIS-90 $[O_2]/[N_2]$ and $[O]/([N_2]+[O_2])$ mixing ratios, imposing the new ratios at a different altitude range, and subsequently redistributing the O, N_2 and O_2 number densities at each model thermospheric pressure level. The column shift estimates that were inferred from the observed-to-modeled OI(135.6)-nm auroral brightness comparisons were presented in two formats; two-dimensional maps encompassing a large area centered on Inuvik's location at horizontal spatial scales of $\sim 10^4$-10^5 km^2 and time series of spatially-averaged column shift values over Inuvik's and Poker Flat's respective locations. The 2-D column shift maps distinguish the spatial morphology of composition variations relative to the model thermosphere, and the point-to-point column shift time series are compared to the vertical wind time series.

Chapter 1 described the global-scale processes that are responsible for the composition and density, wind and temperature patterns observed in the thermosphere.

The thermosphere's horizontal wind system and quasi-equilibrium configuration set up by the Sun's UV and X-ray radiative input was described, ending with a discussion of the high-latitude processes that contribute to and modify the wind system and disturb the equilibrium. High-latitude, intermediate-to-large magnitude vertical winds associated with auroral-related processes and their effects on the thermosphere's state were discussed in detail. A general overview of the thermosphere's structure, composition and photochemistry was presented, leading into a discussion of diffusion and diffusion time scales in the thermosphere and diffusive equilibrium. Lastly, a discussion illustrating the correlation between heating, vertical winds, and composition response was presented.

Chapter 2 described the two instruments that were used in this study. A general overview of Fabry-Perot spectroscopy was presented, and the Inuvik FPS was described in some detail. The POLAR spacecraft UVI instrument was described, as was the POLAR spacecraft's orbital trajectory. The wavelength passbands of the five UVI filters are presented, as is the motivation for the selection of these wavelength ranges.

Chapter 3 described in some detail the data acquisition and data reduction techniques applicable to both data sets that were developed here. How the Inuvik FPS OI(630.0)-nm observations were reduced to spectral widths and Doppler shifts and how the étalon drift was characterized in the Doppler shifts was described. The vertical wind time series from Inuvik were presented and their statistical and geophysical characteristics were described. The techniques used to remove airglow and bin the UVI auroral data, and infer characteristic energy, energy flux, the modeled OI(135.6)-nm auroral brightness and column shifts from UVI observations in conjunction with the outputs of the *Lummerzheim and Lilensten* [1994] auroral model were described. The column shift modification to the MSIS-90 model thermospheric density structure was described, and examples of 2-D column shift maps and time series of spatially-averaged column shift values over Inuvik were presented. Error estimates of the UVI- and model output-inferred auroral parameters are also discussed.

Chapter 4 was separated into two sections. Section 4.1 presented the time series comparisons of Inuvik and Poker Flat vertical wind measurements to spatially-averaged

column shift values. Statistical characteristics of the column shift data sets were first presented, and the techniques which were developed to better interpret the column shift parameter were described, since it was clear from the column shift statistical properties that, on average, the auroral model underestimated the OI(135.6)-nm brightness compared to the observed brightness. A bright-aurora criterion was identified that discarded skeptically-inferred highly-negative column shift estimates associated with the boxes on the 2-D maps that resided at non-auroral-oval latitudes. Boxes on the maps were regions of binned UVI auroral data 1° latitude × 3° longitude, an area of ~110 km × ~120 km = 1.3×10^4 km^2. It was speculated that the boxes residing at non-auroral-oval latitudes potentially were contaminated with residual airglow signal that had not been removed by the airglow-removal algorithm. In general, the observed OI(135.6)-nm brightness was much larger in these boxes than the modeled OI(135.6)-nm brightness, resulting in highly-negative unrealistic column shift values.

The bright-aurora criterion also indicated with more certainty that 1 mW·m^{-2} of energy flux prevailed in a given box based on the general uncertainty in energy flux estimates of 20-35%, which gave more confidence that vertical winds and column shifts may prevail in that particular box. A simple calculation revealed that the mechanical power per unit area P/A required to induce an intermediate-magnitude vertical wind of 30 m·s^{-1} at 200 km altitude is P/A = 3.4 mW·m^{-2} (using the MSIS-90 predicted temperature and total mass density at 200 km). Thermal energy requirements are negligible compared to mechanical energy requirements at the middle- to upper-thermospheric altitudes of $\gtrsim$180 km, and thus, energy flux values of ~1-4 mW·m^{-2} are significant at middle- to upper-thermospheric altitudes, particularly if the range of characteristic energy of the electron precipitation is soft-to-moderate ($\lesssim$1-2 keV), indicating that a significant percentage of its energy is deposited at higher altitudes.

Two examples of an intermediate-magnitude (~30-50 m·s^{-1}) vertical wind-induced composition perturbation, one from the January 3, 2001 and one from the February 28, 2000 vertical wind and column shift time series comparisons, are identified in the relative column shift variation (~35 km) over Inuvik. The composition perturbations were

indicative of a delayed composition effect due to a fairly long-lived (~15 min) intermediate-magnitude vertical wind; *i.e.*, the significant vertical wind events preceded column shift variation over Inuvik the amount of time required to perturb the composition, which was in essence the duration of the vertical wind event. The composition perturbations from each night were also determined to occur at middle- to upper-thermospheric altitudes, based on energy flux and characteristic energy values prevailing over Inuvik at the time of the vertical wind measurements, and the fact that the wind events were not energetic nor long-lived enough or that the relative column shift variation was large enough to indicate a lower- to upper-thermospheric vertical flow cell and composition perturbation.

Cross correlation coefficients at different time lags were also calculated between these time series comparisons, and only one, the January 26, 2001 vertical wind and column shift time series, showed a high degree of correlation at a reasonable time lag. In addition, the two time series both exhibited a significant periodicity at ~3 hr, which may be attributed to equivalent gravity wave oscillations present in both data sets. The time lag of –78 min is also reasonable; *i.e.*, a lower-thermospheric perturbation (identified by the column shift variation) requires ~70 min to reach the upper thermosphere (identified by the vertical wind variation).

Two examples of intermediate- to large-magnitude vertical wind-induced upper-thermospheric composition perturbations were identified over Poker Flat in the CRL-FPS vertical wind and column shift time series comparisons from March 20, 2001. The variations in the CRL-FPS OI(630.0)-nm relative intensity indicated whether upward (decreases in intensity) or downward (increases in intensity) winds prevailed. The relative variations in the column shift values over Poker Flat supported the intensity and wind measurements, and the composition perturbation was indicative of an immediate composition effect; *i.e.*, the vertical wind field had prevailed for some time before moving into the CRL-FPS field of view and had already modified composition in the thermospheric column. Thus, the column shift variations occurred simultaneously with the onset of the intermediate- to large-magnitude vertical winds. These composition

perturbations were also determined to occur at middle- to upper-thermospheric altitudes, based on prevailing energy flux and characteristic energy values over Poker Flat.

One final example of a large-magnitude vertical wind-induced composition perturbation over Inuvik was identified in the November 28, 2000 vertical wind and column shift time series comparison. This was another example similar to the March 20, 2001 time series comparison, where a middle- to upper-thermospheric composition perturbation was determined to occur based prevailing energy flux and characteristic energy values over Inuvik. The variations in the OI(630.0)-nm relative intensity and the relative column shift values over Inuvik supported the vertical wind measurements, both of which occurred simultaneously with the significant wind measurements, indicating that the vertical wind field had prevailed for some time and modified composition in the thermospheric column before moving into the Inuvik FPS field of view.

A more detailed investigation of the 2-D maps of energy flux, characteristic energy, observed and modeled OI(135.6)-nm auroral brightnesses and column shifts identified why one of the column shift estimates in the time series comparison did not support the significant vertical wind during the composition perturbation. The 2-D map presentation also helped explain why the March 20, 2001 and November 28, 2000 column shift data sets were more perplexing than the other column shift data sets, based on their statistical characteristics and the fact that a significant number of highly-negative column shift estimates were retained even after the bright-aurora criterion was applied. These two UVI auroral data sets had been analyzed using *Lummerzheim and Lilensten* [1994] auroral model outputs produced by a high-A_P MSIS-90 model thermosphere. I concluded from the 2-D map analysis that MSIS-90 may be grossly underestimating the O number density at low thermospheric altitudes and possibly overestimates the O_2 number density at middle- to upper-thermospheric altitudes for highly-disturbed geomagnetic parameters. This conclusion was based on the fact that the modeled OI(135.6)-nm auroral brightness was significantly underestimated (65-80%) compared to the observed OI(135.6)-nm brightness when the precipitation's characteristic energy was high ($\gtrsim$4 keV). High characteristic energy precipitation penetrates deep into the thermosphere, and if the O

number density is significantly underestimated by MSIS-90 at low auroral-emission altitudes (~100-120 km), then the modeled OI(135.6)-nm auroral brightness will be significantly underestimated. Furthermore, if MSIS-90 overestimates the O_2 number density at middle- to upper-thermospheric altitudes, then attenuation by O_2 of auroral emissions that fall into the SR continuum (~130-175 nm) which are produced at low auroral-emission altitudes will be significantly affected by overestimation of O_2.

Section 4.2 presented an analysis of the histogram distributions of the Inuvik and South Pole vertical wind measurements and the column shift data sets. The histogram analysis of the column shift data sets was motivated by previous analyses (performed by me) of auroral-latitude vertical wind data sets, which revealed that auroral-latitude vertical winds are a real thermospheric phenomenon and assume a distinct two-Gaussian signature of one narrow and one broad Gaussian, indicative of two distinct classes of vertical winds which prevail in the auroral-latitude thermosphere. Random, small- to intermediate-magnitude vertical winds (~1-30 $m \cdot s^{-1}$), indicative of the full-width at half-maximum of the narrow Gaussian, are due to solar radiative input and the weak Joule and particle-precipitation heating that prevails at auroral latitudes almost all of time. Intermediate- to large-magnitude vertical winds ($\geq$30-50 $m \cdot s^{-1}$), indicative of the full-width at half-maximum of the broad Gaussian, are due to significant auroral-heating events. Presentation of the distributions of the Inuvik and South Pole vertical wind measurements support these conclusions.

A distinct, two-Gaussian signature of one narrow and one broad Gaussian was also identified in the column shift histogram distributions, suggesting that indeed, column shifts are a real thermospheric phenomenon and can be attributed to auroral-latitude vertical wind activity. The column shift histograms were first assembled using a lower threshold of auroral brightness than the one mentioned above on column shift estimates to retain in the data sets. Using this lower brightness threshold, the full-width at half-maximum of the narrow Gaussian in the column shift distributions (~30 km) was indicative of air-parcel height displacements that would be expected from small- to intermediate-magnitude vertical winds. However, the full-width at half-maximum of the

broad Gaussian in the column shift distributions (73-100 km) was generally larger than the range expected of air-parcel height displacements due to intermediate- to large-magnitude vertical winds. Furthermore, the height of broad column shift Gaussian was generally as large as the narrow column shift Gaussian, which would not be expected since intermediate- to large-magnitude vertical wind events are much less frequent than small- to intermediate-magnitude vertical winds. The fact that the broad column shift Gaussian was so pronounced was attributed to the large number of highly-negative unrealistic column shift values that were prevalent in the column shift data sets and were associated with boxes on the 2-D maps that resided at non-auroral-oval latitudes. In addition, the column shift distributions were also biased towards negative values, indicating that the auroral model underestimated the OI(135.6)-nm brightness compared to the observed OI(135.6)-nm brightness.

When the auroral brightness threshold was increased (indicating with more certainty that 1 $mW \cdot m^{-2}$ of energy flux prevailed in a given box), the size of the column shift data sets was reduced considerably, in some cases by a factor of 3. The column shift distributions remained unchanged in that a two-Gaussian signature was still apparent, but the characteristics of the broad Gaussian changed considerably. The width of the narrow Gaussian remained essentially the same (~30 km), while the width of the broad Gaussian took on a range (51-76 km) that would be expected of air-parcel height displacements across 2-3 scale heights due to long-lived, large-magnitude vertical wind events extending from the lower to upper thermosphere. Furthermore, the height of the broad Gaussian decreased significantly, generally by about half, indicating that the bright-aurora threshold rejected a large number of the highly-negative unrealistic column shift values. Most of these rejected column shift estimates resided at non-auroral-oval latitude, which the reevaluated 2-D maps of the column shift revealed.

Nonetheless, even with the application of the bright-aurora criterion, the column shift distributions were still biased towards negative values, indicating that the auroral model continued to underestimate the OI(135.6)-nm brightness compared to OI(135.6)-nm brightness observations. On average, there was a 10-50% difference between the

modeled and observed OI(135.6)-nm brightnesses, and possible reasons for this auroral-model deficiency were considered. For example, I speculated that if MSIS-90 is underestimating the large-scale average atomic oxygen density at each pressure level for a given night, then the negative peak value of the narrow Gaussian of a particular column shift distribution is indicative of how far off MSIS-90 predicted the atomic oxygen number density. A systematic downward column shift equal to the peak value of the narrow Gaussian and applied to the MSIS-90 $[O_2]/[N_2]$ and $[O]/([N_2]+[O_2])$ mixing ratios would redistribute the O, N_2, and O_2 number densities at each thermospheric pressure level and increase the O number density at auroral-emission altitudes, thus increasing the modeled OI(135.6)-nm brightness and centering the narrow Gaussian of the column shift distribution.

One other factor affecting modeled OI(135.6)-nm brightness predictions is the UVI-inferred energy flux. The consensus agreement among UVI auroral modelers is to use 9.3 counts·pixel^{-1} of LBH-L brightness to indicate 1 mW·m^{-2} of energy flux at all characteristic energies. However, the range of this value from auroral model to auroral model is highly variable. The electron transport code of *Lummerzheim and Lilensten* [1994], for example, predicts that a range of 5 to 8 to 5 LBH-L counts·pixel^{-1} is equivalent to 1 mW·m^{-2} of energy flux for the range of 0.1 to 1 to 10 keV characteristic energies, respectively (see Figure 3.26a). On the other hand, the transport code of *Richards and Torr* [1990] computes a value of ~10 counts·pixel^{-1} with a slope much closer to zero for the same range of characterisitic energies [*Lummerzheim*, 2004, private communication]. If a lower-valued LBH-L counts·pixel^{-1} is used to indicate 1 mW·m^{-2} of energy flux, then UVI-inferred energy flux values are increased. Two examples presented at the end of Chapter 4 illustrate this effect. When energy flux appeared to be underestimated across a 2-D map, based on the fact that the modeled OI(135.6)-nm brightness on average was significantly underestimated (by 35%) compared to the observed brightness, the characteristic energy of the precipitation was generally hard ($\gtrsim$4 keV). Thus, a lower-valued LBH-L counts·pixel^{-1} per 1 mW·m^{-2} of energy flux predicted by the *Lummerzheim and Lilensten* [1994] model for high characteristic

energies may be valid here. When energy flux appeared to be reasonably-well estimated, based on the small, on-average difference between the modeled and observed OI(135.6)-nm brightness (~10%), the charateristic energy was soft to moderate in its range, ≲1-2 keV. Thus, the higher-valued 9.3 LBH-L counts·pixel^{-1} per 1 mW·m^{-2} of energy flux used by UVI auroral modelers is valid.

Auroral-modeling issues aside, the column shift parameter has been shown to be a valid measure of vertical wind-induced composition effects. The examples presented in Chapter 4 of the relative column shift variation compared to significant vertical wind measurements supports the conclusion that intermediate- to large-magnitude vertical winds do perturb composition in the auroral-latitude thermosphere and that this perturbation can be quantified. Furthermore, the distribution of column shift values exhibits a distinct two-Gaussian signature, similar to the two-Gaussian signature identified in the distribution of auroral-latitude vertical wind measurements. The range of widths of the narrow (22-36 km) and broad (51-73 km) Gaussians in the column shift distributions (after the bright-aurora criterion is applied) are indicative of air-parcel height displacements that are due to vertical wind magnitudes which are characterized by the range of widths in the narrow (25-36 m·s^{-1}) and broad (46-96 m·s^{-1}) Gaussians of the Inuvik and South Pole vertical wind distributions. If the auroral-modeling deficiencies can be rectified, absolute column shift estimates may be possible, making their comparison to vertical wind measurements more reliable.

5.2 Summary and Future Work

5.2.1 The Inuvik Fabry-Perot Spectrometer

Major upgrades to the Inuvik FPS during the last seven years have significantly improved its reliability and day-to-day capability. The FPS now generates near real-time estimates of vertical winds, relative airglow and/or auroral brightness and temperatures in either the lower or upper thermosphere by observing the OI(557.7)-nm or OI(630.0)-nm emission, respectively, and posts this information on the World Wide Web. The FPS is still capable of horizontal wind measurements as well, if desired. Furthermore, the characterization of the FPS étalon is now done on a daily basis instead of once or twice a

week since the installation of a new laser shutter. In addition, the drift of the étalon due to pressure and temperature variations can be reasonably accounted for using techniques in the post-data-acquistion analysis that take advantage of the pressure and temperature data sets acquired with the FPS image data sets. Lastly, the inherent nature of remote-site facilities can make it difficult to implement fixes to the equipment there. However, in the case of the Inuvik FPS, software upgrades can now be uploaded remotely directly to the FPS operating computer since the installation of a network card into the operating PC and its new-found network connection to a laptop computer, which acts as the communications hub between Fairbanks and Inuvik, the image storage unit, and the data analysis device.

Inuvik provides a unique site for measuring thermospheric vertical winds because of its spatial relation to the quiet-time auroral oval. Vertical wind estimates acquired at Inuvik over the last six years exhibit some unusual—but not unprecedented—properties based on the data sets presented here. These data suggest that thermospheric processes associated with the generation of these vertical winds would also procduce significant composition perturbations at the mesoscale sizes of ~10^4-10^5 km^2. Future work on the Inuvik FPS could, and indeed should, include enclosing the étalon in a pressure-sealed, temperature-controlled chamber, which would eliminate obvious problems with having an étalon exposed to ambient air. A frequency-stabilized laser would be nice as well, eliminating the need for pressure and temperature drift correction since a time-varying estimate of the étalon's drift can be determined from the peak locations of the laser spectra.

5.2.2 Comparing the Modeled OI(135.6)-nm Brightness to Observations: The Column Shift Parameter

For the first time, UVI-inferred energy fluxes and characteristic energies are used to model the OI(135.6)-nm emission in conjunction with the auroral model of *Lummerzheim and Lilensten* [1994]. The modeled OI(135.6)-nm brightness is compared to the UVI-observed OI(135.6)-nm brightness in order to search for discrepancies between the two, potentially identifying mesoscale composition effects. The validity of the assumption that these composition effects are due to vertical winds is pursued through the

development of the column shift, a new model parameter introduced into the electron transport code of *Lummerzheim and Lilensten* [1994] which simulates and parameterizes such vertical-wind effects as height displacement of air parcels (transport), mixing and disruption of diffusive equilibrium. The column shift alters the MSIS-90 neutral thermospheric densities such that the modeled OI(135.6)-nm brightness matches observations.

The spatial morphology of thermospheric composition variations associated with auroral forms relative to the model thermosphere is studied through the use of the two-dimensional maps of the column shift parameter. Organized structures are apparent in these maps, potentially indicating spatially-extended regions of thermospheric up or downwelling over the ~30-60 minutes immediately preceeding the image exposure. In addition, time series comparisons of the column shift estimates to vertical wind measurements from Inuvik and Poker Flat identify several examples of vertical wind-induced composition variations. Though the two time series were generally not correlated, the case-study examples do indicate that, at times, column shifts are due to significant vertical winds.

Systematic errors identified in the column shift data sets through the use of statistical analyses suggested a technique to filter skeptically-inferred column shifts from the physically meaningful column shift estimates. Because the technique amounts to rejection of pixels with low LBH-L brightness, the column shift technique should not be applied except in the presence of bright aurora. However, filtering of the poorly-inferred column shifts did not remove the on-average trend of a given night's column shift data set to form a distribution with non-zero, negative mean. It was speculated that under certain circumstances, this may be attributed to MSIS-90 underestimating the on-average atomic oxygen number densities for a given night, or that energy flux is being underestimated. Further case studies of selected 2-D column shift and characteristic energy maps revealed that energy flux may be underestimated during high characteristic energy aurora. However, due to the great uncertainties associated with auroral modeling in general, the resulting scaling factor of LBH-L brightness to 1 $mW \cdot m^{-2}$ of energy flux

is also quite uncertain. Nonetheless, some of these case studies indicate that the modeled OI(135.6)-nm brightness does on average match the observed brightness, and discrepancies between these brightnesses take on organized and coherent forms, which are distinguished by the 2-D column shift maps, reaffirming that the column shift is physically meaningful and can be used to examine auroral-zone mesoscale composition perturbations at spatial scales of $\sim 10^4$-10^5 km^2.

A next step in the evaluation of these UVI-inferred column shift data sets is to determine a manner in which the energy flux can be reevaluated and recomputed using different auroral model outputs. A possible experiment to further explore the column shift parameter with a different data set would be to collect in conjunction with vertical wind measurements ground-based photometric observations of visible auroral emissions in order to infer energy flux and characteristic energy [*e.g. Lummerzheim et al.*, 1990] and column shifts.

References

Abreu, V. J., G. A. Schmitt, P. B. Hays, J. W. Meriwether Jr., and C. A. Tepley, Atmospheric scattering effects on ground-based measurements of thermospheric winds, *Planet. Space Sci.*, **31**, 303-310, 1983.

Ackerman, M., and E. Van Hemelrijck, Measurement of upper atmospheric winds at 160 and 275 kilometers, *J. Geophys. Res.*, **76**, 3162-3163, 1971.

Ajello, J. M., and D. E. Shemansky, A re-examination of important N_2 cross sections by electron impact with application to the dayglow: the Lyman-Birge-Hopfield band system and NI (119.99) nm, , *J. Geophys. Res.*, **90**, 9845-9861, 1985.

Akasofu, S.-I., The development of the auroral substorm, *Planet. Space Sci.*, **12**, 273-282, 1964.

Akasofu, S.-I., Interplanetary energy flux associated with magnetospheric substorms, *Planet. Space Sci.*, **27**, 425-431, 1979.

Akasofu, S.-I., The solar wind-magnetosphere energy coupling and magnetospheric disturbances, *Planet. Space Sci.*, **28**, 495-509, 1980.

Akasofu, S.-I., Energy coupling between the solar wind and magnetosphere, *Space Sci. Rev.*, **28**, 121-190, 1981.

Anderson, D., and T. J. Fuller-Rowell, "The Ionosphere," Space Environment Topics, SE-14 (1999), 4 pp, Online, Internet, http://www.sec.noaa.gov/info/Iono.pdf, accessed January 21, 2005.

Anger, C. D., T. Fancott, J. McNally, and H. S. Kerr, ISIS-II scanning auroral photometer, *Appl. Opt.*, **12**, 1753-1766, 1973.

Anger, C. D., S. K. Babey, A. L. Broadfoot, R. G. Brown, L. L. Cogger, R. Gattinger, J. W. Haslett, R. A. King, D. J. McEwen, J. S. Murphree, E. H. Richardson, B. R. Sandel, K. Smith, and A. V. Jones, An ultraviolet auroral imager for the Viking spacecraft, *Geophys. Res. Lett.*, **14**, 387-390, 1987.

Armstrong, E. B., Doppler shifts in the wavelength of the OI 6300 line in the night airglow, *Planet. Space Sci.*, **17**, 957-974, 1969.

Aruliah, A. L., and D. Rees, The trouble with thermospheric vertical winds: geomagnetic, seasonal ans solar cycle dependence at high latitudes, *J. Atmos. Terr. Phys.*, **57**, 597-609, 1995.

Atherton, P. D., N. K. Reay, and J. Ring, Tunable Fabry-Perot filters, *Opt. Engin.*, **20**, 807-814, 1981.

Bevington, P. R., Data reduction and error analysis for the physical sciences, 1st ed., Vol. 1, McGraw-Hill Book Company, New York, 1969.

Biondi, M. A., D. P. Sipler, and M. Weinschenker, Multiple aperture exit plate for field-widening a Fabry-Perot interferometer, *Appl. Opt.*, **24**, 232-236, 1985.

Biondi, M. A., and D. P. Sipler, Horizontal and vertical winds and temperatures in the equatorial thermosphere: measurements from Natal, Brazil during August-September 1982, *Planet. Space Sci.*, **33**, 817-823, 1985.

Born, Max, and Emil Wolfe, Principles of optics, 7th (expanded) edition, Cambridge UP, 1999.

Brekke, A., Physics of the upper polar atmosphere, Chichester, Eng., John Wiley & Sons Press, 1997.

Brown, Robert A., Fluid mechanics of the atmosphere, International Geophysics Series, New York, Academic Press, 1991.

Carignan, G. R., B. P. Block, J. C. Maurer, A. E. Hedin, C. A. Reber, and N. W. Spencer, The neutral mass spectrometer on Dynamics Explorer, *Space Sci. Instrum.*, **5**, 429-441, 1981.

Carpenter, D. L., Whistler studies of the plasmapause in the magnetosphere, 1, Temporal variations in the position of the knee and some evidence on plasma motions near the knee, *J. Geophys. Res.*, **71**, 693-710, 1966.

Carpenter, D. L., and R. L. Smith, Whistler measurements of electron density in the magnetosphere, *Rev. Geophys.*, **2**, 415, 1964.

Christensen, A. B., J. H. Hecht, R. L. Walterscheid, M. F. Larsen, and W. E. Sharp, Depletion of oxygen in aurora: evidence for a local mechanism, *J. Geophys. Res.*, **102**, 22,273-22,277, 1997.

Chubachi, S., A special ozone observation at Syowa Station, Antarctica from February 1982 to January 1983, in Atmospheric ozone, Zerefos, C. S. and A. M. Ghazi, eds., D. Reidel Publishing, Dordrecht, 285-289, 1985.

Conde, M., and P. L. Dyson, Thermospheric vertical winds above Mawson, Antarctica, *J. Atmos. Terr. Phys.*, **57**, 589-596, 1995.

Conde, M., and R. W. Smith, Mapping thermospheric winds in the auroral zone, *Geophys. Res. Lett.*, **86**, 5532-5540, 1995.

Conde, M., and R. W. Smith, Phase compensation of a separation scanned, all-sky imaging Fabry-Perot spectrometer for auroral studies, *Appl. Opt.*, **36**, 5441-5450, 1997.

Conde, M., and R. W. Smith, Spatial structure in the thermospheric horizontal wind above Poker Flat, Alaska during solar minimum, *J. Geophys. Res.*, **103**, 9449-9471, 1998.

Conde, M., Analysis of Fabry-Perot spectra of lidar backscatter echoes, In *ANARE Reports*, No. 146, Morris, R. J., and P.J. Wilkinson, eds., 91-114, 2001.

Conde, M., J. D. Craven, T. Immel, E. Hoch, H. Stenbaek-Neilsen, T. Hallinan, R. W. Smith, J. Olson, and Wei Sun, Assimilated observations of thermospheric winds, the aurora and ionospheric currents over Alaska, *J. Geophys. Res.*, **106**, 10,493-10,508, 2001.

Conde, M., Deriving wavelength spectra from fringe images from a fixed-gap single-etalon Fabry-Perot spectrometer, *Appl. Opt.*, **41**, 2672-2678, 2002.

Conde, M., Comparative analysis of Poker Flat FPS data, CEDAR conference, June, 2003, Longmont, CO.

Craven, J. D., A. C. Nicholas, L. A. Frank, D. J. Strickland, and T. J. Immel, Variations in the FUV dayglow after intense auroral activity, *Geophys. Res. Lett.*, **21**, 2793-2796, 1994.

Crickmore, R. I., J. R. Dudeney and A. S. Rodger, Vertical thermospheric winds at the equatorward edge of the auroral oval, *J. Atmos. Terr. Phys.*, **53**, 485-492, 1991.

Dickinson, R. E., and J. E. Geisler, Vertical motion field in the middle thermosphere from satellite drag densities, *Mon. Weather, Rev.*, **96**, 606-616, 1968.

Dickinson, R. E., E. C. Ridley, and R. G. Roble, A three-dimensional general circulation model of the thermosphere, *J. Geophys. Res.*, **86**, 1499-1512, 1981.

Dickinson, R. E., E. C. Ridley, and R. G. Roble, Thermospheric general circulation with coupled dynamics and composition, *J. Atmos. Sci.*, **41**, 205-219, 1984.

Dieminger, W., G. K. Hartmann, and R. Leitinger, eds., The upper atmosphere: data analysis and interpretation, Berlin, Springer Press, 1996.

Doering, J. P., and E. E. Gulcicek, Absolute differential and integral electron excitation cross sections for atomic oxygen 8. The $^3P \rightarrow {}^3S^o$ transition (1356 Å) from 13.9 to 30 eV, *J. Geophys. Res.*, **94**, 2733-2736, 1989.

Dungey, J. W., Interplanetary magnetic field and the auroral zones, *Phys. Rev. Lett.*, **6**, 47-48, 1961.

Edwards, H. D., M. M. Cooksey, C. G. Justus, R. N. Fuller, and D. L. Albritton, Upper-atmosphere wind measurements determined from twelve rocket experiments, *J. Geophys. Res.*, **68**, 3021-3032, 1963.

Evans, J. V., Ionospheric movements measured by incoherent scatter: a review, *J. Atmos. Terr. Phys.*, **34**, 175-209, 1972.

Fairfield, D. H., and L. J. Cahill, Jr., Transition region magnetic field and polar magnetic disturbances, *J. Geophys. Res.*, **71**, 155-169, 1966.

Farman, J. C., B. G. Gardiner, and J. D. Shanklin, Large losses of total ozone in Antarctica reveal seasonal ClO_x/NO_x interaction, *Nature*, **315**, 207-210, 1985.

Field, P. R., and H. Rishbeth, The response of the ionospheric F2-layer to geomagnetic activity: an analysis of worldwide data, *J. Atmos. Solar-Terr. Phys.*, **59**, 163-180, 1997.

Field, P. R., H. Rishbeth, R. J. Moffett, D. W. Idenden, T. J. Fuller-Rowell, G. H. Millward, and A. D. Aylward, Modelling composition changes in F-layer storms, *J. Atmos. Solar-Terr. Phys.*, **60**, 523-543, 1998.

Forbes, J. M., Tidal and planetary waves, *Geophysical Monograph*, **87**, American Geophys. Union, 1995.

Frank, L. A., J. D. Craven, K. L. Ackerson, M. R. English, R. H. Eather, and R. L. Caroillano, Global auroral imaging instrumentation for the Dynamics Explorer mission, *Space Sci. Instrum.*, **5**, 369-393, 1981.

Frank L. A., J. B. Sigwarth, J. D. Craven, J. P. Cravens, J. S. Dolan, M. R. Dvorsky, P. K. Hardebeck, J. D. Harvey, and D. W. Muller, The visible imaging system (VIS) for the POLAR spacecraft, *Space Sci. Rev.*, **71**, 297-328, 1995.

Fujiwara, H., S. Maeda, H. Fukunishi, T. J. Ruller-Rowell, and D. S. Evans, Global variations of thermospheric winds and temperatures caused by substorm energy injection, *J. Geophys. Res.*, **101**, 225-239, 1996.

Fuller-Rowell, T. J., and D. Rees, A three-dimensional, time-dependent, global model of the thermosphere, *J. Atmos. Sci.*, **37**, 2545-2567, 1980.

Fuller-Rowell, T. J., and D. Rees, Derivation of a conservation equation for mean molecular weight for a two constituent gas within a three-dimensional, time-dependent model of the thermosphere, *Planet. Space Sci.*, **31**, 1209-1222, 1983.

Fuller-Rowell, T. J., A two-dimensional, high-resolution, nested-grid model of the thermosphere 1. Neutral response to an electric field "spike", *J. Geophys. Res.*, **89**, 2971-2990, 1984.

Fuller-Rowell, T. J., A two-dimensional, high-resolution, nested-grid model of the thermosphere 2. Response of the thermosphere to narrow and broad electrodynamic features, *J. Geophys. Res.*, **90**, 6567-6586, 1985.

Fuller-Rowell, T. J., D. Rees, S. Quegan, R. J. Moffett, and G. J. Bailey, Interactions between neutral thermospheric composition and the polar thermosphere using coupled global model, *J. Geophys. Res.*, **92**, 7744-7748, 1987.

Fuller-Rowell, T. J., D. Rees, S. Quegan, and R. J. Moffett, Numerical simulations of the sub-auroral *F*-region trough, *J. Atmos. Terr. Phys.*, **53**, 529-540, 1991.

Fuller-Rowell, T. J., D. Rees,, H. Rishbeth, A. G. Burns, T. L. Killeen, and R. G. Roble, Modelling of composition changes during *F*-region stroms: a reassessment, *J. Atmos. Terr. Phys.*, **53**, 541-550, 1991.

Fuller-Rowell, T. J., M. V. Codrescu, R. J. Moffett, and S. Quegan, Response of the thermosphere and ionosphere to geomagnetic storms, *J. Geophys. Res.*, **99**, 3893-3914, 1994.

Fuller-Rowell, T. J., M. V. Codrescu, H. Rishbeth, R. J. Moffett, and S. Quegan, On the seasonal response of the thermosphere and ionosphere to geomagnetic storms, *J. Geophys. Res.*, **101**, 2343-2353, 1996a.

Fuller-Rowell, T. J., D. Rees, S. Quegan, R. J. Moffett, M. V. Codrescu, and G. H. Millward, A coupled thermosphere-ionosphere model (CTIM), In *STEP Handbook of Ionospheric Models*, R. W. Schunk, ed., Utah State University, Logan, UT, 217-238, 1996b.

Germany, G. A., M. R. Torr, P. G. Richards, and D. G. Torr, The dependence of modeled OI 1356 and N_2 Lyman Birge Hopfield auroral emissions on the neutral atmosphere, *J. Geophys. Res.*, **95**, 7725-7733, 1990.

Germany, G. A., M. R. Torr, D. G. Torr, and P. G. Richards, Use of FUV auroral emissions as diagnostic indicators, *J. Geophys. Res.*, **99**, 383-388, 1994a.

Germany, G. A., D. G. Torr, M. R. Torr, and P. G. Richards, The determination of ionospheric conductances from FUV auroral images, *J. Geophys. Res.*, **99**, 388, 1994b.

Germany, G. A., G. K. Parks, M. Brittnacher, J. Cumnock, D. Lummerzheim, J. F. Spann, L. Chen, P. G. Richards, and F. J. Rich, Remote determination of auroral energy characteristics during substorm activity, *Geophys. Res. Lett.*, **24**, 995-998, 1997.

Germany, G. A., D. Lummerzheim, and P. G. Richards, Impact of model differences on quantitative analysis of FUV auroral emissions: total ionization cross sections, *J. Geophys. Res.*, **106**, 12,837-12,843, 2001.

Gladstone, G. R., Simulations of DE 1 UV airglow images, *J. Geophys. Res.*, **99**, 11,441-11,448, 1994.

Gordiets, B. F., M. N. Markov, and L. A. Shelepin, I. R. radiation of the upper atmosphere, *Planet. Space Sci.*, **26**, 933-948, 1978.

Grossmann, K. U., and D. Offermann, Atomic oxygen emission at 63 μm as a cooling mechanism in the thermosphere and ionosphere, *Nature, Lond.*, **276**, 594-595, 1978.

Hanson, W. B., R. A. Heelis, R. A. Power, C. R. Lippincott, D. R. Zuccaro, B. J. Holt, L. L. Harmon, and S. Sanatani, The retarding potential analyzer for Dynamics Explorer-B, *Space Sci. Instrum.*, **5**, 503-510, 1981.

Hargreaves, J. K., The solar-terrestrial environment, Cambridge Atmospheric and Space Sciences Series, Cambridge UP, 1992.

Hays, P. B., R. A. Jones, and M. H. Rees, Auroral heating and the composition of the neutral atmosphere, *Planet. Space Sci.*, **21**, 559-573, 1973.

Hays, P. B., T. L. Killeen, and B. C. Kennedy, The Fabry-Perot interferometer on Dynamics Explorer, *Space Sci. Instrum.*, **5**, 395-416, 1981.

Hecht, Eugene, Optics 2nd edition, Reading, Massachusetts, Addison-Wesley Publishing Company, 1984.

Hecht, J. H., A. B. Christensen, D. J. Strickland, R. R. Meier, Deducing composition and incident electron spectra from ground-based auroral optical measurements: variations in oxygen density, *J. Geophys. Res.*, **94**, 13,553-13,563, 1989.

Hecht, J. H., A. B. Christensen, D. J. Strickland, T. Majeed, R. L. Gattinger, and A. Vallance Jones, A comparision between auroral particle characteristics and atmospheric composition inferred from analyzing optical emission measurements alone and in combination with incoherent scatter radar measurements, *J. Geophys. Res.*, **104**, 33-44, 1999.

Hecht, J. H., D. L. McKenzie, A. B. Christensen, D. J. Strickland, J. P. Thayer, and J. Watermann, Simultaneous observations of lower thermospheric composition change during moderate auroral activity from Kangerlussuaq and Narsarsuaq, Greenland, *J. Geophys. Res.*, **105**, 27,109-27,118, 2000.

Hedin, A. E., J. E. Salah, J. V. Evans, C. A. Reber, G. P. Newton, N. W. Spencer, D. C. Kayer, D. Alcayde, P. Bauer, L. Cogger, and J. P. McClure, A global thermospheric model based on mass spectrometer and incoherent scatter data, MSIS 1, N_2 density and temperature, *J. Geophys. Res.*, **82**, 2139-2147, 1977a.

Hedin, A. E., C. A. Reber, G. P. Newton, N. W. Spencer, H. C. Brinton, H. G. Mayr and W. E. Potter, A global thermospheric model based on mass spectrometer and incoherent scatter data, MSIS 2, composition, *J. Geophys. Res.*, **82**, 2148-2156, 1977b.

Hedin, A. E., A revised thermospheric model based on mass spectrometer and incoherent scatter data: MSIS-83, *J. Geophys. Res.*, **88**, 10,170-10,188, 1983.

Hedin, A. E., MSIS-86 thermospheric model, *J. Geophys. Res.*, **92**, 4649-4662, 1987.

Hedin, A. E., and H. G. Mayr, Characteristics of wavelike fluctuations in Dynamics Explorer neutral composition data, *J. Geophys. Res.*, **92**, 11,159-11,172, 1987.

Hedin, A. E., Extension of the MSIS thermosphere model into the middle and lower atmosphere, *J. Geophys. Res.*, **96**, 1159-1172, 1991.

Heelis, R. A., J. K. Lowell, and R. W. Spiro, A model of the high-latitude ionospheric convection pattern, *J. Geophys. Res.*, **87**, 6339, 1982.

Heelis, R. A., W. B. Hanson, C. R. Lippincott, D. R. Zuccaro, L. H. Harmon, B. J. Holt, J. E. Doherty, and R. A. Power, The ion drift meter for Dynamics Explorer-B, *Space Sci. Instrum.*, **5**, 511-521, 1981.

Heikkila, W. J., and J. D. Winningham, Penetration of magnetosheath plasma to low altitudes through the dayside magnetospheric cusps, *J. Geophys. Res.*, **76**, 883-891, 1971.

Heppner, J. P., and N. C. Maynard, Empirical high-latitude electric field models, *J. Geophys. Res.*, **92**, 4467-4489, 1987.

Hernandez, G., and O. A. Mills, Feedback stabilized Fabry-Perot interferometer, *Appl. Opt.*, **12**, 126-130, 1973.

Hernandez, G., and R. G. Roble, On divergences of thermospheric meridional winds at midlatitudes, *Geophys. Res. Lett.*, **6**, 294-296, 1979.

Hernandez, G., Vertical motions of the neutral thermosphere at midlatitude, *Geophys. Res. Lett.*, **9**, 555-557, 1982.

Hernandez, G., Fabry-Perot interferometers, Cambridge Studies in Modern Optics, Cambridge UP, 1986.

Hernandez, G., R. W. Smith, R. G. Roble, J. Gress, and K. C. Clark, Thermospheric dynamics at the South Pole, *Geophys. Res. Lett.*, **17**, 1255-1259, 1990.

Hicks, T. R., N. K. Reay, and P. D. Atherton, The application of capacitance micrometry to the control of Fabry-Perot etalons, *J. Phys. E: Sci. Instrum.*, **17**, 49-55, 1984.

Hinteregger, H. E., Development of solar cycle 21 observed in EUV spectrum and atmospheric absorption, *J. Geophys. Res.*, **84**, 1933-1938, 1979.

Hodges, R. R., Generation of turbulence in the upper atmosphere by internal gravity waves, *J. Geophys. Res.*, **72**, 3455-3458, 1967.

Houghton, J. T., The physics of atmospheres, Cambridge UP, 1977.

Hunsucker, R. D., and J. K. Hargreaves, A study of gravity waves in ionospheric electron content at L = 4, *J. Atmos. Terr. Phys.*, **50**, 167-172, 1988.

Immel, T. J., Studies of compositional variations in the thermosphere and ionosphere using far-ultraviolet images from DE 1, Ph.D. Thesis, University of Alaska Fairbanks, 1998.

Immel, T. J., J. D. Craven, and L. A. Frank, Influence of IMF B_y on large-scale decreases of O column density at middle latitudes, *J. Atmos. Solar-Terr. Phys.*, **59**, 725-737, 1997.

Innis, J. L., P. A. Greet, and P. L. Dyson, Fabry-Perot spectrometer observations of the auroral oval/polar cap boundary above Mawson, Antarctica, *J. Atmos. Terr. Phys.*, **58**, 1973-1988, 1996.

Innis, J. L., P. L. Dyson, and P. A. Greet, Further observations of the thermospheric vertical wind at the auroral oval/polar cap boundary, *J. Atmos. Solar-Terr. Phys.*, **59**, 2009-2022 1997.

Innis, J. L., P. A. Greet, D. J. Murphy, M. G. Conde, and P. L. Dyson, A large vertical wind in the thermosphere at the auroral oval/polar cap boundary seen simultaneously from Mawson and Davis, Antarctica, *J. Atmos. Solar-Terr. Phys.*, **61**, 1047-1058, 1999.

Innis, J. L., Deceleration of the high-latitude thermospheric wind by polar cap gravity waves, *Geophys. Res. Lett.*, **27**, 3813-3816, 2000.

Innis, J. L., and M. Conde, Thermospheric vertical wind activity maps derived from Dynamics Explorer 2 WATS observations, *Geophys. Res. Lett.*, **28**, 3847-3850, 2001.

Innis, J. L., and M. Conde, High-latitude thermospheric vertical wind activity derived from Dynamics Explorer 2 WATS observations: indications of a source region for polar cap gravity waves, *J. Geophys. Res.*, **107**(A8), 1172, doi:10.1029/2001JA009130, 2002.

Innis, J. L., and M. Conde, Characterization of acoustic-gravity waves in the upper thermosphere using Dynamics Explorer 2 Wind and Temperature Spectrometer (WATS) and Neutral Atmosphere Composition Spectrometer (NACS) data, *J. Geophys. Res.*, **107**(A12), 1418, doi:10.1029/2002JA009370, 2002.

Ishii, M., S. Okano, E. Sagawa, S. Watari, H. Mori, I. Iwamoto, and Y. Murayama, Development of Fabry-Perot interferometers for airglow observations, *Proc. NIPR Symp. Upper Atmos. Phys.*, **10**, 97-108, 1997.

Ishii, M., M. Conde, R. W. Smith, M. Krynicki, E. Sagawa, and S. Watari, Vertical wind observations with two Fabry-Perot interferometers at Poker Flat, Alaska, *J. Geophys. Res.*, **106**, 10,537-10,551, 2001.

Jacchia, L. G., Static diffusion models of the upper atmosphere with emipirical temperature profiles, *Smithsonian Contrib. Astrophys.*, **8**, 215, 1965.

Jacchia, L. G., Thermospheric temperature, density and composition: new models, *Special Report, Smithsonian Contrib. Astrophys.*, **375**, 1977.

Jenkins, G. M., and D. G. Watts, Spectral analysis and its applications, Holden-Day Series in Time Series Analysis, Emerson-Adams Press, Inc., Boca Raton, 1968.

Johnson, F. S., W. B. Hanson, R. R. Hodges, W. R. Coley, G. R. Carignan, and N. W. Spencer, Gravity waves near 300 km over the polar caps, *J. Geophys. Res.*, **107**, 23,993-24,002, 1995.

Kaneda, E., M. Takagi, and N. Niwa, Vacuum aurora television camera, *Proceedings of the twelfth international symposium on space technology and science*, Tokyo, Japan, 233-238, 1977.

Killeen, T. L., J. D. Craven, L. A. Frank, J.-J. Ponthieu, N. W. Spencer, R. A. Heelis, L. H. Brace, R. G. Roble, P. B. Hays, and G. R. Carignan, On the relationship between the dynamics of the polar thermosphere and morphology of the aurora: global-scale observations from Dynamics Explorers 1 and 2, *J. Geophys. Res.*, **93**, 2675-2692, 1988.

Killeen, T. L., A. G. Burns, I. Azeem, S. Cochran, and R. G. Roble, A theoretical analysis of the energy budget in the lower thermosphere, *J. Atmos. Solar-Terr. Phys.*, **59**, 675-689, 1997.

Kivelson, M. G., and C. T. Russell, eds., Introduction to space physics, Cambridge UP, 1995.

Kockarts, G., Nitric oxide cooling in the terrestrial thermosphere, *Geophys. Res. Lett.*, **7**, 137-140, 1980.

Kohl, H., and J. W. King, Atmospheric winds between 100 and 700 km and their effects on the ionosphere, *J. Atmos. Terr. Phys.*, **29**, 1045-1062, 1967.

Krynicki, M. P., R. W. Smith, and G. Hernandez, Thermospheric vertical winds at the South Pole during quiet solar minimum and active solar maximum conditions, CEDAR conference, June, 1998, Boulder, CO.

Krynicki, M. P., D. Lummerzheim, M. Conde, R. W. Smith, M. Brittnacher, and M. Ishii, Verifying thermospheric composition effects due to vertical winds, CEDAR conference, June, 2000, Boulder, CO.

Larsen, M. F., T. R. Marshall, I. S. Mikkelsen, B. A. Emery, A. Christensen, D. Kayser, J. Hecht, L. Lyons, and R. Walterscheid, Atmospheric response in aurora experiment: observations of E and F region neutral winds in a region of postmidnight diffuse aurora, *J. Geophys. Res.*, **100**, 17,299-17,308, 1995.

Larsen, M. F., Winds and shears in the mesosphere and lower thermosphere: results from four decades of chemical release wind measurements, *J. Geophys. Res.*, **107**, doi:10.1029/2001JA000218, 2002.

Luetzelschwab, Carl, DXing on 160m at solar maximum, 23 pp, Online, Internet, http://www.gibbons-clan.com/nwdx2004/K9LA.pdf, **K9LA**, Presentation, NW DX Convention, Seattle, 2004, accessed March 01, 2005.

Lummerzheim, D., M H. Rees, and G. J. Romick, The application of spectroscopic studies of the aurora to thermospheric neutral composition, *Planet. Space Sci.*, **38**, 67-78, 1990.

Lummerzheim, D., and J. Lilensten, Electron transport and energy degradation in the ionosphere: evaluation of the numerical solution, comparison with laboratory experiments and auroral observations, *Ann Geophysicae*, **12**, 1039-1051, 1994.

Lummerzheim, D., M. Brittnacher, D. Evans, G. A. Germany, G. K. Parks, M. H. Rees, and J. F. Spann, High time resolution study of the hemispheric energy flux carried by energetic electrons into the ionosphere during the May 19/20 auroral activity, *Geophys. Res. Lett.*, **24**, 987, 1997.

Lyons, L. R., and M. Schulz, Access of energetic particles to storm time ring current through enhanced radial diffusion, *J. Geophys. Res,* **94**, 5491, 1989.

Mayr, H. G., and H. Volland, Magnetic storm effects in the neutral composition, *Planet. Space Sci.*, **20**, 379-393, 1972.

Mayr, H. G., and H. Volland, A two-component model of the diurnal variations in the thermospheric composition, *J. Atmos. Terr. Phys.*, **35**, 669-680, 1973.

Mayr, H. G., I. Harris, F. Varosi, and F. A. Herrero, Global excitation of wave phenomena in a dissipative multiconstituent medium 1. Transfer function of the earth's thermosphere, *J. Geophys. Res.*, **89**, 10,929-10,959, 1984.

Mayr, H. G., I. Harris, F. Varosi, and F. A. Herrero, Global excitation of wave phenomena in a dissipative multiconstituent medium 2. Impulsive perturbations in the Earth's thermosphere, *J. Geophys. Res.*, **89**, 10,961-10,986, 1984.

Mayr, H. G., I. Harris, F. Varosi, and F. A. Herrero, Global excitation of wave phenomena in a dissipative multiconstituent medium 3. Response characteristics for different sources in the Earth's thermosphere, *J. Geophys. Res.*, **92**, 7657-7672, 1987.

Mayr, H. G., I. Harris, F. A. Herrero, N. W. Spencer, F. Varosi, and W. D. Pesnell, Thermospheric gravity waves: observations and interpretation using the Transfer Function Model, *Space Sci. Rev.*, **54**, 297-375, 1990.

Meier, R. R., Ultraviolet spectroscopy and remote sensing of the upper atmosphere, *Space Sci. Rev.*, **58**, 1-185, 1991.

Meng, C. -I., and R. E. Huffman, Ultraviolet imaging from space of the aurora under full sunlight, *Geophys. Res. Lett.*, **11**, 315-318, 1984.

Meng, C. -I., R. E. Huffman, F. Del Greco, and R. Eastes, *EOS*, **68**, 396, 1987.

Millward, G. H., R. J. Moffett, S. Quegan, and T. J. Fuller-Rowell, A coupled thermosphere-ionosphere-plasmasphere model (CTIP), In *STEP Handbook of Ionospheric Models*, R. W. Schunk, ed., Utah State University, Logan, UT, 239-280, 1996.

Müller-Wodarg, I., and A.D. Aylward, The influence of tides on composition of the thermosphere, *Adv. Space Res.*, **21**, 807-810, 1998.

Murgatroyd, R. J., and R. M. Goody, Sources and sinks of radiative energy from 30 to 90 km, *Quart. J. Roy. Meteorol. Soc.*, **84**, 225-234, 1958.

Murphree, J. S., R. A. King, T. Payne, K. Smith, D. Reid, J. Adema, B. Gordon, and R. Wlochowicz, The Freja ultraviolet imager, *Space Sci. Rev.*, **70**, 421-445, 1994.

Nakamura, J., and H. Kimura, Ionospheric wind and diffusion detected by the sodium cloud method, In *COSPAR Small rocket instrumentation techniques*, Ken-Ichi Maeda, ed., North-Holland Publishing Co. – Amsterdam, 130-134, 1969.

Paxton, L. J., A. B. Christensen, D. C. Humm, B.S. Ogorzalek, C.T. Pardoe, D. Morrison, M.B. Weiss, W. Crain, P.H. Lew, D.J. Mabry, J.O. Goldsten, S.A. Gary, D.F. Persons, M.J. Harold, E.B. Alvarez, C.J. Ercol, D.J. Strickland, and C.-I. Meng, Global ultraviolet imager (GUVI): measuring composition and energy inputs for the NASA Thermosphere Ionosphere Mesosphere Energetics and Dynamics (TIMED) mission, *SPIE Optical Spectroscopic Techniques and Instrumentation for Atmospheric and Space Research III, 3756*, 265-276, 1999.

Perreault, P. and S. -I. Akasofu, A study of geomagnetic storms, *Geophys. J. R. Astr. Soc.*, **54**, 547-573, 1978.

Peteherych, S., G. G. Shephard, and J. K. Walker, Observation of vertical *E*-Region neutral winds in two intense auroral arcs, *Planet. Space Sci.*, **33**, 869-873, 1985.

Press, W. H., S. A. Teukolsky, W. T. Vetterling, and B. P. Flannery, Numerical recipes in C: the art of scientific computing, 2nd ed., Cambridge UP, 1992.

Price, G. D., and F. Jacka, The influence of geomagnetic activity on the upper mesosphere/lower thermosphere in the auroral zone. I. Vertical winds, *J. Atmos. Terr. Phys.*, **53**, 909-922, 1991.

Price, G. D., R. W. Smith, and G. Hernandez, Simultaneous measurements of large vertical winds in the upper and lower thermosphere, *J. Atmos. Terr. Phys.*, **57**, 631-643, 1995.

Prölss, G. W., Magnetic storm associated perturbations of the upper atmosphere: recent results obtained by satellite-borne gas analyzers, *Rev. Geophys.*, **18**, 183-202, 1980.

Prölss, G. W., Thermosphere-ionosphere coupling during disturbed conditions, *J. Geomag. Geoelectr.*, **43**, 537-549, 1991.

Prölss, G. W., Satellite Mass Spectrometer Measurements of Composition Changes, *Adv. Space Res.*, **12**, 10,241-10,251, 1992.

Rees, D., Vertical winds in the lower ionosphere, *J. Brit Interplanet. Soc.*, **22**, 275-284, 1969.

Rees, D., and A. H. Greenaway, Doppler imaging system; an optical device for measuring vector winds. 1. General principles, *Appl. Opt.*, **22**, 1078-1083, 1983.

Rees, D., R. W. Smith, P. J. Charleton, F. G. McCormac, N. Lloyd, and Åke Steen, The generation of vertical thermospheric winds and gravity waves at auroral latitudes – I. Observations of vertical winds, *Planet. Space Sci.*, **32**, 667-684, 1984a.

Rees, D., M. F. Smith, and R. Gordon, The generation of vertical thermospheric winds and gravity waves at auroral latitudes – II. Theory and numerical modelling of vertical winds, **32**, 685-705, 1984b.

Rees, D., Observations and modelling of ionospheric and thermospheric disturbances during major geomagnetic storms: a review, *J. Atmos. Terr. Phys.*, **57**, 1433-1457, 1995.

Rees, M. H., Auroral ionization and excitation by incident energetic electrons, *Planet. Space Sci.*, **11**, 1209, 1963.

Rees, M. H., and R. G. Roble, Excitation of $O(^1D)$ atoms in aurorae and emission of the forbidden OI 6300-A line, *Can. J. Phys.*, **64**, 1608-1613, 1986.

Rees, M. H., Physics and chemistry of the upper atmosphere, Cambridge Atmospheric and Space Sciences Series, Cambridge UP, 1989.

Richards, P. G., and D. G. Torr, Auroral modeling of the 3371 Å emission rate - dependence on characteristic electron energy, *J. Geophys. Res.*, **95**, 10337-10344, 1990.

Richmond, A. D., Gravity wave generation, propagation and dissipation in the thermosphere, *J. Geophys. Res.*, **83**, 4131-4145, 1978.

Richmond, A. D., Thermospheric heating in a magnetic storm: dynamic transport of energy from high to low latitudes, *J. Geophys. Res.*, **84**, 5259-5266, 1979a.

Richmond, A. D., Large-amplitude gravity wave energy production and dissipation in the thermosphere, *J. Geophys. Res.*, **84**,1880-1890, 1979b.

Richmond, A. D., Thermospheric dynamics and electrodynamics, in Solar-terrestrial physics, Carovillano, R. L. and J. M. Forbes, eds., D. Reidel Publishing, Dordrecht, Boston and Lancaster, 523-607, 1983.

Richmond, A. D., E. C. Ridley, and R. G. Roble, A thermosphere/ionosphere general circulation model with coupld electrodynamics, *Geophys. Res. Lett.*, **19**, 601-604, 1992.

Rieger, E., Neutral air motions deduced from barium releases experiments—I. Vertical winds, *J. Atmos. Terr. Phys.*, **36**, 1377-1385, 1974.

Rishbeth, H., R. J. Moffett and G. J. Bailey, Continuity of air motion in the mid-latitude thermosphere, *J. Atmos. Terr. Phys.*, **31**, 1035-1047, 1969.

Rishbeth, H., and O. K. Garriott, Introduction to ionospheric physics, New York, Academic Press, 1969.

Rishbeth, H., Thermospheric winds and the *F*-region: a review, *J. Atmos. Terr. Phys.*, **34**, 1-47, 1972.

Rishbeth, H., R. Gordon, D. Rees, and T. J. Fuller-Rowell, Modelling of thermospheric composition changes caused by a severe magnetic storm, *Planet. Space Sci.*, **33**, 1283-1301, 1985.

Rishbeth, H., T. J. Fuller-Rowell, and D. Rees, Diffusive equilibrium and vertical motion in the thermosphere during a severe magnetic storm: a computational study, *Planet. Space Sci.*, **35**, 1157-1165, 1987.

Rishbeth, H., F-region storms and thermospheric dynamics, *J. Geomag. Geoelectr.*, **43**, 513-524, 1991.

Rishbeth, H., How the thermospheric circulation affects the ionospheric F2-layer, *J. Atmos. Solar-Terr. Phys.*, **60**, 1385-1402, 1998.

Roble, R. G., *The upper atmosphere and magnetosphere*, Geophysics Study Committee, ed., Washington D.C., 57, 1977.

Roble, R. G., R. E. Dickinson, and E. C. Ridley, Global circulation and temperature structure of the thermosphere with high-latitude plasma convection, *J. Geophys. Res.*, **87**, 1599-1614, 1982.

Roble, R. G., and B. A. Emery, On the global mean temperature of the thermosphere, *Planet. Space Sci.*, **31**, 597-614, 1983.

Roble, R. G., E. C. Ridley, A. D. Richmond, and R. E. Dickinson, A coupled thermosphere/ionosphere general circulation model, *Geophys. Res. Lett.*, **15**, 1325-1328, 1988.

Sears, F. W., and G. L. Salinger, Thermodynamics, kinetic theory, and statistical thermodynamics, Reading, Addison-Wesley Publishing Co., 1975.

Shepherd, G. G., T. Fancott, J. McNally, and H. S. Kerr, ISIS-II atomic oxygen red line photometer, *Appl. Opt.*, **12**, 1767, 1973.

Sidi, C., and H. Teitelbaum, Thin shear turbulent layers within the lower thermosphere induced by non-linear interaction between tides and gravity waves, *J. Atmos. Terr. Phys.*, **40**, 529-540, 1978.

Siskind, D. E., C. A. Barth, and R. G. Roble, The response of thermospheric nitric oxide to an auroral storm 1. Low and middle latitudes, *J. Geophys. Res.*, **94**, 16,885-16,898, 1989.

Siskind, D. E., C. A. Barth, D. S. Evans and R. G. Roble, The response of thermospheric nitric oxide to an auroral Storm 2. Auroral latitudes, *J. Geophys. Res.*, **94**, 16,899-16,911, 1989.

Sivjee, G. G., T. J. Hallinan, and G. R. Swenson, Fabry-Perot-interferometer imaging system for thermospheric temperature and wind measurements, *Appl. Opt.*, **19**, 2206-2209, 1980.

Smith, R. W., Neutral winds in the polar cap, in *Exploration of the polar upper atmosphere*, C. S. Deehr and J. Holtet, eds., Reidel, 189-198, 1980.

Smith, R. W., and G. Hernandez, Vertical winds in the thermosphere within the polar cap, *J. Atmos. Terr. Phys.*, **57**, 611-620, 1995.

Smith, R. W., Vertical winds: a tutorial, *J. Atmos. Solar-Terr. Phys.*, **60**, 1425-1434, 1998.

Smith, R. W., G. Hernandez, R. G. Roble, P. L. Dyson, M. Conde, R. Crickmore, and M. Jarvis, Observation and simulations of winds and temperatures in the Antarctic thermosphere for August 2-10, 1992, *J. Geophys. Res.*, **103**, 9473-9480, 1998.

Spencer, N. W., R. F. Theis, L. E. Wharton, and G. R. Carignan, Local vertical motions and kinetic temperature from AE-C as evidence for aurora-induced gravity waves, *Geophys. Res. Lett.*, **3**, 313-316, 1976.

Spencer, N. W., L. E. Wharton, H. B. Niemann, A. E. Hedin, G. R. Carignan, and J. C. Maurer, The Dynamics Explorer wind and temperature spectrometer, *Space Sci. Instrum.*, **5**, 417-428, 1981.

Spencer, N. W., L. E. Wharton, G. R. Carignan, and J. C. Maurer, Thermosphere zonal winds, vertical motions and temperature as measured from Dynamics Explorer, *Geophys. Res. Lett.*, **9**, 953-956, 1982.

Strickland, D. J., D. L. Book, T. P. Coffey, and J. A. Fedder, Transport equation techniques for the deposition of auroral electrons, *J. Geophys. Res.*, **81**, 2755-2764, 1976.

Strickland, D. J., R. R. Meier, J. H. Hecht, and A. B. Christensen, Deducing composition and incident electron spectra from ground based auroral optical measurements: theory and model results, *J. Geophys. Res.*, **94**, 13,527-13,539, 1989.

Strickland, D. J., R. J. Cox, R. R. Meier, and D. P. Drob, Global O/N_2 derived from DE 1 FUV dayglow data: technique and examples from two storm periods, *J. Geophys. Res.*, **104**, 4251-4266, 1999.

Stubbe, P., Vertical neutral gas motions and deviations from the barometric law in the lower thermosphere, *Planet. Space Sci.*, **20**, 209-215, 1972.

Thomas, G. E., and K. Stamnes, Radiative transfer in the atmosphere and ocean, Cambridge Atmospheric and Space Sciences Series, Cambridge UP, 1999.

Thomas, G. E., J. J. Olivero, E. J. Jensen, W. Schroeder, and Q. B. Toon, Relation between increasing methane and the presence of ice clouds at the mesopause, *Nature*, **338**, 490-492, 1989.

Thome, G. D., Incoherent backscatter observations of traveling ionospheric disturbances, *J. Geophys. Res.*, **69**, 4047-4049, 1964.

Torr, M. R., D. G. Torr, M. Zukic, R. B. Johnson, J. Ajello, P. Banks, K. Clark, K. Cole, C. Keffer, G. Parks, B. Tsurutani, and J. Spann, A far ultraviolet imager for the international solar-terrestrial physics program mission, *Space Sci. Rev.*, **71**, 329-383, 1995.

Van Allen, J. A., The geomagnetically trapped corpuscular radiation, *J. Geophys. Res.*, **64**, 1683-1689, 1959.

Vaughan, J. M., The Fabry-Perot interferometer: history, theory, practice and applications, The Adam Hilger Series on Optics and Optoelectronics, Bristol and Philadelphia, IOP Publishing, 1989.

Wardill, P., and F. Jacka, Vertical motions of the thermosphere over Mawson, Antarctica, *J. Atmos. Terr. Phys.*, **48**, 289-292, 1986.

Weimer, D. R., Models of high-latitude electric potentials derived with a least error fit of spherical harmonic coefficients, *J. Geophys. Res.*, **100**, 19,595-19,607, 1995.

Wilksch, P. A., Instrument function of the Fabry-Perot spectrometer, *Appl. Opt.*, **24**, 1502-1511, 1985.

Zuzic, M., L. Scherliess, and G.W. Prölss, Latitudinal structure of thermospheric composition perturbations, *J. Atmos. Solar-Terr. Phys.*, **59**, 711-724, 1997.

Appendix A Introduction to Earth's Solar-Terrestrial Environment

A.1 The Static Atmosphere and Magnetosphere

A detailed understanding of Earth's upper atmosphere (~100-1000 km) is not possible without having a knowledge of the atmosphere below it, the geospace above it and the coupling mechanisms between these regions. Much is already known of the solar-terrestrial environment, and a brief overview of our near-Earth surroundings, the atmosphere and magnetosphere, is presented here. Earth's neutral atmosphere is a composite of many gases, and various classification schemes exist for designating atmospheric regions. Five fairly well-defined regions are distinguishable based on the atmosphere's temperature structure, and Figure A.1 [*Rees,* 1989] illustrates a standard Earth atmosphere. The heights, densities and temperatures of the respective regions, which depend on a variety of influences, vary daily, seasonally and from low to middle to high latitudes. In order of altitude from the ground, the regions are referred to as the troposphere (~0-15 km), the stratosphere (~15-50 km), the mesosphere (~50-90 km), the thermosphere (~90-600 km) and the exosphere (≳600-1000 km). Each "-sphere," except the exosphere, terminates at an upper boundary referred to as a "-pause," which acts as the transition layer between two respective regions and is marked by a reversal in the temperature gradient, except between the thermosphere and exosphere. The troposphere's temperature minimum occurs at the tropopause (*e.g.* ~15 km at low-latitudes, ~8 km at high-latitudes), separating the troposphere from the stratosphere. There is a temperature maximum at the stratopause (~50 km) and another minimum at the mesopause (~90 km). The thermopause's location (~600-1000 km) and temperature maximum are highly variable due to the daily, seasonal and solar-cyclical variability of the Sun's X-ray and UV radiation input and the magnetosphere's constant but varying high-latitude energy inputs into the thermosphere. The ionosphere (~50-1000 km) resides mostly within the thermosphere and exosphere (also extending downward into the mesosphere) and merges with the inner magnetospheric plasma above ~1000 km.

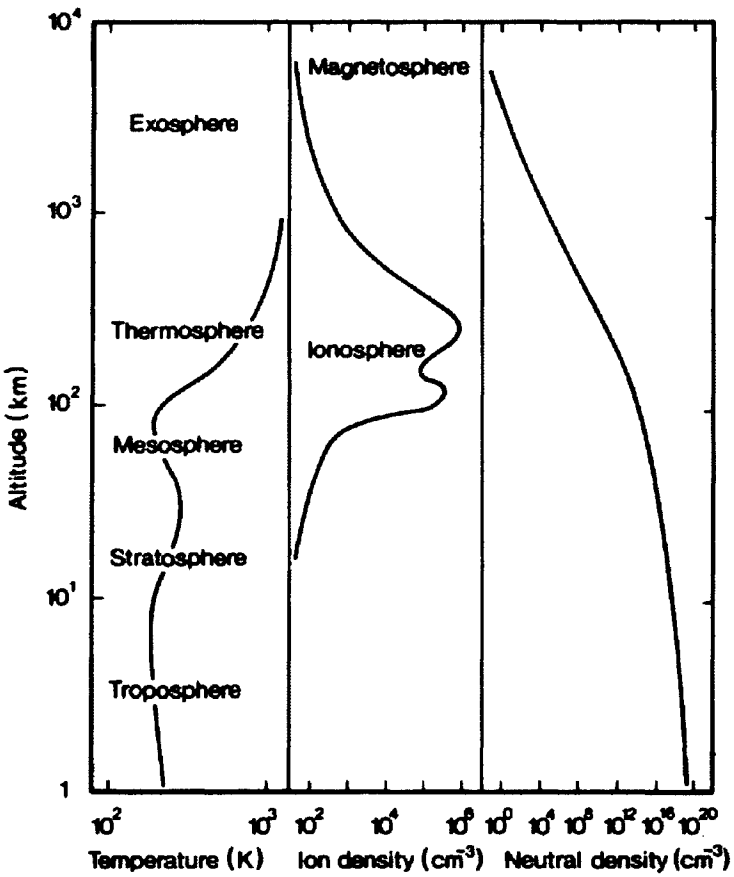

Figure A.1. General structure and composition of Earth's atmosphere. Regions of the atmosphere, temperature and ion and neutral number density distributions are indicated. Heights, densities and temperatures of the respective regions vary daily, seasonally and with latitude [Figure from *Rees*, 1989].

The troposphere, stratosphere and mesosphere are composed of the standard air mixture of 78% molecular nitrogen, 21% molecular oxygen and about 1% Argon (Ar). This condition is a result of Earth's long-term geologic history. Trace amounts of various other gases, such as water vapor (H_2O), carbon dioxide (CO_2), and ozone (O_3) are present as well, but separate short-term processes have determined and continue to regulate their present-day abundances. As was stated in Chapter 1, the atmosphere below ~100 km is well mixed by turbulence and is referred to as the homosphere or turbosphere, which also includes the extreme lower thermosphere (altitudes of ~90-100 km). Composition in the turbosphere remains fairly constant (M = 28.9 amu) up to ~100 km, where the homopause

or turbopause resides. The region above the turbopause, essentially the thermosphere, is referred to as the heterosphere. It is the region where turbulent mixing weakens sufficiently (with increasing altitude) such that constituents separate under gravity. As a result, thermospheric composition varies with altitude. The thermosphere consists of N_2 and O_2 like the atmosphere below, but because species diffusively separate, and because O_2 easily photodissociates into O from solar X-ray and UV radiation and from collisional excitation at auroral latitudes by particle precipitation, O becomes the dominant species above ~200 km [*e.g. Rees*, 1989]. The ionosphere, composed of electrons and a variety of ions, is primarily a product of photoionization but is also due to collisional excitation of neutral species by precipitating particles at high latitudes. Distinct features are present in the ionosphere depending on the latitude, time of day and season. Thermospheric and ionospheric composition are discussed in more detail in Chapter 1. The last vestige of Earth's atmosphere is the exosphere, composed of mostly hydrogen (H) and helium (He) but also some O and N_2. The exosphere is the region in which collisions no longer dominate particle dynamics; *i.e.*, a given particle's mean free path has become larger than the region it occupies, its scale height layer. Exospheric neutral particles can escape into space and tend to move in ballistic orbits governed by Earth's gravity. Charged particle (H^+, He^+, O^+, N^+ and electrons) motion is determined by the near-Earth magnetic field.

Earth's magnetosphere is depicted in Figure A.2 [*Hargreaves*, 1992]. This geomagnetic cavity around Earth is established by Earth's (mostly) dipole magnetic field and its interaction with the solar wind, the continuous stream of electrons and ions coming from the Sun's corona, and the weak solar magnetic field, referred to as the interplanetary magnetic field (IMF). Many sub-regions exist within and around the magnetosphere, each with its own characteristic particle population, dynamics and energetics. The inner magnetosphere, referred to as the plasmasphere, is embedded within the near-Earth closed magnetic field-line region and usually retains a dipolar form except during highly-disturbed geomagnetic conditions associated with intense solar and/or magnetospheric activity. The plasmasphere contains electrons, protons and some heavy ions with typical thermal energies of ~0.1-1 electron volts (eV); *i.e.*, temperatures of ~500-5000 K. The field lines

passing through the plasmasphere's vicinity map down to Earth's low and middle magnetic latitudes, and daytime ionospheric plasma flow up the field lines maintains its particle population. The plasmasphere's lower limit is at ~1000 km, where it merges with the topside ionosphere. The upper limit, the plasmapause, crosses Earth's magnetic equatorial plane at ~3-6 earth radii (R_E) from Earth's center. The location of the plasmapause is dependent on geomagnetic activity and is marked by sudden decreases in electron density of an order of magnitude or more [*e.g. Carpenter and Smith*, 1964; *Carpenter*, 1966].

In the vicinity of the plasmasphere are also the historically-renowned Van Allen radiation belts (not indicated in Figure A.2), the two zones of geomagnetically trapped and peusdo-trapped, very highly-energized charged particles (~1 keV-10 MeV electrons, ~1 keV-50 MeV protons) extending out to ~10 R_E. The particles were inadvertently detected in 1958 by James Van Allen and his group at the University of Iowa while making measurements of cosmic radiation fluxes aboard the Explorer I satellite. Subsequent

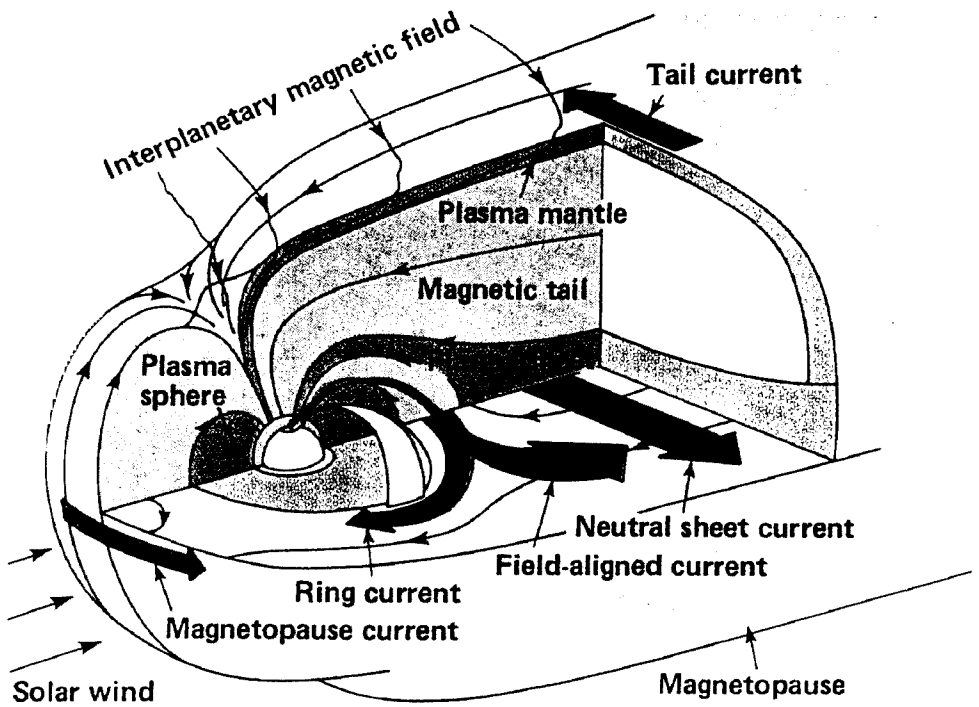

Figure A.2. General structure of Earth's magnetosphere. The various regions, plasma populations and current systems are indicated [Figure from *Hargreaves*, 1992].

satellite measurements throughout 1958 provided a better picture of the entire region [*Van Allen*, 1959]. Van Allen belt particles can damage humans and satellite instrumentation and weakly assist in the ionization of the mid-latitude upper atmosphere when escaping the trapping zones.

At the magnetosphere's outer limit is the magnetopause, the boundary layer separating Earth's immediate geospace from the surrounding solar environment. The magnetopause is established by pressure balance between the solar wind and Earth's magnetic field (the IMF and magnetospheric plasma pressure components are negligible) and is located at ~8-12 R_E on Earth's dayside, ~20-40 R_E on its flanks. A current sheet flows along the magnetopause that cancels the geomagnetic field outside. About 2-3 R_E upstream of the dayside magnetopause is the bow shock (not indicated in Figure A.2), where the solar wind's speed reduces from supersonic to subsonic, turbulently heating the plasma. During intense solar activity (*e.g.*, greatly increased solar wind speeds, ~800 $km \cdot s^{-1}$), the bow shock and magnetopause generally contract and reside much closer to one another. Between the magnetopause and bow shock is the magnetosheath, the region which houses the hotter, slower solar wind plasma. Magnetosheath particles flow turbulently around and past the magnetopause and drive magnetospheric circulation (in turn driving the high-latitude ionospheric circulation) by means of two mechanisms. One is a sort of viscous (but non-collisional) interaction. The other is magnetic reconnection, in which magnetospheric flux tubes merge with IMF flux tubes along the magnetopause, allowing magnetosheath matter to enter the magnetosphere. Neither mechanism as yet is fully understood, but it has been shown that a southward-directed IMF strongly enhances reconnection, magnetospheric circulation and auroral-related activity [*e.g. Dungey*, 1961; *Fairfield and Cahill*, 1966]. Magnetosheath plasma also enters the magnetosphere along Earth's dayside through the longitudinally-extended region referred to as the polar cusp (identifiable in Figure A.2), where the local magnetic flux density is zero. The polar cusp is typically found at magnetic latitudes of ±78° and is ~5° wide. Some magnetosheath particles entering through the cusp region reach the upper atmosphere and have identifiable signatures in the high-latitude daytime ionosphere and

thermosphere [*e.g. Heikkila and Winningham*, 1971]. Most, however, are swept up with the magnetospheric circulation and form the plasma mantle, the thin boundary layer separating the magnetosphere from the magnetosheath along the nightside magnetopause (see Figure A.2). Some magnetospheric plasma is comprised of plasma-mantle particles that have entered the magnetosphere at magnetic reconnection locations.

On Earth's nightside is the magnetosphere's largest sub-structure, the magnetotail. Highly distorted from a dipolar form, the magnetotail is stretched out in the anti-sunward direction from ~10 R_E to as far as ~3000 R_E during intense solar activity. A cross-tail current, driven by a dawn-to-dusk electric field directed across the magnetosphere (which maps down to the high-latitude ionosphere), is located in the neutral sheet region, the central plane of the magnetotail. This current establishes the magnetotail's structure and separates it into two lobes (not indicated in Figure A.2) of opposing field direction. The neutral sheet and cross-tail current are embedded within the plasma sheet, which is an enhancement of the plasma density in the vicinity of the magnetic equatorial plane that extends inward to ~7 R_E in the magnetic equatorial plane and down to the ionosphere at high latitudes (see Figure A.2). The dynamic pressure of the plasma sheet balances the magnetic pressure of the lobes. The plasma sheet consists of plasma from both the ionosphere and the plasma mantle, and during intense solar and/or magnetospheric activity, the plasma sheet supports the ring current [*e.g. Lyons and Schulz*, 1989], a current located at ~5 R_E flowing circularly around Earth that weakens the low-latitude magnetic field at Earth's surface. When reconnection occurs between the lobe fields, particularly during southward IMF, the magnetotail returns to a more dipolar form and releases energy, heating plasma sheet particles and expelling them both toward and away from Earth. Further energization of the Earth-bound plasma sheet particles occurs near the topside ionosphere due to prevailing electric fields located at altitudes of ~1000-5000 km. These highly energized (~0.1-10 keV) precipitating particles spiral down Earth's high-latitude magnetic field lines into the thermosphere at all times, collisionally exciting the thermosphere's constituents and heating the high-latitude thermosphere along with Joule heating processes. During auroral substorms [*Akasofu*, 1964], the ensuing radiative

deactivation of some of the thermosphere's energized constituents generates the beautiful visual display known as the Aurora Borealis and Australis.

A.2 The Sun's Radiative Output

The main source of radiation to Earth is, of course, the Sun. The Sun's radiative spectrum and 11-year solar-cycle variability is described in Table A.1 [*Thomas and Stamnes,* 1999] and Figure A.3 [*Brekke*, 1997]. The Sun behaves essentially as a blackbody at a temperature of ~5800 K, with some notable exceptions. For example, the Far UV radiation (FUV, 100-200 nm) of the Sun originates in the top layers of the Sun's photosphere, which is at an effective blackbody temperature of ~4500 K. The Sun's Extreme UV (EUV, 10-100 nm) and X-ray (<10 nm) radiation mostly emanates from its hot chromosphere (~20,000 K) and very hot corona (~1-2 × 10^6 K), especially during intense solar activity. But for a blackbody at ~5800 K, irradiance peaks in the visible part of the spectrum, 400-700 nm, and the bulk of the Sun's radiative energy output is emitted in this wavelength range. Because of the atmosphere's transparency to these and to Near UV (NUV, 320-400 nm) wavelengths, the Sun's visible radiation reaches Earth's surface, driving the biosphere, heating the land and oceans and generating the weather patterns common to the troposphere. If not for the atmosphere's opacity to other wavelengths, however, life on Earth would not exist. The Sun's more energetic radiation would reach Earth's surface (destroying DNA) and Earth's entire surface IR output (which contributes to heating Earth) would be radiated through the atmosphere and lost into space.

A.3 Radiation Deposition in the Atmosphere: The Unit Optical Depth

Absorption of radiation by Earth's atmosphere is described by the physical discipline of radiative transfer theory. Without going into great detail, a simple relation that describes well the process of radiation absorption by the atmosphere is the Lambert-Beer exponential law [*e.g. Rees*, 1989],

$$I(\lambda, z) = I_\infty(\lambda) \exp[-\tau(\lambda, z)], \qquad \text{(A.1)}$$

where $I(\lambda, z)$ and $I_\infty(\lambda)$ are the irradiance at wavelength λ at altitude z in the atmosphere and at the top of the atmosphere, respectively, and $\tau(\lambda, z)$ is the optical depth. All the physics of

Table A.1. The Sun's output and variability and the atmosphere's response [Table from *Thomas and Stamnes*, 1999].

Sub-region	Range	Variability	Comments
X-rays	$1 < \lambda < 10$ nm	10-100 %	Photoionizes all thermospheric species.
Extreme UV (EUV)	$10 < \lambda < 100$ nm	50 %	Photoionizes O_2 and N_2. Photodissociates O_2.
Far UV (FUV)	$100 < \lambda < 200$ nm	7 %	Dissociates O_2. Discrete electronic excitation of atomic resonance lines.
Middle UV (MUV)			
MUV/UV-C	$200 < \lambda < 280$ nm	1-2 %	Dissociates O_3 in intense Hartley bands. Potentially lethal to biosphere.
MUV/UV-B	$280 < \lambda < 320$ nm	<1 %	Some radiation reaches surface, depending on O_3 optical depth. Damaging to biosphere. Responsible for skin erythema.
Near UV (NUV)			
NUV/UV-A	$320 < \lambda < 400$ nm	<1 %	Reaches surface. Biologically benign, except to eyes. Scattered by clouds, aerosols and molecules.
Visible	$400 < \lambda < 700$ nm	<0.1 %	Absorbed by ocean, land. Scattered by clouds, aerosols and molecules. Primary energy source for biosphere and climate system.
Near IR	$0.7 < \lambda < 3.5$ μm	–	Absorbed by O_2, H_2O in discrete vibrational bands.
Thermal IR	$3.5 < \lambda < 100$ μm	–	Emitted and absorbed by surfaces and IR active gases.

radiation absorption is included in the optical depth parameter, and it is $\tau(\lambda, z)$ which characterizes the attenuation of solar radiation by the atmosphere. For a vertical sun, the optical depth $\tau_{z_0,vert}(\lambda, z_0)$ at altitude z_0 is given by the relation [*Rees*, 1989]

$$\tau_{z_0,vert}(\lambda, z_0) = \sum_j \sigma_j^a(\lambda) \int_{z_0}^{\infty} n_j(z) dz, \tag{A.2}$$

where $n_j(z)$ is the altitude-dependent density profile of any optically-active atmospheric species j within a column of atmosphere of unit area extending from z_0 to the top, and $\sigma_j^a(\lambda)$ is the absorption cross section at wavelength λ of species j. Integration along the column depth and summation over all optically-active species determines the total optical depth of the atmosphere at wavelength λ. Evaluating $\tau(\lambda, z)$ is not necessarily simple,

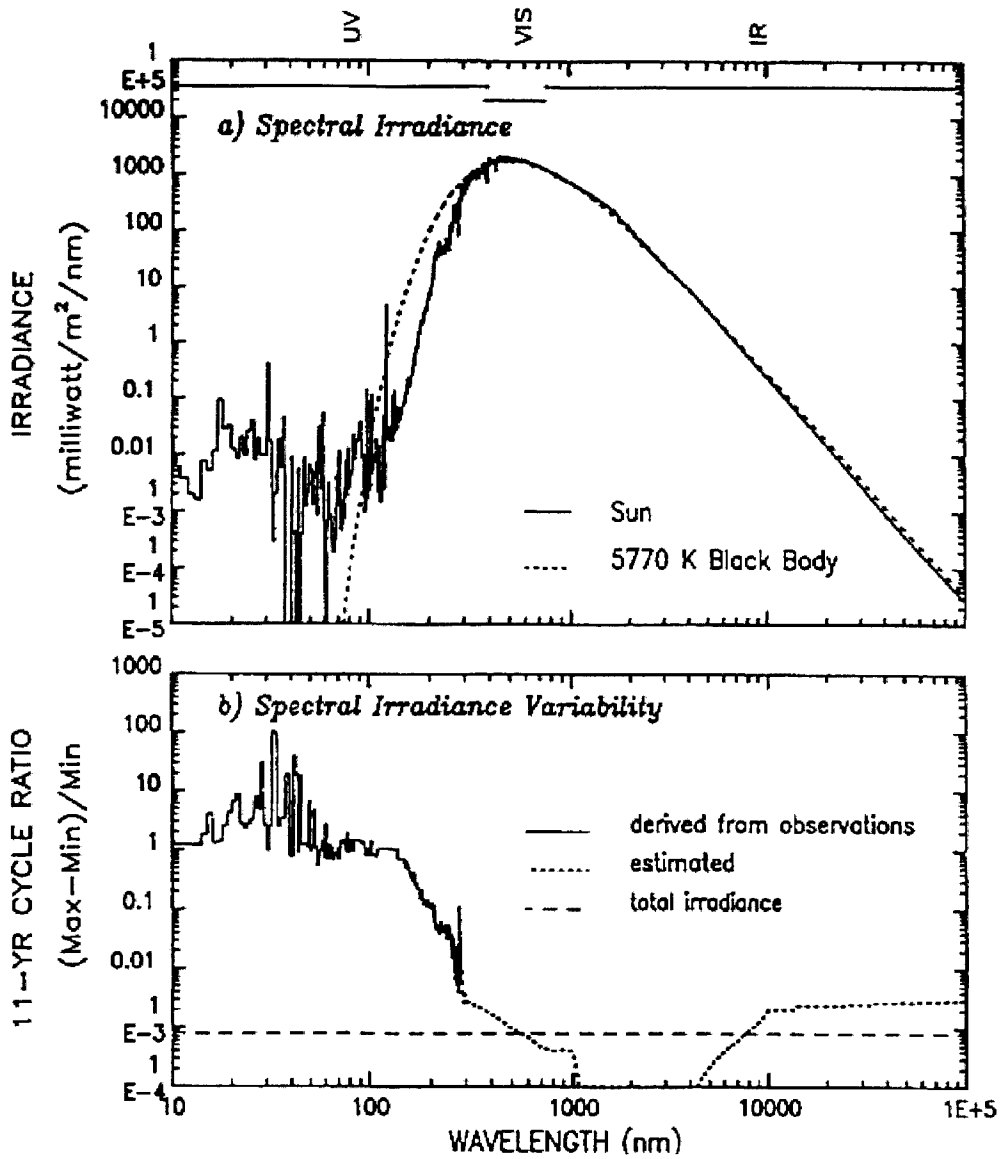

Figure A.3. The Sun's spectral irradiance and variability. The top figure depicts the Sun's radiative output typical for solar minimum conditions and compares it with a blackbody spectrum at 5770 K. The bottom figure highlights the fractional irradiance variability over an 11-year solar cycle [Figure from *Brekke*, 1997].

however. Model atmosphere composition profiles are spatially- and temporally-averaged quantities that are often imprecise, and absorption cross sections must be empirically or experimentally determined and/or calculated using quantum mechanical principles. Also, the expression for $\tau(\lambda, z)$ is more complex in general, dependent on the angle of incidence

of the Sun's rays, the solar zenith angle, and including a component that accounts for scattering of radiation (more quantum mechanics or empirical formulas). But, ultimately, the interpretation of $\tau(\lambda, z)$ remains unchanged. Attenuation of $I_\infty(\lambda)$ incident at the top of the atmosphere by a factor of e^{-1} to $I(\lambda, z)$ at an altitude z within the atmosphere occurs (by definition) at unit optical depth, $\tau(\lambda, z) = 1$, the value at which the competing processes of absorption and (re)emission balance and where heat deposition and photoionization (if relevant to the region) both maximize [*Rishbeth and Garriott*, 1969]. The altitude of unit optical depth for vertically incident radiation is illustrated in Figure A.4 [*Meier*, 1991] for wavelengths in the X-ray (1 nm) to the NUV (350 nm) range and for two MSIS (Mass Spectrometer and Incoherent Scatter) [*Hedin et al.*, 1977a, b; *Hedin*

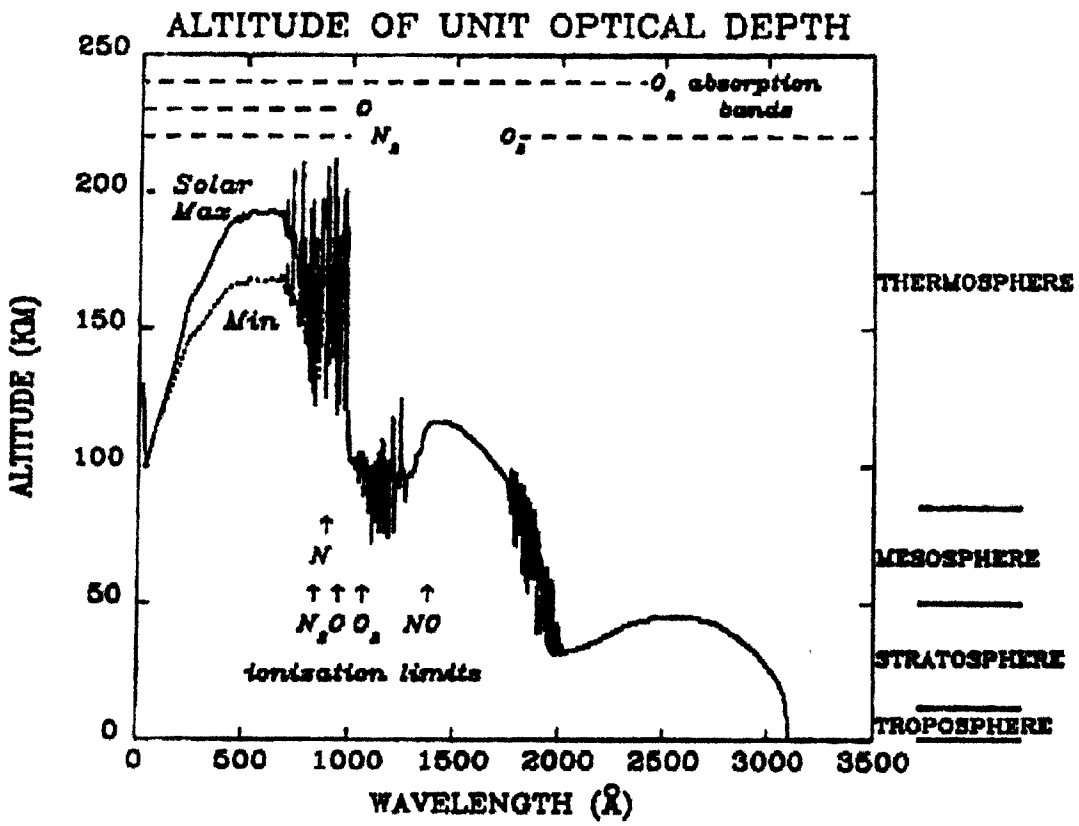

Figure A.4. Altitude of unit optical depth. The altitude at which vertically incident solar UV radiation is reduced by a factor of e^{-1} for two model atmospheres. Absorption bands of O, O_2, O_3 and N_2 are indicated, and arrows denote the wavelength limits for which the ionization of O, O_2, N, N_2 and NO no longer occurs [Figure from *Meier*, 1991].

1983; 1987; 1991] model atmospheres, one indicative of solar maximum conditions and the other of solar minimum conditions. Table A.1 also provides a broad summary of the atmosphere's response to the Sun's input and to Earth's surface IR output as well.

A.4 Radiative Equilibrium: The Effective Surface Temperature

The effective surface temperature T_e is a blackbody property of all planetary bodies dependent on the assumption that the body is in radiative equilibrium with the solar radiative input impacting its surface. For planets with an atmosphere, the input radiation is assumed to reach the surface (no absorption), and the planet's thermal radiative output spectrum is measured from space, but T_e is then indicative of the temperature of the body as measured at the "top" of its atmosphere; *i.e.* where the atmosphere's averaged slant opacity is of order unity. An observed temperature greater than T_e indicates a body with an internal energy source, such as Jupiter. Determining Earth's T_e begins with the expression that describes the column-averaged thermal energy content of a column of Earth's atmosphere of unit area [*e.g. Thomas and Stamnes,* 1999],

$$E^* = \int_0^\infty dz c_p(z)\rho(z)T(z) \equiv c^*_p T^*, \tag{A.3}$$

where $c_p(z)$ is the specific heat per unit mass at constant pressure, $\rho(z)$ is the mass density, and $T(z)$ is the temperature, all at altitude z. T^* is the column-averaged temperature (density-weighted) of the entire column, and c^*_p is the column-averaged specific heat capacity. The time rate of change of the column energy is given by the expression

$$\frac{\partial E^*}{\partial t} = c^*_p \frac{\partial T^*}{\partial t} \equiv N^* = (1-a^*)F^S - F_{TOA}, \tag{A.4}$$

which defines N^*, the mean radiative forcing, as the net flux at the top of the atmosphere. The spherical albedo a^* is the ratio of reflected to incident solar radiation and is equal to ~0.30. F^S, the average solar flux impacting Earth, is determined from the relation

$$F^S = \frac{A_{disk}}{A_{sphere}} S = \frac{\pi \mathrm{R_E}^2}{4\pi \mathrm{R_E}^2} S = \frac{S}{4} = \frac{1369}{4}\ \mathrm{W{\cdot}m^{-2}} = 342\ \mathrm{W{\cdot}m^{-2}}, \tag{A.5}$$

where S is the solar constant (solar energy output integrated over all wavelengths) at one

astronomical unit (1 AU) from the Sun, A_{disk} is the area of the disk of Earth that intercepts the solar radiation, and A_{sphere} is the total surface area that absorbs the radiation. The average absorbed solar radiation by Earth is given by the $(1 - a^*)F^S$ term in Equation A.4 and is equal to 235 W·m^{-2}. F_{TOA} is the outgoing radiation measured at the top of Earth's atmosphere, and for a blackbody, this is given by Stefan's Law,

$$F_{TOA} = \sigma_B T_e^4, \tag{A.6}$$

where σ_B is the Stefan-Boltzmann constant, 5.67×10^{-8} W·m^{-2}·K^{-4}. Assuming that the time rate of change of the column energy equals zero, $\partial T^*/\partial t = N^* = 0$ (*i.e.*, radiative equilibrium), substitution of Equation A.6 into A.4 yields

$$T_e = \left[\frac{(1-a^*)F^S}{\sigma_B}\right]^{1/4} = 255 \text{ K} \tag{A.7}$$

for Earth's effective surface temperature. If observed from space, Earth radiates approximately 235 W·m^{-2} mostly in the far infrared (IR) part of the electromagnetic spectrum (wavelengths $\lambda > 3.5$ μm), and T_e agrees well with Earth's temperature of about 250 K as measured at the top of the atmosphere [*Thomas and Stamnes,* 1999]. Hence, Earth and its atmosphere together are indeed in radiative equilibrium with the Sun's radiative input. T_e, however, does not agree with the actual mean surface temperature of about 290 K.

A.5 The Adiabatic Lapse Rate

The adiabatic lapse rate is a fundamental atmospheric parameter that provides the foundation to understanding the atmosphere's temperature profile. It originates from both the radiative and hydrostatic equilibrium approximations and the ideal gas law (see Chapter 1 for a discussion of hydrostatic equilibrium). Assuming these approximations are valid and that an atmosphere is being heated from below by a hot surface, a heated air mass at the surface will rise and cool by expansion. It will displace cooler, higher-density air above it, and that air will sink and heat. This vertical transport, referred to as convection, disrupts hydrostatic equilibrium locally and establishes a mean temperature gradient from the surface up, which can be determined if the process remains adiabatic;

i.e., if no other heat sources or sinks are at work. For adiabatic processes, the pressure and temperature of an ideal gas obey the expression [*Brekke*, 1997],

$$Tp^{\frac{(1-\gamma)}{\gamma}} = \text{constant}, \tag{A.8}$$

where γ is the ratio of the specific heat capacity at constant pressure to specific heat capacity at constant volume, $\gamma \equiv c_p/c_v$. For diatomic gases such as N_2 and O_2, $c_p = 7R/2$, and for an ideal gas, $c_p - c_v = R$ [*Sears and Salinger*, 1975]. Therefore, at the surface of Earth, $\gamma = 1.4$. Differentiation of Equation A.8 with respect to altitude z (and performing some algebraic operations) yields

$$\frac{\partial T}{\partial z} = \left(\frac{\gamma - 1}{\gamma}\right)\frac{T}{p}\frac{\partial p}{\partial z}. \tag{A.9}$$

Substitution of the barometric equation and the ideal gas law (see Equations 1.1 and 1.2 in Chapter 1) into Equation A.9 yields

$$\frac{\partial T}{\partial z} = \left(\frac{\gamma - 1}{\gamma}\right)\frac{T}{(\rho RT/M)}(-g\rho) = -\left(\frac{\gamma - 1}{\gamma}\right)\frac{Mg}{R} \equiv \Gamma. \tag{A.10}$$

$\Gamma = -9.8$ K·km^{-1} and is called the (dry) adiabatic lapse rate. If Earth's atmosphere were indeed transparent to all radiation and no other energetic processes (*e.g.*, chemical reactions) were at work within it, its temperature profile on average would adhere to Γ due to vertical convection. Furthermore, in the absence of radiation absorption by the atmosphere and other energetic atmospheric processes, the temperature would continue to decline with altitude until the atmosphere terminated at ~50 km, as was believed up to the end of the 19th century [*Rishbeth and Garriott*, 1969]. Of course, this is not the case. The atmosphere's temperature profile does not follow this simplified behavior, as Figure A.1 above indicates, and Figure A.5 [*Thomas and Stamnes*, 1999] below illustrates the turbosphere's varying temperature gradient up to 100 km at different locations. The transition to a positive temperature gradient after the mesopause occurs a little lower in the atmosphere (~85-90 km) than Figure A.5 indicates, but notable is the Standard Atmosphere temperature profile (solid line), a global mean representation, which exhibits a gradient of –5.8 K·km^{-1} up to the tropopause, significantly different than Γ.

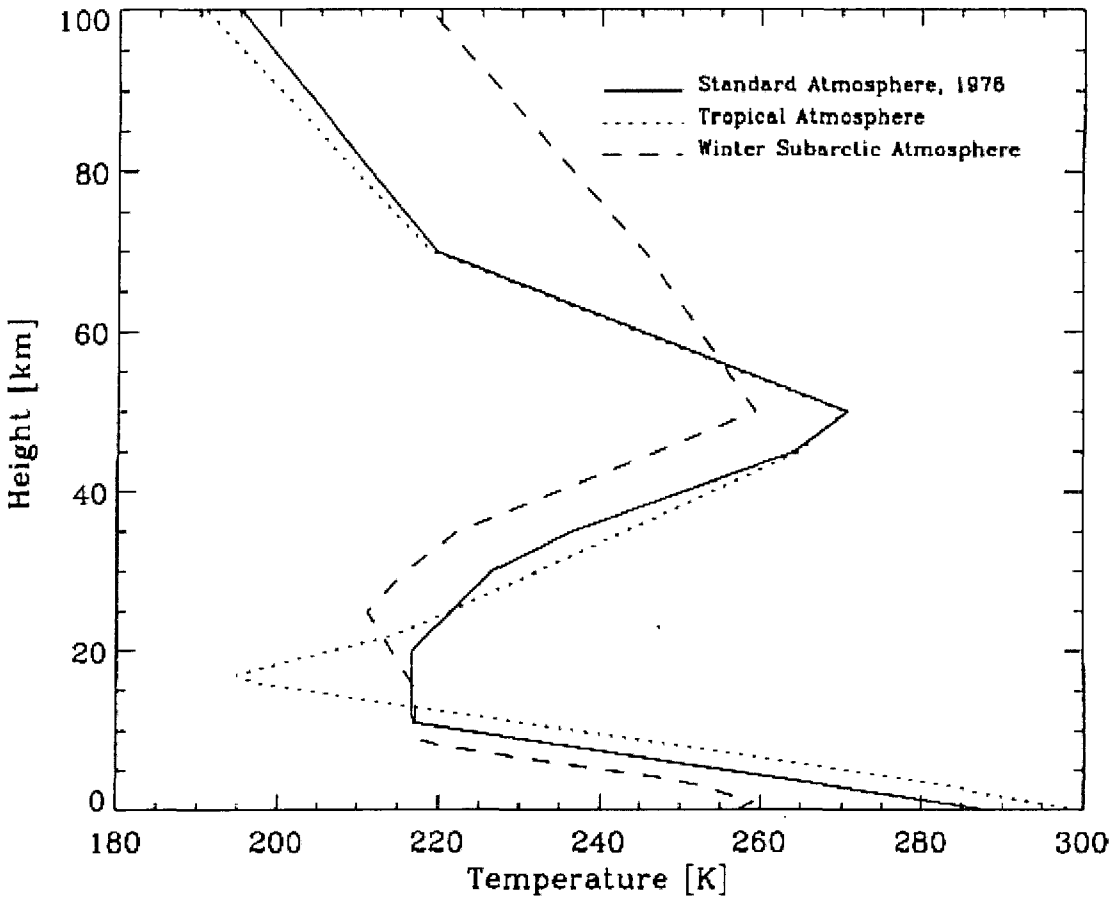

Figure A.5. Empirical model temperature profiles for Earth's atmosphere. Two locations are indicated; the Tropical Atmosphere is valid for latitudes less than 30° and the Subarctic Atmosphere is valid for 30-60° during winter months. The Standard Atmosphere represents a global mean [Figure from *Thomas and Stamnes*, 1999].

A.6 Some Significant Features of the Lower and Middle Atmosphere

As Figure A.4 illustrating the altitude of unit optical depth suggests, absorption of radiation of wavelengths <320 nm—or the lack of it—accounts for much of the heating—or lack of it—and temperature structure in the atmospheric regions above the troposphere. Tropospheric heating results from the absorption of IR radiation emitted by the Sun and Earth's hot surface (which is heated by the Sun's visible radiation), while the troposphere's temperature gradient is controlled by convective transport from the hot surface [*Thomas and Stamnes*, 1999]. Many factors influence the atmosphere's temperature structure

along with the Sun's direct radiative input, and a more comprehensive picture of Earth's radiative energy budget, shown in Figure A.6 [*Thomas and Stamnes*, 1999], is achieved only after the competing processes of radiation absorption, scattering and emission by the land and oceans and by all gases in the atmosphere, both major and minor, are considered together. This requires sophisticated investigations of the differential equation of radiative transfer, which is not discussed here. Of course, dynamical and chemical sources that store radiative energy in the land, oceans, biosphere and magnetosphere and redistribute it from these regions into the atmosphere and from atmospheric region to region must also be included in a complete energy budget of the planet.

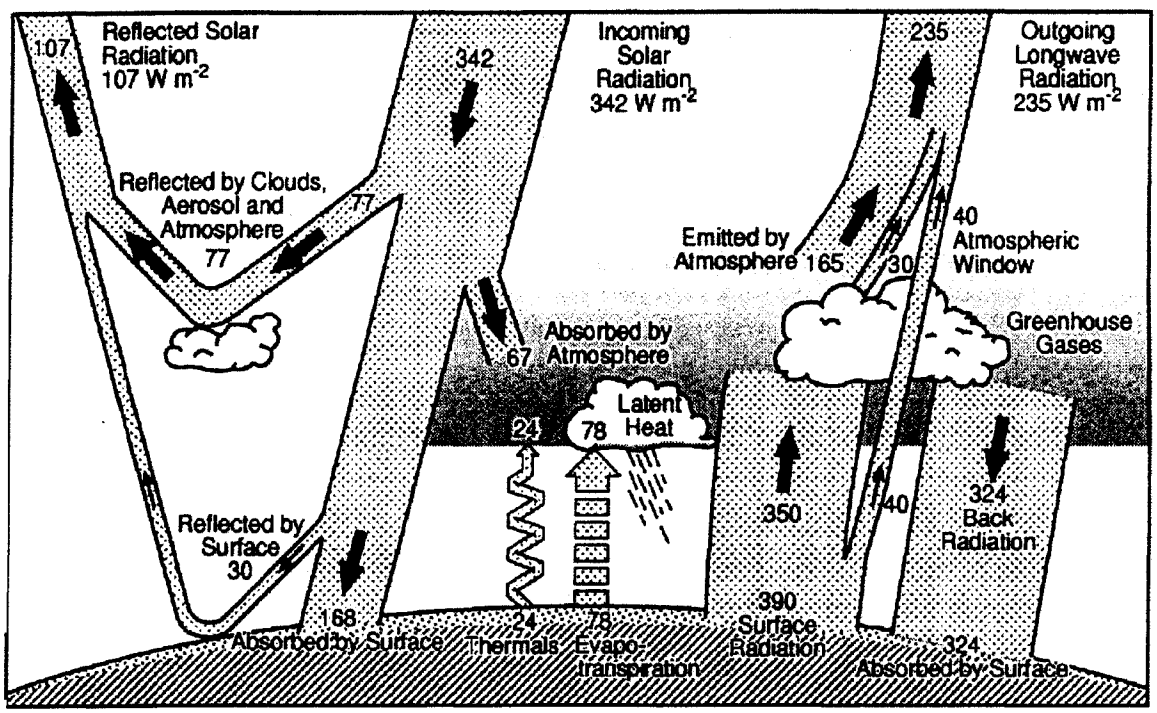

Figure A.6. Earth's radiative energy budget. Of the 342 $W \cdot m^{-2}$ that impacts Earth, 235 $W \cdot m^{-2}$ is absorbed, equaling the amount of outgoing longwave radiation emitted by Earth and its atmosphere and indicating radiative equilibrium. Though much is known of the Sun's radiative and solar wind-driven input and Earth's geophysical response, the many interdependent atmospheric and magnetospheric chemical, dynamical and energetic processes not well understood hinders weather forecasting and atmospheric circulation models' predictive capabilities [Figure from *Thomas and Stamnes*, 1999].

One very important contributor to the atmosphere's temperature structure—and to life in general—is water. Though only a trace gas, its presence in the atmosphere has significant effects on many aspects of atmospheric behavior. For example, the temperature gradient in the troposphere is strongly modified by the presence of water vapor. Condensation of moist air and the release of latent heat raises the troposphere's temperature gradient from that of Γ, which can approach -3 K·km^{-1} depending on the water content of the air [*Thomas and Stamnes*, 1999]. Moreover, tropospheric clouds and polar ice are the principal agents in determining Earth's spherical albedo value. Finally, it is water vapor and the other greenhouse gases in the troposphere (*e.g.*, CO_2, another essential trace gas) which absorb and reradiate IR radiation emitted by Earth's surface and the Sun. Greenhouse gases help to regulate the radiative equilibrium achieved between Earth and the Sun's input, acting as both a heating and cooling mechanism and accounting for the discrepancy between the effective surface temperature T_e and the actual mean surface temperature. Water vapor is by far the most radiatively active greenhouse gas and has an absorption spectrum that spans almost the entire IR output of a ~250 K blackbody [*Thomas and Stamnes*, 1999]. However, the relative importance of two other tropospheric greenhouse gases, CO_2 and methane (CH_4), to the global surface temperature and atmospheric temperature distribution as anthropogenic sources have increased their concentrations—the so-called global warming issue—has become one of the outstanding questions of global change research—studies which examine the past, present and future impact of human activities on the geophysical environment.

Another vitally important trace gas is ozone. Besides behaving as a greenhouse gas in the troposphere, O_3 also absorbs the DNA-damaging UV radiation of wavelengths ~200-320 nm. The optical depth due to O_3 extinction reaches unity between the heights of ~15-50 km (see Figure A.4) at these wavelengths, and subsequent collisions and chemical reactions of the absorption products (O, O_2) with other atmospheric constituents heat the stratosphere, reversing the temperature gradient above the tropopause. The local heating rate maximizes at about 50 km, which marks the approximate location of the stratopause [*Thomas and Stamnes*, 1999]. Like the thermosphere, the stratosphere's

positive temperature gradient makes the stratosphere highly stable. Turbulence is weak, and hydrostatic equilibrium is a dominant feature of stratospheric dynamics. Winds generally flow horizontally, and heated stratospheric air parcels only move vertically across pressure layers until they reach an altitude in which they are back in equilibrium. The little bit of eddy diffusion that does occur in the stratosphere, however, is strong enough at stratospheric temperatures to offset molecular diffusion (as mentioned in Chapter 1, a temperature-dependent process) and keep the stratosphere well mixed. A recently discovered stratospheric phenomenon of serious interest and concern is the "ozone hole" problem. The penetration of UV-B (280-320 nm) radiation through the atmosphere to the ground is strongly sensitive to the total column abundance of ozone, and the well-documented O_3 depletions [*e.g. Farman et al.*, 1985; *Chubachi*, 1985] detected in the Antarctic stratosphere since the mid-1970s—at least partially due to the increase of atmospheric chlorofluorocarbons from anthropogenic sources—has caused considerable anxiety in many scientific communities. Besides the increase in UV-B irradiation at the ground, this ozone depletion also results in an insufficiently heated, very cold (~180 K) Antarctic stratosphere. Polar Stratospheric Clouds (PSCs), which require these cold temperatures to form and which affect ozone chemistry in the spring, have been observed during recent Antarctic winters and may represent a cyclical condition of the ozone layer that humans have yet to quantify or perhaps a more ominous condition associated with global change.

The heating rate due to ozone absorption quickly diminishes above the stratopause, though some absorption does still occur [*Thomas and Stamnes*, 1999]. The absence of a strong radiative heat source between ~50-90 km (see Figure A.4) explains the mesosphere's negative temperature gradient (about -5 K·km^{-1}) and colder temperatures. Vibrational states in CO_2 are excited through collisions, and IR emissions from ozone at 9.6 μm and CO_2 at 15 μm cool the mesosphere, helping to maintain the radiative equilibrium existing from ~30-90 km [*Murgatroyd and Goody*, 1958]. However, though little radiative energy is deposited in the mesosphere, dynamical and chemical sources are important. For example, because the mesopause acts as a heat sink to the thermosphere,

heat energy that is deposited below the turbopause into the extreme lower thermosphere (by radiation or by downward molecular heat conduction from the above thermosphere), gets transported toward the mesopause by convection. Though this source provides little energy to the mesosphere, it represents a significant heat loss to the thermosphere [*Hargreaves*, 1992]. A strong chemical energy source to the upper mesosphere is the recombination of atomic oxygen that has diffused down from the thermosphere (see Chapter 1 for a further discussion of this topic). Lastly, a significant, though much debated, energy source to the mesophere is the dissipation of gravity waves, vertically-propagating buoyancy waves that are generated in the troposphere by turbulence and by winds moving across land features. Some of these waves travel through the stratosphere and reach the mesosphere (some even reaching the thermosphere), where they deposit their momentum and energy near the mesopause by way of such turbulent processes as non-linear breaking and shear instabilities [*e.g. Hodges*, 1967; *Sidi and Teitelbaum*, 1978]. Gravity wave effects on mesospheric dynamics and temperatures continue to be an important topic of atmospheric research. See Appendix B for further discussion of thermospheric buoyancy waves. Another possible global change-related phenomenon, along with PSCs, are Polar Mesospheric Clouds (PMCs), also referred to as "noctilucent clouds" (NLCs) because of their "glow" (due to scattering of sunlight) when seen at high latitudes during summer twilight hours. The very cold mesopause temperature, particularly during polar summers, makes their formation possible, and NLC observations, which have increased in recent years, indicate higher concentrations of water vapor in the mesosphere. It has been speculated that these increasing mesospheric water vapor levels may be due to increasing concentrations of tropospheric methane from anthropogenic sources (*e.g.*, cattle) over the last century and the subsequent chemistry that results in the atmosphere from these methane increases [*Thomas et al.*, 1996].

Appendix B Winds, Tides and Waves in the Thermosphere

B.1 Thermospheric Winds: The Momentum Equation

Achieving insight into the processes that produce the composition, wind and temperature distributions observed in the neutral and ionized thermosphere requires a self-consistent full analysis of the coupled three-dimensional continuity, momentum and energy conservation equations and equation of state of each thermospheric and ionospheric species. The relative importance of the many terms in each equation must also be determined. The momentum equation in its most general form [*Rees*, 1989] is given by (note bold type denotes vector quantites)

$$\rho_j \mathrm{D}_j \mathbf{U}_j / \mathrm{D}t + \nabla \cdot \overline{\overline{\mathbf{P}}}_j = \sum_j n_j \mathbf{F}_j , \tag{B.1}$$

where n_j and $\mathbf{U}_j$ are the number density and velocity of the j^{th} species, respectively, $\overline{\overline{\mathbf{P}}}_j$ is its generalized pressure tensor, ρ_j is its mass density, $\mathbf{F}_j$ are the external body forces acting on the j^{th} species (*e.g.*, gravity, electromagnetic, collisions), and $\mathrm{D}_j/\mathrm{D}t = \partial/\partial t + \mathbf{U}_j \cdot \nabla$ is the convective derivative, where $\mathbf{U}_j \cdot \nabla$ represents velocity changes due to advection. The Coriolis and centripetal acceleration terms, $2\boldsymbol{\Omega} \times \mathbf{U}_{rot}$ and $-\Omega^2\mathbf{r}$, respectively, appear on the left-hand side of Equation B.1 once it is translated to a rotational frame of reference, where $\boldsymbol{\Omega}$ is Earth's angular velocity and $\mathbf{r}$ is the radial vector from Earth's center. The centripetal term is generally negligible (~0.5%) compared to gravity.

In general, much of the atmosphere's large-scale horizontal circulation follows what is referred to as the geostrophic approximation. Because the dayside-to-nightside horizontal pressure gradient is roughly north-south in direction (since solar radiative atmospheric heating varies with latitude), the effect of the latitudinally-varying Coriolis force as air parcels flow away from the diurnal bulge—initially in the negative direction of the pressure gradient—is to balance the pressure-gradient force and blow the wind at right angles to the pressure gradient [*Rishbeth*, 1998]. These two forces are the most dominant in the stratosphere and mesosphere horizontally, and under these

circumstances, the horizontal components of the momemtum equation approximately reduce to [*e.g. Rishbeth and Garriott*, 1969]

$$-2\Omega U_x \sin\phi = \rho^{-1}(\partial p/\partial y),\ \ 2\Omega U_y \sin\phi = \rho^{-1}(\partial p/\partial x), \qquad \text{(B.2}a\text{-}b\text{)}$$

where x and y are the local coordinates at any point in the atmosphere (x is southward, y is eastward in this context), U_x and U_y are the wind speeds, Ω is Earth's angular speed, p is the pressure, ρ is the mass density, and ϕ is the latitude. Also recall from Chapter 1 that the momentum equation reduces to the barometric equation, $\partial p/\partial z = -g\rho$, in the vertical direction. The mean zonal circulation resulting from geostrophic flow is nearly-divergent free, with westward flow prevailing in the summer hemisphere and eastward flow in the winter hemisphere [*Rishbeth*, 1998]. Equations B.2*a-b* can also be combined and rewritten in terms of the latitude,

$$(\rho R_E)^{-1}\partial p/\partial\phi = 2\Omega U \sin\phi, \qquad \text{(B.2c)}$$

where R_E is an earth radius, and U is now specified as a function of latitude and the latitudinal pressure gradient [*Hargreaves*, 1992]. Because the pressure gradient is merely the result of the atmosphere's temperature gradient, these expressions can be further manipulated into forms which give the wind as a function of temperature gradient, referred to as the theory of the thermal wind. In general, global-scale winds in the stratosphere and mesosphere are well explained by Equations B.2*a-c*, with some minor discrepancies [*Hargreaves*, 1992].

Thermospheric winds are also influenced by the Coriolis force, but because the thermosphere interacts with the ionosphere and because the high-latitude thermosphere is dynamically and energetically linked to the magnetosphere, the horizontal components of the momentum equation do not reduce to the geostrophic approximation when applied to the upper atmosphere. Consequently, the thermosphere's circulation patterns are strongly modified from a strictly geostrophic type and from the dayside-to-nightside, solar-radiative-driven pattern discussed in Chapter 1. In the lower thermosphere below ~150 km where ion drag is weak, the Coriolis force tends to dominate the neutral circulation [*e.g. Rees*, 1989; *Rishbeth*, 1998]. In the middle and upper thermosphere ($\gtrsim$150 km), however, ion drag is the limiting force to the pressure-gradient force, and at polar

latitudes, the neutral horizontal circulation tends to follow the ion drift vortices [*Rees*, 1989]. In general, the momentum equation for each neutral species j in vector form reads [*Rishbeth*, 1972],

$$\rho_j[\mathrm{D}_j\mathbf{U}_j/\mathrm{D}t + 2\boldsymbol{\Omega} \times \mathbf{U}_j] = -\nabla p_j - \rho_j \upsilon_{jk}(\mathbf{U}_j - \mathbf{V}_k) + \eta_j \nabla^2 \mathbf{U}_j + \rho_j \mathbf{g}\,, \tag{B.3}$$

where ρ_j is the mass density of the j^{th} constituent, $\mathbf{U}_j$ is its velocity, υ_{jk} is its collision frequency with the k^{th} ions, p_j is its partial pressure, η_j is its coefficient of molecular viscosity, and $\mathbf{V}_k$ is the k^{th} ion's drift velocity. The Coriolis acceleration is given by $2\boldsymbol{\Omega} \times \mathbf{U}_j$, and the centripetal acceleration term $-\Omega^2\mathbf{r}$ is not included. The horizontal pressure-gradient force per unit volume is given by ∇p_j, and $\rho_j \upsilon_{nk}(\mathbf{U}_j - \mathbf{V}_k)$ accounts for the ion drag on the j^{th} neutral species by the k^{th} ions. The force per unit volume due to molecular viscosity is given by $\eta_j \nabla^2 \mathbf{U}_j$, and $\rho_j \mathbf{g}$ is the gravitational force per unit volume. Figures B.1*a-b* [*Jacchia*, 1965; *Kohl and King*, 1967, respectively] below illustrate an early attempt by upper-atmospheric modelers to determine the temperature distribution and the horizontal winds set up by this distribution in the upper thermosphere (~300 km) for moderate solar activity at equinox. Though high-latitude heat sources are not included in the calculation, ion drag and viscosity forces are included, and the modeling approach is similar to the thermal wind concept in that the temperature gradient drives the winds. Though it is not readily apparent from Figure B.1*b*, the neutral wind speeds are generally smaller during the day than at night because ion drag is generally stronger during daytime hours [*Hargreaves*, 1992].

Determining approximate solutions of $\mathbf{U}_j$ from the momentum equation is a challenging task and will not be described in any significant detail here, but a general discussion of the different terms in Equation B.3, the relevant approximations to it (in each dimension) and several figures provides some insights into the details of the dynamics of the thermosphere. To begin with, it is useful to express Equation B.3 in its Cartesian component form at geographic latitude ϕ, where x, y and z are the local Cartesian coordinates at any point in the thermosphere (x is eastward, y is northward, and z is upwards in this context, in contrast to the convention used in Equations B.1*a-b*). The momentum equation then reads [*Rishbeth*, 1972],

a)

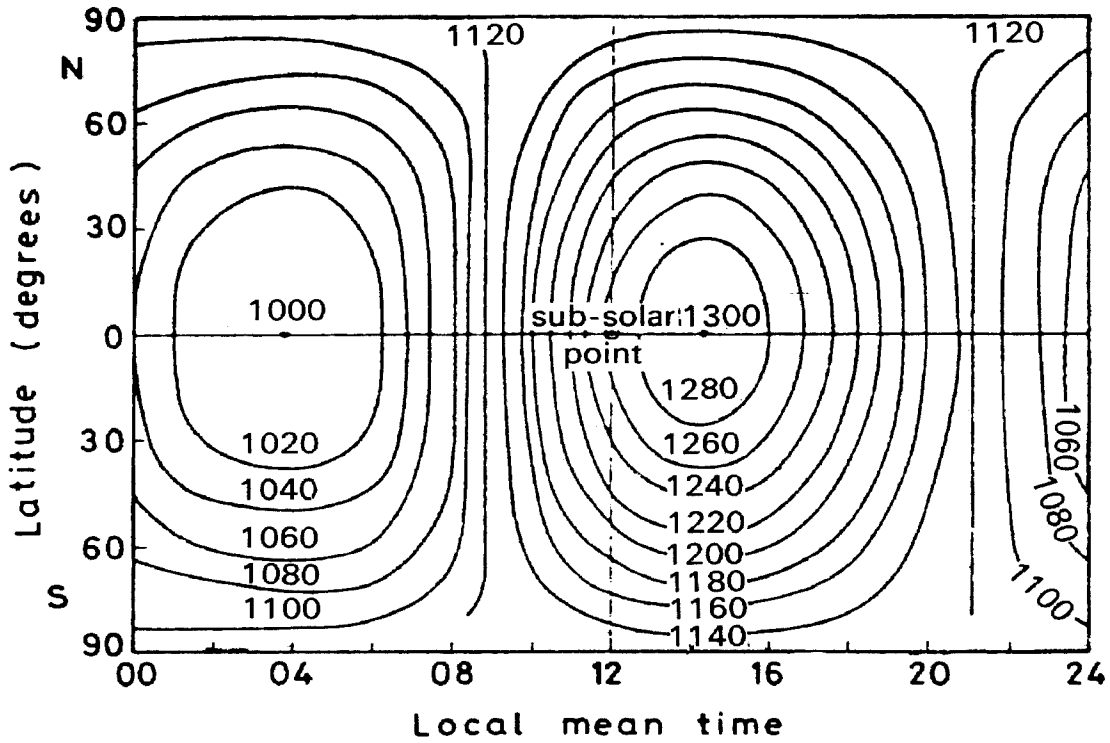

b)

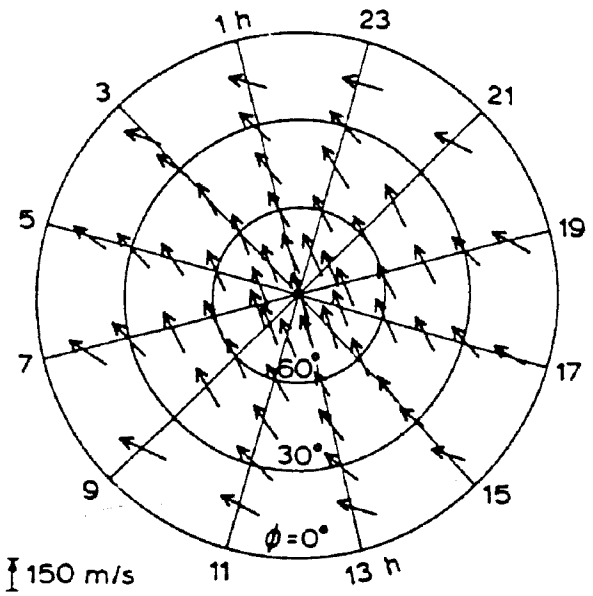

Figure B.1. Temperature and winds in the upper thermosphere. **(a)** Global upper thermospheric temperature distribution in K and **(b)** subsequent computed winds at 300 km in the northern hemisphere for moderate solar activity at equinox. Geographic north is at center of diagram **(b)**, and its perimeter is the equator. High-latitude heat sources are not included [Figures from *Jacchia*, 1965 and *Kohl and King*, 1967, respectively].

$$D_j U_{j,x}/Dt = -\rho_j^{-1}(\partial p/\partial x) + \eta_j \rho_j^{-1}(\partial^2 U_{j,x}/\partial z^2) - \upsilon_{jk}(U_{j,x} - V_{k,x}) + 2\Omega(U_{j,y}\sin\phi - U_{j,z}\cos\phi)$$

$$D_j U_{j,y}/Dt = -\rho_j^{-1}(\partial p/\partial y) + \eta_j \rho_j^{-1}(\partial^2 U_{j,y}/\partial z^2) - \upsilon_{jk}(U_{j,y} - V_{k,y}) - 2\Omega U_{j,x}\sin\phi. \quad \text{(B.4}a\text{-}c\text{)}$$

$$D_j U_{j,z}/Dt = -\rho_j^{-1}(\partial p/\partial z) + \eta_j \rho_j^{-1}(\partial^2 U_{j,z}/\partial z^2) - \upsilon_{jk}(U_{j,z} - V_{k,z}) + 2\Omega U_{j,x}\cos\phi - g$$

In determining $\mathbf{U}_j$, it is necessary to evaluate the equation of motion of each ionic species k because the equation of motion of the j^{th} neutral species depends on the velocity $\mathbf{V}_k$ of the k^{th} ion. It is also necessary to evaluate the continuity equation of each ionic species k because the neutral-ion collision frequency υ_{jk} is proportional to the number density N_k of each ion species (see Appendix C for a more-detailed discussion of collisions and other molecular processes). The ionic equation of motion and continuity equation in vector form are given by [*Rishbeth*, 1972]

$$D_k\mathbf{V}_k/Dt = \mathbf{g} - (N_k m_k)^{-1}\nabla(p_e + p_k) - \upsilon_{kj}(\mathbf{V}_k - \mathbf{U}_j) + e_k m_k^{-1}(\mathbf{E} + \mathbf{V}_k \times \mathbf{B}), \text{ and}$$

$$\partial N_k/\partial t = q_k - l_k(N_k) - \nabla \cdot (N_k\mathbf{V}_k), \quad \text{(B.5}a\text{-}b\text{)}$$

respectively, where m_k is the k^{th} ion's mass, e_k is its charge, q_k and l_k are its production and loss rates, respectively, p_k is its partial pressure, υ_{kj} is its collision frequency with neutral species j ($\upsilon_{kj} = n_j\upsilon_{jk}/N_k$; see Appendix C), p_e is the electron partial pressure, and $\mathbf{E}$ and $\mathbf{B}$ are the local electric and magnetic induction field strengths, respectively. Lastly, it is necessary to evaluate the continuity and energy equations of the j^{th} species since the momentum equation of the j^{th} species is coupled to its number density and temperature. The continuity and temperature equations of the j^{th} species are given by [*Rees*, 1989]

$$\partial n_j/\partial t + \nabla \cdot (n_j\mathbf{U}_j) = P_j - L_j, \text{ and,}$$

$$\frac{\chi}{2}k_B\frac{D_j(n_jT_j)}{Dz} = -\frac{5}{2}n_jk_BT_j\nabla\cdot\mathbf{U}_j - \nabla\cdot\mathbf{q}_j - \overline{\overline{\mathbf{P}}}_j : \nabla\mathbf{U}_j + Q_j - Y_j \quad \text{(B.6}a\text{-}b\text{)}$$

respectively, where P_j and L_j are the production and loss rates of species j, respectively, T_j is its temperature, χ is number of degrees of freedom (3 for monoatomic gases, *e.g.*, O, and 5 for N_2 and O_2), k_B is the Boltzmann constant, and Q_j and Y_j are the local heating and heat loss rates, respectively. The thermal flow vector $\mathbf{q}_j$ is given by $\mathbf{q}_j = -\kappa\nabla T_j$, where κ is the coefficient of thermal conductivity. Compressional heating of species j (or

adiabatic cooling) is given by the $n_j k_B T_j \nabla \cdot \mathbf{U}_j$ term on the right-hand side of Equation B.6*b*, while the viscous heating of species j is determined from the scalar product of the pressure tensor and the velocity gradient, $\overline{\overline{\mathbf{P}}}_j : \nabla \mathbf{U}_j$. Furthermore, depending on which species and what regions of the thermosphere are being investigated, other equations become relevant to the scope of the problem, such as the generalized Ohm's law,

$$\mathbf{J} = \overline{\overline{\boldsymbol{\sigma}}}[\mathbf{E} + (c^{-1})\mathbf{U}_j \times \mathbf{B}], \tag{B.7}$$

and Maxwell's equations,

$$\nabla \times \mathbf{E} = -(c^{-1})\partial \mathbf{B} / \partial t; \ \nabla \times \mathbf{B} = 4\pi (c^{-1})\mathbf{J}, \tag{B.8*a-b*}$$

where **J** is the current density, **E** is the electric field, **B** is the magnetic field, $\overline{\overline{\boldsymbol{\sigma}}}$ is the conductivity tensor, and c is the speed of light. The equation of state, $p_j = n_j k_B T_j$, relates the quantities of temperature, pressure and number density that appear in the other equations and gives the partial pressure of each neutral species j. In general, the temperature of the different neutral species j is the same; *i.e.*, $T_j = T$ for $j = 1, 2, 3, \ldots$ and the neutral gases are in thermal equilibrium. The electron and ion gases generally have temperatures different from the neutral gas and from each other [*Rees*, 1989].

If more than one species of ion exists in a particular altitude range, as is generally the case from ~100-200 km, then separate equations are required for each ionic species. In the F2 region, from ~200-600 km, O^+ is the dominant ion (see Chapter 1 for more details on thermospheric composition), and generally only one ionic equation of motion and continuity equation is required. The Coriolis force can be neglected in Equation B.5*a* because the ion-neutral collision force term, $\nu_{kj}(\mathbf{V}_k - \mathbf{U}_j)$, greatly exceeds the Coriolis force [*Rishbeth*, 1972]. In addition, $D_k\mathbf{V}_k/Dt \sim 0$ in Equation B.5*a* at F2-region altitudes since the time scale for ions to reach their steady-state drift velocity, $(\nu_{kj})^{-1}$, is short, ~1 s [*Rishbeth*, 1972].

Though ions do not flow freely along with the neutral winds because they are constrained by Earth's geomagnetic field, a field-aligned component of the ion motion does exist that is driven by collisions with the neutral horizontal wind field. In the lower thermosphere, collisions between an ion and its neutral neighbors are very frequent, ~10^4

s^{-1}, and as a result, ions tend to follow the neutral flow exclusively, without hindrance from the magnetic field. This is not the case as much in the upper thermosphere, and generally, F-region ion motion is due to plasma diffusion, the neutral wind field, thermal expansion and contraction and electric field drift [*Rishbeth*, 1972]. The result is two-component motion, one that is parallel to the magnetic field lines and one that is perpendicular. The field-aligned velocity component of the ions, $\mathbf{V}_{\parallel}$, is driven by the neutral wind field and is equal to the field-aligned component $\mathbf{U}_{\parallel}$ of the neutral velocity. In vector form, this is given by $\mathbf{V}_{\parallel} = (\mathbf{U} \cdot \mathbf{B})\mathbf{B}/B^2$, and ultimately, $V_{\parallel,x}$, $V_{\parallel,y}$ and $V_{\parallel,z}$ can all be expressed in terms of U_x, U_y and U_z and the magnetic dip and declination angles, I and D, respectively. The drift motion of the ions due to electric fields, given by $\mathbf{V}_{\perp} = (\mathbf{E} \times \mathbf{B})/B^2$, is perpendicular to both **E** and **B**, and $V_{\perp,x}$, $V_{\perp,y}$ and $V_{\perp,z}$ can all be expressed in terms of E_x, E_y, B, I and D. Electric field-induced ion motion has far-reaching consequences in the high-latitude thermosphere, where the large-scale electric field that maps down from the magnetosphere is often very strong, and consequently, the motion of the neutrals strongly couples through ion drag to the ionic motion. In general, the horizontal wind direction of the neutral thermospheric species is governed by the ratio of the Coriolis force to the ion-drag force [*Rishbeth*, 1998]. If ion drag is weak, then the neutral flow will tend to follow the geostrophic approximation. When ion drag is strong (*e.g.*, in the daytime or in the high-latitude upper thermosphere), the winds blow parallel to the pressure-gradient and ion-drag forces [*Rishbeth*, 1998].

The last two processes to consider when evaluating the momentum equation are the advection and molecular viscosity terms, $(\mathbf{U}_j \cdot \nabla)\mathbf{U}_j$ and $\eta_j \nabla^2 \mathbf{U}_j$, respectively. Horizontal advection usually plays a small role in the neutral thermosphere's global-scale dynamics, though not always [*Rishbeth*, 1972]. If neutral wind speeds are much smaller than Earth's rotational speed (*i.e.*, $U_j << R_E\Omega \sim 460$ m·s^{-1}; *e.g.*, during solar minimum), then the quantity $(\mathbf{U}_j \cdot \nabla)\mathbf{U}_j$ is small, but when $\mathbf{U}_j$ is large or there are large spatial gradients in $\mathbf{U}_j$ (*e.g.*, at dusk and dawn or in the thermosphere's polar-cap and high-latitude regions during highly-disturbed geomagnetic activity), then horizontal accelerations of thermospheric neutral species due to advection can be significant. In the past, modeling this force would have

been difficult because of its nonlinearity, but with the advent of more robust computing power and better mathematical techniques for approximating nonlinear differential equations, this acceleration term is now readily included in general circulation models.

The main contribution of molecular viscosity to the dynamics of the thermosphere is to smooth out the wind shears (*i.e.*, the spatial gradients of $\mathbf{U}_j$) that exist in the vertical direction. The variation in wind velocity between two layers of a gas flowing adjacent to one another results in a drag force being exerted on one layer by the other. This drag manifests itself on a molecular level through collisions as a frictional force which imparts a momentum change to the molecules [*Rees*, 1989]. In the thermosphere, where heating, the pressure gradient and ion drag are all height-varying on a scale comparable to the scale height H_j, wind speed is assumed to vary with altitude on a similar scale [*Rishbeth*, 1972]. Because wind shears in the vertical direction are generally the largest, ∇^2 reduces to $\partial^2/\partial z^2$. In evaluating the importance of viscosity, the quantity $\eta_j\rho_j^{-1}$, referred to as the kinematic viscosity, determines the strength of the viscous force in Equations B.4*a-c*, and as mass density ρ_j decreases with altitude, the kinematic viscosity increases. If the altitude variation of U_j is assumed to go as $\exp(\pm z/H_j)$, then the viscous term in Equations B.4*a-c* is $(\eta_j/\rho_j H_j^2)U_j$, and $\eta_j/\rho_j H_j^2$ determines the relative strength of viscosity as it affects thermospheric winds. If $\eta_j/\rho_j H_j^2 > \upsilon_{jk}$, then viscosity is stronger than ion drag, and above ~300-400 km, viscosity dominates such that the variation of U_j with height is small; *i.e.*, $\partial U_j/\partial z \rightarrow 0$. Thus, winds high in the thermosphere blow without altitude variation. Lower in the thermosphere, in the ~100-200 km range, the kinematic viscosity is weak enough such that significant vertical wind shears still exist [*e.g. Larsen*, 2002], and in the high-latitude thermosphere, where ion convection due to the cross-polar cap electric field and the magnetic field drives the neutrals in the direction of the ions, strong velocity shears, which viscosity can not smooth out, are also seen in the horizontal wind field, in both the lower and upper thermosphere [*e.g. Conde and Smith*, 1998; *Conde et al.*, 2001].

Many small- and large-scale spatial and temporal effects that the high-latitude processes of particle precipitation, Joule heating, and ion drag have on the thermosphere's general behavior have been discussed in Chapter 1. Their overall effect on thermospheric

global-scale circulation can be seen in Figure B.2 [*Roble*, 1977], which illustrates the thermosphere's meridional (north-south) circulation from ~100-700 km during varying geomagnetic conditions at both equinox and solstice. During quiet geomagnetic conditions, horizontal flow away from the diurnal bulge due to the Sun's radiative energy input on Earth's dayside dominates, but during active geomagnetic conditions, circulation associated with the high-latitude, magnetospheric-related energy inputs can dominate.

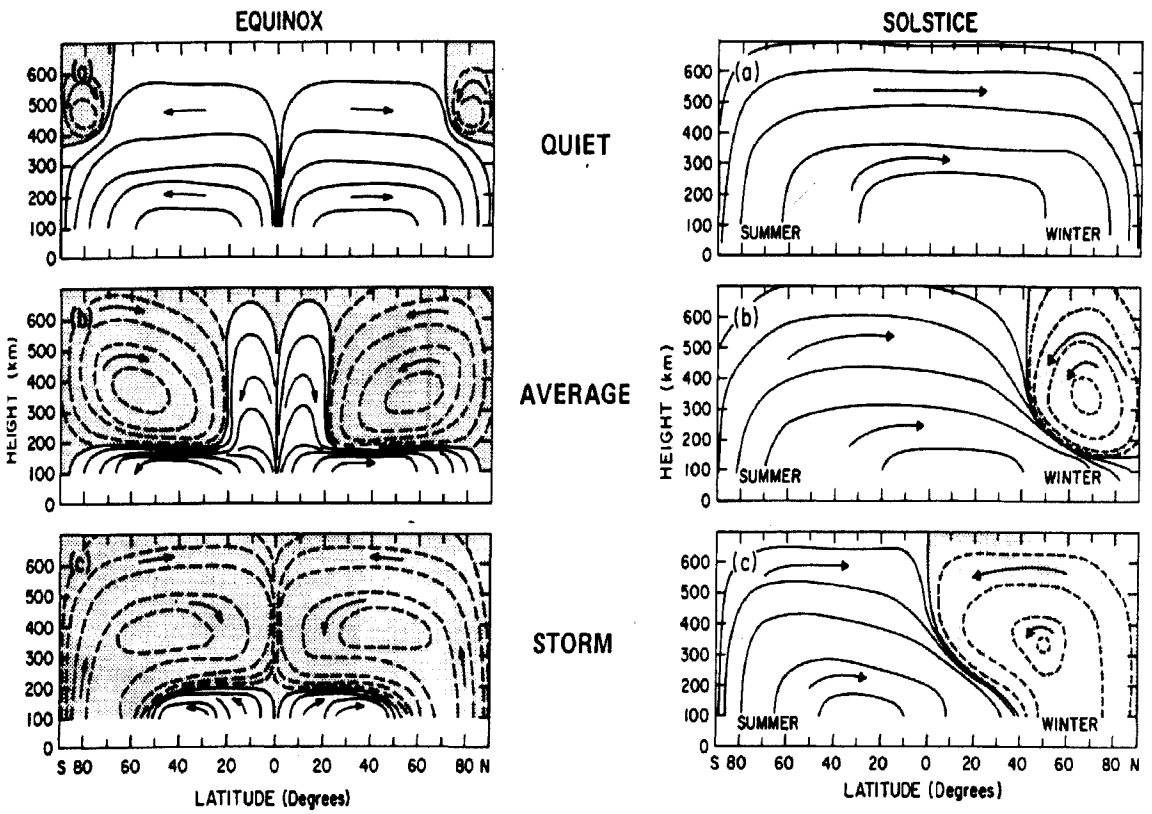

Figure B.2. Thermospheric meridional circulation patterns during quiet and active geomagnetic conditions. High-latitude heating processes modify the thermosphere's overall circulation pattern from a strictly solar radiative-heated pattern. During quiet geomagnetics conditions, radiative heating dominates the circulation. During active conditions, magnetospheric-related heating can dominate [Figure from *Roble*, 1977].

The last component of the momentum equation to discuss is Equation B.4*c*, which describes the vertical component of $\mathbf{U}_j$. Because gravity and the change in pressure are

the strongest forces acting vertically in the atmosphere [*Rishbeth et al.*, 1969; see Section 1.5 in Chapter 1], accelerations due to the other terms in Equation B.4*c* are negligible, and generally, Equation B.4*c* reduces to the barometric equation, $\partial p/\partial z = -g\rho$. However, though it is not apparent from the barometric approximation, vertical winds of an order of magnitude less than horizontal wind speeds do occur in the thermosphere, in and near the aurora and also away from it. Equation B.4*c* is not necessarily practical for ascertaining the details or the magnitudes of this vertical motion, but if $U_{j,x}$ and $U_{j,y}$ are determined from Equations B.4*a-b*, and n_j is known (*e.g.*, from an empirical model), then the neutral continuity equation, $\partial n_j/\partial t = -\nabla \cdot (n_j \mathbf{U}_j)$, can be used to estimate $U_{j,z}$ [*e.g. Rishbeth et al.*, 1969; *Smith*, 1998]. Furthermore, as was discussed in Chapter 1, *Burnside et al.* [1981] employed this method to determine Equation 1.3, $U_{j,z} = W_D = -H\nabla_h \mathbf{U}_h$, and estimate mid- to low-latitude upper-thermospheric vertical winds due to global-scale divergent horizonal winds, using the ideal gas law and hydrostatic equilibrium in conjunction with the neutral continuity equation and FPS OI(630.0)-nm horizontal wind measurements U_x and U_y. Vertical motions in the thermosphere of a variety of types are described in more detail in Chapter 1. As was discussed, vertical wind characteristics such as their small magnitudes at middle to low latitudes (relative to horizontal wind speeds) and their horizontal spatial scales at high latitudes (relative to model grid sizes) continue to make a fully self-consistent computation of $U_{j,z}$—along with $U_{j,x}$, $U_{j,y}$, n_j, N_k, $\mathbf{V}_k$, T_j, T_k and T_e—using global-scale general circulation models a challenging endeavor.

B.2 Thermospheric Tidal Motion

The last two phenomena to consider when investigating thermospheric motions are tides and waves. Neither are discussed here in too much detail, but it is important to mention them, as they are a significant part of the thermosphere's energy budget. Tides, in general, are periodic variations in the atmosphere's global-scale (mostly) horizontally-distributed pressure, temperature and wind patterns due to forcing from the Sun's and Moon's gravitational influence and the Sun's radiative input. Solar radiative input generates diurnal (24-hr period) and other harmonic (12-, 8-hr, *etc.*) tidal oscillations in the troposphere (due to near-IR radiation absorption by water vapor), stratosphere (UV-B

and UV-C absorption by ozone) and thermosphere (EUV, FUV and X-ray absorption) [*e.g. Forbes*, 1995]. In fact, the thermosphere's large-scale horizontal winds set up by the dayside-to-nightside pressure gradient can be regarded as a tidal motion instead of as a "wind" and analyzed using tidal theory. Functions that describe the atmosphere's modes of oscillations are searched for using the equation of motion and a tidal potential function, Ψ. Essentially, the upper thermosphere's horizontal bulk flow set up by the dayside-to-nightside pressure gradient can be regarded as a diurnal tide, with a varying degree of strength (*i.e.*, oscillation amplitude) of ~50-200 $m \cdot s^{-1}$ due to the variable intensity of the Sun's FUV, EUV and X-ray radiation input. In the lower thermosphere and upper mesosphere, a semidiurnal tide dominates, driven more by upward-propagating tides from the troposphere and stratosphere than by *in situ* forcing [*Müller-Wodarg and Aylward*, 1998]. A small lunar tide (with periods related to the lunar day, 24.8 hr) is also discernible in both the upper and lower thermosphere [*Hargreaves*, 1992]. When including the tidal potential function Ψ in the formulation of the previous section, the equation of motion is given by

$$D_j\mathbf{U}_j/Dt + 2\boldsymbol{\Omega} \times \mathbf{U}_j = -\rho_j^{-1}\nabla p_j - \upsilon_{jk}(\mathbf{U}_j - \mathbf{V}_k) + \eta_j\rho_j^{-1}\nabla^2\mathbf{U}_j + \mathbf{g} - \nabla\Psi, \qquad \text{(B.9)}$$

and perturbation theory is used to solve the equation. The analysis is generally performed in spherical coordinates, due to the long period and planetary-scale size of the tidal motions, and certain terms can be neglected depending on which altitude range of the thermosphere is being investigated (*e.g.*, dropping the Coriolis term for upper-thermospheric analysis). Hydrostatic equilibrium is assumed, so the pressure and gravity terms cancel each other. Analytic solutions of Ψ are referred to as Hough functions.

B.3 Thermospheric Buoyancy Motion: Acoustic and Gravity Waves

Besides the long-period, planetary-scale-size wave motions that tides represent, there are also smaller-scale, shorter-period wave motions in the atmosphere referred to as buoyancy waves; *i.e.*, acoustic and gravity waves. In the troposphere, horizontal winds blowing across land features, lightning and surface turbulence produce buoyancy waves. Some waves propagate vertically and increase in amplitude as they travel upward since a given wave's energy density $\frac{1}{2}\rho v_{ph}^2$ must remain constant, where ρ is the atmospheric

mass density and v_{ph} is the wave's phase velocity, $v_{ph} = \lambda/\tau$ (λ is the wavelength, τ is the period). When a wave's amplitude reaches a critical value, the wave will turbulently break and dissipate its energy (see the discussion near the end of Appendix A). Waves break in the upper mesosphere, extreme lower and lower thermosphere, and the lower-thermospheric altitude range where some of these waves break, ~100-120 km, marks the region referred to as the turbopause or homopause, the transition region between the homosphere—the well-mixed lower atmosphere—and the heterosphere—the diffusively-separated upper atmosphere [*e.g. Mayr et al.*, 1997; see references therein].

As was mentioned in Chapter 1, *in situ* generation of acoustic and gravity waves also occurs in the high-latitude thermosphere due to auroral-related processes. These waves generally have periods of minutes to a few hours and wavelengths of a few to several hundred or thousand kilometers (discussed more below), and their propagation speeds generally range from ~100-1000 $m \cdot s^{-1}$ [*e.g. Mayr et al.*, 1984; see references therein]. Because the spatial scale of these disturbances is small (compared to Earth's size) and the periods are relatively short, analysis can be performed in Cartesian coordinates. Also, only pressure-gradient and gravitational forces are considered; hence, their accepted name. If the wave is acoustic, the restoring force of the displaced gas particles is the pressure change of the compressed medium (like a sound wave), and for a buoyancy wave, gravity acts as the restoring force, similarly to its action on a surface ocean wave. The equation of motion reduces to $\partial \mathbf{U}/\partial t = \mathbf{g} - \rho^{-1}\nabla p$ under these circumstances, and also needed in the formulation of the problem are the continuity equation, $\partial\rho/\partial t + \nabla \cdot (\rho \mathbf{U}) = 0$, a relation describing energy conservation, the ideal gas law, $p = nk_BT = \rho RTM^{-1}$, and the adiabatic equation of state, $p\rho^{-\gamma} = \text{const}$, where M is the mean molecular mass (in $kg \cdot kmol^{-1}$), $R = 8.314 \times 10^3$ $J \cdot kmol^{-1} \cdot K^{-1}$ is the ideal gas constant, and γ is the ratio of specific heat capacity at constant pressure to specific heat capacity at constant volume. Plane-wave solutions for perturbations in $\mathbf{U}$, ρ and p of the form $\exp[i(\omega t - k_x x - k_z z)]$ are assumed in order to determine the dispersion relation (*i.e.*, the equation that relates frequency to wavenumber), where ω is the angular frequency of the wave, wavenumber vector $\mathbf{k}$, $\mathbf{k} = k_x\mathbf{x} + k_z\mathbf{z}$ ($k = 2\pi\lambda^{-1}$), is assumed to lie in the xz plane for

simplicity (**x** and **z** are unit vectors), the angle of propagation of the wave, θ, is given by $\tan\theta = k_z/k_x$, x and z are the horizontal and vertical coordinates, respectively, and the phase velocity of the wave, v_{ph}, is given by $v_{ph} = \omega/k$. Without going into further detailed analysis, the dispersion relation is given by [*e.g. Brekke*, 1997]

$$\omega^4 - [(k_x^2 + k_z^2)c_s^2 + \omega_a^2]\omega^2 + k_x^2 c_s^2 \omega_B^2 = 0, \qquad \text{(B.10)}$$

where c_s is the speed of sound, $c_s = (\gamma k_B T m^{-1})^{1/2} = (\gamma RTM^{-1})^{1/2}$, ω_a is the acoustic resonance frequency, $\omega_a = \gamma^{1/2} g c_s^{-1}$, and ω_B is the buoyancy resonance or Brunt-Väisälä frequency, $\omega_B = (\gamma - 1)^{1/2} g c_s^{-1}$. Equation B.10 has two solutions when solved for ω^2, which are given by

$$\omega^2 = \frac{1}{2}\{k^2 c_s^2 + \omega_a^2 + [(k^2 c_s^2 + \omega_a^2)^2 - 4k_x^2 c_s^2 \omega_B^2]^{1/2}\} \text{ and}$$

$$\omega^2 = \frac{1}{2}\{k^2 c_s^2 + \omega_a^2 - [(k^2 c_s^2 + \omega_a^2)^2 - 4k_x^2 c_s^2 \omega_B^2]^{1/2}\}, \qquad \text{(B.11}a\text{-}b\text{)}$$

where $k^2 = k_x^2 + k_z^2$. Transversely-propagating acoustic waves, associated with solution B.11*a*, have the higher frequencies where $\omega > \omega_a$, and longitudinally-propagating gravity waves, associated with solution B.11*b*, have the lower frequencies where $\omega < \omega_B$. At thermospheric altitudes, acoustic waves will have periods of less than or equal to a few minutes, while gravity waves will generally have periods greater than or equal to the Brunt-Väisälä period $\tau_B \approx$ 10-15 min. Waves with frequencies between these two ranges, $\omega_B < \omega < \omega_a$, are evanescent (*i.e.*, they do not propagate), and the two resonance frequencies, ω_a and ω_B, have physical significance. Essentially, the acoustic frequency ω_a is the acoustic-mode natural frequency of the entire atmosphere, when compression acts as the restoring force, while ω_B is the buoyancy-mode natural frequency of the atmosphere, when gravity is the restoring force [*Hargreaves*, 1992]. The atmosphere's buoyancy-mode natural frequency is determined by applying Newton's law, **F** = m**a**, and perturbation analysis to small vertical displacements of an air parcel about its equilibrium position [*Brekke*, 1997], considering only the forces of gravity and pressure. The differential equation for a harmonic oscillator is determined from this analysis, with an oscillation frequency of ω_B.

The three sources of *in situ* thermospheric gravity waves at auroral latitudes are Joule and particle-precipitation heating and the Lorentz force (ion drag momentum coupling) [*Richmond*, 1978]. Recalling from Chapter 1, the Joule heating rate per unit volume Q_J can be estimated from the expression [*e.g. Richmond*, 1978],

$$Q_J = \mathbf{J} \cdot \mathbf{E} = \ldots = \sigma_P(z) E_\perp^2, \tag{1.5}$$

where $\mathbf{J}$ is the current density, $\sigma_P(z)$ is the ionospheric Pedersen conductivity, and $E_\perp$ is the local electric field strength normal to Earth's magnetic field. The Joule heating rate per unit mass Q_J' is given by $Q_J' = \sigma_P E_\perp^2(\rho^{-1})$, and the Lorentz acceleration is given by $\sigma_P E_\perp B(\rho^{-1})$ or $\sigma_H E_\perp B(\rho^{-1})$, where σ_H is the Hall conductivity [*Richmond*, 1978]. The vertical extent of these wave sources is generally two to four scale heights, beginning at an altitude of ~110 km [*Richmond*, 1978]. Atmospheric gravity waves (AGWs) in the thermosphere have been categorized into two classes; large-scale and medium-scale perturbations [*e.g. Mayr et al.*, 1984; see references therein]. Medium-scale disturbances are present in the thermosphere at all latitudes and longitudes, and their excitation is due mostly to the tropospheric sources mentioned at the opening of this section. Some of these waves originate in the auroral zones but do not propagate very far horizontally [*Mayr et al.*, 1984]. They have relatively short periods of 15-60 min, with wavelengths of less than 100 km to about 400 km, and they tend to propagate obliquely upwards with horizontal velocities of 100-250 $m \cdot s^{-1}$ [*Mayr et al.*, 1984]. Large-scale gravity waves generally have longer periods and wavelengths than medium-scale waves, 1-3 hr and 1000-4000 km, respectively [*Mayr et al.*, 1984], and their propagation speed is much faster than medium-scale disturbances (500-1000 $m \cdot s^{-1}$). Large-scale gravity waves can potentially travel large distances to middle and low latitudes [*e.g. Mayr et al.*, 1984; see references therein], and when the amplitude of a large-scale gravity wave reaches a critical magnitude, the wave breaks (similarly to a large ocean wave as it approaches a shallow coast line), imparting its momentum and energy to the surrounding region through viscosity and other turbulent processes.

Thermospheric motion associated with the horizontal component of a propagating gravity wave, when observed overhead from the ground with a Fabry-Perot Spectrometer

(FPS) looking in the zenith direction, would be perceived as a vertical wind. *Hernandez* [1982], using an FPS and observing the upper-thermospheric OI(630.0)-nm airglow emission at the middle-latitude observatory of Fritz Peak in Colorado, measured intermediate-magnitude downward vertical winds of ~40 $m \cdot s^{-1}$, at a latitude where vertical motions of the thermosphere are generally expected to be very small, ~1-2 $m \cdot s^{-1}$ [*e.g. Dickinson and Geisler*, 1968; *Rishbeth et al.*, 1969]. Spectral analysis of the night's vertical wind time series found a ~40 min periodicity in the measurements, and *Hernandez* [1982] attributed this intermediate-magnitude oscillatory thermospheric vertical motion to a large-scale gravity wave passing over the site. Furthermore, an estimation of the total downward height change of the $O(^1D)$-emitting layer due to the downward vertical winds was ~6 km, and though small (compared to the region's scale height), this altitude change would still be expected to affect the $O(^1D)$-emitting layer's chemistry, with an increased emission rate at the lowest altitudes of the emission layer. Small increases observed in the $O(^1D)$ emission rate (3-4 %) during the downward vertical motions agreed with this speculation.

Thermospheric motion attributed to large-scale gravity waves has also been observed in the ionosphere. These oscillatory motions of the ionosphere are referred to as travelling ionospheric disturbances or TIDs. Such techniques as ionosonde measurements of the ionosphere's virtual height profile (*i.e.*, the altitudes at which radio pulses of differing frequencies reflect off the ionosphere) [*e.g. Hunsucker and Hargreaves*, 1988], and incoherent scatter radar measurements of irregularities in the ionosphere's electron distribution [*e.g. Thome*, 1964] have identified TIDs.

Appendix C Molecular Properties of the Thermosphere

C.1 Thermal Equilibrium

In Chapter 1, the ideal gas law, $p = \rho RTM^{-1} = nk_BT$, was used in the formulation of the expression that describes hydrostatic equilibrium in the atmosphere, $\alpha \exp(-z/H)$, where p is the pressure, T is the temperature, M is the mean molecular mass, n is the number density, $k_B = 1.38 \times 10^{-23}$ J·K^{-1} is the Boltzmann constant, $R = 8.314 \times 10^3$ J·kmol^{-1}·K^{-1} is the ideal gas constant, and $H = RT/Mg = k_BT/mg$ is the atmospheric scale height. The ideal gas law is the equation of state of the atmosphere (up to the thermopause) that describes the state variables of pressure, temperature and volume (or mass or number density) as functions of one another. The ideal gas law is a product of the kinetic theory of gases, which relates the bulk properties of a gas to the microscopic behavior of its molecules. A body of gas, however, will not have bulk properties without collisions between the molecules. Collisions allow molecules to influence one another and exchange the information of a system amongst themselves, attaining what is referred to as thermal equilibrium. Additionally, collisions account for the transport of mass (diffusion), momentum (viscosity), energy (heat conduction) and charge (mobility) from one region of a system to another [*Rees,* 1989]. A gas in thermal equilibrium is characterized by a measurable temperature T and can be described in the context of a compressible fluid; *i.e.*, the laws of fluid mechanics can be used to study the gas's physical behavior (a liquid is an incompressible fluid).

The particles of a body of gas in thermal equilibrium exhibit a velocity distribution in three dimensions that is given by the Maxwell-Boltzmann relation (note that boldtype indicates a vector quantity) [*Hargreaves*, 1992],

$$N(\mathbf{v})d\mathbf{v} = 4\pi N_T m^{3/2}(2\pi k_B T)^{-3/2}\mathbf{v}^2 \exp(-m\mathbf{v}^2/2k_BT)d\mathbf{v}, \qquad \text{(C.1)}$$

where $N(\mathbf{v})d\mathbf{v}$ is the number of particles with velocity between $\mathbf{v}$ and $\mathbf{v} + d\mathbf{v}$, N_T is the total number of particles in the system, m is the mass of each particle, T is the absolute temperature, and k_B is the Boltzmann constant. Three important quantities associated

with the random motion of the particles within the body of a gas are determined by taking moments of the distribution function. The most probable speed v_{mp} of a gas particle, the mean speed $\bar{v}$ and the root mean square (RMS) speed v_{rms} are given by the expressions

$$v_{mp} = (2k_B T / m)^{1/2},$$

$$\bar{v} = 2(\pi m)^{-1/2}(2k_B T)^{1/2}, \qquad \text{(C.2}a\text{-}c\text{)}$$

$$v_{rms} = (3k_B T / m)^{1/2},$$

respectively. These quantities do not describe the bulk flow of the gas, which is determined from the momentum equation (see Appendix B), but any bulk flow of the gas is communicated through collisions. The average thermal kinetic energy KE_{ther} of a given gas particle's random motion is related to the bulk property of the gas's temperature through the relation

$$KE_{ther} = \frac{1}{2} m v_{rms}^2 = \frac{3}{2} k_B T, \qquad \text{(C.2}d\text{)}$$

and the RMS speed v_{rms} of the particles of a gas is also referred to as the thermal speed, v_{ther}. Equation C.2*d* does not describe bulk flow kinetic energy. If two or more species are mixed into a composite gas that is in thermal equilibrium (*e.g.*, the gases of the lower and middle atmosphere), the lightest species will have the highest v_{ther} and so on until the heaviest species, which will have the lowest v_{ther}.

C.2 Collisions

In general, collisions that occur in the atmosphere and which account for the molecular processes of diffusion, viscosity and heat conduction are elastic collisions [*Rees*, 1989]. Kinetic energy and momentum are conserved quantities during elastic collisions, and these two conservation laws provide a means of describing the collisional behavior of a gas of one, two or many species in terms of the transfer of momentum between the colliding particles. The collision frequency v of a particle is, simply put, the number of collisions the particle makes per unit time. Considering a gas of two species of particles, of masses m_1 and m_2 and velocities v_1 and v_2, respectively, a species-1 particle colliding with a species-2 particle gains $2(m_1 m_2)(v_2 - v_1)/(m_1 + m_2)$ of momentum

during the collision, while the species-2 particle loses that same amount [*e.g. Hargreaves*, 1992]. If a species-1 particle has υ_{12} collisions per unit time with species-2 particles, then the rate of change of momentum the species-1 particle experiences (*i.e.*, the total force on a species-1 particle due to collisions with species-2 particles), F_{12}, is given by the expression,

$$F_{12} = \upsilon_{12}\frac{2m_1m_2(v_2 - v_1)}{(m_1 + m_2)}. \tag{C.3}$$

The total force per unit volume, F^*_{12}, is given by the expression $F^*_{12} = n_1F_{12}$ and because $F^*_{21} = -F^*_{12}$, a simple relation,

$$n_1\upsilon_{12} = n_2\upsilon_{21}, \tag{C.4}$$

is determined. The principles employed here can be used to determine the drag on satellites due to the thermosphere's constituents [*Hargreaves*, 1992], but these principles do not necessarily provide any insight into the microscopic physics that takes place during the collisions between the molecules.

Generally, in order to determine the collision frequency of a type of particle (call them species 1) with another type (species 2) of particle (*e.g.*, ionospheric electrons with thermospheric neutrals), three quantities must be known, the velocity v_1 of the particle undergoing the collisions, the density n_2 of the particles being collided with and the collision cross section $\sigma_{coll,12}$ between the two species [*e.g. Hargreaves*, 1992],

$$\upsilon_{12} = n_2\sigma_{coll,12}v_1, \tag{C.5}$$

where v_1 is the thermal velocity, $v_{ther,1} = (3k_BT_1/m_1)^{1/2}$. The collision cross section is similar in conception to the absorption cross section for the optical depth (see Equation A.2 in Appendix A) and can be difficult to determine. Quantum mechanical principles must be used to calculate σ_{coll}, or it must be determined empirically. One simplification to using quantum mechanics, particularly for neutral-neutral collisions, is to use the hard-sphere approximation, where the collision cross section of a molecule is given solely by its circular area, $= \pi r^2$, where r is the radius of the molecule, $r \sim 10^{-10}$ m. However, this is only a rough approximation and not to be used in the thermosphere generally because charged particles may polarize neutral molecules during collisions (*e.g.*, electrons induce

a dipole on N_2 and O_2 molecules), and because the coulomb interaction must be included when considering collisions between positively-charged ions and electrons [*Rees*, 1989]. As an example, using the hard-sphere approximation and Equation C.5, the collision frequency for electrons with neutrals, υ_{en}, is roughly given by $\upsilon_{en} \approx [(2 \times 10^{-16}) n_n T_e^{1/2}] \cdot s^{-1}$, where n_n is the density of the particular neutral (*e.g.*, O, O_2, N_2) in MKS units, and T_e is the electron temperature (in K). The quantum mechanical approach, however, determines that the collision cross section of electrons with neutrals, $\sigma_{coll,en}$, is proportional to $T_e^{1/2}$, resulting in $\upsilon_{en} \propto T_e^{1}$, not $T_e^{1/2}$. Empirical expressions determined from a first-principles approach for υ_{en}, the ion-neutral collision frequency, υ_{in}, and the electron-ion collision frequency, υ_{ei} [*Rishbeth and Garriott*, 1969], are

$$\upsilon_{en} = [(5.4 \times 10^{-16}) n_n T_e^{1/2}] \cdot s^{-1},$$
$$\upsilon_{in} = [(2.6 \times 10^{-15}) n_n M_i^{1/2}] \cdot s^{-1}, \qquad \text{(C.6}a\text{-}c\text{)}$$
$$\upsilon_{ei} = \{[59 + 4.18 \ln(T_e^3 / n_e)](10^{-6}) n_e T_e^{-3/2}\} \cdot s^{-1},$$

where M_i is the ion mean molecular mass. If Equation C.4 is used to determine expressions for υ_{ne}, υ_{ni} and υ_{ie}, then M_i becomes the neutral mean molecular mass M_n, n_n becomes n_e and n_i in Equations C.6*a* and *b*, respectively, T_e becomes T_i and n_e becomes n_i in Equation C.6*c*. If charge neutrality holds, then $n_e \approx n_i = N_P$, though this is not the case in the ionosphere's D region, where negatively-charged particles also are present.

C.3 Mean Free Path

An important parameter dependent on the collision cross section that provides some simple insight into thermospheric and exospheric behavior is the mean free path l_f of a particle, the average distance that a particle travels between collisions. The mean free path can be determined from the expression $l_f = v_{ther}/\upsilon$, and thus, as thermospheric temperature increases with altitude, the mean free path also increases. However, the more appropriate expression for l_f, determined from first principles [*Sears and Salinger*, 1975], is $l_f = (n\sigma_{coll})^{-1}$, which ultimately yields $l_f = v_{ther}/\upsilon$. The altitude range where the mean free path of a particle becomes comparable in value to the size of the region the particle occupies (*i.e.*, its pressure scale height $H = k_B T/mg$ layer) marks the location of

the thermopause and the beginning of the exosphere. At the thermopause, hydrostatic equilibrium breaks down, and gases no longer are in thermal equilibrium.

As an example, take two thermospheric constituents, species 1 and 2, to both be atomic oxygen, the dominant species from ~200-600 km. At 600 km, the O density is $n_O \approx 10^{12}$ atoms·m^{-3}. Using the hard-sphere approximation for the collision cross section between O atoms, $\sigma_{coll,OO}$ is given by $\sigma_{coll,OO} \sim \pi r^2 = 3.14 \times 10^{-20}$ m^2. For a thermospheric temperature of 1000 K at 600 km, the O collision frequency with other O atoms is $\upsilon_{OO} \sim 4 \times 10^{-5}$ s^{-1}, and the time between collisions is $\tau_{OO} \sim (\upsilon_{OO})^{-1} \sim 7$ hours, which is not very many collisions. The scale height at 600 km is $H_O = k_B T/m_O g \sim 50$ km, and the mean free path is $l_{f,O} \sim 3.18$ x 10^7 m = 31,800 km, which is 3 orders of magnitude greater than the scale height. The thermopause generally resides at about this altitude, dependent on solar radiative and geomagnetic conditions. Moving down to ~300 km, where the temperature is $T \approx 800$ K and $n_O \approx 10^{15}$ atoms·m^{-3}, then $H_O \sim 40$ km, $l_{f,O} \sim 30$ km, $\upsilon_{OO} \sim 0.04$ s^{-1} and $\tau_{OO} \sim 25$ s. This is a long enough time between collisions that a fraction of O atoms in the ^{1}D state (radiative half-life of ~110 s) will release their excess energy in the form of radiation and produce the λ630.0-nm red-line airglow and auroral emission. Still lower, at say 150 km, $T \approx 500$ K, and O atoms will collide with N_2 and O_2 molecules as often as with other O atoms. Taking $n_{tot} \approx 10^{18}$ atoms·m^{-3}, $H_O \sim 25$ km, $l_{f,O,neutrals} \sim 30$ meters, $\upsilon_{O,neutrals} \sim 30$ s^{-1} and $\tau_{O,neutrals} \sim 0.05$ s, which is still enough time between collisions that a fraction of O atoms in the ^{1}S state (radiative half-life of ~0.9 s) will descend to the ^{1}D state and radiate, producing the λ557.7-nm green-line airglow and auroral emission.

C.4 General Diffusion Principles and Ion Diffusion in the Upper Thermosphere

When pressure, density or temperature gradients exist between regions of a particular gas or between one gas and another background gas, molecules move in the opposite direction of the gradient (in addition to their random thermal motion) until pressure is equalized [*e.g. Rees*, 1989]. In the case of large-scale gradients, such as the atmosphere's dayside-to-nightside horizontal pressure gradient, the process results in bulk flow (*i.e.*, winds), but at smaller scales, the process is referred to as diffusion. The flux Φ_j of the j^{th} constituent,

$$\mathbf{\Phi}_j = n_j \mathbf{v}_j, \tag{C.7}$$

where n_j and $\mathbf{v}_j$ are the j^{th} constituent's number density and diffusion velocity (not the thermal or bulk velocities), respectively, is also described by Fick's law,

$$\mathbf{\Phi}_j = -D_j \nabla n_j, \tag{C.8}$$

where D_j is the diffusion coefficient of the j^{th} constituent. Thus, the diffusion velocity can be written as

$$\mathbf{v}_j = -(D_j/n_j)\nabla n_j. \tag{C.9}$$

Assuming an isothermal atmosphere and that production and loss are negligible compared to transport, substitution of Equation C.9 into the j^{th} constituent's continuity equation,

$$\partial n_j/\partial t = -\nabla\cdot(n_j \mathbf{v}_j), \tag{C.10}$$

yields the diffusion equation

$$\partial n_j/\partial t = -\nabla\cdot\{n_j[-(D_j/n_j)\nabla n_j]\} = \ldots = D_j \nabla^2 n_j, \tag{C.11}$$

which describes the time rate of change of the j^{th} constituent's number density n_j at any point in space.

An expression for the molecular diffusion coefficient D_j of the j^{th} constituent can be derived by examining the simple case of a gas at constant temperature exhibiting a horizontal pressure gradient in one dimension. Particles of the gas that are diffusing will exert a drag force per unit volume on each other due to collisions, which is given by Equation C.3,

$$F_j^* = n_j F_j = n_j \upsilon_j m_j \nu_j. \tag{C.12}$$

This force per unit volume is equal to and in the opposite direction of the pressure gradient,

$$\partial p_j/\partial x = -\, n_j \upsilon_j m_j \nu_j. \tag{C.13}$$

However, differentiation of the ideal gas law, $p_j = n_j k_B T_j$, yields another expression for the pressure gradient (if T_j remains constant),

$$\partial p_j/\partial x = k_B T_j(\partial n_j/\partial x). \tag{C.14}$$

Substitution of $\partial n_j/\partial x$ from Equation C.7, $\partial n_j/\partial x = -(n_j \nu_j/D_j)$, into Equation C.14 yields

$$\partial p_j/\partial x = k_B T_j\,[-(n_j \nu_j/D_j)]. \tag{C.15}$$

Finally, equating Equations C.14 and C.15 yields

$$D_j = k_B T_j / m_j \upsilon_j \tag{C.16}$$

as the j^{th} constituent's molecular diffusion coefficient.

To investigate diffusion in the thermosphere in the vertical direction, it is necessary to include gravity in the formulation that yielded Equation C.16. Examining the diffusion of a species-1 minor gas (*e.g.*, the ion-electron plasma) through the thermosphere's species-2 background gas (*e.g.*, O atoms), the species-1 diffusion coefficient D_1 depends on its own temperature and on its collision frequency, υ_{12}, with the background gas, $D_1 \propto T_1 \upsilon_{12}^{-1}$. However, because the species-1 collision frequency depends on the density of the background gas, $\upsilon_{12} = n_2 \sigma_{coll,12} v_1$, the species-1 diffusion coefficient is inversely proportional to the density of the background gas, $D_1 \propto T_1^{1/2} n_2^{-1}$. Therefore, molecular diffusion is stronger high in the thermosphere and becomes weaker as a gas diffuses downward. For a species-1 minor gas diffusing through a species-2 background gas, the sum of the forces per unit volume acting on the minor gas is

$$\partial p_1 / \partial z = - n_1 m_1 g - n_1 \upsilon_{12} m_1 w_1, \tag{C.17}$$

where w_1 is the vertical diffusion speed of the minor gas. Upward z is taken to be positive. After some algebra, Equation C.17 yields

$$w_1 = -(D_1/n_1)[\partial n_1/\partial z + n_1/H_1], \tag{C.18}$$

where $H_1 = k_B T_1 / m_1 g$ is the species-1 pressure scale height. Equation C.18 gives an approximate expression for w_1 because T_1 changes with altitude in the thermosphere. This topic is addressed in Chapter 1, Section 1.2.2 as it relates to neutral diffusion. In the upper thermosphere, however, Equation C.18 is suitable because the temperature gradient is nearly zero. The altitude distribution of the minor gas is not necessarily given by H_1 either, which is instead described by the distribution height [*Hargreaves*, 1992],

$$\delta_1 = [-n_1^{-1}(\partial n_1/\partial z)]^{-1}. \tag{C.19}$$

The distribution height is examined more closely below. Substitution of Equation C.18 into the species-1 continuity equation, $\partial n_1/\partial t = -\partial(n_1 w_1)/\partial z$, yields

$$\partial n_1/\partial t = \partial/\partial z[D_1(\partial n_1/\partial z + n_1/H_1)], \tag{C.20}$$

an equation that describes the time rate of change of the species-1 density n_1 in the vertical direction.

In the upper thermosphere above the F2-layer peak N_mF2 ($h_mF2 \sim 300$ km), where temperature varies little with altitude and ion production and recombination are negligible, the time and altitude variation of the ions (mostly O^+) and electrons is governed by Equations C.18 and C.19,

$$w_P = -(D_P/N_P)[\partial N_P/\partial z + N_P/H_P], \tag{C.21}$$

and

$$\partial N_P/\partial t = \partial/\partial z[D_P(\partial N_P/\partial z + N_P/H_P)], \tag{C.22}$$

where $n_e = n_i = N_P$ is the ion and electron density, w_P is the ion diffusion speed, D_P is the ambipolar or plasma diffusion coefficient $D_P = k_B(T_i + T_e)/m_i\upsilon_{in}$, and H_P is the plasma scale height $H_P = k_B(T_i + T_e)/m_ig$. T_i is the ion temperature, T_e is the electron temperature, m_i is the ion mass, and υ_{in} is the ion-neutral collision frequency. The ions and electrons tend to drift as a single gas with respect to the neutrals (mostly O atoms) because a polarization field develops if ions and electrons separate [*Rees*, 1989]. The plasma diffusion coefficient and scale height are determined by performing a force analysis for the electrons and ions similarly to Equation C.16, necessarily including the electrostatic force between them and making several approximations based on $m_e << m_i$. Though Equations C.21-22 govern the plasma's behavior above the F2 peak, the discussion in Chapter 1, Section 1.2.1 showed that during the day, the F2 layer below and up to its peak is in quasi-equilibrium, since $\partial N_P/\partial t$ is smaller than the other terms in the continuity equation [*Rishbeth*, 1998]. The equilibrium density N_P at each altitude up to the peak is roughly given by $N_P \sim q/\beta \sim I_\infty[O]/(k'[O_2]+k''[N_2])$ since ion production and loss roughly balance. The escalating trend this relation gives for the equilibrium density ceases, however, because of the upward diffusion of ions away from the F2 peak (described more below), recalling from Section 1.2.1 that N_mF2 occurs at an altitude h_mF2 where β loss and diffusive loss are comparable; *i.e.*, where $\beta \approx D_P/H_O^2$, as will be shown accordingly.

Above the F2-layer peak, the plasma assumes a distribution that follows Equations C.21-22, which is approximately given by [*Hargreaves*, 1992]

$$N_P = N_{P,0}\exp[-(z - z_0)/\delta_P]. \tag{C.23}$$

where $N_{P,0}$ is the plasma density at some fixed height z_0 (*e.g.*, $z_0 = h_mF2$, $N_{P,0} = N_mF2$).

Equations C.21-22 can be further simplified to study the time dependence of N_P and examine some limiting cases of δ_P. For example, if there is no net vertical diffusion (*i.e.*, $\partial N_P/\partial t = 0 = w_P$), and the upper-thermospheric plasma is in a quasi-equilibrium state (*e.g.*, at night), then both equations reduce to

$$\partial N_P/\partial z = -(N_P/H_P), \tag{C.24}$$

which gives $\delta_P = H_P$ as the distribution height from Equation C.20 [*Hargreaves*, 1992]. Thus, the plasma above the F2-layer peak is in hydrostatic and diffusive equilibrium and assumes an exponential distribution given by $N_P = N_{P,0}\exp[-(z - z_0)/H_P]$.

Other examples which investigate the characteristics of δ_P and the time dependence of N_P require carrying through the derivative $\partial/\partial z$ on the right-hand side of Equation C.22. To begin with, assume that the atomic oxygen density profile n_O is roughly given by the hydrostatic equilibrium solution

$$n_O \approx n_{O,0}\exp[-(z - z_0)/H_O] \tag{C.25}$$

above the F2-layer peak, where $n_{O,0}$ is atomic oxygen's density at altitude z_0, and H_O is its scale height ($= k_B T_O/m_O g$). This is a reasonable assumption since the diffusive equilibrium solution reduces to the hydrostatic solution when the vertical temperature gradient is negligible (see Chapter 1, Section 1.2.2), as is the case in the upper thermosphere. The plasma's diffusion coefficient, which depends on the density of the O gas, is then given by

$$D_P \approx D_{P,0}\exp[(z - z_0)/H_O], \tag{C.26}$$

where $D_{P,0}$ is the plasma's diffusion coefficient at altitude z_0. Equation C.26 highlights the altitude dependence of the plasma diffusion coefficient, which increases with increasing altitude. Carrying through the derivative $\partial/\partial z$ in Equation C.22 and using the expressions for n_O and D_P gives

$$\partial N_P/\partial t = D_P[\partial^2 N_P/\partial z^2 + (H_P^{-1} + H_O^{-1})\partial N_P/\partial z + N_P(H_P H_O)^{-1}]. \tag{C.27}$$

Finally, substitution of $N_P = N_{P,0}\exp[-(z - z_0)/\delta_P]$ into Equation C.27, execution of the derivatives on N_P, and some algebra yields [*Hargreaves*, 1992]

$$\partial N_P/\partial t = N_P[D_P(\delta_P^{-1} - H_P^{-1})(\delta_P^{-1} - H_O^{-1})]. \tag{C.28}$$

Equation C.28 describes the time dependence of N_P, and the diffusion velocity w_P can be written as

$$w_P = -D_P(-\delta_P^{-1} + H_P^{-1}). \quad \text{(C.29)}$$

The solution to Equation C.28 is given by

$$N_P = N_{P,0}\exp[-\gamma_P(t - t_0)], \quad \text{(C.30)}$$

where $N_{P,0}$ is the plasma's density at some time t_0, and

$$\gamma_P \equiv D_P(\delta_P^{-1} - H_P^{-1})(\delta_P^{-1} - H_O^{-1}) \sim D_P/\delta_P^2. \quad \text{(C.31)}$$

In this context, γ_P is a parameter that estimates the loss rate of plasma due to diffusion, and if $\delta_P \approx H_O$ then $\gamma_P \approx D_P/H_O^2$. This can be shown by taking $\partial N_P/\partial t = 0$ in Equation C.28, in which case (after some algebra), two solutions for δ_P are determined. One of the solutions from this approximation was already determined above, when $\delta_P = H_P$ and the plasma is in diffusive equilibrium. The second solution, $\delta_P = H_O$ and $\gamma_P \approx D_P/H_O^2$, however, results in a non-zero plasma diffusion speed, $w_P \neq 0$,

$$w_P = D_P(H_O^{-1} - H_P^{-1}). \quad \text{(C.32)}$$

Equation C.32 generally yields a non-zero plasma diffusion speed w_P because H_P is generally greater than H_O, and this solution represents an unchanging distribution of ions and electrons with a steady upward flow of plasma [*Hargreaves*, 1992]. Thus, γ_P represents the loss rate of ionospheric constituents due to the upward diffusion of ions through the O gas, and the altitude where recombination loss is comparable to upward diffusive loss marks the location of the F2-layer peak; *i.e.*, where $\beta \approx \gamma_P \approx D_P/H_O^2$.

C.5 Viscosity

One final molecular process relevant to the thermosphere's behavior is molecular viscosity. A variation of wind velocity between two layers of a gas flowing adjacent to one another—wind shear—results in a drag force being exerted on one layer by the other. This drag manifests itself on a molecular level through collisions as a frictional force that imparts a momentum change to the molecules [*Rees*, 1989]. The force per unit volume $\mathbf{F}^*$ is proportional to the spatial gradients and is in the opposite direction of the bulk flow velocity $\mathbf{v}$. $\mathbf{F}^*$ is given by the expression $\mathbf{F}^* = -\eta\nabla^2\mathbf{v}$, where η is the coefficient of viscosity [*e.g. Rishbeth*, 1972]. Viscosity's main contribution to the thermosphere's behavior is to reduce wind speeds and smooth out the wind shears. These effects are discussed in more detail in Appendix B.

Appendix D Fabry-Perot Spectroscopy

D.1 The Ideal Fabry-Perot Interferometer

The first Fabry-Perot interferometer, originally referred to as an étalon, was developed in the late 1800s by Charles Fabry and Alfred Perot [*e.g.*, see *Vaughan*, 1989 or *Hernandez*, 1986 and references therein for further history and information]. The ideal étalon consists of two perfectly flat semi-transparent mirrors of infinite extent held perfectly parallel at a fixed separation. A piece of polished glass of index of refraction n' mirrored on both sides or two separate plates with their silvered surfaces facing each other (with index of refraction n between them) can act as an étalon cavity, as Figure D.1 shows [*Born and Wolf*, 1999]. When a monochromatic wavefront is incident upon the étalon at an arbitrary angle θ to the normal of the plates, the wavefront will be partially reflected and partially transmitted at the first interface. Figure D.1 is somewhat idealized because it shows only one incoming light ray of a wavefront, when in actuality, it is the infinite number of wavefronts passing into the étalon cavity that all undergo multiple reflections within the cavity and multiple transmissions through each end of the cavity. Each reflected and transmitted wave component is of weaker amplitude than the preceding component, and positive-powered lenses L and L' properly located, will superimpose and focus the divided wavefronts [*e.g. Hecht*, 1984; *Born and Wolf*, 1999]. The interfering partial wavefronts, in the transmitted case, produce a set of bright circular rings on a dark background, and in the reflected case, a set of dark rings on a light background. The rings are referred to as fringes of equal inclination, and are circular if the optical axis of each focusing lens L and L' is perpendicular to the plate face. The location of the fringes depends on the radiation's wavelength λ and angle of incidence θ, and on the index of refraction n' and thickness h of the plate (or the gap between the two plates).

One way to consider an étalon's effect on incident radiation is that the étalon transforms the incident radiation's intensity distribution from a wavelength domain to an angular displacement domain [*Hernandez*, 1986]. Put in another context, the wavelength

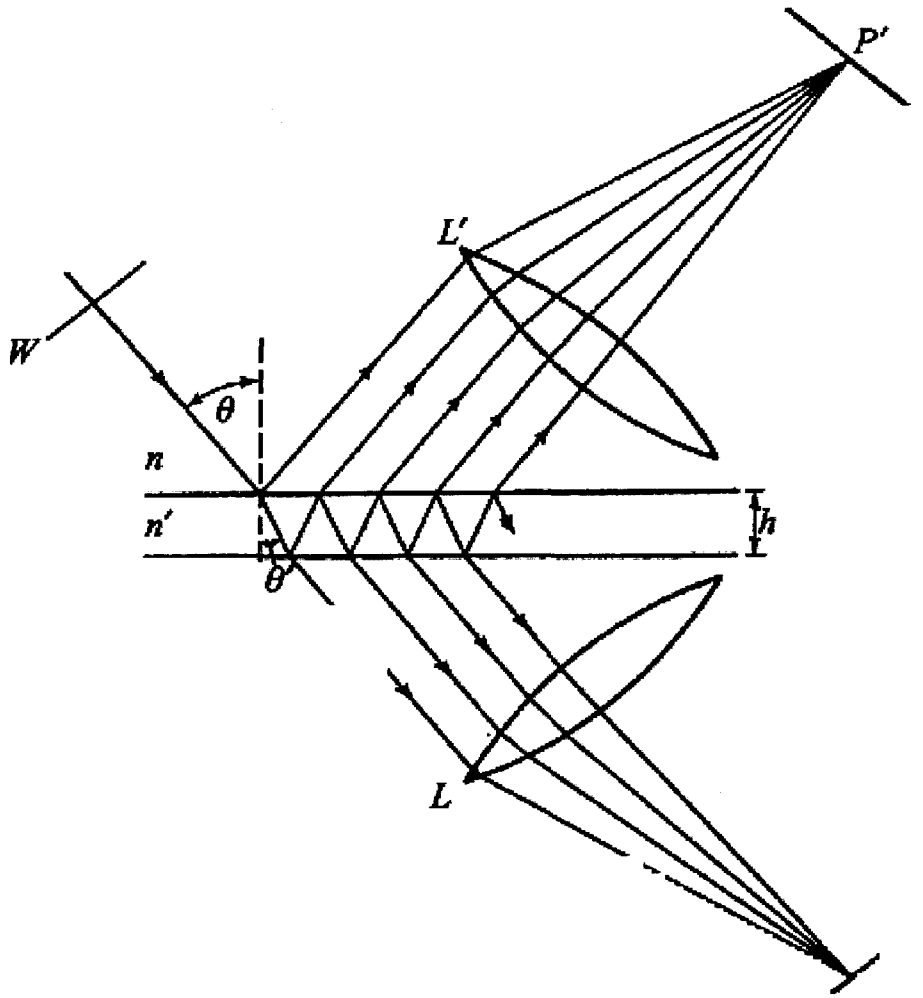

Figure D.1. Multiple-beam interference in an ideal Fabry-Perot étalon. The plane-parallel plate has thickness h, an index of refraction n' and reflection and transmission amplitude coefficients r and t, respectively. A wavefront incident at an arbitrary angle θ to the normal of the plate surface will undergo mulitple reflections and transmissions [Figure from *Born and Wolf*, 1999].

spectrum of a radiation source can be determined from its étalon-induced radial intensity distribution, provided the radiation's bandwidth is small compared with the étalon's free spectral range [*Conde*, 2002], a spectroscopic parameter that will be defined soon. A set of Fabry-Perot transmitted fringes is shown below in Figure D.2 [*Hernandez*, 1986]. The mathematical expressions describing the transmitted and reflected intensity distributions of an ideal étalon, referred to as the Airy formula, are determined by considering the effect

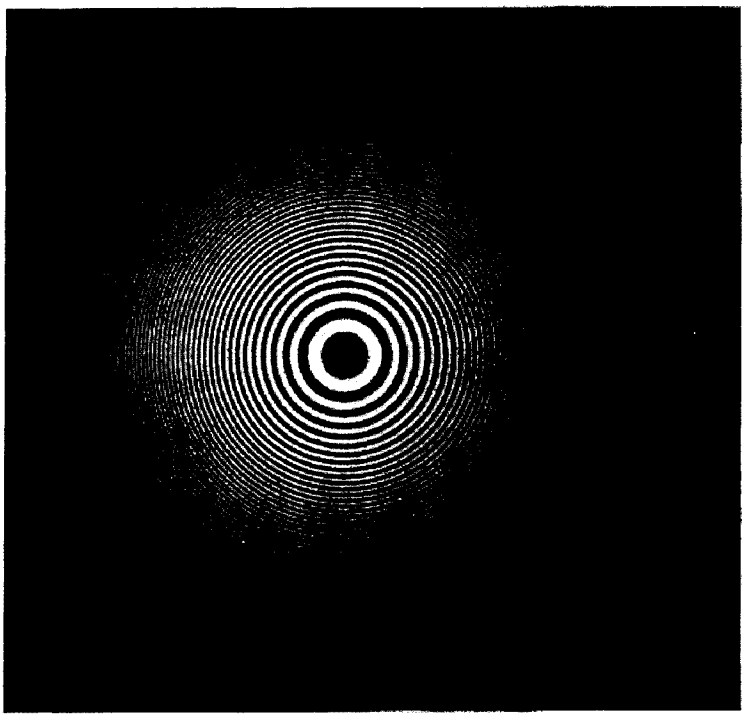

Figure D.2. Transmitted radiation fringes of a Fabry-Perot étalon. Transmitted radiation is the mercury line at λ546.1 nm [Figure from *Hernandez*, 1986].

that multiple reflections has on the radiation's incident wavefronts [*e.g.*, see derivation in *Hecht*, 1984]. The reflected and transmitted electric field scalar amplitudes, $E_{TOT,R}$ and $E_{TOT,T}$, respectively, of the incident radiation are given by the expressions [*Hecht*, 1984]

$$E_{TOT,R} = E_0 e^{i\omega t}\left[\frac{r[1-e^{-i\delta}]}{1-r^2 e^{-i\delta}}\right], \text{ and}$$

$$E_{TOT,T} = E_0 e^{i\omega t}\left[\frac{1-r^2}{1-r^2 e^{-i\delta}}\right], \qquad \text{(D.1}a\text{-}b\text{)}$$

where E_0 is the initial scalar amplitude of the incoming wave, t is the time, r and τ are the reflection and transmission amplitude coefficients shown in Figure D.1 going from the air into the plate, r' and τ' are the reflection and transmission amplitude coefficients going from the plate to the air, and δ is the phase difference between interfering wavefronts. The reflection and transmission amplitude coefficients r, τ, r', and τ' obey the expressions

$r' = -r$ and $\tau'\tau = 1 - r^2$, which are known as the Stokes relations [*Hecht*, 1984]. The phase difference is determined from the optical path length P between the interfering beams, where P represents the path a wavefront traverses due to the actual distance it covers while also accounting for the index of refraction of the medium that the wavefront is traversing. In general, the optical path length between a source S and an observer K is [*Hecht*, 1984]

$$P = \int_S^K n(s)ds\,, \tag{D.2}$$

where $n(s)$ is the index of refraction of the medium the wavefront is traversing and is a function of position s. The optical path length between two interfering wavefronts in an étalon cavity determined from Equation D.2 [*e.g.*, see derivation in *Hecht*, 1984] is

$$P = (2n'h)\cos\theta, \tag{D.3}$$

and in general, the phase difference δ is given by

$$\delta = kP \pm \phi, \tag{D.4}$$

where $k = 2\pi\lambda^{-1}$ is the vacuum wave number, and λ is the radiation's wavelength. The phase shift ϕ is due to the metallic mirrors, and for most applications can be omitted if the width h of the plate (or the gap between the two plates) is sufficiently large [*Hecht*, 1984]. In general, the phase difference δ between interfering wavefronts in an étalon cavity is

$$\delta = (4\pi n'h\lambda^{-1})\cos\theta, \tag{D.4}$$

The total reflected and transmitted irradiances (flux densities) I_R and I_T, respectively, are determined by multiplying Equations D.1*a-b* by their complex conjugates, which yields

$$I_R = I_0\left[\frac{F\sin^2(\delta/2)}{1+F\sin^2(\delta/2)}\right], \text{ and}$$

$$I_T = I_0\left[\frac{1}{1+F\sin^2(\delta/2)}\right]. \tag{D.5a-b}$$

The initial irradiance I_0 of the incoming radiation is given by $I_0 = c\epsilon_0 E_0^2/2$, where c is the speed of light, and ϵ_0 is the permeability of free space. F is the coefficient of finesse and is

$$F = 4R/(1-R)^2, \tag{D.6}$$

where R is the reflectance of the plate's mirrored surface and is given by $R = r^2$ if there is little or no absorption in the mirror material [*Hecht*, 1984]. The transmittance T of the

mirrored surface is $T = \tau'\tau = 1 - r^2 = 1 - R$. In general, the quantities of reflectance and transmittance of incident radiation of initial flux density I_i at a reflecting and transmitting interface (*e.g.*, glass) are defined by their ratios of reflected and transmitted flux, I_{RFL} and I_{TRN}, respectively, to the incident flux [*Hecht*, 1984],

$$R \equiv \frac{I_{RFL}\cos\theta_{RFL}}{I_i\cos\theta_i} = \frac{I_{RFL}}{I_i}, \text{ and}$$

$$T \equiv \frac{I_{TRN}\cos\theta_{TRN}}{I_i\cos\theta_i}, \qquad \text{(D.7}a\text{-}b\text{)}$$

where θ_i is the wavefront's angle of incidence, θ_{RFL} is the wavefront's angle of reflection, $\theta_{RFL} = \theta_i$ (Law of Reflection), and θ_{TRN} is the wavefront's transmission or refraction angle, where $n'\sin\theta_{TRN} = n\sin\theta_i$ (Snell's Law).

The Airy formula, $\tilde{A}(\delta)$, which is named after George Biddell Airy for his work on this subject in 1831 [*e.g.*, see *Vaughan*, 1989], is defined by Equation D.5*b* describing the transmission of radiation through an étalon relative to the incident radiation,

$$\tilde{A}(\delta) \equiv I_T/I_0 = \tilde{A}(\theta) = [1 + F\sin^2(\delta/2)]^{-1}. \qquad \text{(D.8)}$$

The Airy formula is periodic in δ. When $\delta = 2\pi m$ for the transmitted beams, where $m = 0, 1, 2, 3,\ldots$, constructive interference is said to occur, the beams are in phase, and $\tilde{A}(\delta) = 1$. Destructive interference occurs when $\delta = 2\pi(m + 1/2)$, the beams are out of phase, and $\tilde{A}(\delta) = (1 + F)^{-1}$. The shape of the function $\tilde{A}(\delta)$ depends on the value of F and thus on the reflectance R, with typical values of R ranging from ~0.7-0.95 for the mirror materials used on étalon plates (metal and dielectric films). R also varies from material to material depending on the wavelength range being resolved. Figure D.3 [*Hecht*, 1984] below shows $\tilde{A}(\delta)$ for different values of δ and R. If some fraction of the initial flux density I_0 is absorbed by the film, which is referred to as the absorptance A, then $R + T + A = 1$ and the transmitted flux density I_T instead is given by [*Hecht*, 1984]

$$I_T = I_0[1 - A(1 - R)^{-1}]^2\tilde{A}(\delta). \qquad \text{(D.9)}$$

D.2 Relevant Spectroscopic Quantities

Spectroscopy is the science of determining the wavelength spectrum of a radiation-emitting source. Knowledge of the different wavelengths present in a spectrum can reveal

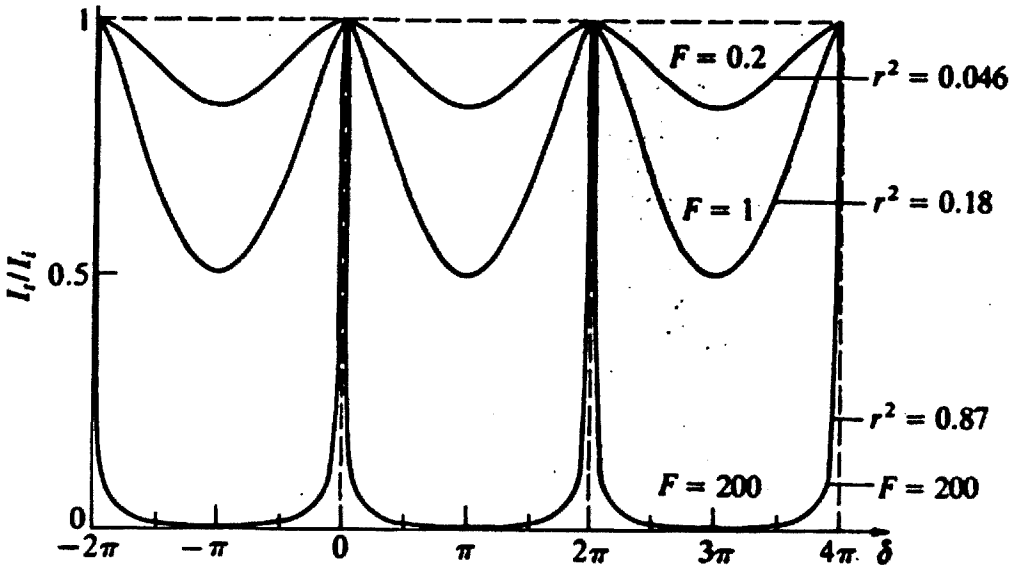

Figure D.3. The Airy formula. Representing the transmitted radiation of an étalon, the periodic function $\tilde{A}(\delta)$ is shown for different values of the reflectance $R = r^2$ and δ. As R increases, the transmitted flux density becomes very small, except for narrow peaks centered about values of $\delta = 2\pi m$, $m = 0, 1, 2, 3,\ldots$ F is the coefficient of finesse defined above in Equation D.6 [Figure from *Hecht*, 1984].

information on the processes occurring in the atoms or molecules emitting the radiation, or, as is the case in this thesis, precise determination of a particular wavelength and its comparison to an absolute wavelength reference using the Doppler formula and Maxwell-Boltzmann relations yields the bulk flow speed and temperature of the emitting particles. The better the capability of a spectroscopic device to resolve the wavelength or many wavelengths present in a spectrum, the better the understanding of the processes generating that spectrum. A spectroscopic device's ability to resolve a wavelength spectrum is defined by several quantities, and the étalon is ideal for studies that demand precise detail of an isolated emission line.

The sharpness of an étalon's transmitted fringes are measured by the full width of the fringes at the half-maximum of the intensity, fwhm $\equiv \zeta$. The quantity is also referred to as the full-width at half-height (fwhh). Some workers choose instead to quote the half-width at half-max (hwhm), which is also referred to as half-width at half-height (hwhh). Also quoted by some is the full- (or half-) width at one-over-*e* [*e.g. Hecht*, 1984].

Considering an ideal étalon, if there is a change in phase $\Delta\delta$ from $\delta = 2\pi m$, then the transmitted flux density through the étalon drops from its peak value of $\tilde{A}(\delta) = 1$. When the transmitted flux density drops to one-half its maximum value, $\tilde{A}(\delta) = ½$, there is a change in phase $\Delta\delta$ of $\delta_{1/2}$ (in radians), which can be determined by solving

$$\tilde{A}(\delta) = ½ = [1 + F\sin^2(\delta_{1/2}/2)]^{-1}, \tag{D.10}$$

which yields (using the approximation $\sin^{-1}F^{-1/2} \approx F^{-1/2}$)

$$\delta_{1/2} \approx 2F^{-1/2}. \tag{D.11}$$

Therefore, the full-width at half-maximum ζ for an ideal étalon is

$$\zeta = 2\delta_{1/2} = 4F^{-1/2} = 8R^{1/2}/(1 - R). \tag{D.12}$$

Thus, for the ideal case, the fwhm is determined only by the étalon's reflectance R. In reality, however, such things as coating defects, lack of parallelism, finite plate size, and non-monochromatic light sources, act to broaden an étalon's fringes relative to the ideal ζ.

Another spectroscopic parameter of an étalon used to measure the sharpness of the étalon's fringes is its ideal reflectivity finesse N_R, which is defined as the ratio of the separation between adjacent transmitted maxima $I_{T,max}$ (2π) to the fwhm,

$$N_R = 2\pi/\zeta = \pi R^{1/2}/(1 - R). \tag{D.13}$$

For typical values of reflectance, $R \sim 0.9$, $N_R \approx 30$. An increasing R and N_R implies tighter fringes, which is desirable but also presents a problem because the transmitted flux density passing through the étalon decreases with the étalon's increasing reflectance. This is revealed by determining the peak transmission of an étalon $(I_T/I_0)_{max}$ from Equation D.9. Letting $\tilde{A}(\delta) = 1$, the peak transmission is given by [*Born and Wolf*, 1999]

$$(I_T/I_0)_{max} = [1 - A(1 - R)^{-1}]^2, \tag{D.14}$$

which decreases with increasing R. Thus, the maximum flux density that can pass through an étalon decreases with the étalon's increasing reflectance. Conversely, an étalon's contrast factor C is defined by the peak transmission divided by the minimum transmitted flux density, $(I_T/I_0)_{max}/(I_T/I_0)_{min}$ [*Born and Wolf*, 1999],

$$C = (I_T/I_0)_{max}/(I_T/I_0)_{min} = 1 + F = [(1 + R)/(1 - R)]^2 = 1 + 4N_R^2/\pi^2, \tag{D.15}$$

where $(I_T/I_0)_{min} = [1 - A(1 - R)^{-1}]^2/(1 + F)$ is determined by setting $\tilde{A}(\delta) = (1 + F)^{-1}$ in Equation D.9. The contrast factor increases with increasing R and acts as a measure of

how distinct the peaks of the transmitted flux density are relative to the background transmitted flux density. This is illustrated in Figure D.3, which shows the peaks becoming more pronounced as R increases. In general, an étalon's real finesse N is less then N_R due to real-world effects, and thus, the peak transmission and contrast factor are also reduced. These issues are discussed in the next section.

As was mentioned above, the discussion up to this point has assumed that the étalon is transmitting monochromatic light, but real light sources are not monochromatic. There is always wavelength broadening around the peak wavelength associated with the thermal agitation of the emitting particles, and radiation sources generally have a distribution of wavelengths present in their spectra. When more than one wavelength is present in a spectrum, the wavelengths are often said to be just resolvable if they fulfill the Rayleigh criterion. The Rayleigh criterion is defined as follows; assuming that two separate peaks I_a and I_b of equal irradiance, $I_a = I_b = I_{max}$, are present in a spectrum at locations δ_a and δ_b, respectively, the combined irradiance of the two peaks, I_s, at the center of the saddle point between the peaks fulfills the Rayleigh criterion if the value is $8/\pi^2$ times the irradiance of the peaks, $I_s = (8/\pi^2)I_{max} \approx 0.81 I_{max}$. The $8/\pi^2$ value is arbitrary but was deemed appropriate by Lord Rayleigh through the assessment of the resolution capabilities of such imaging systems as telescopes, diffraction gratings and prisms [*e.g.*, see discussion in *Hecht*, 1984]. When $I_s = 0.81 I_{max}$, the wavelengths are said to be resolved, as Figure D.4 below [*Born and Wolf*, 1999] shows. If this is the case, then the criterion for the minimum phase difference between the two peaks, $\Delta\delta_{min} \equiv \epsilon$, for an ideal étalon [*Born and Wolf*, 1999] is

$$\epsilon = 2.07\pi/N_R. \tag{D.15}$$

In reality, ϵ is defined by the real finesse N and not the ideal finesse N_R.

The phase difference ϵ can be translated into a wavelength difference through the original expression for the phase difference δ, $\delta = (4\pi n' h\lambda^{-1})\cos\theta = 2\pi m$. Differentiating this equation yields an expression for $\Delta\delta$ in terms of $\Delta\lambda$,

$$\Delta\delta = -(4\pi n' h\lambda^{-2}\cos\theta)\Delta\lambda = -2\pi m(\Delta\lambda/\lambda). \tag{D.16}$$

Setting $\Delta\delta = \epsilon$ in Equation D.16 then yields an expression for $(\lambda/\Delta\lambda)_{min}$, which is referred to as the resolving power $\mathbf{R} \equiv (\lambda/\Delta\lambda)_{min}$. For near normal incidence of radiation at the étalon,

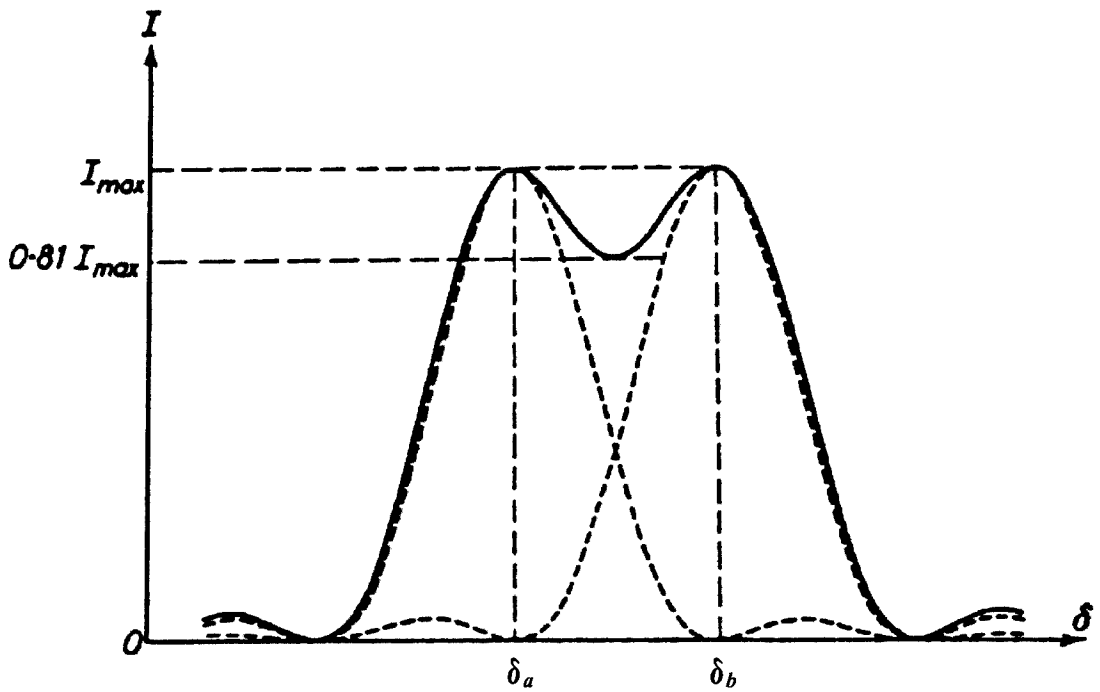

Figure D.4. The Rayleigh Criterion for resolvable fringes. When the saddle point of the combined irradiances from the two wavelengths, each of irradiance I_{max}, is $(8/\pi^2)I_{max}$, then the two wavelengths are said to be resolved [Figure from *Born and Wolf*, 1999].

$\theta \approx 0°$, which is often the case for many FPS designs, and $\cos\theta \approx 1$. Under these circumstances, the resolving power is given by

$$\mathbf{R} = (\lambda/\Delta\lambda)_{min} \approx 2n'h\lambda^{-1}N_R = 0.97mN_R, \qquad \text{(D.17)}$$

though, in general, $\mathbf{R} = 2n'h\lambda^{-1}N_R\cos\theta$. If an étalon with a reflectance of $R = 0.9$ is observing a wavelength of 520 nm and $n'h = 10$ mm (n of air is ~1), then the resolving power of the étalon is $\mathbf{R}_{FPS} \approx 10^6$. This value is comparable to a diffraction grating's resolving power, and in general an order of magnitude greater than that of a prism's. Of course, in reality $\mathbf{R}_{FPS}$ is dependent on the real finesse and not the ideal finesse. It is also sometimes convenient to express the resolving power in terms of wave number, which is referred to as the resolving limit $(\Delta\kappa)_{min}$. The wavenumber κ is given by $\kappa = \lambda^{-1}$ and differentiation of this equation yields $\Delta\kappa = \Delta\lambda/\lambda^2$. Therefore,

$$(\Delta\kappa)_{min} = \lambda^{-1}(\Delta\lambda/\lambda)_{min} \approx (2n'hN_R)^{-1}. \qquad \text{(D.18)}$$

For the above example, $(\Delta\kappa)_{min} \approx 0.02$ cm^{-1}. The resolving power can also be written in terms of frequency $v = n'c/\lambda$, c being the speed of light, and $(\Delta v)_{min}$, referred to as the minimum resolvable bandwidth, is given by $(\Delta v)_{min} \approx c(2n'hN_R)^{-1}$.

Another quantity that is relevant to the performance of an étalon is its free spectral range. When two or more wavelength components are present in a light source, two or more fringe systems will be transmitted through the étalon. If the wavelength difference between the two components is appreciably large, then the two fringe systems will be sufficiently resolvable. However, if the wavelength difference is further increased, the displacement of the fringe patterns becomes larger than the difference between adjacent maxima of either fringe pattern, and "overlapping" of orders is said to occur under these circumstances. The phase difference $\Delta\delta$ is still given by $\Delta\delta = (4\pi n'h\lambda^{-2}\cos\theta)\Delta\lambda$, but $\Delta\lambda$ is now sufficiently large such that $\Delta\delta = 2\pi$. The difference in wavelength when this occurs is referred to as the free spectral range, $\Delta\lambda \equiv(\Delta\lambda)_{fsr}$, and is thus given by

$$(\Delta\lambda)_{fsr} = \lambda^2(2n'h\cos\theta)^{-1}. \qquad \text{(D.19)}$$

For near normal incidence and following along with the above example, $(\Delta\lambda)_{fsr} = 0.14$ Å. The free spectral range $(\Delta\lambda)_{fsr}$ can also be written in terms of wavenumber, and $(\Delta\kappa)_{fsr} = (\Delta\lambda)_{fsr}/\lambda^2 = (2n'h)^{-1} = 0.5$ cm^{-1} for the above example.

As the previous discussion indicates, if one attempts to increase the resolving power of an étalon by increasing the width h, the free spectral range will decrease, which can be undesirable if a source's wavelength spread is larger than the free spectral range or if the overlapping of orders occurs from two closely-packed wavelengths. The desired quality of an étalon is for its resolving power and free spectral range to both be as large as possible, and this feature, in theory, is limited by the ideal reflectivity finesse; *i.e.*, $(\Delta\lambda)_{fsr}/(\Delta\lambda)_{min} = N_R$. In practice, the feature is limited by the real finesse; *i.e.*, $(\Delta\lambda)_{fsr}/(\Delta\lambda)_{min} = N$. If several wavelengths are present in a light source and are closely-packed together and $(\Delta\lambda)_{fsr}$ is not large enough to prevent overlap of orders, then other means must be used to filter out the unwanted wavelengths.

One final quantity to discuss that pertains to an étalon's performance is its étendue U, also referred to as its throughput; *i.e.*, its light-gathering capability. In general, U of a

spectrometer is given by the product of its collection solid angle Ω and the source area observed A. For an étalon, U is simply a function of the étalon plates' coated area A_{plate}, which determines the observed area, and the maximum angle of incidence θ_{max} of the incoming radiation at the étalon relative to the plate normal, which determines the collection solid angle. To increase the throughput of an FPS, the plate diameter can be increased, which increases the likelihood that plate defects may appear, requiring higher quality (and more expensive) plates. See Chapter 2 for further discussion of étendue as it pertains to the Inuvik Fabry-Perot Spectrometer.

D.3. Deviations from Ideal: Determining an Étalon's Instrument Function

As has been indicated several times, the transmission properties of an étalon are modified from the ideal by real-world effects. Plate defects, deviations from parallelism and the finite-sized plates all broaden the transmission passband of an étalon relative to the Airy profile that is characteristic of that étalon's measured reflectance R [*e.g. Wilksch*, 1985]. Characterization of these imperfections is needed before an étalon's instrument function can be determined; *i.e.*, the mathematical function $I(\delta)$, $I(\lambda)$, or $I(\nu)$ that describes its working passband. Techniques have been developed for accomplishing this task, and a few details of some of these techniques are discussed here. The method used for the characterization of the étalon located in Inuvik, NT, Canada is discussed in detail in Chapter 2 on instrumentation and Chapter 3 on data acquistion and analysis.

A general first step in ascertaining an étalon's instrument function is to determine its reflectance R. A simple technique for this [*e.g.*, see *Hernandez*, 1986 and references therein] involves detection of radiation of a broadband source, such as white light, with and without the étalon in the path of the detector. The transmission function of an étalon can be written alternatively to Equation D.9 above and is given by [*Hernandez*, 1986]

$$I_T = I_0[1-A(1-R)-1]^2(1-R)(1+R)^{-1}\left(1+\sum_{m=1}^{\infty} R^m \cos(m\delta)\right). \qquad \text{(D.20)}$$

If the bandpass wave number of the source, $\Delta\kappa_{source}$, is much greater than the étalon's free spectral range, $\Delta\kappa_{source} >> (\Delta\kappa)_{fsr}$, then Equation D.20 can be shown to reduce to [*Hernandez*, 1986]

$$I_T = I_0[1 - A(1-R)^{-1}]^2(1-R)(1+R)^{-1} = I_0[T^2(1-R^2)^{-1}] \quad \text{(D.21)}$$

using $R + T + A = 1$. Therefore, the reflectance is found to be

$$R = [1 - T^2(I_0/I_T)]^{1/2}, \quad \text{(D.22)}$$

where $T^2 = T_1T_2$ (T_1 and T_2 are each mirror's transmittance). Because T_1, T_2, I_0, and I_T are all measurable quantites, R can be determined. From this, the coefficient of finesse F and the ideal finesse N_R are known, and the ideal form of the Airy profile $\tilde{A}(\delta)$ associated with that étalon is determined. This does not yet yield the étalon's true instrument function, however, because the plates' defects and their finite extent will alter the étalon's performance by reducing its resolving power and finesse and ultimately modifying the form of its instrument function [*Wilksch*, 1985]. In addition, as the reflectance $R \rightarrow 1$, the real finesse N approaches a limiting finesse value N_d [*Hernandez*, 1986] which depends exclusively on the plates' defects and their finite extent, further limiting the sharpness of the fringes no matter how high a reflectance is achieved.

An example of a common plate defect [*Born and Wolf*, 1999; *Vaughan*, 1989] is a slight spherical curvature to the plates. Figure D.5 [*Vaughan*, 1989] illustrates the defect. This defect can result during a plate's polishing process when the plate's edge is of poorer quality than its center [*Vaughan*, 1989]. The defect may also result from strain due to an étalon's mounting, which potentially produces curvature in one or two dimensions. An étalon's spherical-curvature defect can be characterized by a finesse N_{sd} which reduces the étalon's real finesse N relative to its ideal finesse N_R. If the étalon gap width $n'h$ changes by λ/q between the center and the edge of the interferometer's aperture, where q defines the smoothness of the plates relative to the wavelength λ being observed, then N_{sd} is given by $N_{sd} = q/2$ [*Born and Wolf*, 1999]. Plates can be polished to $\lambda/200$ or $\lambda/150$, but generally, $\lambda/100$ is the best that is achieved [*Born and Wolf*, 1999], resulting in N_{sd} = 50-100. Table D.1 below [*Born and Wolf*, 1999] illustrates the effect that a slight spherical curvature will have on the real finesse and the peak transmission compared to the ideal scenario. It is seen from the table that when $N_R \geq N_{sd}$, an increase of the reflectance R does little to increase the real finesse N (*i.e.*, the fringes do not get sharper), though the increase in R continues to reduce the peak transmission accordingly.

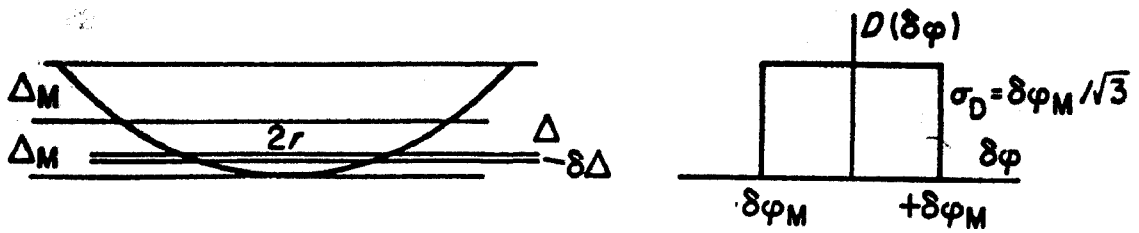

Figure D.5. Schematic representation of an étalon plate's spherical-curvature defect. The left-hand figure depicts the actual defect, while the right-hand figure is the "top-hat" distribution, the defect's mathematical representation $D(\delta\phi)$ as a function of the phase ϕ. Note that here, phase is represented by ϕ, not δ as has been the case in the text. Here, δ is instead the mathematical equivalent of "the change in." The gap width is given by $d + \Delta$, where d is the mean width, and varies from $d - \Delta_M$ at the center of the plates to $d + \Delta_M$ at the edges due to the defect being present on one of the plates. The surface area δS of a tiny piece of the étalon with gap between $d + \Delta$ and $d + \Delta + \delta\Delta$ is $\delta S = D(\Delta)\delta\Delta$, where the interferometer is composed of all these tiny étalons. The phase decoupling $\delta\phi$ at $d + \Delta$ from mean gap d is $\delta\phi = 4\pi\Delta\lambda^{-1}$, and $\delta S = 2\pi r\delta r$ between Δ and $\Delta + \delta\Delta$, where r is the radius to Δ. If the defect's radius of curvature is e, then $2e\Delta \approx r^2$, which can be differentiated to give $\delta\Delta = 2r\delta r$. Thus, $D(\Delta) = D(\delta\phi) = \delta S/\delta\Delta = \pi$ between $\phi - \delta\phi_M < \phi < \phi + \delta\phi_M$. The standard deviation of the distribution is σ_D [Figure from *Vaughan*, 1989].

A spherical-curvature defect not only reduces an étalon's real finesse relative to its ideal finesse, but it also redistributes the étalon's instrument function $I(\delta)$ relative to that of the Airy profile that would be inferred using strictly the measured reflectance R. However, $I(\delta)$ can be determined by convolving the étalon's R-inferred Airy profile with the distribution function (or kernel) representing the spherical-curvature defect. The details that explain how a mathematical representation of a spherical-curvature defect is acquired

Table D.1. Effect of slight spherically-curved plates on an étalon's finesse. Plates are filmed with fresh silver, used at λ520.0 nm and $n'h$ changes by 52 Å from the center to edges [Table from *Born and Wolf*, 1999].

Plane-Parallel Plates		Spherically-Curved Plates with $N_{sd} = 50$ ($\lambda/100$)	
Ideal Finesse N_R	Max Transmission T_{max}	Finesse N	Max Transmission T_{max}
25	0.59	22	0.55
50	0.44	36	0.34
75	0.30	42	0.20
100	0.20	45	0.11
125	0.13	46	0.06

are described in the caption to Figure D.5. In general, a defect can be represented by some distribution function $D(\delta)$ (recall δ is phase), which will change the response of the étalon; *i.e.*, $I(\delta) \neq \tilde{A}(\delta)$. The new étalon response $I(\delta)$ is determined from the convolution integral between $\tilde{A}(\delta)$ and $D(\delta)$; *i.e.*,

$$I(\delta) = \int_{-\infty}^{\infty} \tilde{A}(\delta - \delta')D(\delta')d\delta', \tag{D.23}$$

and in the case of the spherical-curvature defect, Equation D.23 looks like

$$I(\delta) = \int_{-\delta_M}^{\delta_M} \pi\tilde{A}(\delta - \delta')d\delta'. \tag{D.24}$$

Note that here, δ represents the phase, as opposed to in Figure D.5, which uses ϕ to represent phase and δ to represent the mathematical equivalent of "the change in." In general, a defect's effect may be to broaden, skew, or shift (or all of these) the étalon's instrument function from $\tilde{A}(\delta)$. Another typical étalon problem is a lack of parallelism, shown in Figure D.6 [*Vaughan*, 1989] with its characteristic distribution function.

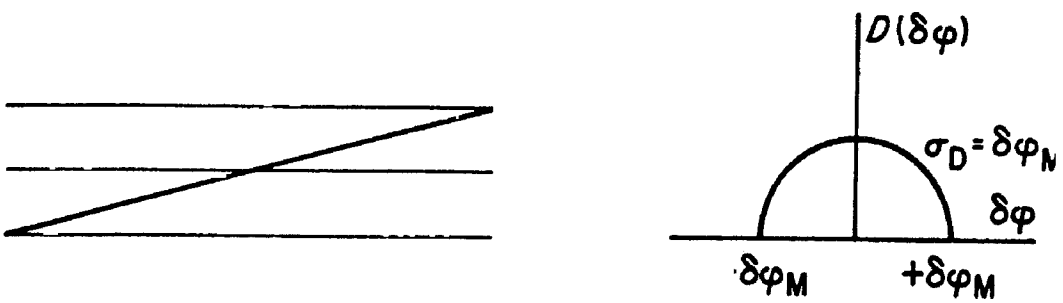

Figure D.6. Schematic representation of an étalon lacking parallelism. The figure on the left-hand side shows the lack of parallelism and the right-hand figure represents its characteristic distribution function as a function of phase. Notation is as in Figure 3.5 [Figure from *Vaughan*, 1989].

When using an étalon to observe the wavelength spectrum of a distant radiation source, the étalon's instrument function will have a similar effect on the source's wavelength distribution as a plate defect has on the instrument function; *i.e.*, the source's

true wavelength spectrum $S(\lambda - \lambda')d\lambda$ is modulated by the instrument function $I(\lambda')$ [or $I(\delta')$, $I(m')$] into the observed source spectrum $E(\lambda)$, where $d\lambda$ is the wavelength spread. $E(\lambda)$ is given by the convolution of $I(\lambda')$ and $S(\lambda - \lambda')d\lambda$

$$E(\lambda) = \int_{-\infty}^{\infty} S(\lambda - \lambda')I(\lambda')d\lambda'. \tag{D.25}$$

In addition, the effect of the finite plate size will be to further modulate the the observed spectrum from true source spectrum [*Wilksch*, 1985] and must be included in the convolution integral as well,

$$E(\lambda) = \int_{-\infty}^{\infty} S(\lambda - \lambda')I(\lambda')F(\lambda')d\lambda', \tag{D.26}$$

where $F(\lambda')$ is the plates' applicable distribution function. The method employed for determining the instrument function of the étalon at Inuvik, NT, Canada does not depend on any of the techniques discussed here and instead utilizes a clever software approach in conjunction with exposures of the étalon to a Helium-Neon laser source, which is further described in Chapter 2.

Appendix E Cross Correlation and Lomb-Scargle Spectral Analysis of Unevenly-Sampled Time Series

E.1 The Lomb-Scargle Normalized Periodogram

Because the Inuvik FPS time series of vertical wind measurements are an unevenly sampled data set, standard Fast Fourier Transform methods for determining the power spectrum of the time series are not applicable. The Inuvik FPS sky observations are made approximately every 4 min, but breaks in the sky observations occur approximately every 20 min so that a laser observation can be performed (for characterization of the étalon) and every 3.6 hr so that FP image data can be transferred to the storage unit (laptop). However, spectral analysis of unevenly sampled data can be performed using the Lomb-Scargle normalized periodogram [*e.g. Press et al.*, 1992]. Spectral power $P_N(\omega)$ as a function of angular frequency $\omega = 2\pi f$ is given by

$$P_N(\omega) = \frac{1}{2\sigma^2}\left\{\frac{[\sum_j (h_j - \bar{h})\cos\omega(t_j - \tau)]^2}{\sum_j \cos^2\omega(t_j - \tau)} + \frac{[\sum_j (h_j - \bar{h})\sin\omega(t_j - \tau)]^2}{\sum_j \sin^2\omega(t_j - \tau)}\right\}, \quad \text{(E.1)}$$

where h_j are the wind measurements at times t_j, $\bar{h}$ is the mean value of the time series given by

$$\bar{h} = \frac{1}{N}\sum_j h_j, \quad \text{(E.2)}$$

σ^2 is the variance in the time series, given by

$$\sigma^2 = \frac{1}{N-1}\sum_j (h_j - \bar{h}), \quad \text{(E.3)}$$

N is the total number of measurements, and $j = 1, 2, \ldots, N$. The offset value τ is given by

$$\tan(2\omega\tau) = \frac{\sum_j \sin(2\omega t_j)}{\sum_j \cos(2\omega t_j)}, \quad \text{(E.4)}$$

which leaves $P_N(\omega)$ independent of any shifting in the times t_j by some constant [*Press et al.*, 1992]. The offset value τ makes Equation E.1 identical to the equation that is obtained if the harmonic content of a data set at frequency ω is estimated by linear least-

squares fitting to the model $h(t) = A\cos(\omega t) + B\sin(\omega t)$ [*Press et al.*, 1992]. Thus, Equation E.1 weights the data on a 'per point' basis rather than a 'per time interval' basis [*Press et al.*, 1992].

In trying to determine if a given time series exhibits a periodic signal, a quantitative means must be utilized to determine if the maximum peak in the spectrum $P_N(\omega)$ is significant. In asking if the maximum peak is significant, the null hypothesis is that the time series of data values are independent Gaussian random values [*Press et al.*, 1992]. For the case of the maximum peak in a Lomb-Scargle periodogram, the null hypothesis can be tested rigorously. If the null hypothesis is true, then $P_N(\omega)$ has an exponential probability distribution of unit mean; *i.e.*, the probability that $P_N(\omega)$ is between some z and $z + dz$ is $\exp(-z)dz$ [*Press et al.*, 1992]. If some M independent frequencies are scanned for in the time series, then the probability that none of the frequencies give values larger than z is $(1 - e^{-z})^M$. Therefore,

$$P(>z) = 1 - (1 - e^{-z})^M \tag{E.5}$$

is the probability that the null hypothesis is false [*Press et al.*, 1992]. $P(>z)$ is referred to as the significance level of the maximum peak in $P_N(\omega)$, and a small $P(>z)$ indicates a highly significant periodic signal. In general, if $P(>z) < 0.05$, then the periodicity associated with the maximum peak in $P_N(\omega)$ is considered highly significant. Generally, the number of independent frequencies M depends on the number of frequencies sampled, the number of data points N, and their spacing [*Press et al.*, 1992], but in the cases of when the data points are approximately equally spaced or when the sampled frequencies fill (oversample) the frequency range from 0 to the Nyquist frequency, M is about equal to N [*Press et al.*, 1992].

Two examples are shown here of $P_N(\omega)$. Figure E.1 shows the Lomb-Scargle periodogram of the Inuvik FPS vertical wind time series from the night of January 26, 2001. Figure E.1 reveals that this vertical wind time series exhibits a strong periodicity at 3.2 hr. When evaluating a Lomb-Scargle spectrogram, only the maximum peak in the power spectrum can be considered in regards to determining whether the time series exhibits significant periodicity at the frequency of the maximum.

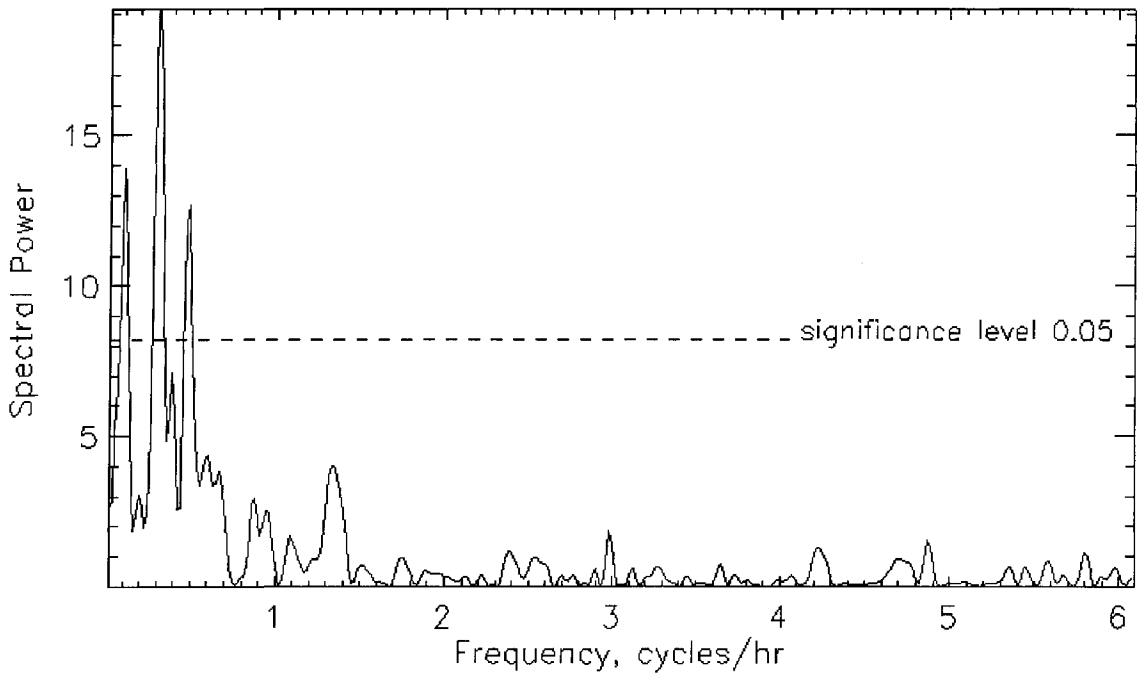

Figure E.1. Lomb-Scargle periodogram of the Inuvik FPS time series of vertical wind measurements on Jan 26, 2001. When evaluating a Lomb-Scargle spectrogram, only the maximum peak in the power spectrum can be considered in regards to evaluating the significance of the periodicity identified in the original time series. The maximum normalized power of 19.1 occurs at a frequency of 0.31 hr^{-1} with a significance of 0.00004. The corresponding period is 3.2 hr. See the text for more discussion.

Generally, when a strong periodicity is identified in a time series of thermospheric vertical wind measurements, the periodicity can be attributed to gravity wave oscillations in the thermosphere, if the periodicity is greater than the Brunt-Väisälä period. Appendix B discusses gravity wave properties in more detail, and the January 26, 2001 vertical winds and column shifts over Inuvik are discussed in Chapter 4. If the periodicity of the vertical wind time series is due to gravity wave oscillations, then an estimate of the wave's amplitude can be determined from the normalized power of the maximum peak in $P_M(\omega)$. That was done here as well, which determined that the wave amplitude associated with the maximum peak in Figure E.1 is ~30 $m \cdot s^{-1}$. A sinusoid with this amplitude is superimposed on the January 26, 2001 vertical wind time series shown in Figure E.2. The phase between the sinusoid and the vertical wind time series must be determined since

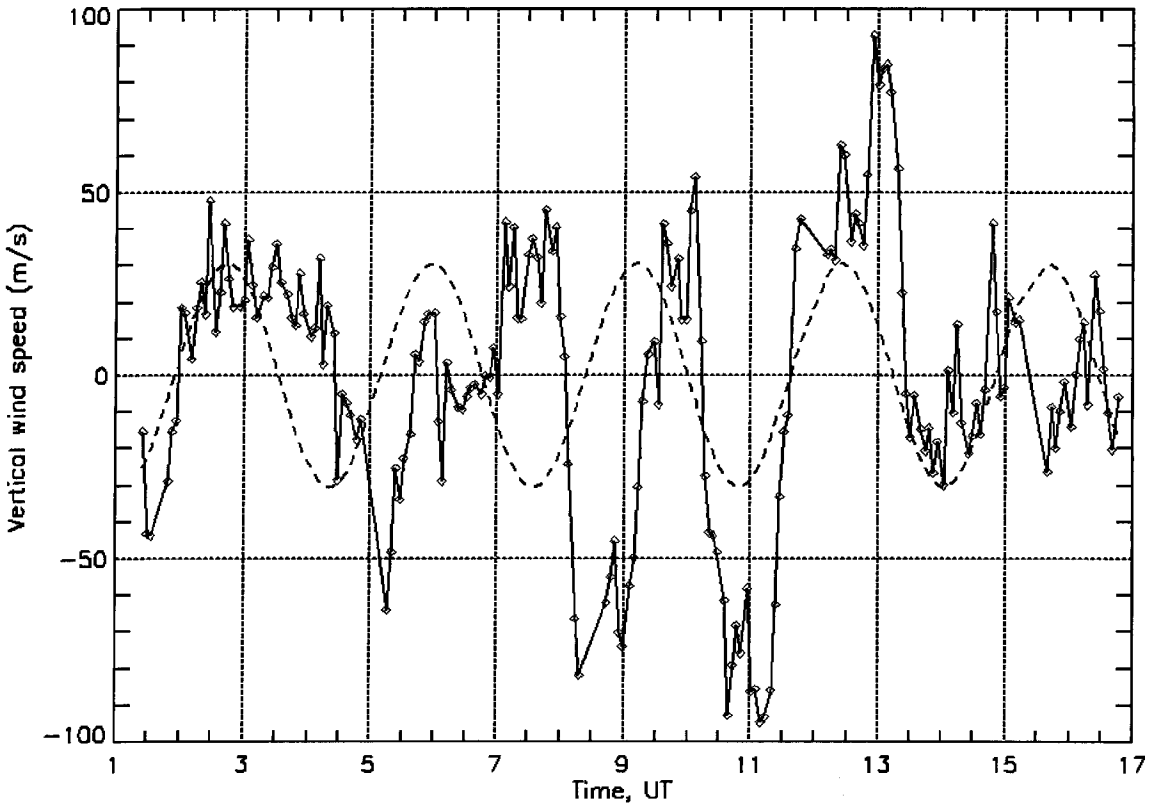

Figure E.2. Sinusoidal wave superimposed on the Jan 26, 2001 vertical wind time series. The wave's amplitude is ~30 $m \cdot s^{-1}$. See the text for more discussion.

the Lomb-Scargle method loses this information. The phase between the sinusoid and the original time series was determined by subtracting the value of the sinusoid at each data point from the vertical wind measurements for an array of lags. The lag which yielded the minimum variance to the corrected wind data determined the phase.

Recall from Chapter 4 that this night's column shift time series over Inuvik also exhibited strong periodicity. The Lomb-Scargle periodogram for the column shift time series is shown in Figure E.3. The column shift time series showed a strong periodicity at 3.4 hr, and the superimposed sinusoid is shown in Figure E.4. The sinusoidal wave has an amplitude of ~30 km. Recall from Chapter 4 the discussion on this data set. The vertical wind and column shift time series are highly correlated (see the next section), which is attributed to equivalent gravity wave activity identified in both time series.

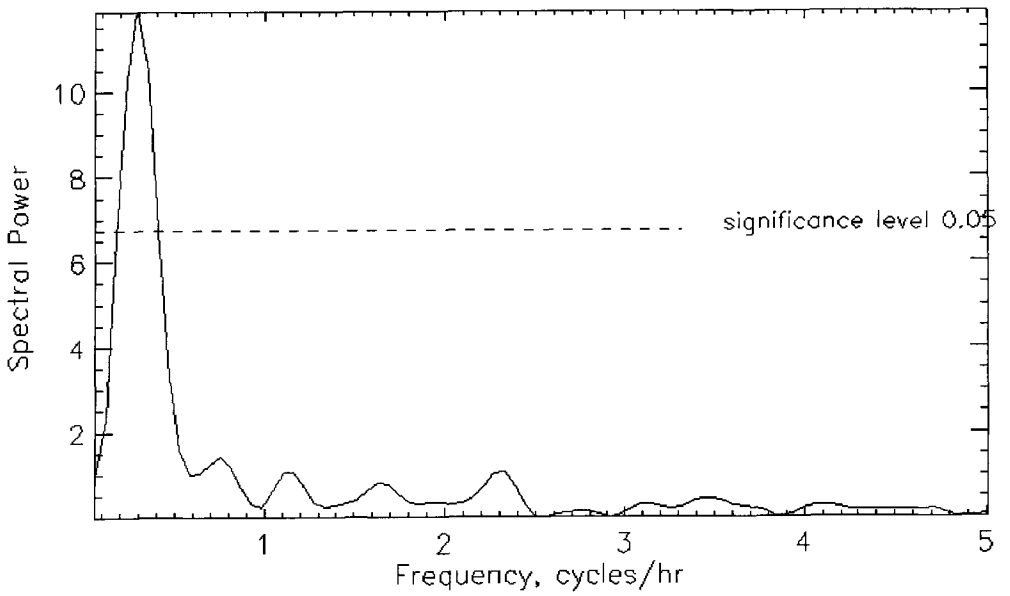

Figure E.3. Lomb-Scargle periodogram of the time series of column shifts over Inuvik on Jan 26, 2001. The maximum normalized power of 11.9 occurs at a frequency of 0.29 hr^{-1} with a significance of 0.0003. The corresponding period is 3.4 hr.

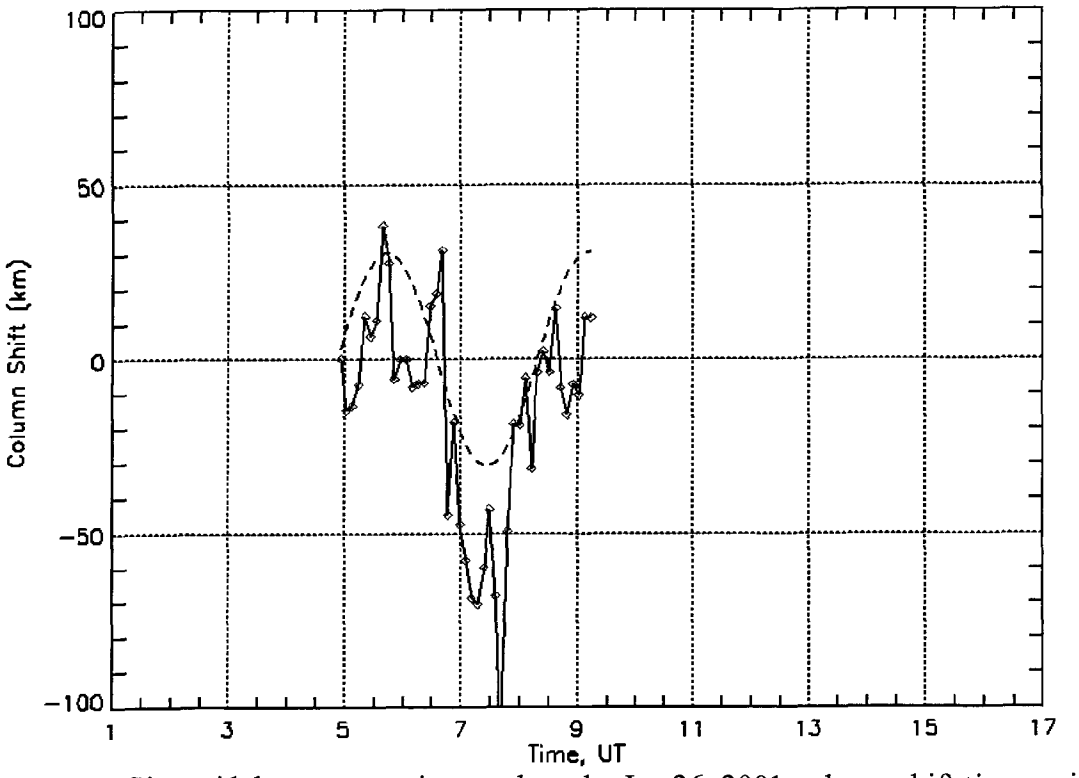

Figure E.4. Sinusoidal wave superimposed on the Jan 26, 2001 column shift time series. The wave's amplitude is ~30 km.

E.2 Cross Correlation Analysis of Two Time Series

As was shown in Section 1 of Chapter 4, a cross correlation calculation was performed between each of the time series of vertical winds and column shifts. Given two N-element sample data sets X and Y, calculation of the correlation coefficient quantifies the degree of fit to a linear model of the data sets. The correlation coefficient r is given by [*e.g. Press et al.*, 1992]

$$r = \frac{\frac{1}{N-1}\sum_{j=0}^{N-1}\left[x_j - \left(\sum_{k=0}^{N-1}\frac{x_k}{N}\right)\right]\left[y_j - \left(\sum_{k=0}^{N-1}\frac{y_k}{N}\right)\right]}{\left\{\frac{1}{N-1}\sum_{j=0}^{N-1}\left[x_j - \left(\sum_{k=0}^{N-1}\frac{x_k}{N}\right)\right]^2\right\}^{1/2}\left\{\frac{1}{N-1}\sum_{j=0}^{N-1}\left[y_j - \left(\sum_{k=0}^{N-1}\frac{y_k}{N}\right)\right]^2\right\}^{1/2}}, \tag{E.6}$$

where x_j and y_j are the elements of X and Y, respectively, and j = 1, 2, ..., N. The correlation coefficient is a direct measure of how well two sample populations vary together, and a value of r = +1 or r = –1 indicates a perfect fit to a positive or negative linear model, respectively. A value of r close to +1 or -1 indicates a high degree of correlation and a good fit to a linear model, while a value of r close to 0 indicates a poor linear model fit [*Press et al.*, 1992].

The cross correlation calculation of two sample N-element sample populations X and Y computes the correlation coefficient $r_{xy}(L)$ as a function of the lag L between the two data sets, which is given by

$$r_{xy}(L) = \frac{\sum_{j=0}^{N-L-1}(x_{j+L}-\bar{x})(y_j-\bar{y})}{\left\{\left[\sum_{j=0}^{N-1}(x_j-\bar{x})^2\right]\left[\sum_{j=0}^{N-1}(y_j-\bar{y})^2\right]\right\}^{1/2}} \quad \text{for } L<0$$

$$r_{xy}(L) = \frac{\sum_{j=0}^{N-L-1}(x_j-\bar{x})(y_{j+L}-\bar{y})}{\left\{\left[\sum_{j=0}^{N-1}(x_j-\bar{x})^2\right]\left[\sum_{j=0}^{N-1}(y_j-\bar{y})^2\right]\right\}^{1/2}} \quad \text{for } L\geq 0 \tag{E.7}$$

where L = $-N$ + 2, $-N$ + 3, ..., –2, –1, 0, 1, 2, ..., N – 3, N – 2 is the lag between the elements of X and Y.

Cross correlation calculations were performed between the seven Inuvik FPS time series of upper-thermospheric vertical winds and column shifts. The CRL-FPS upper- and lower-thermospheric vertical winds were both cross correlated with the time series of column shifts over Poker Flat. Because the column shift temporal resolution was ~6 min, ~4 min for the Inuvik vertical winds and ~2 min for the CRL-FPS vertical winds, wind values were interpolated to the times of the column shifts before the cross correlation was computed. For the cases where column shift data was missing within the range of the column shift time series, a column shift value was interpolated for a particular time. This was the case, for example, in the December 9 and 22, 2000 vertical wind and column shift time series comparisons (see Chapter 4). If too much column shift data was missing, the column shift time series were split into sections, as was the case for the January 3, 2001 and February 28, 2000 time series comparisons.

The only time series comparison to exhibit a high degree of correlation at a realistic time lag is from January 26, 2001. The cross correlation calculation is shown in Figure E.5.

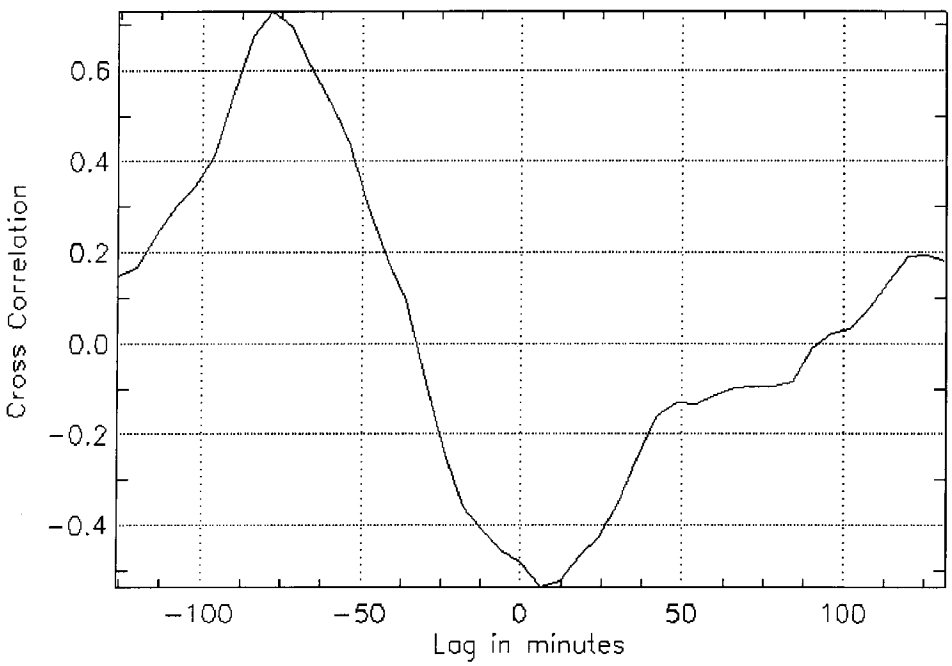

Figure E.5. Cross correlation calculation between the time series of vertical wind measurements and column shift values on Jan 26, 2001. The maximum correlation coefficient of 0.73 occurs at a time lag of −78 min. See the text for more discussion.

The Inuvik FPS vertical wind measurements and column shift values prevailing over Inuvik were shown in Chapter 4 and above in Figure E.2 and E.4. The cross correlation calculation computed a maximum correlation coefficient of 0.73 which occurred at a time lag –78 min. This time lag indicates that the variation in the column shift values leads the variation in the vertical wind estimates. Other cross correlation calculations are shown in Chapter 4. The January 26, 2001 column shift time series did not have any missing data and the integer lag L was converted into a time-lag array using the temporal resolution value of the column shift measurements. These two time series, in showing a high degree of correlation at the particular time lag of –78 min, also exhibited significant periodicities of ~3 hr, as was revealed by the Lomb-Scargle periodogram calculations shown in the previous section. The geophysical significance of the high correlation and similar periodicities was discussed in Chapter 4.